Modeling of reactor antineutrino spectra

Lorenzo Périssé

To cite this version:

Lorenzo Périssé. Modeling of reactor antineutrino spectra. Nuclear Experiment [nucl-ex]. Université Paris-Saclay, 2021. English. NNT : 2021UPASP069 . tel-03538198

HAL Id: tel-03538198
https://theses.hal.science/tel-03538198

Submitted on 20 Jan 2022

Modeling of reactor antineutrino spectra

Modélisation de spectres antineutrino de réacteur

Thèse de doctorat de l'Université Paris-Saclay

École doctorale n° 576, particules hadrons énergie et noyau : instrumentation, image, cosmos et simulation (PHENIICS)

Spécialité de doctorat: Physique des particules

Unité de recherche: Université Paris-Saclay, CEA, Département de Physique des Particules, 91191, Gif-sur-Yvette, France

Référent: Faculté des sciences d'Orsay

Thèse présentée et soutenue à Paris-Saclay,
le 20 septembre 2021, par

Lorenzo PÉRISSÉ

Composition du jury

Alessandra Tonazzo Professeure des universités, Université Paris-Diderot	Présidente
José Busto Professeur des universités, Aix-Marseille Université	Rapporteur & Examinateur
Patrick Huber Professeur, Virginia Tech	Rapporteur & Examinateur
Jaime Dawson Chargée de recherche, CNRS - APC	Examinatrice
Laurent Simard Maître de conférence, Université Paris-Saclay	Examinateur

Direction de la thèse

Xavier Mougeot Ingénieur-chercheur (HDR), CEA Paris-Saclay, Université Paris-Saclay	Directeur de thèse
Matthieu Vivier Ingénieur-chercheur, CEA Paris-Saclay	Co-encadrant de thèse
Anthony Onillon Docteur, CEA Paris-Saclay	Co-encadrant de thèse

Thèse de doctorat

NNT: 2021UPASP069

DE LA RECHERCHE À L'INDUSTRIE

cea

Irfu
Institut de recherche
sur les lois fondamentales
de l'Univers

Laboratoire National
LNHB
Henri Becquerel

Cette thèse est dédiée à Amélie.

Remerciements

En préambule de ce manuscrit, je souhaiterais remercier celles et ceux qui m'ont aidé à atteindre cet objectif que représente la thèse de doctorat. Pendant ces trois années, j'ai été formé à devenir un chercheur, et ce n'est pas sans mal et sans embuche que j'ai pu accomplir ce projet.

C'est tout d'abord grâce aux efforts combinés de Matthieu Vivier et Xavier Mougeot, mes deux directeurs de thèse à l'Irfu et au LNHB, qui m'ont donné l'opportunité de travailler sur les neutrinos de réacteur nucléaire. À ce duo s'ajoute Anthony Onillon, postdoctorant à l'Irfu et au SERMA qui m'a accompagné durant l'ensemble de ma thèse et m'a formé sur de nombreux sujets. Pour leur enseignement et leur aide qui m'ont permis de m'améliorer dans mon travail, je les remercie tous les trois.

Je tiens aussi à remercier les autres chercheurs de l'Irfu qui m'ont offert leur aide et leur soutient tout au long de ma thèse, en particulier Guillaume Mention et Thierry Lasserre, mais aussi Alain Letourneau et David Lhuillier pour leur aide lors du développement du code BESTIOLE. Je remercie aussi tous les stagiaires et thésards de l'Irfu pour nos moments de convivialité lors de nos déjeuners hebdomadaires du vendredi, avec une mention spéciale à Paul Kot, Joe Jonhson et Alex Wex qui ont partagé mon quotidien dans le groupe des neutrinos de basse énergie. Ces remerciements sont aussi adressés à tout le personnel de l'Irfu qui a fourni assistance et soutient à tous les chercheurs pendant ces années. À tous les membres de mon jury, Alessandra Tonazzo, José Busto, Patrick Huber, Jaime Dawson et Laurent Simard, qui ont accepté de relire mon manuscrit et m'ont apporté avis et conseils afin de l'améliorer, j'adresse mes plus sincères remerciements.

Enfin, merci à mes amis et à ma famille, à eux qui ont su m'épauler. Une pensée toute particulière va à Amélie, qui m'accompagne depuis tant d'années et pour davantage encore, qui m'a totalement soutenu durant la rédaction de mon manuscrit. Je souhaiterais adresser un dernier mot de remerciement à mon professeur de Physique-Chimie de Terminale, René Chavignon, qui m'a transmis son plaisir des sciences et sans qui je ne me serais peut-être pas tourné vers la Physique.

Contents

Appendices

List of Figures

List of Tables

List of Symbols and Abbreviations

$\boldsymbol{v}$	Bold scripts refer to a vector quantity, except if mentionned otherwise.
$\boldsymbol{v}\boldsymbol{w}$	Scalar product between two vectors $\boldsymbol{v}$ and $\boldsymbol{w}$. Also written $\boldsymbol{v}\cdot\boldsymbol{w}$.
$\mathbb{1}$	Identity operator. The identity matrix of dimension n may be written $\mathbb{1}_n$.
δ_{ij}	Kronecker delta, equal to 1 if $i=j$ and 0 otherwise.
$\epsilon_{i_1\ldots i_n}$	Levi-Civita symbol, verifying $\epsilon_{\ldots i_p \ldots i_q \ldots} = -\epsilon_{\ldots i_q \ldots i_p \ldots}$.
$\eta_{\mu\nu}$	Minkowsky metric, related to a space-time interval of $\mathrm{d}s^2 = -\,\mathrm{d}t^2 + \,\mathrm{d}\mathbf{r}^2$.
$\sigma_{i=1,2,3}$	Pauli matrices, verifying $[\sigma_i, \sigma_j] = 2i\epsilon_{ijk}\sigma_k$. They are given by $\sigma_1 = \begin{pmatrix} 0 & 1 \\ 1 & 0 \end{pmatrix}$, $\sigma_2 = \begin{pmatrix} 0 & -i \\ i & 0 \end{pmatrix}$, and $\sigma_3 = \begin{pmatrix} 1 & 0 \\ 0 & -1 \end{pmatrix}$, to which is added $\sigma_0 = \mathbb{1}_2$.
$\gamma_{\mu=0,1,2,3}$	Dirac matrices, verifying $\{\gamma_\mu, \gamma_\nu\} = 2\eta_{\mu\nu}$. In the Dirac basis they are given by $\gamma_0 = \begin{pmatrix} \mathbb{1}_2 & 0 \\ 0 & -\mathbb{1}_2 \end{pmatrix}$, $\gamma_1 = \begin{pmatrix} 0 & \sigma_1 \\ -\sigma_1 & 0 \end{pmatrix}$, $\gamma_2 = \begin{pmatrix} 0 & \sigma_2 \\ -\sigma_2 & 0 \end{pmatrix}$, $\gamma_3 = \begin{pmatrix} 0 & \sigma_3 \\ -\sigma_3 & 0 \end{pmatrix}$, to which is added $\gamma_5 \equiv i\gamma_0\gamma_1\gamma_2\gamma_3 = \begin{pmatrix} 0 & \mathbb{1}_2 \\ \mathbb{1}_2 & 0 \end{pmatrix}$.
BR	Branching ratio.
CC	Charged current.
CEνNS	Coherent elastic neutrino-nucleus scattering.
CL	Confidence level.
CFY	Cumulative fission yield.
DOF	Degrees of freedom.
EC	Electron capture.
EFY	Effective fission yield.
FF	Fission fragment.
FD	Forbiddenness degree.
FP	Fission product.
FY	Fission yield.
GA	Gallium anomaly.
HPGe	High-purity germanium detector.
HM	Huber-Mueller.

IBD	Inverse β-decay.
IFY	Independent fission yield.
LS	Liquid scintillator.
MC	Monte-Carlo.
NC	Neutral current.
NEES	Neutrino-electron elastic scattering.
PS	Plastic scintillator.
PWR	Pressurized water reactor.
RAA	Reactor antineutrino anomaly.
SM	Summation model.
TAGS	Total Absorption γ-ray Spectroscopy.
WM	Weak magnetism.

When the meaning of a symbol is not explicitly introduced in the chapters, it will always refer to one of the abbreviations above. In all the chapters, the equations will always be written in relativistic units where $c = \hbar = m_e = 1$, except if mentioned otherwise. All the figures have been made by my own means except if specified in the caption.

Introduction

The work of a physicist is dedicated to explain the grand scheme of Nature by studying the mechanisms at work behind experiments. Nature's complexity has always surpassed scientists' expectations, and its minute study has regularly led to discoveries that have completely modified our understanding of Physics. The birth of the neutrino has been the forerunner of such discoveries. The existence of the neutrino was predicted by Wolfgang Pauli in 1930, in order to explain the observation of continuous spectra in β-decays [1]. The neutrino was described as an electrically neutral particle with spin $1/2$ and positive mass, and was soon incorporated into the first theory of β-decays developed by Enrico Fermi in 1934 [2]. The Fermi theory drew the path of two decades of theoretical works and experiments, and the neutrino existence was finally confirmed in 1953. This prowess was performed by Frederick Reines and Clyde Cowan, who detected antineutrinos emitted from the Savannah River nuclear reactor using a scintillation detection technique based on the inverse β-decay (IBD) process [3]. The zoology of neutrinos was then completed by two other flavors of neutrino: the muon neutrino, observed in 1962 at the Brookhaven Alternating Gradient Synchrotoron [4], and the tau neutrino, discovered in 2000 by the Direct Observation of the NeUtrino Tau experiment [45]. But neutrinos had still not revealed all their mysteries.

In 1968, only one third of the predicted flux of neutrino emitted from the Sun was measured at the Homestake experiment [6]. This solar neutrino deficit was confirmed by the Soviet-American Gallium Experiment [7], the Gallium Experiment [8] and the Gallium Neutrino Observatory [8] in the 1990s. The solar neutrino problem was followed by the atmospheric neutrino problem, in which only half of the predicted neutrinos arising from cosmic ray collisions in the upper atmosphere were observed by underground water Cherenkov detectors such as IMB [9], Kamiokande [10] and Super-Kamiokande [11]. A possible origin of the solar and atmospheric neutrino deficits was described by the theory of neutrino flavor oscillations, postulated in 1962 by Ziro Maki, Masami Nakagawa and Shoichi Sakata after the detection of the muon neutrino, and based on the neutrino-antineutrino oscillation proposed by Bruno Pontecorvo the same year. The atmospheric and solar neutrino deficits were confirmed to originate from neutrino oscillations with conclusive measurements from Super-Kamiokande [11] and the Sudbury Neutrino Observatory [12], respectively in 1998 and 2001. This became an important observation as the neutrino oscillations highlighted with certainty the non-zero mass of neutrinos.

Most of the experiments observing neutrino oscillation can be interpreted in an oscillation framework consisting in three massive neutrino states. These massive neutrino states are related to the flavor neutrino states through the complex 3×3 Pontecorvo-Maki-Nakagawa-Sakata (PMNS) matrix. The oscillation phenomenon then originates from the fact that the neutrino mass eigenstates do not coincide with the flavor eigenstates. Based on a phenomenology deduced from experiments, the PMNS matrix can be parametrized by three mixing angles and a phase inducing the violation of the $\mathcal{CP}$ symmetry in neutrino oscillations. The oscillation probabilities also depend on the differences between the squared mass of the massive eigenstates. Two of the mixing angles have been measured in solar and atmospheric neutrino experiments. The third mixing angle has been measured by observing the neutrino and antineutrino fluxes emitted from accelerators as well as from nuclear reactors.

Regarding nuclear reactors, a reevaluation of the predictions of the reactor antineutrino spectrum in 2011 [13, 14] has led to a systematic deficit of measured antineutrinos in twenty reactor experiments, significant at the level of 2.8σ and called the reactor antineutrino anomaly (RAA) [15]. The RAA cannot be explained by the three known mixing angles, and is not the only discrepancy between experiments and predictions in that case. For instance, the measured and theoretical neutrino capture rates on gallium observed in the Gallium Experiment and in the Soviet-American Gallium Experiment differ significantly from one another even after including the three-flavor oscillation effects, and constitutes the gallium anomaly [16]. The LSND and MiniBooNE anomaly refers to the inconsistent results of the eponymous experiments with respect to predictions including the solar and atmospheric oscillation parameters [17, 18]. All these anomalies can be explained in the framework of neutrino oscillation if additional sterile neutrinos are considered. These sterile neutrinos could mix with the other neutrino mass states but could not interact with the flavor states. Would sterile neutrinos exist, that would be a clear evidence for physics beyond the Standard Model. However, the sterile neutrino interpretation of the RAA has been mostly excluded by recent very short baseline reactor experiments, and no evidence for an experimental bias has been detected in any reactor experiment. Furthermore, IBD antineutrino experiments conducted at short and long baselines from nuclear reactors have revealed two other significant differences on the rate and on the shape of the measured spectra compared to state-of-the-art predictions. The validity of the predictions is then questioned as the source of the discrepancies observed in reactor experiments. This last lead has motivated a revision of reactor antineutrino spectrum modelings.

In this context, a revisited prediction of reactor antineutrino spectra using the summation method has been developed and is presented in this work. The first chapter comes back on the experimental discoveries related to the neutrino, introducing its properties in parallel. The different experimental anomalies revealed in the last decades are also presented, as well as their role in the development of the sterile neutrino hypothesis. The second chapter is dedicated to the different types of nuclear reactor as sources of antineutrinos. The fission chain reaction and the resulting fission and activation products, the two sources of antineutrino emission in reactors, are described. The different modelings used to predict reactor antineutrino spectra are introduced, along the experimental anomalies observed in IBD reactor experiments. The $V - A$ theory of β-decay used to model each β-decay contributing to a reactor antineutrino spectrum is detailed in the third chapter. The impact of each correction is discussed at the level of a single transition, with an emphasis on the differences with former modelings. Evaluated nuclear data and their inclusion in the revisited prediction is the topic of the fourth chapter. A thorough description of uncertainties associated to both the modeling and the nuclear data is also presented. The comparison of the improved summation modeling with other state-of-the-art predictions, as well as some IBD datasets collected by recent short and long baseline reactor experiments, is finally addressed in the last chapter.

1

Physics of the neutrino

Contents

The goal of this first chapter is twofold: to give a short overview of the Standard Model of particle physics and to introduce the neutrino properties. A review of the experiments that show evidence of the neutrino existence and its properties are presented. Open questions about the properties and nature of neutrinos are also briefly addressed, and an overview of experiments investigating these questions is presented.

From here onwards, and for all chapters, neutrinos and antineutrinos of any flavor may be referred to as *neutrinos* if the context is clear enough to identify the particle.

1.1 The Standard Model of particle physics

The Standard Model is a theory describing elementary particles and how they interact together. Elementary particles composing the Standard Model are sorted based on their spin, as pictured in Fig. 1.1. They are called bosons if their spin is an integer, for they obey the Bose-Einstein statistics. They are named fermions if their spin is half an integer, and they follow the Fermi-Dirac statistics. The relation between the spin and the particle statistics was brought forth by Markus Fierz and Wolfgang Pauli in 1939 [19, 20].

1.1.1 Fermions

Fermions are distributed into three generations, or families. A generation is composed of two quarks and two leptons, plus the associated antiparticles (antiquarks and antileptons) which have the same mass and spin but opposite quantum number (*e.g.* electric charge, color charge). The first generation is made of the up (u) and down (d) quarks, the electron (e^-) and its neutrino (ν_e). In the second generation are found the charm (c) and strange (s) quarks, the muon (μ) and its neutrino (ν_μ). The top (t) and bottom (b) quarks, the tau (τ) and its neutrino (ν_τ) constitute the last generation of fermions. It was showed in 1989 at the Large Electron-Positron collider (LEP) that the number of active families is only three, except if hypothetical generations have neutrinos with masses of the order of $m_Z/2$ or higher [21]. The different types of quarks and neutrinos are referred to as *flavors*. Fermion masses become larger going from the first generation to the third, except eventually for neutrinos for which the mass ordering is not known yet. Apart from that, fermions of different families behave the same way, with identical electromagnetic and weak couplings.

1.1.2 Bosons

There are currently five identified types of bosons entering the composition of the Standard Model. Four of them are called *gauge bosons* and convey the fundamental interactions between particles:

- electromagnetic interaction acts between electrically charged particle through the exchange of a photon (γ);
- weak interaction acts between fermions through the exchange of three different bosons: W^+ and W^- are exchanged in *charged currents* (CC), and Z^0 is emitted in *neutral currents* (NC);
- strong interaction acts between particles having a color charge (green, blue and red) through the exchange of eight different gluons (g). The particles having a color charge are the quarks and the gluons themselves. The strong interaction increases when two colored particles are pulled away. This is the reason why quarks are confined into hadrons or mesons, which color must be neutral.

Gravitation, the last fundamental interaction, is not described by the Standard Model. The hypothesized associated boson is the graviton — which has a zero mass, zero electric charge, and a spin 2 — but it has never been observed. The fifth boson is the Brout-Englert-Higgs boson, or simply called the Higgs boson (H). In the Standard Model, the mass of particles results from their interaction with the Higgs boson, except for neutrinos which may acquire their mass differently.

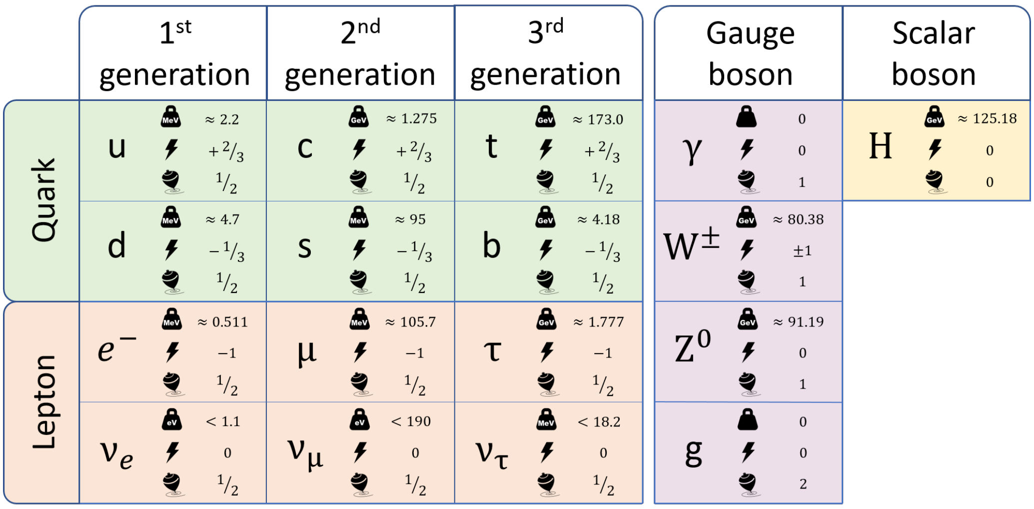

	1st generation	2nd generation	3rd generation	Gauge boson	Scalar boson
Quark	u MeV ≈ 2.2 $+^{2}/_{3}$ $^{1}/_{2}$	c GeV ≈ 1.275 $+^{2}/_{3}$ $^{1}/_{2}$	t GeV ≈ 173.0 $+^{2}/_{3}$ $^{1}/_{2}$	γ 0 0 1	H GeV ≈ 125.18 0 0
	d MeV ≈ 4.7 $-^{1}/_{3}$ $^{1}/_{2}$	s MeV ≈ 95 $-^{1}/_{3}$ $^{1}/_{2}$	b GeV ≈ 4.18 $-^{1}/_{3}$ $^{1}/_{2}$	$W^{\pm}$ GeV ≈ 80.38 ±1 1	
Lepton	e^- MeV ≈ 0.511 −1 $^{1}/_{2}$	μ MeV ≈ 105.7 −1 $^{1}/_{2}$	τ GeV ≈ 1.777 −1 $^{1}/_{2}$	Z^0 GeV ≈ 91.19 0 1	
	ν_e eV < 1.1 0 $^{1}/_{2}$	ν_μ eV < 190 0 $^{1}/_{2}$	ν_τ MeV < 18.2 0 $^{1}/_{2}$	g 0 0 2	

Figure 1.1: The three families of fermions (left chart) and the different bosons (right chart) of the Standard Model, with their mass, electric charge and spin. To each fermion is associated an antiparticle with opposite quantum numbers. Mass values (or limits) of bosons, quarks, ν_μ and ν_τ are taken from [22], and the ν_e mass limit is taken from [23].

1.1.3 Electroweak model and symmetry breaking

Symmetries of a system refer to the set of transformations leaving it invariant. These transformations can be described in the framework of group theory, which has proven to be a powerful mathematical tool to build physics theories. The Standard Model relies on group theory to describe fields and their symmetries, particles being excited states of these fields. The Lagrangian equations of a system of fields must be invariant under the associated symmetry groups. For instance, the Poincaré group, which represents relativistic invariance, includes space-time translations, space rotations, and special Lorentz transformations *e.g.* boosts. The other symmetries of the Standard Model, called gauge symmetries, are $SU(3)_C \otimes SU(2)_L \otimes U(1)_Y$. $SU(3)_C$ is the color symmetry group for quarks and gluons and describes the strong interaction. $SU(2)_L \otimes U(1)_Y$ describes the electroweak interaction which unifies the weak interaction and electromagnetism. $SU(2)_L$ and $U(1)_Y$ are respectively the isospin and hypercharge groups. Weak interaction and electromagnetism are then understood as being two expressions of the same force. Below the electroweak scale, given by the $W^{\pm}$ and Z^0 masses, the electroweak force spontaneously breaks into weak interaction and electromagnetism, and the two interactions can be treated separately. Electromagnetism is very well described by Quantum Electrodynamics (QED), based on the group $U(1)_Q$. To date, there is no clear deviation from experiments. On the other hand, weak interaction is partly described by the Fermi theory and the $V - A$ theory. However, these theories have some inherent limitations. For instance, they are not renormalizable (*i.e.* divergent quantities appearing in these theories cannot be regularized), contrary to QED. This led to the development of the electroweak model, which has successfully reconnected observations with theory.

Spontaneous symmetry breaking mentioned earlier is of utmost importance in the Standard model. Indeed, mass terms are not gauge invariant and thus cannot be introduced into the Lagrangian. Hence, all fields should be massless in the Standard Model, which is in contradiction with the experimental fact that some particles do have a mass. The Higgs mechanism was then suggested to give mass to particles while respecting the gauge invariance [24–26]. In this mechanism, a new scalar field is introduced with the following properties: it couples to fermion and boson fields, it respects the gauge symmetries of the Standard Model, and it self-interacts with a quadratic potential. At low energy, this quadratic potential has an infinite number of degenerated states with minimal energy. By choosing a specific ground state, called the *vacuum expectation value* or *vev*, the symmetry is said to be spontaneously broken. The *vev* does not respect the initial symmetry $SU(2)_L \otimes U(1)_Y$ anymore, but is invariant under $U(1)_Q$. The scalar field can then be parameterized around this ground state by introducing the Higgs field H. When the parametrization with the Higgs field is put back into the Lagrangian, the five bosons H, $W^{\pm}$, Z^0 and γ appear along with suitable mass terms for all fields. Coupling the Higgs field to fermion also returns fermion mass terms, although it is a more complicated matter for neutrinos as it will be seen in Sec. 1.4.1.

The Standard Model is one of the completions of modern physics. Highly predictive, its many successes are not shadowed by any significant deviation from experiments. In 2012, the observation of the Higgs boson by two experiments, A Toroidal LHC ApparatuS (ATLAS) and the Compact Muon Solenoid (CMS), has secured the correctness of the Standard Model [27, 28]. However, the theory is incomplete. For instance, there are 18 free parameters that must be measured (3 coupling constants, 2 Higgs parameters, 9 fermion masses, 4 parameters for the Cabibbo-Kobayashi-Maskawa matrix describing quark mixing). Their value cannot be explained in the Standard Model and suggest that they find an origin in a more fundamental theory. The Standard Model is also not able to account for gravity, and is not valid at very high energy where the strong, weak and electromagnetic interactions become of the same magnitude. Dark matter and dark energy, described by the $\Lambda - CMD$ model, do not fit in the Standard Model. Finally, neutrinos are assumed to be massless in the Standard Model but have been measured to oscillate between flavors which is a proof of their non-zero mass. This phenomenon has motivated many experiments and offers a possible window to new physics beyond the Standard Model.

1.2 The neutrino through the XX$^{\text{th}}$ century

1.2.1 Birth of the neutrino

As the story goes, it all started with the discovery — somewhat accidental — of radioactivity by Henri Becquerel in 1896. While searching for phosphorescence, the emission of light by a material after it has been exposed to an external light, Becquerel stumbled upon the fact that uranium salt emitted its own radiation without being excited by light [29–31]. The different types of radiation, denominated as α, β and γ, were then later revealed by Ernest Rutherford [32] and Paul Villard [33]. During the early XX$^{\text{th}}$ century, β particles were identified as electrons and several experiments from Walter Kaufmann and Becquerel supported the idea of a continuous β spectrum. The physicist's community did not accept it until 1914, when James Chadwick performed a decisive measurement of the β spectra of ^{214}Pb and ^{214}Bi [34]. This continuous spectrum was a thorn in the side of physicists, as it questioned the conservation of energy. Instead of giving up on the energy conservation principle, an idea supported by Niels Bohr, Wolfgang Pauli came upon a solution in 1930, a "desperate way out"[1] as he called it in its famous letter to the Tübingen conference [1]. He suggested that β-decays were emitting another particle in addition to the electron. The neutrino, as it would be called a few years later, was predicted by Pauli to be electrically neutral, with spin $^1/_2$ and positive mass. It would carry away the missing energy and additional $^1/_2$ spin in β-decays, therefore saving energy conservation and solving the nucleus spin problem. In 1934, Enrico Fermi formulated its theory of β-decay [2] and incorporated the neutrino in the model. This theory became the first theory of weak interaction, and predicted the spectra of both electron and antineutrino in a three-body decay:

$$n \longrightarrow p + e^- + \bar{\nu}_e. \tag{1.1}$$

In 1934, Hans Bethe and Rudolf Peierls advanced that if a neutrino is created during a β-decay, surely the opposite annihilation process must exist [35]. They mention inverse β-decay (IBD) to be the most interesting process to study neutrinos:

$$\bar{\nu}_e + p \longrightarrow n + e^+. \tag{1.2}$$

Bethe and Peierls estimated the cross-section of IBD to be less than 10^{-44} cm^2 for a 2 MeV incoming neutrino. It corresponds to a penetrating power of about 10^{16} km in solid matter, and they concluded that the neutrino was very unlikely to be ever detected due to its very low probability of interaction. Fortunately enough, they were wrong. The antineutrino was clearly identified twenty years later by the Poltergeist Project led by Frederick Reines and Clyde Cowan. The experiment initially took place in 1953, using the Handford nuclear plant as an intense neutrino source. The result only hinted at the neutrino existence, the cosmic background being too important. The experiment was completely redesigned and relocated at the Savannah River nuclear plant in 1956, where the neutrino was unmistakably detected [3]. A 10-ton detector was built to detect IBD events through two correlated signals: a prompt signal coming from the positron annihilation, and a delayed signal from the neutron capture. The detector consisted in two tanks filled with $CdCl_2$-doped water, sandwiched between three layers of scintillator. The protons in the water would provide the IBD targets, and the cadmium from $CdCl_2$ would capture the moderated neutron. Each scintillator block had 110 photomultipliers tubes (PMT) connected inside in order to record the scintillation light emitted from the positron deceleration and annihilation and the neutron capture. They reported an average IBD cross-section in agreement within 5% with the predicted cross-section of $(6.3 \pm 1.6) \times 10^{-44}$ cm^2 [3].

1.2.2 Parity violation and neutrino helicity

Until 1956, the weak interaction was assumed to conserve parity as any other interaction. A fermion is mathematically described by a spinor ψ, solution of the Dirac equation. Spinors can be split into two chiral states, called left-handed and right-handed spinors, under the action of the chiral projection operators P_L and P_R. The left and right-handed spinors are then identified by their transformation under the Lorentz group:

$$P_L = \frac{1}{2}(\mathbb{1}_4 - \gamma_5), \qquad P_R = \frac{1}{2}(\mathbb{1}_4 + \gamma_5), \tag{1.3}$$

$$\psi_L = P_L\psi, \qquad \psi_R = P_R\psi. \tag{1.4}$$

---

[1] "einen verzweifelten Ausweg" in the original text.

For fermions, the parity transformation $\mathcal{P} : (t, x, y, z) \longmapsto (t, -x, -y, -z)$ switches together the two chiral states, $\mathcal{P} : \psi_{L,R} \longmapsto \psi_{R,L}$. The parity operator is γ_5 and its eigenvalues are ± 1. In 1956, Tsung-Dao Lee and Chen-Ning Yang reviewed all experimental informations and concluded that there was no evidence to refute nor support parity conservation in weak interactions, and they proposed an experiment to directly test $\mathcal{P}$-conservation in β-decay [36]. This experiment was conducted later that year by Chien-Shiung Wu [37]. The experiment consisted in measuring the angular distribution of electrons emitted by β-decays of polarized ^{60}Co nuclei (*i.e.* having their spin in the same state) [37]. The β-decay of ^{60}Co leads to an excited state of ^{60}Ni which then emits two γ-rays:

$$^{60}\mathrm{Co} \to {}^{60}\mathrm{Ni}^* + e^- + \bar{\nu}_e \to {}^{60}\mathrm{Ni} + 2\gamma + e^- + \bar{\nu}_e.$$

The emission of γ-rays is an electromagnetic process that satisfies the parity symmetry. The photon emission should thus be isotropic for polarized ^{60}Co nuclei, and their degree of polarization can be checked by measuring the anisotropy of the γ-rays. When comparing the distribution of the emitted electrons with the one of γ-rays, an asymmetry was observed providing unequivocal proof of $\mathcal{P}$-violation in weak interactions [37].

One year later, Maurice Goldhaber and his collaborators carried out an experiment to measure the helicity of neutrinos [38]. The helicity of a particle is the projection of its spin along the direction of its momentum, $h = \boldsymbol{\sigma p}/p$. For massive fermions, the helicity of the two chiral states can be positive and negative. Indeed, one can always find a reference frame where the particle motion is reversed while the spin stays the same, hence reversing the helicity. On the other hand, the helicity of a massless fermion is a relativistic invariant. Goldhaber's team measured the γ-ray emission following the capture of an orbital electron in $^{152}\mathrm{Eu}^{\mathrm{m}}$:

$$^{152}\mathrm{Eu}^{\mathrm{m}} + e^- \to {}^{152}\mathrm{Sm}^* + \nu_e \to {}^{152}\mathrm{Sm} + \gamma + \nu_e.$$

$^{152}\mathrm{Sm}^*$ returns to its ground-state by emitting a photon, whose spin is related to the neutrino's helicity due to momentum conservation. Measuring the γ-ray polarization then directly gives access to the neutrino helicity. This was achieved by filtering out a specific helicity with a magnet. More photons could be measured when the magnetic field of the magnet was letting left-handed photons go through. It was concluded that the neutrinos have a negative helicity. A similar experiment was conducted by J. C. Palathingal in 1970 with antineutrinos [39]. The antineutrino helicity was measured by determining the circular polarization of gamma rays emitted by ^{203}Hg and resonantly scattered by ^{203}Tl nuclei. The experiment concluded that antineutrinos have positive helicity. Fermi had already discussed the fact that the neutrino mass was extremely small if not zero [2]. The detection of only negative helicity neutrinos and positive helicity antineutrinos led to the conclusion that neutrinos (antineutrinos) were massless and left-handed (right-handed). They were introduced as such in the Standard Model. As a result, the theory of weak interaction was built by grouping left-handed spinors of a generation into a doublet representation of $SU(2)_L$, while each right-handed spinors were left into singlet representations of $SU(2)_L$ as they do not take part in the weak interaction.

1.2.3 The different flavors of neutrino

In 1962, a second type of neutrino, ν_μ, was observed at Brookhaven Alternating Gradient Synchrotoron (AGS) [4]. A 15 GeV proton beam was aimed at a beryllium target in order to produce pions. The pions would then decay in flight according to $\pi^\pm \to \mu^\pm + \nu_\mu(\bar{\nu}_\mu)$. The resulting flux of particles traveled 21 m to strike a 13.5 m thick iron wall, stoping most of the muons. Neutrino interactions were then observed in a 10-ton aluminum spark chamber located behind the wall. In the case that ν_μ were the same as ν_e, the expected neutrino interactions would have been $\nu_\mu(\bar{\nu}_\mu)+n \to p+e^-(e^+)$ and $\nu_\mu(\bar{\nu}_\mu)+n \to p+\mu(\mu^+)$. Electron-like events and muon-like events, respectively identified in the spark chamber by electromagnetic showers and single tracks, would have been detected in similar proportion. However, only muons remained once the electrons coming from contaminant kaon decays were accounted for, thus confirming that ν_μ were indeed different from ν_e.

The discovery of the τ lepton in 1975 by Martin Perl and his colleagues at the Stanford Linear Accelerator Center (SLAC) in Stanford, California, logically led to question the existence of a third neutrino [5]. The question was partly solved in 1989, when the LEP at CERN, in Switzerland, and the SLAC Linear Collider (SLC) in Stanford determined that there were only three species of light neutrinos [40–43]. The different experiments studied the process $e^- + e^+ \to$ hadrons. This process cross-section depends on the decay width of Z^0, which itself depends on the number of neutrinos that couple to Z^0. The most up-to-date result from the Z^0 decay width measurement for the number of light active neutrinos is $N_\nu = 2.9840 \pm 0.0082$ [44]. It is noteworthy that this measurement only accounts for massive neutrinos with $m < m_Z/2$ that couples to Z^0. Hence, it is possible that other types of neutrinos exist as long as one of these two conditions is not respected. In particular, the existence of a sterile neutrino is still allowed in the Standard Model. Finally, the ν_τ was observed in 2000 by the Direct Observation of the NeUtrino Tau (DONUT) experiment, at Fermilab [45]. A 800 GeV proton beam struck a tungsten target, producing charmed mesons D_S. D_S would then decay as $D_S \to \tau + \bar{\nu}_\tau$, closely followed by the τ decay producing an additional ν_τ. The produced neutrino beam, composed of 5% of ν_τ and $\bar{\nu}_\tau$ in equivalent proportion, reached a detector 36 m downstream made of stainless steel sheets, interleaved with emulsion plates where the interaction products were detected. DONUT successfully identified the τ as the only lepton created at the vertex of the neutrino interaction, thus proving that ν_τ was distinct from ν_e and ν_μ.

1.3 Deciphering the neutrino oscillations

The neutrino saga could have reached an end here, if not for the intriguing ability of neutrinos to oscillate between the different flavors. Experimentally confirmed in 1998 by Super-Kamiokande [11], the oscillation phenomenon was first suggested by Bruno Pontecorvo in 1957 [46]. He proposed that a neutrino could oscillate into an antineutrino, based on the analogous case of kaon transition $K^0 \to \bar{K}^0$. With the discovery of the muon neutrino ν_μ in 1962 at Brookheaven [4], Ziro Maki, Masami Nakagawa and Shoichi Sakata elaborated the same year a theory of flavor neutrino oscillation [47]. They proposed that the neutrino flavor eigenstates were a mixture of mass eigenstates. In that case, neutrinos would have a non-zero mass, giving them the property to oscillate between flavors while as they propagate in space. The probability for a neutrino to oscillate between n flavors is then a function of several mixing angles θ_{ij} and squared-mass differences $\Delta m^2_{ij} \equiv m^2_i - m^2_j$, with $i, j \leq n$.

In the following, the framework of neutrino oscillation is first introduced. Then, experiments that have paved the way for the discovery of neutrino oscillations and measured the oscillation parameters are presented. A summary of the key characteristics (baseline, mean energy of the neutrino flux, detector technology) of past, current and future neutrino oscillation experiments is presented in Fig. 1.6 at the end of the section.

1.3.1 Neutrino oscillation framework

1.3.1.1 Oscillation in vacuum

The oscillation of neutrino between different flavors can be derived in the framework of quantum field theory [48], although this phenomenon is very well described in a first approach by quantum mechanics [49]. Neutrino flavors ν_α are coherent superpositions of mass eigenstates ν_i, related through the complex unitary Pontecorvo-Maki-Nakagawa-Sakata (PMNS) matrix U_{PMNS}. In quantum mechanics, a pure flavor state ν_α produced in a CC process is given by

$$|\nu(t=0)\rangle = |\nu_\alpha\rangle = \sum_i U^*_{\alpha i} |\nu_i\rangle \,. \tag{1.5}$$

Note that the complex conjugate of the PMNS matrix is involved here. That is because the neutrino state $|\nu_\alpha(\boldsymbol{p})\rangle$ with momentum $\boldsymbol{p}$ is obtained by the action of the creation operator $a^\dagger_\alpha(\boldsymbol{p})$ on the vacuum [50]. In quantum field theory, the neutrino field $\nu_\alpha(\boldsymbol{r})$ annihilates a neutrino flavor ν_α so that $\nu_\alpha = \sum_i U_{\alpha i}\nu_i$. For antineutrino, the complex conjugate is replaced with the usual PMNS matrix in quantum mechanics, $|\bar{\nu}_\alpha\rangle = \sum_i U_{\alpha i} |\bar{\nu}_i\rangle$, and reciprocally in quantum field theory. The massive neutrino states are eigenstates of the free Hamiltonian, and propagates in vacuum as plane waves according to the Schrödinger equation:

$$|\nu(t)\rangle = \sum_i U^*_{\alpha i} e^{-iE_i t} |\nu_i\rangle = \sum_i U^*_{\alpha i} e^{-iE_i t} \sum_\beta U_{\beta i} |\nu_\beta\rangle \,, \tag{1.6}$$

with $E_i = \sqrt{\boldsymbol{p}^2 + m_i^2}$ the energy of the massive state ν_i, and with the approximation that all massive eigenstates have the same momentum $\boldsymbol{p_i} = \boldsymbol{p}$[1], *i.e.* neutrino masses are negligible with respect to their energies. The amplitude of probability at time t for a flavor ν_α to have oscillated into a flavor ν_β is then given by

$$P_{\nu_\alpha \to \nu_\beta} = |\langle \nu_\beta | \nu(t) \rangle|^2 = \left| \sum_i U^*_{\alpha i} U_{\beta i} e^{-iE_i t} \right|^2 . \tag{1.7}$$

Considering ultra-relativistic neutrinos for which $E \simeq p$ and $E_i \simeq p + m_i^2/2E$, the probability to observe a flavor ν_β at a distance $L \simeq t$ from the site of emission of a flavor ν_α is given after some calculations by

$$\begin{aligned} P_{\nu_\alpha \to \nu_\beta}(L,E) = \delta_{\alpha\beta} &- 4 \sum_{i<j} \mathfrak{Re}\left[U_{\alpha i} U^*_{\beta i} U^*_{\alpha j} U_{\beta j}\right] \sin^2\left(\frac{\Delta m^2_{ij} L}{4E}\right) \\ &+ 2 \sum_{i<j} \mathfrak{Im}\left[U_{\alpha i} U^*_{\beta i} U^*_{\alpha j} U_{\beta j}\right] \sin^2\left(\frac{\Delta m^2_{ij} L}{2E}\right) , \end{aligned} \tag{1.8}$$

with $\delta_{\alpha\beta}$ the Kronecker delta. For antineutrino oscillations, the sign of the imaginary term in Eq. 1.8 is flipped. It can be noted that oscillations manifest only if the massive states

---

[1] The exact quantum mechanics treatment is based on the wave-packet description of wavefunctions. If appropriate coherence conditions are satisfied, the approximations made here result in the same oscillation probability as the proper derivation. See [51] for a detailed explanation.

are non-degenerate, *i.e.* $\Delta m^2_{ij} \neq 0$. Oscillation probabilities with $\alpha \neq \beta$ are called *transition probabilities* $P_{\nu_\alpha \to \nu_\beta}$ and are studied in *appearance experiments*. In this type of experiment, an increase or apparition of a given neutrino flavor is investigated compared to the emission source. Oscillations with $\alpha = \beta$ define *survival probabilities* $P_{\nu_\alpha \to \nu_\alpha}$, studied in *disappearance experiments* where the decrease of a neutrino flavor is investigated compared to the emission source. The two types of oscillation experiments are complementary and investigate different elements of the PMNS matrix.

1.3.1.2 Three-flavor oscillation

If one considers the three usual neutrino flavors $(\nu_e, \nu_\mu, \nu_\tau)$ and three massive states (ν_1, ν_2, ν_3), the PMNS matrix can be parametrized using three mixing angles θ_{ij} and a $\mathcal{CP}$-violation phase $\delta_{\mathcal{CP}}$ [49]. The 3-flavor oscillation derived from Eq. 1.8 then depends on two squared-mass differences in addition to the three mixing angles. The third squared-mass difference is constrained by the other two:

$$\Delta m^2_{31} = \Delta m^2_{32} + \Delta m^2_{21}. \tag{1.9}$$

The phenomenology of experiments has shown that neutrino oscillations can be described by three sectors where the oscillation associated to one of the mixing angles dominates over the others. U_{PMNS} can then be factorized as the product of three rotation matrices associated to each sector, with a $\mathcal{CP}$-violation phase conventionally included in the θ_{13} rotation matrix:

$$U_{PMNS} = \begin{pmatrix} 1 & 0 & 0 \\ 0 & c_{23} & s_{23} \\ 0 & -s_{23} & c_{23} \end{pmatrix} \begin{pmatrix} c_{13} & 0 & e^{-i\delta_{\mathcal{CP}}} s_{13} \\ 0 & 1 & 0s \\ -e^{i\delta_{\mathcal{CP}}} s_{13} & 0 & c_{13} \end{pmatrix} \begin{pmatrix} c_{12} & s_{12} & 0 \\ -s_{12} & c_{12} & 0 \\ 0 & 0 & 1 \end{pmatrix}, \tag{1.10}$$

with $c_{ij} = \cos\theta_{ij}$, $s_{ij} = \sin\theta_{ij}$. All neutrinos play an equivalent role in the $\mathcal{CP}$-violation which only appears in a 3-flavor framework. Furthermore, two additional $\mathcal{CP}$-violating phases should be introduced if neutrinos were Majorana particles, *i.e.* if neutrinos and antineutrinos were the same particles:

$$U_{PMNS} \to U_{PMNS} \times \mathrm{diag}(e^{i\phi_{M1}}, e^{i\phi_{M2}}, 1). \tag{1.11}$$

The Majorana phases cancel out in the term $U_{\alpha j} U^*_{\beta j}$ of Eq. 1.8. Hence, Dirac and Majorana neutrinos cannot be distinguished by studying oscillations, leaving only $\delta_{\mathcal{CP}}$ to play a role in oscillations. The term $U^*_{\alpha i} U_{\beta i} U_{\alpha j} U^*_{\beta j}$ in Eq. 1.8 being real for $\alpha = \beta$, the survival probability is identical for neutrinos and antineutrinos. It follows that the $\mathcal{CP}$-violation can only be studied in appearance experiments.

1.3.1.3 Two-flavor oscillation

In most of the experiments, it is appropriate to consider only two flavors of neutrino[1]. For an experiment set at a baseline L and detecting neutrinos of energy E, a careful tuning of L/E allows to be maximally sensitive to a specific Δm^2_{ij}, justifying the use of the 2-flavor framework. Subleading terms in Eq. 1.8 are then neglected as a first approximation, resulting in an effective

---

[1] The 2-flavor and plane waves approximations are usually enough to interpret the data of neutrino oscillation experiments. However, the 3-flavor formalism and corrections may be required to properly explain experimental data. The corrections come from different origins: oscillation in matter, effect due to the quantum field nature of particles, and $\mathcal{CP}$-violation effects [50].

oscillation probability governed by a single mixing angle θ and a single squared-mass difference Δm^2. Flavor and mass states are then related by

$$\begin{pmatrix}\nu_\alpha \\ \nu_\beta\end{pmatrix} = \begin{pmatrix}\cos\theta & \cos\theta \\ \sin\theta & -\sin\theta\end{pmatrix} \begin{pmatrix}\nu_1 \\ \nu_2\end{pmatrix}. \tag{1.12}$$

When put back in Eq. 1.8, the result for transition probabilities is

$$\begin{aligned} P_{\nu_\alpha\to\nu_\alpha}(L,E) + P_{\nu_\alpha\to\nu_\beta}(L,E) &= 1, \\ P_{\nu_\alpha\to\nu_\beta}(L,E) &= \sin^2 2\theta \sin^2\left(\frac{\Delta m^2 L}{4E}\right). \end{aligned} \tag{1.13}$$

The oscillation phase $\frac{\Delta m^2 L}{4E}$ is responsible for the oscillation frequency, whereas the oscillation amplitude depends only on the mixing angle θ:

- if $\frac{\Delta m^2 L}{E} \ll 1$, the oscillations are practically unnoticeable, $P_{\nu_\alpha\to\nu_\beta} = 1$ and $P_{\nu_\alpha\to\nu_\beta} = 0$;
- if $\frac{\Delta m^2 L}{E} \gg 1$, the required precision to resolve the oscillations is increasingly important, and if not enough, the oscillation effect is averaged out to a constant equal to $\langle P_{\nu_\alpha\to\nu_\alpha}\rangle = \frac{1}{2}\sin^2 2\theta$;
- if $\frac{\Delta m^2 L}{E} \sim 2\pi$, the oscillation is at its peak of amplitude and the sensitivity to Δ_m^2 is optimal. This is the best value to measure simultaneously $\sin^2 2\theta$ and Δm^2.

Fig. 1.2 shows the $\bar{\nu}_e \to \bar{\nu}_e$ survival probability typically observed in reactor experiments, in the 3-flavor and 2-flavor frameworks. It can be seen that a 2-flavor description is only accurate in a given region of L/E where one oscillation dominates (the θ_{13} oscillation in the case of the short baseline curve, and the θ_{12} oscillation for the long baseline curve).

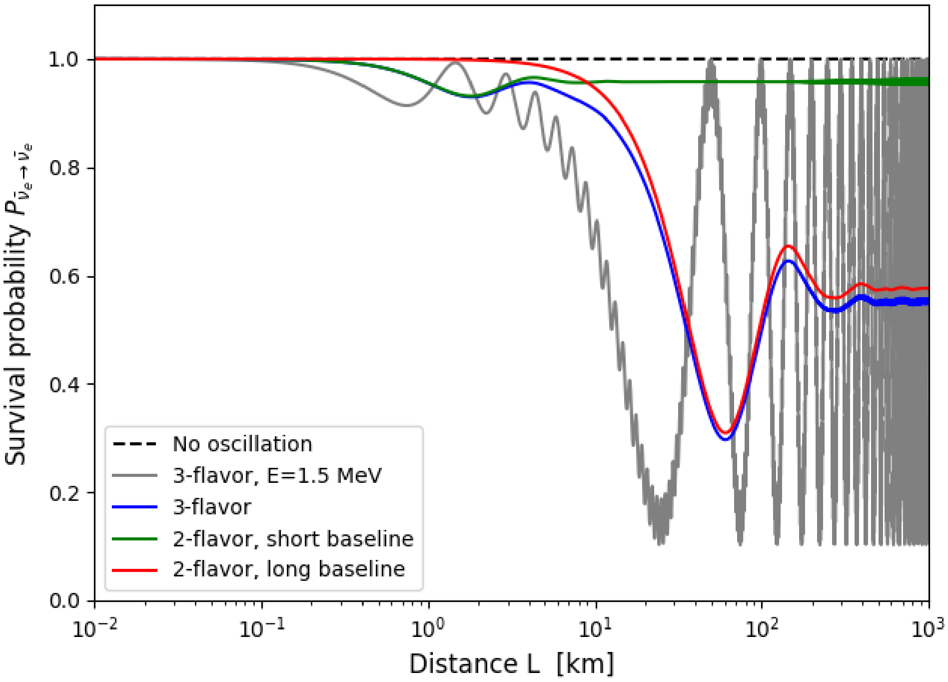

Figure 1.2: Survival probability for a $\bar{\nu}_e$ to be detected as a $\bar{\nu}_e$ after traveling a distance L. The grey curve shows the 3-flavor oscillation probability for a neutrino with energy $E = 1.5$ MeV. The blue curve represents the 3-flavor oscillation probability averaged over a neutrino spectrum detected at a rector experiment. The red and green curves represent respectively the 2-flavor oscillation probability for long baseline experiments $L \sim \mathcal{O}(100\text{ km})$, and for short baseline experiments $L \sim \mathcal{O}(1\text{ km})$. The considered mixing parameter values are from the normal ordering case from Tab. 1.1.

Parameter	Global fit	
	Normal ordering	Inverted ordering
θ_{12} (°)	$33.44^{+0.77}_{-0.74}$	$33.45^{+0.78}_{-0.75}$
θ_{23} (°)	$49.2^{+0.9}_{-1.2}$	$49.3^{+0.9}_{-1.1}$
θ_{13} (°)	8.57 ± 0.12	8.60 ± 0.12
$\delta_{\mathcal{CP}}$ (°)	197^{+27}_{-24}	282^{+26}_{-30}
Δm^2_{21} (10^{-5} eV^2)	$7.42^{+0.21}_{-0.20}$	$7.42^{+0.21}_{-0.20}$
Δm^2_{31} (10^{-3} eV^2)	$2.517^{+0.026}_{-0.028}$	
Δm^2_{32} (10^{-3} eV^2)		-2.498 ± 0.028

Table 1.1: Global fit of neutrino oscillation parameters from [52]. The best-fit is done considering all PMNS parameters at once in the case of Normal Ordering or Inverse Ordering. Uncertainties are given at the $\pm 1\sigma$ level.

The 2-flavor formula Eq. 1.13 has been widely used to describe oscillations observed in experiments measuring solar and atmospheric neutrinos. In the 3-flavor framework, the solar parameters are identified by convention with the oscillation between ν_1 and ν_2 and thus define the 1-2 sector. The squared mass difference is initially degenerated as the probability Eq. 1.13 only depends on the squared sinus of the oscillation phase. This degeneracy can be lifted by studying matter effects, as neutrinos and antineutrinos oscillate with uneven probabilities when traveling through matter. The sign of Δm^2_{21} is given by the oscillation of solar neutrinos in the star such that $m_2 > m_1$:

$$\Delta m^2_{sol} = \Delta m^2_{21} > 0. \tag{1.14}$$

The measured atmospheric parameters are such that $\Delta m^2_{atm} \gg \Delta m^2_{sol}$, and can be identified with either $|\Delta m^2_{32}|$ or $|\Delta m^2_{31}|$. This implies, according to Eq. 1.9:

$$\Delta m^2_{atm} \simeq \left|\Delta m^2_{32}\right| \simeq \left|\Delta m^2_{31}\right| \gg \Delta m^2_{21} > 0. \tag{1.15}$$

The massive eigenstates can then be arranged in two ways. The first possibility is $m_1 < m_2 < m_3$, characterized by $\Delta m^2_{31} > 0$, and is known as the *normal mass ordering* or normal hierarchy. The second, characterized by $\Delta m^2_{31} < 0$, yields $m_3 < m_1 < m_2$ and is known as the *inverted mass ordering* or inverted hierarchy. The mass ordering $m_1 < m_3 < m_2$ is not consistent with Eq. 1.15 and is excluded. The global fit made in [52] and reproduced in Tab. 1.1 favors the normal ordering at the level of 2.7σ compared to the inverted ordering.

Leaving aside a few anomalies that will be discussed in Sec. 1.4, the compilation of all experimental results about neutrino oscillation are consistent with the 3-flavor oscillation and the U_{PMNS} parametrization given in Eq. 1.10. The oscillation parameter best values, obtained through a global fit over all the mixing parameters [52], are reported in Tab. 1.1.

1.3.2 The 1-2 sector and solar neutrinos

The parameters θ_{12} and Δm^2_{21} have been mainly measured by studying solar neutrinos, earning them the name of *solar parameters*. The high energy fusion processes by which the Sun and stars in general burn, namely the reactions belonging to the *pp* chain and the CNO cycle, release a very intense and pure ν_e flux. In low-energy solar neutrino experiments, where

$\Delta m^2_{31} L/E \gg 1$ and $\Delta m^2_{21} L/E \gtrsim 1$, the oscillation governed by Δm^2_{31} is averaged and the 2-flavor ν_e survival probability is thus led by θ_{12} and Δm^2_{21}:

$$P(\nu_e \to \nu_e) = 1 - \sin^2 2\theta_{12}\ \sin^2\left(\frac{\Delta m^2_{21} L}{4E}\right). \tag{1.16}$$

In 1960, Raymond Davis Jr. and John Bahcall conducted an experiment located in the Homestake gold mine at Lead, South Dakota [6]. Its goal was to make the first measurement of the solar ν_e flux. The Homestake detector was based on the CC process

$$\nu_e + {}^{37}\mathrm{Cl} \to {}^{37}\mathrm{Ar} + e^-. \tag{1.17}$$

With a threshold of 0.814 MeV, the charged current process described in Eq. 1.17 prevents the measurement of most of the solar neutrino flux, and is mainly sensitive to ν_e from ^{8}Be, ^{7}Be and *pep*. The Homestake detector contained 615 tons of C_2Cl_4 and was located at 1.478 km underground in order to reduce the production of ^{37}Ar induced by cosmic rays [53]. The resulting ^{37}Ar was then extracted by purging the tank with helium gas and separated from the helium with a suitable absorber. The argon sample could then be chemically purified. The number of recovered ^{37}Ar atoms, which is a radioactive isotope decaying by electron capture (EC), was measured by proportional counters. The measured neutrino flux of 2.56 ± 0.23 SNU (1 SNU $= 10^{-36}$ event/target/s) returned to be three times lower than expected [6, 53], as seen in Fig. 1.3a. The accuracy of both the measurement and the predictions were first questioned, but after a few years the doubt was cast aside as no error was highlighted. The deficit of two thirds in the measured solar neutrino flux constituted the *solar neutrino problem*. Pontecorvo reckoned the same year that the oscillation phenomenon could be the reason for the solar neutrino problem [54, 55].

During the 1990s, three conclusive experiments were carried out using detection through radiochemical extraction: the Soviet-American Gallium Experiment (SAGE) in Baksan, U.S.S.R. [7], the Gallium Experiment (GALLEX) [8] and its successor the Gallium Neutrino Observatory (GNO) [8] both conducted at the Gran Sasso Underground Laboratory in Italy. The detection involved the CC process

$$\nu_e + {}^{71}\mathrm{Ga} \longrightarrow {}^{71}\mathrm{Ge} + e^- \tag{1.18}$$

and the extraction by a selective oxidation of the produced ^{71}Ge from the liquid metal gallium, using a weakly acidic H_2O_2 solution [56]. The threshold of this process is 0.234 MeV, giving access to the *pp* neutrinos. SAGE, GALLEX and GNO measured about half of the expected neutrino rate and reached the same conclusion: the solar neutrino problem was not an experimental artifact and was indicating new neutrino properties.

The solar neutrino problem came to an end in 2001, with the combined analysis of Super-Kamiokande (Super-K) and the Sudbury Neutrino Observatory (SNO) experiment [12]. Super-K and SNO were using water Cherenkov detectors. In such detectors, charged particles produced in neutrino interactions happening in water radiate photons when they exceed the speed of light in water. These Cherenkov photons are emitted in a cone centered on the produced ultra-relativistic charged particle. The cone pattern allows Cerenkov detectors to be sensitive to the direction of the incoming neutrino, which is not possible with radiochemical experiments. Furthermore, Cherenkov detectors are sensitive to neutrino-electron elastic scattering (NEES) in addition to CC. The SNO Cherenkov detector contained heavy water ^2H_2O which allowed the ^8B neutrinos to be detected through NC in addition to CC and NEES:

$$\begin{aligned} \text{NEES:} \quad & \nu_{e,\mu,\tau} + e^- \longrightarrow \nu_{e,\mu,\tau} + e^-, && (1.19) \\ \text{CC:} \quad & \nu_e + {}^2\text{H} \longrightarrow e^- + p + p, && (1.20) \\ \text{NC:} \quad & \nu_{e,\mu,\tau} + {}^2\text{H} \longrightarrow \nu_{e,\mu,\tau} + p + n. && (1.21) \end{aligned}$$

The low energy of solar neutrinos makes it impossible to produce μ and τ leptons through CC processes similar to Eq. 1.20, thus making the CC process only sensitive to ν_e. NEES is preferentially sensitive to ν_e because the cross-section with ν_e is about six times higher than with ν_μ and ν_τ. On the contrary, NC is sensitive to all active flavors with equal cross-section. By comparing the measurements of the three reactions, SNO provided a model independent test of neutrino oscillations. The neutrino deficit was still present in NEES and CC data, however the neutrino flux measured via NC was consistent with solar models as shown in Fig. 1.3a, providing a compelling evidence in favor of ν_e oscillation into a mixed state $\nu_\mu + \nu_\tau$.

The Kamioka Liquid Scintillator Antineutrino Detector (KamLAND) experiment, located in the former site of KamiokaNDE, also provided important results in the solar sector by providing an independent and precise measurement of the solar parameters. Indeed, the $\bar{\nu}_e$ survival probability investigated in reactor experiments also fits Eq. 1.16 for long baselines of hundreds of kilometers, as seen in Fig. 1.2 where the 2-flavor θ_{12} oscillation dominates in this region. With 55 nuclear reactors located at an average baseline of 180 km, KamLAND was designed to measured $\bar{\nu}_e$ produced by these reactors via IBD [57]. KamLAND demonstrated for the first time the disappearance of reactor $\bar{\nu}_e$ with a clear dependency in L/E. The measured oscillation parameters provided a strong constraint for solar neutrinos, a large mixing angle remaining the only solution consistent with KamLAND's results [57]. The allowed parameter space showing the agreement between the results of KamLAND and solar experiments can be seen in Fig. 1.3b [58], and the current best-fit for the solar parameters Δm^2_{21} and θ_{12} are displayed in Tab. 1.1 [52].

1.3.3 The 2-3 sector and atmospheric neutrinos

While the brainstorming about the solar neutrino problem was foaming, the massless neutrino hypothesis was also challenged by a second problem coming from atmospheric neutrinos. These neutrinos result from the collision of cosmic rays with nuclei in the upper atmosphere. The collisions produce particle showers, followed by hadron and lepton decays which produce neutrinos with energies from 0.1 GeV and up to a few TeV [50]. The neutrino production is dominated by the following processes (and their charge conjugates):

$$\begin{aligned} \pi^+ &\longrightarrow \mu^+ + \nu_\mu, && (1.22) \\ \mu^+ &\longrightarrow e^+ + \nu_e + \bar{\nu}_\mu. && (1.23) \end{aligned}$$

The flux ratio $\nu_\mu/\nu_e \equiv {}^{\nu_\mu+\bar{\nu}_\mu}/_{\nu_e+\bar{\nu}_e}$ was then expected to be about 2. In a 2-flavor scenario, the ν_μ disappearance is led by θ_{23} and $\Delta m^2_{31} \simeq \Delta m^2_{32}$:

$$P(\nu_\mu \to \nu_\mu) = 1 - \sin^2 2\theta_{23}\ \sin^2\left(\frac{\Delta m^2_{31} L}{4E}\right). \tag{1.24}$$

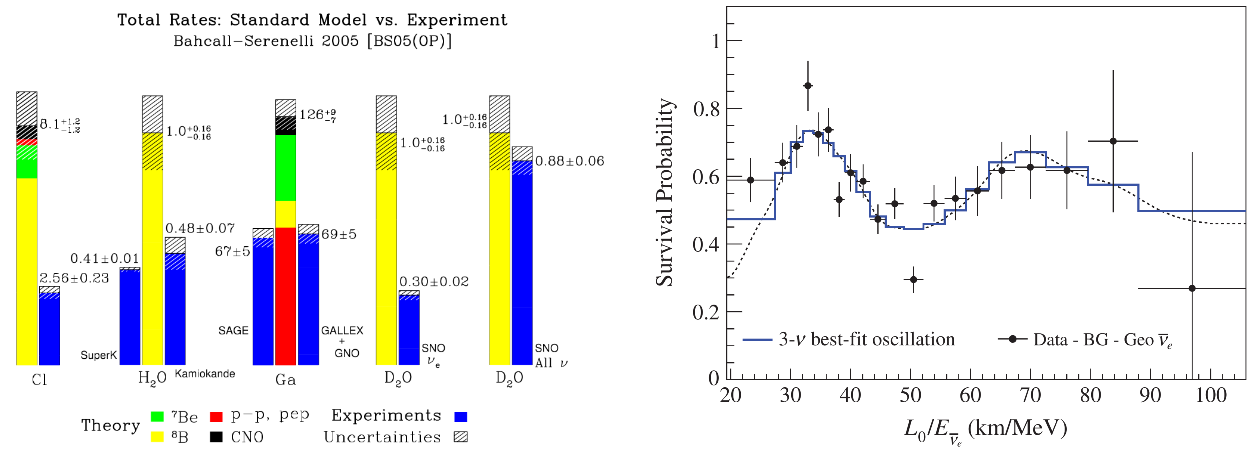

(a) Solar neutrino rates.

(b) KamLAND $\bar{\nu}_e$ survival probability.

Figure 1.3: **(a)** Comparison of the expected versus measured solar neutrino fluxes for several experiments. The numbers at the top of each column are in units of SNU (1 SNU = 10^{-36} event/target/s). The figure is taken from [59]. **(b)** Ratio of the observed $\bar{\nu}_e$ spectrum to the no-oscillation expectation as a function of $L_0/E_{\bar{\nu}_e}$ from the KamLAND data, where $L_0 = 180$ km is the flux-weighted average reactor baseline. The dotted curve and the blue histogram show the best-fit survival probability curve based on the three-flavor framework. The figure is taken from [58].

However, the measured ν_μ/ν_e ratio was reported at almost half this value by deep underground water Cherenkov detectors such as IMB [9], Kamiokande [10] and its successor Super-Kamiokande [11]. This deficit came to be known as the *atmospheric neutrino problem*. Atmospheric neutrinos can interact with nuclei via CC. Each possible resulting particle ($e^\pm, \mu^\pm, \pi^\pm$) creates a specific Cherenkov cone pattern in the detector and is identified that way. The flavor of atmospheric neutrinos can then be traced back. By 1998, the neutrino oscillation $\nu_\mu \to \nu_\tau$ was undoubtly disclosed by Super-K results as the cause of the atmospheric neutrino problem [11]. The zenith angle distribution of μ-like events significantly differed from predictions in absence of neutrino oscillation while e-like events were in agreement as shown in Fig. 1.4a.

The oscillations observed initially in atmospheric neutrinos was later precisely measured in particle accelerator experiments generating neutrino beams, among which one can cite KEK to Kamioka (K2K) [60], Main Injector Neutrino Oscillation Search (MINOS) [61], Oscillation Project with Emulsion-tRacking Apparatus (OPERA) [62], Tokai to Kamioka (T2K) [63], NuMI Off-axis ν_e Appearance (NOνA) [64]. A review on experiments using neutrino beams generated from particle accelerators can be found in [50, 65]. Neutrino accelerator experiments consists in producing pions and kaons through the interaction of a high intensity proton beam on a target [65]. The produced mesons are sorted based on their electric charge by a magnetic device called the horn. The decay of positive mesons results in a neutrino beam mainly composed of ν_μ, while negative meson decays generate a $\bar{\nu}_\mu$ beam. In such experiments, the measurement is obtained by comparing the neutrino beam composition in two detectors, called the near detector and the far detector. The near detector is located a few hundreds of meters downstream the proton beam target, and measures the flavor composition of the non-oscillated neutrino beam. Based on the initial composition, the expected spectra at the far detector is compared to the measured one. The far detector is typically located several hundreds of kilometers away, and the flux energy is tuned in order to have a maximum sensitivity to Δm^2_{32} to probe the atmospheric sector. The final beam composition is determined by identifying the products of neutrino interactions happening in the far detector, allowing for

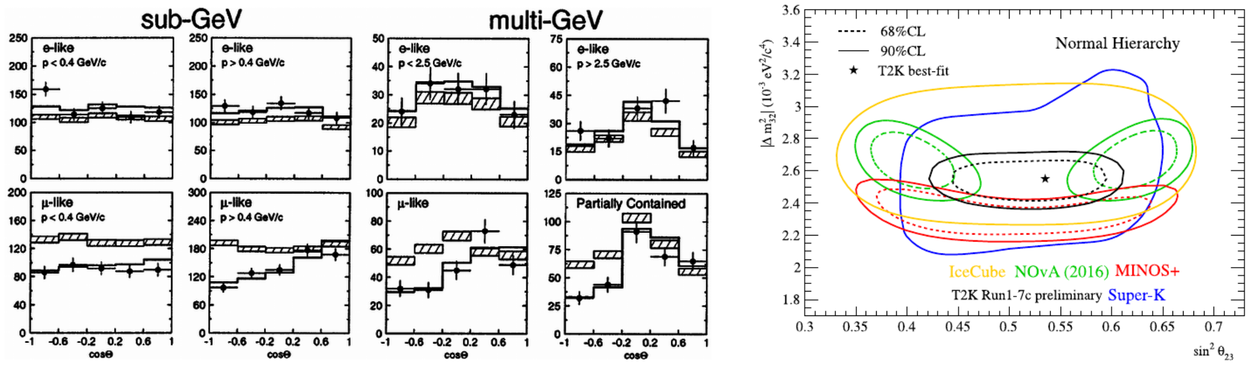

(a) μ-like and e-like events in Super-Kamiokande.

(b) Atmospheric parameters.

Figure 1.4: **(a)** Zenith angle distributions of μ-like and e-like events in Super-Kamiokande. The distribution of fully and partially contained multi-GeV μ-like events are separated. A fully contained event deposits all of its Cherenkov light in the inner detector contrary to partially contained events which have an exiting track and deposit some of the Cherenkov light in the outer detector. The hatched region shows the Monte Carlo expectation for no oscillations normalized to the data with statistical errors. The bold line is the best-fit expectation for $\nu_\mu \to \nu_\tau$ oscillations with the overall flux normalization fitted as a free parameter. The figure is taken from [11]. **(b)** Confidence regions in the plane Δm^2_{32} versus $\sin^2\theta_{23}$ for T2K, Super-K, Minos+, NOνA and IceCube DeepCore. The figure is taken from [50].

a model-independent measurement of the oscillation parameters. Both ν_μ and $\bar{\nu}_\mu$ disappearance experiments can be conducted with accelerator, as well as ν_e and $\bar{\nu}_e$ appearance experiments [65]. The agreement between long-baseline accelerator and atmospheric experiments can be seen in Fig. 1.4b [50], and the current best-fit for the atmospheric parameters Δm^2_{32} and θ_{23} are showed in Tab. 1.1 [52].

1.3.4 The 1-3 sector and reactor neutrinos

A detailed presentation about reactor neutrinos is made in Ch. 2. The contribution of reactor experiments to our understanding of neutrino oscillations is presented here. Starting in the 1980s, neutrino oscillations have been investigated in short-baseline experiments near nuclear reactors. Nuclear reactors produce an intense and pure flux of $\bar{\nu}_e$ of about 2×10^{20} $\bar{\nu}_{\rm e}.{\rm GW}_{\rm th}.{\rm s}^{-1}$, making them ideal to study $\bar{\nu}_e$ disappearance. The energy range of reactor neutrinos expends up to 20 MeV with an average energy of about 1.5 MeV. With detector located around 2 km, reactor experiments are preferentially sensitive to Δm^2_{13} if the condition $\Delta m^2_{21} L/E \ll 1$ is satisfied, and $\bar{\nu}_e$ the survival probability in the 2-flavor framework becomes:

$$P(\bar{\nu}_e \to \bar{\nu}_e) = 1 - \sin^2 2\theta_{13}\ \sin^2\left(\frac{\Delta m^2_{31} L}{4E}\right). \tag{1.25}$$

Until now, reactor experiments have been designed based on the same principle than the Reynes and Cowan experiment. $\bar{\nu}_e$ are detected through the IBD process in a volume filled with liquid-scintillator doped with a neutron absorber. The $\bar{\nu}_e$ interaction produces a positron and neutron which are responsible for a prompt and a delayed signal.

The first reactor experiments designed to investigate the 1-3 oscillation had their detectors set at a distance less than 100 m from reactor cores (Institut Laue–Langevin (ILL), Bugey 3 and its successor Bugey 4 in France [66–68], Gösgen in Switzerland [69], Rovno and Krasnoyarsk in USSR [70, 71], and Savannah River, USA [72]). They measured an antineutrino rate in agreement with the predictions at the time. The global measured over predicted ratio $R = \phi(\bar{\nu}_e)_{meas}/\phi(\bar{\nu}_e)_{pred} = 0.976 \pm 0.024$ was consistent with the no-oscillation hypothesis [15].

In the 1990s, a second series of reactor experiments began with extended baseline around 1 km, such as the CHOOZ experiment in the French Ardennes and the Palo Verde experiment in Arizona, USA. These experiments set an upper limit on θ_{13}, with CHOOZ's limit being the most stringent result for several year. These experiments were limited by their use of a single detector, thus requiring a prediction to be compared with the measured spectrum. The rate prediction uncertainty of about 2% was one of the principal sources of uncertainty and limitation [73]. Another limitation was the quality of the Gd-loaded scintillator liquid, whose optical clarity decreased over time [74].

The θ_{13} oscillation has also been investigated at long baseline accelerator experiments through the appearance channel $\nu_\mu \to \nu_e$, already mentioned in Sec. 1.3.3. Using a 2-flavor analysis, the K2K and MINOS accelerator experiments determined an upper limit on θ_{13} [75, 76], and T2K was the first experiment to favor a non-zero value at 2.5σ in 2011 [63]. An important limitation of accelerator experiments is due to the characterization of the background events [75].

The last mixing parameter θ_{13} was subsequently measured by Daya Bay in China in 2012 [77], promptly followed the same year by Double Chooz in France [78] and the Reactor Experiment for Neutrino Oscillation (RENO) in South Korea [78], whose key characteristic and results are summarized in Tab. 1.2. These three experiments have made use of a near and a far detector, using the same principle as for long-baseline accelerator experiments. The near detector is located close to the reactor core to measure the non-oscillated $\bar{\nu}_e$ flux, and the far detector measures the $\bar{\nu}_e$ disappearance. The θ_{13} oscillation results in a rate deficit and in a shape distortion of the far spectra with respect to the near one. Oscillation parameters in the 1-3 sector can then be inferred by comparing the spectra measured in the near and far detectors. The detection systematic uncertainties of the near and far detectors are expected to be strongly correlated for identical detectors. Therefore, the systematic uncertainties should cancel out in the θ_{13} measurement. Furthermore, the near and far detector positions are optimized to be on the isoflux line of the reactors. This implies that the near and far detectors receive the same flux contributions from each reactor. The flux predictions in the near and far detectors are expected to be strongly correlated. As such, thus uncertainties on the predictions are expected to cancel out in the θ_{13} measurement. An experiment with multiple identical detectors then strongly cancel out the systematic uncertainties associated to both the detector and the flux prediction. As a result, the sensitivity on θ_{13} is increased compared to single detector experiments that rely on a flux prediction to normalize the emitted flux. The difference between Daya Bay, Double Chooz and RENO comes from the number of reactors and their thermal power, as well as from the number of identical detectors that are used and their overburden. The layout of each experiment is shown in Fig. 1.5. All three experiments are using Gd-doped liquid scintillator detectors. Daya Bay is also employing water Cherenkov detectors to improve the rejection of spallation neutron and cosmic rays, and have laid the most precise measurement of θ_{13} until now [77]:

$$\sin^2 2\theta_{13} = 0.0841 \pm 0.0027\ (\text{stat}) \pm 0.0019\ (\text{syst}). \tag{1.26}$$

The current best-fit for the parameters Δm^2_{31} and θ_{13} are presented in Tab. 1.1 [52].

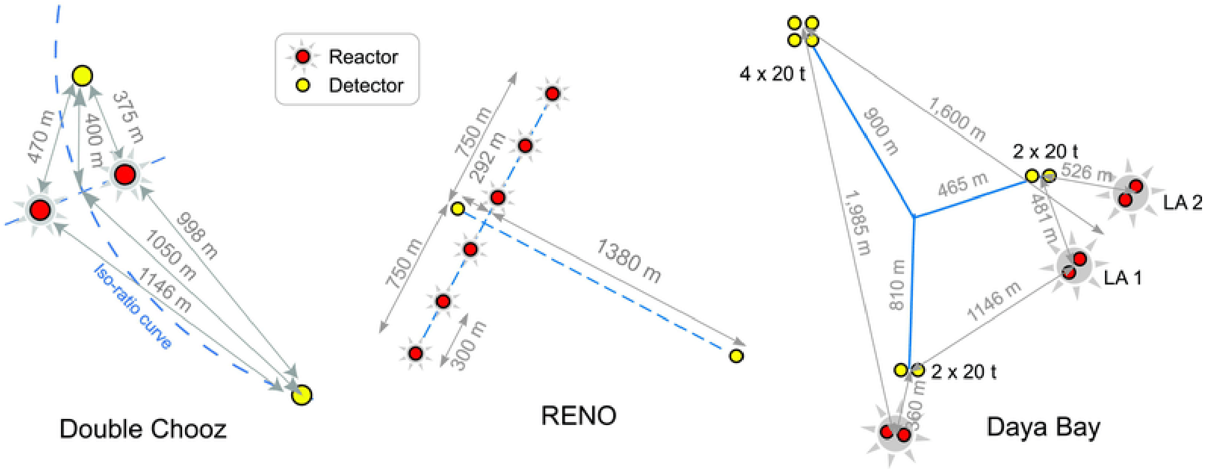

Figure 1.5: Schematic view of the reactor cores ad the detectors for the Daya Bay, Double Chooz and RENO experiments. The dashed curve in the Double Chooz scheme is the far flux iso-ratio curve, where any detector located on this curve will receive the same flux contribution from each reactor as the far detector. The figure is taken from [82].

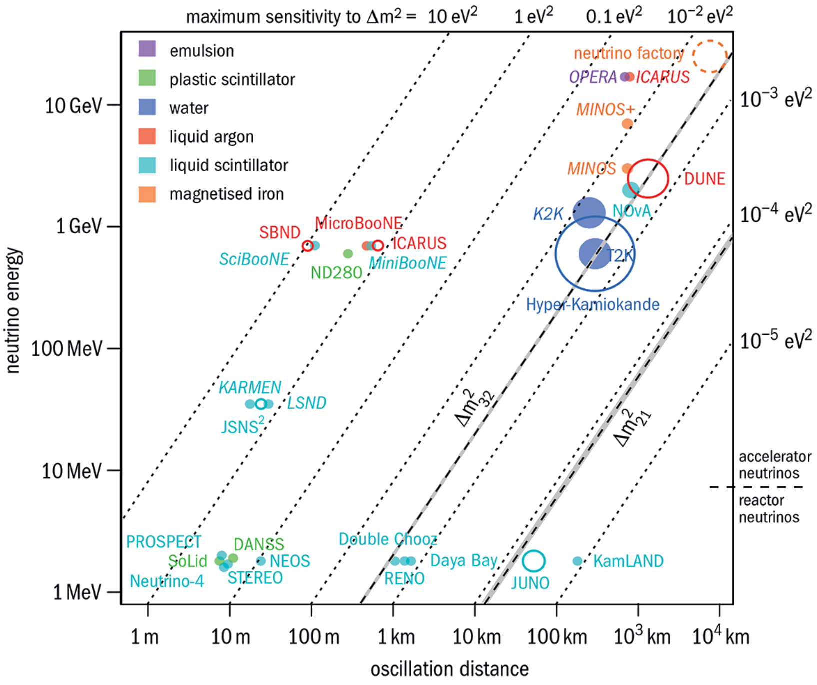

Figure 1.6: Sensitivity domain of neutrino oscillation experiments using reactor or accelerator beam as neutrino source. The experiments are sorted according to the peak energy of the neutrino flux and to the experiment baseline. Experiments in italic are completed. Open markers indicate future projects. The size of the marker is proportional to the detector mass when it is greater than 5 kton, and its color represents the neutrino target material. The figure is taken from CERN courier, credit to M. Rayner [83].

Experiment	**Power** [GW_{th}]	**Baseline** [m]	**Overburden** [m.w.e]	**Mass** [ton]	**Technology**	**Result** $\sin^2 2\theta_{13} \pm$ stat $\pm$ syst
Daya Bay [79]	17.4	520 - 570 - 1590	250 - 265 - 860	20	Gd LS	$0.0841 \pm 0.0027 \pm 0.0019$
Double Chooz [80]	8.5	400 - 1000	115 - 400	8	Gd LS	$0.105 \pm 0.005 \pm 0.013$
RENO [81]	16.4	290 - 1380	70 - 260	16	Gd LS	$0.086 \pm 0.006 \pm 0.005$

Table 1.2: Detector and reactor characteristics in the Double Chooz, RENO and Daya Bay experiments, studying the θ_{13} oscillation of neutrinos. The different weighted baselines of the experiment halls of an experiment are listed in the ”Baseline” column, idem for their overburden. All the detectors of an experiments are similar otherwise, with identical fiducial volume.

1.4 Pending questions

The observation of neutrino oscillations has answered many problems. Nonetheless, some questions remain open. For instance, the existence of $\mathcal{CP}$-violation in neutrino oscillations, the nature of the neutrino, and its mass which cannot be explained by the Standard Model. Indeed, on one hand they seem to be massless, because neutrinos (antineutrinos) are always measured as left-handed (right-handed), and on the other hand the oscillation phenomenon underlines the existence of a neutrino mass.

1.4.1 Dirac or Majorana nature

The characteristic of a Dirac fermion is that it acquires its mass through the Higgs mechanism, as mentioned in section 1.1.3. A Yukawa interaction couples the left and right spinors of a fermion with the Higgs field in order to generate a mass term. Neutrinos have been introduced in the Standard Model as massless particles based on the empirical fact that no right-handed neutrino has so far been observed. However, neutrinos could acquire their mass through the Higgs mechanism if right-handed neutrinos are introduced as singlets of $SU(2)_L$. Singlets of $SU(2)_L$ would not interact via weak interaction, but could participate in the Higgs mechanism via a Yukawa coupling. In that case, the small neutrino mass would be the direct result of a Yukawa coupling far smaller than the Yukawa couplings associated to other leptons [49].

There exists another Lorentz invariant mass term based on the charge conjugated fermion, *i.e.* the antifermion. Neutrino and antineutrino can then be combined into a single particle call a Majorana neutrino which its own antiparticle. The introduction of a Majorana mass term in the Lagrangian results in the existence of physical processes which violate the lepton number by two units. If neutrinos are Majorana particles, the see-saw mechanism provides an elegant explanation for the smallness of neutrino masses. The Majorana or Dirac nature of the neutrino is thoroughly investigated. One of the most promising leads is the existence of the rare neutrinoless double β-decay ($0\nu\beta\beta$) process, whose current half-life limit has been experimentally set to 10^{25}-10^{26} years [84]. This decay is investigated by a worldwide program of experiments such as GERDA [85], Majorana [86], CUPID-0 [87], NEMO-3 [88–90], Aurora [91], CUORE [92], KamLAND-Zen [93] or EXO-200 [94]. The goal set for the next decade is to improve the limit on the $0\nu\beta\beta$ half-life by one or two orders of magnitude [84].

1.4.2 Absolute mass scale

Neutrino oscillations are sensitive to the difference of squared-mass as shown in Eqs.1.8 and 1.13. The individual mass cannot be measured in oscillation experiments and must be determined otherwise. For now, only upper limits have been put on the flavor neutrino masses (see the values reported in Fig. 1.1). One of the most sensitive methods to measure the absolute neutrino mass scale is to use a kinematic approach. For instance, the spectrum shape of an electron emitted in a β-decay is slightly distorted near the transition maximal energy depending on the $\bar{\nu}_e$ mass value [2]. Likewise, the ν_e mass can be investigated by considering an electron capture or a β^+ decay of a carefully chosen isotope. Note that the distortion of the spectrum shape also depends on the neutrino mixing [49]. Indeed, the kinematic measurement actually concerns the effective neutrino mass which results from neutrino oscillations. The measured spectrum results from separate decay modes emitting different neutrino flavors. The spectrum shape near the endpoint is actually sensitive to an effective mass given by

$$m_\nu^2 = \sum_k |U_{ek}|^2 \, m_k^2, \tag{1.27}$$

and can be considered as the effective electron neutrino mass in β-decay [49]. However, as long as the effect of neutrino mixing on the spectrum are small, m_ν and m_{ν_e} can be confounded. The kinematic study of τ decays and of pion decays can also provide a measurement of ν_τ and ν_μ masses.

To investigate the $\bar{\nu}_e$ mass, the tritium β-decay is a privileged isotope because it has a low endpoint ($E_0 = 18.57$ keV), a suitable lifetime ($t_{1/2} = 12.32$ yr) and a simple nuclear structure ($V - A$ theory can be used without fearing nuclear correction):

$$^3\text{H} \rightarrow {}^3\text{He} + e^- + \bar{\nu}_e. \tag{1.28}$$

Two past experiments, Mainz [95] and Troitsk [96], put a limit on the $\bar{\nu}_e$ mass based on the tritium decay. The two collaborations have merged in a joint collaboration, the Karlsruhe Tritium Neutrino experiment (KATRIN), which has currently the most stringent result. Results delivered in 2021 have reported an effective electron neutrino mass square of $m_\nu^2 = 0.26 \pm 0.34$ eV^2, setting the best upper limit on the $\bar{\nu}_e$ mass to date [97]:

$$m_\nu < 0.8 \text{ eV (90\% CL)}. \tag{1.29}$$

where CL means confidence level. Cosmological observations have also helped put a limit on the sum of neutrino masses. The measurement of the Lyα forest power spectrum combined with results from baryonic acoustic oscillations and cosmic microwave background data have resulted in the upper limit [98]

$$m_{\nu_e} + m_{\nu_\mu} + m_{\nu_\tau} \leq 0.14 \text{ eV (90\% CL)}. \tag{1.30}$$

1.4.3 Mass hierarchy

The mass hierarchy, or mass ordering, is the arrangement of the neutrino mass eigenstates as schematically showed in Fig. 1.7a. The mass ordering has not yet been determined experimentally. One possibility to investigate the mass ordering is given in the context of $0\nu\beta\beta$ (see the related experiments listed in Sec. 1.4.1). If neutrinos are Majorana particles, the ν_e mass can be approximated by an effective mass $m_{\beta\beta}$ based on the smallest mass eigenstate and the different squared-mass differences [99]. The effective mass then reduces to one out of three formulas depending on whether the mass ordering is normal, inverted or degenerated. The allowed phase space regarding the relation between the effective Majorana mass $m_{\beta\beta}$ and the lightest neutrino mass is shown in Fig. 1.7b.

A second possibility is to use reactor experiments with baselines $L \sim 50$ km. At this distance, the 3-flavor $\bar{\nu}_e$ disappearance probability $P(\bar{\nu}_e \to \bar{\nu}_e)$ is governed by the three squared-mass differences. A precise measurement of the shape of the reactor spectrum could infer the sign of Δm^2_{31} and assess the mass hierarchy. This is particularly investigated in the Jiangmen Underground Neutrino Observatory (JUNO). JUNO is a next-generation reactor experiment featuring a 20 ktons liquid scintillator detector used for IBD detection [100]. The detector should start operating in 2022. In addition to reactor neutrinos, it will be sensitive to supernova neutrinos, geo-neutrinos, solar neutrinos and atmospheric neutrinos. While its primary goal is to measure the mass hierarchy, it also aims to measure the mixing parameters Δm^2_{21}, Δm^2_{31} and $\sin^2\theta_{12}$ with a precision of less than 1%, and can investigate the sterile neutrino hypothesis and exotic physics like proton decays [100].

Another solution is to study the appearance channels $\nu_\mu \to \nu_e$ and $\bar{\nu}_\mu \to \bar{\nu}_e$ in accelerator experiments. The sensitivity of oscillation to matter effect leads to an asymmetry in the transition probabilities $\nu_\mu \to \nu_e$ and $\bar{\nu}_\mu \to \bar{\nu}_e$ [101]. In the case of normal hierarchy, the neutrino oscillations are favored compared to antineutrino oscillations and vice versa in the case of inverted hierarchy. This will be investigated in the Deep Underground Neutrino Experiment (DUNE) for instance. DUNE is a long-baseline accelerator experiments whose detector is located at the Homestake Mine, South Dakota, 1300 km from the Fermilab main injector where a 120 GeV proton beam incident on a graphite target generates ν_μ and $\bar{\nu}_\mu$ beams [101]. Important matter effect due to the presence of electrons and the absence of positrons in the Earth will take place, and the asymmetry can reach up to $\pm 40\%$ at the peak flux [101]. This asymmetry due to the matter effect is larger than the maximal possible asymmetry associated with the $\mathcal{CP}$-violating phase, $\delta_{\mathcal{CP}}$. Hence, both the mass ordering and the $\mathcal{CP}$-violating phase should be determined by DUNE. DUNE is expected to determine the mass hierarchy at the 5σ level for any value of $\delta_{\mathcal{CP}}$ after 2 years of running [102]. The other goals of DUNE is to measure precisely the parameters governing the $\nu_\mu \to \nu_e$ and $\bar{\nu}_\mu \to \bar{\nu}_e$ oscillations, to test the 3-flavor oscillation paradigm by studying ν_μ disappearance and ν_e appearance, to search for proton decay and eventually to detect the ν_e flux from a core-collapse supernova [101].

1.4.4 Violation of CP symmetry

As mentioned in Sec. 1.3.1.2, neutrino flavor oscillations also depend on a $\mathcal{CP}$-violation phase, $\delta_{\mathcal{CP}}$. The violation of the $\mathcal{CP}$ symmetry would translate into different oscillation probabilities in vacuum for neutrino and antineutrinos, which could help to understand the baryon asymmetry observed in the Universe [50]. A necessary condition to observe the $\mathcal{CP}$-violation in neutrino oscillation experiments is that all three mixing angles must be nonzero, a requirement that has been met in 2012 with the measurement of θ_{13}. Moreover, $\delta_{\mathcal{CP}}$ must be different from zero and π ($\mathcal{CP}$-conservation) and all neutrino masses should be different, mirroring the criteria for $\mathcal{CP}$-violation in the quark sector [50]. The $\mathcal{CP}$-violation effects are proportional to $\sin(\Delta m^2_{21} L/4E)$, and can only be observed in experiments measuring the subdominant oscillations governed by this squared mass difference. As such, the involved experiments must have long baselines of several hundreds of km.

An important program of long-baseline accelerator experiments will investigate $\delta_{\mathcal{CP}}$ in the coming years. First results reported by T2K in the search for $\mathcal{CP}$-violation in neutrino

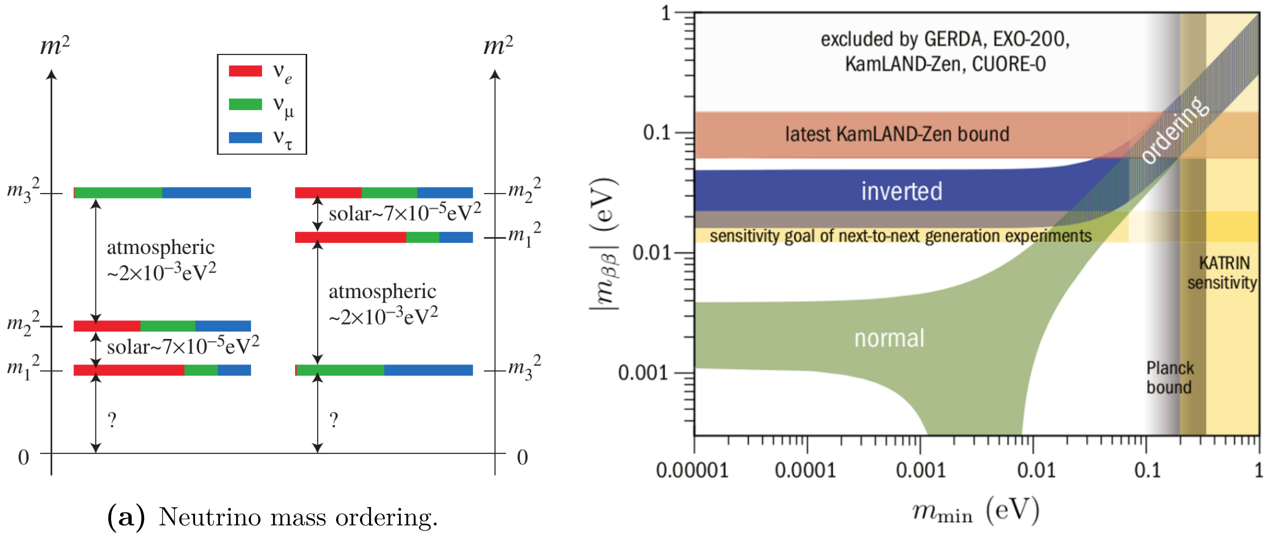

(a) Neutrino mass ordering.

(b) Exclusion limits of mass orderings.

Figure 1.7: **(a)**: Neutrino mass state ordering in the case of a normal (left) or inverted (right) hierarchy. The probability for a mass state to be projected onto a given flavor state is represented by the color segments in each rectangle. The figure is taken from [103]. **(b)**: Allowed region for the effective Majorana mass $m_{\beta\beta}$ versus the lightest neutrino mass. The figure is taken from [104].

oscillations exclude the $\mathcal{CP}$-conservation at 90% CL [105]. As the DUNE high energy ν_μ beam and large baseline will enhance the impact of the matter effect, the $\delta_{\mathcal{CP}}$ effect is decoupled from the mass ordering, allowing a measurement of $\delta_{\mathcal{CP}}$ for both hierarchies. DUNE is then expected to observed $\mathcal{CP}$-violation in neutrino oscillations to a precision of 3σ with an exposure of 5 years for 50% of all $\delta_{\mathcal{CP}}$ values [102].

Although $\mathcal{CP}$-violation is not a priority for JUNO's program, it can be used as a complement to conventional beam experiments [106]. Coupled to a cyclotron producing $\bar{\nu}_\mu$, JUNO would only be sensitive to the appearance of $\bar{\nu}_e$ in comparison with beam experiments. The $\bar{\nu}_e$ spectrum depends on the $\delta_{\mathcal{CP}}$ value and the measurement is independent of the mass hierarchy [106]. It is estimated that a 3σ significance can be reached for 22% of all $\delta_{\mathcal{CP}}$ values, where the dominant influence comes from the θ_{23} uncertainty.

1.4.5 Experimental anomalies, a hint toward additional neutrino species ?

The vast majority of experiments fits in the PMNS framework. Nonetheless, some tensions — or anomalies as they are called — between predictions and experiments have been observed. These results, if not caused by experimental artifacts, can be interpreted as a new oscillation channel with a fourth heavier sterile neutrino in the short baseline region $L/E \sim 1$ m.MeV^{-1} [15]. This neutrino would not weakly interact but could oscillate with other neutrinos. As such, the PMNS matrix is extended to a 4×4 matrix in a 3+1 model, U^{3+1}_{PMNS}, with a new massive eigenstate ν_4. According to the anomalies described thereafter, ν_4 would be the heaviest massive state such that $\Delta m^2_{41} \simeq 1$ eV^2. In the limit where Δm^2_{41} governs the oscillation and the other squared-mass differences can be neglected, the transition probability given at Eq. 1.8 reduces to:

$$P_{\nu_e \to \nu_e} = P_{\bar{\nu}_e \to \bar{\nu}_e} = 1 - \sin^2 2\theta_{ee} \sin^2 \left(\frac{\Delta m^2_{41} L}{4E} \right), \tag{1.31}$$

$$P_{\nu_\mu \to \nu_e} = P_{\bar{\nu}_\mu \to \bar{\nu}_e} = \sin^2 2\theta_{\mu e} \sin^2 \left(\frac{\Delta m^2_{41} L}{4E} \right), \tag{1.32}$$

where $\theta_{ee} \simeq \theta_{14}$ and $\theta_{\mu e}$ are effective mixing angles expressed in term of the U^{3+1}_{PMNS} entries. The experimental anomalies could be explained by the presence of more than one sterile neutrino (*e.g.* 3+2 scheme and 1+3+1 scheme [107, 108]). Even though tensions between the data can be slightly reduced when considering additional sterile neutrinos, the improvement seems to be mainly a statistical effect due to an increase in the number of free parameters [107, 108]. While the possibility of additional sterile neutrinos has still not been excluded, the 3+1 scheme is usually privileged for its simplicity in associating a new oscillation effect at short-baseline to one new particle. Thus, only the 3+1 scheme will be considered in the following. Other explanations for these anomalies are not excluded and are privileged, such as biases in experiments or in predictions. This last possibility will be discussed in the next chapter in the context of reactor experiments.

1.4.5.1 Gallium anomaly

GALLEX and SAGE both initially investigated the solar neutrino problem and ν_e disappearance as mentioned in Sec. 1.3.2. They found significant deficits in the measured solar neutrino flux with respect to the expected flux. To ensure the trustworthiness of their results, a check of the experimental techniques used to detect ν_e was performed. The detectors were exposed to intense radioactive sources of several tens of PBq of ^{51}Cr (as well as ^{37}Ar for SAGE), with well known activities and level energies. The energy of the emitted neutrino and the exposure conditions were close to those of a solar experiment. ^{51}Cr and ^{37}Ar both decay via electron capture:

$$^{51}\text{Cr} + e^- \longrightarrow {}^{51}\text{V} + \nu_e, \tag{1.33}$$

$$^{37}\text{Ar} + e^- \longrightarrow {}^{37}\text{Cl} + \nu_e. \tag{1.34}$$

In both experiments, the resulting ν_e were detected by interacting with ^{71}Ga to produce ^{71}Ge as in Eq. 1.18. The source activity could be directly measured by several techniques: the calorimetric method, the total gas volume, the total gas mass, using a proportional counter, the method of isotopic gas dilution (see [109–111] for more details). The measured source activity is then compared to the activity deduced from the measured production rate of ^{71}Ge. In all cases the measured event rate was lower than expected. Considering all the measurements, the average ratio of measured to estimated ^{71}Ge production is 0.86 ± 0.05 [16]. This deficit, significant at almost 3σ with respect to the no oscillation hypothesis, constitutes the *Gallium anomaly* (GA). This anomaly could be interpreted by an additional short-baseline ν_e disappearance as given by Eq. 1.31 in addition to the known neutrino oscillations [16]. The parameter space allowed by the Gallium anomaly data for this new oscillation is

$$\Delta m^2_{41} > 0.35 \text{ eV}^2 \text{ (99\% CL)}, \qquad \sin^2 2\theta_{ee} > 0.07 \text{ (99\% CL)}. \tag{1.35}$$

This deficit could also be partially explained by an overestimation of the transitions to two excited states of ^{71}Ge. In the absence of such transitions, the anomaly would reduce to a significancy level of 1.7σ [16]. A second contribution to this deviation could come from the estimation of the cross-section of the processes Eq. 1.17 and 1.18. Based on advanced nuclear computation, the cross-sections have been reevaluated to be 3.0% lower in [112], which would decrease the GA significance to 2.3σ.

1.4.5.2 LSND and MiniBooNE anomaly

The Liquid Scintillator Neutrino Detector (LSND) experiment was a short-baseline accelerator experiment started in 1993 at Los Alamos [17]. It was measuring $\bar{\nu}_e$ appearance from a $\bar{\nu}_\mu$ beam. The detector consisted in 167 tons of mineral oil with a low concentration of scintillating additive. The low scintillator concentration allows the detection of both Cherenkov and scintillation light. LSND provided the first evidence for $\bar{\nu}_\mu \rightarrow \bar{\nu}_e$ oscillations, with a 3.8σ significant excess of electron neutrino events with respect to the no-oscillation hypothesis [17]. However, the resulting mixing parameters were not consistent with the known solar and atmospheric parameters, with LSND pointing toward at least one neutrino having a mass greater than 0.4 eV [17].

The MiniBooNE experiment was then build at the Fermilab to test the LSND anomaly through the $\nu_\mu \rightarrow \nu_e$ and $\bar{\nu}_\mu \rightarrow \bar{\nu}_e$ oscillation channels [113]. The ν_μ ($\bar{\nu}_\mu$) beam, coming from pion decay, was intercepted at a L/E value close to the one from LSND, with L and E both an order of magnitude higher than LSND [114]. The background as well as the systematic uncertainties were different, thus making MiniBooNE an independent check of LSND results. Located at 500 m from the beam source, the detector consisted in a 806 tons of mineral oil using both scintillation and Cherenkov light for detection. The latest MiniBooNE analysis showed a 4.8σ significant excess of ν_e and $\bar{\nu}_e$ events observed in the range $200 < E < 1250$ MeV [18]. These excesses are consistent with the excess of events reported by LSND, both in energy and magnitude, and the analysis from [18] disfavors a background origin to explain these events. To properly interpret these results in a 2-flavor framework, a fourth neutrino is required that would generate ν_e through $\nu_\mu \rightarrow \nu_{new} \rightarrow \nu_e$, and equivalently for antineutrinos. The combined best-fit for LSND and MiniBooNE data is [113]

$$\Delta m^2_{41} = 0.041 \text{ eV}^2, \qquad \sin^2 2\theta_{\mu e} = 0.96. \tag{1.36}$$

The MicroBooNE experiment, currently taking data, has been designed as a check for MiniBooNE results, using the same beam facility and almost the same baseline than MiniBooNE. The detection technology is based on a Liquid Argon Time Projection Chamber (LArTPC), which can distinguish between electromagnetic showers of electron or photon origin with high efficiency. With this enhanced discrimination capacity, MicroBooNE is expected to address the origin of the ambiguous low energy electromagnetic excess seen in MiniBooNE at the level of 5σ [115].

1.4.5.3 Reactor antineutrino anomaly

Experimental discrepancies in the context of reactor experiments are addressed in the next chapter (see Sec. 2.3.1.1), with a proper introduction to reactor physics. One of them is presented here for its role in the emergence of the light sterile neutrino hypothesis. Before reactor experiments used near and far detectors to measure oscillations, experiments consisted in a single detector and the $\bar{\nu}_e$ flux emitted by the reactor core was analyzed with respect to a prediction accounting for the different isotopes of uranium and plutonium contributing to the flux. In the 1980s, such predictions for ^{235}U, ^{239}Pu and ^{241}Pu were proposed following electron spectrum measurements made at the Institut Laue-Langevin (ILL) [116–119]. From the measured electron energy spectra, $\bar{\nu}_e$ spectra were derived using the so-called conversion method, as described in Sec. 2.2.3.2.

Until 2011, the neutrino rates measured in various past reactor neutrino experiments with baseline inferior to 100 m were in reasonable agreement with the predictions, with an average ratio of observed event rate to predicted rate of 0.976 ± 0.024 [15]. In 2011, two independent reevaluations of the conversion method applied on the ILL measurements were performed [13, 14]. Consistent results led to an average increase of 3% of the $\bar{\nu}_e$ flux compared to previous calculations. Concurrently, the IBD cross-section was reevaluated based on the latest neutron mean lifetime, leading to an increase of about 0.4% [15]. Based on these newly predicted spectra and IBD cross-section, the ratio of the expected neutrino rate over the predicted one $R = \phi(\bar{\nu}_e)_{meas}/\phi(\bar{\nu}_e)_{pred}$ was recalculated in 19 short-baseline experiments ($L < 100$ m) [15]. The global analysis highlighted an average deficit of 0.943 ± 0.023, called the *Reactor Antineutrino Anomaly* (RAA). The current average ratio $\langle R \rangle = 0.934 \pm 0.024$ with a significance level of 2.8σ and is shown in Fig. 1.8 [120]. The corresponding best-fit is:

$$\Delta m^2_{41} = 0.48 \text{ eV}^2, \qquad \sin^2 2\theta_{ee} = 0.14. \tag{1.37}$$

1.4.5.4 The landscape of sterile neutrino experiments

All the anomalies discussed above could be addressed if a fourth sterile neutrino with a mass of about 1 eV^2 plays a role in oscillations in the region $L/E \sim 1$ m.MeV^{-1}. A global fit taking into account the four anomalies (gallium, LSND, MiniBooNE, RAA) disfavored the no-oscillation hypothesis at 99.8% C.L [15]. A series of experiments have then been designed to get a clear evidence or disproof about sterile neutrinos. Reactor experiments are especially suitable to perform very short baseline measurements at $L \sim 10$ m where this new oscillation is expected to appear. These reactor experiments will be discussed in Sec. 2.3.1.1. These experiments are still based on detecting $\bar{\nu}_e$ through IBD taking place in scintillator medium, as in former reactor experiments. However, the shortness of the baseline prevents the use of an even nearer detector. In order to scan different values of L, and hence measure a neutrino detection rate as a function of L/E, the detector is either segmented or moved at different baselines from the reactor core. At the moment, the results of these experiments seem to favor the null oscillation hypothesis (see discussion in Sec. 2.3.1.1 of the next chapter).

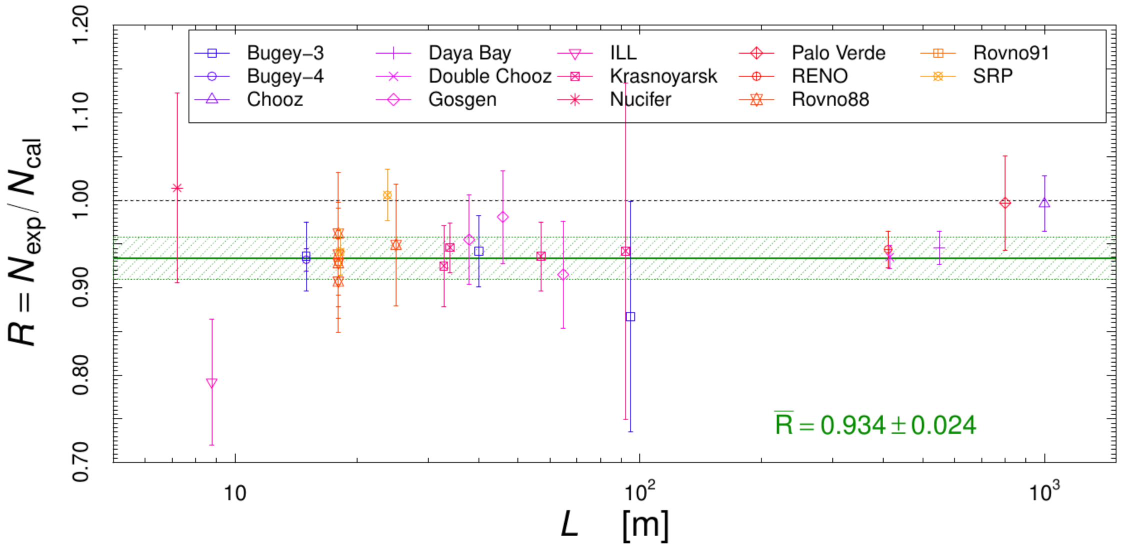

Figure 1.8: Ratio of observed to predicted IBD events for 14 reactor experiments, as a function of the baseline L. The green band shows the average ratio $\langle R \rangle$ and its 1σ uncertainty. The figure is from [120].

Sterile neutrinos are also investigated in non reactor experiments, a number of which are summarized along their key characteristics in Fig. 1.6. Designed to measure the effective neutrino mass, KATRIN can also constrain the mass of a fourth neutrino mass state and investigate its electronic flavor composition [121]. The mixing with a sterile neutrino would manifest as a distortion of the β spectrum at a few eV near the endpoint. The results, probing m_4 in the range 2 to 40 eV, have shown no significant sterile neutrino signal [121]. The KATRIN sensitivity, peaking around $m_4 \sim 20$ eV, excludes $|U_{e4}^2| \geq 2 \times 10^{-2}$ where U_{e4} is an element of the U_{PMNS}^{3+1} matrix and defines the mixing of electronic neutrinos with a fourth mass state. This search is complementary to reactor oscillation experiments and constrains the reactor sector for $\Delta m_{41}^2 \geq 10$ eV^2, excluding the allowed GA and RAA parameter space for 100 eV^2 $< \Delta m_{41}^2 <$ 1000 eV^2.

Accelerator-based experiments can also search for sterile neutrino oscillation signatures in their data. MINOS and MINOS+ are long-baseline accelerator experiments initially studying the atmospheric oscillation sector. A ν_μ beam of about 3 GeV is generated from the Fermilab's proton beam, and is intercepted by two detectors located at 1.04 km and 735 km [122]. The detectors can measure the ν_μ disappearance which is sensitive to oscillations involving sterile neutrinos at these energies and baselines. A combined fit of the two experiments did not show evidence of sterile neutrinos and has set the most stringent limit on $\sin^2 2\theta_{24} < 0.008$ (95% CL) for $\Delta m_{41}^2 > 10 \times 10^{-2}$ eV^2. IceCube is an experiment investigating neutrinos from extraterrestrial origins. Measuring atmospheric neutrinos as part of its background, IceCube can also study the impact of the mixing of a light sterile neutrino with active neutrino states on the atmospheric ν_μ flux [123]. Located at the geographic South Pole, IceCube is a Cherenkov detector measuring the disappearance of atmospheric neutrinos. IceCube has found no evidence for anomalous ν_μ and $\bar{\nu}_\mu$ disappearance in two independent analysis. The combined LSND and MiniBooNE allowed region has been excluded at 99% CL and the constraint on sterile to muon neutrino oscillation has been extended to $\sin^2 \theta_{24} \leq 0.02$ for $\Delta m^2 \sim 0.3$ eV^2 (90% CL). The MINOS/MINOS+ and IceCube results are in tension with those of LSND and MiniBooNE. While this θ_{24} oscillation takes no part in the RAA and possible active-sterile oscillations at reactor experiments, it shows that the sterile neutrino is a heavily disputed hypothesis not only in the reactor sector.

Numerous other experiments will also test the sterile neutrino hypothesis in the upcoming years. The LSND and MiniBooNE anomalies will also be tested by the Fermilab SBN Program, which consists of three experiments installed near the Booster Neutrino Beam-line (BNB): SBND (100 m from the beam target), MicroBooNE (470 m from the beam target) and ICARUS (600 m from the beam target) [124]. The BNB is a proton beam with a 0.7 GeV neutrino energy peak. It is used to search for ν_e appearance and ν_μ disappearance. The SBN program aims to cover 99% of the LSND-allowed region with a 5σ significance by studying the baseline dependence of the low energy excess in ν_e appearance and disappearance. The JSNS^2 experiment will test the LSND anomaly at the J-PARC installation in Japan [125]. A 3 GeV proton beam incident on a neutron target made of mercury produces muons at rest which decay via $\mu^+ \to e^+ + \bar{\nu}_\mu + \nu_e$. JSNS^2 will search for $\bar{\nu}_e$ appearance from the $\bar{\nu}_\mu$ beam, with a liquid scintillator detector located at 24 m from the mercury target. Hyper-Kamiokande is a long-baseline accelerator experiment, with two Cherenkov detectors located at 295 km from the J-PARC. Together with DUNE, they are sensitive to a possible mixing with sterile neutrinos and will complete the mixing parameter region $\Delta m_{41}^2 < 10 \times 10^{-2}$ eV^2 [126].

Finally, active-sterile oscillation can be observed through Coherent Elastic Neutrino-Nucleus Scattering (CEνNS) [127]. While neutrino of any energy can interact through this channel, in practice the detector sensitivity results in a threshold of at least a few hundreds keV. This process is investigated in experiments measuring reactor $\bar{\nu}_e$ fluxes, and can provide a complementary test to IBD experiments. A more complete description of this process is done in Sec. 2.3.2 of the next chapter with a review of on-going experiments.

1.5 Summary

In hindsight, unraveling the properties of the neutrino has helped to establish the electroweak sector of the Standard Model, with for instance the discovery of the violation of the parity symmetry in weak interactions. The properties of neutrinos actually went beyond expectations, with the discovery of the neutrino flavor oscillations, suggesting the existence of neutrino masses. Many questions revolving around the neutrino mass, its origin and the smallness of its absolute scale, are currently under investigation. The Dirac or Majorana nature of the neutrino is also actively researched. With decades of research performed with different sources of neutrinos, the oscillation phenomenon is now well documented. Oscillations fit in a robust theoretical framework, albeit not yet included in the Standard Model. All the parameters entering the standard PMNS matrix have been measured to different degrees of precision, at the exception of the $\mathcal{CP}$-violating phase which investigation is now within reach of future accelerator-based experiments after θ_{13} has been precisely measured by reactor experiments.

With the increase of precision in detection techniques, new anomalies not fitting this standard paradigm have been observed, such as the gallium anomaly, the LSND and MiniBooNE anomaly and the reactor antineutrino anomaly. A possible explanation for these anomalies is the existence of a new oscillation channel with a sterile neutrino with a mass of the order of 1 eV. The sterile neutrino hypothesis is thoroughly investigated as it could be another evidence for physics beyond the Standard Model. In particular, very short-baseline reactor experiments are well suited to test the sterile neutrino hypothesis and will soon address its existence. Nuclear reactors are at the origin of an intense neutrino flux, and are presented in this context in Ch. 2.

2

Reactor neutrinos and physics motivation

Contents

Reactor neutrinos are the topic of this chapter, from their production in reactors to their detection. The first section describes the chain reaction of fission at the origin of the power generation in a reactor. The composition of the fuel used in a nuclear reactor is also presented. The different sources of reactor $\bar{\nu}_e$ are presented in the second section. A review of the different methods that can be used to predict the flux and energy spectra of these sources is described. The interaction processes most commonly used in reactor experiments to detect neutrinos are presented in a third section. The different anomalies between the measured IBD rates and spectra of reactor experiments and the predictions are discussed in the last section.

2.1 Nuclear reactors

A nuclear reactor is a device that produces energy through the fission of heavy nuclei. It can be used for electrical power generation in nuclear power plant, military or research purpose. Commercial and research reactors differ in their purpose, but both are sources of an enormous flux of antineutrinos, typically 2×10^{20} $\bar{\nu}_{\mathrm{e}}$/s per $\mathrm{GW_{th}}$. While the power of research reactors is lower compared to commercial reactors, it is possible to install a detector at a closer distance from the reactor core. Nuclear reactors then constitute ideal tools to study the neutrino properties as they balance its very low interaction probability, give access to a pure $\bar{\nu}_e$ flux, and do not need to be build. The fission chain reaction and the interaction processes that result in the emission of antineutrinos at commercial and research reactors are presented in this section.

2.1.1 Fission chain reaction

A fission is a process where a heavy nucleus splits into two lighter nuclei[1] called fission fragments. Fission results from the competition between the nuclear binding energy and the Coulomb repulsion due to the protons. A fission can be spontaneous or induced by an incident particle. The non-spontaneity of fission for some nuclei is due to the existence of an energy threshold of a few MeV, preventing the splitting in normal circumstances [129]. This extra energy is brought by the incident particle, a neutron in the case of nuclear reactor. Once the energy wall is overcome, an induced fission releases about 200 MeV of energy. Most of it (82%) comes from the kinetic energy of the fission fragments [130]. The rest of the energy comes from the emission of β particles, γ-rays and neutrons from the fission fragments and their subsequent fission products, either directly after the fission (11%) or after a delay (7%). The energy is then released in the surrounding environment and results in heat radiation from the reactor core. As neutrinos easily escape the nuclear core, their energy does not contribute to the radiated 200 MeV.

Nuclear reactors generate energy at a steady pace by keeping fissions occurring through a controlled chain reaction. On average, about 2.5 neutrons are emitted per fission [129]. They can either be absorbed by the fuel or the structural materials of the reactor core, leak from the core or induce another fission. The new fission would give birth to neutrons of the next generation, maintaining the chain reaction. The chain reaction is then characterized by the effective multiplication factor k_{eff} expressed as [131]

$$k_{eff} = P_{NL}\frac{n_f}{n_a} = \frac{n_f}{n_a + n_l}, \tag{2.1}$$

with P_{NL} the non-leakage probability, n_l the number of neutrons that have leaked, n_a the number of neutrons absorbed among the neutrons emitted per fission and n_f the number of neutrons not absorbed and available to induce a new fission. At each generation of neutron, the

---

[1] Ternary fissions, where the heavy nucleus splits into three lighter nuclei, are rare events occurring in approximately 0.1% of the cases [128]. Quaternary fissions are even rarer, occurring in less than 1 out of 10^7 fissions.

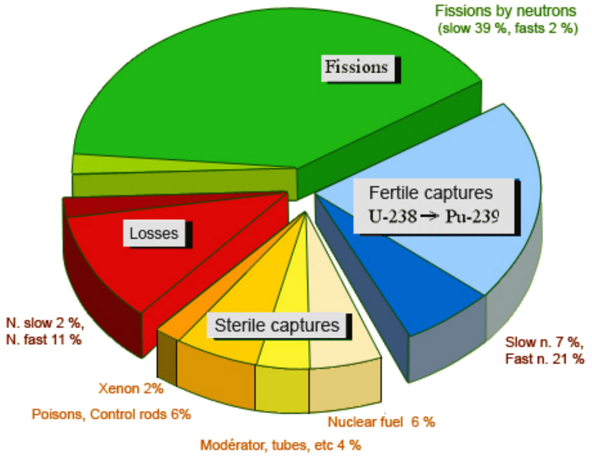

Figure 2.1: Balance of thermal and fast neutrons in a pressurized water reactor. Only 40% of fission neutrons are used to sustain the chain reaction. The figure is taken from [132].

neutron population is multiplied by k_{eff}. The chain reaction is self-sustaining when $k_{eff} = 1$, and the reactor is said to be critical with a neutron population kept constant. If $k_{eff} > 1$, the production of neutron exceeds the absorption and the leakage and the reactor is supercritical, with a neutron population increasing for each generation. On the other hand, if $k_{eff} < 1$, the absorption and leakage of neutrons are greater than the production and the reactor is subcritical, with a decreasing neutron population. During a cycle of irradiation, the modification of the fuel inventory content is responsible for a change of the fission and absorption rates, which result in a decrease of k_{eff}. In order to counter-balance this effect, the reactor starts operating in a supercritical state. The criticality is ensured and controlled by the use of neutron poisons, which are isotopes with high neutron absorption cross-sections that will compete with the fission. A tuning of the poison concentrations can compensate for the local surges of power due to temperature and neutron irradiation effects, and even shut down the chain reaction for safety reasons [130]. The management of the poison concentrations also allows to counterbalance the decrease of the neutron flux along the fuel depletion and to ensure that the power is uniformly distributed over the core. The balance of neutrons in a commercial reactor is shown in Fig. 2.1.

2.1.2 Fission neutrons

Between 0 and 7 neutrons are evaporated by the fission fragments before they interact with matter, approximately 10^{-7} s after the fission [133]. These prompt neutrons have an energy spectrum, also called fission spectrum, well approximated by a Maxwell distribution peaked at 2 MeV [133]. Prompt neutrons make more than 99% of the neutron flux resulting from a fission, the remaining ones being delayed neutrons emitted a few moments after the occurance of a β-decay [133]. The time gap between the fission and the emission of delayed neutrons ranges from the second to the minute, far greater than the few microseconds a neutron spends on average in a reactor before being absorbed or leaked. This time lapse corresponds to the time between the fission and the β-decay of a fission fragment, the prompt neutron emission being comparatively instantaneous. Delayed neutrons are less energetic than prompt ones, with an energy between 0.2 and 0.6 MeV [133], and are fundamental in the control of the criticality of the reactor. By increasing the effective neutron lifetime in the reactor, delayed neutrons smooth the variation of the criticality following an increase or a decrease of the neutron flux, allowing a better control of the chain reaction [133]. For instance, a neutron population would grow through 40 000 generations in one second without delayed neutrons. For a supercriticity

	^{235}U	^{238}U	^{239}Pu	^{241}Pu
Prompt neutrons n_p	2.414	2.486	2.871	2.929
Delayed neutrons n_d	0.017	0.044	0.006	0.016
$n_d/(n_p + n_d)$ [%]	0.70	1.77	0.22	0.55

Table 2.1: Average number of prompt and delayed neutrons emitted per fission induced by a thermal neutron for ^{235}U, ^{239}Pu and ^{241}Pu and induced by a fast neutron for ^{238}U. The data are obtained from the ENDF/B-VIII.0 database [134].

state of $k_{eff} = 1.0001$, the reactor thermal power would be enhanced by a factor 55 during that same second [133]. With delayed neutrons, there are only 13 effective neutron generations per second, and the power increases by a factor 1.001 during that one second instead, allowing to control the evolution of a reactor with much more ease [133].

Once emitted, neutrons interact with surrounding nuclei via elastic scattering as well as inelastic scattering at high energy [133]. During these processes, the neutron energy decreases after each collision[1]. The neutron slows down from 20 000 km/s (speed of a 2 MeV neutron) to a few kilometers per second (neutron speed for a hundredth of eV). This process is called *thermalization* or *moderation*, and neutrons end up in a state near thermal equilibrium with the environment. Neutrons in this state of quasi thermal equilibrium are called thermal neutrons. In nuclear reactors, the thermalization is optimized by the use of a medium called moderator. The energy spectrum of neutrons in the moderator is then made of three components displayed in Fig. 2.2 [133]. The high energy part of the spectrum is the fast component, which can be conventionally defined for $E_n > 10$ keV. The fast component is the residual of the fission neutron spectrum after thermalization, which is reflected by the Maxwell-like distribution around 2 MeV. The sharp dips in the fast regime reflect the resonances in the elastic scattering cross-sections of the moderator and other structural elements [131]. The thermal component constitutes the low energy part of the spectrum, with $E_n < 0.625$ eV as a convention [137]. This component reflects the neutron distribution after thermalization. It can be approximated by a Maxwell-Boltzmann distribution peaked around the temperature of thermal agitation[2], only slightly shifted toward high energy as the thermal equilibrium is not completely reached. The epithermal regime lies in between. The sharp dips observed in this energy range correspond to resonances in the capture and fission cross-sections of fissionable isotopes [131].

2.1.3 Thermal and fast neutron reactors

Nuclear reactors fall into one of two categories, depending on the type of neutrons used to induce fission. Thermal reactors are based on thermalized neutrons in order to take advantage of the high fission cross-section associated to thermal neutrons as showed in Fig. 2.3. These reactors require the use of a moderator, which is a relatively dense medium composed of light nuclei [130]. In addition, the light nuclei should also have a low neutron capture cross-section. As the average energy loss per elastic collision is inversely proportional to the target nuclei mass, neutrons are thermalized all the faster the lighter the nuclei. The moderator must be contiguous to the fuel location so that neutron losses are minimized, not jeopardizing the probability to make a fission. Its proximity with the fuel makes the moderator a candidate of

---

[1] The neutron energy can occasionally increase during thermalization due to thermal agitation. However, the overall effect is still a decrease of the neutron energy.

[2] The energy associated to the thermal agitation at $T = 293.15$ K is $kT = 0.0253$ eV [133].

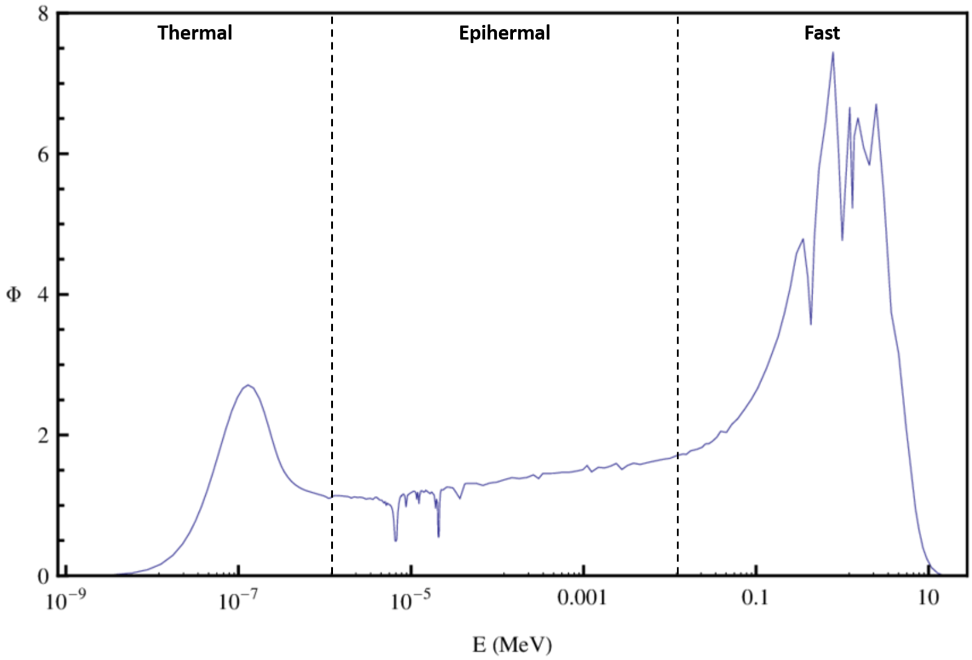

Figure 2.2: Neutron energy spectrum in a PWR and associated to a fresh fuel made of UO_2 enriched at 3.1%. The ordinate axis is given as a flux per unit lethargy $\mathrm{d}\phi/\mathrm{d}\ln E$. Thus, the displayed height of the neutron spectrum increases with higher energies. The low energy bump reflects the thermalization of neutrons, and the high energy bump corresponds to the fission spectrum of neutrons. The figure is taken from [135].

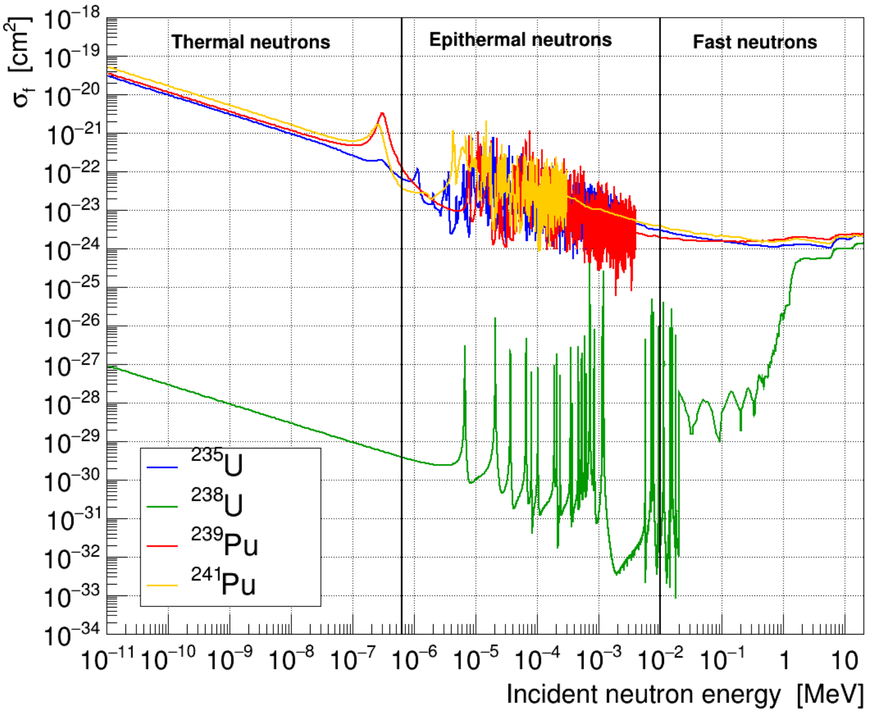

Figure 2.3: Fission cross-section of the main fissionable isotopes ^{235}U, ^{238}U, ^{239}Pu and ^{241}Pu. The data are obtained from the JEFF-3.3 database [136].

choice to also act as the coolant, which is the heat transfer medium. Water (H_2O) and heavy-water (^2H_2O) have high heat capacities, and are used as a combined moderator and coolant in pressurized water reactors and boiled water reactors. However, the hydrogen in natural water has a high neutron capture cross-section resulting in a significant loss of thermal neutrons [130]. The use of natural water as a moderator then forbids the use of natural uranium as fuel. Other media have the appropriate properties to act as moderator. For instance graphite — should it be purified from boron and present in large volume next to the fuel — can be used to moderate neutrons from natural uranium [130].

In fast neutron reactors, the use of a moderator is excluded. To minimize neutron energy losses, the reactor core is compact, and the coolant is not composed of light nuclei as they slow down neutrons. The coolant can then be made of gases to compensate an undesired increase of the moderation efficiency on light nuclei with a low density media (*e.g.* carbon dioxide, helium), or by using molten metals which have better heat capacity than gases (*e.g.* lead, bismuth, potassium, sodium) [130]. To compensate for the low fission cross-section associated to fast neutrons, the fuel must be highly enriched in fissile isotopes and the neutron flux must be higher than in thermal reactor. Additionally, fast neutron reactors run at higher temperatures increasing the power efficiency of the reactor. The breeding of fertile isotopes into fissile isotopes is possible in fast neutron reactors thanks to the high neutron flux and its positive neutron balance [130]. For example, neutron captures on ^{238}U result in the production of ^{239}Pu (see reaction 2.2). Finally, fast neutron reactors are suitable for fuel regeneration with more fissile isotopes produced than consumed [133].

Fast neutron reactors are compact reactor allowing for fertile breeding and fuel regeneration. However, they require challenging materials for the coolant and for the fuel, and present inherent radiological and chemical risks [138]. Thermal reactors have then been the standard to produce energy across the world for decades. Most of the commercial reactors currently running are thermal reactors, while fast neutron reactor are mainly limited to a few research reactors or for breeding purpose [139]. Reactor neutrino experiments are all located near thermal nuclear reactors. As such, only these reactors are considered in the following.

2.1.4 Pressurized water reactors

Approximately 67% of the commercial reactors are pressurized water reactors (PWR) [139]. Besides research reactors, only PWR are used as neutrino sources in reactor experiments. In France, a PWR-N4 reactor type is typically run at a thermal power of 4270 $\mathrm{MW_{th}}$ [140]. A scheme of the general principle of a PWR is showed in Fig. 2.4.

In a PWR, fuel assemblies are located in the reactor vessel and immersed in water (used as moderator and coolant) constituting the primary loop (see Fig. 2.5a). A pressure of 155 bars is applied by the pressurizer to the water of the primary circuit in order to maintain its liquid state [130]. The water enters from the bottom of the core vessel at a temperature of about 290 °C. There, it passes through the assemblies and as it exits from the top of the core, the water temperature has increased by about forty degrees. It then reaches a steam generator where the water exchanges its heat with the water from the secondary loop.

The water in the secondary loop is kept under 70 bars of pressure, and gets vaporized in the steam generator when in contact with the water from the primary circuit. The vapor is sent in a series of turbines coupled to alternators which generate electricity. When exiting the turbines, the vapor is sent to the condenser where it is cooled down to return to its liquid state, before being send back to the steam generator.

The tertiary loop supplies the condenser with fresh water to cool the vapor exiting the turbines. Depending on the nuclear power plant location, the fresh water comes from a river, from the sea or from another closed circuit. The water in the tertiary loop is cooled down in cooling towers. About one third of the energy released by fissions is converted into electricity. The other two thirds are evacuated in the tertiary loop, where the water temperature does not increase by more than a few tens of degrees.

2.1.4.1 Fuel composition

PWR fuel is made of uranium dioxide (UO_2) lowly enriched in ^{235}U. UO_2 is contained into sintered pellets of 8 mm diameter and 14 mm height [137]. Pellets are stocked together in shell of zirconium alloy of 4 m length, constituting a fuel rod as shown in Fig. 2.5a. Fuel rods are filled with helium with a spring to maintain the fuel pellets at the top. The fission fragments produced in gaseous form will fill the space as the spring is compressed. The number of assemblies and rods per assemble depends on the PWR type. For a typical PWR-N4 reactor used in France, there are 264 rods per assembly with 205 assemblies per core [140]. The UO_2 mass contained in a fresh assembly is about 608 kg, for a total fuel mass of about 125 tons in a reactor core [142]. A few tens of empty tubes ensure the mechanical rigidity of the structure and can host control rods. Finally a single tube at the center of the assembly is dedicated to flux monitoring instruments [130]. Depending on the output nuclear power, hundreds of assemblies are packed in a core in a cylindrical pattern.

The abundance of ^{235}U in natural uranium — a mix of ^{238}U (99.27%), ^{235}U (0.72%), and some traces of ^{234}U (0.005%) [143] — is not enough to sustain the chain reaction in a PWR. PWR require the use of fuel enriched in fissile isotopes, such as ^{235}U or ^{239}Pu. The initial enrichment in ^{235}U of fresh fuel is typically between 3% and 5% of the uranium mass[1] [130]. ^{235}U is the only isotope found in nature that is fissile, *i.e.* that can fission under a thermal neutron flux.

2.1.4.2 Fuel evolution and reactor cycle

Other fissile isotopes must be produced artificially using fertile isotopes. ^{239}Pu is produced by neutrons captures on ^{238}U:

$$^{238}_{92}\mathrm{U} \xrightarrow{(n,\gamma)} {}^{239}_{92}\mathrm{U} \xrightarrow[t_{1/2}=23\ \mathrm{min}]{\beta^-} {}^{239}_{93}\mathrm{Np} \xrightarrow[t_{1/2}=2.4\ \mathrm{days}]{\beta^-} {}^{239}_{94}\mathrm{Pu}, \tag{2.2}$$

where (n, γ) is a radiative capture, *i.e.* a neutron capture followed by the emission of one or more γ-rays. In a PWR, about 7% of thermal neutrons and 21% of fast neutrons are used to generate ^{239}Pu, as shown in Fig. 2.1. ^{239}Pu α-decays with a half-life of 2.4×10^4 years, which makes it practically stable during a cycle of irradiation besides fissions. However, it can capture neutrons leading to the production of ^{241}Pu:

$$^{239}_{94}\mathrm{Pu} \xrightarrow{(n,\gamma)} {}^{240}_{94}\mathrm{Pu} \xrightarrow{(n,\gamma)} {}^{241}_{94}\mathrm{Pu}, \tag{2.3}$$

making ^{235}U, ^{238}U, ^{239}Pu and ^{241}Pu the principal isotopes sustaining the chain reaction in a PWR. They produce more than 99% of the thermal power released by a reactor core, and

---

[1] A second type of fuel used in PWR is the MOX, a mix of a few percents of PuO_2 (made by recycling the plutonium produced in standard assemblies) and UO_2 (made of natural uranium or with uranium depleted down to 0.2%) [130]. For safety reason, the use of MOX fuel is limited to a third of the assemblies, the two other thirds being standard UO_2 assemblies.

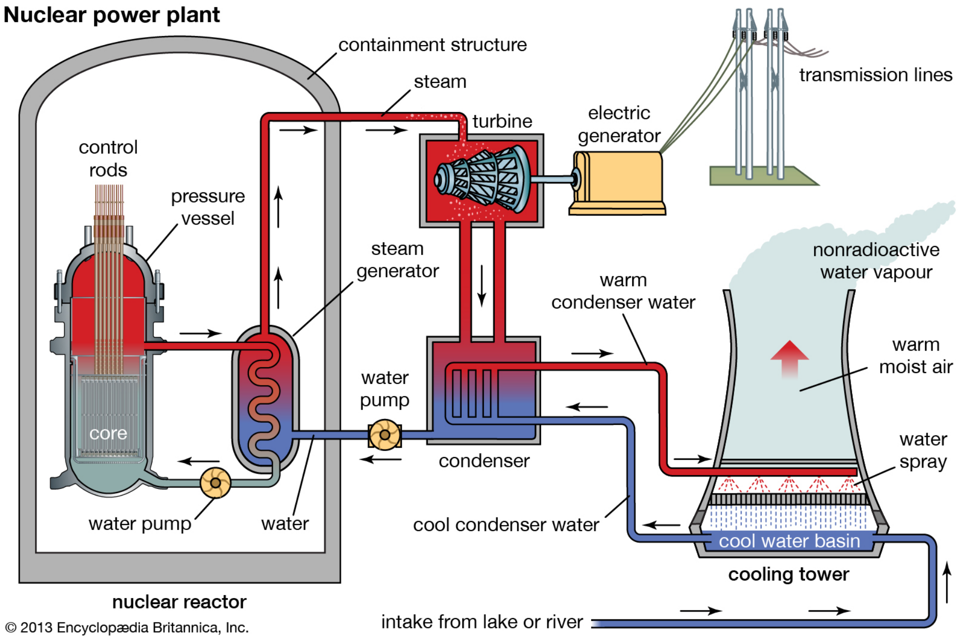

Figure 2.4: Schematic view of the working principle of a water reactor. See text for more details. The figure is taken from Encyclopædia Britannica [141].

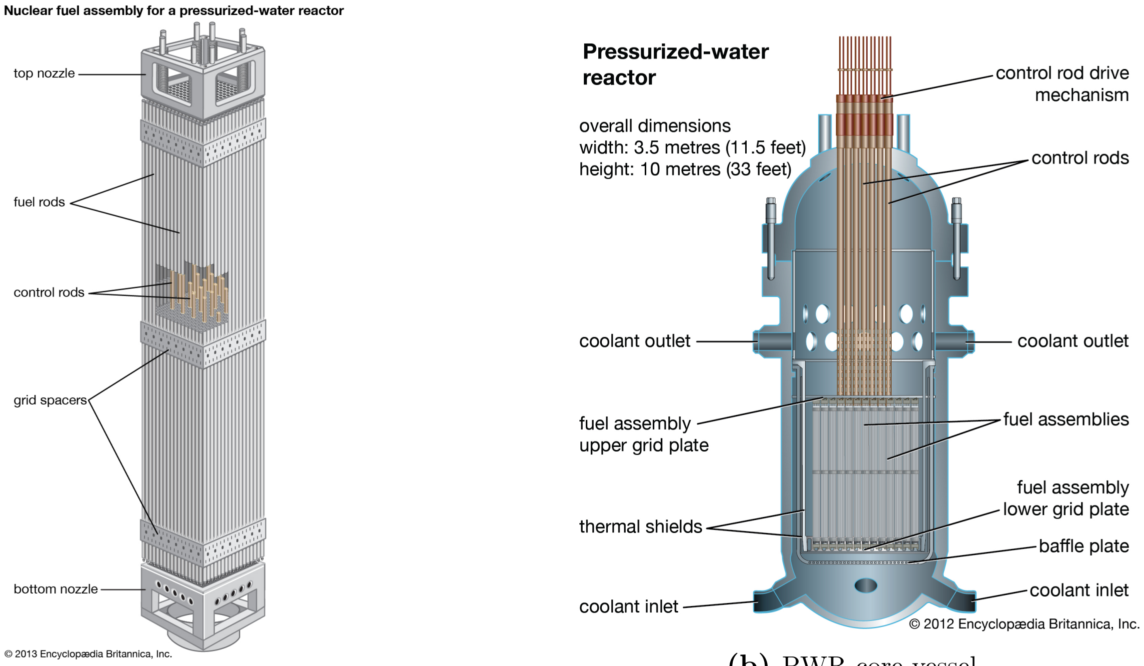

(a) Assembly.

(b) PWR core vessel.

Figure 2.5: Schematic view of an assembly **(a)** and cross view of a PWR core vessel **(b)**. The figures are taken from Encyclopædia Britannica [141].

the inventory of fission products is built almost entirely from their fissions. Other fissionable isotopes produced during irradiation such as ^{236}U, ^{240}Pu or ^{242}Pu only have a minor contribution to the fission. These secondary isotopes can be neglected in the chain of fission, their fission rate being marginal.

The amount of energy extracted from a nuclear fuel is called burnup [137]. The burnup at time t is expressed as:

$$B(t) = \frac{\int_0^t \mathrm{d}t'\; P_{th}(t')}{M_f}, \tag{2.4}$$

with P_{th} the instantaneous thermal power delivered by the reactor in MW$_{\mathrm{th}}$, M_f the initial mass of heavy nuclei in tons. The burnup is usually expressed in thermal megawatt day per ton (MWd/t). The burnup characterizes the fuel depletion regardless of the power history. The burnup is an interesting variable as the inventory of a nuclear fuel only depends on its initial enrichment and its burnup in first approximation.

The fresh fuel is made of ^{238}U and ^{235}U. The total fission rate is then dominated by the fission of ^{235}U at first, with a small contribution of ^{238}U. During a cycle of irradiation, ^{239}Pu and ^{241}Pu are produced while ^{235}U is depleted. Hence, the fission rates of ^{239}Pu and ^{241}Pu increase while the ^{235}U fission rate decreases over time. The mass and the fission fraction of ^{238}U are approximately constant during a cycle. A typical example of the evolution of the fission fractions — which are the isotope fission rates normalized to the total fission rate — in UO$_2$ assemblies are showed in Fig. 2.6a.

Reactors typically operate at their nominal power for periods of about one year which are called reactor cycles. Between two cycles, the reactors are stopped for a few weeks[1] and burnt fuel assemblies are discharged and replaced with fresh fuel assemblies. The length of the cycles, of the refueling period, and the number of discharged assemblies depend on the type of reactor. Typically, about one third of the assemblies are discharged during a refueling period. The ordering of the remaining assemblies and the fresh ones is arranged to flatten the neutron flux across the core to prevent local power rising, to optimize the global power delivery and to limit the number of fast neutrons that could harm the reactor vessel protecting the core [130]. An assembly is typically irradiated during three cycles, for about 15 GWd/t per cycle and around 30 to 50 GWd/t after three cycles. The evolution of the fission fractions in a reactor core over one irradiation cycle is showed in Fig. 2.6b. The averaged fission fractions of ^{235}U, ^{238}U, ^{239}Pu, and ^{241}Pu over a 12-month reactor cycle are typically of 56%, 9%, 29% and 6% for a PWR-N4 [145].

2.1.5 Research reactors

Contrarily to commercial reactors, the purpose of research reactors is not to produce electricity. Instead, they are used as neutron sources for non-destructive testing, studying the behavior of materials and nuclear fuels, production of radioisotopes or in the case of interest as neutrino sources. Each research reactor has its own design, and run at a thermal power typically below 100 MW$_{\mathrm{th}}$ [146–149]. The operation times of research reactors are typically of a couple of months, and their fuel is made of highly enriched uranium formed into different compounds according to the reactor design. Fission then predominantly originates from ^{235}U in research reactors, with an ^{235}U fission fraction typically above 99%. Only four research reactors host very short baseline experiments: STEREO at the ILL reactor in France [146], PROSPECT at the ORNL reactor in the USA [147], Neutrino-4 at the SM-3 reactor in Russia [148], and SoLid at the BR2 reactor in Belgium [149]. Because of its numerous uses in the context of $\bar{\nu}_e$ experiment, a brief description of the ILL reactor is given.

---

[1] Typically six to eight weeks in France [144].

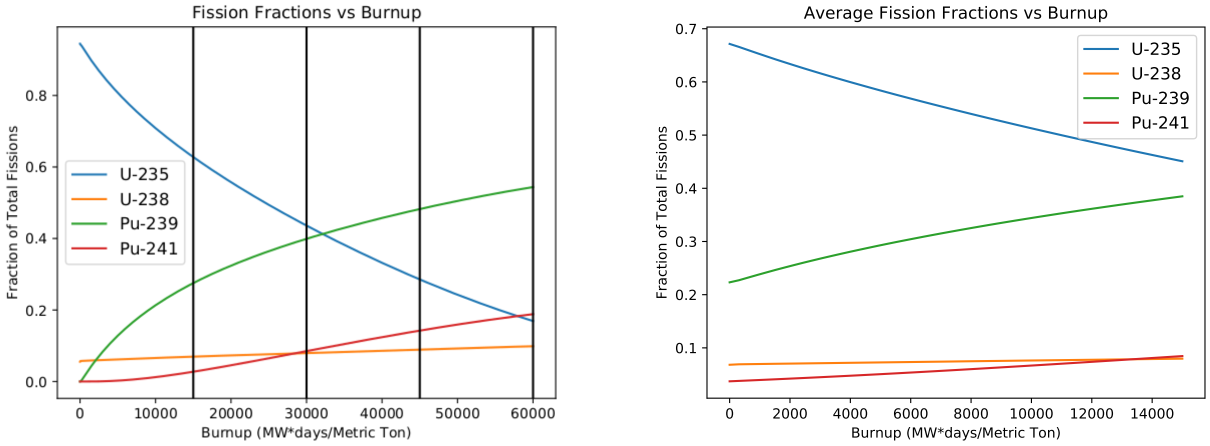

(a) Assembly evolution.

(b) Reactor core evolution.

Figure 2.6: Fission fraction evolution with respect to the burnup in an assembly **(a)** and in a reactor core **(b)** using UO_2 fuel enriched at 4%. The core is loaded with one third of fresh assemblies, one third of assemblies irradiated up to 15 GWd/t, and another third of assemblies irradiated up to 30 GWd/t. The back lines in **(a)** indicate typical stages at which core refueling occurs.

The High Flux Reactor at the ILL

The High Flux Reactor (HFR) located at the Institut Laue-Langevin only has a single fuel element arranged in a hollow cylinder of 40 cm diameter [150]. The fuel element is contained in a tank of 2.50 m diameter filled with heavy water serving as coolant and moderator, as shown in Fig. 2.7. A light water pool of 6 m diameter surrounds the heavy water tank to ensure the biological shielding. For the purpose of different experiments, 13 horizontal beam tubes and 4 inclined beam tubes guide the neutron flux out to 100 m from the core [150].

The fuel consists in 10 kg of uranium aluminide (UAl_x) enriched at 93%, and arranged in 280 curved plates cladded in aluminum alloy [151]. The production of plutonium is marginal, with an average ^{239}Pu fission fraction over a 50-days cycle of 0.7%. The fission fractions of ^{238}U and ^{241}Pu are completely negligible. The HFR has a nominal thermal power of 58.3 $\mathrm{MW_{th}}$, and operates for cycles of about 50 days before shutting down for refueling and maintenance operations [146]. The fuel element is replaced every cycle. The resulting neutron flux inside the moderator is about 1.5×10^{15} neutron/cm^2/s, making it one of the highest continuous fluxes worldwide.

The HFR is particularly suitable to conduct very short baseline neutrino oscillation experiments due to its compact core and small overall dimensions. Detectors can then be located closer to the core than in the case of a commercial reactor, which increases the receive $\bar{\nu}_e$ flux and balances the lower thermal power. For instance, a detector located at 10 m from the HFR receives the same $\bar{\nu}_e$ flux than if it was located at 85 m from a PWR-N4 core.

2.1.6 Distribution of fission products

Fission fragments (FF) are the primary nuclei directly produced from fission, after neutron evaporation but before the emission of delayed neutrons [153]. They are to be differentiated from the fission products (FP) which include the FF as well as the isotopes subsequently generated by the FF decays and neutron activation.

The fraction of a FF produced per fission is called independent fission yield (IFY). As showed in Fig. 2.8, the IFY distribution has a characteristic double bump profile approximately

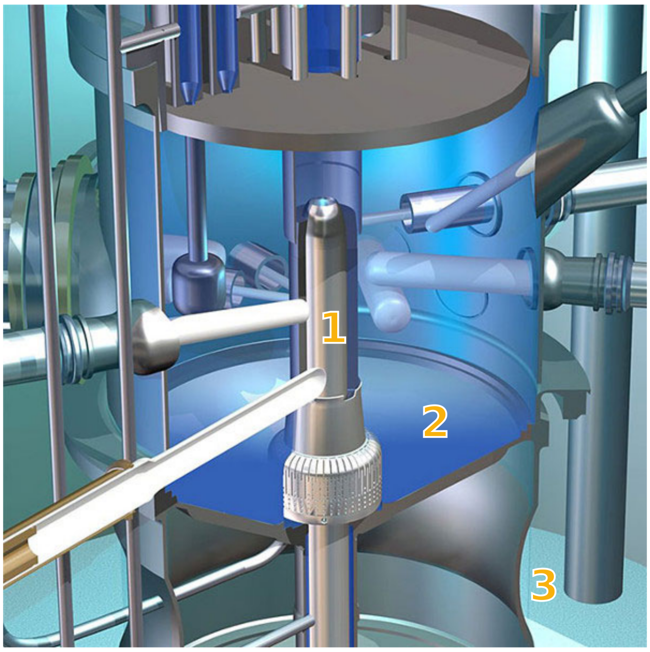

Figure 2.7: 3D cross section of the HFR at the ILL. The fuel element (1) is located at the center of the heavy water tank (2), itself immersed in pool of natural water (3). The figure is taken from [152].

symmetric about the center, reflecting the fact that FF are preferentially produced around the magic numbers of nucleons[1] [137]. An island of very light nuclei ($A \lesssim 20$) is present due to ternary and quaternary fissions. The distribution depends on the incident neutron energy and on the fissioning isotope. The resulting $\bar{\nu}_e$ energy spectrum will then be specific to each fissioning isotope. IFY are normalized to the number of FF produced per fission which is 2[2]. For the ^{235}U fission yields (FY) obtained for a thermal neutron flux, the most probable FF are centered around A=95 and A=140 and are obtained in 6.5% of the fissions, while a symmetric fission with A=118 occurs only in 0.012% of the cases. FF with equal masses are favored when the energy of the incident neutron increases. For neutrons with energy of tens of MeV, the valley observed in IFY distribution nearly disappears [131].

FF and their daughter nuclei are usually rich in neutrons. They can decay through different channels, which can be gathered into three categories summarized in Tab. 2.2: decays with emission of at least one electron (B^-), electron capture and decays with emission of at least one positron (B^+) and isomeric transitions (IT). A summary of the particle emission in FF is presented in Tab. 2.3. About 90% of the FF are β^- emitters due to being neutron rich, with only 10% being already stable. The neutrons emitted after a β-decay are the delayed neutrons. The α particles, protons, positrons and ν_e emitted subsequently to a β-decay are negligible. Hence, the FF mostly β-decay to become stable isotopes.

All FP eventually become stable nuclei at the end of the decay chains. FF are continuously produced throughout the fission chain reaction. On the other hand, FP are produced from the decays and processes involving FF and other FP. The evolution of the FP inventories under a neutron flux is then described by the Bateman equation [137, 154]. By solving the Bateman equations simultaneously for a set of FP and an input neutron flux, one can obtain a picture of the inventory of FP at any irradiation time. If the production rate of a FP is constant, it

---

[1] A magic number of nucleons, either protons or neutrons, corresponds to nucleons arranged into complete shells within the nucleus. A nucleus with a magic number of protons or of neutrons is particularly stable.

[2] If the ternary and quaternary fissions are considered, the IFY from the JEFF-3.3 database [136] sum up to 2.0019 for ^{235}U, 2.0016 for ^{238}U, 2.0024 for ^{239}Pu and 2.0020 for ^{241}Pu.

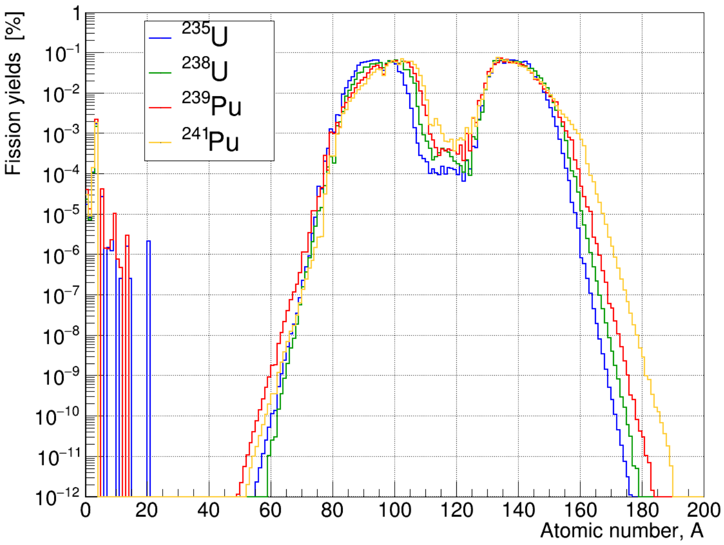

Figure 2.8: Distribution of independent thermal fission yields of ^{235}U, ^{239}Pu and ^{241}Pu and of independent fast fission yields of ^{238}U. The fission yields are taken from the JEFF-3.3 database [136].

will be balanced by the FP decay rate after several half-lives, and the FP population will reach an equilibrium state [131]. The population of FP with short half-lives compared to the reactor core operating time will then be proportional to the reactor power. On the other hand, the population of FP with long half-lives will build linearly with the burnup.

The fractions of FP obtained after all the products have reached equilibrium — technically for an infinite amount of time due to very long-lived nuclei — are called cumulative fission yields (CFY). Once the FP decay rates have reached an equilibrium state, up to hundred more stable nuclei have appeared, constituting now about 20% of the FP. Similarly, the number of β^- emitters increase for all four actinides, with a final repartition of about 80%. Finally, the FY values change and result in β^- and $\bar{\nu}_e$ fluxes about three times higher than for IFY, as shown in Tab. 2.2. This mostly reflects the cascade of β-decays of FP. Note, however, that the other particle fluxes are only slightly modified.

The IFY and CFY are provided by libraries such as ENDF/B-VIII.0 [134], JEFF-3.3 [136] and JENDL/FPY-2011 [156] for three types of incident neutron fluxes. The high-energy, fast and thermal fission yields correspond respectively to an incident neutron energy of 14 MeV, 400 keV and 0.0253 eV. The FY are evaluated based on experimental data as well as on models. For instance, the JEFF-3.3 database is built by performing a statistical analysis of a database of experimental measurements to estimate a set of recommended IFY and CFY and their corresponding uncertainties [136, 153]. For each fissioning isotope, the FY are also predicted based on a suitable model along uncertainties based upon the model parameter uncertainties. The modeled FY are then adjusted to fit the recommended FY along other physical constrains such as the conservation of mass and of charge. Hence, the evaluated FY provide a set of data consistent with experiments that take into account all the FP according to the models. Let us point out that the distribution of the low-yield FP is extremely model-dependent and can thus vary in a significant way between different libraries and even between different versions of a library. On the contrary, the high-yield FP have much more consistent FY throughout the different libraries. Hence, the detail of the decay categories and of the types of emitter from Tab. 2.2 and Tab. 2.3 can vary from one library to another.

Categories of decay		
B^-	B^+	IT
β^-	β^+	it
$\beta^-{}_{\text{meta 1}}$	EC	$it_{\text{meta 1}}$
$\beta^-{}_{\text{meta 2}}$		$it_{\text{meta 2}}$
(β^-, n)		
$(\beta^-, 2n)$		
(β^-, α)		
(β^-, p)		
(β^-, d)		
(β^-, t)		
$\beta\beta2\nu$		

Table 2.2: Categories of decay occurring in fission products. The subscript "meta n" means that the daughter nucleus is the n$^{\text{th}}$ metastable isomer. EC stands for "electron capture". The data are obtained from the NUBASE2020 database [155].

				Emitted particle						
		Isotope	**Number of FP**	s	$\beta^-/\bar{\nu}_e$	ν_e	α	n	p	IT
Independent	**Number of emitters**	^{235}U	873	85	771	7	2	192	0	59
		^{238}U	771	45	722	1	0	193	0	44
		^{239}Pu	1006	127	832	19	1	191	1	69
		^{241}Pu	958	101	834	9	0	197	0	63
	Number of particle emitted per fission	^{235}U	873	-	1.93	7.08e-11	7.30e-7	1.41e-2	-	-
		^{238}U	771	-	1.96	5.01e-14	-	3.20e-2	-	-
		^{239}Pu	1006	-	1.89	5.92e-7	2.48e-8	6.08e-3	9.78e-12	-
		^{241}Pu	958	-	1.94	6.69e-11	-	1.23e-2	-	-
Cumulative	**Number of emitters**	^{235}U	983	150	793	7	2	192	0	60
		^{238}U	935	130	778	2	0	193	0	55
		^{239}Pu	1093	176	851	19	3	191	1	70
		^{241}Pu	1071	163	860	9	0	197	0	66
	Number of particle emitted per fission	^{235}U	983	-	6.06	2.35e-10	7.31e-7	1.56e-2	-	-
		^{238}U	935	-	7.15	1.69e-13	-	3.83e-2	-	-
		^{239}Pu	1093	-	5.49	5.98e-7	6.32e-7	6.43e-3	9.78e-12	-
		^{241}Pu	1071	-	6.25	9.41e-11	-	1.39e-2	-	-

Table 2.3: Types of emitters and associated fluxes of particle for thermal FP of ^{235}U, ^{239}Pu and ^{241}Pu, and for fast FP of ^{238}U. The data are given right after a fission (Independent) or after reaching an equilibrium state in the rate of production of FP (Cumulative), and the fluxes are obtained respectively from IFY and CFY. Stable nuclei are reported in the column s. Decays listed in Tab. 2.2 that produce two types of particle are accounted for both types of emitter and fluxes. As most of the B^+ decays are actually EC, only the ν_e fluxes are reported. The data are obtained from the NUBASE2020 database [155] and from the JEFF-3.3 database [136].

As a first approximation, the thermal FY are a good representation of the true FY distribution associated to a neutron flux having a Maxwellian distribution centered on the thermal agitation energy [137]. Similarly, the fast FY correspond in a first approximation to the FY obtained under a combined flux of fast and epithermal neutrons. To properly estimate the FY in a reactor, the thermal (fast) FY must be weighted by the fission fractions associated to thermal (fast and epithermal) neutrons. The thermal (fast) FY remain a good first approximation of the true FY distributions of ^{235}U, ^{239}Pu and ^{241}Pu (^{238}U) in a PWR [137].

2.2 Reactor antineutrino sources

In nuclear reactors, $\bar{\nu}_e$ are emitted from two types of sources, described in the next section. The majority of $\bar{\nu}_e$ are emitted during the cascade of β-decays of FP. Another component of the $\bar{\nu}_e$ flux indirectly originates from neutron activation and decay chains on the structural material and on the fuel of the reactor.

2.2.1 Antineutrinos from fission

The successive β-decays of a FF result on average in the emission of three $\bar{\nu}_e$ until the stable isobar is reached. This is reflected in the number of $\bar{\nu}_e$ emitted per fission when the FP decay rates are in an equilibrium state, which is approximately 6 $\bar{\nu}_e$/fission as seen in Tab. 2.3. In comparison, the number of $\bar{\nu}_e$ emitted per fission of ^{235}U is of 4.40 $\bar{\nu}_e$/fission after 12 hours of irradiation, and of 4.65 $\bar{\nu}_e$/fission after 36 hours of irradiation[1]. Hence, approximately four $\bar{\nu}_e$ are emitted per fission at these time steps, and equivalently FF have already decayed twice in average. A PWR emits typically 6 $\bar{\nu}_e$/fission on average over a 12-month core cycle [145]. Consequently, the majority of β^- emitters are formed and reach an equilibrium state during the first days of a reactor operation.

As the chains of β-decays approach stable states, the energy released per decay decreases while the decay half-lives increase [129]. As a rule of thumb, short-lived FP contribute to the high energy part of the $\bar{\nu}_e$ spectrum, while long-lived FP contribute to the low energy part. The fission $\bar{\nu}_e$ spectrum at low energy will then build up over time, contrarily to the high energy part of the neutrino spectrum that is almost stable a few days after the beginning of the reactor operation. The long-lived FP then contribute to the so called off-equilibrium corrections to the $\bar{\nu}_e$ spectrum. This is illustrated in Fig. 2.9, showing a ^{235}U $\bar{\nu}_e$ spectrum at different moments of a reactor cycle at the ILL.

Compared to a PWR, research reactors have a lower thermal power by two about orders of magnitude. Therefore, the fission rates and thus the number of emitted $\bar{\nu}_e$ are equivalently lower. Furthermore, a shorter operation time limits the $\bar{\nu}_e$ flux contribution of long-lived nuclei that accumulate with time, as seen in Fig. 2.9.

For instance, at the energy threshold of the IBD process, the $\bar{\nu}_e$ spectrum becomes stable at the 1% level only after about 100 days of irradiation [13]. Thus, the fission $\bar{\nu}_e$ spectrum of a research reactor is not in an equilibrium state and the resulting $\bar{\nu}_e$ flux is lower than for a commercial reactor. The $\bar{\nu}_e$ spectrum is also impacted by the different fission fractions, which typical evolution for a PWR is shown in Fig. 2.6. Indeed, the $\bar{\nu}_e$ spectra of ^{235}U, ^{238}U, ^{239}Pu, and ^{241}Pu are not identical due to the differences between the associated FY distributions. The

---

[1] These values are based on FY computed for an irradiation of 12 h and 36 h under a thermal neutron flux of 3.3×10^{14} n $\cdot$ cm^{-2} $\cdot$ s^{-1}. This flux corresponds to the typical neutron flux in the HFR core.

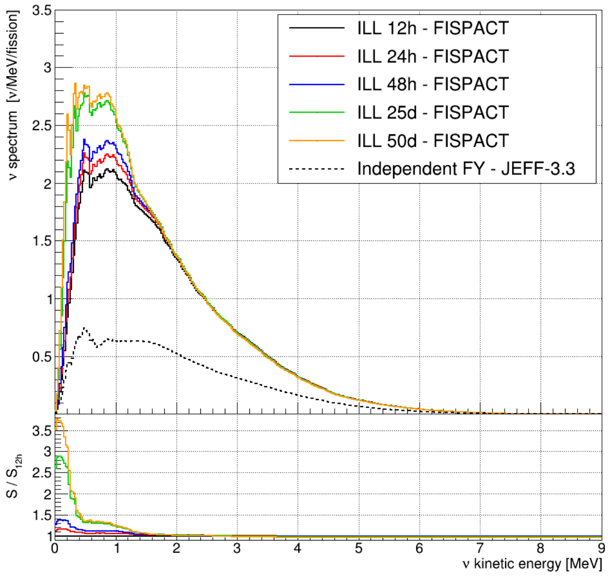

Figure 2.9: Fission $\bar{\nu}_e$ spectra of ^{235}U at 12 hours, 1 day, 2 days, 25 days, and 50 days after the beginning of a reactor cycle of the HFR. The fission yields have been computed with FISPACT-II [157]. The ratios of each $\bar{\nu}_e$ spectrum with the spectrum at 12 hours are represented in the subplot. The dotted line in the upper plot represents the ^{235}U spectrum computed with independent fission yields from the JEFF-3.3 database [136].

typical average fission fractions of the four actinides measured over a period of data taking are summarized in Tab. 2.4 for an experiment conducted at a commercial reactor and at a research reactor. Due to the dominant fission fraction contribution from ^{235}U in PWR and research reactors, the fission $\bar{\nu}_e$ spectra of a PWR and of a research reactor remain close in shape.

Among the FP, a few β^- emitters with non negligible yields are susceptible to decay via $\beta\beta2\nu$. Such decays have half-lives of the order of 10^{18} years or greater and are unlikely to happen during an irradiation cycle. Thus, the associated $\beta\beta2\nu$ neutrino flux are negligible.

2.2.2 Antineutrinos from activation

In addition to the $\bar{\nu}_e$ produced by fission, contribution from $\bar{\nu}_e$ produced by activation of fuel and structural material is expected. Neutron activation results in a sizable $\bar{\nu}_e$ flux if several requirements are met: the activated element is present in a relative abundance, it has an important neutron capture cross-section, and the daughter element of the activation process β-decays with a low half-life. These information are summarized in Tab. 2.4 for the relevant elements for commercial and research reactors described below.

In a PWR, the main contribution of the activation $\bar{\nu}_e$ flux comes from the β-decays of ^{239}U ($t_{1/2}$ = 23.45 min) and ^{239}Np ($t_{1/2}$ = 2.36 d), issued from the ^{238}U chain capture (see Eq. 2.2). The average number of neutron captured on ^{238}U per fission event is 0.62 over a core cycle [145]. Thus, the two β-decays result in the emission of 1.24 $\bar{\nu}_e$ with energy up to 0.71 MeV for the β-decay of ^{239}U and 1.26 MeV for the one of ^{239}Np. The emission rates of these neutrinos are at equilibrium a few days after the beginning of a core cycle, and contribute to about 17% of the emitted $\bar{\nu}_e$ on average over a reactor cycle. While the $\bar{\nu}_e$ are emitted below the IBD threshold, they are not negligible for CEνNS experiments. For a research reactor highly enriched in ^{235}U, only a few percents of ^{238}U is present in the fuel (7% in the HFR fuel

[158]). Neutron capture on ^{238}U is thus a minor process, and the $\bar{\nu}_e$ contribution from the two β-decays of ^{239}U and ^{239}Np are expected to be negligible.

A second contribution comes from the β-decay of ^{237}U produced in the reactions:

$$^{1}\mathrm{n} + {}^{236}_{92}\mathrm{U} \longrightarrow {}^{237}_{92}\mathrm{U} + \gamma, \tag{2.5}$$

$$^{1}\mathrm{n} + {}^{238}_{92}\mathrm{U} \longrightarrow {}^{237}_{92}\mathrm{U} + 2n, \tag{2.6}$$

where the ^{236}U is produced in about 14% of the neutron captures on ^{235}U[1]. These two processes have low cross-sections and result in a low production rate of ^{237}U. For a PWR at mid-operation time, the process 2.5 results in the emission of 0.018 $\bar{\nu}_e$/fission, while the reaction 2.6 yields 0.003 $\bar{\nu}_e$/fission [160], emitting in total about 0.3% of the $\bar{\nu}_e$ flux on average over a reactor cycle. The half-life of ^{237}U is 6.75 days and has its ν_e spectrum extends up to 0.45 MeV, which makes it impossible to detect with IBD nor with current detector technology based on the CEνNS process (see Sec. 2.3.2). Hence, the $\bar{\nu}_e$ contribution of ^{237}U is not relevant for reactor experiments and can be neglected.

In the control rods and in the zirconium alloy sheets of a PWR, the main activated β^- emitters are ^{95}Zr, ^{97}Zr, ^{95}Nb and ^{97}Nb [160]. Their respective β-decay half-lives are 64.03 days, 16.75 hours, 34.99 days and 72.1 minutes [161]. With short half-lives, ^{97}Zr and ^{97}Nb neutrino rates can be considered as constant. However the population of ^{95}Zr and ^{95}Nb will reach an equilibrium after several months, and only at this moment their neutrino rates will be stabilized. The combined yield of these four isotopes is 0.01 $\bar{\nu}_e$/fission at mid-operation time, and the $\bar{\nu}_e$ spectra of these four isotopes extends to 2 MeV. Considering the low combined yield with respect to the total $\bar{\nu}_e$ flux, their contribution can be neglected.

Two minor sources of β^- emitter are produced on the gadolinium used as neutron poison, and on the water used as moderator. The gadolinium contained in some of the fuel rods results in a typical yield of about 10^{-3} $\bar{\nu}_e$ per fission [160], and is the highest $\bar{\nu}_e$ source among poisons. By capturing fast neutrons, the oxygen contained in the water produces ^{16}N which emits about 10^{-5} $\bar{\nu}_e$ per fission. Hence, the poison and nitrogen $\bar{\nu}_e$ fluxes are negligible.

The structural materials employed in research reactor differ from that composing a PWR. Detailed studies of relevant nonfuel $\bar{\nu}_e$ emitters for IBD experiments were conducted for the HFR in [151], and for the high flux isotope reactor (HFIR) located at the Oak Ridge National Laboratory (ORNL) in [162, 163]. Let us point out that such studies are specific to each research reactor, and that further studies might be required to identify relevant activated elements for future CEνNS experiments with lower thresholds.

The HFR contains a large amount of aluminum in the fuel element, the beam tubes and the heavy water vessel [151]. The major activation contribution then comes from

$$^{1}\mathrm{n} + {}^{27}\mathrm{Al} \longrightarrow {}^{28}\mathrm{Al} + \gamma, \tag{2.7}$$

which contributes to about 26% of all radiative captures in the reactor core, with ~ 0.35 neutrons absorbed on ^{27}Al per fission event. The β-decay of ^{28}Al has a half-life of 2.25 minutes and emits $\bar{\nu}_e$ with energy up to 2.86 MeV. The next contribution comes from the radiative capture on ^{55}Mn located in the heavy water tank, absorbing ~ 0.06 neutron per fission:

$$^{1}\mathrm{n} + {}^{55}\mathrm{Mn} \longrightarrow {}^{56}\mathrm{Mn} + \gamma. \tag{2.8}$$

The $\bar{\nu}_e$ spectrum of ^{56}Mn has a half-life of 2.58 hours and extends up to 2.85 MeV. Because of their low half-lives, the ^{28}Al and ^{56}Mn activities reach an equilibrium state promptly into the

---

[1] According to the cross-section for incident thermal neutrons from the JENDL-4.0 database [159].

	Element	**Process**	**Cross-section**	**Daughter**	**$\mathrm{T}_{1/2}$**	**E_0**	**Event/fission**		
			[b]			[MeV]	PWR	HFR	HFIR
Fission	^{235}U	fission					0.559	0.993	0.998
	^{238}U	fission					0.088	-	-
	^{239}Pu	fission					0.291	0.007	0.002
	^{241}Pu	fission					0.062	-	-
Activation (fuel)	^{238}U	(n,γ)	2.68	^{239}U	23.45 min	1.26	0.62	-	-
				$^{239}\mathrm{Np}^{\dagger}$	2.36 d	0.71	0.62	-	-
Activation (structure)	^{27}Al	(n,γ)	0.23	^{28}Al	2.25 min	2.86	-	0.346	0.18
	^{55}Mn	(n,γ)	13.28	^{56}Mn	2.579 h	2.85	-	0.058	-
	^{9}Be	(n,α)	0.05*	^{6}He	0.806 s	3.51	-	-	0.015
	^{51}V	(n,γ)	4.92	^{52}V	3.743 min	2.54	-	-	0.007

Table 2.4: Summary of the $\bar{\nu}_e$ sources in PWR, at the HFR and at the HFIR. For activated elements, the β^- emitters at the origin of the $\bar{\nu}_e$ emission are listed in the "Daughter" column (†: ^{239}Np is produced from the β-decay of ^{239}U). Cross-sections are taken from the JENDL-4.0 database [159] for incident thermal neutrons (*: for fast neutrons if the process has a high energy threshold). The "Event/fission" column corresponds to fission fractions for the "Fission" rows and to the number of $\bar{\nu}_e$ emitted per fission event for the "Activation " rows. PWR, HFR and HFIR values are respectively averaged over a 12-month cycle [145], a 50-day cycle [151] and a 25-day cycle [162, 163]. The hyphen means that the process is either negligible or absent.

cycle. Their respective contribution to the total $\bar{\nu}_e$ flux are then of about 5% and 1%. With endpoint energies above the IBD threshold, they constitute non-negligible $\bar{\nu}_e$ contributions that must be taken into account in IBD and CEνNS experiments.

Besides ^{28}Al[1], the most important activation $\bar{\nu}_e$ sources at the HFIR are ^{6}He produced in the neutron capture on the beryllium reflectors[2], and ^{52}V originating from ^{51}V loaded in special rods irradiated for experimental purpose. ^{6}He and ^{52}V have significant activities compared to the HFIR fission rate. The ^{6}He and ^{52}V contributions to the total $\bar{\nu}_e$ flux are proportional to the reactor power due to their low half-lives (806.7 ms and 3.74 min). Due to their high endpoint energies (3.50 MeV and 3.974 MeV respectively), the $\bar{\nu}_e$ contributions from ^{28}Al, ^{6}He and ^{52}V are not negligible in IBD and CEνNS experiments [164]. For example, their contributions at 2 MeV to the total $\bar{\nu}_e$ spectrum are approximately of 8% for ^{28}Al, and 1% for ^{6}He and ^{52}V combined. The ratios of the ^{6}He and ^{52}V activities to the fission rate are respectively about 0.015 and 0.007 at the middle of a 25-day cycle [163].

2.2.3 Prediction of the neutrino flux and spectrum

At a given time t, the number of $\bar{\nu}_e$ emitted by a reactor core with energy between E and $E + \mathrm{d}E$ is expressed as

$$N_r(E,t) = \frac{\mathrm{d}\phi_r(E,t)}{\mathrm{d}E\mathrm{d}t} = \frac{P_{th}(t)}{\sum_f \alpha_f(t)\left\langle E_f\right\rangle}\left(\sum_f \alpha_f S_f(E,t) + \sum_a y_a S_a(E,t)\right). \tag{2.9}$$

---

[1] At the HFIR, the number of $\bar{\nu}_e$ emitted per fission event from the β-decay of ^{28}Al lies between 0.15 and 0.20 [163]. The ^{56}Mn activity at the HFIR is two order of magnitude below the one of ^{28}Al, and is thus negligible.

[2] Reflectors are located on the most radially outward region of the HFIR, and moderate neutrons that will be transported in beam tubes or reflect them back into the core to sustain the chain reaction.

	^{235}U	^{238}U	^{239}Pu	^{241}Pu
$\langle E_f$ [MeV]$\rangle$	202.36 ± 0.26	205.99 ± 0.52	211.12 ± 0.34	214.26 ± 0.33
$\bar{\nu}_e$/fission	6.08	7.16	5.50	6.26
$\bar{\nu}_e$/fission > 1.8 MeV	1.88	2.56	1.54	2.01
$\langle \sigma_{IBD} \rangle$ [10^{-43} cm^2/fis]	6.50	10.32	4.72	6.93

Table 2.5: Mean energy released per fission in a PWR and number of $\bar{\nu}_e$ emitted per fission and IBD mean cross-section per fission of ^{235}U, ^{238}U, ^{239}Pu and ^{241}Pu. The mean energies are taken from [165]. The different values have been computed with CFY from the JEFF-3.3 database and with the BESTIOLE software (see Ch. 3).

P_{th} is the thermal power released in the core. α_f, $\langle E_f \rangle$ and S_f are the fission fractions, mean energies per fission released in the core (reported in Tab. 2.5[1]) and $\bar{\nu}_e$ spectra of the f^{th} fissioning isotope ($f = {}^{235}\text{U}, {}^{238}\text{U}, {}^{239}\text{Pu}, {}^{241}\text{Pu}$). y_a is the $\bar{\nu}_e$ yield associated to the activation $\bar{\nu}_e$ source a and S_a is the associated $\bar{\nu}_e$ spectrum. A reactor $\bar{\nu}_e$ spectrum thus results from the overlapping of hundreds $\bar{\nu}_e$ spectra of FP and activated elements depending on the reactor features.

With approximately 200 MeV, 6.0 fission $\bar{\nu}_e$ and 1.3 activation $\bar{\nu}_e$ released per fission, a PWR core emits about 2.3×10^{20} $\bar{\nu}_e$/s per GW$_{\text{th}}$ on average over a rector cycle. The neutrino flux is purely electronic, with a majority of $\bar{\nu}_e$ and a negligible amount of ν_e. Almost 75% of the $\bar{\nu}_e$ flux is emitted below 1.8 MeV, and about 17% of the flux originate from non-fission process. 99.9% of the $\bar{\nu}_e$ flux is emitted below 7 MeV, as illustrated by the cumulative distribution function of a typical reactor $\bar{\nu}_e$ spectrum in Fig. 2.10b. Only a handful of isotopes have a spectrum extending up to 10 MeV and above.

Commercial power plants consist usually in several nuclear reactors. At a given location L, the local $\bar{\nu}_e$ flux originating from all nearby reactor cores distant by L_r is

$$N_{\bar{\nu}_e}(E,t,L) = \sum_r \frac{P_{\bar{\nu}_e \to \bar{\nu}_e}(E, L_r)}{4\pi L_r^2} N_r(E,t), \tag{2.10}$$

where the $\bar{\nu}_e$ survival probabilities $P_{\bar{\nu}_e \to \bar{\nu}_e}$ are taken into account for each reactor source term, and the denominator $4\pi L_r^2$ accounts for the isotropic emission of $\bar{\nu}_e$. This formulation is correct as long as the reactor core can be treated as a point-like source of $\bar{\nu}_e$. If L_r is low compared to the dimension of the reactor core, it may be necessary to consider the spatial dependence of the $\bar{\nu}_e$ emission in the core.

Three methods can be used to predict the antineutrino spectrum of a nuclear reactor, and are described in the next sections.

2.2.3.1 Summation model

In the summation method (SM), the spectra of all the thousands of β^- transitions contributing to a reactor $\bar{\nu}_e$ spectrum are modeled individually and summed together. The fission $\bar{\nu}_e$ spectrum of a fissionable isotope f is then given as

$$S_f(E,t) = \sum_p \mathcal{Y}_p^f(t)\ S_p(E), \tag{2.11}$$

---

[1] To obtain the mean energy released and deposited in the core, one must correct the mean energy released per fission for the energy loss from $\bar{\nu}_e$ escaping the reactor, for the energy not yet released due to long-lived FP present in the decay chains, and for the added energy originating from radiative neutron captures on structural elements [165]. Hence, the mean energy released per fission has a small dependency on the type of reactor and can slightly change over a core cycle.

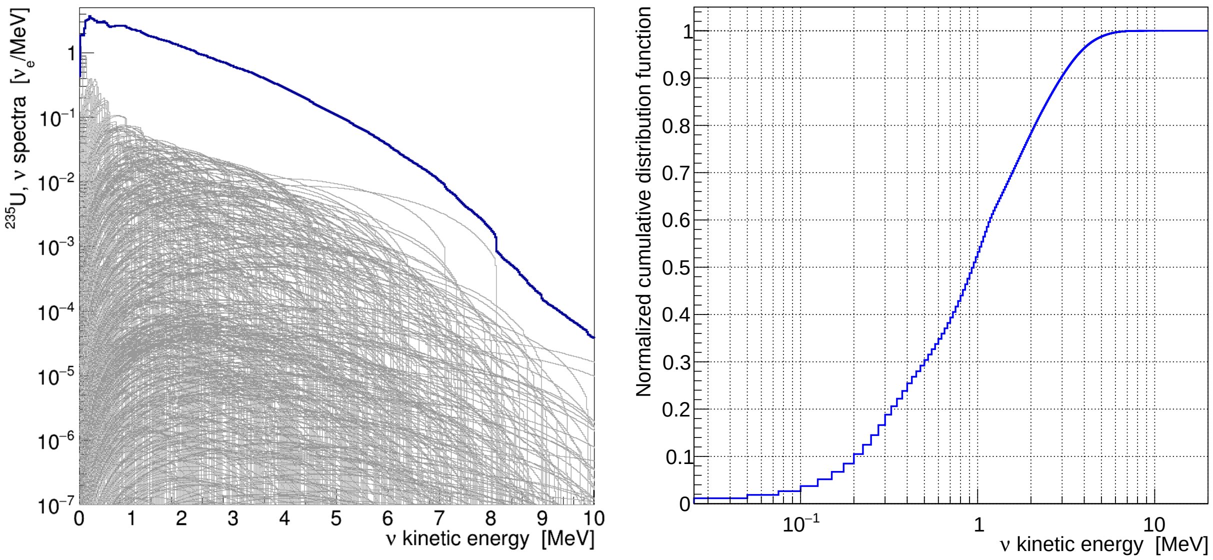

(a) Summation model of ^{235}U.

(b) Cumulative distribution function.

Figure 2.10: **(a)** Summation model of the ^{235}U antineutrino spectrum made with BESTIOLE (in blue) along all the isotope spectra entering its composition (in grey). **(b)** Cumulative distribution function of a reactor spectrum for fission fractions and activated elements averaged over a 12-month reactor cycle. The CFY from the JEFF-3.3 database have been used.

where $\mathcal{Y}_p^f(t)$ is the FY at time t of the FP p derived from the fission of f. The spectrum S_p of a fission product results from the superimposition of the spectra of its β^- transitions (also called branches), as illustrated for ^{235}U in Fig. 2.10a. The probability to decay through a given transition over the total decay probability is called branching ratio, which add up to unity if the isotope is a pure β^- emitter and to less than one otherwise. A FP spectrum is then expressed as

$$S_p(E) = \sum_b \mathcal{B}_b^p \; S_b(E, E_{0b}), \tag{2.12}$$

with $\mathcal{B}_b^p$ the branching ratio of the transition b, and E_{0b} its endpoint. The spectra at the branch level are modeled in the framework of the $V - A$ theory, and will be thoroughly discussed in Ch. 3. Calculation of a branch spectrum requires a large amount of nuclear data. Nuclear data are compiled in evaluated nuclear databases such as ENSDF [161], JENDL [159], or CENDL [166]. An accurate prediction based on the SM require a complete knowledge of the β-decay schemes of all FP and activated isotopes, as well as an unbiased modeling. Both requirements are currently not fulfilled.

One of the first SM was proposed by J. F. Perkins and R. W. King in 1958 [167]. Several SM were proposed during the 1970s following the steady improvement in nuclear and fission data [168–170]. For instance, about 60% of FP had a completely unknown decay scheme in 1968 [168], while this is the case for less than 30% of the FP today. Moreover, a systematic bias in the decay scheme of many relevant FP was pinpointed in 1977 and known as the Pandemonium effect [171]. This is an overestimation of the β-feedings of low energy levels due to the low-efficiency of high purity germanium detectors at high γ-ray energy (see Sec. 4.1.2). This effect was discussed in the context of reactor spectra as soon as in the early 1980s [172–175]. In all these summation calculations, the approximation was made that each β-decay of a FP could be modeled as an allowed transition[1] of a point-like nucleus. This approximation was consistent in regards to the completeness and precision of the available nuclear data, even though it would necessarily introduce a bias in the shape of the predicted $\bar{\nu}_e$ spectra.

In 2011, the SM was refined by the Saclay group by including correct calculation of unique forbidden transitions and additional corrections at the level of a β-decay [13]. The obtained fission spectra would differ by less than 1% with previous spectra based on allowed transitions only. However, uncertainties higher than 10% were considered over the whole spectra, mainly derived from the estimated impact of missing information in nuclear databases and from the difference with reference measured β spectra. A second refined SM was proposed in 2012 by the Subatech group [176]. Correct unique forbidden transitions were also included in this model, which differed from Saclay's SM in its set of corrections (see Sec. 3.6). This SM has been used since then by the Subatech group to emphasize the impact of Pandemonium-free nuclear data, reflecting the progress made in correcting this systematic effect in relevant FP during the last two decades [176–179]. They have shown that correcting this bias significantly reduces the discrepancies observed between SM predictions and experimental data [178]. Let us point out that several approximations in the β-decay modeling are still employed in these two SM, namely the $\lambda_k = 1$ and the ξ approximations, both discussed in Ch. 3. The important impact of these approximations on fission spectra has been recently addressed in a study from Hayen et al. [180, 181]. Especially, the contribution of non-unique forbidden transitions has been shown to exceed 50% at 6 MeV. With a more appropriate modeling of these transitions, the shape of a $\bar{\nu}_e$ spectrum can be locally modified by 5% [181].

The SM is the only model that can make a prediction over the full energy range of reactor neutrinos. Additionally, it allows to conduct sensibility studies for any fissionable isotope and type of fuel, to evaluate the off-equilibrium effects due to long-live FP on a reactor spectrum, and can be used to predict the spectra of spent fuel and even of geoneutrinos. Another example is the study of the fine structure of a reactor $\bar{\nu}_e$ spectrum, also called microscopic structure. A reactor $\bar{\nu}_e$ spectrum is made of thousands of transition $\bar{\nu}_e$ spectra, each presenting a sharp edge at the endpoint energy due to the Coulomb correction (see Sec. 3.4.3). As a result, a reactor $\bar{\nu}_e$ spectrum has a fine structure due to the discontinuities at the edge of each transition spectrum. The fine structure can be associated to specific isotope spectra using the SM, and can be used to address the completeness of nuclear databases. An energy resolution at the percent level or below is necessary to measure this fine structure [182], and no experiment is able to detect it at the moment. Similarly, a detection in bins of 100 keV or less is necessary to observe the fine structure [183]. The Taishan Antineutrino Observatory (TAO) is a satellite experiment of JUNO that should start in 2022, and is expected to achieve such energy resolution [184]. TAO is a ton-level liquid scintillator detector, and is expected to have a statistical uncertainty below 1% in the energy range of 2.5–6 MeV after three years of data taking, enough to constrain the fine structure at the 1% level with a bin width of about 30 keV. As already mentioned, the major weakness of the SM is that its prediction capacity depends entirely on the completeness and precision of evaluated nuclear databases and on the considered modeling. Recent SM studies have highlighted the necessity to improve the modeling of β-decays as well as the evaluation of nuclear data for relevant FP [178, 179, 181].

---

[1] The different types of β^- transitions will be introduced in Ch. 3. For now, let us keep in mind that allowed transitions are easily computed and well known, while the treatment of non-unique forbidden transitions is usually dismissed through approximations.

2.2.3.2 Predictions from aggregated β spectrum measurements at reactors

In a β-decay, the decay energy is shared between the electron and the neutrino if one neglects recoil effects[1]. There is then a unique correspondence between the spectra of the emitted fermions. Hence, it is only natural to wonder if a $\bar{\nu}_e$ spectrum could be inferred from a measured β spectrum, which is the basis for the conversion method (CM).

A first CM was proposed by C. O. Muehlhause and S. Oleska in 1957 to convert an aggregated β spectra measured at a reactor [185], and was further developed by Carter et al. [186]. The principle of this first CM was to fit a measured β spectrum using a continuous distribution of virtual allowed transitions. At each energy, the spectra of the virtual branches were weighted by the distribution of endpoint energies estimated from evaluated nuclear data. The virtual β spectra were then converted into its associated $\bar{\nu}_e$ spectrum based on energy conservation at the branch level. This CM was estimated to be about 10% accurate [174, 175]. It required an analytic fit of the measured β spectrum that needed to be extrapolated up to 3 MeV beyond the maximum required $\bar{\nu}_e$ energy. Moreover, the converted $\bar{\nu}_e$ spectrum was slightly dependent on the averaged atomic number Z considered when building the distribution of endpoint energies.

In the early 1980s, a second CM was conceived by Klaus Schreckenbach and his colleagues [116–119]. Although conceptually similar, this second CM did not require an analytic fit nor an extrapolation of the β spectrum. The continuous distribution of allowed transitions was replaced by a finite set of about thirty virtual branches. These virtual transitions were selected based on the distribution of the average nuclear charge $\bar{Z}$ with respect to the endpoint energy to optimally fit different measured β spectra. The $\bar{Z}$ distribution was also built from evaluated nuclear data, displaying a small dependency depending on the considered data. The input β spectra used by Schreckenbach's group were the aggregated β spectra of the FP derived from the thermal fission of ^{235}U, ^{239}Pu and ^{241}Pu [116–119]. The three β spectra were obtained by irradiating target foils for 12 to 43 hours with a thermal neutron flux generated by the HFR at the ILL. The resulting aggregated β spectra were measured by the BILL magnetic spectrometer in magnetic field steps of 50 keV [187]. Except for energy bins above 7 MeV yielding poor statistic, all other binned data displayed statistical uncertainties at the percent of even sub-percent level, leaving the absolute normalization of the measured spectrum as the main source of uncertainty, around 3% (90% CL) with a weak energy dependency. The spectrum data were published in 250 keV bins, but the original data were recently released with a smaller binning of 100 keV (50 keV for ^{235}U) [188]. The uncertainty due to the conversion procedure from Schreckenbach's CM was less than 5% below 8 MeV. The total uncertainty on the converted $\bar{\nu}_e$ spectra was then lying between 5% around 2 MeV and 8% at 7 MeV, with statistical uncertainties superior to 10% dominating beyond. The electron spectrum from ^{238}U could not be measured at the ILL as it fissions under a fast neutron flux, but an experiment was recently performed at the scientific neutron source FRM II in Garching [189]. The aggregated β spectrum of ^{238}U was measured by irradiating target foils of natural uranium with a thermal and a fast neutron flux during 53 hours. The emitted β spectrum was then recorded with a spectrometer and normalized with respect to the ILL measurement of the ^{235}U β spectrum.

The CM was revisited in 2011 independently by the Saclay group [13] and Patrick Huber [14] using the same β spectra than Schreckenbach. In Saclay's approach, the SM was employed to build approximately 90% of the β spectra [13]. Thus, it benefited from a distribution of β branches close to the physical one, partly corrected from the Pandemonium effect, and corrections could be applied at the branch level. The remaining residuals with the ILL spectra

---

[1] The magnitude of recoil effects is $\mathcal{O}(E_0/AM_N) \sim 10^{-4}$ where E_0 is the endpoint energy, A is the mass number and M_N the average nucleon mass [14].

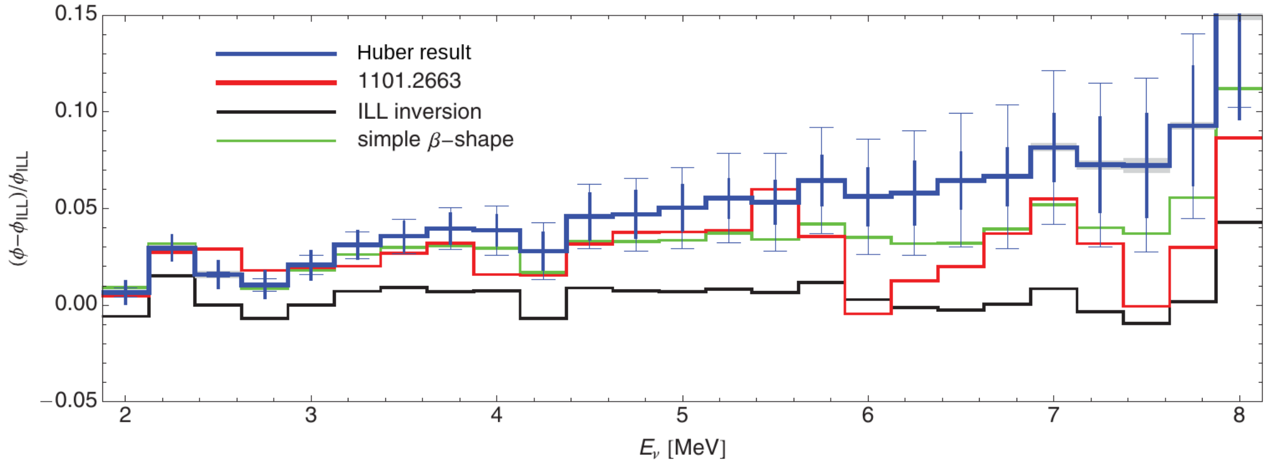

Figure 2.11: Relative residual with respect to the ILL $\bar{\nu}_e$ spectrum of ^{235}U for Huber's conversion model (blue line) and Saclay's conversion model (red line). The black line represents the Schreckenbach's conversion model reproduced by Huber as a check. The green line shows the result of Huber's conversion model when using the same description of β-decay as in Saclay's conversion model. The figure is taken from [14].

was compensated using five virtual branches. The contribution of virtual branches was reduced by an order of magnitude compared to previous CM, and the uncertainty due to the conversion procedure was reduced down to 1-3%. The $\bar{\nu}_e$ spectra derived from Saclay's CM display a +3% normalization shift compared to Schreckenbach's CM [13]. Below 4 MeV, this shift is generated by the implementation at the branch level of the SM of two corrections, the weak magnetism and the Coulomb correction induced by the finite-size of the parent nucleus. In comparison, these two corrections were applied as an effective linear correction over the total $\bar{\nu}_e$ spectra in Schreckenbach's CM, overestimating the negative correction at low $\bar{\nu}_e$ energy [13]. At higher energy, the main origin of the shift is the parametrization of the $\bar{Z}$ distribution used to select the virtual β transitions which differs from the one use in Schreckenbach's CM.

In Huber's CM, the conversion was solely based on virtual branches: 30 branches for ^{235}U, 23 for ^{239}Pu and 25 for ^{241}Pu. Evaluated nuclear data were only used to build the distribution of the average nuclear charge $\bar{Z}$. Since $\bar{Z}$ is an average quantity, its variation from modification in the nuclear database is small [14]. The theoretical framework used to model each virtual branch was also improved, including corrections previously omitted such as finite-size effects, screening, radiative QED and weak magnetism corrections. Contrarily to the SM which suffer from high uncertainties due to nuclear database inputs, Huber's CM uncertainties originating from nuclear data are limited to less than 1% for ^{235}U and less than 3% for ^{239}Pu and ^{241}Pu. The modeling and normalization uncertainties propagated to the converted $\bar{\nu}_e$ spectra remain inferior to 3%. Finally, the statistical uncertainty increases with energy and become larger than for the initial ILL β spectra, dominating the total uncertainty above 5 MeV (above 7 MeV for ^{235}U). Huber's CM also concluded to an upward $2.4 - 3.2\%$ shift in the $\bar{\nu}_e$ spectra of the three isotopes [14]. Similarly to Saclay's results, the shift below 4 MeV finds its origin in the implementation of the weak magnetism and of the Coulomb finite-size corrections at the branch level. Above 5 MeV, the shift also derives from the new form of the $\bar{Z}$ distribution, as well as from the contribution of the screening correction applied to virtual branches. The relative residuals with the ILL spectra of the Saclay and Huber's CM for ^{235}U are showed in Fig. 2.11, where the upward shifts can clearly be seen. The measured β spectra of the four fissionable isotopes and their associated conversion $\bar{\nu}_e$ spectra are showed in Fig. 2.12.

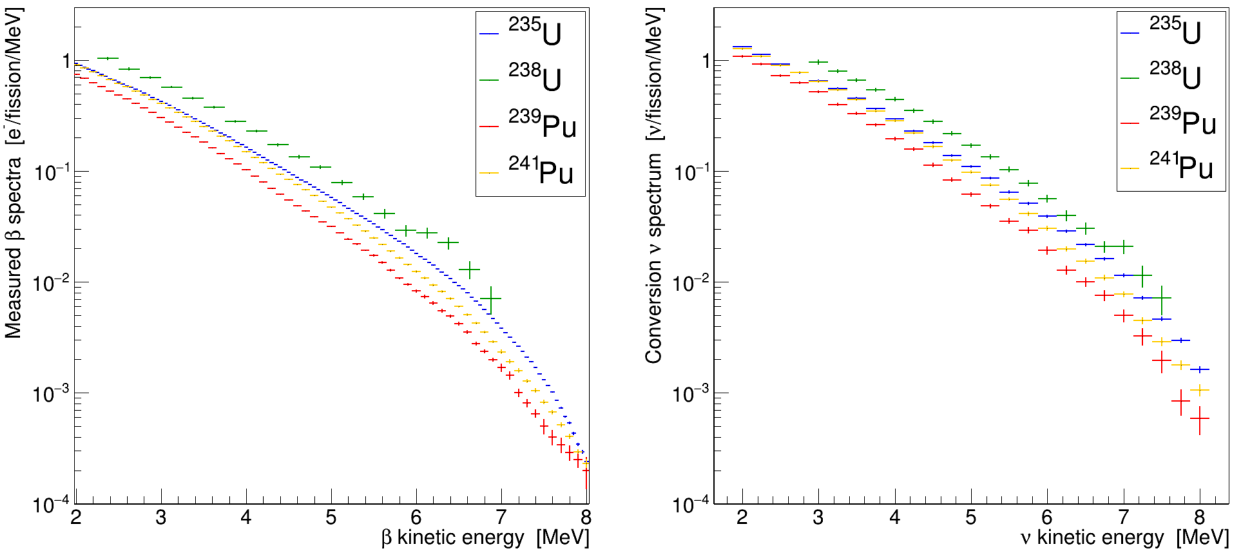

(a) Measured β spectra.

(b) Conversion $\bar{\nu}_e$ spectra.

Figure 2.12: **(a)** Data of the ILL electron spectra of ^{235}U, ^{239}Pu and ^{241}Pu in 50 keV bins [188], and electron spectrum of ^{238}U from [189]. The displayed uncertainties consists in the quadratic sum of the statistical and normalization uncertainties. **(b)** Conversion $\bar{\nu}_e$ spectra of ^{235}U, ^{239}Pu and ^{241}Pu from [14], and of ^{238}U from [189]. The uncertainties consists in the quadratic sum of the CM uncertainty, statistical uncertainty and normalization uncertainty.

The CM spectra are currently considered as the most reliable predictions and are widely used in reactor experiments. Yet they still have several weaknesses. Only a handful of measurements of the ^{235}U aggregated β spectrum have been attempted, with the BILL measurement being the most accurate one [116, 118, 185, 186, 190]. Regarding the aggregated spectra of ^{238}U, ^{239}Pu and ^{241}Pu, the FRM II and the BILL experiments are the only occurrence of such measurements. These spectra have been used in all recent CM as reference β spectra. Thus, any bias in these experiments directly impact the CM's results. For instance, a recent study has concluded that the ILL normalization of the ^{235}U β spectrum was possibly overestimated by 5% [191, 192]. The ^{238}U β spectrum from the FRM II should also suffer from this bias as it was normalized with respect to the ILL ^{235}U spectrum [188]. Another lead is a possible inconsistency between the ^{235}U and ^{239}Pu normalizations of the ILL β spectra [193]. The normalizations of the ILL β spectrum measurements were determined by a relative approach based on irradiating a calibration target with a well known (n, e^-) cross-section for thermal neutron. A study is currently ongoing to investigate if a possible bias in the different parameters used at the ILL to perform the relative normalization could contribute to the RAA. Another limitation of the CM is the use of virtual branches that remain an effective tool to reproduce an aggregated β spectrum. If the fitting procedure of the virtual transitions ensures that an aggregated β is reproduced at the subpercent level, the converted $\bar{\nu}_e$ spectrum depends on the modeling of the virtual branches. For instance, the presence of unique and non-unique forbidden transitions is not accounted for in recent CM. Yet, it is known from [181] that a unique or non-unique forbidden spectrum differs significantly from an allowed spectrum. Even though the contribution of many unique and non-unique transitions could somewhat cancel out in a SM, taking into account the existence of such transitions in a CM could have an impact due to the limited number of virtual branches. Due to the short irradiation times of the ILL and FRM II experiments, long-live nuclei are not taken into account in the CM. Off-equilibrium corrections are then required to account for these nuclei present in the reactor spectra of PWR and research reactors. The CM also depends on the binning of the measured β spectra, currently limited to a hundreds of keV. Finally, CM predictions are limited to the energy range of the measured β spectra. As the $\bar{\nu}_e$ flux is negligible above 8 MeV (see Fig. 2.10b), the upper energy limit of the measurement of about 8-9 MeV is not an issue. However, the ILL measurements are limited to 2 MeV for ^{235}U and 1.5 MeV for ^{239}Pu and ^{241}Pu, and the FRM II ^{238}U measurement is limited to 2.25 MeV. This prevents the use of the CM below these energies, which are of interest for CEνNS experiments.

2.2.3.3 Predictions from antineutrino spectrum measurements at reactors

A third method to predict reactor neutrino spectra is becoming conceivable. With the recent high-precision measurements of antineutrino reactor spectra at Daya Bay (^{235}U and ^{239}Pu) and at research reactors (^{235}U), a possible solution would be to use these experimental spectra to make a prediction and forego entirely the theoretical predictions [194]. The drawback would be the complete dependency to the experimental features.

For instance, all experiments at the moment detect neutrinos through the IBD process which has a threshold of 1.806 MeV, thus restricting predictions to energies superior to the IBD threshold. For commercial reactors such as Daya Bay, deriving a data-driven prediction also requires to extract the isotopic positron energy spectra associated to the different actinides [194]. Uncertainties arising from the isotopic extraction procedure then encompass detector and modeling uncertainties. The former consists in uncertainties associated to the detection efficiency, to energy nonlinearity models, to the different energy scale between detectors, and due to the energy loss occurring in the detector [194]. The modeling uncertainties originate from input spectra used in the extraction analysis. For instance, ^{238}U and ^{241}Pu are respectively modeled with Mueller's SM and Huber's CM in [195]. Finally, the positron energy spectrum measured during an IBD experiment (see Sec. 2.3.1) must be unfolded into a generic antineutrino energy spectrum weighted by the IBD cross-section. This procedure takes into account the detector response and contributes to the total uncertainty of the prediction. The total uncertainty of the unfolded $\bar{\nu}_e$ spectra of ^{235}U is 3.5% between 3 MeV and 6 MeV [194]. The uncertainty is of 5% in the same energy range for the combination of the unfolded $\bar{\nu}_e$ spectra of ^{239}Pu and ^{241}Pu. Statistical and modeling uncertainties dominate the total uncertainties with a contribution of a couple of percents each.

Another limitation of such data-driven model is that it cannot address the microscopic structure of a neutrino spectrum. Thus, the contributions of individual FP or of a specific modeling feature at the level of a β-decay cannot be investigated. However, it can be used to validate theoretical models, to address the content of evaluated nuclear databases, and it provides interesting and complementary data to study the composition of reactor neutrino fluxes.

2.3 Reactor antineutrino detection

For any given neutrino interaction process, the number of $\bar{\nu}_e$ with energy E interacting in a detector is given by

$$N_d(E,t,L) = \ n_t \ \epsilon \ \sigma(E) \ N_{\bar{\nu}_e}(E,t,L), \tag{2.13}$$

where n_t is the number of targets in the detector, ϵ is the detector efficiency, and σ is the considered process cross-section. There are many processes involving an incident antineutrino. Below 100 MeV, neutrino interactions are dominated by CC and NC interactions with nuclei, and most importantly by the IBD and by elastic scattering processes such as CEνNS [196]. The IBD detection technique was pioneered by Reines and Cowan for the first detection of the neutrino and is since widely used in reactor experiments, while CEνNS is investigated in a new generation of reactor experiments.

2.3.1 Inverse β-decay detection technique

The IBD process is a CC interaction where a $\bar{\nu}_e$ collides with a proton to produce a neutron and a positron:

$$\bar{\nu}_e + p \longrightarrow e^+ + n. \tag{2.14}$$

The IBD possesses an energy threshold due to the difference of mass between the initial and final particles and also to some degree to the relativistic behavior of the neutrino. In the laboratory frame where the proton is at rest, the threshold is defined as

$$E_{thr} = \frac{(m_e + m_n)^2 - m_p^2}{2m_p} = 1.806 \text{ MeV}, \tag{2.15}$$

where m_e, m_n and m_p are respectively the positron, neutron and proton mass. For energies below 20 MeV, the weak interaction is clearly dissociated from electromagnetism following the spontaneous symmetry breaking mentioned in Ch. 1. As such, the IBD process is best treated as a current-current interaction in the framework of the $V - A$ theory [197].

Depending on the considered energy scale, the IBD cross-section can be expressed in several ways [198]. The approximation derived in [197] for IBD on a free proton is suitable for energy below 20 MeV, and is the one used in this work. At the first order in the neutron recoil $\mathcal{O}(1/M)$, with M the average nucleon mass, the differential IBD cross-section is expressed as

$$\frac{\mathrm{d}\sigma_{IBD}}{\mathrm{d}\cos\theta}^{(1)} = \frac{\sigma_0}{2}\left[1 + \frac{(1-\lambda^2)}{(1+3\lambda^2)} v_e^{(1)} \cos\theta\right] E_e^{(1)} p_e^{(1)} - \frac{\sigma_0}{2}\frac{\Gamma}{M} E_e^{(0)} p_e^{(0)}, \tag{2.16}$$

where θ is the angle between the $\bar{\nu}_e$ and positron directions in the laboratory, and $\lambda = |g_A/g_V|$ is the ratio of axial-vector to vector coupling constants whose value is taken from [199]. The normalizing constant σ_0 yields

$$\sigma_0 = \frac{G_F^2 \cos^2\theta_C}{\pi}(1 + \Delta_{inner}^R)\left(1 + 3\lambda^2\right), \tag{2.17}$$

with G_F the Fermi constant, θ_C the Cabbibo angle, and Δ_{inner}^R the energy-independent inner or universal electroweak radiative corrections. Alternatively, σ_0 can be normalized to the β-decay of the free neutrons mean lifetime τ_n:

$$\sigma_0 = \frac{2\pi^2}{m_e^5 f^R \tau_n}, \tag{2.18}$$

with f^R the phase-space factor of the free neutron β-decay [200, 201]. This last expression is commonly used to model the IBD cross-section and was used in the reevaluation of reactor $\bar{\nu}_e$ spectra that has led to the RAA [15]. The energy E_e of the outgoing positron at the zeroth and first order are given by

$$E_e^{(0)} = E - \Delta, \qquad E_e^{(1)} = E_e^{(0)} - T_n, \tag{2.19}$$

with E the $\bar{\nu}_e$ energy, $\Delta = m_n - m_p$ and T_n is the neutron kinetic energy due to the recoil given at first order in $\mathcal{O}(1/M)$ by

$$T_n = \frac{EE_e^{(0)}}{M}(1 - v_e^{(0)}\cos\theta) + \frac{y^2}{M}, \tag{2.20}$$

	Constant value		
	1999	2011	2020
λ	1.2670	1.2695(29)	1.2762(5)
G_F [10^{-5} GeV^{-2}]	1.16639(1)	1.16637(1)	1.1663787(6)
$\sin\theta_C$	0.2265	0.2255(10)	0.2278(6)
f	3.706	3.706	3.706
Δ^R_{inner}	0.024	0.024	0.02467(22)
σ_0 [10^{-43} cm$^2 \cdot$ MeV^{-2}]	0.953	0.956(4)	0.964(1)
τ_n [s]	886.7(19)	885.7(8)	879.4(6)
f^R	1.71465(15)	1.71465(15)	1.71517(9)
σ_0 [10^{-43} cm$^2 \cdot$ MeV^{-2}]	0.955(2)	0.956(1)	0.963(1)

Table 2.6: Values of the constants used in the IBD cross-section. The 1999, 2011 and 2020 values are respectively taken from [204], [15] ans [199].

with $y^2 = (\Delta^2 - m_e^2)/2$. The momentum p_e and velocity v_e of the positron are defined at each order by

$$p_e^{(i)} = \sqrt{E_e^{(i)2} - m_e^2}, \qquad v_e^{(i)} = p_e^{(i)}/E_e^{(i)}, \tag{2.21}$$

Finally, the Γ term encompasses the recoil and weak magnetism corrections [197].

$$\begin{aligned}\Gamma =& 2\lambda\frac{(1+f)}{(1+3\lambda^2)}\left[\left(2E_e^{(0)}+\Delta\right)\left(1-v_e^{(0)}\cos\theta\right)-\frac{m_e^2}{E_e^{(0)}}\right]\\ &+\frac{(1+\lambda^2)}{(1+3\lambda^2)}\left[\Delta\left(1+v_e^{(0)}\cos\theta\right)+\frac{m_e^2}{E_e^{(0)}}\right]\\ &+\left(1+\frac{(1-\lambda^2)}{(1+3\lambda^2)}v_e^{(0)}\cos\theta\right)\left[\left(E_e^{(0)}+\Delta\right)\left(1-\frac{\cos\theta}{v_e^{(0)}}\right)-\Delta\right],\end{aligned} \tag{2.22}$$

where $f = \mu_p - \mu_n$ is the anomalous nucleon magnetic moment. In [202, 203], an outer radiative correction δ_{rad} is proposed, taking into account the effect of bremsstrahlung on the process 2.14. Eq. 2.16 must then be multiplied by $(1 + \delta_{rad})$. The total IBD cross-section is obtained by integrating numerically Eq. 2.16 over θ.

The different constants employed in Eq. 2.16 and its subsequent terms are reported in Tab. 2.6, where it can be seen that the the cross-section normalization σ_0 has increased by 1.2% during the last decades. This evolution is driven by the change in the neutron lifetime and equivalently in λ. Indeed, τ_n and λ are related in the measurement of the up and down quark mixing element of the Cabibbo–Kobayashi–Maskawa matrix, $|V_{ud}|$, although λ can also be measured independently from the angular correlation between the neutron spin and the emitted electron in neutron decay [15]. For the expression based on the neutron lifetime, the change between 2011 and 2020 is significant with respect to the uncertainty. This is due to the significant decrease of the neutron lifetime during the decade. The norm uncertainty of the IBD cross-section is dominated by the uncertainty on σ_0, itself led by the uncertainty on λ or τ_n. As a result, the cross-section uncertainty over the whole energy range is 0.1%.

Compared to the zeroth order, the implementation of the first order correction slightly diminishes the IBD cross-section as the recoil correction increases with higher energies [197].

The cross-section is decreased by 0.1% in the vicinity of the threshold and by 0.5% at 10 MeV. The folding of the reactor $\bar{\nu}_e$ spectrum (rapidly falling off with energy) with the IBD cross-section (rising with energy) results in an IBD spectrum starting at 1.806 MeV and peaking around 4 MeV, as shown in Fig. 2.13b. The main limitation of the IBD process comes from its threshold, preventing the detection of approximately 75% of a PWR flux among which lies the activation neutrino component (see Sec. 2.2.2). For research reactors, the activation component can contribute to a few percents to the $\bar{\nu}_e$ flux above the IBD threshold. The IBD cross-section for reactor $\bar{\nu}_e$ is approximately 6×10^{-43} cm^2 per fission, as shown by the IBD mean cross-sections per fission (or IBD yield) reported in Tab. 2.5.

Several types of IBD detectors based on organic scintillator are commonly employed in reactor experiments. A scintillator is a transparent material[1] that emits flashes of light when a charged particle goes through it, losing its energy along its passage, or if a γ-ray interacts with it. Scintillator detectors are based on hydrogenous material providing the proton target for the IBD as well as the medium for detecting the outgoing positron. The resulting neutron is either captured on the scintillator protons or on specifically added targets such as cadmium, gadolinium or lithium. These added targets are selected for their high neutron capture cross-section in order to increase the capture probability of the IBD neutron, but also to decrease the mean capture time of the neutron in order to easily reject backgrounds.

The IBD products are detected as a very specific pulse pair delayed from one another. The first signal, or *prompt signal*, is due to the deceleration and annihilation of the positron with a nearby electron, producing two back-to-back 511 keV photons. The resulting light intensity is proportional to the energy of the positron plus the two 511 keV photons, and is collected by photodetectors. The photodetectors turn the light into an electric signal proportional to the flash intensity. The visible prompt energy is

$$E_{vis} = E_{\bar{\nu}_e} + 2 \times 0.511 \text{ MeV} - E_{thr} - T_n \simeq E_{\bar{\nu}_e} - 0.784 \text{ MeV}, \tag{2.23}$$

where the neutron kinetic energy T_n depends on the diffusion angle as seen in Eq. 2.20. In practical case, the average of T_n over the diffusion angle is employed to determine the prompt energy [205]. The second pulse, or *delayed signal*, comes from the capture of the neutron after thermalization. The energy released by the neutron capture and the time difference between the prompt and delayed signals depends on the capture target and on its concentration. The typical orders of magnitude are 8 MeV and 30 μs for a capture on Gd, and 2.2 MeV and 200 μs on hydrogen [206]. Illustration of an IBD interaction is shown in Fig. 2.13a. The detected spectrum in an IBD experiment is thus the prompt positron spectrum, which can be unfolded into an IBD $\bar{\nu}_e$ spectrum. Due to unavoidable detector effects (quenching[2], detector resolution, energy loss occurring in the detector, detection efficiency), the IBD spectrum is not simply given as the prompt spectrum offset by 0.784 keV. Instead, the unfolding procedure is based on a response matrix containing the probability for a $\bar{\nu}_e$ of a given energy to be measured with a specific prompt energy [207].

Most of the reactor experiments use liquid scintillator (LS) in which the neutron target is directly loaded. For instance, Double Chooz, Daya Bay and RENO use Gd-LS detectors. Two reactor experiments, DANSS (Detector of the reactor AntiNeutrino based on Solid Scintillator) and SoLid (Search for oscillation with a ^{6}Li detector), use plastic scintillator (PS) with the neutron targets (respectively Gd and Li) contained in a coated screen attached to the PS strips

---

[1] The requirement is usually a high transparency for photon with wavelength above 400 nm.

[2] Quenching is the dissipation of the deposited energy via other processes than scintillation. It results in a loss of visible energy, decreasing the light emission efficiency of the scintillator. The emitted scintillation light following a deposition depends on the particle that has deposited the energy.

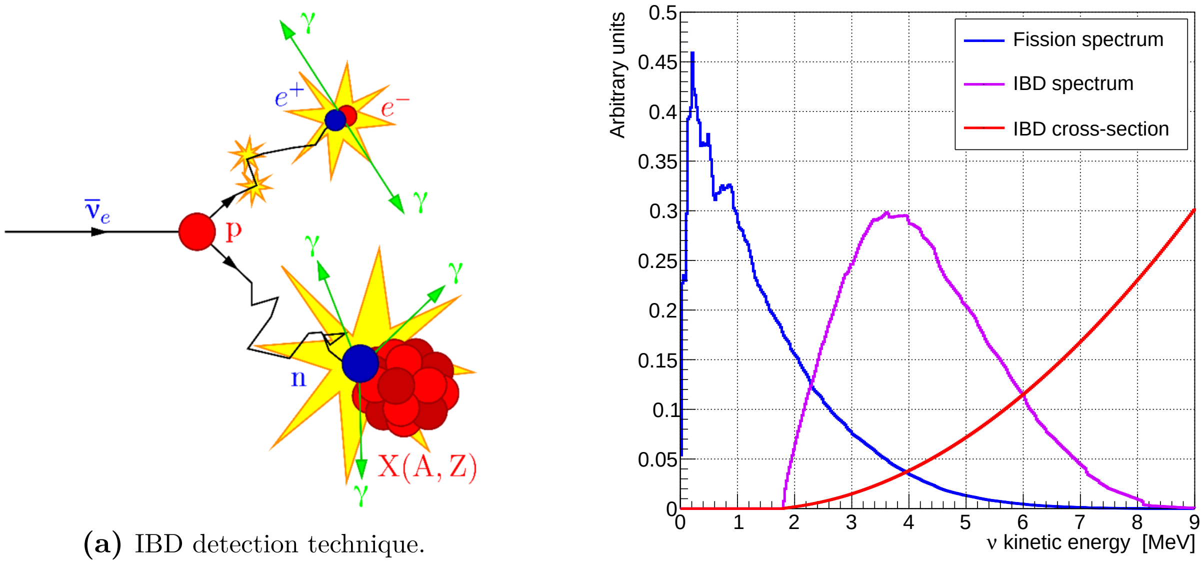

(a) IBD detection technique.

(b) IBD spectrum.

Figure 2.13: **(a)** Scheme of the coincident signal signing the IBD process. The positron slows down and annihilates almost instantaneously with a nearby electron, producing two back-to-back 511 keV photons. The neutron is moderated and then captured on a specific nucleus. **(b)** Illustration of the fission neutrino spectrum of ^{235}U, the IBD cross-section, and the resulting IBD spectrum. The fission spectrum is computed with CFY from the JEFF-3.3 database.

[208, 209]. The choice of the target loading also depends on the size of the detector and if the detector is segmented into several units. For instance, Gd-LS is not optimal for compact detectors or highly segmented detectors as γ-rays can escape from the detector. Instead, PROSPECT and SoLid use ^{6}Li as a neutron target, $n + {}^6\mathrm{Li} \rightarrow \alpha + {}^3\mathrm{H}$. The emitted α particle and the tritium are mostly localized and the heavy charged products allow a clear particle identification [147].

Background events in IBD detection come from other processes also giving rise to a coincident prompt and delayed signal in the detector. The main backgrounds are induced by accidental coincidences mostly due to the natural radioactivity, and by cosmic muon spallation products [184]. An important case of the latter type is the fast neutron background due to cosmic muon induced neutrons [210]. These energetic neutrons can recoil off a proton before being captured. A second important cosmic induced background comes from the (β^-, n) decay of neutron rich nuclei such as ^{9}Li and ^{8}He produced in cosmic muon interactions [210]. These decays will mimic IBD candidates over the whole energy spectrum due to large Q_β superior to 10 MeV. Finally, there may be an important reactor correlated background depending on the reactor type and on the baseline. For instance, fast neutrons generated from fission could result in a prompt proton recoil and a delayed capture signal. To discriminate these backgrounds, different cuts are applied. They consist in associating a window of acceptable values regarding the energy of an event, the coincidence time between two events, or the topology of an event [151]. Another type of selection cut consists in rejecting all events after observing a muon-induced event.

Source of uncertainty	Emitted uncertainty [%]	IBD uncertainty [%]
Spectrum prediction	1.4	2.4
Fission fraction	0.4	0.6
Fission energy	0.3	0.3
Reactor power	0.5	0.5
Cross section	-	0.1
Distance	-	0.01
Total	1.6	2.5

Table 2.7: Uncertainty budget on the $\bar{\nu}_e$ flux emitted by a PWR and the flux detected in an IBD experiment, assuming values from [211] and Huber-Mueller spectra.

2.3.1.1 Reactor antineutrino anomaly

In 2011, a comparison between the Huber-Mueller (HM) model[1] and the IBD rates from 19 short-baseline experiments revealed a deficit of the measured mean cross-section per fission [15], whose current value of $(6.6 \pm 2.4)\%$ is significant at the level of 2.8σ [120]. Before that, the experimental data and the predictions were consistent with an average ratio of observed event rate to predicted rate of 0.976 ± 0.024 [15]. The increased deficit originated partly from the 3% upward shift of recent $\bar{\nu}_e$ spectrum predictions compared to former predictions. The remaining discrepancy came from the updated value of the free neutron lifetime revising the IBD cross-section, leading to an increase of about 0.4%. This deficit is called the Reactor Antineutrino Anomaly (RAA) and has been confirmed since then by recent reactor experiments at PWR and research reactors.

Establishing an accurate prediction of a reactor neutrino spectrum is not an easy task, and CM and SM predictions have their own limitations as it was previously discussed. In the ratio of the measured over the predicted mean cross-section per fission, the uncertainty is dominated by the prediction, as shown in Tab. 2.7 detailing the typical uncertainty budget in an IBD experiment conducted at a PWR [211]. The ratio measured by Daya Bay is 0.952 ± 0.014 (exp) $\pm\, 0.023$ (model), where the dominant experimental uncertainty come from the uncertainty on the number of target protons [212]. In STEREO, which measures a pure ^{235}U flux, the observed to predicted ratio is 0.948 ± 0.008 (stat) $\pm\, 0.023$ (syst) $\pm\, 0.023$ (model), where the two first uncertainties are experimental [158].

Hence, the RAA could find its origin in a bias in the models not accounted for in the uncertainty budget, from an experimental bias in the normalization of the ILL β spectra used as inputs for the CM predictions, or from a bias in the normalization of the predictions induced by the CM. A last possibility is the existence of a sterile neutrino, already discussed in Ch. 1. An incorrect prediction of the ^{235}U mean cross-section per fission as the sole origin of the RAA is favored at almost 3σ with respect to having a sterile neutrino oscillation as solely responsible for the RAA [158]. Additionally, in the absence of sterile neutrino oscillation, global fits to all $\bar{\nu}_e$ rate measurements show a 3σ preference for a bias in the modeling of a specific actinide over a common mismodeling of all CM predictions [213].

The hypothesis of a sterile neutrino oscillation is disfavored from recent very-short baseline experiments, whose key characteristics are summarized in Tab.2.8 and in Fig. 1.6. DANSS,

---

[1] The Huber-Mueller model refers to the converted spectra of ^{235}U, ^{239}Pu and ^{241}Pu obtained from Huber's CM together with the ^{238}U spectrum predicted with the SM from Saclay group.

Experiment	**Power** [$\mathrm{MW_{th}}$]	**Baseline** [m]	**Overburden** [m.w.e]	**Target material**	**Segment**
DANSS [214]	3100	10.7 - 12.7	50	Gd layer PS	2D
NEOS [216]	2800	24	20	Gd LS	none
STEREO [151]	55	10	15	Gd LS	1D
PROSPECT [147]	80	7 - 13	surface	^{6}Li LS	2D
Neutrino-4 [148]	100	6 - 12	surface	Gd LS	2D
SoLid [149]	50 - 80	5.5 - 12	10	^{6}Li layer PS	3D

Table 2.8: Overview of the on-going experimental efforts for detecting active-sterile oscillation at a nuclear reactor, along with their key experimental parameters. The detector technology is based on liquid scintillator (LS) or on plastic scintillator (PS), possibly segmented into a 1D, 2D, or 3D array. Baseline given as an interval means that the detector can be moved in this interval

STEREO and PROSPECT have respectively performed a measurement of the flux of a commercial reactor (Kalinin Nuclear Power Plant, Russia) and of two research reactors (HFR at ILL in France, and HFIR at ORNL in the USA) where the RAA has been observed for a pure ^{235}U $\bar{\nu}_e$ flux. With a total of 2.1 millions IBD events, DANSS excludes a large part of the sterile neutrino parameter space including the best-fit obtained from the RAA and the GA [209, 214]. After 179 days of reactor-on data, STEREO's data are compatible with the null oscillation hypothesis and the best-fit point of the RAA is rejected at more than 99.9% CL [151]. Finally, PROSPECT disfavors the RAA best-fit point at 2.5σ based on 50 000 IBD events [215]. NEOS' result is consistent with the other very-short baseline reactor experiments, excluding a significant part of the RAA allowed region and superimposing with Bugey-3 and Daya Bay exclusion limits [216]. Located at the SM-3 research reactor in Russia, Neutrino-4 is the only very-short baseline reactor experiment reporting a 2.8σ significant oscillation effect close to the RAA allowed region [148]. Neutrino-4 results still exclude the allowed area from the combined RAA and gallium anomaly at 99.7% CL. This result is in manifest tension with the limits obtained by the other reactor measurements, and further analysis are expected to be delivered. The different exclusion contours of very-short baseline experiments are shown in Fig. 2.14.

2.3.1.2 Shape distortion anomaly

In addition to the RAA, predicted IBD spectra exhibit a significant shape difference with the measured IBD spectrum in most experiments. Once the predicted IBD spectra and the measured spectra are normalized to the same integral, an excess of IBD events is observed in the range 4 to 6 MeV with respect to the predictions. The upward deviation is compensated by a deficit over the rest of the spectrum. These deviations are not consistent with the systematic uncertainties. At first order, the distortions can be approximated by a Gaussian centered at 5 MeV and with amplitude of about 10% and standard deviation of about 0.5 MeV. The spectral distortion was first reported by Double Chooz [218], promptly followed by RENO [219, 220] and Daya Bay [205, 212]. These three distortions are showed in Fig. 2.15. This shape anomaly is also observed in the recent very short baseline reactor experiments, at both commercial and research reactors. The deviation measurements of NEOS [216], PROSPECT [164] and STEREO [207] are shown in Fig. 2.16. DANSS does see a spectral deformation but cannot claim yet that it is consistent with the 4-6 MeV deviation due to the high sensitivity of the spectrum shape with

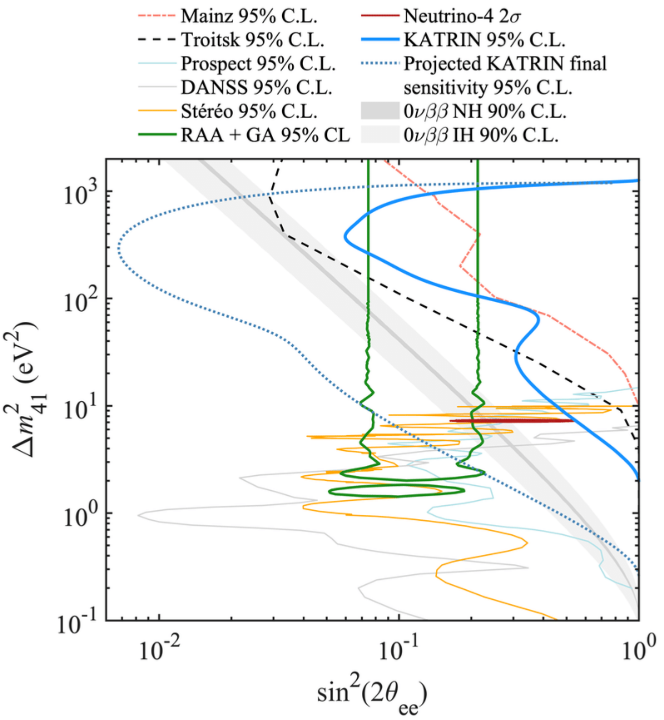

Figure 2.14: Exclusion limits of short-baseline reactor neutrino experiments in the $(\sin^2(\theta_{ee}), \Delta m^2_{41})$ plane. The 95% CL exclusion limit from the analysis of KATRIN's data [121] is shown in blue. The combined GA and RAA allowed region is delimited in green. The figure is from [121].

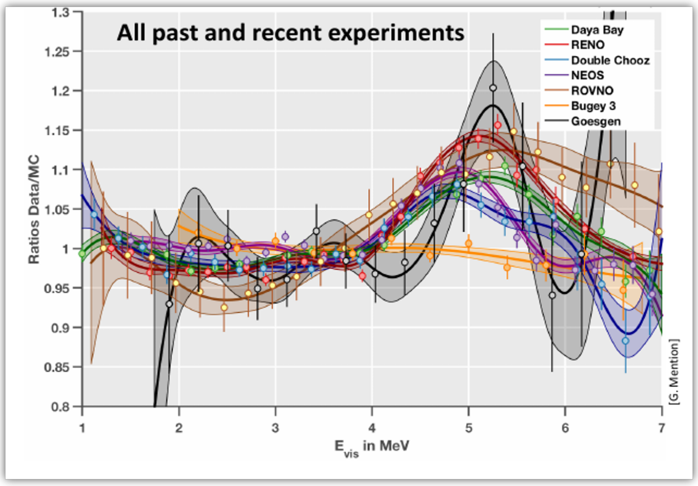

Figure 2.15: Ratio of the measured to the predicted IBD spectrum with respect to the prompt energy in past and present reactor experiments. The figure is taken from [217].

respect to the energy scale. The systematical uncertainty on the measured spectrum shape, mainly dominated by detector-related uncertainties, are of the same order of magnitude than the uncertainties on the predictions. However, the statistical uncertainty can dominate the experimental uncertainty in some experiment, *e.g.* PROSPECT [215]. The Bugey 3 experiment does not observe a significant shape deviation, even when compared to recent predictions [217].

Several possible origins for these deviations have been mentioned in the literature. The distortions observed in different experiments are not always consistent with each other, which could possibly point toward residual biases in the detector energy scale calibration [217]. It also was shown that the excess rates were strongly correlated with the reactor power, which

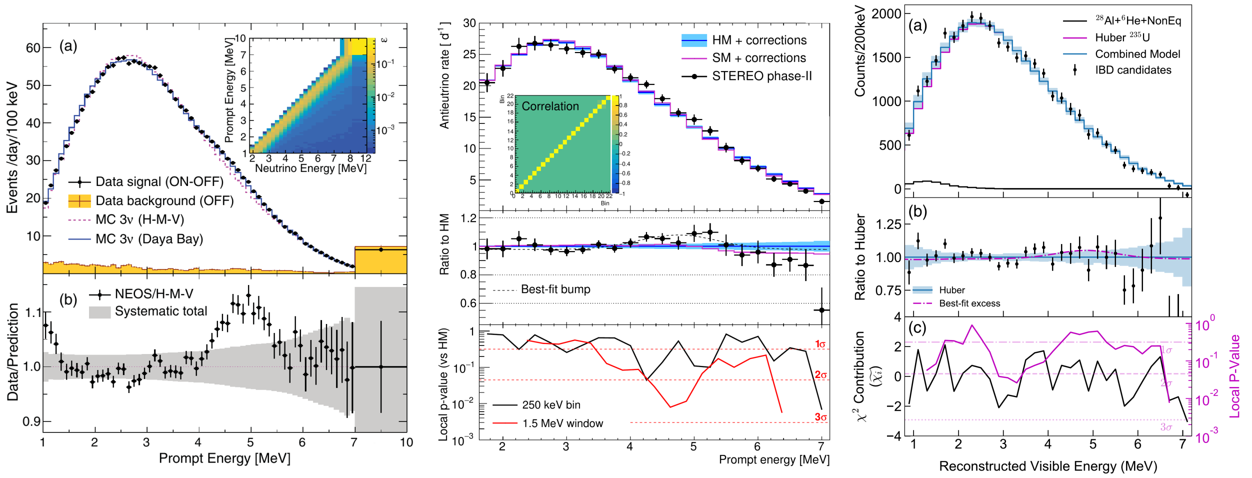

(a) NEOS. **(b)** STEREO. **(c)** PROSPECT.

Figure 2.16: Spectral distortion anomaly from NEOS [216], PROSPECT [164] and STEREO [207] with respect to the prompt energy. For STEREO and PROSPECT, the local standard deviation is shown in the bottom panel. NEOS is conducted at a commercial PWR and measures a $\bar{\nu}_e$ flux originating from the four actinides, while PROSPECT and STEREO measure a pure ^{235}U flux.

discarded backgrounds to be at the origin of this deviation [218]. A misprediction in the model or an underestimated uncertainty budget are to this day the favored explanations. The bias due to unaccounted forbidden transitions in CM predictions was shown to be potentially important while it is not considered in the Huber-Mueller prediction. The corrections applied to forbidden decays have underestimated uncertainties, while these decays can make up to 30% of the neutrino flux [221]. Furthermore, the inclusion in a SM of correct forbidden spectrum shapes based on nuclear shell model computation results in an upwards shift of 1-2% of the neutrino spectrum in the 4-5 MeV range [181]. These two studies point towards an underestimation of the theoretical uncertainties.

A pending question would then be if the shape anomaly originates from one fissionable isotope in particular or from several. At Daya Bay, the IBD spectra of ^{235}U and ^{239}Pu were extracted from the global IBD spectrum based on the prompt spectrum evolution as a function of fission fractions. As a result, a spectral distortion is observed for both isotopes, with the ^{235}U discrepancy being more significant than the ^{239}Pu one due to smaller uncertainties [195]. Moreover, a combined analysis of NEOS and Daya Bay concluded that ^{239}Pu (^{241}Pu) was disfavored at 3.3σ (3.9σ) as the unique source of the spectral distortion [222]. This is further confirmed by PROSPECT and STEREO measuring an almost pure ^{235}U neutrino flux and which have indeed observed a spectral deformation. Additionally, the PROSPECT spectrum disfavors at 2.4% the hypothesis that ^{235}U is the sole responsible for the deviation. Finally, PROSPECT and Daya Bay spectra are consistent with the hypothesis that all isotopes play an equal role in the deviation.

2.3.1.3 Antineutrino flux correlations with fuel composition

The four actinides contribute differently to a reactor IBD flux due to their different fission rates and their different mean IBD cross-sections per fission. As a result, the reactor IBD mean cross-section per fission is correlated to the reactor core fuel composition, and is expected to change over time. The IBD yield evolution as a function of the fission fractions of ^{235}U and ^{239}Pu was measured by Daya Bay in 2017 [223] and by RENO in 2019 [224].

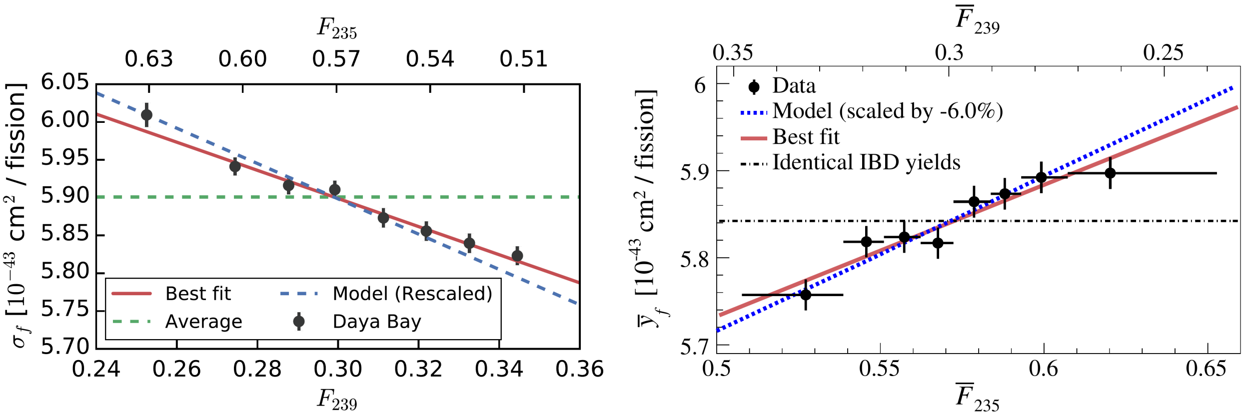

(a) Daya Bay. **(b)** RENO.

Figure 2.17: Evolution of the measured IBD yield per fission with respect to the predicted ^{235}U and ^{239}Pu fission fractions at Daya Bay [223] and RENO [224].

Daya Bay observed a linear fuel-dependent variation in the IBD yield, shown in Fig. 2.17a. Their analysis rejected the hypothesis of a constant $\bar{\nu}_e$ flux at the 10σ level [223]. Moreover, they observed a dependency of the IBD spectrum with the fuel composition and rejected the hypothesis of a constant $\bar{\nu}_e$ energy spectrum at the 5σ level. The variation of the IBD spectrum over time was found to agree with the variation of the predictions scaled to the same integral. However, the slope of the variation of the measured IBD yield exhibited a difference with the slope of the predicted IBD yield evolution, significant at 3.1σ. This discrepancy indicates that an overall deficit between the predictions and the measured flux is not induced by equal fractional deficits from the primary fission isotopes [223]. This could be interpreted as an issue in the modeling of the reactor $\bar{\nu}_e$ flux, with unequal biases on the actinide $\bar{\nu}_e$ spectrum predictions.

RENO also observed a linear dependency between the evolution of the ^{235}U fission fraction and the evolution of the IBD yield, as shown in Fig. 2.17b. The hypothesis of a constant $\bar{\nu}_e$ flux was rejected by RENO's analysis at the 6.6σ level [224]. The variation of the measured IBD yield was fitted with the HM prediction of the IBD yield variation, and no significant deviation was observed at the 1.3σ level.

A bias in the predictions of the four actinide IBD yields could be at the origin of the IBD yield fuel-dependent anomaly, which further motivates to reevaluate the models. In particular, SM predictions could bring interesting insight about the contribution of each actinide to the fuel-dependent $\bar{\nu}_e$ flux change observed at reactors. This has been mentioned in two studies [178, 225], in which different SM predictions of the fuel-dependent variation of the total IBD yield were compared with Daya Bay measurement. In both analysis, the slope of the IBD yield evolution determined by Daya Bay showed a better agreement with the SM predictions than with the HM prediction. However, uncertainties on the IBD yields predicted with the SM were not presented in either study due to the difficulty of assessing a reliable uncertainty budget for SM predictions [178, 225]. This highlights not only the need to reevaluate the SM model, but also the necessity to establish a complete and reliable uncertainty budget for SM predictions in order to quantitatively discuss the agreement between SM model and experimental data.

2.3.2 Coherent elastic neutrino-nucleus scattering

Predicted in 1974 [226, 227], the CEνNS process is a NC interaction where a neutrino of any flavor scatters coherently[1] on all the nucleons of a nucleus:

$$\nu_\alpha + {}^A_Z X \longrightarrow \nu_\alpha + {}^A_Z X. \tag{2.24}$$

The condition for a coherent scattering is satisfied when the momentum transfer q is small compared to the inverse of the nucleus size R, $qR \ll 1$ [229]. The typical inverse size of a nucleus is in the range 25 to 150 MeV, which make reactor antineutrinos fully satisfying the coherence condition. Same as for IBD, the CEνNS process is treated as a four-fermion interaction. As a NC interaction, all flavors of neutrino and antineutrino participate with the same cross-section. The differential cross-section with respect to the recoil energy T of a nucleus of mass M is expressed as [229]:

$$\frac{\mathrm{d}\sigma_{CE\nu NS}}{\mathrm{d}T} = \frac{G_F^2 M}{2\pi}\left[(G_V+G_A)^2 + (G_V-G_A)^2\left(1-\frac{T}{E}\right)^2 - \left(G_V^2 - G_A^2\right)\frac{MT}{E^2}\right], \tag{2.25}$$

where E is the incoming neutrino energy, and the constant G_V and G_A are defined by

$$G_V = [g_V^p Z + g_V^n N]\, F_V(q^2), \tag{2.26}$$

$$G_A = [g_A^p (Z_\uparrow - Z_\downarrow) + g_A^n (N_\uparrow - N_\downarrow)]\, F_A(q^2), \tag{2.27}$$

with Z and N the number of protons and neutrons, and $Z_{\uparrow\downarrow}$ and $N_{\uparrow\downarrow}$ the number of protons and neutrons with spin up ($\uparrow$) and down ($\downarrow$). Another expression of the process cross-section is commonly found in the literature, based on equal neutron and proton form factors [230]. While neglecting the form factor dependence can have an important impact on the cross-section, the agreement of these two approximations is reasonable for incident $\bar{\nu}_e$ with less than 20 MeV, *i.e.* for reactor neutrinos [231]. This is also reasonable as, in many cases, the axial-vector form factor Eq. 2.27 can be neglected which results in similar expressions [229]. The values of NC vector and axial-vector couplings to protons $g^p_{V/A}$ and to neutrons $g^n_{V/A}$ are summarized in Tab. 2.9. The coupling values used in this work are the ones including radiative corrections.

Finally, the neutral weak vector and axial-vector form factors $F_{V/A}(q^2)$ encompass the weak charge distribution of the nucleons as a function of the momentum transfer[2]. An effective approximation, employed in this work, is to assume identical form factors $F_V = F_A$ [232]. Several analytic expressions exists for this nuclear form factor, such as the Fermi form factor [233] or the Helm form factor [234], the latter being used in this work. Form factors tends to unity at small momentum transfer $q^2 \ll M^2$, a deviation from unity describing the loss of coherence in the scattering process. The impact of the form factor on the CEνNS cross-section is small for reactor neutrinos [231], and the discrepancies between different form factor expressions is negligible.

The total cross-section is then obtained by integrating numerically Eq. 2.25 between $T = 0$ and T_{max} given by

$$T_{max} = \frac{2E^2}{(M+2E)}. \tag{2.28}$$

---

[1] A coherent scattering conserves the integrity of nucleons in neutrino-quark interactions, allowing an effective description of the neutrino interaction with nucleons. The nucleon current is then represented as a sum of vector and axial currents [228].

[2] The form factor is defined as the Fourier transform of the weak charge distribution.

	g_V^p	g_V^n	g_A^p	g_A^n
Tree level	$1/2 - 2\sin^2\theta_W$	-1/2	1/2	-1/2
With radiative corrections	0.0301	-0.5116	0.4995	-0.5120

Table 2.9: Values of neutral current vector and axial-vector couplings to protons $g_{V/A}^p$ and to neutrons $g_{V/A}^n$ used in the CEνNS cross-section. The first row gives the coupling expressions at tree level, while the second row displays the values with radiative corrections based on the values given in Table 10.3 from [199]. θ_W is the Weinberg angle.

The CEνNS cross-section scales with the squared number of neutrons, $\sigma_{CE\nu NS} \sim N^2$, which can be seen in Fig. 2.18 with the cross-section calculated without any energy threshold applied (solid lines). It can thus exceed the IBD cross-section by more than two orders of magnitude. A CEνNS interaction is detected by measuring the nucleus recoil energy typically lying in the sub-keV regime for reactor $\bar{\nu}_e$. Even though CEνNS is a thresholdless process, the detector threshold T_{thr} implies than only neutrinos with an energy over an effective threshold E_{thr} given by $T_{thr} = 2E_{thr}^2/(M + 2E_{thr})$ will be detected, as illustrated in Fig. 2.19a. For instance for a germanium target, a 10 eV detector threshold can detect neutrinos down to 0.58 MeV, and a 100 eV detector threshold requires a minimum neutrino energy of 1.84 MeV. Hence, the CEνNS process could potentially give access to neutrinos below the IBD threshold. In particular, it could give access to the $\bar{\nu}_e$ emitted from activated element in PWR. The actual number of CEνNS events occurring in the detector is obtained by integrating the differential cross-section between T_{thr} and T_{max}. As E_{thr} increases with the nucleus mass for a given recoil energy threshold T, the cross-section of composite targets displays multiple components, as seen in Fig. 2.18. The CEνNS cross-section being given as the average over all the nuclei of the target[1], the behavior displayed for low neutrino energy is based on the recoil of light nuclei. As the neutrino energy increases, the recoil of heavier nuclei takes the upper hand in the total cross-section behavior. Note that the different cross-section components of a composite target appear increasingly with higher detector thresholds. For instance, in Fig. 2.18, the tungsten cross-section appears distinctively in the CaWO$_4$ cross-section above 2 MeV for a 50 eV recoil energy threshold, while it is indistinguishable for a zero recoil energy threshold.

A neutrino of a given energy will be able to produce a range of recoil energies. Thus, the detection of a CEνNS signal smears out the reactor neutrino spectrum into a recoil spectrum. Therefore, the neutrino energy cannot be measured with CEνNS contrary to the IBD process. The recoil spectrum is obtained by folding the differential cross-section over the neutrino spectrum and then by integrating it over the neutrino energy:

$$S_{recoil}(T) = \int_{E_{thr}}^{E_{max}} \mathrm{d}E \; S_r(E) \; \frac{\mathrm{d}\sigma_{CE\nu NS}}{\mathrm{d}T}(E,T). \tag{2.29}$$

The recoil spectra obtained for several target materials are shown in Fig. 2.19b, where it can be seen that the light and heavy nucleus components of the CaWO$_4$ cross-section each produces a specific component of the CaWO$_4$ recoil spectrum (the light oxygen and calcium component corresponding to the higher recoil energy component). Using Eq. 2.28, the recoil energy extends up to 13 keV for an incoming 10 MeV neutrino scattering on oxygen, and up to 3 keV for a scattering on germanium.

Contrarily to the time and space correlated IBD signal, the CEνNS signal is a standalone recoil that can be spoiled by many processes inducing a nuclear recoil. Thus, ultra-low energy threshold detectors with high background discrimination capabilities are two necessary

---

[1] For each nuclei, the cross-section results from the average over the abundance of their respective isotopes.

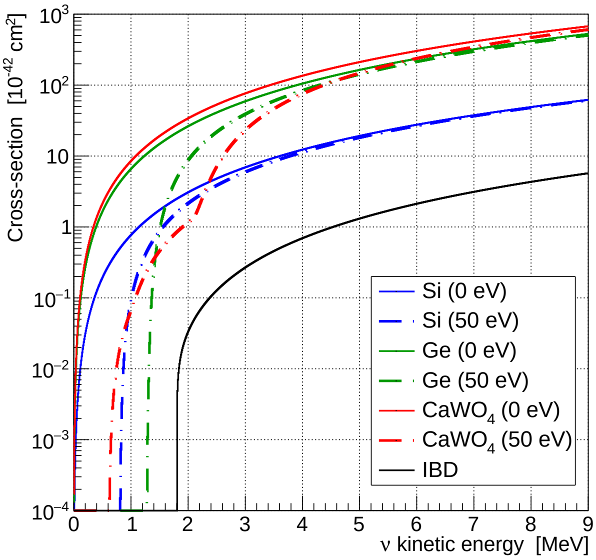

Figure 2.18: CEνNS cross-sections for different target materials and detector recoil energy thresholds (T_{thr} = 0 eV or 50 eV).

requirements to properly exploit a CEνNS signal. One of the biggest challenges of a reactor CEνNS experiment is then to discriminate and to characterize the different backgrounds in a yet unexplored sub-keV energy regime, which essentially explains why CEνNS has yet to be measured in a reactor experiment. For instance, the NUCLEUS experiment aims to reach a background count rate of 100 counts $\cdot$ keV^{-1} $\cdot$ kg^{-1} $\cdot$ day^{-1} for a recoil threshold of 20 eV. With a 10 g detector, NUCLEUS is expected to observe CEνNS with a sensitivity of 4σ after one year of measuring time in a pessimistic scenario where the residual backgrounds rise exponentially over the expected signal [235].

2.3.2.1 CEνNS experiments at nuclear reactors

CEνNS is a promising tool to explore the Standard Model at low energy, and holds a broad field of research: measurement of the Weinberg angle at low momentum transfer [235], investigating a possible neutrino magnetic dipole moment [236], application in supernovae detection, citing only a few among many. Most notably, CEνNS is a robust probe to test the sterile neutrino hypothesis as it is a NC interaction and thus is flavor insensitive [237]. In 2017, the CEνNS process was observed for the first time by the COHERENT experiment with a 6.7σ confidence level [238]. Neutrinos emitted by the Spallation Neutron Source (SNS) at the ORNL were detected by a 14.6 kg Na-doped CsI scintillator detector with a 4 keV recoil threshold. The SNS generates the most intense pulsed neutron beams in the world by striking accelerator-driven 1 GeV protons with a mercury target. The proton-mercury interaction produces pions that decay at rest into a flavor mix of neutrinos yielding energies up to 50 MeV (still in the good range for coherent scattering). In 2020, the COHERENT collaboration reported a second observation at 3.5σ of CEνNS using the 24 kg liquid Argon scintillator detector CENNS-10 with 20 keV recoil threshold, confirming the N^2 dependence of CEνNS [239]. In addition to the already well-tested scintillation technique, numerous technologies and target materials are investigated in planned or undergoing experiments to detect and explore CEνNS. Especially, the experiments set at nuclear reactors are presented below and their key characteristics are summarized in Tab. 2.10.

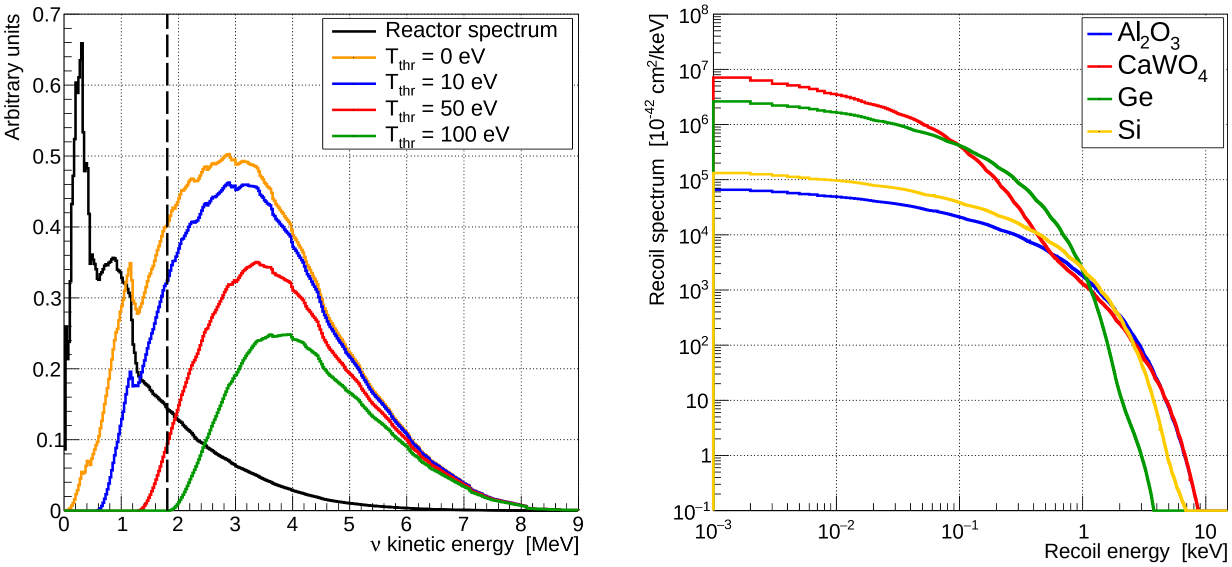

(a) Cross-section.

(b) Energy spectrum.

Figure 2.19: **(a)** Reactor $\bar{\nu}_e$ spectrum and energy spectrum of $\bar{\nu}_e$ detected with CEνNS for several germanium detector thresholds. The vertical dotted line indicates the IBD threshold. The reactor spectrum is computed with CFY from the JEFF-3.3 database [136], activation $\bar{\nu}_e$ yields and fission fractions from [145]. **(b)** CEνNS recoil spectrum for several target materials and a zero detector threshold, considering the same reactor spectrum as in (a).

Various detection technologies are currently investigated to observe CEνNS from reactor neutrinos as seen in Tab. 2.10, the two most common being cryogenic detectors and HPGe point-contact detectors. Cryogenic detectors measure the temperature rise following an energy deposition in a crystal kept at a low temperature $\sim \mathcal{O}(\mathrm{mK})$ to ensures a small heat capacity. Such detectors are sensitive to sub-keV energy depositions and have the advantage to avoid quenching effects at those recoil energies. Cryogenic detectors will be deployed in NUCLEUS, Ricochet and at the Mitchell Institute Neutrino Experiment at Reactor (MINER).

NUCLEUS

The NUCLEUS experiment will be located at the very near site of the Chooz nuclear power plant [235]. During the first phase of NUCLEUS, the detector will consist of two superimposed $CaWO_4$ and Al_2O_3 arrays [240]. The use of different targets will improve the background discrimination, CEνNS interactions yielding different spectra on the two types of calorimeter while neutrons are expected to induce similar signals due to the scattering on oxygen [235]. The targets are installed in a cryostat surrounded by two Germanium and Silicon cryogenic veto detectors for active background discrimination. A 0.5 g Al_2O_3 prototype has already achieved a 19.7(9) eV threshold [241]. NUCLEUS will measure the absolute CEνNS rate and has to rely on a reactor neutrino flux prediction. The prediction will significantly contribute to systematic uncertainty to the measurement [235]. The first phase NUCLEUS-10g should begin to take data in 2022 and aim to achieve a 10% precision on the CEνNS cross-section, while the second phase NUCLEUS-1kg planned for 2024 should reach a 1% precision.

Ricochet

The Ricochet experiment will deploy germanium and zinc cryogenic calorimeters at 8 m from the ILL research reactor. The semiconductor properties of Ge and the superconducting nature of Zn should allow to identify particles and to discriminate between nuclear recoils and electromagnetic backgrounds. The goal for the first phase is to push particle identification down to 50 eV using a 1.3 kg payload. Ricochet will benefit from the STEREO background characterization. In addition to the usual cosmic-ray, γ-ray and natural radioactivity background, the proximity from the reactor core will induce a high level of reactor correlated background. In 2024, Ricochet is expected to detect 20 events per day which should lead to a 1% precision measurement of the CEνNS rate after a year.

MINER

The MINER detector consists of Ge and Si cryogenic calorimeters, with an adaptative baseline fom 1 m to 3 m thanks to a movable reactor core, allowing a precise test of the sterile neutrino hypothesis [242]. Campaigns to study the neutron and γ-ray backgrounds have been conducted [127]. It results that for a planned 10 kg payload and 100 eV threshold, MINER is expected to observe CEνNS at 5σ within a few months to a year. The first data-taking are ongoing, and its phase-2 should be operational in 2021 and run for a few years.

CONUS

The Coherent elastic Neutrino nucleus Scattering (CONUS) experiment started in 2018 with four HPGe point-contact (HPGe PC). With a recoil threshold of 300 eV in electron-recoil equivalent (eV$_{\mathrm{ee}}$) and exposures of reactor-on and off data of respectively 248.7 kg $\cdot$ days and 58.8 kg $\cdot$ days, no hint for a CEνNS signal has been observed yet, setting a constraint on the CEνNS signal in the fully coherent regime with reactor antineutrinos [243]. Additional statistics and sensitivity improvements are expected in the upcoming years.

νGeN

During the first phase of the Neutrino–Ge Nucleus (νGeN) experiment, four HPGe PC detectors will be deployed at 14 m from a reactor core, using the shiedling from the former experiment GEMMA [244]. The experiment aims to achieve a threshold of 350 eV$_{\mathrm{ee}}$, which should allow the detection of up to tens of CEνNS events per day [244]. Another goal of νGeN will be to measure the neutrino magnetic moment, whose best current limit has been set by GEMMA [245]. The νGeN detectors has been produced and tested, and preparations for the measurements at KNPP are ongoing.

TEXONO

The TEXONO collaboration have installed a HPGe PC detector at the Kuo-Sheng Neutrino Laboratory, 28 m away from a commercial reactor core. The physics program of TEXONO is vast, investigating on neutrino electromagnetic properties and dark matter in addition to pursuing sterile neutrinos and CEνNS signals. One of TEXONO's goal with respect to CEνNS is to test the nuclear coherency in the energy range of reactor neutrinos [246, 247]. With an achieved energy threshold of about 200 eV$_{\mathrm{ee}}$, CEνNS has not yet been observed by TEXONO. Efforts to lower backgrounds and energy threshold are ongoing, and data taking and analysis are continuing.

Experiment	**Power** [MW_{th}]	**Baseline** [m]	**Overburden** [m.w.e]	**Technology**	**Payload** [kg]	$\mathbf{T_{thr}}$ [eV]
NUCLEUS [235]	2×4250	59	3	$Al_2O_3/CaWO_4$ cryo. det.	0.01	20 (nr)
				Ge/Si cryo. det.	1	20 (nr)
Ricochet [253]	58	8	~ 10	Ge/Zn cryo. det.	1.3-10	50 (nr)
MINER [127]	1	$1 \leftrightarrow 3$	15	Ge/Si cryo. det.	$\mathcal{O}(10)$	100 (nr)
CONUS [254]	3900	17	$15 \rightarrow 45$	HPGe PC	3.7	300 (ee)
νGeN [244]	3000	$10 \leftrightarrow 14$	70	HPGe PC	1.6	350 (ee)
TEXONO [247]	2900	28	30	HPGe PC	1.5	200 (ee)
CONNIE [248]	3800	30	surface	Si CCD	~ 0.1	$40 \rightarrow 7$ (ee)
NEON [250]	2800	24	20	NaI[Tl]	15	200 (ee)
RED-100 [255]	3000	19	65	Dual-phase liquid Xe	160	250 (ee)

Table 2.10: Overview of the on-going experimental efforts to detect CEνNS at nuclear reactors, along with their key experimental parameters. The reported energy thresholds are expressed in electron-recoil equivalent (ee) or nuclear-recoil equivalent (nr) energy.

CONNIE

The Coherent Neutrino Nucleus Interaction Experiment (CONNIE) detector consists in an array of 14 charge-coupled devices (CCD) made of silicon, imprinted by particle tracks when they pass through the CCDs [248]. The array geometry has been designed for track and shower identification, used to distinguished diffusion hits (due to nuclear recoils and X-rays) from background events (due to muons and electrons). CONNIE can currently detects the ionization energy of nuclear recoils down to 40 eV, and aim to reach of 7 eV threshold for ionization energy [249]. CONNIE's last results show no excess of CEνNS event in the reactor-on data with respect to reactor-off, putting an upper limit on the CEνNS rate at about 40 times above the expectation [248].

NEON

The Neutrino Elastic-scattering Observation with NaI (NeON) detector is located at the same reactor complex than NEOS and RENO, 24 m away from a reactor core, and thus benefits from their background studies. Made of six units of NaI(Tl) scintillator crystals based on the COSINE-100 experiment detector design, NeON display a 200 eV_{ee} [250]. The NeON-phase 1 is planned to last until 2022.

RED-100

The Russian Emission Detector (RED-100) is a noble gas two-phase emission detector [251], whose principle was proposed more than 50 years ago [252]. In such detectors, ionization electrons are produced in a condensed noble gas following the primary particle interaction, and are moved by applied electric fields toward a gas phase above the liquid surface where they are detected as single-electron events. Based on the detector tests, CEνNS events resulting in at least four single electron events should be detected. The data taking should start in 2021.

2.4 Summary

The chain reaction occurring in a nuclear reactor results in a intense flux of $\bar{\nu}_e$ of about $2{\times}10^{20}$ $\bar{\nu}_\mathrm{e}$/s per GW_th, making commercial and research reactors suitable $\bar{\nu}_e$ sources for neutrino experiments. This flux is produced by four fissionable isotopes in a PWR (^{235}U, ^{238}U, ^{239}Pu, ^{241}Pu), and almost entirely from ^{235}U in a research reactor. It results in about 6 $\bar{\nu}_e$ emitted per fission in both types of reactors, with a dominant ^{235}U contribution followed by ^{239}Pu in PWR, respectively $\sim$ 55% and $\sim$ 30% on average over a rector cycle. The neutron flux produced by the chain reaction also activates several isotopes that can contribute up to 10% to 20% to a reactor $\bar{\nu}_e$ flux, depending on the fuel and on the structural material. Thus, significant differences are expected in the $\bar{\nu}_e$ flux and spectra emitted by a PWR and a research reactor. Although the thermal power of a research reactor is lower by two orders of magnitude compared to a PWR, it is compensated by its compactness that allows to conduct experiment closer to the core.

Reactor experiments have exhibited discrepancies between predictions and experimental data. The RAA is a rate discrepancy significant at almost 3σ between measurements and predictions based on recent conversion models that is observed in all IBD experiments. A new generation of IBD reactor experiments located at very short baseline has been deployed to investigate the sterile neutrino hypothesis as a possible explanation to the RAA. At the moment, a significant part of the RAA allowed region has been excluded, and a bias from the predictions is now favored as the origin of the RAA. Such bias could also explain the shape difference observed between measured IBD spectra and predictions. Additionally, the bias in the predictions is at the origin of a discrepancy with the fuel-dependent IBD yield variation measured at Daya Bay. Conversion models, used in all recent predictions, display uncertainties of about 2-3% that dominate the uncertainty of the RAA. These uncertainties from the conversion models are on par with experimental ones regarding the spectrum shape anomaly, while the experimental uncertainty dominates the analysis of the fuel-dependent IBD yield variation. Another possibility to predict reactor spectra is the summation method. However, current summation models display a 10% uncertainty mainly due to incomplete nuclear databases, or are lacking uncertainties due to the complexity of the task.

Conversion and summation models both exhibit significant limitations, and must be refined in order to address the RAA, the shape discrepancy and the fuel-dependent IBD yield evolution. Reactor spectra must also be predicted down to 0 MeV for the upcoming CEνNS experiments, which is not possible with conversion models. The thresholdless CEνNS process will allow to measure the reactor $\bar{\nu}_e$ flux below the IBD threshold of 1.8 MeV, where lies up to 75% of the flux. Activation $\bar{\nu}_e$ (from fuel activation and structural material activation) that cannot be detected in IBD experiments conducted at commercial reactors can then contribute significantly to the $\bar{\nu}_e$ flux measured in future CEνNS experiments. The prediction will contribute significantly to the systematic uncertainty of the measurement, and must present a reliable uncertainty budget below the IBD threshold. In this context, the summation method and the associated uncertainties have been revisited using an advanced theory of β-decay and recent nuclear data, which is the topic of Ch. 3 and 4.

3

Improved modeling of β-decay spectra

Contents

The formalism used to describe the energy spectra of the electron and the antineutrino emitted during a β-decay is introduced in this chapter. Evaluated nuclear data and their inclusion as modeling parameters for reactor spectra will be treated in Ch. 4. The different terms necessary to build a β transition spectrum are presented along the associated covariance matrices. The modeling of these terms is discussed in the context of an improved modeling with respect to the former BESTIOLE model. The previous version of the BESTIOLE software was employed by the Saclay group in 2011 to build the predictions previously mentioned in Sec. 2.2.3. Lastly, this improved modeling of $\bar{\nu}_e$ spectra is compared to other state-of-the-art β-decay models such as BetaShape, another software also developed at CEA. Even though BetaShape has been initially developed for β spectrum modeling, it is completely suitable to predict the associated $\bar{\nu}_e$ spectra.

In this chapter, the term "endpoint energy" will be used for both the maximum kinetic energy reachable by the electron and neutrino, E_0, but also for the total energy available for a transition $W_0 = E_0 + m_e$.

3.1 The BESTIOLE software

Beta Energy Spectrum Tool for an Improved Optimal List of Elements (BESTIOLE) is a software developed at CEA whose purpose is to model the electron and neutrino spectra of β-decays. Written in C++ with the ROOT framework [256], it takes as input a text file database that contains the details of the different transitions for all the isotopes of interest. Such file will be referred to as a BESTIOLE database, and its composition is presented in Ch. 4. BESTIOLE saves in a ROOT file the β and $\bar{\nu}_e$ spectra of each isotope along with their respective covariance matrices. BESTIOLE was developed in 2011 by the Saclay group to model fission $\bar{\nu}_e$ spectra [13]. In the following, the modeling ingredients of this prediction will be referred to as the BESTIOLE-2011 version, or B-11 for short. Starting from the B-11 version, the BESTIOLE modeling has been improved step by step in the present work by lifting several approximations and refining some terms. Furthermore, a thorough work has been done to characterized the related uncertainties. More broadly, all uncertainties have been reviewed and are presented either in this chapter for the modeling ones, or in Ch. 4 for the data-origin uncertainties. The improved BESTIOLE modeling, labeled as B-21, is presented in this chapter along the formalism used to describe β and $\bar{\nu}_e$ spectra, and is put in perspective with B-11.

3.2 Fermi's golden rule

Many authors have participated in the development of the theory of the weak interaction. It started in its early days as Fermi's theory of β-decay. The $V - A$ structure of the weak interaction was then disclosed step by step, on the basis of both theoretical (such as Gamow and Teller's work [257, 258] and Feynman and Gell-Man's work [259]) and experimental work (for instance the Wu experiment [37]). Finally, the weak force was unified with electromagnetism into a single electroweak interaction by Glashow, Weinberg and Salam [260–262]. However, one does not need to invoke such an advanced theory as the electroweak interaction breaks distinctively into the weak force and electromagnetism at low energy. The equations detailed in the following sections are mainly based on the work of Behrens and Bühring [263], which specifically describes the β-decay as a low energy weak interaction process.

Soon after Pauli proposed the existence of the neutrino to explain the continuity of beta spectra, Fermi developed his theory of β-decay [2]. In the latter, the Hamiltonian H_β associated to the weak interaction is treated as a perturbation of a more general Hamiltonian. The overall results are encompassed by the famous Fermi's Golden Rule that relates the decay probability per unit of time (or transition rate) between an initial state $|i\rangle$ and a final state $|f\rangle$[1] with the interaction Hamiltonian H_β. In short form, the Golden Rule is written as

$$\Gamma_{if} = 2\pi \int |T_{if}|^2 \, \delta(E_i - E) \mathrm{d}n, \tag{3.1}$$

---

[1] To simplify the writing, the notation $|f\rangle$ will be associated to both the final nucleus and the final state of the whole system. The same applies to $|i\rangle$. The context will differentiate between the two uses.

where dn is the density of states *i.e.* the number of states accessible for outgoing particles with energy between E and $E + \mathrm{d}E$, E_i is the initial total energy of the system, and T_{if} is the transition matrix element related to H_β in first order of perturbation theory through [263]:

$$(2\pi)^4\delta^4(p_f - p_i)T_{if} = -\langle f|\int H_\beta(x)\mathrm{d}^4x\,|i\rangle\,, \tag{3.2}$$

with p_i and p_f the four-momenta of the initial and final system states. This formulation of the interaction density comes from the assumption that the interaction is local, with the involved particles interacting at the same vertex. In the case of a β-decay, Eq. 3.1 can be rewritten as [263]

$$\Gamma_{if} = \frac{1}{(2\pi)^5}\sum_s\int |T_{if}|^2\,\delta^4(p_f + p_e + p_\nu - p_i)\;\mathrm{d}p_f\;\mathrm{d}p_e\;\mathrm{d}p_\nu, \tag{3.3}$$

where the sum over all final nuclear spin projections s explicitly appears, and the density of states has been developed and then simplified. In first approximation, the transition matrix element can be considered as kinematic-independent *i.e.* $\sum_s |T_{if}|^2 = \text{const.}$ A kinematic term, related to the density of states and called the phase space factor (or statistical factor), can then be extracted and integrated over separately. The probability $P(W_e)$ for an electron to be emitted with a total energy between W_e and $W_e + \mathrm{d}W_e$ is then given as the differential of Γ_{if} with respect to dW_e, resulting into [263]:

$$P(W_e)\;\mathrm{d}W_e = \frac{\sum_s |T_{if}|^2}{(2\pi)^3}\;(W_0 - W_e)^2 p_e W_e\;\mathrm{d}W_e, \tag{3.4}$$

where $p_e = \sqrt{W_e^2 - m_e^2}$ is the norm of the electron three-momentum, and W_0 is the maximum energy available for the transition also called endpoint energy.

Finally, after a tedious development, the squared transition matrix element can be expressed as the product of two functions $F(Z, W_e)$ and $C(W_e)$ called respectively the *Fermi function* and the *shape factor*. The main effect of the electromagnetic interaction between the nucleus and the emitted electron are encompassed in $F(Z, W_e)$, while nuclear structure effects are gathered in $C(W_e)$. The weak magnetism is an effect of the shape factor commonly treated as a correction, and as such it is explicitly taken out from the shape factor. Another important correction to β-decay spectra originates from QED, the outer radiative corrections δ_R. At last, the electron spectrum can be expressed as

$$P(W_e)\;\mathrm{d}W_e = K\;F(Z, W_e)\;C(W_e)\;(W_0 - W_e)^2 p_e W_e\;(1 + \delta_R^{e^-} + \delta_{WM})\;\mathrm{d}W_e, \tag{3.5}$$

where all the constants have been gathered in a single normalization factor K. The spectrum of the antineutrino emitted simultaneously is given as a mirror of Eq. 3.5 based on energy conservation $W_\nu + W_e = W_0$, at the exception of the outer radiative correction which is specific to the outgoing lepton, $\delta_R^{e^-} \to \delta_R^{\bar{\nu}_e}$ (see Sec. 3.5.3). In this work, electron and neutrino spectra are used to define probability distributions so that $K = 1/\int P(W_e)\mathrm{d}W_e$. All the terms entering Eq. 3.5 will be discussed considering that the transition spectra are normalized to unity.

3.3 The current-current structure of the weak interaction

The first attempt of a β-decay Hamiltonian was made by Fermi in 1934, inspired by the current-current structure of electromagnetism [2]. The Hamiltonian proposed by Fermi for the free neutron decay was

$$H_\beta = \frac{G_F}{\sqrt{2}} J_\mu L^\mu + h.c., \tag{3.6}$$

where G_F is the Fermi constant, $J_\mu = \bar{\psi}_p \gamma_\mu \psi_n$ is the nucleon current, $L^\mu = \bar{\psi}_e \gamma^\mu \psi_\nu$ is the lepton current and $h.c.$ stands for "hermitian conjugate". $\psi_{x=p,n,e,\nu}$ are the particle field operators and $\bar{\psi} = \psi^\dagger \gamma_0$. In Fermi's theory, J_μ and L^μ both transform as vector quantities under Lorentz transformations. However, Gamow and Teller showed in 1936 that Eq. 3.6 was not the most general Hamiltonian that could describe a β-decay [257]. The matrix element of the weak interaction must be Lorentz invariant, which restricts the possible forms of the current-current interaction. Only five types of currents, called bilinear covariants and listed in Tab. 3.1, satisfy the Lorentz invariance condition [264]. However not all five of the bilinear covariants play a role in the weak interaction. The parity violation demonstrated by Chien-Shiung Wu in 1957 proved the vector and axial-vector nature of the lepton current:

$$L^\mu = \bar{\psi}(g_V \gamma^\mu - g_A \gamma^\mu \gamma_5)\phi. \tag{3.7}$$

Additionally, the parity was shown to be maximally violated *i.e.* $g_V = \pm g_A$. Experimentally, this translates into the observation of only left-handed neutrinos (right-handed antineutrinos). It connects with the fact that the lepton current can be rewritten with the chiral projectors P_L and P_R leaving only the left-handed (right-handed) component of the neutrino (antineutrino) bispinor to play a role in the interaction.

The correct $V - A$ structure of the Hamiltonian is finally expressed as

$$H_\beta = \frac{G_F}{\sqrt{2}} \left[\bar{\psi}_p \gamma_\mu (1 + \lambda\gamma_5)\psi_n\right] \left[\bar{\psi}_e \gamma^\mu (1 + \gamma_5)\psi_\nu\right] + h.c., \tag{3.8}$$

where $\lambda = -g_A/g_V$. The field operators $\psi_{x=p,n,e,\nu}$ can be expanded in terms of creation/annihilation operators and free wave spinors, which leads *in fine* to the following transition matrix element or the β-decay of the free neutron [263]:

$$T_{if} = \frac{G_F}{\sqrt{2}} \left[\bar{u}_p \gamma_\mu (1 + \lambda\gamma_5) u_n\right] \left[\bar{u}_e \gamma^\mu (1 + \gamma_5) v_\nu\right], \tag{3.9}$$

where u and v are respectively the free wave bispinors of a particle and an antiparticle.

3.3.1 Structure of the nuclear current

The β-decay of a nucleus is quite different of the free neutron decay, which the aforementioned Hamiltonian is actually related to. A nucleus is a composite system consisting in many bound nucleons interacting with each other. Many-body effects take place inside the nucleus and therefore nucleons should not be treated as free particles [263]. The nucleon current from Eq. 3.7 is then substituted with the more general expression

$$\bar{\psi}_p(x)\gamma_\mu(1 + \lambda\gamma_5)\psi_n(x) \longrightarrow \langle f|\, V_\mu(x) + A_\mu(x)\, |i\rangle, \tag{3.10}$$

Type	Current
Scalar	$\bar{\psi}\phi$
Pseudoscalar	$\bar{\psi}\gamma_5\phi$
Vector	$\bar{\psi}\gamma^\mu\phi$
Axial-vector	$\bar{\psi}\gamma^\mu\gamma_5\phi$
Tensor	$\bar{\psi}(\gamma^\mu\gamma^\nu - \gamma^\nu\gamma^\mu)\phi$

Table 3.1: List of the five bilinear covariants that can be combined into a Lorentz-invariant current-current matrix element. ψ and ϕ are fields operators.

where $V_\mu(x)$ and $A_\mu(x)$ are the vector and axial-vector nuclear currents. The associated transition matrix element is then given by:

$$T_{if} = -\frac{G_F}{\sqrt{2}} \langle f| V_\mu(0) + A_\mu(0) |i\rangle \left[\bar{u}_e\gamma^\mu(1+\gamma_5)v_\nu\right]. \tag{3.11}$$

The next step is to perform a multipole expansion of the nuclear current in spherical harmonics ordered by power of qR, where $q^\mu = p_f^\mu - p_i^\mu$ is the four-momentum transfer between initial and final nuclear states and R is the nuclear radius. The advantage of this expansion is to split the kinematic dependency from the nuclear structure effects which are model dependent. The latter are encompassed in form factors F_k and F_{kl} which are function of $q^2 = q^\mu q_\mu$. The time and space components of the nuclear current are then rewritten as

$$\begin{aligned}\langle f| V_0(0) + A_0(0) |i\rangle = \sum_{l,m} (-1)^{J_f - M_f}\sqrt{4\pi(2J_i+1)} \begin{pmatrix} J_f & l & J_i \\ -M_f & m & M_i \end{pmatrix} \\ \times \overline{Y_l^m}(\hat{\boldsymbol{q}}) \frac{(qR)^l}{(2l+1)!!} F_l(q^2),\end{aligned} \tag{3.12}$$

$$\begin{aligned}\langle f| \boldsymbol{V}(0) + \boldsymbol{A}(0) |i\rangle = \sum_{k,l,m} (-1)^{J_f - M_f}\sqrt{4\pi(2J_i+1)} \begin{pmatrix} J_f & k & J_i \\ -M_f & m & M_i \end{pmatrix} \\ \times \overline{\boldsymbol{Y}_{kl}^m}(\hat{\boldsymbol{q}}) \frac{(qR)^l}{(2l+1)!!} F_{kl}(q^2).\end{aligned} \tag{3.13}$$

The $J_{i,f}$ and $M_{i,f}$ are the spin and magnetic quantum numbers of the initial and final nuclear states, $\overline{Y_l^m}(\hat{\boldsymbol{q}})$ and $\overline{\boldsymbol{Y}_{kl}^m}(\hat{\boldsymbol{q}})$ are respectively the complex conjugates of the scalar and vector spherical harmonics [263], $\hat{\boldsymbol{q}} = \boldsymbol{q}/|\boldsymbol{q}|$ is the directional vector of the three-momentum, l is the relative orbital angular momentum between the initial and final nuclear states, k is the relative total angular momentum, and $\begin{pmatrix} j_1 & j_2 & j_3 \\ m_1 & m_2 & m_3 \end{pmatrix}$ is a Wigner 3-j symbol. The nuclear information is fully contained in the form factors $F_{kls} = \begin{cases} F_k\delta_{kl}, & \text{if } s=0 \\ F_{kl}, & \text{if } s=1 \end{cases}$, which are sorted according to angular momentum conservation. Form factors have the role of reduced transition matrix elements and describe the transition between two nuclear states. They can be determined from experiments or from theory using a nuclear modeling. In the latter case, they can be calculated analytically or numerically if the assumption is made that the nucleons inside the nucleus are free particles, which is called the *impulse approximation* [265]. Note that the final proton emitted in a β-decay is also considered as free in this approximation. In the impulse approximation, all nucleons inside the nucleus are considered as independent free nucleons on their mass-shell, *i.e.* each of them satisfies the free Dirac equation [263]. Meson-exchange corrections and other many-body effects are thus neglected.

β-decay type	l	s	$\Delta J = \lvert J_f - J_i \rvert = l + s$	$\pi_f \pi_i$
Allowed	0	0,1	0,1	$+$
1st non-unique forbidden	0,1	0	0,1	$-$
nth non-unique forbidden	n	0	n	$(-1)^{\Delta J}$
nth unique forbidden	n	1	$n+1$	$(-1)^{\Delta J - 1}$

Table 3.2: β-decays classification and associated selection rules. The form factors selected with these rules are only the lowest order terms from the multipole expansion. For instance, in the case of non-unique transitions, Fermi form factors with $s = 1$ also play a role at a higher order.

3.3.2 Selection rules and β-decay classification

As in electromagnetic transitions, each order of the multipole expansion Eq. 3.12 and 3.13 is associated to a change in angular momentum l. Due to the conservation of momentum in β-decays, these units of l must be carried away by the emitted electron-neutrino pair. Additionally, the parities of the initial and final states must differ by a factor $(-1)^l$ as it is the parity associated to an angular momentum l. Hence, a transition between an initial state $(J_i \pi_i)$ and a final state $(J_f \pi_f)$ selects terms from the mutipole expansion such that

$$J_i = J_f + l + s, \tag{3.14}$$

$$\pi_i \pi_f = (-1)^l, \tag{3.15}$$

with $l = l_e + l_\nu$ the total lepton angular momentum and $s = s_e + s_\nu$ the total lepton spin. The spin s can be either 0 or 1, corresponding respectively to an antiparallel or a parallel electron-neutrino spin. The former is associated to vector form factors while the latter is associated to axial-vector form factors, defining respectively Fermi and Gamow-Teller transitions.

While the triangular rule for angular momentum allows terms of multiple orders of l in the expansion, it is adequate to only consider the terms with the lowest power of l which are dominant. Indeed, the magnitude of each term of the multipole approximately decreases by 10^2 to 10^4 for each unit increase of l [266]. Thus, the assumption done in this work is to consider only the terms associated to $\Delta J = |J_f - J_i|$, neglecting higher power terms. The classification of β-decays based on these selection rules are summarized in Tab. 3.2. The selection rules for a n^{th} unique forbidden transition only leave a single form factor among the sereval ones implied in a n^{th} non-unique transition, hence the name ”unique” [263].

Let us point out that meson-exchange corrections can be neglected in allowed and unique forbidden transitions [267, 268]. However, neglecting meson-exchange effects in non-unique forbidden transition can have an important impact, and it is necessary to correct the matrix elements to include such interactions between nucleons. Nevertheless, non-unique forbidden transitions require a dedicated computational approach as it will be explained in Sec. 3.5.1, and the impulse approximation is assumed to be valid for the following equations.

3.4 Coulomb correction to the weak Hamiltonian

To treat properly a β-decay, the electromagnetic interaction must be taken into account between the nucleus and the β particle in addition to the weak interaction. However, the electromagnetic interaction is several orders of magnitude stronger than the weak interaction, and thus the total Hamiltonian $H_T = H_\beta + H_C$ cannot be treated in perturbation theory.

The β-decay is assumed to happen punctually in time at $t = 0$. Thus it is still treated as a perturbation at $t = 0$, while the electromagnetic interaction acts distinctively before and after $t = 0$ on the particles through H_C^i and H_C^f. The introduction of the electromagnetic Hamiltonian impacts the lepton current such that the expansion of the electron field operators ψ_e in Eq. 3.8 must now be done in terms of distorded spinors ϕ_e instead of free spinors. The distorded spinors are then solutions of the Dirac equation in presence of a Coulomb potential V_C^f. The neutrino field operator ψ_ν is still expanded in terms of free spinor as neutrinos do not interact through electromagnetism. Considering the multipole expansion of the nuclear current introduced earlier, it is suitable to also expand the electron and neutrino spinor onto a spherical basis:

$$\phi_e = \sum_{\kappa_e,\mu_e} a_{\kappa_e}^{\mu_e} \phi_{\kappa_e}^{\mu_e}, \tag{3.16}$$

$$\psi_\nu = \sum_{\kappa_\nu,\mu_\nu} b_{\kappa_\nu}^{\mu_\nu} \phi_{\kappa_\nu}^{\mu_\nu}, \tag{3.17}$$

where μ and κ are respectively the eigenvalues of the spin operator $\hat{J}_z$ and the operator $\hat{K} = \beta[\boldsymbol{\sigma}\hat{\boldsymbol{L}} + \mathbb{1}_4]$,

$$\hat{J}_z \phi_\kappa^\mu = \mu \phi_\kappa^\mu, \tag{3.18}$$

$$\hat{K} \phi_\kappa^\mu = \kappa \phi_\kappa^\mu. \tag{3.19}$$

The κ eigenvalue is related to the angular momentum eigenvalue l through $\kappa = \left\{ \begin{array}{ll} -(l+1) = -(j+\frac{1}{2}) & \text{, if } j = l + \frac{1}{2} \\ l = j + \frac{1}{2} & \text{, if } j = l - \frac{1}{2} \end{array} \right.$ or equivalently $l = \left\{ \begin{array}{ll} \kappa & \text{, if } \kappa > 0 \\ |\kappa| - 1 & \text{, if } \kappa < 0 \end{array} \right.$. The spherical waves ϕ_κ^μ are defined by

$$\phi_\kappa^\mu(\boldsymbol{r}) = \begin{pmatrix} \text{sign}(\kappa) f_\kappa(r) \chi_{-\kappa}^\mu(\hat{\boldsymbol{r}}) \\ g_\kappa(r) \chi_\kappa^\mu(\hat{\boldsymbol{r}}) \end{pmatrix}, \tag{3.20}$$

with $\hat{\boldsymbol{r}} = \boldsymbol{r}/|\boldsymbol{r}|$ the radial directional vector and χ_κ^μ given by

$$\chi_\kappa^\mu(\hat{\boldsymbol{r}}) = i^l \sum_{m=-\frac{1}{2},\frac{1}{2}} \langle l, \mu - m; 1/2, m | j\mu \rangle \, Y_l^{\mu-m}(\hat{\boldsymbol{r}}) \chi^m, \tag{3.21}$$

with $\langle j_1 m_1; j_2 m_2 | JM \rangle$ a Clebsch-Gordan coefficient and $Y_l^{\mu-m}$ a spherical harmonic. χ^m are the Pauli spinors with m the magnetic quantum number, $\chi^{1/2} = \begin{pmatrix} 1 \\ 0 \end{pmatrix}$ and $\chi^{-1/2} = \begin{pmatrix} 0 \\ 1 \end{pmatrix}$. It should be noted that physically the orbital momentum l is ill-defined due to the relativistic treatment of the Dirac equation, with f_κ and g_κ related to different values of l. The proper physical parameter to describe the system is κ as it belongs to the set of commuting operators $\{H_T, \hat{K}, \hat{J}_z\}$. The radial dependency of the lepton wavefunction is contained in the radial wavefunctions f_κ and g_κ, called respectively the small and large wavefunction components, while the spin-orbital functions depend only on the $\hat{\boldsymbol{r}}$-direction. If the nucleus is assumed spherical, *i.e.* the nuclear potential is symmetric through rotation, the Coulomb information is completely encoded in the radial functions f_κ and g_κ.

The functions f and g are then solutions of the coupled radial Dirac equations:

$$\begin{cases} \dfrac{\mathrm{d}f_\kappa}{\mathrm{d}r} - \dfrac{\kappa - 1}{r} f_\kappa + [W_e - m - V(r)]\, g_\kappa = 0, \\ \\ \dfrac{\mathrm{d}g_\kappa}{\mathrm{d}r} + \dfrac{\kappa + 1}{r} g_\kappa - [W_e + m - V(r)]\, f_\kappa = 0. \end{cases} \tag{3.22}$$

While analytical solutions of f_κ and g_κ exist for null and point-like nuclear potential [263], they can be expressed as power series expansion for any other potential. Close to the origin, the expansion is

$$\begin{Bmatrix} f_\kappa(r) \\ g_\kappa(r) \end{Bmatrix} = \alpha_\kappa \frac{(p_e r)^{|\kappa|-1}}{(2\,|\kappa|-1)!!} \sum_{n\geq 0} \begin{Bmatrix} a_{\kappa,n} \\ b_{\kappa,n} \end{Bmatrix} r^n, \tag{3.23}$$

where α_κ is a normalization factor called *Coulomb amplitude*, and $a_{\kappa,n}$ and $b_{\kappa,n}$ are iteratively defined parameters whose expression depends on the potential. The Coulomb amplitudes for different values of κ can be combined into functions of interest called *Coulomb functions* which are detailed in the next sections.

3.4.1 Numerical resolution of the Dirac equation

For a general potential, α_κ, $a_{\kappa,n}$ and $b_{\kappa,n}$ must be computed numerically at each energy of interest. Based on a numerical algorithm issued from the work of Behrens and Bühring [263], a program named Directives for an Improved Result of the Amplitudes of Coulomb (DIRAC) has been developed in this work to solve the radial Dirac equations and to compute the Coulomb amplitudes for any energy. An outline of the numerical algorithm is presented here and in App. A, while the analytical details can be found in [263]. The method consists in solving Eq. 3.22 using local power-series expansions of the electron radial wavefunctions on a grid. Starting by evaluating f_κ and g_κ near $r=0$, they are solved for each point of the grid and each solution is connected back to the former point's solution until $r=R_2$, where the power-series associated to $r\to+\infty$ is assumed to be correct. The propagated series are then compared with the asymptotic power-series in R_2. The reconnection of the different power-series near $r=R_2$ gives the value of the Coulomb amplitude α_κ.

The radial wavefunctions must be precisely evaluated up to R_2 (see App. A), which must be large enough to allow the convergence of the asymptotic power-series. As a result, DIRAC algorithm is time consuming. Computing a Coulomb function from 0 MeV up to a tens of MeV can last a tens of minutes. To avoid a significant loss of time, the program DIRAC generates tables of Coulomb functions for each β emitter (referred to as *Coulomb tables*), from 0 MeV up to the isotope Q_β energy. The Coulomb tables are then interpolated in BESTIOLE to include the Coulomb functions in the β and $\bar{\nu}_e$ spectra.

While Coulomb tables already exist such as those of Behrens and Jänecke [269], the increasing precision of β-decay measurement requires an update of these tables over a more complete grid of energy. In the Behrens and Jänecke's tables, Coulomb functions derived for potentials of spherical nuclei with a uniform charge distribution inside but without atomic screening (referred to as "finite-size Coulomb functions" in the following) are evaluated at 40 energies below 10 MeV. Coulomb tables associated to potentials of spherical nuclei with a uniform charge distribution and screened by an atomic cloud of electrons (referred to as "screened Coulomb functions" in the following) provide values only for a handful of energies below 5 MeV. Moreover, the Coulomb tables were computed using outdated atomic Coulomb potentials, which will be discussed in Sec. 3.4.2 and 3.4.3. The new tables computed with DIRAC are made of several hundreds points up to the isotope Q_β energy, diminishing the inaccuracy due to the interpolation method used to include the Coulomb functions. The energy steps are selected so that the tables can be interpolated by a linear function or a higher polynomial without a significant loss of precision. The relative precision of a linearly interpolated point between two tabulated values does not exceed $10^{-4}\%$ with respect to the exact function value, making interpolation effects negligible.

In the very low β energy region (or equivalently the region very close to the endpoint for neutrino spectra), Coulomb functions of interest present a non linear behavior, namely the Fermi function and the λ_k functions (see Sec. 3.4.3 and 3.5). While previous Coulomb tables were tabulated down to a kinetic β energy of 2.5 keV, the new tables have been extended down to 10 eV. Non linear behaviors that can play an important role at low β energy and near-endpoint $\bar{\nu}_e$ energy are then accurately taken into account.

Behrens and Jänecke's Coulomb functions have been computed with the same algorithm from [263] and have been perfectly reproduced by DIRAC up to the last decimal. As a secondary check, the numerical wavefunctions obtained with DIRAC reproduce well below 1% the analytical solutions of Eq. 3.22 up to R_2 in the case of a null and a point-like nuclear potential. The remaining discrepancies are explained by the truncation in the power series and by the size of the steps taken through the grid. Improving the precision on the wavefunctions has no significant impact, modifying the β and $\bar{\nu}_e$ spectra by less than 10^{-2}% if the step size is halved for instance. The Coulomb functions computed by DIRAC are thus well determined for any energy and for any non trivial potential. Finally, it allows the B-21 modeling to be independent from other less accurate Coulomb tables.

3.4.2 Modeling of the nuclear radius

The nuclear radius of an isotope enters the computation of the Coulomb functions when defining the potential seen by the emitted electron. It is also used in the power series expansion near the origin ($r = 0$) at the first step of the DIRAC algorithm, as well as in the analytical expression of the Fermi function for a point-like potential. The finite size of a nucleus has an impact on the Coulomb functions and thus on the spectra of the emitted β and $\bar{\nu}_e$ particles. In Behrens and Jänecke's Coulomb tables [269], the nuclear radii are based on the uniform-density liquid drop model which assumes a uniform charge distribution [270].

If these nuclear finite-size effects are not accounted for via Coulomb functions, they must be included through a correction in which the nuclear radius plays a role. In the B-11 model, a Coulomb correction induced by the finite size of the nucleus is included [13]. The correction is linear in the nuclear radius and is taken from [202]. In a second model developped at Subatech by Fallot et al. [176], discussed in more detailed in Sec. 3.6, the electromagnetic and weak interaction finite-size corrections are polynomial taken from [271] whose dominant behaviors are linear in the nuclear radius and in the endpoint energy. Nuclear radii of β emitters are determined in both models with the so-called Elton formula [272]:

$$R = 1.121\ A^{1/3} + 2.426\ A^{-1/3} - 6.614\ A^{-1}, \tag{3.24}$$

with R given in fm. The Elton formula is more refined than the liquid drop model and considers a charge distribution with a finite surface thickness [272]. The two models do not consider any nuclear radius uncertainty.

Nuclear radii used in DIRAC, and thus in B-21, are based on Angeli's experimental root mean square (RMS) charge radii [273]. When no measurement is available for an isotope, the R_{RMS} charge radius is approximated by [270]

$$R_{RMS} = \left[r_0 + \frac{r_1}{A^{2/3}} + \frac{r_2}{A^{4/3}} + a_Z \frac{Z - Z_{stab}}{A} \right] A^{1/3}, \tag{3.25}$$

where A and Z are the mass and charge numbers, and $Z_{stab} = 1/(1.98 + 0.016 A^{2/3})$ is the proton number associated to the line of stability for a given A. This formula is especially well suited

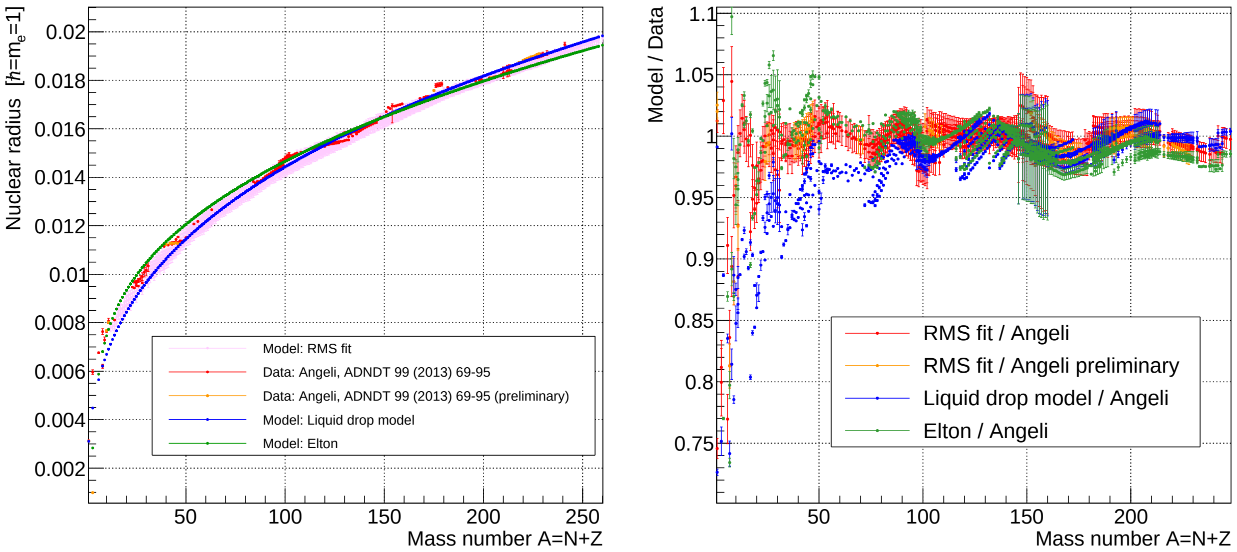

(a) Nuclear radii of β emitters.

(b) Model/Data ratios.

Figure 3.1: **(a)** Nuclear radii of β emitters based on different models and on experimental data. **(b)** Ratios of model over experimental data. Only experimental uncertainties have been propagated to the Elton formula and the liquid drop model ratios, while uncertainties from Eq. 3.25 are propagated in addition to the experimental ones to the ”RMS fit” ratios.

for nuclei off the stability line [270], such as β emitters. The parameters a_Z and $r_{i=1,2,3}$ were simultaneously fitted by Angeli based on a list of experimental RMS charge radii from 1999 [270]:

$$r_0 = 0.897 \text{ fm}, \qquad r_1 = 1.362 \text{ fm}, \qquad r_2 = -2.247 \text{ fm}, \qquad a_Z = 0.398 \text{ fm}.$$

The R_{RMS} uncertainty associated to Eq. 3.25 is the same for any A and Z, $\sigma(R_{RMS}) = 0.0574$ fm. It is adequate to model a nucleus by a uniformly charged sphere whose radius R reproduces the experimental $R_{RMS} = \sqrt{\langle r^2 \rangle}$. The RMS charge radius is related to the shell-model radius R_{sh} via [274]

$$R_{RMS}^2 = R_{sh}^2 + \frac{3}{2}\left(a_p^2 - \frac{b^2}{A}\right), \tag{3.26}$$

where $a_p = 0.65$ fm and $b \simeq A^{1/6}$ fm give sufficiently accurate results. Finally, the radius R of a uniformly charged sphere is given by [274]

$$R^2 = \frac{5}{3}R_{sh}^2 = \frac{5}{3}\left[R_{RMS}^2 - \frac{3}{2}\left(a_p^2 - \frac{b^2}{A}\right)\right]. \tag{3.27}$$

Nuclear radii computed from experimental RMS charge radii are compared with three nuclear radius models in Fig. 3.1: the liquid drop model, the Elton formula, and the uniformly charged sphere model based on RMS charge radii calculated with Eq. 3.25 (labeled as ”RMS fit” in the figure). Nuclear radii computed with the liquid drop model differ up to 4% from experimental data for $A > 90$. No uncertainty are given on the liquid drop model in [269], and the observed differences are significant in that case. For nuclear radii in this range of mass number, the shapes of the β and $\bar{\nu}_e$ spectra can be typically impacted by 0.1% and up to 0.3% at the level of a transition, depending on whether the Coulomb functions have been computed with nuclear radii based on the liquid drop or on experimental data. This illustrates the necessity to generate upgraded Coulomb tables with accurate nuclear radius values based on experimental data. Because the nuclear finite-size effects decrease for low mass numbers A, the impact of the different nuclear radius modelings on Coulomb functions is not important for low A. The range of mass numbers where the nuclear finite-size impact is sizable coincides with the range where the liquid drop model, the Elton formula and the "RMS fit" have similar values. Thus, similar deviations arise at the level of a transition spectrum for each nuclear radius model and for $A > 90$.

Nuclear radii modeled with "RMS fit" differ by less than 2% from experimental values down to $A = 15$. The corresponding ratios, shown in Fig. 3.1b, fall below one standard deviation from unity. An update of the fitted parameters of Eq. 3.25 based on more recent experimental evaluations is thus not necessary. When an isotope RMS charge radius has not been measured, the "RMS fit" model is more appropriate than the liquid drop model to generate Coulomb tables. Nuclear radii based on the Elton formula differ from experimental data by less than 5% down to $A = 15$, although these differences remain larger up to 2% than those due to the "RMS fit", underlining the better agreement of the latter with experimental data as expected. Regarding the finite-size corrections used in B-11 and in the Subatech modeling, using either the Elton formula or experimental data can impact the shapes of transition β and $\bar{\nu}_e$ spectra up to 0.2% for B-11 and 0.4% for the Subatech modeling. For both models, the differences exhibit a linear dependency in the nuclear radius and in the endpoint. This again stresses the necessity to use experimental data and Eq. 3.25 at the level of a transition, even for modelings disregarding the use of Coulomb tables.

Nuclear radii estimated with "RMS fit" are correlated due to the strong correlation between the fitted parameters or due to experimental systematic uncertainties [270]. Additionally, nuclear radii play a role in several terms of Eq. 3.5, therefore correlating the uncertainties of the different spectrum terms. However, the nuclear radius uncertainty is negligible in regards to the other sources of uncertainty, and as it will be seen in the following sections. As such, the correlations induced by the nuclear radius have a minor impact with respect to the total uncertainty and their computation is neglected in B-21.

3.4.3 Computation of the Fermi function

If one carries dutifully the multipole expansion, the squared transition matrix element can be expressed as a linear combination of form factors multiplied by squared coulomb amplitudes. It is common to factorize out the Coulomb amplitudes from the first order terms and write

$$F(Z, W) = \frac{\alpha_1^2 + \alpha_{-1}^2}{2p_e^2}. \tag{3.28}$$

This function is commonly called the Fermi function, and encodes the distortion of the electron wavefunction due to the daughter nuclear charge. It can be interpreted as the ratio of the electron density at the nucleus boundary over the one at infinity where the wavefunction is a plane wave [275]. Note that the impact of the Fermi function is independent of the type of transition as it can be considered as the zeroth order of the multipole expansion.

In the case of a point-like nucleus, an analytical Fermi function F_0 can be derived [2]:

$$F_0(Z, W) = 4(2p_eR)^{2(\gamma-1)} e^{\pi y} \frac{|\Gamma(\gamma + iy)|^2}{|\Gamma(1 + 2\gamma)|^2}, \tag{3.29}$$

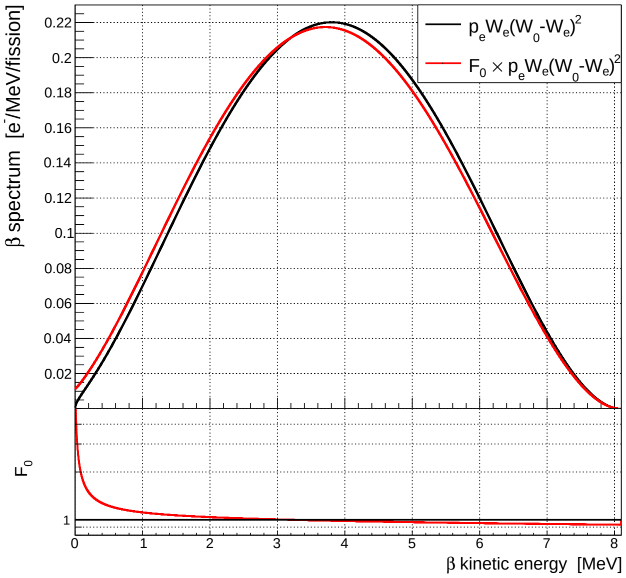

Figure 3.2: Impact of the point-like Fermi function on a β spectrum. The spectra are associated to a virtual transition based on ^{92}Rb as the father nucleus. The black curve represents the phase space factor on its own, while the red curve also includes the point-like Fermi function. Both spectra are normalized to unity. Their ratio is presented in the subplot.

where Γ is the complex gamma function, with $\gamma = \sqrt{1-(\alpha Z)^2}$ and $y = \alpha Z \frac{W_e}{p_e}$. The impact of this point-like Fermi function on a β spectrum is shown in Fig. 3.2. Its effect, and more generally the effect of the Fermi function computed with any potential, is to increase the transition probability at low β energy (high $\bar{\nu}_e$ energy), which results from the attractive interaction between the electron and the daughter nucleus. It results in a typical sharp edge at the endpoint energy of a transition $\bar{\nu}_e$ spectrum. Due to the normalization to unity of the spectra, the probability at high β energy (low $\bar{\nu}_e$ energy) is decreased in return, which is shown in the ratio in the lower panel of Fig. 3.2. This ratio is actually the Fermi function up to a factor equal to the ratio of normalization constants. The Fermi function in the lower panel increases up to 25 when the kinetic energy tends to zero, but the scale is limited to 5 to improve the readability.

The Fermi function in Eq. 3.28 is then expressed as $F = F_0 L_0$. The correction $L_0 = F/F_0$ encompasses the information relative to the spatial extension of the nucleus and its screening. While the analytical point-like Fermi function Eq. 3.29 was used in the B-11 model [13], the Fermi function used in B-21 is based on the Coulomb tables computed with DIRAC. The impact of finite size and atomic screening on the Fermi function and thus on the spectra are now discussed.

3.4.3.1 Potential of a uniformly charged spherical nucleus

The potential V_1 of a spherically extended nucleus is considered. The nucleus is modeled by a sphere of radius R, with a charge ζ uniformly distributed through its volume:

$$V_1(r) = \begin{cases} -\frac{\alpha\zeta}{2R}\left[3-\left(\frac{r}{R}\right)^2\right] & \text{, if } 0 \leq r \leq R, \\ -\frac{\alpha\zeta}{r} & \text{, if } r \geq R. \end{cases} \tag{3.30}$$

This finite-size potential is compared to a point-like potential in Fig. 3.3 in the case of ^{92}Rb.

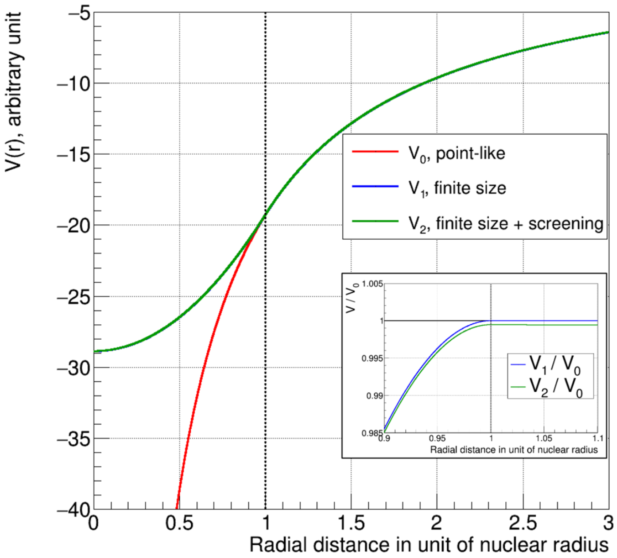

Figure 3.3: Comparison of the nuclear potential models investigated in this work, in the case of ^{92}Rb. V_0 is the potential of a point-like nucleus. V_1 is associated to a uniformly charged spherical nucleus, and V_2 further includes an atomic screening. The inset shows the ratio of V_1 and V_2 with V_0 as they are not distinguishable in the main plot. The fact that V_2 is slightly lower than V_1, as seen in the inset, stands true at any radial distance.

The ratios of transition β spectra computed with finite-size Fermi functions over ones with point-like Fermi functions are shown in Fig. 3.4a, for all β-decays listed in ENSDF [161]. The different terms cancel out in the ratios which resume to $L_0^{V_1}$ up to a multiplying factor equal to the ratio of the normalization constants. The effect of introducing a nuclear finite-size is to increase the transition probability at low β energy, thus amplifying the shift toward low β energies induced by F_0.

The correction due to the finite size of the nucleus is approximately linear with respect to energy. Its value at zero β kinetic energy is then a good indicator of how distorted a spectrum is, considering a null correction in the middle of the spectrum and an approximately mirrored correction at the endpoint. For the vast majority of transitions, the amplitude of the finite-size correction at zero kinetic energy lies at the percent level, typically 1-2%, or even less as shown in Fig. 3.4b.

Considering two transitions with identical endpoints, the finite-size correction will be higher for the transition originating from the nucleus with the highest A and Z, as seen in Fig. 3.4b. Conversely, the different transitions of an isotope are distributed along a line where the highest corrections occur for transitions with the highest endpoints. This is due to the fact that the finite-size Fermi function is monotonic and decreases when β energy increases. While the Fermi function is the same for all transitions of a given isotope, its impact on the normalized spectrum is driven by the relative difference between its highest value (when the β kinetic energy tends to zero) and its lower value (at the endpoint value). Hence, the higher the endpoint, the higher the difference between the two extreme values, and the higher is the amplitude of the finite-size correction.

In the former BESTIOLE model B-11, the nuclear finite-size correction to the Fermi function was taken into account through $P(W) \to P(W)\,[1 + a_C E]$ [13], with $a_C = -\frac{10}{9}\frac{Z\alpha R}{m_e}$ [202]. This correction reproduces the linear behavior of the numerical Fermi function observed in Fig. 3.4a, but with a smaller amplitude. The B-11 correction can differ up to 4%. The B-11 correction

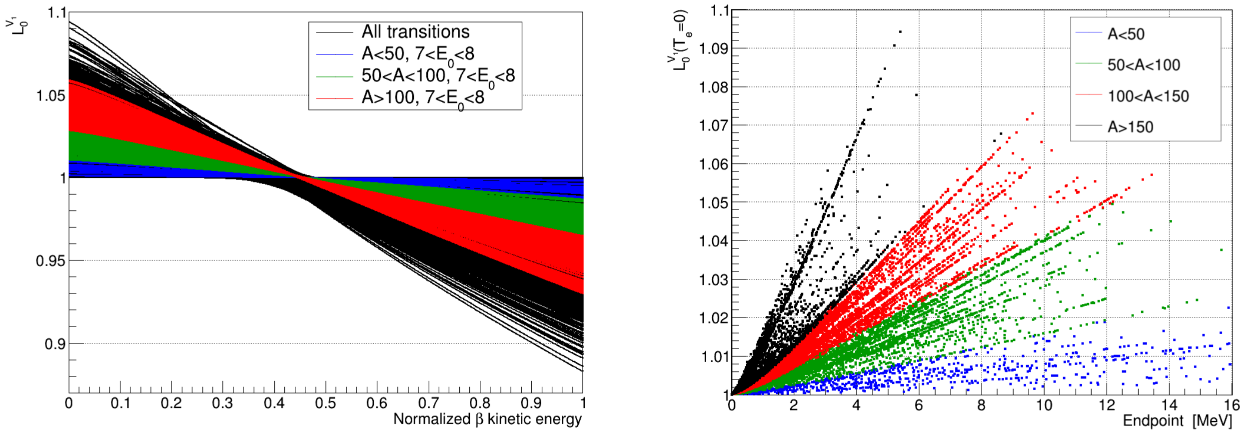

(a) Impact of the finite-size Fermi function.

(b) Deviation at zero kinetic energy.

Figure 3.4: **(a)** Impact of the nuclear finite-size effects on the Fermi function. Each curve represents the ratio of transition β spectra, where the numerator is computed with a finite-size Fermi function $F_0 L_0^{V_1}$ and the denominator with a point-like Fermi function F_0. The x-axis is the normalized kinetic energy of the β particle, E/E_0. Nuclear data from ENSDF have been used [161]. **(b)** Distribution of the correction $L_0^{V_1}$ at zero β kinetic energy with respect to the transition endpoint. Points that are aligned represent the different transitions of an isotope.

being proportional to the nuclear radius, the maximum differences are observed for high A nuclei while almost no difference is displayed for smaller nuclei. In addition, nuclear radii were estimated with the Elton formula in B-11 instead of experiment-based data [13], which can impact β and $\bar{\nu}_e$ spectra up to 0.2% at the level of a transition. Note that this difference is linearly dependent on the nuclear radius and on the endpoint energy. A similar conclusion can be made for the Coulomb finite-size correction considered in the Subatech modeling, except that this correction has a larger amplitude than the numerical Fermi function up to 2%. The impact of using the Elton formula instead of experimental data is also about 0.2% at maximum with the same dependencies.

3.4.3.2 Potential of a uniformly charged spherical nucleus with atomic screening

The second investigated potential V_2 is for a spherical nucleus of radius R, with charge ζ uniformly distributed through its volume, and screened by a cloud of $\zeta - 1$ atomic electrons. In the range where the electron cloud effect is effective, the screened potential has the form:

$$V(r) = -\frac{\alpha\zeta}{r}\sum_{i=1}^{N} a_i e^{-\beta_i r}, \tag{3.31}$$

with

$$\sum_{i=1}^{N} a_i = 1. \tag{3.32}$$

The a_i, β_i are free parameters that can be adjusted according to the considered atom. In the following results, the parameters derived by Salvat are considered [276]. For Salvat's parameters, $N = 3$ provides an accurate modeling of the screened potential for any atom [277]. The majority of formula and parametrizations for screened potentials proposed in the literature rely on the Thomas-Fermi statistical model of the atom, which is non-relativistic and fails in the regions of large potential gradients and of small electron densities [276, 278]. The screening functions are then unreliable at small and large distances from the nucleus, which are regions of interest for the screening effect [276]. The model and parametrization proposed in [276] and used in this work is based on Dirac-Hartree-Fock-Slater calculations which incorporates the main relativistic effects. This ensures the reliability of the Salvat's potentials for large atomic numbers and at any radial distance.

The potential V_2 must be quadratic inside the nucleus and reconnects with a single charge point-like potential at infinity[1]. Two radial limits R_1 and R_2 are introduced. The asymptotic point-like behavior is assumed to be correct for $r \geq R_2$, while the screened potential Eq. 3.31 is employed for $R \leq r \leq R_1$. The two forms are smoothly transited over in the region $R_1 \leq r \leq R_2$, where the exponential in Eq. 3.31 is replaced by a polynomial ensuring continuity at R_1 and R_2. All these requirements lead to the expression [277]:

$$V_2(r) = \begin{cases} -\frac{t_1}{R} + \frac{t_2}{R}\left(\frac{r}{R}\right)^2 & ,\forall r \in [0, R], \\ -\frac{\alpha\zeta}{r}\left\{1 - C + C\sum_i a_i e^{-\beta_i r} + C\sum_i a_i\left[1 - (1+\beta_i R)e^{-\beta_i R}\right]\right\} & ,\forall r \in [R, R_1], \\ -\frac{\alpha\zeta}{r}\left\{1 - C + C\left[\sigma t_3^2 + \mu t_3^3 + \nu t_3^4\right]\right\} & ,\forall r \in [R_1, R_2], \\ -\frac{\alpha\zeta}{r}(1 - C) & ,\forall r \in [R_2, +\infty], \end{cases} \tag{3.33}$$

with

$$\begin{aligned} C &= \frac{\zeta-1}{\zeta}, & t_1 &= \frac{3\alpha\zeta}{2}\left[1 - \frac{2}{3}CR\sum_i a_i\beta_i e^{-\beta_i R}\right], \\ t_2 &= \frac{\alpha\zeta}{2}, & t_3 &= \frac{r-R_2}{R_1-R_2}, \\ \sigma &= \frac{D_2}{2} - 3D_1 + 6D_0, & \mu &= -D_2 + 5D_1 - 8D_0, \\ \nu &= \frac{D_2}{2} - 2D_1 + 3D_0, & D_0 &= \sum_i a_i e^{-\beta_i R_1} + \sum_i a_i\left[1 - (1+\beta_i R)e^{-\beta_i R}\right], \\ D_1 &= (R_2 - R_1)\sum_i a_i\beta_i e^{-\beta_i R_1}, & D_2 &= (R_2 - R_1)^2\sum_i a_i\beta_i^2 e^{-\beta_i R_1}. \end{aligned} \tag{3.34}$$

The screening should manifest mostly at low momentum where the electron De Broglie wavelength is at the scale of atomic dimensions [275]. This is seen in Fig. 3.5a showing the ratios of transition β spectra computed with finite-size and screened Fermi functions over ones with only finite-size Fermi functions. The different terms cancel out in the ratios which resume to the screening distortion $L_0^{V_2}/L_0^{V_1}$ up to a multiplying factor equal to the ratio of the normalization constants. The screening correction peaks at low energy, while the correction at higher energy is almost linear and lower in amplitude. The main effect of the screening on the Fermi functions is then to slightly shift back the β spectra toward high energies with respect to the finite-size Fermi function. The screening correction in Fig. 3.5a is indeed opposite to the finite-size correction in Fig. 3.4a, with an amplitude approximately twice lower, typically of 0.5-1%. Qualitatively, this is due to the fact that the shape of the screened potential in Fig. 3.3 is close to the shape

---

[1] The difference between the $Z+1$ charge of the daughter nucleus and its Z electron inherited from the father nucleus is seen from infinity as a single charge.

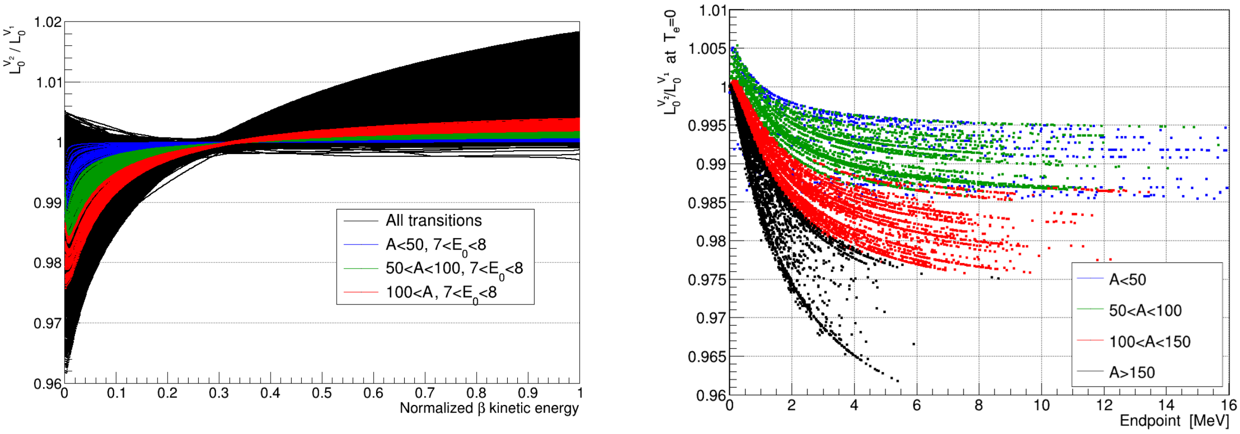

(a) Impact of the screened Fermi function.

(b) Deviation at zero kinetic energy.

Figure 3.5: (a) Impact of the screening effect on the Fermi function. Each curve represents the ratio of transition β spectra, where the numerator is computed with a finite-size Fermi function with screening $F_0 L_0^{V_2}$ and the denominator with a finite-size Fermi function $F_0 L_0^{V_1}$. Nuclear data from ENSDF have been used[161]. **(b)** Distribution of the deviation $L_0^{V_2}/L_0^{V_1}$ at zero β kinetic energy with respect to the transition endpoint. Points that are aligned along a single curve represent the different transitions of an isotope.

of the finite-size potential and is slightly smaller in magnitude, $\forall\ r\ \ |V_2(r)| < |V_1(r)|$. Hence it can be interpreted as a weaker finite-size potential, and the associated correction is expected to be weaker while going in the same direction.

However, a specific effect of the screening on the Fermi function is that a non-monotonic behavior usually arises in $L_0^{V_2}$ at very low energy, contrarily to $L_0^{V_1}$ which is monotonic. This is seen in Fig. 3.5a when the ratio suddenly increases back when the β energy tends to zero. In the case of low endpoint transitions ($E_0 < 1.2$ MeV) for which the non-monotonic behavior dominates completely, the screening correction can even enhance the correction initiated by the finite-size Fermi function instead of reducing it. This is limited to a few transitions as seen in Fig. 3.5b, where the screening correction at zero kinetic energy is plotted against the endpoint energy. The ratio $L_0^{V_2}/L_0^{V_1}$ is then greater than one when the kinetic energy tends to zero, and slowly flatten below unity at higher energy.

In the 2011 version of BESTIOLE, B-11, the impact of the atomic screening on the Fermi function was not taken into account. While the screening impact may be less important than the one of finite-size, it can play a significant role in the shape of $\bar{\nu}_e$ spectra. Indeed, the maximum deviation in β spectra is usually located near 0 MeV, which translates to a maximum deviation at the endpoint for $\bar{\nu}_e$ spectra. Thus, the screening can be an important addition to B-11 in the context of IBD predictions.

Uncertainty on the Fermi function

In the DIRAC computation, uncertainties on the Coulomb functions originate from the nuclear potential modeling and from the numerical resolution of the Dirac equation. Uncertainties in the numerical resolution of the Dirac equation come from several assumptions such as the cut-off in the power series development of the solutions, the choice of the asymptotic radius R_2, and the choice of the grid size. Their impact has been thoroughly studied and has been checked to be negligible compared to the model uncertainties.

The modeling uncertainties come from assumptions including the nuclear radius and the shape and amplitude of the considered nuclear potential, which are the only model-dependent features in DIRAC. The impact of the nuclear radius on the Fermi function was investigated by perturbing the value of R by $\pm 1\sigma$. Due to the small nuclear radius uncertainties, the Fermi function is modified linearly. The Fermi function uncertainty due to the nuclear radius uncertainty is very low once propagated to the spectra, below 0.1% for all energies and all transitions. Compared to the other uncertainties which will be discussed in this work, the propagation of the nuclear radius uncertainty on the Fermi function is negligible. For the Salvat's potential, no parameter uncertainty is given in [276]. Furthermore, the screening parameters are constrained from Eq. 3.32 and thus are correlated. Hence, the parameter uncertainties cannot be inferred in a simple manner. However, Salvat's parameters are well known for providing a robust modeling of screened potential compared to experiments [277]. As such, it is appropriate to neglect the uncertainty arising from Salvat's parameter uncertainties, thus not treating the screened potentials as a source of uncertainty. Hence, the total Fermi function uncertainty is negligible and will not be considered in the improved model B-21.

3.5 Computation of shape factors

What remains from the squared matrix element after taking out the Fermi function is encapsulated in a term C called the shape factor [263]:

$$C(W_e) = \sum_{k_e,k_\nu,k} \lambda_{k_e} \left\{ M_k^2(k_e,k_\nu) + m_k^2(k_e,k_\nu) - 2\frac{\mu_{k_e}\gamma_{k_e}}{k_e W_e} M_k(k_e,k_\nu) m_k(k_e,k_\nu) \right\}, \tag{3.35}$$

where $\gamma_{k_e} = \sqrt{k_e^2 - \alpha^2 Z^2}$, and $k_{e,\nu} = |\kappa_{e,\nu}|$ with κ the eigenvalue of the K operator as defined in Eq. 3.19. k must satisfies a triangular rule with j_e and j_ν as well as with J_i and J_f [278]. λ_{k_e} and μ_{k_e} are Coulomb functions given by:

$$\lambda_{k_e} = \frac{\alpha_{-k_e}^2 + \alpha_{k_e}^2}{\alpha_{-1}^2 + \alpha_1^2}, \tag{3.36}$$

$$\mu_{k_e} = \frac{\alpha_{-k_e}^2 - \alpha_{k_e}^2}{\alpha_{-k_e}^2 + \alpha_{k_e}^2} \frac{k_e W_e}{\gamma_{k_e}}. \tag{3.37}$$

The terms $M_k(k_e,k_\nu)$ and $m_k(k_e,k_\nu)$ contain the leptonic and nuclear information encoded in form factors, and depend on the electron and neutrino momenta.

The computation of shape factors is usually a complicated process. However, one can assume for allowed and unique forbidden transitions that only the dominant matrix elements contribute and that the lepton wavefunctions are constant in the nuclear volume. Hence, the nuclear current component can be split from the dynamical lepton factor for allowed and unique forbidden β-decay [263]. The allowed shape factor is treated as a constant and does not play a role in normalized spectra. For unique forbidden transitions, the shape factor depends on a single form factor that is factorized out and absorbed in the spectrum normalization. The shape factors of 1^{st}, 2^{nd} and 3^{rd} unique forbidden transitions then only depend on the lepton kinematics and describe the deviation of a spectrum from an allowed shape [263].

$$1^{\text{th}} \text{ unique forbidden:} \quad C_1 \propto p_\nu^2 + \lambda_2 p_e^2, \tag{3.38}$$

$$2^{\text{nd}} \text{ unique forbidden:} \quad C_2 \propto p_\nu^4 + \frac{10}{3}\lambda_2 p_\nu^2 p_e^2 + \lambda_3 p_e^4, \tag{3.39}$$

$$3^{\text{rd}} \text{ unique forbidden:} \quad C_3 \propto p_\nu^6 + 7\lambda_2 p_\nu^4 p_e^2 + 7\lambda_3 p_\nu^2 p_e^4 + \lambda_4 p_e^6. \tag{3.40}$$

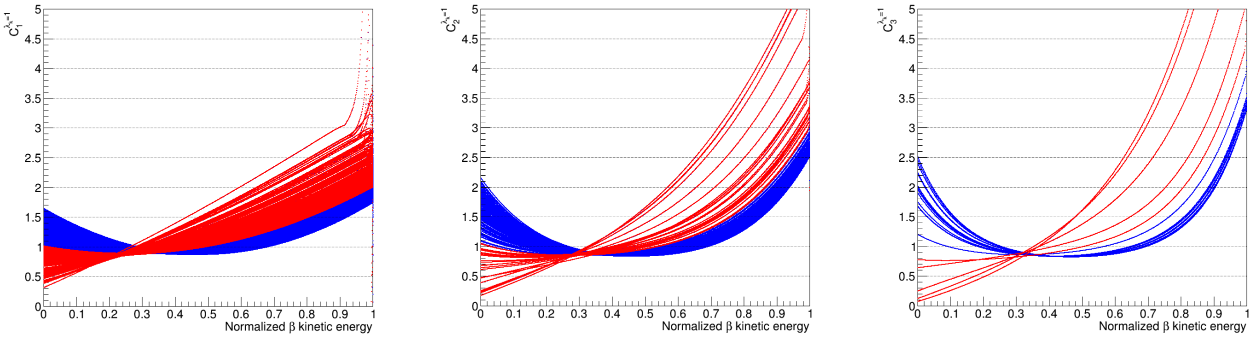

(a) 1st unique. **(b)** 2nd unique. **(c)** 3rd unique.

Figure 3.6: Shape factors in the "$\lambda_k = 1$" approximation in the case of 1st **(a)**, 2nd **(b)** and 3rd **(c)** unique forbidden transitions. Each curve represents the ratio of transition β spectra computed with the "$\lambda_k = 1$" approximation over ones constrained to an allowed shape. The red curves are associated to transitions with endpoint below 1.5 MeV (1 MeV for 1st unique forbidden transitions). The ratios of transitions with endpoints superior to these energies are displayed in blue. Nuclear data from ENSDF have been used [161].

These λ_k functions are almost constant at high energy, and thus a common approximation employed in B-11 and other summation models [13, 176] has been to set them equal to unity, *i.e.* $\forall k\ \lambda_k = 1$. Fig. 3.6 shows the ratios of transition β spectra computed with the "$\lambda_k = 1$" approximation over ones constrained to an allowed shape in the case of 1st, 2nd and 3rd unique forbidden transitions. The ratios resume to the shape factors $C^{\lambda=1}$ in the "$\lambda_k = 1$" approximation up to a factor equal to the ratio of normalization constants. The shape of the shape factor depends on the endpoint. For endpoints below a certain value typically of 1-1.5 MeV, the shape factor is monotonic and increases with energy so that the β spectrum is shifted toward high energies as illustrated by the red curves in Fig.. 3.6. For higher endpoints, the shape factor is curved downwards and is asymmetrical due to the difference between the lepton masses, with higher values toward the endpoint. Its effect is then to lower the central region of the spectra and to increase the lateral regions. The shape factors in Eq. 3.38-3.40 are functions of the β energy and of the endpoint. The modification of the allowed beta spectrum through the shape factor then increases with higher endpoints. For identical endpoints, it increases with the forbiddenness degree due to the order of the associated polynomial. The impact of shape factors on β and $\bar{\nu}_e$ spectra is important, with a distortion that can reach up to several hundreds of percents locally in some cases, significantly modifying the allowed shape.

In the B-21 model, the λ_k functions are interpolated from the Coulomb tables computed with the DIRAC program. They include corrections originating from the finite size of the nucleus and from its screening. The λ_k functions computed with DIRAC increase below 0.1 MeV by five to ten orders of magnitude depending on the isotope. Above 0.1 MeV, the λ_k are actually not constant, starting below unity and increasing linearly by a few percents over a tens of MeV (these behaviors are displayed for the λ_2 functions in App. A). The modification of the shape factors by lifting up the "$\lambda_k = 1$" approximation is presented in Fig. 3.7a showing the ratios of transition β spectra computed with λ_k based on finite-size potentials over ones with the "$\lambda_k = 1$" approximation. The ratios resume to a ratio of shape factors $C^{V_1}/C^{\lambda_k=1}$ up to a factor equal to the ratio of normalization constants. The shape factors computed with the numerical λ_k are increased below 0.1 MeV and above 5 MeV. At energies in-between, the shape factors are decreased. Note that the 0.1 MeV and 5 MeV points are approximated and the corresponding energies actually depend on the exact behavior of the λ_k for each isotope. For transitions with endpoints below 5 MeV, the finite-size correction to the shape factors is monotonic and shifts the β spectra toward low energy with respect to the "$\lambda_k = 1$" approximation. It can be seen that the amplitude of the finite-size correction to the shape factors decreases when the endpoint energy increases. Additionally, for identical endpoints the amplitude of the correction increases with the daughter nucleus mass and charge numbers A and Z. For transitions with endpoint above the IBD threshold, the typical value of the finite-size correction at zero β kinetic energy lies between 5 to 10 % and can even reach 20%.

For all isotopes and all energies, the λ_k functions computed with screening are lower than those computed without (the screening effects on the λ_2 functions are displayed in App. A). The impact is especially important at very low β energy, where the λ_k are decreased by 20 to 30% on average. In the shape factor formulas Eq. 3.38-3.40, the λ_k are associated to powers of the electron momentum while the highest power of the neutrino momentum is left alone. The dominant behavior at low β energy then comes from the highest power of p_ν which is not impact by the screening effect. The screening effects on the λ_k mostly impact the terms with power of p_e. The screening effects on the shape factor are then to decrease the shape factor when the β energy increases. Moreover, considering a transition of a nucleus with a given endpoint energy, the shape factor decrease is more important for a 3rd unique forbidden transition than for a 2nd unique forbidden transition, and similarly between a 2nd and a 1st unique forbidden transition. The screening effects on the shape factors are presented in Fig. 3.7b, showing the ratios of transition β spectra where the λ_k are computed with finite-size effects and with or without screening. The ratios resume to a ratio of shape factors C^{V_2}/C^{V_1} up to a factor equal to the ratio of normalization constants. Due to the normalization of transition β spectra, the screening correction to the shape factor increases the β spectra at low energy and decreases them at higher energy, with a typical impact of $\sim 0.5\%$ This is observed for transitions with endpoints above 1.8 MeV, *i.e.* for the black, green and red curves in Fig. 3.7b. Part of the transitions with endpoints below 1.8 MeV (blue curves) also display this behavior. However, one can see that part of the transitions with endpoints below 1.8 MeV are actually decreased at low β energy. This corresponds to transitions with endpoint typically below 0.5 MeV. For these low endpoint transitions, the highest power of p_e cannot be neglected compared to the highest power of p_ν in the low β energy region. The behavior at low β energy is then no longer dominated by p_ν as it was previously the case. Because the p_e contribution is impacted by the screening effects on the λ_k, the decrease of the shape factors can be more important at low β energy. As a result, the low endpoint transition β spectra are shifted toward high energies. For all transitions, the amplitude of the screening correction to the shape factor increases with A and Z and decreases for higher endpoints.

The discussion about the Fermi function uncertainties conducted in Sec. 3.4.3.2 can be applied to all the Coulomb functions. In the same fashion, the propagation of the numerical uncertainties in the resolution of the Dirac equations has been checked to have a negligible impact on the shape factors and thus are neglected, and the potential modeling is not treated as a source of uncertainty. Finally, the nuclear radius uncertainties propagate linearly on the Coulomb functions. In the case of shape factors, the propagation of the nuclear radius uncertainty results in an uncertainty whose amplitude is below 0.3% for all energies and all transitions. Although it can be sizable at the level of the single transition, the uncertainty due to the nuclear radius uncertainty is inferior to $10^{-2}\%$ once propagated to a reactor spectrum. Therefore, the nuclear radius can be neglected as a source of uncertainty compared to the other uncertainties discussed in this work. Thus, no uncertainty on the shape factor is considered in the improved modeling B-21 for 1st, 2nd and 3rd unique forbidden transitions. However, an uncertainty must be considered for non-unique forbidden transitions.

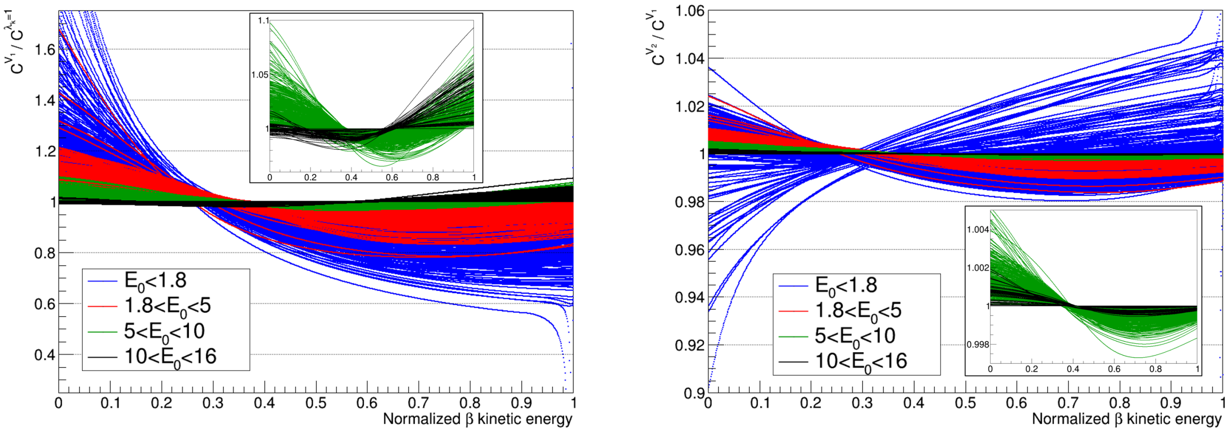

(a) Finite-size effect versus "$\lambda_k = 1$". **(b)** Screening effect.

Figure 3.7: Impact of the nuclear finite-size effect and of the atomic screening effect on the shape factors. Each curve represents the ratio of transition β spectra where: **(a)** the numerator is computed with shape factors based on potentials of finite-size nuclei and the denominator with shape factors in the "$\lambda_k = 1$" approximation; **(b)** the numerator is computed with shape factors based on potentials of finite-size nuclei with screening and the denominator with finite-size shape factors only. Nuclear data from ENSDF have been used [161].

3.5.1 ξ-approximation

The spectrum shape of a 1st non-unique forbidden transition deviates from an allowed form. The amplitude of this deviation is significant when the corresponding transition endpoint W_0 is large enough, *i.e.* only if $W_0 R \gg \alpha Z$ [263]. The physical interpretation of $\alpha Z/R$ is the Coulomb energy of the emitted electron at the nuclear radius [279]. When this energy is large compared to the total decay energy, the terms in $M_k(k_e, k_\nu)$ and $m_k(k_e, k_\nu)$ from Eq. 3.35 associated with a factor $W_0 R$ can be neglected in front of those associated with αZ. This is called the ξ-approximation:

$$2\xi = \frac{\alpha Z}{R} \gg W_0. \tag{3.41}$$

If the ξ-approximation is satisfied, the spectra of 1st non-unique transitions can be approximated with an allowed shape [279]. A conservative criterion can be $2\xi/W_0 > 100E_0/W_0$ [280], which is satisfied only by transitions with endpoint below 0.4 MeV as seen in Fig. 3.8. If one considers a weaker criterion $2\xi/W_0 > 10$, transitions satisfying the ξ-approximation appear up to 3 MeV. Because non-unique transitions are very complicated and foremost very time consuming to compute, the ξ-approximation is often applied to all non-unique transitions without any theoretical argument [280]. A n^{th} non-unique forbidden transition is then approximated as a $(n-1)^{\text{th}}$ unique forbidden transition with the same change of total angular momentum. This ξ-approximation extrapolation has been applied to every modeling up to now, including B-11. That is also the case in this work, where an attempt to build a credible and conservative uncertainty associated to the ξ-approximation is performed and included in B-21. This will be done in Sec. 4.2.1, after introducing the covariance matrix formalism. Note that under the conservative criterion, all the non-unique $\bar{\nu}_e$ spectra relevant for IBD spectra would not be correctly modeled under the ξ-approximation.

Non-unique transitions are estimated to contribute to at least 29% of the ^{235}U fission flux of β particles and antineutrinos, and to at least 43% of the corresponding IBD flux[1]. It is then of utmost importance to provide a valid uncertainty to the ξ-approximation especially because it is abusively applied to all non-unique transitions. The eight transitions listed in Tab. 3.3 are among the top 10 contributors to a reactor IBD flux, both for PWR and research reactors. These transitions alone make up about 23% of the ^{235}U IBD flux and about 53% of its non-unique component[2]. Beside ^{139}Cs, these transitions are also among the most relevant non-unique transitions when considering the 5-7 MeV window of the IBD spectrum. They all are ground-state to ground-state 1st non-unique forbidden transitions, and none of them satisfy the ξ-approximation as showed by the ratio ξ/E_0 in Tab. 3.3.

The computation of non-unique form factors based on complete nuclear structure computation is excessively time consuming, requiring several days of computation for a single transition. The most important non-unique transitions from ^{92}Rb and ^{96}Y have already been computed at CEA by Xavier Mougeot, using a detailed nuclear structure based on the shell model. The non-unique shape factor Eq. 3.35 and the required Coulomb functions have been computed numerically, incorporating the impact of atomic screening and of nuclear finite-size. In the impulse approximation, transitions are described as the transformation of a single nucleon, and nuclear states as a superposition of nucleon states. The transition matrix element between single nucleon bound states is expressed in function of the small and large components of wavefunctions of all the particles (nucleons and leptons), integrated over the whole radial space [263, 284]. The transition matrix element of the total nuclear state is then given as a sum of products of single particle matrix elements weighted by one-body transition densities, with the sum running over the superposition of all possible nucleon states. The one-body transition densities are provided by the NuShellX program [285], a nuclear structure code based on the spherical shell model and Hamiltonians fitted on experimental data in specific mass regions. A radiative correction based on [286] for β spectra[3] and on [287] for $\bar{\nu}_e$ spectra is applied on the non-unique transitions obtained in this advanced computation. Due to the complexity of computing a non-unique transition, the non-unique forbidden β and $\bar{\nu}_e$ spectra of ^{92}Rb and ^{96}Y have been computed over 1 keV energy steps and the energy and emission probabilities have been written into text files. These text files are then interpolated by BESTIOLE at runtime. The remaining transitions from Tab. 3.3 are expected to be included in the B-21 modeling in a second step.

The $\bar{\nu}_e$ spectra of the ^{92}Rb and ^{96}Y non-unique transitions are displayed in Fig. 3.9 along their ratio with their ξ-approximated versions, which are allowed spectra. Hence, their ratio resumes to the non-unique shape factor C^{NU} up to a factor equal to the ratio of normalization constants. For these two 1st non-unique forbidden transitions, the impact of the non-unique shape factor is to increase the spectrum near 0 MeV (15% for ^{92}Rb and 2% for ^{96}Y) and near the endpoint (40% for ^{92}Rb and 25% for ^{96}Y). The spectra are slightly decreased at the middle by a few percents in both transitions due to the normalization of the spectra at unity. While the spectrum shapes are particularly impacted in the energy window of interest for IBD, the IBD flux of the ^{92}Rb transition poorly changes with a mere 0.1% decrease. The ^{96}Y transition

---

[1] As it will be seen in Ch. 4, the forbiddenness degree of some transitions cannot be obtained from evaluated nuclear databases. They are then identified as allowed transitions, whereas they could be non-unique forbidden transitions.

[2] These values are obtained with the improved modeling B-21 described in this chapter, with the optimal database described in the next chapter and with the cumulative FY from the JEFF-3.3 database [136]. These numbers are expected to change with a complete description of non-unique spectra, but remain valid as a first approximation of the IBD flux.

[3] This β spectrum radiative correction differs by less than 0.5% from the one used in the improved BESTIOLE modeling B-21 and detailed in Sec. 3.5.3.

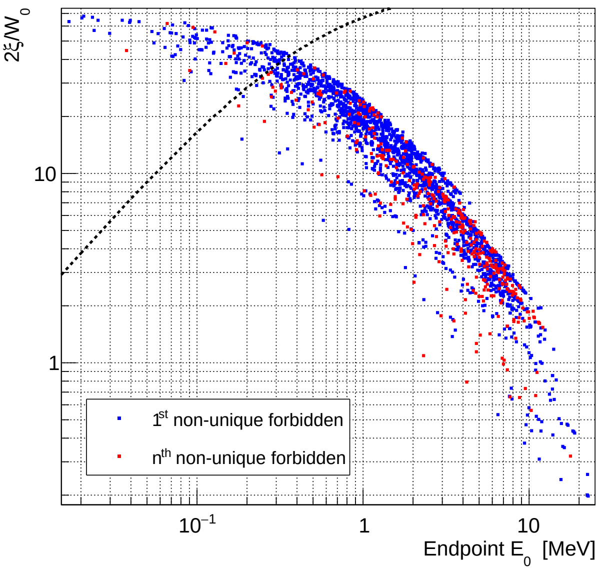

Figure 3.8: Distribution of the criterion $2\xi/W_0$ with respect to the kinetic endpoint E_0 for all transitions in ENSDF [161]. Blue points are associated to 1^{st} non-unique forbidden transitions, while red points are related to higher order non-unique forbidden transitions. Allowed and unique forbidden transitions are not represented as they are not concerned by the ξ-approximation. The black dotted line represents the conservative criterion $2\xi/W_0 = 100E_0/W_0$. The kinetic endpoint E_0 is related to the total decay energy by $W_0 = E_0 + m_e$.

Isotope	BR [%]	E_0 [MeV]	$J_i\pi_i$	$J_f\pi_f$	ξ/E_0	Contrib IBD [%]	Contrib NU [%]
^{92}Rb	87.5†	8.09	0−	0+	1.2	6.50	14.59
^{96}Y	95.5	7.10	0−	0+	1.4	5.54	12.44
^{142}Cs	46.4†	7.33	0−	0+	1.7	1.95	4.37
^{140}Cs	35.5†	6.22	1−	0+	2.1	1.86	4.17
^{135}Te	62	6.05	7/2−	7/2+	2.0	1.84	4.13
^{95}Sr	55.7	6.09	1/2+	1/2−	1.6	1.72	3.87
^{93}Rb	35	7.47	5/2−	5/2+	1.3	1.66	3.72
^{139}Cs	84.5	4.21	7/2+	7/2−	3.0	1.46	3.27

Table 3.3: List of the most important non-unique transitions to the IBD spectrum of a PWR and of a research reactor. The endpoints (E_0) and spin-parity data ($J\pi$) are taken from ENSDF [161]. The branching ratios (BR) are taken from ENSDF except for those marked with a "†" which comes from TAGS measurements. The ^{92}Rb data comes from [281], ^{142}Cs from [282] and ^{140}Cs from [283]. Their contribution to the ^{235}U IBD flux and to the non-unique component of said flux is displayed in the two last columns. All together, these eight transitions contribute at 50.6%, 42.6%, 47.8% and 41.8% to the non-unique component of the IBD flux of ^{235}U, ^{238}U, ^{239}Pu and ^{241}Pu respectively.

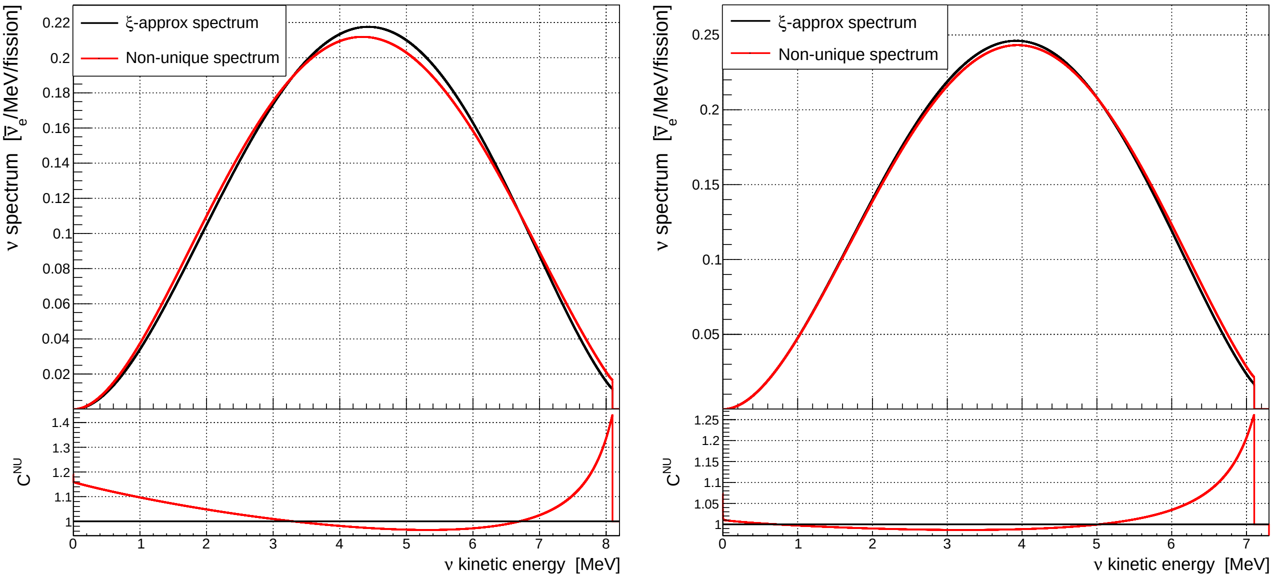

(a) ^{92}Rb. **(b)** ^{96}Y.

Figure 3.9: Non-unique and ξ-approximated $\bar{\nu}_e$ spectra of the main transitions of ^{92}Rb **(a)** and ^{96}Y **(b)**. The spectra in the top panel are normalized to unity. The non-unique spectra are based on the advanced modeling described in Sec. 3.5.1.

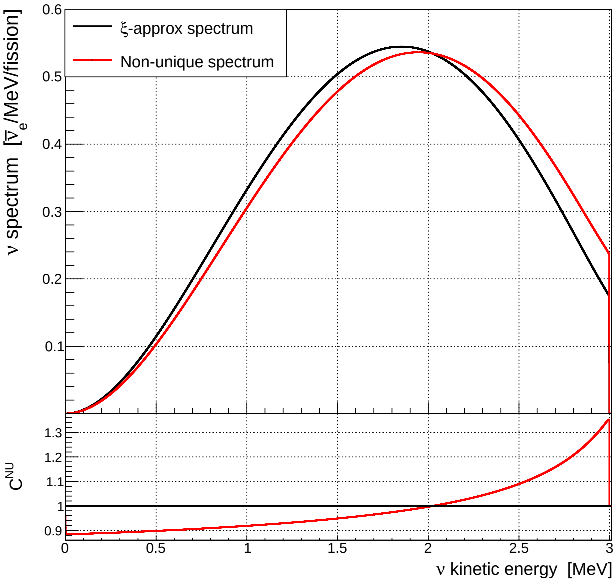

Figure 3.10: Non-unique and ξ-approximated $\bar{\nu}_e$ spectra of the main transitions of ^{144}Pr. The spectra in the top panel are normalized to unity. The non-unique spectra are based on the advanced modeling described in Sec. 3.5.1.

IBD flux is more impacted, with an increase of 1.8%. Finally, the ^{92}Rb transition spectrum is depleted in the 5-7 MeV range as opposed to the ^{96}Y transition spectrum which is inflated in the very same region. This stresses the necessity to properly address the ξ-approximation as the mismodeling of non-unique transitions could play a role both in the RAA and the spectral shape anomaly. As such, an uncertainty associated to the ξ-approximation will be estimated for each non-unique forbidden transition. This uncertainty will be derived by comparing different modelings, and will be discussed in Sec. 4.2.1.

In another context, a revision of geoneutrino spectra based on the B-21 modeling is currently undergoing at CEA. For this geoneutrino study, the advanced computation has been performed for four other non-unique forbidden transitions belonging to four isotopes of interest for geoneutrinos, namely ^{212}Bi ($1^- \rightarrow 0^+$, E_0 = 2.25 MeV), ^{214}Bi ($1^- \rightarrow 0^+$, E_0 =3.27 MeV), ^{234m}Pa ($0^- \rightarrow 0^+$, E_0 =2.27 MeV) and ^{144}Pr ($0^- \rightarrow 0^+$, E_0 =3.00 MeV). ^{144}Pr is the 44th top contributor to the ^{235}U IBD flux with a 0.44% contribution, and the 23rd top contributor to the associated IBD non-unique component with a 0.90% contribution. The $\bar{\nu}_e$ spectra of the ^{144}Pr non-unique transition is displayed in Fig. 3.10 along the ratio with its allowed ξ-approximated spectrum. The non-unique correction shifts the $\bar{\nu}_e$ spectrum toward high energy, with an increase of 35% at the endpoint. The ^{144}Pr correction is monotonic contrarily to the ^{92}Rb and ^{96}Y corrections. The three other isotopes unfortunately do not contribute to reactor spectra. Nonetheless, these four transitions will help to define an estimated uncertainty associated to the ξ-approximation in Sec. 4.2.1.2.

3.5.2 Weak magnetism and other induced currents

Due to the strong interaction between hadrons, the nucleons have a finite size and an internal structure. The strong interaction gives rise to new currents referred to as induced currents or recoil currents, and the nucleon current from Eq. 3.7 must then be modified accordingly. In the impulse approximation, the most general form for the nucleon current is then

$$\langle p| V_\mu(0) |n\rangle = i\ \bar{u}_p \left[\gamma_\mu - g_M \sigma_{\mu\nu} q^\nu + i g_S q_\mu\right] u_n, \tag{3.42}$$

$$\langle p| A_\mu(0) |n\rangle = i\ \bar{u}_p \left[\lambda \gamma_\mu \gamma_5 - g_T \sigma_{\mu\nu} \gamma_5 q^\nu + i g_P \gamma_5 q_\mu\right] u_n, \tag{3.43}$$

where $\sigma_{\mu\nu} = i[\gamma^\nu, \gamma^\mu]/2$. The couplings $g_{X=M,S,T,P}$ are dependent on q^2. However the q^2 dependency is very weak and only brings a correction an order of magnitude lower that can be dismissed. The term associated to g_M is called *weak magnetism* (WM)[1] , while the other recoil currents are simply called the induced scalar, pseudoscalar and tensor currents. These currents are of order $\mathcal{O}(q/M)$ with M the nucleon mass. While all recoil currents play a role in β-decays, WM is the most important and other induced currents can be neglected. A WM correction should therefore be added to each vector reduced transition matrix elements.

In the absence of a dedicated calculation of the shape factor that includes these induced currents, an analytical WM correction must be derived and applied at the level of a transition spectrum. At the spectrum level, the WM correction arises from the interference of the magnetic moment of the vector current with the spin of the axial current [221]. In the impulse approximation and truncating the orbital angular momentum current, WM carries no nuclear structure dependency and is completely related to the anomalous magnetic moments of the nucleons, μ_p and μ_n for the proton and neutron respectively [278]. Therefore, the WM correction is identical for all allowed Gamow-Teller transitions [202]. A first WM correction for allowed transitions was derived in the 1980s [202, 203] and was used in previous summation models [13]. In 2014, WM corrections for 1st forbidden transition operators was for the first time proposed by Hayes et al. [221]. This WM correction takes the form:

$$P(W) \rightarrow P(W)\left[1 + \delta_{WM}(W_e, W_\nu)\right], \tag{3.44}$$

where the δ_{WM} associated to different transition operators are summarized in Tab. 3.4.

---

[1] The name *weak magnetism* is due to the operator $\sigma_{\mu\nu}$ being also associated to the magnetic form factor in QED, which describes the anomalous magnetic moment of fermions.

Transition type	$\Delta J\pi$	$\delta_{WM}(W_e, W_\nu)$
Allowed GT	1+	$\frac{2}{3}\frac{\mu_p-\mu_n-1/2}{\lvert\lambda\rvert M}\left(W_e\beta^2 - W_\nu\right)$
1^{st} non-unique forbidden GT	0−	0
1^{st} non-unique forbidden GT	1−	$\frac{\mu_p-\mu_n-1/2}{\lvert\lambda\rvert M}\frac{(p_e^2+W_\nu^2)(\beta^2 W_e-W_\nu)+2\beta^2 W_e W_\nu(W_\nu-W_e)/3}{p_e^2+W_\nu^2-4\beta^2 W_e W_\nu/3}$
1^{st} unique forbidden GT	2−	$\frac{3}{5}\frac{\mu_p-\mu_n-1/2}{\lvert\lambda\rvert M}\frac{(p_e^2+W_\nu^2)(\beta^2 W_e-W_\nu)+2\beta^2 W_e W_\nu(W_\nu-W_e)/3}{p_e^2+W_\nu^2}$
Allowed F	0+	0
1^{st} non-unique forbidden F	1−	0

Table 3.4: Fractional weak magnetism corrections of allowed and 1^{st} forbidden reduced transition matrix elements. The type of the transition associated to the matrix elements is given in the first column, and the selection rule in the second column with $\Delta J = |J_i - J_f|$ and $\pi = \pi_i \pi_f$. A Gamow-Teller (GT) operator is related to a total lepton spin eigenvalue $s = 1$, while a Fermi (F) operator is associated to $s = 0$. μ_p and μ_n are the proton and neutron magnetic moments, and $\beta = p_e/E_e$. The tab is reproduced from [221].

As explained in Sec. 3.3.2, only the main reduced transition matrix element is considered to define and model a transition. Thus, the WM correction used in this work essentially resumes to the correction of the main matrix element. While allowed Gamow-Teller and Fermi transitions can easily be differentiated solely based on the spins and parities of initial and final states, the leading operator of a 1^{st} non-unique forbidden transition cannot be identified without advanced computation. Thus, there is no clear prescription for 1^{st} non-unique forbidden transitions, not to mention higher order unique and non-unique forbidden transitions for which no correction is available. Four approximations (labeled H1 to H4) to treat forbidden transitions have been proposed in [221] and are summarized below. For each one, all unique forbidden transitions are treated as 1^{st} unique forbidden GT, and all non-unique forbidden transitions are treated as:

- allowed GT (H1);
- 1^{st} unique GT (H2);
- 1^{st} non-unique GT with $(\Delta J\pi) = 0-$ (H3);
- 1^{st} non-unique GT with $(\Delta J\pi) = 1-$ (H4).

A fifth approximation (labeled H5) is considered here, for which 1^{st} non-unique forbidden transitions with $\Delta J\pi = 0-$ and $\Delta J\pi = 1-$ are differentiated, the former having no WM and the latter being treated as 1^{st} non-unique forbidden GT. In H5, higher non-unique forbidden transitions are treated as allowed GT. Before the WM correction of 1^{st} forbidden transitions was determined in [221], the formerly used prescription (labeled H6) in B-11 for instance had been to apply the allowed Gamow-Teller WM correction to all transitions [13]. The impact of the WM correction on allowed and 1^{st} forbidden transitions is presented in Fig. 3.11, showing the ratios of β spectra computed with and without WM. The general impact of the WM is to bend the β spectra toward high energy, with a distortion almost linear and symmetric. The amplitude of the distortion only depends on the endpoint energy. For transitions with an endpoint above the IBD threshold, the amplitude of the distortion increases approximately linearly with the endpoint. For non-unique forbidden transitions, the distortion due to the WM is maximal with the prescription H4 which is based on the 1^{st} non-unique forbidden correction

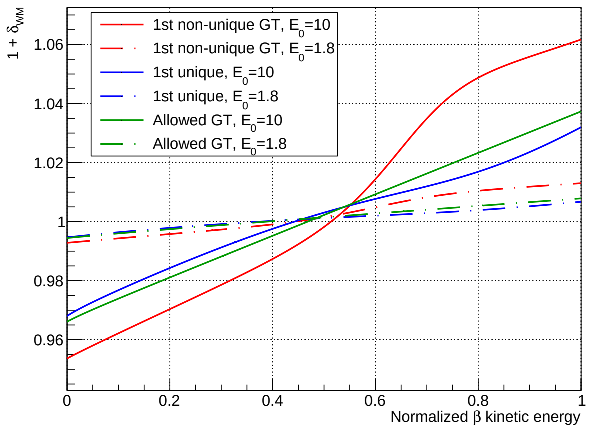

Figure 3.11: Ratio of β spectra computed with and without weak magnetism correction. The ratios resume to $1 + \delta_{WM}$ up to a ratio of normalization constants. The correction only depends on the endpoint and on the forbiddenness degree. The different colors of the curves (red, blue, green) refer to different types of transitions, while the curve styles (solid, dashed) refer to different endpoint energies.

(see Fig. 3.11. The distortion is null with H3, and intermediary with H1, H2 and H6 (which treats non-unique forbidden transitions in a similar manner than H2).

The WM corrections of 2^{nd} and higher non-unique forbidden transitions are based on an approximations, and the choice to apply or not a correction is arbitrary for 1^{st} non-unique forbidden transitions. Moreover, the WM corrections of allowed and 1^{st} unique forbidden transitions are based on initial assumptions such as a truncated orbital current, the absence of meson currents and of hadronic or nuclear structure. An uncertainty associated to the WM correction at the level of a transition spectrum must then be derived to account for a potential bias in the modeling of a transition. This uncertainty will be estimated by comparing the modeling of a transition with and without WM, and will be discussed in detailed in the next chapter, in Sec. 4.2.1.1. The impact of the six prescriptions for the WM correction on reactor neutrino spectra will be discussed in Ch. 5.

3.5.3 Radiative correction from QED

Even though weak interaction processes such as β-decays are well described by the $V - A$ theory at first order, divergences appear in the perturbation expansion of weak interactions at higher orders [263]. Such divergences also appear in QED and in the electroweak theory, however they can be overcome by a redefinition of masses and of coupling constants. This procedure is called renormalization, and cannot be applied in the $V - A$ theory due to new infinite terms appearing at each order of the perturbation series. As a result, some effects induced by electroweak interactions cannot be described with the $V - A$ theory. While neutral currents can be neglected in the phenomenology of β-decays, electromagnetic effects must be included in the so-called radiative corrections described in QED.

The radiative corrections can be separated into inner and outer radiative corrections, where the former depends on the details of the weak and strong interactions inside the nucleus while the latter is independent from them [288]. The inner radiative correction is nucleus-independent and is related to the lepton-hadron electroweak interaction in loop diagrams [289, 290]. The inner correction is typically included into effective coupling constants impacting the normalization of β-decay spectra. It is thus not necessary to consider the inner radiative correction due to the normalization of β and $\bar{\nu}_e$ spectra at unity in B-21. The outer radiative correction on the other hand depends on the nucleus and on the energy. It originates from the exchange of virtual photons and from internal bremsstrahlung. An important feature of the outer correction is that it differs for electron and neutrino due to the contribution of internal bremsstrahlung [287]. The outer radiative correction is only considered up to the first order in α in this work. The impact of higher order terms in $\alpha(\alpha Z)^n$, discussed in [278], is neglected in the improved modeling. The outer correction for electrons is then given by [288]

$$P(W) \to P(W)\left[1+\frac{\alpha}{2\pi}g(W,W_0)\right], \tag{3.45}$$

with

$$\begin{aligned} g(W,W_0) = {} & 3\ln\left(\frac{m_p}{m_e}\right) - \frac{3}{4} - \frac{4}{\beta}\mathrm{Li}_2\left(\frac{2\beta}{1+\beta}\right) \\ & + 4\left[\frac{\tanh^{-1}\beta}{\beta}-1\right]\left[\frac{W_0-W}{3W}-\frac{3}{2}+\ln\left(\frac{2[W_0-W]}{m_e}\right)\right] \\ & + \frac{\tanh^{-1}\beta}{\beta}\left[2(1+\beta^2)+\frac{(W_0-W)^2}{6W^2}-4\tanh^{-1}\beta\right], \end{aligned} \tag{3.46}$$

where $\beta = p/W$ is the electron ratio of momentum over total energy, m_p is the proton mass, and $\mathrm{Li}_2(x) = \int_0^x \mathrm{d}t\ln(1-t)/t$ is the dilogarithm function. For neutrinos, the function g must be replaced by its neutrino counterpart h [287]:

$$\begin{aligned} h(W_\nu,W_0) = {} & 3\ln\left(\frac{m_p}{m_e}\right) + \frac{23}{4} - \frac{8}{\beta}\mathrm{Li}_2\left(\frac{2\beta}{1+\beta}\right) \\ & + 8\left[\frac{\tanh^{-1}\beta}{\beta}-1\right]\ln\left(\frac{2[W_0-W_\nu]\beta}{m_e}\right) \\ & + 4\frac{\tanh^{-1}\beta}{\beta}\left[\frac{7+3\beta^2}{8}-2\tanh^{-1}\beta\right]. \end{aligned} \tag{3.47}$$

The strong interaction is neglected in Eq. 3.46 and 3.47, which are valid for the decay of nucleons devoid of any hadronic structure, such as in the impulse approximation [291]. Recoil effects are also neglected in g and h [291]. Hence, the radiative correction only depends on the endpoint energy as illustrated in Fig. 3.12, with an amplitude increasing with the endpoint. The impact of the radiative correction on β spectra is important, inducing a distortion up to 10% for endpoints above 10 MeV. However, the effect is small on $\bar{\nu}_e$ spectra, with a distortion below 1% for any endpoints.

These formulas have been derived in the case of an allowed transition. Nonetheless, the usual approximation considered here and in other models [13, 176] is to apply Eq. 3.46 and 3.47 to all forbidden transitions. The validity of this approximation is not well known, and as such an uncertainty associated to the outer radiative correction is derived for forbidden transitions in B-21. Due to the small impact of the radiative correction on $\bar{\nu}_e$ spectra, the conservative choice is made to also derive an uncertainty for allowed transitions. This uncertainty is estimated by comparing the modeling of transitions with and without outer radiative corrections, and will be discussed in more details in Sec. 4.2.1.1.

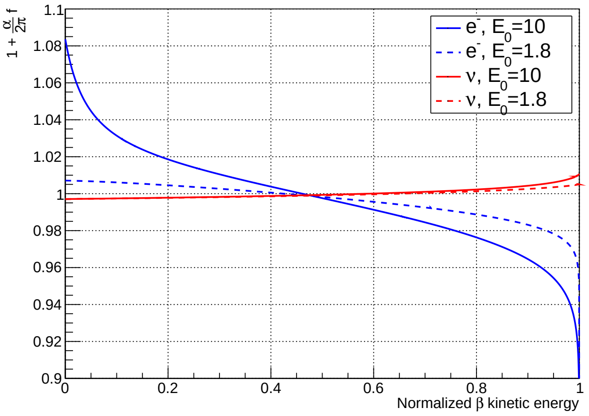

Figure 3.12: Ratios of β and $\bar{\nu}_e$ spectra computed with and without radiative corrections. The ratios resume to $1+\frac{\alpha}{2\pi}f$ up to a factor equal to the ratio of normalization constants, with $f = g$ ou h. The correction only depends on the endpoint. Blue and red curves are respectively associated to β and $\bar{\nu}_e$ spectra. Solid lines result from an $E_0 = 10$ MeV, while dotted lines are associated to $E_0 = 1.8$ MeV.

3.6 Comparison with other ab-initio models

A comparison of the improved BESTIOLE modeling B-21 with other modelings available in the literature has been conducted. An in-depth comparison should be done case by case and transition-wise. As it is a task most certainly too tedious to conduct over thousands of transitions, the study is restricted to a hypothetical transition following the example from [14] with $E_0 = 10$ MeV and for a nucleus with $Z = 46$ and $A = 117$. The virtual transition is either modeled as an allowed Fermi or Gamow-Teller (differing in B-21 only by the weak magnetism correction), or a 1st, 2nd or 3rd unique forbidden transition. This method is expected to give a comprehensive overview of the impact of the different modelings on a typical β-decay. Three models whose ingredients are summarized in Tab. 3.5 are compared with B-21 and are detailed below.

The first model is the former BESTIOLE computation dating back to 2011 and labeled B-11 [13], whose differences with B-21 have been introduced all along the chapter. The difference in the allowed Fermi spectrum shown in Fig. 3.13a has two origins. The linear part comes from the weak magnetism that is null for allowed Fermi transitions in B-21 and non-null in B-11. The curvature and the small twist near the endpoint is due to the screening effects in the numerical Fermi functions. For the allowed Gamow-Teller spectra, displayed in Fig. 3.13b, the weak magnetism correction is similar in B-21 and B-11. The difference then comes only from the screening of the numerical Fermi functions. For the ratios of 1st, 2nd and 3rd unique forbidden spectra, presented respectively in Fig. 3.13c, 3.13d and 3.13e, the discrepancies mainly originate from the "$\lambda_k = 1$" approximation used in B-11.

The second model has been developed at Subatech by Fallot et al. [176] (labeled F-12) and has been used in recent summation models [176, 178]. In this approach, spectra at the transition level are modeled according to the prescription from Huber [14]. The main difference with B-21 is that F-12 uses analytical finite-size and screening corrections to the Fermi function originating respectively from [271] and [263]. These corrections behave similarly to the numerical ones discussed in Sec. 3.4.3, with a linear dependency on the nuclear radius and on the endpoint (see. Fig. 3.4 and 3.5). Their amplitude however differs from the numerical corrections, with a difference reaching up to 2% for the finite-size correction and up to 1% for the screening correction. This difference comes from the analytical approximation, and in second from the

	B-21	B-11 [13]	F-12 [176]	BS-2.1 [292]	Magnitude	Comment
Fermi function	Numeric	Eq. 3.29, point-like	Eq. 3.29, point-like	Numeric	≥ 10	—
Shape factor	Numeric	$\lambda = 1$	$\lambda = 1$	Numeric	≥ 1	ξ-approx. applied in all models. ξ-approx. uncertainty estimated in B-21.
Coulomb finite-size	Numeric	Analytic from [202]	Analytic from [271]	Numeric	~ 1	—
Atomic screening	Numeric	—	Analytic from [263]	Analytic from [293]	0.1	B-21 and BS-2.1 use potentials from [276].
Weak interaction finite-size	—	—	[271]	—	0.01	Correction from [271] is $\leq 4\%$ for every isotopes and energies.
Weak magnetism	[221]	[202]	[202]	—	0.1	[221] is forbidden degree-wise. Uncertainty estimated in B-21.
Radiative correction	β from [288] ν from [287]	β from [288] ν from [287]	β from [288] ν from [287]	β from [286] ν from [287]	0.1 for β 0.01 for ν	[286] more accurate than [288] and differ $\leq 0.5\%$. Uncertainty estimated in B-21.
Nuclear radius	Data from [273] & fit from [270]	Elton formula from [294]	Elton formula from [272]	Liquid drop model from [269]	0.001	—

Table 3.5: Details of the four different models for β-decays. The "Numeric" tag refers to the Coulomb tables computed with DIRAC for B-21, and to a similar program effective at running-time in BS-2.1. The listed magnitudes are the maximal deviations observed in normalized spectra with B-21, among all the isotopes from the ENSDF database [161].

use of the Elton formula for nuclear radii instead of experiment-based data (weighting $\leq 0.4\%$, similar to the difference observed with B-11). Note that for transitions with endpoints below 2 MeV and high Z (typically $Z > 50$), the F-12 screening correction can differ by $\pm 5\%$ from the numerical screening correction, this deviation being solely due to the analytical formula. While the analytical formula of these corrections can reproduce the tabulated values from [269], the formula can neither cope with the fine behavior displayed at very low β energy (high $\bar{\nu}_e$ energy) nor adapt to other nuclear and screening models than the ones they were designed to fit initially. Additionally, the "$\lambda_k = 1$" approximation is employed in F-12. The F-12 weak magnetism correction resumes essentially to the allowed Gamow-Teller correction from Tab. 3.4 used in B-21, and is applied to all types of transition. The radiative correction in F-12 and B-21 are identical. A last correction is applied in F-12, originating from the impact of the nuclear finite-size on the weak interaction itself. The correction is estimated based on Gamow-Teller transitions and is applied to all transitions. All isotopes considered, the impact of this weak-interaction finite-size on normalized $\bar{\nu}_e$ spectra is of about 4% at maximum near 0 MeV and endpoints. The different corrections used in F-12 have been implemented in BESTIOLE. Thus, the differences observed with B-21 in the hypothetical transitions in Fig. 3.13 do not result from an algorithm bias. The impact of the F-12 corrections on the allowed hypothetical transition can be found in Fig.1 of [14]. When comparing B-21 with F-12 in the case of the forbidden unique transitions (Fig. 3.13c-3.13e), the major difference comes from the "$\lambda_k = 1$" approximation used in the latter. The impact of this approximation eludes the other corrections except for allowed transitions, for which the impact of the weak interaction finite-size and of the Coulomb finite-size becomes foremost. The five ratios of F-12 over B-21 show a sharp increase near the endpoint. This is due to the F-12 screening correction which starts, for β spectra, above a transition-dependent threshold, thus ending a few keV before the endpoint for $\bar{\nu}_e$ spectra.

The third model is based on the BetaShape program (version 2.1, labeled BS-2.1) [284, 292] which is one of the state-of-the-art program to compute β and $\bar{\nu}_e$ spectra at the isotope level. As in B-21, numerical finite-size corrections to the Fermi function and to the λ_k functions based on the algorithm from [263] are employed in BS-2.1. The screening correction is however based on the analytical formula from [293] and adapted to the Salvat potentials [276]. While it reproduces the main behavior of the numerical screening correction, it is not reliable at very low β energy (high $\bar{\nu}_e$ energy). The impact of the nuclear radius values used in BS-2.1 is negligible in both the finite-size numerical correction and the analytical screening. The BS-2.1 radiative correction for β spectra is taken from [286]. This radiative correction is more accurate than the one from B-21, with a difference on the transition spectra of $\lesssim 0.5\%$ depending on the endpoint energy. However, the $\bar{\nu}_e$ radiative correction remains identical with B-21. The BS-2.1 model does not incorporate a weak magnetism correction. Weak magnetism apart, the difference between B-21 and BS-2.1 $\bar{\nu}_e$ spectra mainly originates from the screening correction. This can be seen in the allowed Fermi transition case Fig. 3.13a, where the weak magnetism is null in both B-21 and BS-2.1. The analytical screening is consistent with the B-21 numerical screening almost over the full energy range. The sharp decrease near the endpoint observed in the five BS-2.1 to B-21 ratios (see Fig. 3.13) is due to the BS-2.1 analytic screening whose accuracy collapses around the endpoint (around 0 MeV in the case of β spectra). A second sharp deviation is present near 0 MeV and originates from a difference in the algorithms of BS-2.1 and B-21. In BetaShape, the spectra are computed at several energy steps. The output files return then a list of energies and associated emission probabilities. On the other hand, BESTIOLE computes spectra as histograms whose bins hold the integral of Eq. 3.5 (or the equivalent neutrino formula) between the lower and higher limits of the bins. If BESTIOLE is modified to return values in a similar manner to BetaShape, the low energy discrepancy in Fig. 3.13a is reduced. Note that this algorithm difference also participates to the sharp decrease of the last high energy bins. Regarding the sharp increase at 0 MeV, it is also partly due to the different extrapolation methods used in B-21 and BS-2.1 to model the Fermi function close to 0 MeV. While this deviation appears important in magnitude, it is located around 0 MeV where the spectrum is almost null and therefore its impact on the spectrum shape is completely negligible. Except in the allowed Fermi transition case, the difference between B-21 and BS-2.1 is driven by the WM correction as seen in the approximately linear difference following the weak magnetism behavior displayed in Fig. 3.11. Finally, let us point out that 50 β^- emitters found among FP have experimental shape factors defined in BetaShape. These experimental shape factors, determined from β spectrum measurements in a given energy window, reproduce the measured β spectra once combined with the statistical factor. Among these isotopes, 15 have a Q_β above the IBD threshold, and only 4 have non negligible fission yields: ^{90}Y ($Q_\beta = 2.28$ MeV), ^{139}Ba ($Q_\beta = 2.31$ MeV), ^{140}La ($Q_\beta = 3.76$ MeV) and ^{140}Pr ($Q_\beta = 3.00$ MeV). However, their Q_β energies combined to the shape of their $\bar{\nu}_e$ spectra result in very small contributions to a reactor IBD flux. For instance, their contributions to the ^{235}U IBD flux are inferior to 0.1% for ^{90}Y and ^{139}Ba, and inferior to 0.01% for ^{140}La and ^{140}Pr. Therefore, the experimental shape factors have not been included in B-21.

Every model compared to B-21 exhibits small fluctuations near the endpoint which reflect the fine behavior of the numerical Fermi function below 20 keV. These fluctuations tend to flatten with better screening modeling, and are almost non-existent for BS-2.1 while they are clearly visible in B-11 as a small twist in the ratio. The five $\bar{\nu}_e$ spectra of the hypothetical transitions are impacted by a couple of percents at the middle of the spectrum and around the endpoint, which are the spectrum portions of interest regarding IBD spectra. The low energy part of the $\bar{\nu}_e$ spectra is also impacted, though the 5-10% deviations at 0 MeV are not relevant due to the low value of the $\bar{\nu}_e$ spectra in this energy range. Note that the magnitude of these differences depends on the endpoint energy as the impact of the Fermi function and of the shape factor on a β-decay spectrum have been shown to be endpoint-dependent. These results then highlight the importance to properly model β and $\bar{\nu}_e$ spectra and their uncertainties, especially when a limited number of transitions dominate the case of study, such as in reactor neutrino experiments where 40 transitions contribute to about half of the IBD flux.

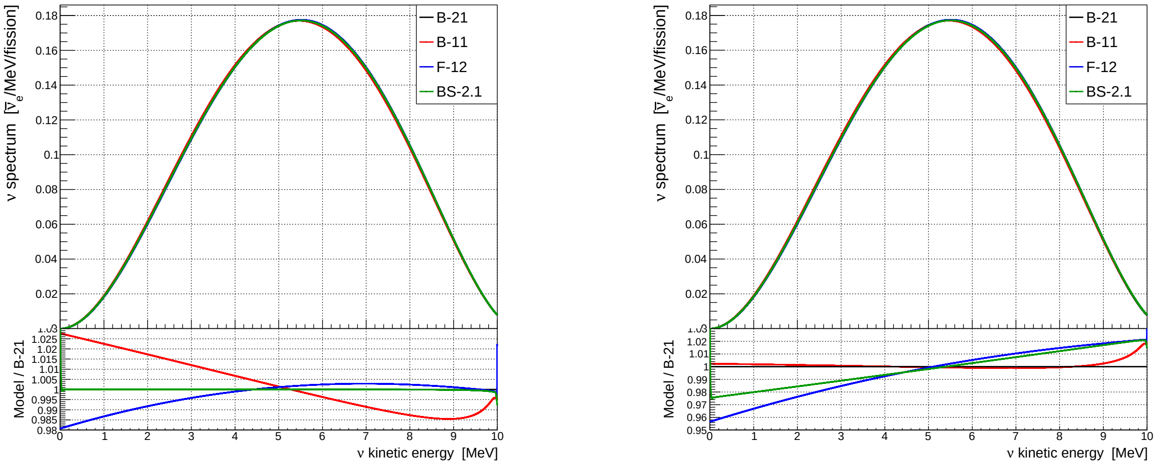

(a) Allowed Fermi.

(b) Allowed Gamow-Teller.

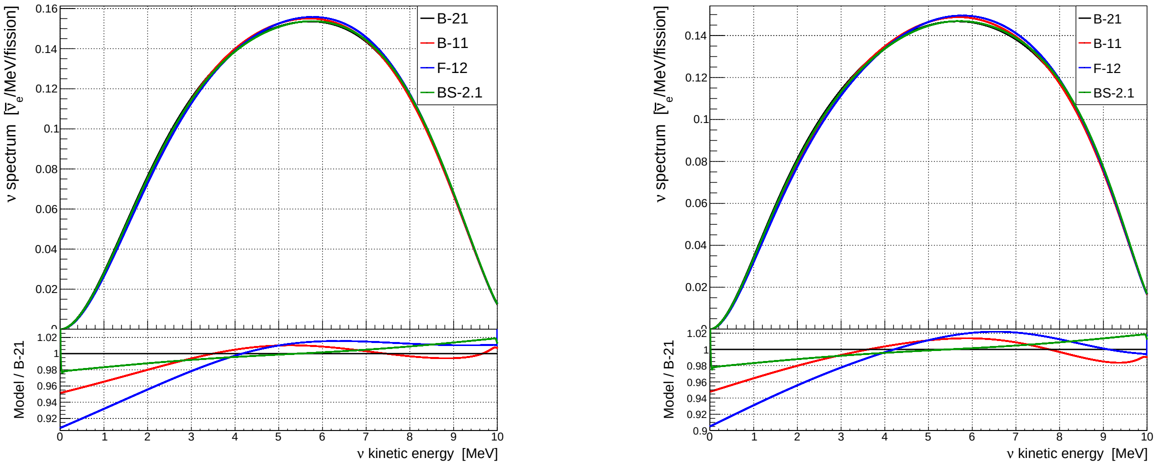

(c) 1^{st} unique.

(d) 2^{nd} unique.

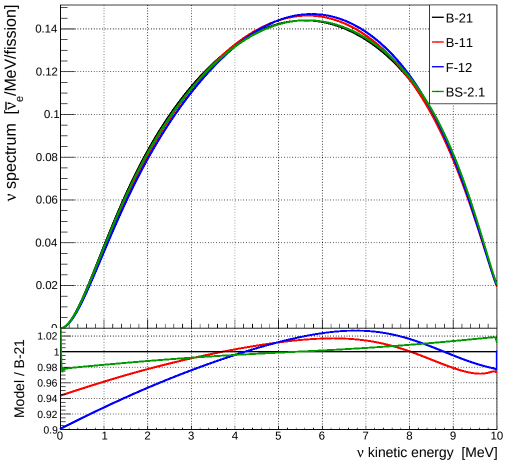

(e) 3^{rd} unique.

Figure 3.13: Comparison of the $\bar{\nu}_e$ spectrum of a hypothetical transition with $\{E_0 = 10\text{ MeV}, Z = 46, A = 117\}$. The virtual transition is modeled as an allowed Fermi **(a)**, allowed Gamow-Teller **(b)**, 1^{st} **(c)**, 2^{nd} **(d)** or 3^{rd} **(e)** unique forbidden transition. The top panels show the $\bar{\nu}_e$ spectra modeled with B-21, B-11, F-12 and BS-2.1, while the bottom panels show the ratio of the spectra over the B-21 spectrum. The allowed Fermi and Gamow-Teller plots differ only by the weak magnetism correction applied in B-21, null in the former.

3.7 Summary

Starting from the Fermi's golden rule, the transition probability of a β-decay has been studied in detail. The most important corrections to the β and $\bar{\nu}_e$ spectra and their relation to the selection rules associated to allowed and forbidden β-decay transitions have been discussed.

A home-made program called DIRAC has been implemented in order to lift the $\lambda_k = 1$ approximation commonly used to calculate the shape factors, as well as to include two important effects in the calculation of the Fermi function and of the shape factor: the spatial extension of the nucleus and the atomic screening. Coulomb tables made with DIRAC can be computed for any potential, grant the B-21 spectra to be independent from outdated Coulomb tables, and limit the bias introduced by an interpolation method.

At the level of a transition, the typical impact of the finite size of the nucleus on the shape of the β and $\bar{\nu}_e$ spectra is about 1-2% induced by the Fermi function. The impact of lifting the $\lambda_k = 1$ approximation and including the finite-size effect on the shape factor is about 5-10%. The effect of the screening is opposite to the finite-size effect, with a typical impact of about 0.5-1% induced by the Fermi function and of about 0.5% induced by the shape factor. The uncertainties on the Coulomb functions computed with DIRAC are small and can be neglected. However, it is worth to stress that uncertainties on the screening parameters are missing and thus could not be studied. Uncertainties associated to Salvat's screening parameters could have an impact on the screening correction. No nucleus deformation has been taken into account so far in all the different models presented in this chapter, and the relevance of the spherical nucleus model could be investigated in a future work to assess an uncertainty.

The computation of non-unique forbidden shape factors is currently out of reach for a general use. Their study was limited to the two most important non-unique forbidden transitions contributing to the IBD flux of a reactor spectrum, associated to ^{92}Rb and ^{96}Y, and to an additional non-unique forbidden transition from ^{144}Pr derived in the context of geoneutrinos. An advanced computation of the non-unique forbidden shape factors has shown a significant impact of the shape of these two transition $\bar{\nu}_e$ spectra, superior to 2% at the middle of the spectra and up to several tens of percents at the endpoint energies. Additional non-unique transitions will be computed in future studies, with the aim to include the top 10 contributors to IBD spectra in a first step and then more.

Finally, using up-to-date analytical weak magnetism and outer radiative corrections, the improved BESTIOLE modeling has been compared with three other β-decay modelings described in the literature. The new B-21 modeling displays important differences on the shape of β and $\bar{\nu}_e$ spectra at the level of a transition compared to the other models.

Lastly, it must be stressed that many theoretical ingredients entering the complete description of β-decays have been left out (see Tab. 7 from [278] for an overview). Although they usually are orders of magnitude below the spectrum corrections discussed here and can be easily dismissed in most cases, they may be relevant in some rare instances and should be studied individually. The modeling of non-unique forbidden transitions remains nonetheless the critical point to improve.

Nuclear data must be coupled to the spectrum modeling presented in this chapter in order to produce summation spectra. The treatment of nuclear data is the topic of the next chapter, along the treatment of the uncertainties associated to both the nuclear data and the modeling.

4

Revision and improvement of the treatment of nuclear data

Contents

In this chapter, the making of a database of transitions with up-to-date nuclear data is explained step by step. The content of the different sources of nuclear data entering the database is detailed and discussed with respect to their relevancy. In a second part, a particular attention is paid to the propagation of both the nuclear data uncertainties and uncertainties coming from the β-decay modeling. Their treatment in the improved modeling B-21 is presented and is compared with the former BESTIOLE uncertainty propagation.

4.1 Evaluated nuclear data

Improving the BESTIOLE modeling at the transition level constituted the first stage in reviewing the summation method. One must then establish a list of all the isotopes contributing to the spectrum of interest, in this case a reactor neutrino spectrum. The second stage consists in retrieving all the relevant nuclear data for these isotopes: decay scheme of the parent nucleus, spin and parity of the initial and final nuclear states, transition endpoint energies, branching ratios, β^- intensity and fission yields.

This section reviews how these nuclear data have been used to model a β spectrum at the isotope level. Several evaluations of the same nuclear data often exist, and are sometimes not in agreement. The choices to prioritize one evaluation over the others are also discussed here.

4.1.1 Nuclear decay data

The only comprehensive database of nuclear decay data, encompassing all known nuclei, is the Evaluated Nuclear Structure Data Files (ENSDF). This database is the result of a continuous international effort of the Nuclear Structure Decay Data (NSDD) network coordinated by the International Atomic Energy Agency (IAEA) over the last 50 years [161]. The database is managed and maintained by the Nuclear Decay Data Center (NNDC) at the Brookhaven National Laboratory (BNL), USA. An ENSDF evaluation can be found for approximately 70% of the fission products (FP) entering the composition of a reactor spectrum, which corresponds to more than 600 isotopes and several thousands of transitions. Properties of nuclear levels and β transitions, among other quantities that are not of interest for our study, are determined by evaluators based on all available experimental data and are synthesized in ENSDF files, which are written in a standardized format.

For the purpose of extracting β-decay data from the hundreds of ENSDF files, the ENSDF++ program has been used[1]. The program was already used in 2011 to build a part of the database employed in BESTIOLE [13]. When building the 2021 BESTIOLE database from the ENSDF data files, it has appeared that some of the nuclear data were mistreated in 2011. For instance, branching ratios were not normalized to the β^- intensity, available spin and parity information were not entirely included, nuclear data uncertainties were not retrieved correctly. A detailed review of the ENSDF data has been conducted in this work and is presented thereafter. It emphasizes the treatment of the nuclear and decay data and the associated uncertainties in order to include them in BESTIOLE. Several classes of the ENSDF++ program have been rewritten in order to improve the quality of the 2021 BESTIOLE database. The aim of the introduced features is threefold: compensating for missing data in ENSDF files, correcting data that have been previously misread in BESTIOLE, and improving the consistency between information present in ENSDF and those included in BESTIOLE.

---

[1] The program is available on Github [295]

4.1.1.1 Branching ratio

In ENSDF, the branching ratio (BR) uncertainty is provided either as a numerical value or as one of the five tags summarized in Tab.4.1. In the 2011 BESTIOLE database, all BR were treated as Gaussian variables with the central value and uncertainty equal to those given in ENSDF, with null uncertainties associated to the tags. For the 2021 review, specific treatments of the different tags have been implemented in ENSDF++.

The ”AP” tag stands for ”approximated”. In that case, the branching ratio from the source article is given as an approximation or relies on weak arguments. There are 297 transitions concerned by this tag, and an arbitrary 10% relative uncertainty has been set on their BR which is then treated as Gaussian distributed. This 10% value has been chosen because it approximately equals the median value of the distribution of relative BR uncertainties, as shown in Fig. 4.1, making it a reasonable assumption.

The four other tags ”LE”, ”LT”, ”GE” and ”GT” signify respectively ”less or equal to”, ”less than”, ”greater or equal to” and ”greater than”. They imply that the BR actually lies inside an interval whose only known information is the upper (or lower) limit. There are 823 transitions concerned by these tags. In B-11, the uncertainties associated to these tags were set to zero with the BR equal to the limit, which is pretty optimistic and does not make full use of the ENSDF information. In this work, all the BR values inside the interval are treated as equivalently probable. The associated distributions are then uniform laws as detailed in Tab.4.1, and require a redefinition of the BR central value and uncertainty. Regarding BR tagged with ”GE” and ”GT”, the associated upper limit is determined by subtracting all the other BR to the isotope β^- intensity (I_β).

There are 533 transitions with a recorded BR uncertainty equal to zero in ENSDF. When checking the ENSDF files, this is usually commented as an indication of poor argued uncertainty in the original article. Hence, a null uncertainty in ENSDF should not be treated as such. On the contrary, null uncertainties should be a warning to search for the original publication in order to assess a BR uncertainty on those transitions. Evaluating the BR central value and respective uncertainty for these particular transitions is beyond the scope of the present work. For simplicity, a relative 10% uncertainty has been assumed, mirroring the 10% set on the BR tagged as ”approximated” in ENSDF.

Data provided in ENSDF	Associated distribution in BESTIOLE	Number of transitions
$\mathrm{BR} \pm \sigma(\mathrm{BR})$	$\mathcal{N}(\mathrm{BR}, \sigma(\mathrm{BR})^2)$	10 084
$\mathrm{BR} \pm 0$	$\mathcal{N}(\mathrm{BR}, (\mathrm{BR}/10)^2)$	533
BR AP	$\mathcal{N}(\mathrm{BR}, (\mathrm{BR}/10)^2)$	297
BR LE	$\mathrm{Unif}(0, \mathrm{BR})$	809
BR LT	$\mathrm{Unif}(0, \mathrm{BR})$	
BR GE	$\mathrm{Unif}(\mathrm{BR}, I_\beta - \sum_{B \neq BR} B)$	14
BR GT	$\mathrm{Unif}(\mathrm{BR}, I_\beta - \sum_{B \neq BR} B)$	

Table 4.1: Branching ratio information as provided in the ENSDF and BESTIOLE databases. In the 2021 BESTIOLE database, branching ratios and the corresponding uncertainties are respectively equal to the central values and the standard deviations of the distributions listed in the second column. There are 11 737 β^- transitions read from ENSDF [161]. The number of β^- transitions concerned by each case is reported in the third column.

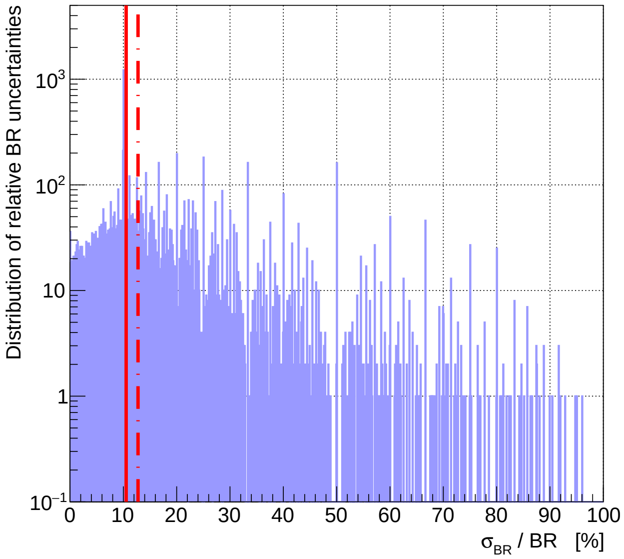

Figure 4.1: Distribution of relative branching ratio uncertainties. The data are taken from the ENSDF database for all transitions with available branching ratio uncertainty [161]. The red dotted line represents the median value for all values, equal to 12.7%. The red solid line represents the median when considering only relative uncertainties inferior to 30%, and is set at 10.5%.

4.1.1.2 β^- intensity

I_β represents the number of β-decays an isotope undergoes for 100 decays. In the B-11 modeling, the BR were normalized when their sum was greater than 1, in which case the BR were scaled down to have a sum equal to 1. In the B-21 modeling, the BR are always normalized to I_β. The most important fission products all have I_β equal to unity or very close to one. Hence, the impact of normalizing the BR of an isotope to I_β on the fission $\bar{\nu}_e$ spectrum of the four actinides is very small. Below 4 MeV, the ^{239}Pu $\bar{\nu}_e$ spectrum is decreased by 0.2%, and the difference is inferior to 0.1% for the other actinides. Above 4 MeV, the $\bar{\nu}_e$ spectra of the four actinides are typically impacted by about 0.2%. The IBD flux of the four actinides is reduced by about 0.1%[1].

The I_β uncertainty are given in ENSDF either as a numerical value or as one of five tags similar to the tags associated to the BR uncertainties, discussed in Sec. 4.1.1.1. The different cases summarized in Tab.4.1 can be applied to I_β. For the "LE" and "LT" tags, the associated uniform distributions are defined over $[0; I_\beta]$, and over $[I_\beta; 1]$ for the "GE" and "GT" tags. A specific case concerns isotopes that are full β emitter, *i.e.* for which $I_\beta = 1$. In that case, the I_β uncertainty is rigorously null, which concerns most of the important FP. Contrarily to the BR normalization, the scaling of BR uncertainties is more complicated due to the necessity to consider I_β and its uncertainty. This will be discussed in Sec. 4.2.2.

4.1.1.3 Endpoint energy

In BESTIOLE, the endpoint E_0 of a transition is computed based on the isotope Q_β energy, the energy of the excited level E_{lvl} of the daughter nucleus, and the metastable energy E_{parent} of the parent nucleus when it is not in a ground-state.

$$E_0 = Q_\beta + E_{parent} - E_{lvl} \tag{4.1}$$

---

[1] Value obtained with cumulative fission yields (CFY) from the JEFF-3.3 database [136].

The Q_β energy is equal to the mass difference between the initial and final states of the whole system.

$$Q_\beta = M({}^{A}_{Z}X_i) - M({}^{A}_{Z+1}X_f) - m_e - m_{\bar{\nu}_e} \tag{4.2}$$

The Q_β value can be obtained from several sources. In this work, the Q_β values have been taken from the Atomic Mass Evaluation database from 2020 (AME2020) [296]. For each isotope, the authors have evaluated the methodology of multiple experiments from the literature [297]. A weight has been attributed to each measurement representing its confidence, and a least squared analysis has then been performed to obtain a fitted Q_β for each β-decay. It results that the Q_β evaluation from AME2020 is more robust than a single source measurement. The fitted Q_β uncertainty is slightly reduced compared to the propagated uncertainty of the mass difference.

When applicable, the energy of the metastable parent nuclei, E_{parent}, and the corresponding uncertainties are taken from ENSDF. If the information is not available in ENSDF, E_{parent} is taken from the NUBASE2020 database [155]. Finally, the energy levels E_{lvl} are listed in the ENSDF data files. The Q_β, E_{parent} and E_{lvl} uncertainties are always treated as Gaussian distributed in BESTIOLE. It is worth to mention that the "AP" tag can be attributed to the E_{lvl} uncertainty in ENSDF. In that case, a 10% relative uncertainty is assumed and is limited to 50 keV. The endpoint uncertainty is then computed as the quadratic sum of $\sigma(Q_\beta)$, $\sigma(E_{parent})$ and $\sigma(E_{lvl})$.

4.1.1.4 Spin and parity of nuclear states

Spin and parity data of the parent and daughter nuclear levels are provided in ENSDF. The spin-parity information of a nuclear state can be known accurately or, if experimental data of good quality is missing, it can be given as a list of possible spins and parities or left blank.

When a transition has different possible spin-parity combinations between the parent and daughter nuclear states, many hypothetical forbiddenness degrees (FD) are possible. In the former BESTIOLE database, the prescription was to only consider the lowest FD from the list. While it is understandable, as transitions with lower FD usually have a higher probability to occur, it does not fully convey the experimental lack of knowledge about the transition. In the 2021 BESTIOLE database, each hypothetical transition is considered as equally possible. The spectrum of the transition is then given as the average of all possible spectra, giving a larger weight to redundant FD in the list. This concerns about 2500 transitions in ENSDF, among which approximately 2000 belong to FP. This treatment can have a sizable impact at the level of an isotope. However, due to the superimposition of hundreds of FP spectra, the impact at the level of a fission spectrum is very small. The shapes of the fission $\bar{\nu}_e$ spectra change by less than 0.1% below 4 MeV, and they are typically decreased up to 0.2% above 4 MeV.

When the FD of a transition cannot be determined, due to either the parent or daughter spin (or both) being a blank entry in the ENSDF database, the transition is assumed to be allowed. If the parity of the daughter nuclear state is unknown, it is assumed to be the same as the one of the parent nuclear state, and vice versa. Further details about the treatment of the spin-parity uncertainty in BESTIOLE are given in Sec. 4.2.4.

4.1.2 Correction of the Pandemonium effect

4.1.2.1 Pandemonium effect

The usual method to obtain the decay scheme of an isotope is to measure the γ-ray intensities consecutive to the deexcitation of the daughter nucleus levels, which are fed by the β-decays of the parent nucleus. Correcting these emission intensities from internal conversion, one obtains the γ transition probabilities that can then be used to deduce the β branching ratios. The measurement of the γ-rays has been largely performed with High Purity Germanium detectors (HPGe) [298]. This type of detector has a high energy resolution and can detect individual γ-ray transitions. However, their detection efficiency strongly decreases with increasing γ-ray energies, resulting for high-energy γ-rays at best in large intensity uncertainties, and at worst in strongly biased intensities or undetected photons. The β-feedings of the daughter nucleus levels can then be ill-evaluated during the decay scheme reconstruction, overestimating the β-feeding of low-energy levels and underestimating or even missing higher energy levels. Furthermore, a ground-state to ground-state transition does not emit any γ-ray, and its BR is usually deduced with the balance of the decay scheme from the β-feedings of the higher levels, gathering somehow all the misinformation. This bias was first mentionned in 1977 by Hardy et al. [171]. Using a Monte-Carlo approach, they simulated the γ-cascade of a virtual nucleus named "Pandemonium" and its detection with a HPGe detector. They found out that a non-negligible amount of the γ-ray intensity actually remained unobserved with HPGe detectors when compared to the simulation. This pure measurement effect, named the Pandemonium effect and illustrated in Fig. 4.2a, is more probable as the complexity of the cascade of γ-rays increases with level density and Q_β energy. As a result, the normalization of each transition spectrum of an isotope impacted by the Pandemonium effect is biased, which induces an underestimation of the isotope β and $\bar{\nu}_e$ spectra at low energy and an overestimation at high energy.

The Pandemonium effect is known to have an important impact on fission spectra and thus on IBD and CEνNS spectra [13, 176, 299]. Fig. 4.2b shows the $\bar{\nu}_e$ spectrum of ^{92}Rb modeled with ENSDF data and with data corrected from the Pandemonium effect from [281], illustrating the impact of the Pandemonium effect on an isotope. Among the 40 top contributors to the ^{235}U IBD flux, 19 have been identified to be subject to the Pandemonium effect. As such, these 19 isotopes present decay data that are likely affected by the Pandemonium effect in the ENSDF database. A list of isotopes potentially impacted by the Pandemonium has been proposed in [300], and has been reproduced in Tab.B.1 presented in App. B. Indeed, the evaluated data in ENSDF have not been updated yet with recent data corrected from the Pandemonium effect. It is noteworthy that some ENSDF data files are mentioning recent measurements not affected by the Pandemonium effect and not yet included in ENSDF. Reactor $\bar{\nu}_e$ spectra present an important bias with the summation method above 2 MeV, if the Pandemonium effect is not corrected [13, 176, 179]. There are two experimental methods to obtain Pandemonium-free experimental data for β-decays, and special care has been given to include these data into the BESTIOLE database.

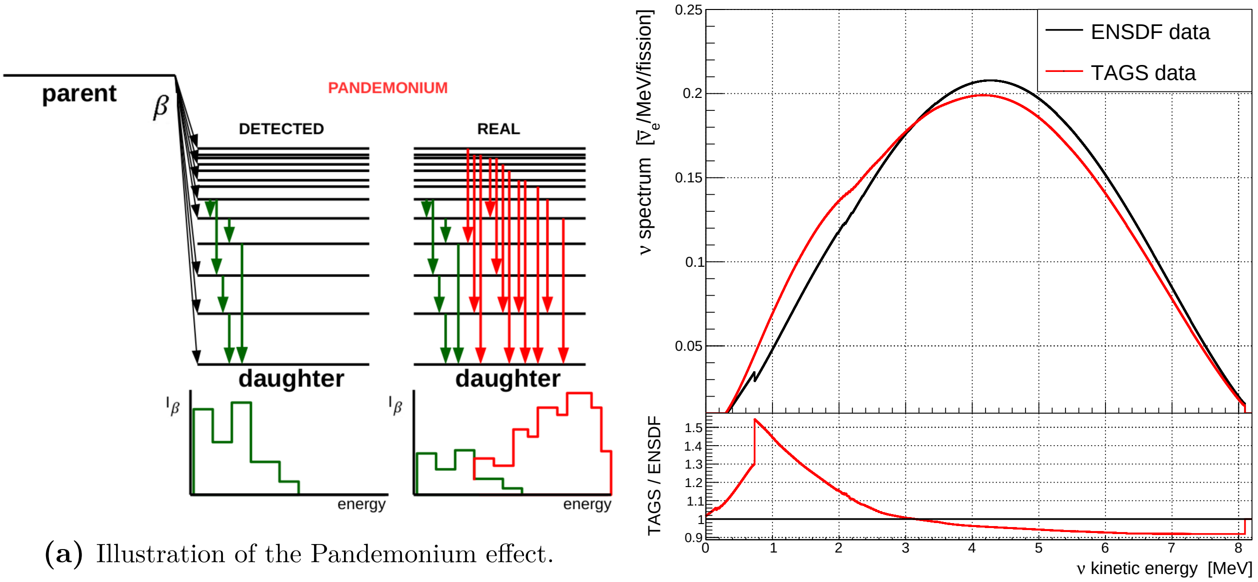

(a) Illustration of the Pandemonium effect.

(b) Pandemonium effect in ^{92}Rb.

Figure 4.2: **(a)** Schematic representation of the Pandemonium effect and how it can affect the measured β-feedings of a daughter nucleus. The γ-rays emitted from high energy levels (in red) are hidden to HPGe detectors, resulting in an overestimation of the β-feedings of low energy levels (in green). The figure is taken from [283]. **(b)** Impact of the Pandemonium effect on the ^{92}Rb neutrino spectrum, where the TAGS spectrum is corrected from Pandemonium.

4.1.2.2 Total Absorption Gamma Spectroscopy measurements

The first method is to apply a Total Absorption γ-ray Spectroscopy (TAGS) technique to measure the β-feedings of an isotope [301], uncovering many of the undetected levels with high-energy resolution spectroscopy. Contrarily to a HPGe detector, a TAGS detector have a modest energy resolution (*e.g.* NaI(Tl) detectors) and a maximized efficiency. It aims at detecting the total energy of the γ-cascade following a β-decay instead of individual γ-rays, avoiding the Pandemonium systematic error. Large scintillator crystals are used to cover a solid angle of approximately 4π, at the center of which is located the radioactive isotope to be measured. The experimental γ spectrum must be deconvoluted from the response function of the spectrometer to obtain the β^- intensity distribution.

Greenwood campaign

A first campaign of TAGS measurements was conducted in 1997 by Greenwood et al. at the Idaho National Engineering Laboratory's (INEL) isotope separation on-line (ISOL) facility [302]. The decay schemes of 49 isotopes were updated with TAGS data, listing the energy levels of transitions along with their BR and respective uncertainties [302]. In order to incorporate Greenwood's measurements into the BESTIOLE database, the data must be translated into the appropriate format. Such evaluation has been carried out in 2011 to build the database employed with B-11 [13]. Upon reviewing it, it turned out that some information were not properly implemented: there was no endpoint energy uncertainties, the transitions were all treated as allowed, and the β^- intensities were not taken into account. A new evaluation of Greenwood's data, detailed below, has been done in this work. Additionally, the transition information associated to Greenwood's data have been implemented in BESTIOLE using the

AME2016 database[303] for the computation of the Q_β energies and with the NUBASE2016 database [304] for the energies of the metastable levels and β^- intensities.

The systematic approach conducted in this work consists in matching the isotope levels measured by Greenwood with levels documented in ENSDF. For each transition from Greenwood's data, the level energy is compared to the level energies from ENSDF data. If a correspondence can be established between Greenwood's data and ENSDF data, typically for level energies differing by less than 1σ based on their associated uncertainty from ENSDF, ENSDF data are used to fill in the spin-parity data and the energy level uncertainty that are not provided in [302]. When a Greenwood level is not consistent with any level from ENSDF, a null energy uncertainty is associated and the transition is considered as allowed. The energy levels associated to a daughter nucleus are then selected from Greenwood's data.

In Greenwood's analysis, the placement and number of new energy levels are not always physical, but rather indicate that a certain amount of β-feeding is necessary to fit the measured spectrum. Such effective energy levels are referred to as pseudolevels. In this new evaluation, pseudolevels have an energy uncertainty set to 50 keV, which corresponds to the energy resolution of the TAGS detector used in [302], and are treated as allowed transitions. Endpoint energies are then computed with Eq. 4.1 and the associated uncertainties are given as quadratic sums of the Q_β, metastable and level uncertainties.

The BR from Greenwood's data have been incorporated into the BESTIOLE database with the same prescription as for ENSDF data, described in Sec. 4.1.1.1 and summarized in Tab.4.1. Unresolved energy regions are present in 27 isotopes measured by Greenwood. While the number and the energies of the levels located in these regions are known, the associated BR cannot be exactly determined. Instead, a unique BR and a unique uncertainty are associated to all the unresolved energy levels in a region. In the 2011 evaluation, the choice was made to associate the full BR value and uncertainty to a single transition in the region, the one with the highest endpoint energy. In the 2021 evaluation, the BR value from Greenwood's data and its uncertainty, B_G and σ_{B_G}, have been split between the n energy levels located in an unresolved region. The BR distribution associated to each transition is then modeled as a uniform law defined in $[0; {}^{2B_G}/_{n}]$, considering all the BR in the interval as equivalently probable in the absence of further information. Hence, the BR of each branch is equal to $B' = B_G/n$, and the associated uncertainty is $\sigma_{B'} = {}^{2B'}/_{\sqrt{12}}$. In order to reproduce σ_{B_G} as established in [302], correlations must be introduced between the newly determined BR. The correlation coefficients between each couple of BR are set to the same value, so that each BR has an equal contribution in reproducing σ_{B_G}, and no transition is favored[1]. The correlation coefficient $\rho_{B'}$ is then given by

$$n\sigma_{B'}^2 + n(n-1)\rho_{B'}\sigma_{B'} = \sigma_{B_G}^2 \qquad \Longrightarrow \qquad \rho_{B'} = \left(\frac{\sigma_{B_G}^2}{\sigma_{B'}^2} - n\right)\frac{1}{n(n-1)} \tag{4.3}$$

Correlation matrices for these Greenwood isotopes have been specifically implemented in BESTIOLE, and are always applied as prior correlation matrices during the propagation of the BR uncertainties (see Sec. 4.2.2.1 for a detailed explanation of the propagation of the BR uncertainty).

Three fission products with important fission yields and with a non-negligible contribution to a reactor IBD flux are concerned by this new prescription on unresolved levels: ^{141}Cs, ^{143}La and ^{145}Ba. They contribute respectively to 1.2%, 0.6% and 0.5% to the IBD flux of ^{235}U[2].

---

[1] Associating a uniform law may not be adequate in some cases (*e.g.* ^{142}Ba, ^{143}Ba, ^{144}Ba, ^{145}La, ^{145}Ce, ^{146}Ce, ^{148}Ce, ^{147}Pr, ^{154}Nd, ^{156}Pm, ^{157}Sm, ^{158}Sm), resulting in unphysical correlations higher than 1 or lower than −1. A Gaussian distribution $\mathcal{N}(B_G/n, {}^{\sigma^2_{B_G}}/_{n})$ is then considered for the BR of the impacted levels.

[2] These values are obtained by computing the ^{235}U IBD flux with CFY from the JEFF-3.3 database [136].

Fig 4.3 shows the $\bar{\nu}_e$ spectra of the three isotopes modeled with the new 2021 prescription and with the former 2011 prescription, along with the corresponding ratios of spectra. For ^{141}Cs, an initial BR value of 35.6% is distributed over three energy levels differing by up to 50 keV, and whose corresponding endpoint energies are close to the Q_β energy. Hence, the superimposition of the three transition $\bar{\nu}_e$ spectra differ significantly from a single transition spectrum extending up to the Q_β energy. The impact on ^{141}Cs is thus very important, with a $\bar{\nu}_e$ spectrum increased by 7% at 3 MeV and decreased by more than 10% above 4 MeV. The $\bar{\nu}_e$ spectrum of ^{143}La is similarly impacted, with an initial total BR value of 77% distributed over three energy levels separated by 40 keV, and whose corresponding endpoint energies are close to the Q_β energy. As a result, the ratio seen in the bottom plot of Fig. 4.3b is very similar to the ratio from Fig. 4.3a, showing an important impact on the ^{143}La $\bar{\nu}_e$ spectrum that is increased by 10% at 2 MeV and decreased by more than 10% above 3 MeV. However, the $\bar{\nu}_e$ spectrum of ^{145}Ba is almost unchanged. Although there are two unresolved energy levels separated by 65 keV and with corresponding endpoint energies close to the Q_β energy, the low value of the initial total BR of 7% results in a small contribution from the two transitions spectra to the isotope $\bar{\nu}_e$ spectrum. The combined IBD yield of ^{141}Cs, ^{143}La and ^{145}Ba is decreased by 5.5% in total with the new 2021 prescription for unresolved energy levels. At the level of a reactor spectrum, using the 2021 prescription instead of the 2011 prescription for unresolved energy levels results typically in a decreased of the IBD yield slightly higher than 0.1%.

Including spin and parity data taken from ENSDF in the evaluation of Greenwood's data results in the most important impact in the new prescription. As it has been shown in Ch. 3, the shape of an allowed spectrum differs significantly from those of unique forbidden spectra. Therefore, allowing transitions based on Greenwood's data to be modeled as unique forbidden transitions instead of being forced to be allowed transition can have a significant impact on the shape of an isotope $\bar{\nu}_e$ spectrum. As a result, the contribution of isotope spectra modeled with Greenwood's data to a reactor IBD flux is increased. The ^{235}U and ^{239}Pu IBD fluxes are typically increased by 0.3% with respect to the former 2011 prescription, and the ^{238}U and the ^{241}Pu fluxes by 0.2%.

Among the 49 Greenwood's isotopes, 44 have been included into the 2021 BESTIOLE database as reported in Tab.B.1 of App. B. These 44 Greenwood's isotopes are prioritized over ENSDF data, while the remaining five isotopes have been remeasured during recent TAGS campaigns.

Recent TAGS campaigns

To improve the calculations of decay heat and reactor spectra, two meetings were held in 2009 [305] and 2014 [300] following the recommendations of the Subgroup 25 of the OECD-NEA Working Party on International Evaluation Cooperation of the Nuclear Science Committee. The purpose of these meetings was to establish a list of potential candidates to the Pandemonium effect. The isotopes were sorted in prioritizing order to be measured (or remeasured) with the TAGS technique. This list has been partly reproduced in Tab.B.1, presented in App. B. There is currently no single place sourcing all the TAGS measurements, and retrieving all these valuable experimental data is a consequent piece of work. The information summarized in Tab.B.1 gives a broad picture of the current status of the work related to TAGS measurements, including the multiple TAGS measurements that have been carried out since then at the Jyväskylä University and at the Oak Ridge National Laboratory. Some of the most important isotopes subject to the Pandemonium effect still have to be measured, but the majority of them have already been taken care of.

The 2021 BESTIOLE database includes 34 recent TAGS measurements (see Tab.B.1). These recent TAGS data are prioritized over both Greenwood's data and ENSDF data. The TAGS data have been coupled to ENSDF decay scheme data in a similar manner than for Greenwood's data.

4.1.2.3 Direct β spectrum measurement

The second possibility to obtain Pandemonium-free data is to make a direct measurement of the β spectrum. In 1990, Tengblad et al. have measured separately the continuous β and γ spectra following the decay of 111 short-lived FP [306, 307]. The γ spectra and a first set of β spectra were measured at the isotope-separator-on-line facility OSIRIS at Studsvik (Sweden), and the remaining β spectra of these FP were measured at the ISOLDE facility (CERN). The β spectra were measured over an energy range from 0.25 MeV to 14 MeV [306, 307]. The 111 FP, mostly short-lived and with high Q_β, make up for about 90% of the expected $\bar{\nu}_e$ flux above 6 MeV [306].

The drawback of this method is that it does not give any access to the decay scheme data nor to the $\bar{\nu}_e$ spectrum, which must be modeled with the conversion method. To include Tengblad's measurements into the BESTIOLE database, it is necessary to convert them into a proper data format. This was done in 2011 by the Saclay group, by applying the conversion procedure mentioned in Sec. 2.2.3.2 to each Tengblad β spectrum individually [13]. The Tengblad β spectra were well reproduced by two to six allowed virtual transitions depending on the isotopes. The endpoint energies and the BR of these virtual transitions were finely tuned to best fit the β spectra from [307]. The characteristics of these branches were then stored in a text file in the BESTIOLE format.

While the conversion procedure can reproduce the β spectra within less than a percent of accuracy over the whole energy range, nothing guarantees that the associated $\bar{\nu}_e$ spectra are perfectly reproduced by the set of allowed branches. Therefore, the branching ratio and the endpoint energy uncertainties were deliberately overestimated in the 2011 study to compensate for this potential bias. As a result, the considered BR relative uncertainty was typically greater than 50%, and the relative endpoint uncertainty could reach up to 30%. The study performed in 2011 has been included in the 2021 BESTIOLE database, with the β^- intensities and the corresponding uncertainties updated from the NUBASE2016 database.

The presence of overestimated uncertainties is an argument against using Tengblad's spectra. While being conservative, it would also go against the initial point to propose a reviewed and reliable uncertainty budget. Therefore, it has been decided to prioritize TAGS data over Tengblad's data. Tengblad's data being Pandemonium free, they are still prioritized over ENSDF data. From the 111 measured β spectra, 44 are consistent with the ENSDF data and thus need not to be employed [13]. Among the remaining 67 isotopes measured by Tengblad, 24 have also been TAGS measured. Hence, the 2021 BESTIOLE database includes 43 isotopes measured by Tengblad.

4.1.3 Modeling of missing nuclei

After including the different experimental sources to model spectra, 779 isotopes listed as β emitters in NUBASE2020 [155] are still missing from the BESTIOLE database. Among them, 253 are FP contributing to reactor spectra. For these isotopes, β-decay data have not been measured and their contribution must be estimated using an effective modeling. These missing FP usually exhibit a high Q_β far above the IBD threshold, and thus have very short half-lives making them difficult to measure. They contribute typically to a couple of percents of a reactor $\bar{\nu}_e$ flux and to about 5% of the IBD mean cross-section per fission of a reactor spectrum.

In 2011, the missing isotopes were held responsible for the difference between the summation spectra and the ILL β spectra [13]. The contribution of missing isotopes to a reactor $\bar{\nu}_e$ spectrum was then modeled using the conversion method presented in Ch. 2. An uncertainty encompassing the "Missing information" in nuclear databases was then associated to the contribution of missing nuclei [13, 308]. The "Missing information" uncertainty was evaluated based on different scenarios to model the missing nuclei as well as from the difference with the ILL β spectra. It resulted in a dominating uncertainty on reactor $\bar{\nu}_e$ spectra, ranging from 10% at 2 MeV and up to 20% at 8 MeV.

A second approach, considered in [176, 308] and in this work, is to model each isotope spectrum individually using an effective modeling. Even though β-decay data for missing isotopes are not available, their Q_β energies and β^- intensities are respectively listed in the AME2020 database [296] and in the NUBASE2020 database [155]. These two information give the possibility to constrain the uncertainty on the shape of the isotope spectrum, the uncertainty on the normalization of the spectrum being given by the uncertainties coming from I_β and from the fission yields. Two effective modelings have been investigated for missing nuclei.

The Gross theory of β-decay

This theory, elaborated in the 1970s, describes the β-decay properties of an isotope by replacing the discrete level scheme with a continuum of levels, and the nuclear matrix element with the average of the squared norm of the matrix element multiplied by the density of final states [309, 310]. A single-nucleon energy is assumed to exist with a distribution based on the Fermi gas model. Moreover, each nucleon is assumed to decay with a given probability as a result of the single-particle β-decay operator. Several trial forms of this decay probability distribution have been investigated in [309]. The Gross theory is widely used in the Japanese Evaluated Nuclear Data Library (JENDL) to compensate for missing experimental data. However, only the β spectra obtained with the Gross theory are provided in JENDL. In former summation predictions [15, 176], data from the JENDL database were included in fourth order of priority, after TAGS data, Tengblad's data and ENSDF data. In [13], the aggregate β spectra computed with JENDL data were converted into the $\bar{\nu}_e$ spectra with the conversion method. In this work, the Gross theory of allowed transitions has been implemented in BESTIOLE based on the work from [309]. The isotope $\bar{\nu}_e$ spectra can then be computed with the Gross theory, with an uncertainty on the normalization derived from $\sigma(I_\beta)$ and an uncertainty on the shape derived from $\sigma(Q_\beta)$. However, the uncertainty on the shape may be underestimated for small values of $\sigma(Q_\beta)$.

The Q_β effective modeling

The second investigated modeling for missing nuclei is the Q_β effective modeling, previously used in [13, 176], where an isotope is modeled with m virtual allowed Gamow-Teller transitions. Each transition has a BR equal to I_β/m, and the transition endpoint energies are spread at regular intervals equal to Q_β/m. High uncertainties are associated to the BR and to the endpoint energies to cover the lack of information on the decay schemes of these isotopes. The BR uncertainty is then set equal to 20% of the BR, and the uncertainties on the endpoint energies are equal to 10% except for the highest endpoint for which $\sigma(E_0) = \sigma(Q_\beta)$. In [308], this effective model has been tested with $m = 1$ and $m = 5$, while in [176] the model was employed with $m = 3$. In [13], the number of branches has been based on a fit of the distributions of the endpoints and branching ratios in the ENSDF database. The fit was then extrapolated to the missing nuclei.

Selection of the effective modeling for missing isotopes

The Gross theory of β-decay and four Q_β effective modelings are compared in Fig. 4.4 with aggregate $\bar{\nu}_e$ spectra of FP whose decay data are fully available and complete in ENSDF. The different Q_β effective modelings are for 1 branch, 3 branches, 5 branches, and for a number of branches based on a fit from ENSDF data. For the Q_β modeling based on a fit, the number of branches is determined by fitting the number of branches as a function of the Q_β energy for isotopes present in the ENSDF database. The fit is then extrapolated to the missing isotopes.

In a first study, only the isotopes whose decay date are provided in ENSDF without missing information are considered to constitute the reference spectrum. This amounts to 183 isotopes. Each isotope spectrum is then weighted by its corresponding cumulative fission yield for ^{235}U from the JEFF-3.3 database to produce a $\bar{\nu}_e$ spectrum. This $\bar{\nu}_e$ spectrum corresponds to about 25% of the expected total reactor $\bar{\nu}_e$ flux, to approximately 8% of the expected $\bar{\nu}_e$ flux above the IBD threshold, and to only 5% of the expected reactor IBD flux. Similarly, the 183 isotopes are modeled with the five different effective modelings. It can be seen in Fig. 4.4a that each effective modeling performs poorly in reproducing the reference $\bar{\nu}_e$ spectrum. The Q_β effective modeling with one branch overestimates the reference spectrum, and the resulting difference exceeds those obtained with the other modelings. The four other modelings are all overestimated below 1 MeV and underestimated between 1 MeV and 8 MeV. For the Q_β modelings, this is explained by the fact that an isotope modeled with either one of the four Q_β modelings is distorted toward low energy due to the stacking of transition spectra. The distortion thus increases in the low energy region with the number of branches used in the Q_β effective modeling. It is noteworthy that the difference is in only between the shape of the aggregate spectra, the normalization being conserved for each isotope. On the other hand, isotope β and $\bar{\nu}_e$ spectra modeled with the Gross theory are skewed toward low energies, leaving the spectra depleted in the high energy region. The amplitude of the differences of the four modelings with the reference spectrum are similar up to 3 MeV and of about 40%. Beyond 3 MeV, the Q_β modeling with 3 branches is the one with the smallest deviation, exhibiting a 20% difference. The difference above 8 MeV is much less relevant as more than 99.9% of a reactor $\bar{\nu}_e$ flux is emitted below 7 MeV.

Above 3 MeV, the spectra in Fig. 4.4a are dominated by a small number of isotopes whose contribution appear as sharp edges in the reference spectrum: ^{101}Nb and ^{98}Nb contribute identically and dominate up to 4.6 MeV, then ^{97}Y dominates up to 6.8 MeV and ^{150}La dominates up to 8.4 MeV. The different effective modelings are not accurate to model a single isotope, and the observed differences are then not surprising. The comparison of the five effective modelings has then been conducted for a $\bar{\nu}_e$ spectrum including isotopes from ENSDF with partially missing decay data, thus increasing the number of FP contributing to the total spectrum to

570. Transition with missing decay data are then modeled as allowed transition, as explained in Sec. 4.1.1.4. The hundreds of FP spectra average out, and the resulting $\bar{\nu}_e$ spectrum is more representative of an aggregate fission spectrum than the spectrum computed with 183 isotopes. These 570 FP typically contribute to $\sim$ 95% of the reactor IBD flux. The $\bar{\nu}_e$ spectra obtained with ENSDF data or modeled with the different effective modelings are presented in Fig. 4.4b. The conclusion is similar than for the previous case, and the Q_β modeling with 3 branches exhibits the smallest difference with the reference spectrum in the range 2 MeV to 7 MeV, between 10% and 20%. Hence, the Q_β modeling with 3 branches is selected to model the 227 missing isotopes in B-21.

4.1.4 Fission yield libraries

Fission yield (FY) data are compiled in several modern nuclear libraries such as JEFF (European database) [136], ENDF (USA database) [134], and JENDL (Japanese database) [159] for the most important ones. These FY libraries are based on the combination of experimental data, theoretical data and semi-empirical models. It is important to stress that the different FY libraries do not evolve independently, and on the contrary are supported by international cooperation of the organizations maintaining the libraries up-to-date. As a result, the different FY libraries share many information and evaluated data.

In this work, the JEFF-3.3 library has been used. The JEFF-3.3 evaluation is the latest evaluation of the European library of FY [136] and follows the general evaluation methodology employed by the United Kingdom evaluation UKFY-3.7 based on the work presented in Mills' PhD [153]. The FY from the JEFF-3.3 database are based on 7720 experimental measurements reviewed up to 2016. FY averages are obtained from different measurements by performing a down-weighting of discrepant assessments based on χ^2 tests [153]. Separate analysis have been conducted for independent and cumulative FY, whose average values and uncertainties have been used as inputs in a model fitting procedure. The resulting fit has then been interpolated and extrapolated to missing FY which have few available experimental measurements or none. The JEFF-3.3 library then provides a set of consistent FY data for the FP of ^{235}U, ^{238}U, ^{239}Pu and ^{241}Pu along with the corresponding uncertainties. However, the information present in JEFF-3.3 and in other FY libraries is restricted to only the variances. The existing correlations between the FY, necessarily induced by conservation during the fission process for instance (*e.g.* charge and particle conservation laws), are not available in these libraries [136]. Indeed, the complexity of determining FY correlations is a worldwide recognized problem [311].

Over the last decade, this issue has become an important topic, and the possibility to evaluate FY correlations have been recently investigated [311–316]. The content of these studies could not be appreciated at a sufficient level in this work to be incorporated. As a result, both the intra-actinide and inter-actinide FY correlations are considered null in this work. The case of fully correlated FY is not physical, as for instance the number of fission fragments produced during a fission is constrained to 2, which necessarily introduces negative correlations between the FY. As such, the case of fully correlated FY will only be mentioned for information purposes.

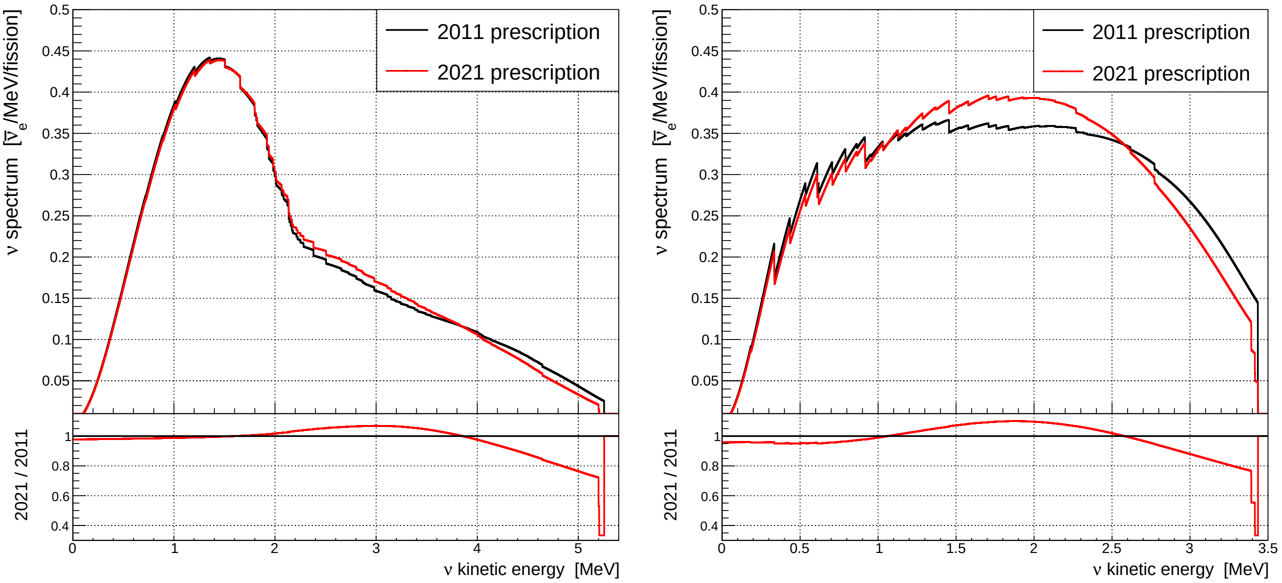

(a) ^{141}Cs. **(b)** ^{143}La.

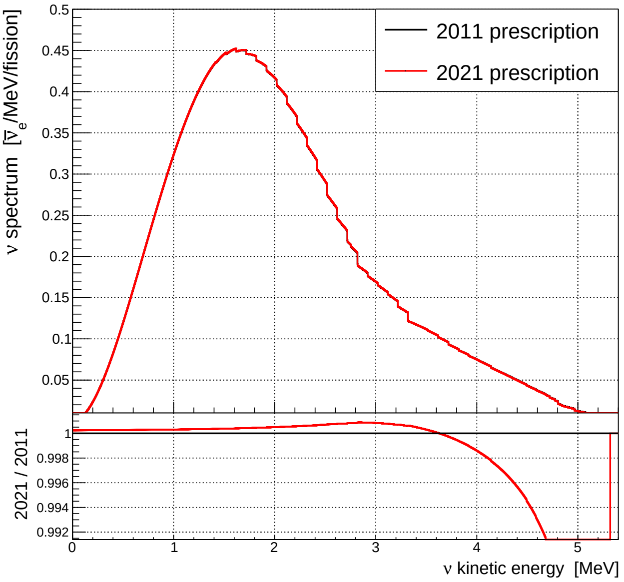

(c) ^{145}Ba.

Figure 4.3: Antineutrino spectra of ^{141}Cs **(a)**, ^{143}La **(b)** and ^{145}Ba **(c)** modeled with B-21, using Greenwood's data and the 2021 or the 2011 prescription regarding the unresolved energy levels from Greenwood's data. The subplots show the ratios of the spectrum modeled with the 2021 prescription over the spectrum computed with the 2011 prescription.

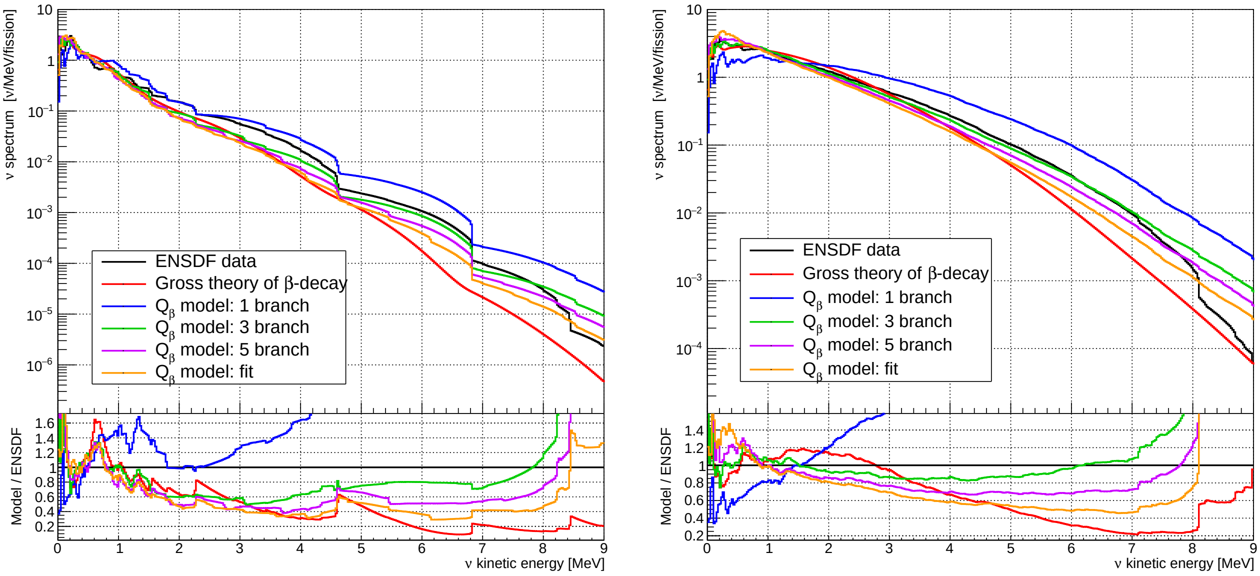

(a) $\bar{\nu}_e$ spectrum of 183 fission products.

(b) $\bar{\nu}_e$ spectrum for 570 fission products.

Figure 4.4: Comparison of different Q_β effective modelings and of the Gross theory of β-decay with an aggregate antineutrino spectrum made of 183 fission products **(a)** or 570 fission products **(b)** modeled with ENSDF data. The bottom panels show the ratios of each effective modelings with the spectrum modeled with ENSDF data.

4.2 Treatment of uncertainties

The values and uncertainties of the parameters characterizing the β-decays of each FP are extracted from different sources and compiled into a common format in the BESTIOLE database. Uncertainties are treated through a covariance matrix approach. The β and $\bar{\nu}_e$ spectrum uncertainties are propagated using either an analytical method, the Jacobian matrix formalism, or a Monte-Carlo (MC) simulation, depending on the source of uncertainty. Both methods are presented in App. C. Between the 2011 and the 2021 versions of BESTIOLE, the two propagation methods have been completely revisited. Several features previously not accounted for in B-11 have been included in the B-21 propagation of uncertainties, such as the correlations between the branches of an isotope induced by the correlations between the endpoint energies or between the BR. Additionally, modeling uncertainties are estimated by comparing different modelings of a branch spectrum. The improvements made in the treatment of the uncertainty sources are reviewed in this section after introducing them for a reactor spectrum.

The spectrum of a FP p is given by:

$$S_p(E) = \sum_b \mathcal{B}_b^p \; S_b(Z_p, A_p, E, E_{0b}), \tag{4.4}$$

where $\mathcal{B}_b^p$ and $S_b(Z_p, A_p, E, E_{0b})$ are respectively the BR and the spectrum of the branch b of the FP. Z_p and A_p are the charge and mass numbers of the FP. The branch spectrum has been described in length in Ch. 3. Parameters entering the calculation of a branch spectrum can be correlated to those entering the calculation of another one, inducing branch-to-branch correlations. The covariance matrix V_p^k associated to the spectrum of an isotope p for an uncertainty source k is then given by:

$$V_p^k = \sum_{b_i} V_{b_i}^{k_i} + \sum_{\substack{b_i, b_j \\ b_i \neq b_j}} V_{b_i b_j}^{k_i k_j}, \tag{4.5}$$

where the first sum is over the covariance matrix associated to the spectrum of each branch b_i and induced by the uncertainty on the parameter k_i, and the second sum is over the cross-term covariance matrices associated to the spectra of the branches b_i and b_j and induced by the correlations between the branch parameters k_i and k_j.

In the hypothesis that the uncertainty sources are not correlated, each source of uncertainty k can be analyzed independently and its impact on a FP spectrum can be described by a covariance matrix V_p^k uncorrelated with those of other parameters. The total covariance matrix V_p of an isotope spectrum is then calculated as the sum of the covariance matrix for each parameter:

$$V_p = \sum_k V_p^k. \tag{4.6}$$

The uncertainties on the isotope spectrum energy bins are then given by the squared roots of the diagonal elements of V_p.

The aggregate spectrum of all the FP of a fissionable isotope f is given by:

$$S_f(E) = \sum_p \mathcal{Y}_p^f \; S_p(E), \tag{4.7}$$

where $\mathcal{Y}_p^f$ is the FY of the FP p. The total covariance matrix V_f of a fission spectrum is then given by:

$$V_f = \sum_p \left(\mathcal{Y}_p^f\right)^2 V_p + \sum_p V_p^{\mathcal{Y}} + \sum_{\substack{p_i, p_j \\ p_i \neq p_j}} V_{p_i p_j}^{\mathcal{Y}_{p_i}^f \mathcal{Y}_{p_j}^f}. \tag{4.8}$$

where the first sum is the uncorrelated weighted sum of the total covariance matrix of each FP spectrum, the second sum is over the covariance matrix of each FP spectrum induced by the FY uncertainties, and the third sum is over the cross-term covariance matrices of FP spectra induced by the correlations between the FY. It is worth to stress that because a reactor $\bar{\nu}_e$ spectrum is described as a sum of the individual FP spectra weighted by their FY, potential correlations between the FY could led to significant changes in the uncertainty budget.

Finally, the average reactor spectrum per fission S_r is given by the sum of each fission spectrum weighted by the corresponding fission fraction α_f:

$$S_r(E) = \sum_f \alpha_f \; S_f(E), \tag{4.9}$$

There exist correlations between the fission fractions induced by the reactor fuel evolution and due to the normalization of the sum of fission fractions to unity. As such, cross-term covariance matrices associated to fission spectra and induced by the fission fraction correlations must be considered. Additionally, many FP spectra contribute to several fission spectra. The total covariance matrix of a reactor spectrum is then given as:

$$\begin{aligned} V_r = \sum_f \alpha_f^2 \; V_f + \sum_f V_f^{\alpha_f} + \sum_{\substack{f_i, f_j \\ f_i \neq f_j}} V_{f_i f_j}^{\alpha_{f_i} \alpha_{f_j}} \\ + \sum_{\substack{f_i, f_j \\ f_i \neq f_j}} \alpha_{f_i} \alpha_{f_j} \sum_p \mathcal{Y}_p^{f_i} \mathcal{Y}_p^{f_j} V_p, \end{aligned} \tag{4.10}$$

where the second sum is over the covariance matrices of fission spectra induced by the fission fraction uncertainties, the third sum is over the cross-term covariance matrices of fission spectra induced by the correlations between the fission fractions, and the fourth sum is related to the correlations of the FP spectra between different fission spectra. If the $\bar{\nu}_e$ emitted by activated elements have a significant contribution to the $\bar{\nu}_e$ spectrum in the energy range of interest, their covariance matrices must be added to the total covariance matrix of a reactor $\bar{\nu}_e$ spectrum weighted by the square of the activation $\bar{\nu}_e$ rate.

The different covariance matrices previously presented contain the information about the uncertainties on the shape and on the normalization of the FP spectra, fission spectra and reactor spectra. Uncertainties on the normalization of a FP arise due to the FY uncertainty, and in the case of a β^- intensity inferior to 1 (see Sec. 4.1.1.2). In order to conserve the normalization of a spectrum, the covariance matrix associated to the uncertainty on the shape of the spectrum is constrained according to:

$$\sum_{ij} V_{ij} = 0, \tag{4.11}$$

where V_{ij} is the covariance between the energy bins i and j of a spectrum. Beside the two uncertainties on the normalization mentioned above, all the covariance matrices associated to a FP spectrum describe uncertainties on the spectrum shape, and thus must satisfy this condition. Let us point out that an uncertainty source that is responsible for an uncertainty on the shape of the reactor spectrum without inducing an uncertainty on its normalization will nonetheless be responsible for an uncertainty on the normalization of the corresponding IBD or CEνNS spectrum.

At the level of a branch spectrum, the parameters whose uncertainties are propagated in BESTIOLE are the BR, the endpoint energies and the spin-parity data. Additionally, modeling uncertainties associated to the weak magnetism (WM) correction, to the outer radiative correction and to the modeling of non-unique forbidden transitions (see Ch. 3) are considered. The covariance matrices associated to these modeling uncertainties are estimated by comparing different modelings of a branch spectrum, and the method is presented in the next section. At the level of an isotope spectrum, the uncertainty on the β^- intensity is propagated. Moreover, the different branch spectra of an isotope can be correlated through their BR and through their endpoint energies. The correlations between the branch spectra induced by the nuclear radius parameter are neglected due to its small impact on the modeling of a branch spectrum (see Sec. 3.4.2). At the level of a fission spectrum, the FY uncertainties are propagated and the FY are considered uncorrelated, as mentioned in Sec. 4.1.4. Finally, the fission fraction uncertainties are propagated on a reactor spectrum and the correlations between the fission fractions are taken into account.

4.2.1 Modeling uncertainties

In this section, a general method is discussed to generate a covariance matrix associated to the modeling of a β transition spectrum. This allows to estimate uncertainties and covariance matrices for a branch spectrum associated to the WM correction, to the outer radiative correction and to the modeling of non-unique forbidden transitions, for which theoretical uncertainties cannot be derived easily or have not been defined in the literature. Because there is no uncertainty to propagate, the covariance matrices are generated instead to take into account a potential bias in the modeling of the WM, of the outer radiative corrections and of the non-unique forbidden transitions. The method consists in arbitrarily defining an energy dependent uncertainty on the branch spectrum, using different modelings of the spectrum when available. This modeling uncertainty must conserve the normalization of the branch spectrum, and as such a covariance matrix that satisfies the constraint Eq. 4.11 is generated. It is noteworthy that this method relies on arbitrary choices that may influence the final uncertainty budget. Despite these limitations, this uncertainty budget is constructed to be conservative.

The covariance matrix associated to a modeling uncertainty is estimated by comparing two modelings of a β transition spectrum. The modeling uncertainty is defined accordingly to the difference ΔP between the two modeled spectra. The two spectra act like extreme cases which are considered as the upper and the lower limits of a uniform distribution. The modeling uncertainty σ_m is thus set as the standard deviation of the uniform distribution, $\sigma_m = \Delta P/2\sqrt{3}$. To ensure the constraint from Eq. 4.11, the energy regions where ΔP has the same sign (positive or negative) are fully correlated. Energy regions where the signs are opposite are fully anticorrelated. An illustration of this method is presented in Fig. 4.5. The choice of a uniform distribution and the limits of this distribution for a given energy bin are arbitrary, and can be tuned to increase or decrease the amplitude of the uncertainty. A covariance matrix generated with this method presents one or several points where the estimated uncertainty is null, corresponding to the energy values where the two spectrum modelings cross each other. The superimposition of thousands of branch spectra averages out the modeling uncertainties and thus reduces the impact of having null uncertainties for these energies.

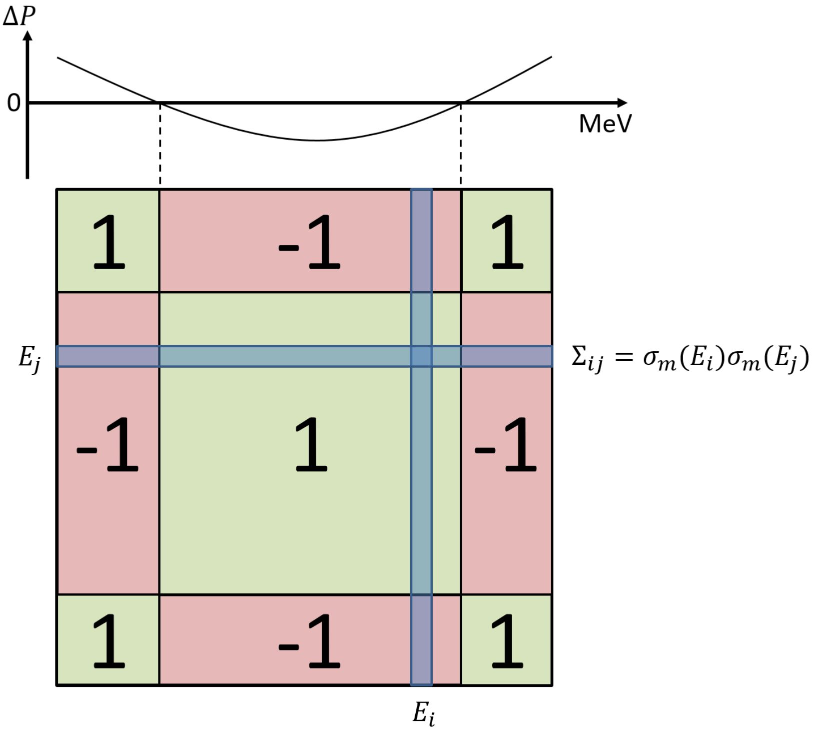

Figure 4.5: Illustration of the method to generate a matrix associated to a modeling uncertainty. The energy regions where the absolute difference ΔP between two modelings of a spectrum has the same sign (positive or negative) are fully correlated in the correlation matrix below. Regions with opposite signs are fully anticorrelated. The associated covariance matrix Σ is given by $\Sigma_{ij} = \sigma_m(E_i)\sigma_m(E_j)$, where E_i is the energy bin i and $\sigma_m(E_i) = \Delta P(E_i)/2\sqrt{3}$.

4.2.1.1 Weak magnetism and outer radiative correction uncertainties

As mentioned in Sec. 3.5.2, the WM corrections of non-unique forbidden transitions are based on approximations while the WM corrections of allowed and 1^{st} unique forbidden transitions are based on assumptions such as a truncated orbital current, the absence of meson currents and of hadronic or nuclear structure. Regarding the outer radiative correction, it is only defined for allowed transitions and is applied as such to all forbidden transitions. These approximations can induce a bias in the modeling of a branch spectrum, and there is no simple method to verify their validity. A conservative approach is then to consider the difference induced on a branch spectrum by these corrections as a maximum uncertainty.

An uncertainty is defined for both the WM correction and the outer radiative correction for each transition, based on the method presented in Sec. 4.2.1. At the level of a transition, the covariance matrix associated to the WM uncertainty is estimated by comparing the transition spectrum with and without WM correction, where the WM correction is described in Sec. 3.5.2. The conservative choice is made to symmetrize the uniform distribution considered in the procedure to take into account a possible bias induced by applying an incorrect WM correction on certain transitions, as the WM correction is not well defined for every transition. This amounts to multiply by a factor two the uncertainties derived with the covariance matrix generation method, $\sigma_m = \Delta P/\sqrt{3}$, where ΔP is the difference between the two spectrum modelings.

Similarly, the covariance matrix associated to the uncertainty on the outer radiative correction is estimated by comparing the transition spectrum with and without the radiative correction as defined in Sec. 3.5.3. As for the WM correction, the same conservative choice to symmetrize the uniform distribution is considered, in order to account for a possible bias induced by an incorrect outer radiative correction applied on certain transitions. The derived uncertainty at the level of a transition is then $\sigma_m = \Delta P/\sqrt{3}$, where ΔP is the difference between the two spectrum modelings.

4.2.1.2 Non-unique forbidden transitions

A nuclear shell model calculation has been performed to compute the three 1st non-unique forbidden transitions of ^{92}Rb, ^{96}Y and ^{144}Pr, as explained in Sec. 3.5.1. The modeling based on the nuclear shell model is more reliable than the ξ-approximation in which the three spectra are assumed to have an allowed shape. However, an uncertainty is still considered to account for a potential mismodeling of the non-unique forbidden shape factors. The method described in Sec. 4.2.1 is then used to define an uncertainty by comparing the spectra computed with nuclear shell model calculation and the allowed spectra assumed in the ξ-approximation. The amplitude of the uncertainty is defined at each energy bin by $\sigma_{NU} = \Delta P/2\sqrt{3}$, where ΔP is the difference between the two spectrum modelings. The resulting correlation matrices and fractional uncertainties are displayed in Fig. 4.6.

In addition to the non-unique forbidden transitions calculated with the nuclear shell model, a modeling uncertainty is also considered for all non-unique forbidden transitions modeled with the ξ-approximation. In Sec. 3.5.1, it was shown that the ξ-approximation used to model non-unique forbidden transitions is not appropriate for most of the transitions. Because these transitions contribute to approximately 40% of the IBD spectrum, it is critical to account for the potential bias induced by the appropriate or inappropriate use of this approximation.

The three non-unique forbidden transitions of ^{92}Rb, ^{96}Y and ^{144}Pr, along with the three non-unique forbidden transitions of ^{212}Bi, ^{214}Bi and ^{234m}Pa computed with nuclear shell model calculation in the context of geoneutrinos (see Sec. 3.5.1), are compared with their modelings in the ξ-approximation in Fig.4.7. For ^{144}Pr, the non-unique shape factor shifts the spectrum toward high energy while the opposite happens for ^{212}Bi, ^{214}Bi and ^{234m}Pa. The non-unique shape factors of ^{92}Rb and ^{96}Y increase the spectra near 0 MeV and near the endpoint, and decrease the spectra around their center. Additionally, the non-unique shape factors seem to depend on the spin difference between the parent and daughter nuclear state, ΔJ. For $\Delta J = 1$, *i.e.* for ^{212}Bi and ^{214}Bi, the non-unique forbidden shape factors are approximately linear. For $\Delta J = 0$, *i.e.* for ^{144}Pr, ^{234m}Pa, ^{92}Rb and ^{96}Y, the non-unique forbidden shape factors exhibit either concave or convex curvatures. Finally, the deviation due to the non-unique shape factors ranges from a few percents up to 30% at 0 MeV. Near the endpoint, the deviation ranges from about 7% up to more than 40%. The impact of non-unique forbidden shape factors have also been studied in [181]. They investigated 36 first non-unique forbidden transitions by calculating the corresponding shape factors with a nuclear shell model calculation and using the same formalism from Behrens and Bürhing [263] as in this work. A positive or negative slope is exhibited by most of the non-unique shape factors that they have computed. To summarize, no real trend in the non-unique shape factor is observed with the six transitions based on nuclear shell model and calculated in this work. Nonetheless, an approximately monotonic slope seems to be a dominant characteristic among the non-unique forbidden shape factors.

The method described in Sec. 4.2.1 is then used to estimate a covariance matrix for each non-unique transition improperly modeled with the ξ-approximation. A virtual spectrum is thus defined for each non-unique transition in order to be compared with the ξ-approximated spectrum. These spectra are defined as extreme cases associated to the mismodeling. The uncertainty derived from the comparison between the two spectra must be representative enough to describe a potential mismodeling for any transition. As such, the derived uncertainty is

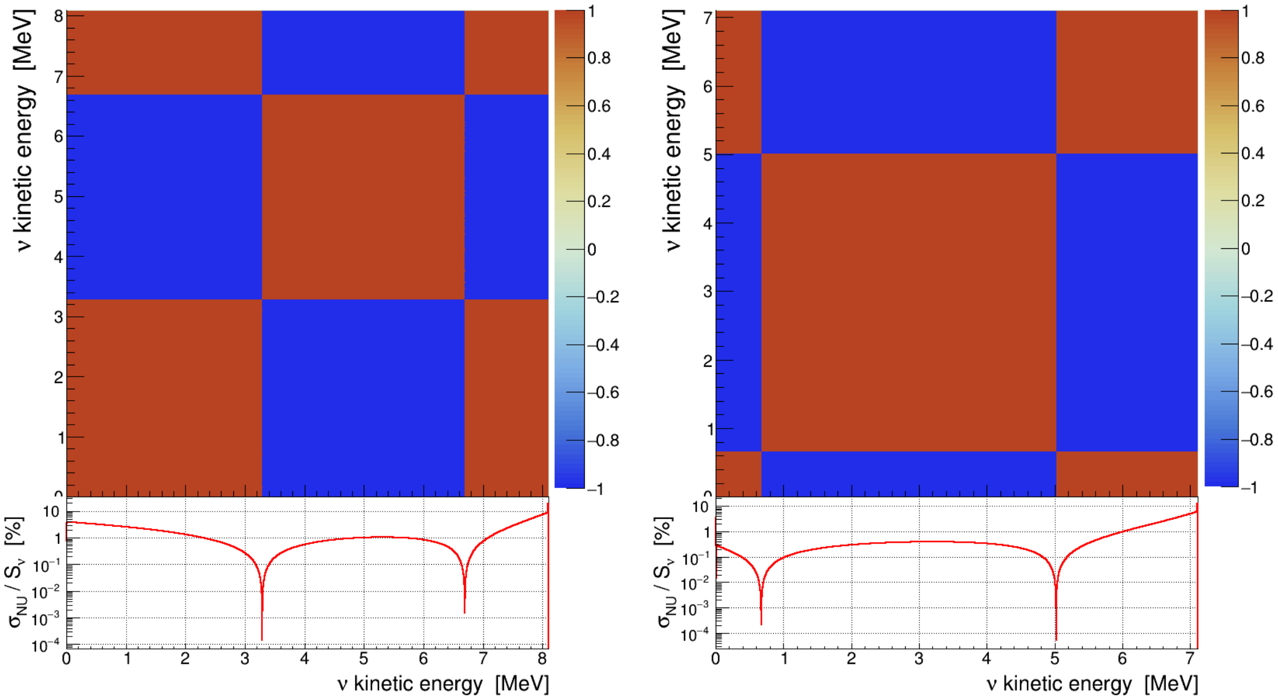

(a) ^{92}Rb.

(b) ^{96}Y.

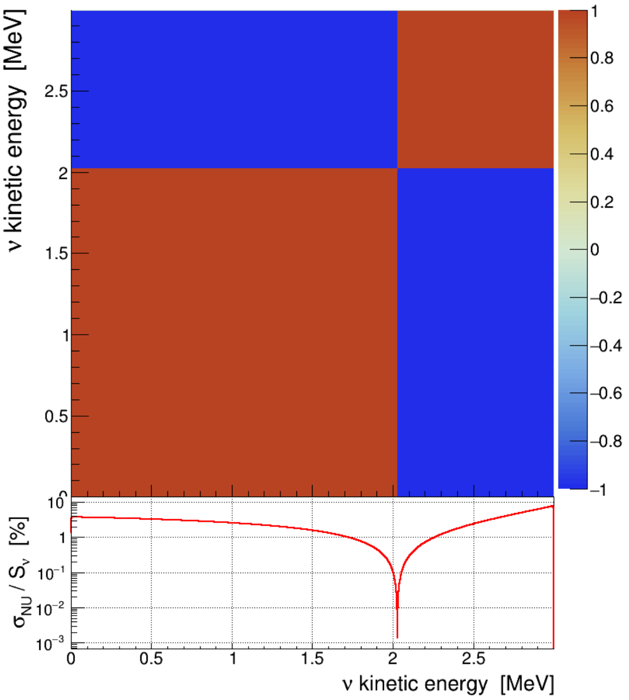

(c) ^{144}Pr.

Figure 4.6: Correlation matrices and fractional uncertainties associated to the modeling of the non-unique forbidden shape factor of the main transition of ^{92}Rb **(a)**, ^{96}Y **(b)** and ^{144}Pr **(c)**. The matrices and uncertainties result from the method proposed to generate covariance matrices for modeling uncertainties detailed in Sec. 4.2.1. The uncertainties are obtained by comparing the transition spectra modeled with nuclear shell model calculation and modeled with the ξ-approximation. The amplitudes of the uncertainties are defined by $\sigma_{NU} = \Delta P/2\sqrt{3}$, where ΔP is the difference between the two spectrum modelings.

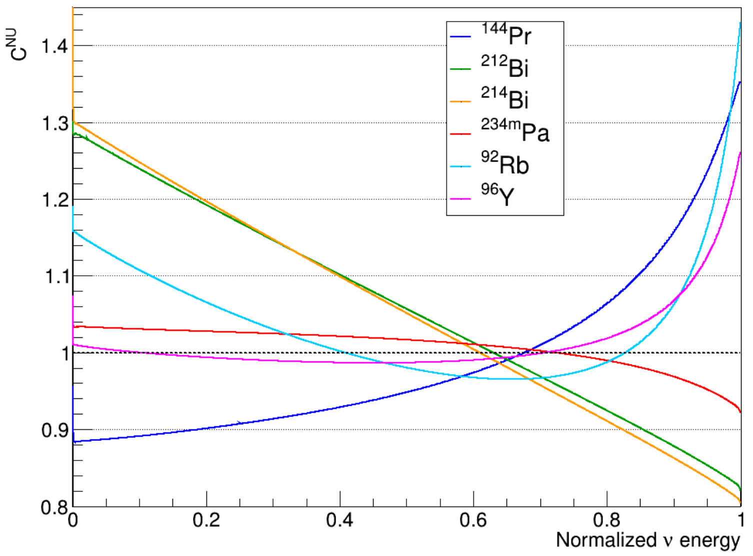

Figure 4.7: Ratio of non-unique forbidden $\bar{\nu}_e$ spectra over ξ-approximated spectra for the main non-unique forbidden transitions of a rector IBD flux (^{92}Rb and ^{96}Y) and of a geoneutrino flux (^{212}Bi, ^{214}Bi, ^{234m}Pa and ^{144}Pr). In each case, the ξ-approximated spectrum is an allowed spectrum, and the ratios resume to the non-unique shape factors C^{NU} up to a factor equal to the ratio of normalization constants. The x-axis is the normalized kinetic energy of the antineutrino, E/E_0.

expected to cover the different cases among the six non-unique forbidden transitions presented in Fig. 4.7. The virtual spectrum is generated by selecting the profile and the amplitude of a deviation with respect to the ξ-approximated spectrum. According to the non-unique forbidden shape factors from Fig. 4.7, a linear deviation would be a perfect match for ^{212}Bi and ^{214}Bi, and would make a rough approximation for ^{144}Pr and ^{234m}Pa. The amplitude of the linear deviation for $\bar{\nu}_e$ spectra is set at 0% at 0 MeV and at 150% at the endpoint energy (conversely for β spectra). The virtual spectrum is then generated based on this linear deviation and is normalized to unity. This procedure has been performed for each non-unique forbidden transition present in the ENSDF database. After normalization, the virtual spectra always exhibit a deviation of at least -30% at 0 MeV, and at least +30% at the endpoint energy. The amplitude of the derived correction covers the different deviations induced by the non-unique forbidden shape factors observed in Fig. 4.7. This virtual spectrum is finally used in the method presented in Sec. 4.2.1 and compare to the non-unique forbidden spectra modeled with the ξ-approximation to generate a covariance matrix. The uniform distribution considered in the procedure is symmetrized to take into account that the deviation induced by a non-unique forbidden shape factor could be either described approximately as a positive slope or as a negative slope. This is a conservative choice which amounts to multiply by a factor two the uncertainties derived with the covariance matrix generation method, $\sigma_{NU} = \Delta P/\sqrt{3}$, where ΔP is the difference between the virtual spectrum and the ξ-approximated spectrum.

4.2.2 Propagation of branching ratio and β^- intensity uncertainties

In the former BESTIOLE version, the BR were assumed to follow a Gaussian distribution, and no correlation was considered between the BR of a given isotope. The total BR uncertainty for an isotope was then equal to the quadratic sum of the BR uncertainties of each transition. With this treatment, the contribution of BR uncertainties to the uncertainty budget of a reactor spectrum is overestimated. This is due to the fact that the total BR uncertainty of an isotope is not constrained to the β^- intensity uncertainty.

The β^- intensity and its uncertainty are two information documented in ENSDF and in the NUBASE2020 database that must be used when possible, in order to be consistent with experimental data. This has been implemented in B-21 by developing a MC simulation. For each isotope, a MC is run over its BR values. Constraints are introduced during the MC, which generates correlations between the BR of an isotope that allow to reproduce the uncertainty on the β^- intensity. The obtained covariance matrix associated to the BR is then used to propagate the BR uncertainties on the isotope spectrum according to Eq. 4.5.

During the MC, the BR values are randomly sampled from Gaussian distributions defined as $\mathcal{N}(\mu_{\text{BR}}, \sigma(BR)^2)$, where the central value μ_{BR} and the BR uncertainty $\sigma(BR)$ have been described in Sec. 4.1.1.1. When a negative BR is drawn during the MC, the iteration is canceled and started anew, as a negative BR would be unphysical. After sampling the BR, the β^- intensity is randomized from its associated distribution, and the randomly sampled BR are scaled such that their sum is equal to the random β^- intensity. This second constraint allows the final BR covariance matrix to reproduce the I_β uncertainty and introduces correlations between the BR of an isotope.

4.2.2.1 Maximization of the branching ratio uncertainty

BR provided in ENSDF comes from experiments and there might exist correlations between the BR of an isotope due to systematic experimental uncertainties. Moreover, correlations are introduced when the BR are normalized by the evaluators to I_β. However, these correlations are not provided in ENSDF. Because there is not a unique BR covariance matrix consistent with experimental data for isotopes having three or more transitions, the phase space of BR correlations is investigated in B-21 in order to evaluate a conservative covariance matrix. A criterion is required to qualify the conservativeness of a covariance matrix. In this study, it has been chosen to maximize the BR uncertainty with respect to the IBD spectrum. Indeed, as mentioned in Sec. 4.2, both uncertainties on the shape and on the normalization of an isotope spectrum can produce an uncertainty on the normalization of the corresponding IBD spectrum. The amplitude of the induced normalization uncertainty depends on the isotope covariance matrix and thus on the correlations. The maximization criterion favors positive correlations between the BR of high endpoint transitions, as branches with endpoint energies below the IBD threshold have no weight in the IBD spectrum. A second criterion investigated in BESTIOLE is to maximize the BR uncertainty with respect to the CEνNS spectrum.

In order to investigate different sets of correlations between the BR of an isotope, a prior correlation matrix between the BR is introduced during the MC. Instead of being randomized independently during the MC, the BR are randomly sampled and correlated using the Cholesky decomposition of the prior correlation matrix. The correlated BR are then scaled to a randomized I_β value as previously. As a result, the final BR correlations are modified and depend on the prior correlation matrix. It is worth to stress that the Cholesky decomposition can only be used to generate normal correlated variables. Thus, the BR redefined in the BESTIOLE database based on uniform distributions (see Sec. 4.1.1.1) are randomized from a Gaussian distribution modeled by the central value and the uncertainty associated to the uniform distribution. The prior correlation matrix must be a random matrix to explore the phase space of BR correlations. A random matrix must satisfy several very constraining conditions to be used as a correlation matrix: it must be symmetric, semi-positive definite, and its eigenvalues must be positive or null. Hence, generating a correlation matrix by randomly sampling its entries is time consuming.

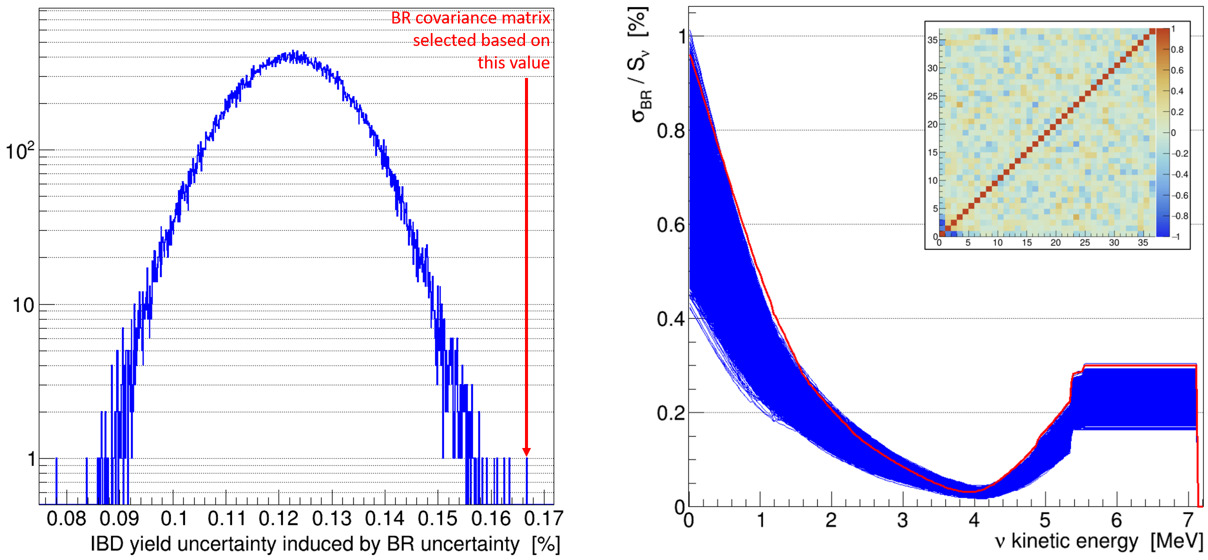

(a) IBD maximization criteria.

(b) Fractional uncertainty.

Figure 4.8: Result of the algorithm maximizing the BR uncertainty with respect to the IBD yield of ^{96}Y. The maximizing matrix has been selected from a batch of 10 0000 covariance matrices, each generated with a MC of 5000 iterations. **(a)** Distribution of the relative IBD yield uncertainty induced by the BR uncertainty. Each entry is associated to one random BR covariance matrix from the batch. **(b)** Distribution of the ^{96}Y neutrino spectrum fractional uncertainty induced by the BR uncertainty. The curve associated to the maximizing matrix is represented in red. The inset plot represents the BR correlation matrix associated to the maximizing covariance matrix.

A convenient method to generate a random correlation matrix in a negligible computing time is the onion algorithm [317], which is used in B-21 to generate the prior correlation matrix. Starting with a 2×2 correlation matrix, the onion algorithm consists in growing the matrix one row and one column at a time until reaching a $n \times n$ matrix, with n the number of transitions of an isotope. For isotopes without transition above the IBD threshold, the prior correlations are considered null.

To explore the phase space of BR correlations, a batch of BR covariance matrices is generated using random prior correlation matrices. The maximization criterion is applied to each of these matrices, and the random BR covariance matrix resulting in the maximum IBD (CEνNS) rate uncertainty is selected. With this approach, the final BR covariance matrix is the most conservative matrix of the batch, but not necessarily the most conservative matrix in general because the correlation phase space is not fully explored. Nonetheless, the randomness of the maximization algorithm allows to reproduce to some extent the phase space. If the size of the batch is large enough, it can be considered as a proper representation of the phase space of BR correlations. With the introduction of constraints and correlations, the post-MC BR uncertainties can slightly differ from their original value provided in ENSDF. The maximization procedure is illustrated in the case of ^{96}Y in Fig. 4.8. The ^{96}Y decay scheme is shown in Fig. 4.9. The BR uncertainty is dominated by the transitions to the ground-state, to the 1581 keV energy level and to the 1750 keV energy level, which are also the main transitions above the IBD threshold. As such, the maximization mostly impacts the correlations between the BR of these three transitions numbered 1 to 3 in the inset correlation matrix in Fig. 4.8.

It has been mentioned in Sec. 4.1.2.2 that 27 isotopes measured during the TAGS campaign conducted by Greenwood et al. present unresolved energy levels in their decay scheme [302].

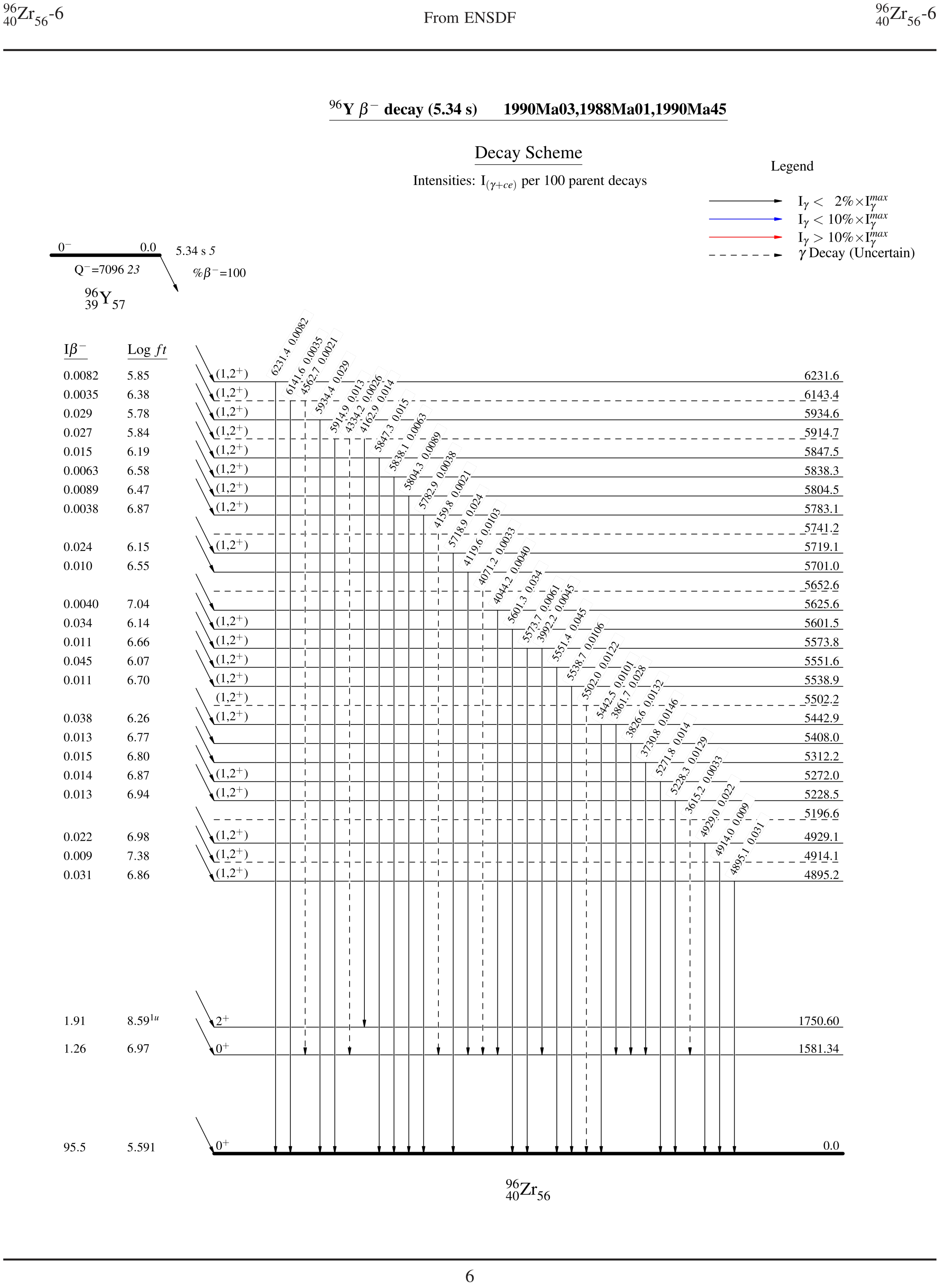

Figure 4.9: Decay scheme of ^{96}Y from ENSDF [161].

Correlations have been specifically introduced between the BR of the energy levels present in these unresolved regions to reproduce Greenwood's data. The randomization of the coefficients of the prior correlation matrix is not conducted for these specifically implemented correlation coefficients. Instead, the onion algorithm grows the random prior correlation matrix starting from the specifically implemented correlation matrix.

4.2.3 Propagation of endpoint energy uncertainties

Endpoint uncertainties are usually dominated by the Q_β uncertainty, as shown in Fig. 4.10. For 91% of the transitions listed in the ENSDF database, the ratio $\sigma(Q_\beta)/\sigma(E_0)$ lies between 0.99 and 1. This proportion increases to 96% for the interval 0.90 to 1. For transition belonging to fission products of ^{235}U, 93% of them have a ratio above 0.99 and 98% have a ratio greater than 0.9. Because the same Q_β value is used to compute the endpoint energies of all the branches constituting an isotope, a first and conservative approximation is then to considered the endpoint energies as fully correlated between the branches.

Endpoint uncertainties are propagated with a MC simulation. Random spectra of each transition contributing to the isotope spectra are generated while randomly sampling the endpoint value into the associated Gaussian distribution. Additionally, the randomized endpoint values were constrained to be positive ("$E_0 > 0$" constraint). For isotopes with correlated endpoints between the branches, the endpoints are not generated independently. Instead, at each iteration of the MC, a unique value is randomly generated in the normal distribution $N(0,1)$. This value is then appropriately scaled and normalized with respect to the endpoint central value and uncertainty of each branch, allowing to generate fully correlated endpoint values for all the branches of an isotope.

For the 1st non-unique forbidden transition computed with the nuclear shell model (see Sec. 3.5.1), a simplified approach was used to propagate the endpoint uncertainty on the β and on the $\bar{\nu}_e$ spectra as a MC would have resulted in an unrealistic computation time. As a first approximation, the endpoint uncertainties are considered small enough so that they can be propagated linearly on the spectra. Their impact on the β and $\bar{\nu}_e$ spectra is then interpreted as a simple perturbation of the energy range over which the transition spectra range, while not affecting the spectrum shapes. At each iteration of the MC, endpoint uncertainties can thus be propagated by contracting or by dilating the spectra accordingly to the randomly generated endpoint. The spectra are then normalized to unity. For 1st non-unique forbidden transition modeled with the ξ-approximation, this method was found to reproduce with a good accuracy the spectrum uncertainty estimated with a proper MC. The difference between the two generated spectrum uncertainties was below 20%. It can also be noted that for branches modeled with nuclear shell model calculations, the endpoint uncertainty is not a dominant systematic uncertainty. The total uncertainty is dominated by modeling systematic uncertainties as described in Sec. 4.2.1.2.

At each iteration of the MC, the isotope spectrum is calculated as a sum of the random transition spectra. For the very rare cases of isotopes with high endpoint uncertainties, typically $\sigma(E_0) \geq E_0/5$ which concerns less than 0.8% of the transitions included the 2021 BESTIOLE database, random endpoint values generated with negative or null value are rejected and resampled.

Let us point out that for a given transition, the spectrum calculated as the average of the random spectra exhibits differences with the spectrum modeled with the evaluated endpoint value. Indeed, a bin value is not a linear function of the endpoint, which can be easily seen

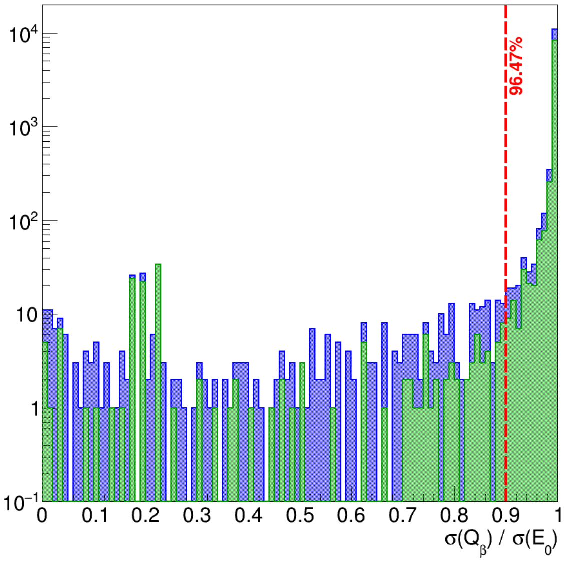

Figure 4.10: Distribution of the ratio of Q_β uncertainties over endpoint uncertainties for β^- transitions from the ENSDF database. The distribution in green represents the ratio for transitions belonging to fission products of ^{235}U. The Q_β and E_0 uncertainties are described in Sec. 4.1.1.3. For 96.5% of the transitions listed in ENSDF, the ratio is greater or equal to 0.9 as indicated by the red line.

from Eq. 3.5. These differences are negligible at low energy, and become relevant only close to the endpoint energy, typically in the $\pm\sigma(E_0)$ interval around the endpoint energy. Before the endpoint energy, the average spectrum is going to be underestimated and after the endpoint, where the spectra are expected to be null, the average spectrum will exhibit non null values. The additional constraint "$E_0 > 0$" applied on the sampled value can eventually further increase the differences if $\sigma(E_0)$ is significantly high. As a result, the uncertainty on the shape of the spectrum modeled with the evaluated endpoint value can be overestimated around the endpoint energy. These effects manifest as sharp dips around the endpoint energies in the corresponding fractional uncertainties, as illustrated in Fig. 4.11c in the case of ^{96}Y. Despite these limitations, the use of a covariance matrix framework remains a valid approach to propagate endpoint uncertainties. Indeed, these differences appear only when modeling a spectrum with an energy binning of the order of the endpoint uncertainty. For 85% of the transitions of FP, the endpoint uncertainties are below 25 keV, and the induced differences does not appear or are not significant with an energy binning of 25 keV.

The impact of correlating the endpoint energies is usually small with respect to the corresponding fractional uncertainties, as shown in Fig. 4.11c in the case of ^{96}Y, due to the small uncertainties on the endpoints. The impact increases for larger uncertainties. Nonetheless, the correlations between the energy bins of a spectrum can be impacted even for small endpoint uncertainties. In the case of ^{96}Y, the correlations between the endpoint energies result in a very localized anchor point associated to the main transition of ^{96}Y, as seen in the correlation matrix and fractional uncertainties in Fig. 4.11b. For uncorrelated endpoint energies, the anchor points associated to transitions with the second and third highest BR values manifest in the correlation matrix around 5 MeV in Fig. 4.11a.

For isotopes modeled with Tengblad's data or for missing isotopes modeled with the Q_β effective modeling, endpoints are not correlated. Tengblad's isotopes are modeled with virtual transitions whose endpoint uncertainties have been chosen independently. Similarly, the

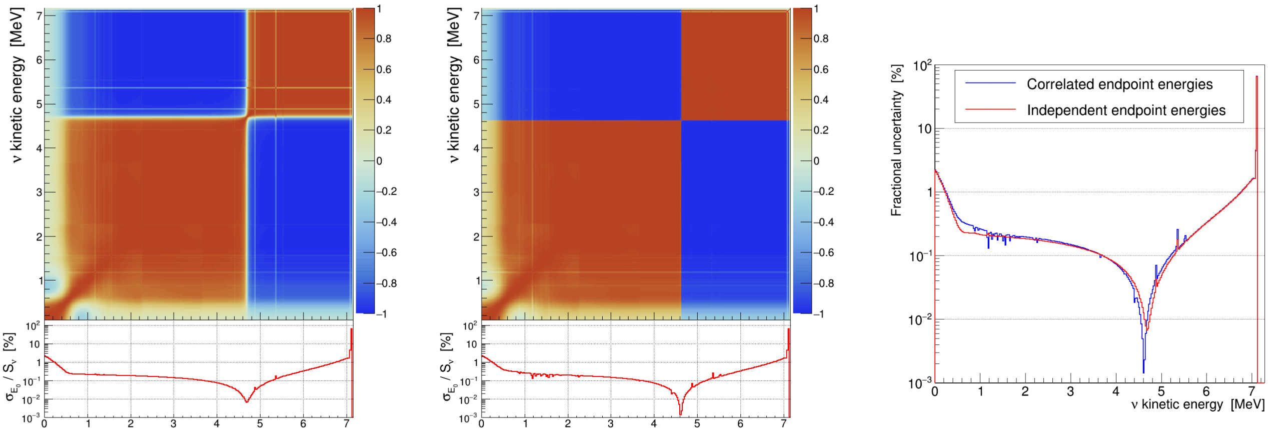

(a) Uncorrelated endpoints.

(b) Correlated endpoints.

(c) Fractional uncertainties.

Figure 4.11: Correlation matrix associated to the endpoint uncertainty for the ^{96}Y $\bar{\nu}_e$ spectrum in the case of independent endpoint energies **(a)** or correlated endpoint energies **(b)**. **(c)** Impact of the endpoint correlations on the fractional uncertainty associated to the endpoint uncertainty of ^{96}Y.

uncertainties on the endpoint energies of the virtual branches modeled with the Q_β effective modeling have been chosen independently.

In the 2011 version of BESTIOLE, a convergence criterion was defined to stop the MC over the endpoint energies. The covariance matrix was considered converged when the relative variation of each energy bin of the covariance matrix was less than 10^{-3} between two iterations. Two issues arise with this criterion. First, the MC can stop in some rare case at an early stage where the convergence criterion is met while some bins are still relatively far from their "true" value. Second, the precision of the MC on each energy bin of the covariance matrix is not known. In the 2021 version of BESTIOLE, the convergence criterion has been removed in favor of a more robust approach. The same number of iterations is used to compute the endpoint covariance matrix of all isotopes. If the endpoint uncertainty of a transition is small enough to be propagated linearly on the spectra, the energy bin values should behave approximately as Gaussian variables except around the endpoint energy as mentioned previously, and the precision of the MC on the diagonal elements of the covariance matrix of the transition spectrum can then be estimated from the number of iterations (see App. C). The uncertainty on the endpoint energy is typically propagated using 20 000 iterations in B-21, which corresponds to a precision of about 1% on the diagonal elements.

4.2.4 Uncertainties associated to spin-parity

Spin-parity uncertainty

In the reviewed model B-21, the propagation of the spin-parity uncertainties is combined with the propagation of the endpoint uncertainty and a single covariance matrix is calculated. As explained in Sec. 3.4.3 and 3.5, the spectrum correction induced by the Fermi function and the shape factor depend to a certain extent on the transition endpoint. Thus, computing the endpoint and spin-parity covariance matrices together allows to integrate the impact of the endpoint on the different types of transition. When a transition has multiple possible FD due to the multiplicity of nuclear state spin-parities, a FD is uniformly and equiprobably sampled among the available FD at each iteration of the MC. For a transition with unknown FD, the FD is uniformly and equiprobably sampled between allowed, 1st, 2nd and 3rd unique forbidden degrees. If n possible FD are available for a transition and if the effect of the endpoint on the transition spectrum is neglected, the value of an energy bin can be modeled with a discrete distribution with n values or less if there is some redundancy between the available FD. The spin-parity uncertainty of the bin is then equal to the standard deviation of the discrete law. This is a simplified view as the transition endpoint is randomized simultaneously.

Weak magnetism, outer radiative correction and ξ-approximation uncertainties

For a transition having multiple possible spin-parities, and thus multiple available FD, the spectrum is given as the average over the possible spectra. This implies that different WM corrections which depend on the FD are taken into account in the spectrum. As such, the covariance matrix associated to the WM modeling uncertainty must reflect this multiplicity. If there are n available FD for a transition, the covariance matrix associated to the WM modeling uncertainty is obtained by summing the n covariance matrices for the WM modeling uncertainty associated to each FD weighted by $1/n^2$. Additionally, if some of the FD are redundant[1], their WM modeling uncertainties are fully correlated and additional cross-term covariance matrices must be added. This last point is mandatory to get back identical covariance matrices induced by the WM modeling uncertainty in the case of a single FD or multiple but identical FD. With this approach taking into account the multiplicity of available FD, the WM modeling uncertainty associated to a transition with several different FD can decrease compared to a WM modeling uncertainty derived from a single FD. On the other hand, the WM modeling uncertainty based on multiple FD can increase compared to a null WM modeling uncertainty associated to a single FD.

The multiplicity of FD for a transition is taken into account in a similar manner in order to generate a covariance matrix for the outer radiative correction and for the ξ-approximation. Compared to an uncertainty based on a single FD, the uncertainty associated to the outer radiative correction based on multiple FD will be decreased if the FD are not all equal. This is due to the fact that the uncertainties associated to the modeling of the outer radiative correction are considered uncorrelated for different FD.

Regarding the modeling uncertainty associated to the ξ-approximation and based on multiple FD, it is increased compared to a modeling uncertainty based on a single FD associated to an allowed or unique forbidden transition. On the contrary, the modeling uncertainty associated to the ξ-approximation and based on multiple FD is decreased compared to a modeling uncertainty based on a single FD associated to a non-unique forbidden transition.

4.3 Summary

The construction of a database using recent sources of experimental data such as the ENSDF library and Pandemonium-free data from TAGS data and Tengblad's measurements has been presented in this chapter. The reading of ENSDF data has been revised to improve the consistency of modeled spectra with experimental data, by including notably the β^- intensity of FP and the possibility to take into account multiple available spin-parity data. Additionally, the TAGS data measured by Greenwood have been included in B-21 following a new prescription, resulting in more consistent spectra and in a reliable uncertainty budget. These revisions have a potentially important impact at the level of an isotope, with a difference of up to

---

[1] A distinction is made between Fermi and Gamow-Teller allowed transitions as their WM corrections are not equivalent.

10% observed on the shapes of isotope spectra relevant to a reactor IBD flux. However, the superimposition of hundreds of FP spectra reduces the impact of these revisions at the level of a reactor spectrum, with typically an impact on the shape of the order of 0.1%. The data from 34 recent TAGS experiments have also been included, and are expected to reduce the systematic bias originating from the Pandemonium effect.

A complete review of the propagation of evaluated nuclear data uncertainties and of modeling uncertainties has been conducted in BESTIOLE. A Monte-Carlo simulation has been developed to propagate the uncertainties associated to evaluated nuclear data. This simulation account for potential correlations between the branches of an isotope. While correlations can exist between the branching ratios of an isotope, they are not known. This simulation consists in generating randomly sampled correlation matrices associated to the branching ratios and in selecting the one maximizing a criterion that has been chosen for our study. A comparison with experimental correlations between branching ratios would allow to conclude on the validity of this simulation.

Finally, a method has been proposed to model uncertainties accounting for potential mismodelings of a branch spectrum. This method has been applied to derive modeling uncertainties for non-unique forbidden transitions modeled with the ξ-approximation or with nuclear shell model calculations, and which contribute significantly to a reactor spectrum. The bias induced by the abusively used ξ-approximation is difficult to estimate, and even though the method proposed in this work is probably too crude to pretend otherwise, it is expected to be sufficiently conservative.

The different methods developed in this chapter to propagate experimental and modeling uncertainties will be applied and discussed in the case of a reactor spectrum in the next chapter.

5

Revised summation modeling of a reactor antineutrino spectrum

Contents

In the first section of this chapter, the fission spectra of ^{235}U, ^{238}U, ^{239}Pu and ^{241}Pu are discussed in regards with the modeling of β and $\bar{\nu}_e$ transitions described in Ch. 3 and the revised uncertainty model described in Ch. 4. The new fission β spectra are then compared with measurements performed at the ILL in the 1980s [117–119] and at the FRM II in Garching in the early 2010s [189] in a second section. In the third section, the $\bar{\nu}_e$ fission spectrum predictions derived for the four actinides with the revised summation method are compared with other theoretical predictions. Finally, IBD spectrum predictions derived in this work are compared with experimental data in the last section.

In the following studies, all the spectra have been computed as histograms with energy bins of 25 keV. The value of an energy bin is equal to the integral of the analytical spectrum over the bin energy range computed with the Gauss-Legendre integration method using 10 nodes. For each isotope, a batch of 5000 random correlation matrices between the BR of the considered isotope has been generated, each matrix being generated with a Monte-Carlo (MC) simulation of 10 000 iterations (see Sec. 4.2.2). The matrix from this batch maximizing the IBD yield uncertainty induced by the BR uncertainties is selected as reference for the uncertainty propagation. The covariance matrix of each isotope spectrum induced by the uncertainties on the endpoint energies and on the spin-parities have been computed with a MC of 20 000 iterations (see Sec. 4.2.3).

5.1 Revised fission spectra

The modeling of reactor β and $\bar{\nu}_e$ spectra have been revised using an improved modeling of the β transition spectra as detailed in Ch. 3, and using updated nuclear data sources as described in Ch. 4. In this improved modeling, labeled B-21, the Fermi function and the unique forbidden shape factors take into account the effect of the spatial extension of the nucleus and the effect of the atomic screening. Moreover, the λ_k functions used in the calculation of the unique forbidden shape factors have been computed with a homemade program to lift the ”$\lambda_k = 1$” approximation. Two additional corrections are considered at the level of a transition spectrum, the outer radiative correction from [287, 288] and the weak magnetism (WM) from [221]. The $\bar{\nu}_e$ fission spectra of the four actinides computed with CFY from the JEFF-3.3 database [136] are displayed in Fig. 5.1a. Regarding the WM correction, several prescriptions can be considered for the non-unique forbidden transition and are discussed in the first section.

A detailed uncertainty budget for the four actinide $\bar{\nu}_e$ spectra is presented in the second section. The uncertainties propagated on the FP spectra and then on the total fission spectra originate from the BR, the β^- intensity, the endpoint energies and the spin-parity data. Additionally, modeling uncertainties associated to the WM, to the outer radiative correction and to the modeling of non-unique forbidden transitions are considered. The FY uncertainties are also propagated on the fission spectra, assuming that the FY are uncorrelated. The total fractional uncertainties of the four actinide $\bar{\nu}_e$ fission spectra are presented in Fig. 5.1b.

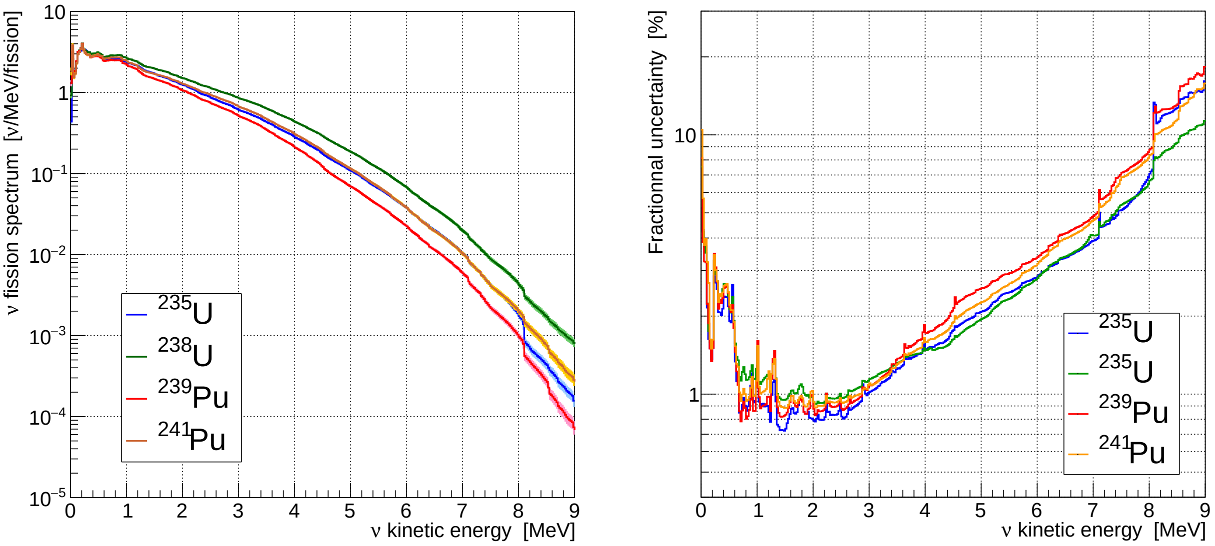

(a) Fission spectra.

(b) Fractional uncertainties.

Figure 5.1: **(a)** Antineutrino fission spectra of ^{235}U, ^{238}U, ^{239}Pu and ^{241}Pu and **(b)** the corresponding total fractional uncertainties in function of the neutrino kinetic energy. The spectra have been computed with CFY from the JEFF-3.3 database [136].

5.1.1 Selection of the weak magnetism correction

The WM prescriptions H1 to H4 correspond to the four prescriptions proposed in [221]. For each one, all unique forbidden transitions are treated as 1st unique forbidden Gamow-Teller, and all non-unique forbidden transitions are treated as:

- allowed Gamow-Teller (H1);
- 1st unique Gamow-Teller (H2);
- 1st non-unique Gamow-Teller with $(\Delta J\pi) = 0-$ (H3);
- 1st non-unique Gamow-Teller with $(\Delta J\pi) = 1-$ (H4).

In the prescription H5, 1st non-unique forbidden transitions with $\Delta J\pi = 0-$ and $\Delta J\pi = 1-$ are differentiated, the former having no WM and the latter being treated as 1st non-unique forbidden Gamow-Teller, and higher non-unique forbidden transitions are treated as allowed Gamow-Teller. In the prescription H6, the allowed Gamow-Teller WM correction is applied to all transitions [13].

The impact of each WM prescription on the ^{235}U fission spectrum is displayed in Fig. 5.2, showing the ratios of the spectra modeled with and without WM correction. The impact of the six prescriptions on the three other actinides fission spectra are similar both in amplitude and in shape. The six prescriptions have a close effect below 3 MeV and differ by up to a couple of percents above. For $\bar{\nu}_e$ spectra, there is a small increase below 2 MeV and a decrease beyond, and conversely for the β spectra. The differences induced by the WM corrections on the $\bar{\nu}_e$ spectra is less than 0.2% below 2 MeV, and reach between 0.3% and 1.5% at 6 MeV depending on the prescription. The impact on the β spectra is slightly larger at 6 MeV, between 0.4% and 3%. The maximum deviation is observed with the prescription H4, which is expected because the WM correction is maximal for all non-unique forbidden transitions. The deviation is minimal for H3, for which a null WM correction is considered for all non-unique forbidden transitions. Finally, the deviation is intermediate with H1, H2 and H6. These behaviors reflect the treatment of non-unique forbidden transitions under each prescription. Because the WM correction that should be applied on non-unique transitions is unknown, one of the intermediate prescriptions H1, H2 or H6 would seem appropriate. We dismissed the prescription H6 because forbiddenness degrees are not distinguished and the WM is always equal to the correction of an allowed transitions. The WM modeling uncertainties associated to H1 (shown as the red bands in Fig. 5.2) and H2 are almost identical, and each allows to cover approximately the spectra associated to these intermediate prescriptions. The difference induced by the choice of either H1 or H2 on $\bar{\nu}_e$ spectra is inferior to 0.1% below 7 MeV, and the H1 prescription is chosen hereafter.

The correlation matrix and the fractional uncertainty as a function of the energy induced by the WM on the $\bar{\nu}_e$ and β total fission spectra were generated using the method described in Sec. 4.2.1.1 and can be observed in the case of ^{235}U in Fig. 5.3. The uncertainties induced by the WM are lower than 0.1% below 5 MeV, and reach a maximum of 0.7% for the β spectrum and 0.5% for the $\bar{\nu}_e$ spectrum above 7 MeV. The fact that the WM modeling uncertainties are assumed to be uncorrelated in our model between the branches of an isotope and between the FP results in a small uncertainty on the fission spectra due to the superimposition of thousands of branches. The resulting uncertainties are negligible compared to the uncertainties induced by the other uncertainty sources, as seen in Fig. 5.5.

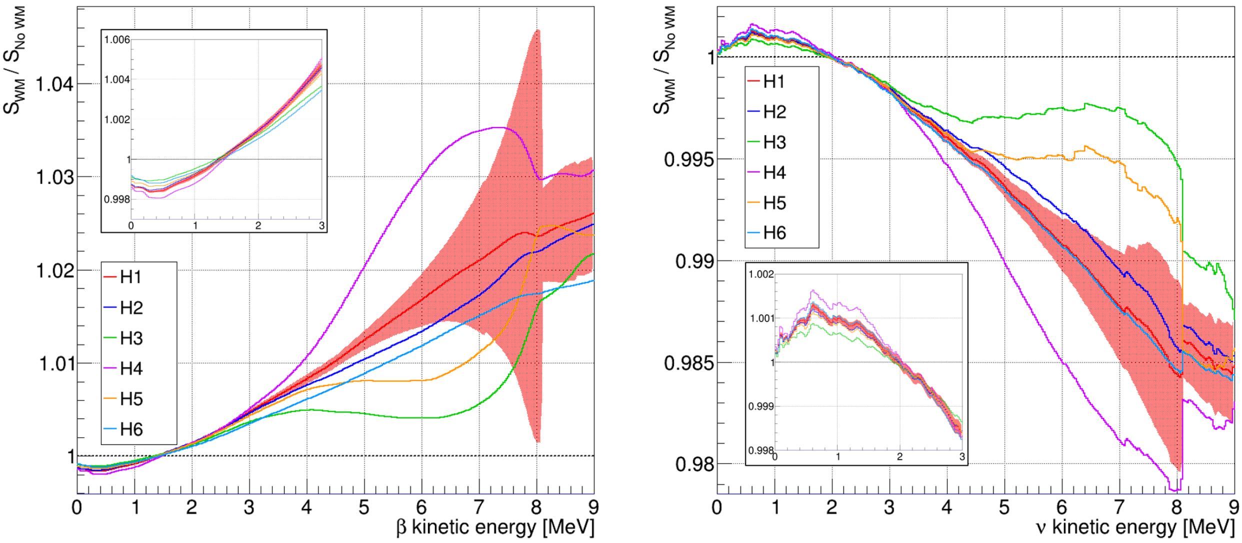

(a) WM impact on β spectrum.

(b) WM impact on $\bar{\nu}_e$ spectrum.

Figure 5.2: Ratios of the β fission spectra **(a)** and of the $\bar{\nu}_e$ fission spectra **(b)** of ^{235}U computed with and without weak magnetism with the six prescriptions. The fission spectra have been computed with CFY from the JEFF-3.3 database [136]. The red bands represent the uncertainties induced on the fission spectra by the weak magnetism modeling for the H1 prescription.

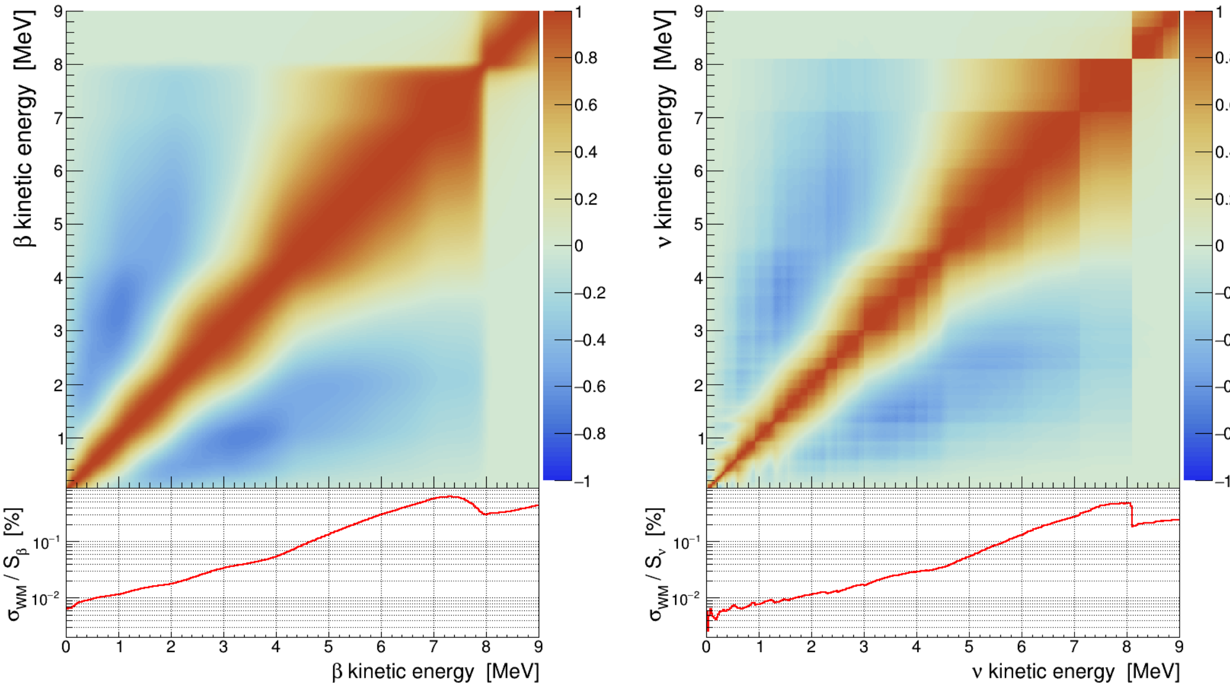

(a) β fission spectrum.

(b) $\bar{\nu}_e$ fission spectrum.

Figure 5.3: Correlation matrix and fractional uncertainty induced by the weak magnetism modeling uncertainty on the β fission spectrum **(a)** and on the $\bar{\nu}_e$ fission spectrum **(b)** of ^{235}U. The spectra have been computed with the H1 prescription for weak magnetism and with CFY from the JEFF-3.3 database [136].

5.1.2 Impact of the revised modeling

Improving the modeling of β-decay spectra at the level of individual transitions has a small impact on the actinide $\bar{\nu}_e$ fission spectra, which are modified by less than 0.2% above 1 MeV. This is shown by the green curve in Fig. 5.4a, representing the ratio of the ^{235}U $\bar{\nu}_e$ fission spectrum computed with the set of correction from B-21 over the spectrum computed with the set of correction from B-11. Both sets of corrections have been detailed in Tab. 3.3.

Regarding the WM correction, using the H1 prescription in B-21 instead of the H6 prescription used in B-11 results in an increase of less than 0.1% above 2 MeV, as shown by the red curve in Fig. 5.4a. This is expected as these two prescriptions have a similar impact on $\bar{\nu}_e$ fission spectra as seen in Sec. 5.1.1.

The effect of the finite size of the nucleus on the Fermi function is modeled with a linear analytic correction in B-11 and with a numerical correction in B-21 exhibiting a linear behavior. At the level of individual transitions, the difference between the B-21 and the B-11 corrections is small, typically a couple of percents at the endpoint energy for high A nuclei and large endpoint energy transitions. Using the B-21 numerical correction instead of the B-11 analytic correction then results in a small increase of the $\bar{\nu}_e$ fission spectrum of about 0.1% above 5 MeV, as shown by the blue curve in Fig. 5.4a with respect to the red curve.

Most of the transitions contributing to a $\bar{\nu}_e$ fission spectra are allowed transitions or 1$^{\text{st}}$ non-unique forbidden transitions, as seen in Fig. 5.4b. In B-21, 1$^{\text{st}}$ non-unique forbidden transitions are either ξ-approximated to allowed transitions or are computed with nuclear shell model calculations for the main non-unique forbidden transitions of ^{92}Rb, ^{96}Y and ^{144}Pr (see Sec. 3.5.1). In each case, the shape factors of these transitions (given either as a constant or computed with nuclear shell model calculation) are not impacted by the $\lambda_k = 1$ approximation (see Sec. 3.5). The numerical correction of the shape factors used in B-21 only impacts unique forbidden transitions and higher non-unique forbidden transitions, which make up about 10% of the $\bar{\nu}_e$ fission spectra up to 5 MeV and above 8 MeV. As a result, lifting the $\lambda_k = 1$ approximation results in a small increase of the $\bar{\nu}_e$ fission spectra, up to 0.2% between 1 MeV and 5 MeV and above 8 MeV, as shown by the purple curve in Fig. 5.4a with respect to the blue curve. Let us point out that the impact of lifting the $\lambda_k = 1$ approximation is also less important on a $\bar{\nu}_e$ fission spectrum than at the level of individual transitions due to transition spectra averaging out in a fission spectrum.

Finally, the impact of the numerical correction for the atomic screening on the Fermi functions and on the shape factors used in B-21 is shown by the green curve in Fig. 5.4a. Due to the smaller contributions from unique forbidden transitions and from 2$^{\text{nd}}$ and higher non-unique forbidden transitions, the observed effect is mainly due to the screening correction of the Fermi functions which applies to all transitions. At the level of a transition, the effect of the screening correction on the Fermi function is opposite to the effect of the finite-size correction. The effect is then to decrease the $\bar{\nu}_e$ spectrum in the high-energy region (see Sec. 3.4.3.2). Moreover, the amplitude of the correction increases with higher endpoint energies. This behavior can be observed at the level of a $\bar{\nu}_e$ fission spectrum, as shown by the green curve which is lower than the purple curve above 1 MeV and whose difference increases with higher energies.

The large differences observed in the purple and green curves below 0.5 MeV are due to a handful of isotopes that dominate in this energy region and for which the impact of the B-21 modeling is sizable.

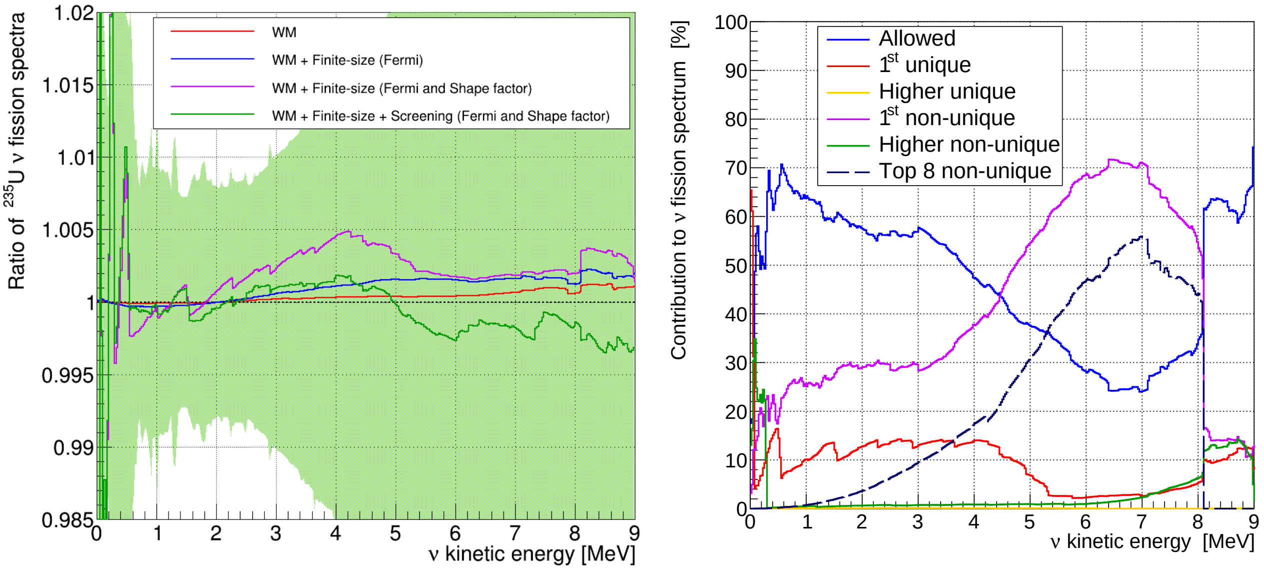

(a) B-21 modeling impact on the ^{235}U $\bar{\nu}_e$ spectrum.

(b) Transitions in the ^{235}U $\bar{\nu}_e$ spectrum.

Figure 5.4: (a) Ratio of ^{235}U $\bar{\nu}_e$ fission spectra computed with B-21 and with B-11. For all the ratios, the spectra at the denominator are computed with the corrections from B-11 as detailed in Tab. 3.5. The blue, red, purple and green curves each includes additional corrections used in B-21 as detailed in the text, and the differences with the spectra at the denominator are written in the legend. The green band represents the final B-21 ^{235}U spectrum uncertainty. **(b)** Contributions from the different transition types to the ^{235}U $\bar{\nu}_e$ fission spectrum. The contributions in solid lines sum up to 100%. The dashed line represents the contribution of the 8 most important non-unique forbidden transitions (see Tab. 3.3). The spectra have been computed with CFY from the JEFF-3.3 database [136].

5.1.3 Uncertainty budget

The systematic breakdown per uncertainty source on the $\bar{\nu}_e$ flux, the IBD yield and the CEνNS yield calculated for a germanium detector with a 20 eV recoil energy threshold are shown in Tab. 5.1. The correlation matrix of the ^{235}U $\bar{\nu}_e$ fission spectrum and the fractional uncertainties induced by each uncertainty source are displayed in Fig. 5.5. The detail of the correlation matrix per uncertainty source for the four actinide fission spectra can be found in App. E, along with the inter-actinide correlation matrices induced by the contribution of identical FP in the total fission spectra.

The ^{235}U total fractional uncertainty is about 1% between 1 MeV and 3 MeV, and increases with energy. The fractional uncertainty is about 2% at 5 MeV and reaches up to 10% at 8 MeV. The increase of the fractional uncertainties is mostly due to the fact that the number of contributing isotopes decreases when energy increases. Uncertainties induced by the FY uncertainties dominate the uncertainties of $\bar{\nu}_e$ fission spectra above 2 MeV and generate positive correlations between the energy bins. The FY uncertainties result in an uncertainty on the $\bar{\nu}_e$ flux of 0.30%, 0.55%, 0.35% and 0.50% for respectively ^{235}U, ^{238}U, ^{239}Pu and ^{241}Pu when the FY are assumed to be uncorrelated. If the FY are assumed to be fully correlated, these uncertainties increase respectively to 3.63%, 6.91%, 4.56% and 7.25%. This extreme case illustrates the range for the $\bar{\nu}_e$ flux uncertainty induced by FY uncertainties, although it is important to stress that the fully correlated case is extremely unphysical. While potential correlations between the FY could lead to an underestimation of the uncertainty on the $\bar{\nu}_e$ flux in our current uncertainty budget, it is expected that the actual induced uncertainty is closer to that of uncorrelated FY.

		Normalization uncertainty [%]				
	Source	^{235}U	^{238}U	^{239}Pu	^{241}Pu	PWR
Flux	FY	0.30	0.55	0.35	0.50	0.21
	BR+I_β	0.03	0.03	0.04	0.03	0.03
	α	-	-	-	-	0.24
	Total	0.31	0.55	0.35	0.50	0.33
$\langle\sigma_{IBD}\rangle$	FY	1.07	1.15	1.26	1.25	0.69
	BR+I_β	0.63 (0.49)	0.70 (0.53)	0.62 (0.48)	0.64 (0.48)	0.61 (0.47)
	NU	0.49	0.42	0.42	0.41	0.45
	E_0+$J\pi$	0.19	0.24	0.25	0.25	0.20
	WM	0.04	0.03	0.03	0.03	0.03
	RC	0.01	0.01	0.01	0.01	0.01
	σ	0.10	0.10	0.10	0.10	0.10
	α	-	-	-	-	0.65
	Total	1.35 (1.29)	1.44 (1.36)	1.49 (1.43)	1.49 (1.43)	1.24 (1.18)
$\langle\sigma_{CE\nu NS}\rangle$	FY	0.87	0.99	1.00	1.03	0.57
	BR+I_β	0.47 (0.36)	0.53 (0.40)	0.45 (0.35)	0.46 (0.35)	0.45 (0.35)
	NU	0.34	0.29	0.30	0.28	0.31
	E_0+$J\pi$	0.14	0.18	0.17	0.18	0.15
	WM	0.02	0.02	0.02	0.02	0.03
	RC	0.01	<0.01	0.01	0.01	0.03
	α	-	-	-	-	0.55
	Total	1.06 (1.01)	1.17 (1.12)	1.15 (1.11)	1.18 (1.14)	0.97 (0.93)
	Total <1.8 MeV	0.65	0.87	0.71	0.78	0.72
	Total >1.8 MeV	1.13	1.23	1.24	1.25	1.04

Table 5.1: Breakdown of the systematic uncertainties of a reactor $\bar{\nu}_e$ flux per fission, of the IBD yield $\langle\sigma_{IBD}\rangle$ and of the CEνNS yield $\langle\sigma_{CE\nu NS}\rangle$ computed for a Ge detector with a 20 eV recoil energy threshold. The uncertainties are induced by nuclear data uncertainties (FY: fission yield, BR: branching ratio, I_β: β^- intensity, E_0: endpoint energy, $J\pi$: spin-parity) and modeling uncertainties (NU: modeling of non-unique transitions, WM: weak magnetism, RC: radiative correction, σ: cross-section, α: fission fraction). The uncertainties in the "PWR" column have been derived for fission fractions averaged over a 12-month cycle (see Tab. 2.4), and include the activated elements ^{239}U and ^{239}Np whose spectra and uncertainties are given in App. F. The uncertainty on the fission fractions is discussed later in the text. The uncertainties in brackets in the "BR+I_β" and "Total" rows are obtained when there is no maximization criterion applied (see Sec. 4.2.2.1). The $\langle\sigma_{CE\nu NS}\rangle$ uncertainties below and above 1.8 MeV are relative to the CEνNS yields below and above 1.8 MeV.

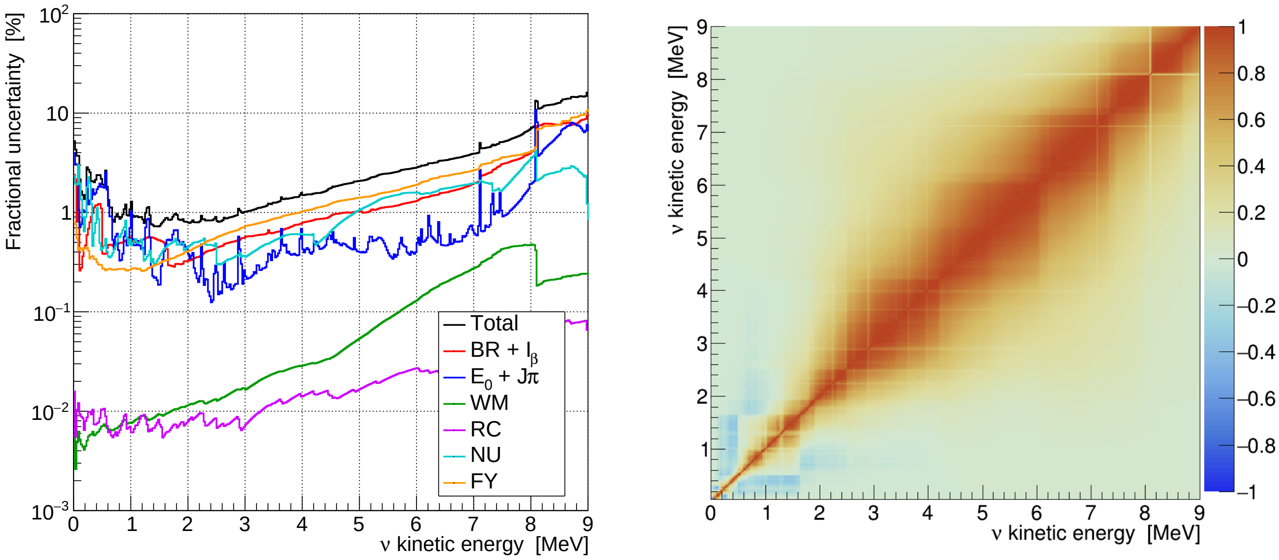

(a) ^{235}U $\bar{\nu}_e$ fission spectrum uncertainties. **(b)** ^{235}U $\bar{\nu}_e$ fission spectrum correlations.

Figure 5.5: **(a)** Fractional uncertainties of the ^{235}U $\bar{\nu}_e$ fission spectrum induced by nuclear data uncertainties (BR: branching ratios, I_β: β^- intensity, E$_0$: endpoint energy, $J\pi$: spin-parity, FY: fission yield) and modeling uncertainties (WM: weak magnetism, RC: radiative correction, NU: modeling of non-unique transitions). **(b)** Correlation matrix of the ^{235}U $\bar{\nu}_e$ fission spectrum associated to the total uncertainty. The spectrum has been computed with CFY from the JEFF-3.3 database [136].

The uncertainties induced by the modeling uncertainties of non-unique transitions, by the uncertainties on BR and I_β, and by the uncertainties on endpoint energies and spin-parities are approximately of the same order, about 1% or less between 0.5 MeV and 5 MeV and a few percents beyond. They dominate the spectrum uncertainties below 2 MeV. These uncertainties constrain the spectrum shape at the level of an isotope, and induce anticorrelations between the energy bins of a FP spectrum. These anticorrelations manifest in the total correlation matrix of the ^{235}U $\bar{\nu}_e$ fission spectrum below 2 MeV (see Fig. 5.5b), where these uncertainties dominate. The uncertainties induced by the modeling uncertainties on the WM and on the radiative correction have the lowest contribution to the total uncertainty, which is expected as these corrections have a small impact at the level of a transition spectrum (see Sec. 3.5.2 and 3.5.3).

The impact of correlating the endpoint energies of an isotope is negligible on the fractional uncertainties as well as on the induced uncertainties on the IBD and CEνNS yields, which vary by less than 0.01% in absolute. The maximizations of the IBD and CEνNS yield uncertainties induced by the BR uncertainties have a small impact on the corresponding uncertainties, which are increased by about 30% in relative. They remain secondary behind the uncertainties induced by the FY uncertainties, and the impact of this maximization is to increase the total uncertainty by about 0.06% in absolute, which is small.

The contribution from non-unique forbidden transitions to a fission spectrum is important, making up about 50% of the spectrum at 5 MeV as shown in Fig. 5.4b. However, the uncertainties associated to the modeling of non-unique forbidden transition are relatively small at the level of the actinide IBD yields, about 0.5% as shown in Tab. 5.1, and thus despite an attempt to make conservative choices made when deriving the modeling uncertainties (see Sec. 4.2.1). The two dominant non-unique forbidden transitions, issued from ^{92}Rb and ^{96}Y, benefit from a more reliable nuclear shell model calculation and contribute respectively to 6.5% and 5.5% of the ^{235}U IBD yield. A third non-unique forbidden transition issued from ^{144}Pr

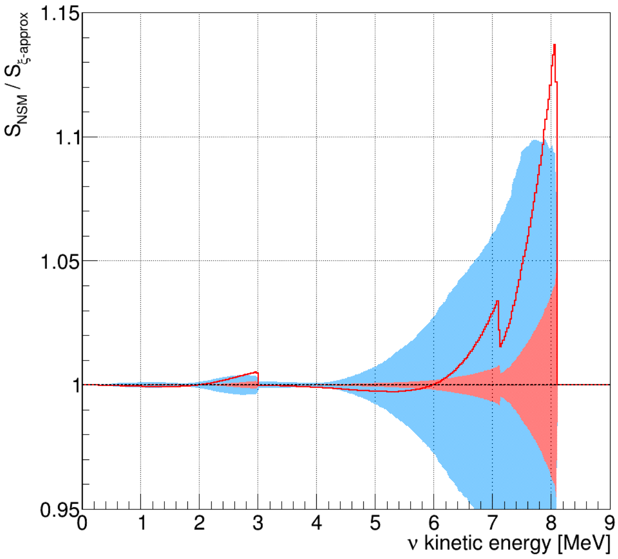

Figure 5.6: Ratio of the ^{235}U antineutrino spectrum computed with and without nuclear shell model calculation for the three main non-unique forbidden transitions issued from ^{92}Rb, ^{96}Y and ^{144}Pr. In the spectrum at the numerator, the three non-unique forbidden transitions are computed with nuclear shell model and the red band represents their associated modeling uncertainty in that case. In the spectrum at the denominator, the three non-unique forbidden transitions are ξ-approximated to allowed transitions the blue band represents their associated modeling uncertainty in that case.

is computed with nuclear shell model calculation, and has a small contribution of about 0.4% to the ^{235}U IBD yield. Moderately small uncertainties have been derived in Sec. 4.2.1.2 for this reliable modeling based on nuclear shell model calculation, which in turn induce relatively small uncertainties on the IBD yields of ^{92}Rb, ^{96}Y and ^{144}Pr respectively of about 0.01%, 0.5% and 3.2%. With the reliable modeling of non-unique forbidden transitions, the ^{92}Rb IBD yield decreases by 0.1%, the ^{96}Y IBD yield increases by 1.8%, and the ^{144}Pr IBD yield increases by 12.6% compared to the case where these three transitions are ξ-approximated to allowed transitions. The impact on the ^{235}U IBD yield is small, with an increase inferior to 0.2%. Nonetheless, the impact on the shape of the ^{235}U $\bar{\nu}_e$ fission spectrum is sizable, as seen in Fig. 5.6 showing the ratio of the ^{235}U $\bar{\nu}_e$ spectrum computed with and without nuclear shell model calculation for these three branches. The ^{235}U spectrum is increased by about 0.5% at 3 MeV due to the change in ^{144}Pr, and the combined changes from ^{92}Rb and ^{96}Y result in a decrease of about 0.3% at 5 MeV and an important increase of 3% at 7 MeV. The red band in Fig. 5.6 represents the small uncertainty associated to the modeling of these three branches with nuclear shell model calculation. The blue band, on the other hand, represents the large uncertainty associated to the ξ-approximation of these three branches. It can be seen that the uncertainty associated to the ξ-approximation covers correctly the $\bar{\nu}_e$ fission spectrum computed with nuclear shell model calculation, thus supporting the assumption that the bias induced by the ξ-approximation is correctly taken into account by this modeling uncertainty. The other important non-unique forbidden transitions typically contribute each less than 2% of the ^{235}U IBD yields, and have relatively large IBD yield uncertainties induced by the modeling uncertainties for non-unique forbidden transitions, typically between 5% and 10% of their respective IBD yield. The uncertainty induced by each of these FP on the ^{235}U IBD yield is less than 0.2%, as shown in Fig. 5.7b, and result in the $\sim$ 0.5% induced IBD uncertainty for ^{235}U.

Bloc structures can be observed in the correlation matrices of the fission spectrum, such as in Fig. 5.7a. The structures appear more clearly for correlation matrices associated to $\bar{\nu}_e$ spectra

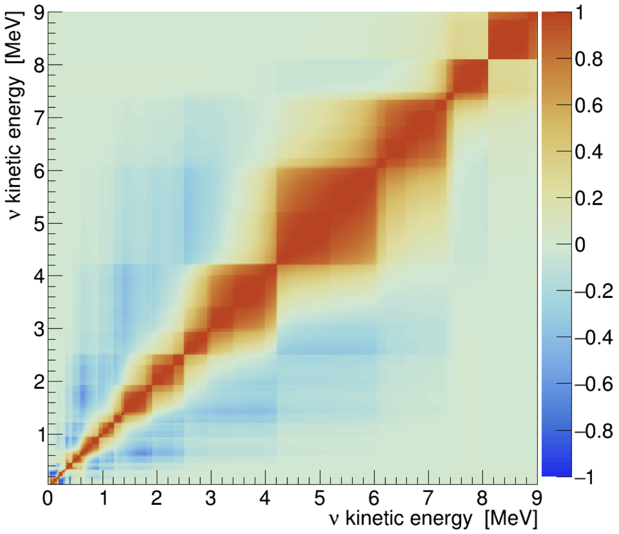

(a) ^{235}U correlations from non-unique modeling.

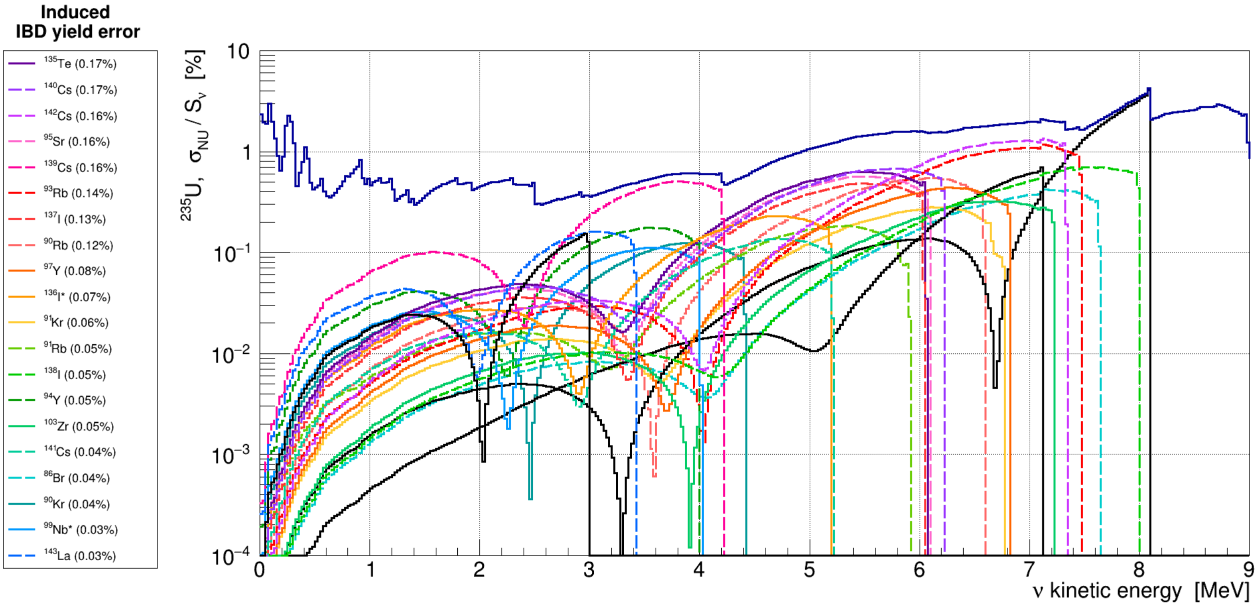

(b) ^{235}U fractional uncertainties due to non-unique transition modeling.

Figure 5.7: **(a)** Correlation matrix and **(b)** fractional uncertainties of the ^{235}U $\bar{\nu}_e$ fission spectrum induced by the uncertainties on the modeling of non-unique forbidden transitions. The 20 main contributors to the ^{235}U IBD yield uncertainty induced by the non-unique modeling uncertainties are highlighted in the list, along with their respective modeling uncertainties with respect to the ^{235}U IBD yield. The fission product spectra are modeled with ENSDF data (solid line) or with TAGS data (dashed line). The main non-unique forbidden transitions of ^{92}Rb, ^{96}Y and ^{144}Pr have been computed with nuclear shell model calculation and their modeling uncertainty are represented by the three black curves. The spectra have been computed with CFY from the JEFF-3.3 database [136].

due to the sharp edges present at the maximum energies of FP $\bar{\nu}_e$ spectra, and result from the fact that the uncertainties of certain FP or group of FP dominate in a restrained energy range. For instance, the structures around 7 MeV and 8 MeV in the correlations induced by the non-unique modeling uncertainties, in Fig. 5.7a, mostly come from ^{142}Cs, ^{93}Rb and ^{92}Rb.

The FP spectra whose uncertainties dominate the IBD yield uncertainty are presented in Fig. 5.8b in the case of ^{235}U. It is noteworthy that the FP dominating the uncertainties are not necessarily the ones that dominate the IBD yield. Several isotopes modeled with Tengblad's data or with the Q_β effective modeling appear in the list of the top contributors to the IBD yield uncertainties of the four actinides. For these isotopes, the dominant uncertainties are induced by the BR and by the endpoint energy for which large uncertainties have been considered in order to accommodate for a potential mismodeling introduced by the use of this very approximate modeling (see Sec. 4.1.2.3 and 4.1.3).

At the level of a reactor $\bar{\nu}_e$ spectrum, the spectrum of a FP contributing to several actinide total fission spectra is fully correlated between the fission spectra and introduces correlations between them. As such, the predicted IBD yields of each fissioning actinide are strongly correlated. It results that the induced uncertainty on the total IBD yields is $\sim 0.6\%$, about the same as for each actinide IBD yield. Oppositely, the absence of correlation between the FY of the different actinides results in a smaller IBD yield uncertainty induced by the FY uncertainties for a PWR spectrum than the IBD yield uncertainty of each actinide. The IBD yield uncertainty induced by the FY uncertainties for a PWR spectrum is $\sim 0.7\%$, and contributes about the same than the IBD yield uncertainty induced by the BR, the I_β and the fission fraction uncertainties. Regarding the fission fractions, each reactor experiment has its own estimation of fission fraction uncertainties and correlations that depend on the reactor parameters and the data taking period. The uncertainties on the ^{235}U and ^{239}Pu fission fractions typically range from 3% to 5%, while the uncertainties on ^{238}U and ^{241}Pu are typically between 5% and 10% [205, 318–320]. For the calculations reported in Tab. 5.1, uncertainties of 5% have been considered for ^{235}U and ^{239}Pu, uncertainties of 10% have been considered for ^{238}U and ^{241}Pu, and the correlations between the fission fractions have been taken from [205] as a first approximation.

5.1.4 Contribution from the different nuclear data sources

The contribution of each data source to the $\bar{\nu}_e$ fluxes and to the IBD and CEνNS yields is shown in Tab.5.2. The data sources are: ENSDF data, TAGS data, Tengblad's data and isotopes with missing nuclear data modeled with the Q_β effective modeling with 3 branches. The contribution to the four actinide $\bar{\nu}_e$ spectra derived from each data source is showed in Fig. 5.9, and the corresponding fractional uncertainties with respect to the fission spectra are displayed in Fig. 5.10.

The two dominant contributions are from ENSDF and TAGS data. Above 1.5 MeV, FP modeled with ENSDF data contribute between 40% and 50% to the fission spectra, and isotopes modeled with TAGS data contribute between 30% and 40%. The contributions are about of the same amplitude, even though the number of FP modeled with TAGS data are five times lower than the number of FP modeled with ENSDF data. This underlines the fact that most of the important FP of a reactor spectrum are modeled with TAGS data, for which a potential bias in the BR of an isotope is less likely. Although, this does not mean that a potential mismodeling of the FP using TAGS data is not possible, because many present non-unique forbidden transitions (*e.g.* ^{140}Cs and ^{142}Cs, see Tab. 3.3). Considering that the candidate isotopes that will be TAGS measured in the future (see Tab. B.1 from App. B) are

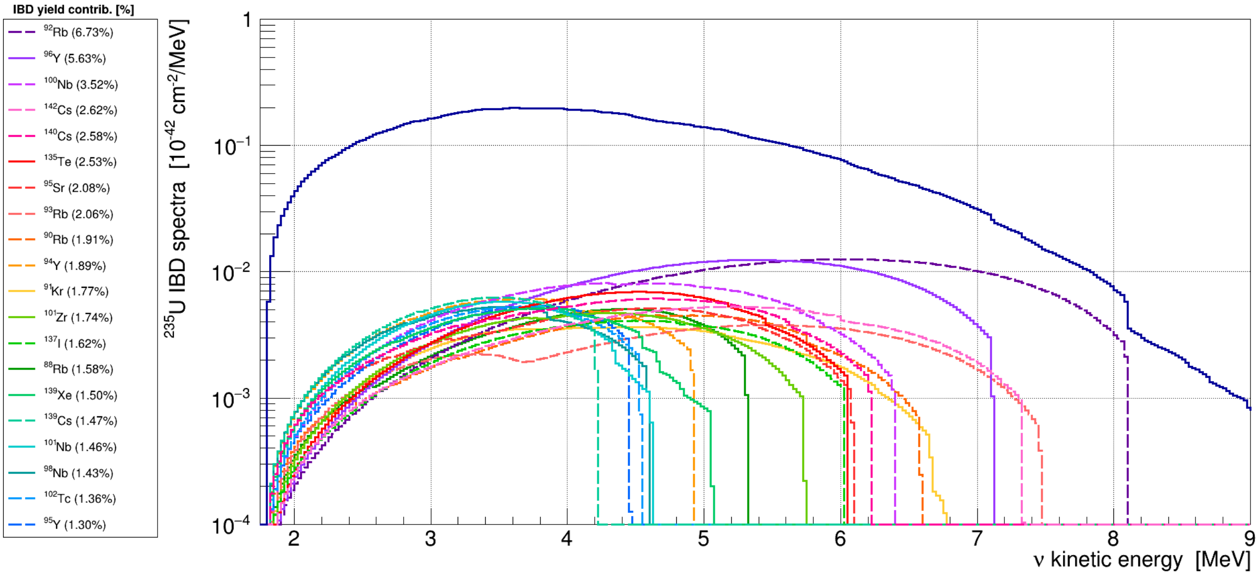

(a) Top 20 contributors to the ^{235}U IBD spectrum.

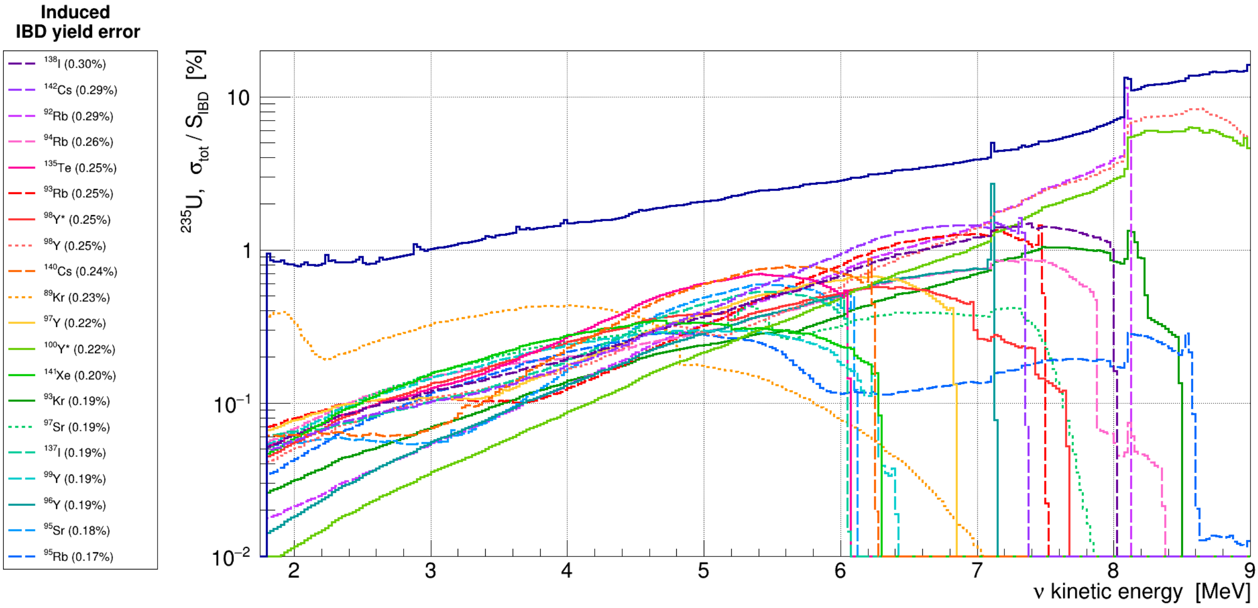

(b) Top 20 contributors to the ^{235}U IBD spectrum uncertainty.

Figure 5.8: (a) Top 20 contributors to the ^{235}U IBD spectrum. **(b)** Total fractional uncertainty of the ^{235}U IBD spectrum. The 20 main contributors to the ^{235}U IBD yield uncertainty are highlighted in the list, along with their respective uncertainty with respect to the ^{235}U IBD yield. The fission product spectra are modeled with ENSDF data (solid line), with TAGS data (dashed line) or with Tengblad's data (dotted line). The main transitions of ^{92}Rb and ^{96}Y have been computed with nuclear shell model calculation. The spectra have been computed with CFY from the JEFF-3.3 database [136].

		FP	Flux [$\bar{\nu}_e$/fis]	$\langle\sigma_{IBD}\rangle$ [10^{-43} cm^2/fis]	$\langle\sigma_{CE\nu NS}\rangle$ [10^{-41} cm^2/fis]
^{235}U	ENSDF	460	3.614 ± 0.012	2.62 ± 0.05	4.79 ± 0.07
	TAGS	71	1.874 ± 0.010	2.91 ± 0.06	5.05 ± 0.07
	Tengblad	43	0.494 ± 0.009	0.72 ± 0.04	1.27 ± 0.06
	Missing isotopes	219	0.095 ± 0.003	0.25 ± 0.02	0.39 ± 0.02
	Potential TAGS	42	1.222 ± 0.009	1.08 ± 0.03	2.19 ± 0.05
	Total	793	6.078 ± 0.019	6.50 ± 0.09	11.50 ± 0.12
^{238}U	ENSDF	431	4.075 ± 0.028	4.47 ± 0.09	7.45 ± 0.12
	TAGS	70	2.022 ± 0.022	3.33 ± 0.07	5.70 ± 0.10
	Tengblad	43	0.751 ± 0.013	1.50 ± 0.07	2.45 ± 0.09
	Missing isotopes	234	0.316 ± 0.010	1.02 ± 0.06	1.51 ± 0.08
	Potential TAGS	42	1.278 ± 0.016	1.34 ± 0.04	2.60 ± 0.06
	Total	778	7.163 ± 0.039	10.32 ± 0.15	17.15 ± 0.20
^{239}Pu	ENSDF	519	3.514 ± 0.014	2.05 ± 0.04	3.95 ± 0.06
	TAGS	71	1.546 ± 0.010	1.97 ± 0.04	3.64 ± 0.06
	Tengblad	43	0.337 ± 0.007	0.40 ± 0.02	0.75 ± 0.03
	Missing isotopes	218	0.107 ± 0.005	0.31 ± 0.03	0.46 ± 0.04
	Potential TAGS	42	1.025 ± 0.010	0.83 ± 0.03	1.76 ± 0.05
	Total	851	5.503 ± 0.019	4.72 ± 0.07	8.80 ± 0.10
^{241}Pu	ENSDF	497	3.961 ± 0.027	3.33 ± 0.07	5.96 ± 0.10
	TAGS	71	1.639 ± 0.012	2.29 ± 0.05	4.13 ± 0.07
	Tengblad	43	0.448 ± 0.009	0.69 ± 0.03	1.20 ± 0.05
	Missing isotopes	249	0.213 ± 0.008	0.62 ± 0.05	0.94 ± 0.06
	Potential TAGS	42	1.175 ± 0.016	1.08 ± 0.04	2.21 ± 0.06
	Total	860	6.261 ± 0.032	6.93 ± 0.10	12.23 ± 0.14

Table 5.2: Breakdown of the data source contribution to each actinide $\bar{\nu}_e$ flux, their corresponding IBD yield $\langle\sigma_{IBD}\rangle$ and their corresponding CEνNS yield $\langle\sigma_{CE\nu NS}\rangle$ computed for a Ge detector with a 20 eV recoil threshold. The propagated uncertainties are those listed in Tab. 5.1. The sum of the contribution calculated with ENSDF data, TAGS data, Tengblad's data and of missing isotopes (*i.e.* isotopes with missing nuclear data) results in the total contribution. The "Potential TAGS" rows refer to the contribution of Pandemonium-candidate isotopes currently modeled with ENSDF data or part of the missing isotopes (see App. B). The number of β emitters modeled from each data source are given in the "FP" columns. The uncertainties include a maximization of the BR uncertainties with respect to either $\langle\sigma_{IBD}\rangle$ or $\langle\sigma_{CE\nu NS}\rangle$ (see Sec. 4.2.2.1).

currently modeled with ENSDF data, a potential Pandemonium effect could be present up to 8.5 MeV and could lead to an overestimation of $\bar{\nu}_e$ fission spectra above the IBD threshold. Let us stress that this potential bias is not taken into account in the current uncertainty budget. This could have an important impact on the predicted IBD and CEνNS yields as these candidate isotopes have significant contributions.

The isotopes modeled with Tengblad's data contribute to about 10% of the spectra and have relatively large uncertainties in regards with their spectral contribution. This reflects the large uncertainties assumed on their BR and on their endpoint energies to take into account a possible bias in their modeling (see Sec. 4.1.2.3). As a result, the aggregate spectra of FP modeled with Tengblad's data present uncertainties induced by BR and endpoint energy uncertainties of the same amplitude or even larger than the uncertainties induced by FY uncertainties. The IBD yield uncertainty induced by FP modeled with Tengblad's data is about 5% of their contribution.

The contribution from nuclei with no evaluated data and modeled with the Q_β effective modeling with 3 branches increases with the energy. At 2 MeV, these missing isotopes contribute between 2% and 5% of the fission spectra, and they contribute between 5% and 11% at 6 MeV. Their contribution increases significantly beyond 6 MeV to reach between 20% and 40% at 8 MeV. This increase reflects the fact that the missing nuclei usually have large Q_β energies and thus are expected to have a more important contribution at high energy. However, it could also reflect that the bias induced by the Q_β effective modeling increases with the energy. It was shown in Sec. 4.1.3 that the Q_β effective modeling with 3 branches was underestimating aggregate spectra by 20% below 6 MeV and could overestimate aggregate spectra by more than 10% above 6 MeV. Thus, the contribution from missing isotopes could be at the origin of a bias on the shape of a fission spectra resulting in a possible overestimation of the fission $\bar{\nu}_e$ spectra above 6 MeV. As a result, the IBD and CEνNS yields could also be overestimated. The uncertainties associated to the missing isotopes are about 8% of their spectral contribution, and similarly for the uncertainty induced on their IBD yield contribution. However, this may not be enough to cover the potential bias induced by the Q_β effective modeling, which could be about 20%. Further improvement of this uncertainty is foreseen.

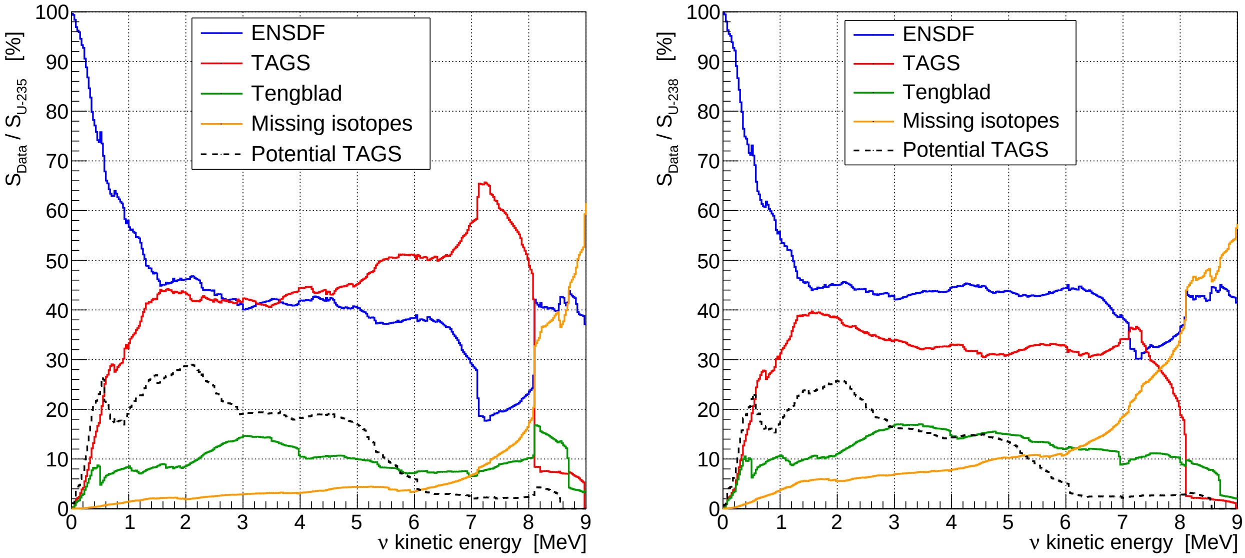

(a) ^{235}U.

(b) ^{238}U.

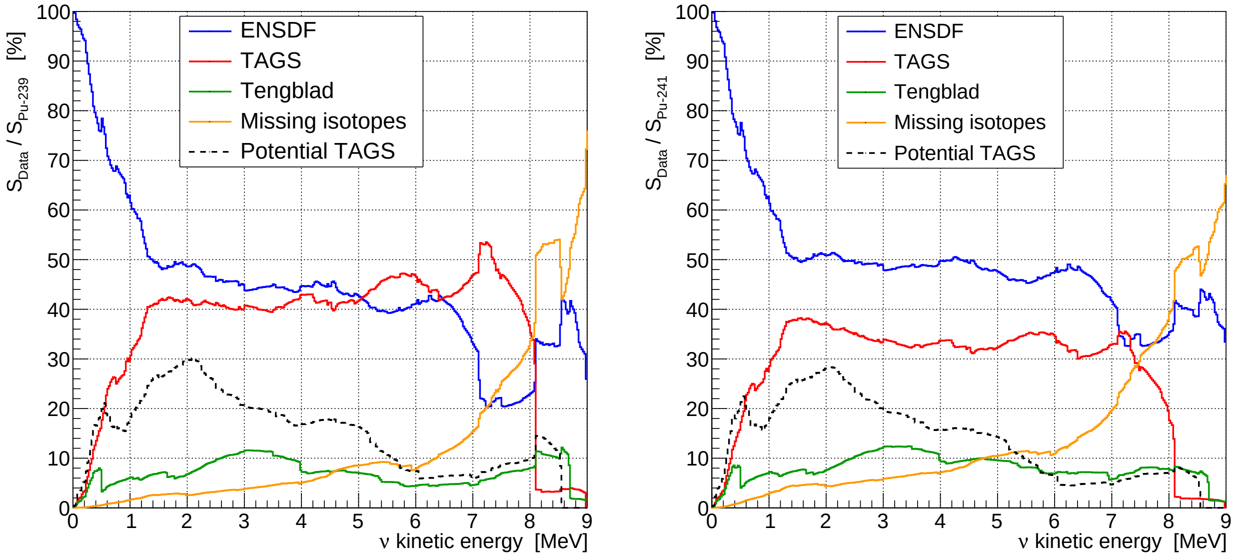

(c) ^{239}Pu.

(d) ^{241}Pu.

Figure 5.9: Contributions to the $\bar{\nu}_e$ fission spectrum of ^{235}U, ^{238}U, ^{239}Pu and ^{241}Pu derived from the ENSDF data, TAGS data, Tengblad's data and from missing isotopes (*i.e.* isotopes with missing nuclear data). The "Potential TAGS" contribution is based on the TAGS candidates listed in App. B. The other contributions in solid lines sum up to 100%. The spectra have been computed with CFY from the JEFF-3.3 database.

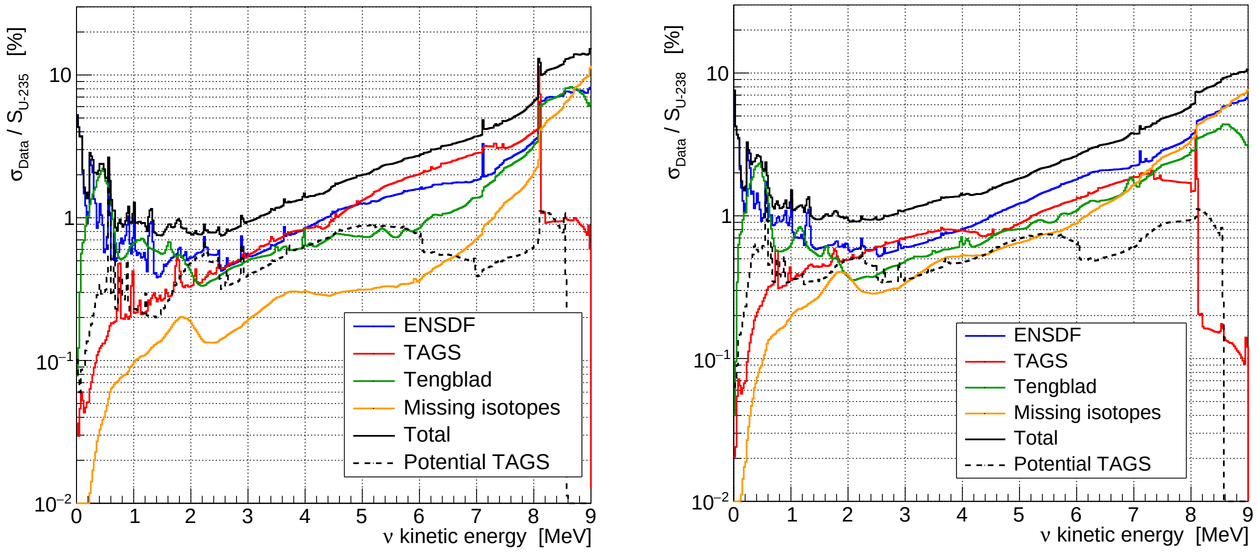

(a) ^{235}U. **(b)** ^{238}U.

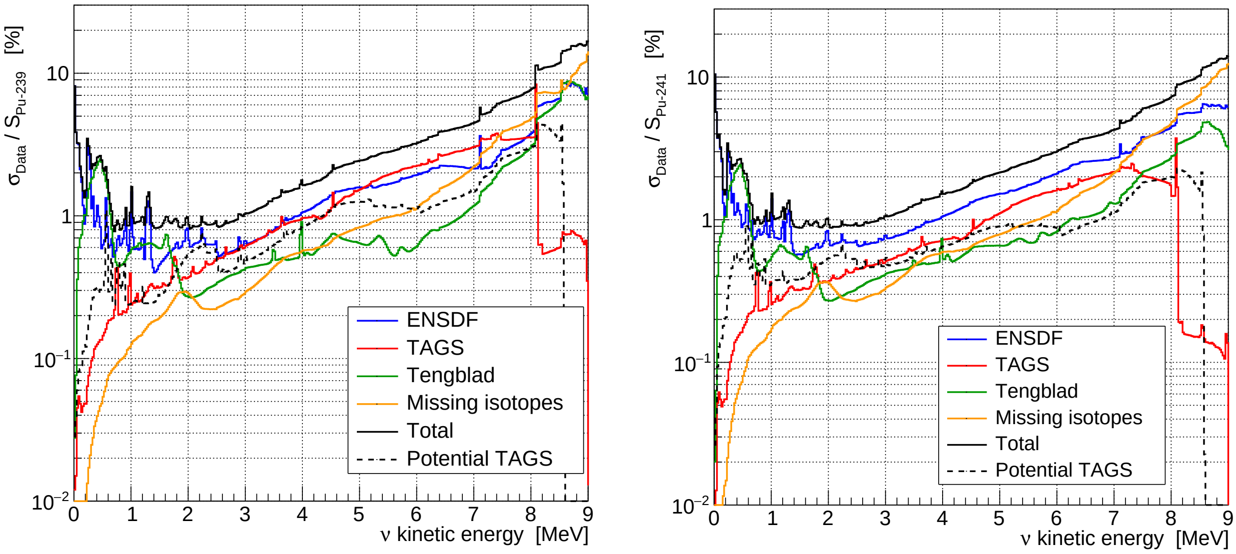

(c) ^{239}Pu. **(d)** ^{241}Pu.

Figure 5.10: Fractional uncertainties associated to the different data sources contributing to the $\bar{\nu}_e$ fission spectra of ^{235}U, ^{238}U, ^{239}Pu and ^{241}Pu. The contributions are derived from the ENSDF data, TAGS data, Tengblad's data and from missing isotopes (*i.e.* isotopes with missing nuclear data). The "Potential TAGS" contribution is based on the TAGS candidates listed in App. B. The fractional uncertainties in solid lines sum quadratically to the total fractional uncertainty (black solid line). The spectra have been computed with CFY from the JEFF-3.3 database.

5.2 Comparison with β spectrum measurements

The aggregate FP β spectra of ^{235}U, ^{239}Pu and ^{241}Pu measured with the BILL spectrometer by Schreckenbach et al. in the 1980s [116–119] are currently used in the conversion models predicting the $\bar{\nu}_e$ fission spectra of these actinides in IBD experiments. The experimental conditions of these measurements — during which target foils were irradiated by a thermal neutron flux produced by the HFR at the ILL — differ from the real irradiation conditions of a research or a commercial reactor core. Their irradiation time was shorter, a couple of days compared to several weeks for research reactors or several months for commercial reactors, which induces off-equilibrium effects in the aggregate β spectra. Even though, these aggregate spectra are expected to be similar to those originating from reactors at an early stage of a reactor cycle.

Measurements conducted at the ILL

During the 1980s campaign, the ^{235}U β spectrum was measured thrice after the start of the target foil irradiation, totaling a measuring time of 15 h of irradiation [118]. With this exposure time to neutrons, the β activities of FP with endpoint energies larger than 3 MeV are expected to reach equilibrium. The ^{235}U spectrum changes by less than 1% above 3 MeV for a increased amount of exposure time, according to the off-equilibrium effects estimated in [13]. Below 5 MeV, only the data recorded during the third run after a 12 h exposure time were used in the provided β spectrum to limit the impact of off-equilibrium effects [118]. Similarly, three runs were conducted to measure the ^{239}Pu β spectrum, performed 6 h, 23 h and 38 h after the start of the irradiation [117]. Between 23 h and 38 h, the spectrum changes by less than 1.2% above 1.5 MeV, and the ^{239}Pu β spectrum is expected to be at equilibrium above 1.5 MeV after 38 h of irradiation. Thus, only the data recorded after 36 h of irradiation were used in the provided ^{239}Pu β spectrum [117]. The ^{241}Pu β spectrum was measured through several runs during a 45-h long irradiation campaign [119]. An equilibrium was reached above 2 MeV after an exposure of 24 h, and only the data obtained after 37 h of exposure were adopted in the provided β spectrum below 3.5 MeV. The ^{238}U spectrum could not be measured at the ILL as it fissions under a fast neutron flux which is not produced at the ILL. For each measurement, uncorrelated statistical uncertainties are provided along with uncertainties on the normalizations of the measurements. These uncertainties are represented in Fig. 5.11 based on the recently republished data [188]. The uncertainties on the spectrum normalizations dominate below $\sim$ 6 MeV, while statistical uncertainties are dominant beyond. Furthermore, the statistical uncertainties exceed 10% above $\sim$ 8 MeV.

Measurement conducted at the FRM II

In the early 2010s, the aggregate β spectrum of ^{238}U was measured by Haag et al. at the FRM II research reactor in Garching [189]. Only the data measured between 11 h and 53 h after the start of irradiation were kept in the provided β spectrum. Two identical target foils of natural uranium were irradiated, one with a thermal neutron beam and the other by a fast neutron beam generated by the FRM II. Both the ^{235}U and ^{238}U β spectra were thus measured at Garching. The ^{235}U measurement was then normalized to the ^{235}U β spectrum measured at the ILL, thus allowing to normalize the ^{238}U β spectrum to the ILL data. Systematic uncertainties connected to the unknown detector efficiency, to the unexpected energy dependence of the detector response function, and to the weakly known neutron-beam profile and intensity were then suppressed in the ^{238}U spectrum analysis [189]. The ^{238}U and ^{235}U spectra are correlated through this normalization, and any bias in the ^{235}U normalization will appear in the ^{238}U spectrum normalization. In addition to the uncertainty induced by the

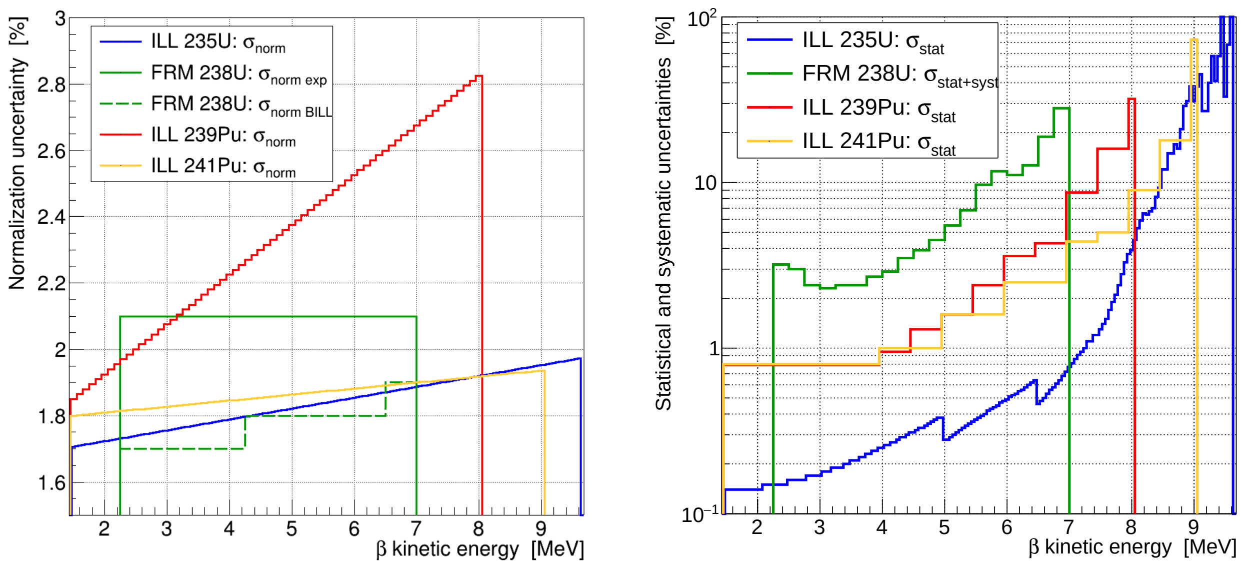

(a) Normalization uncertainties.

(b) Statistical uncertainties.

Figure 5.11: Uncertainties on the β spectra measured at the ILL and at the FRM II. **(a)** Uncertainties on the normalization of the β spectra, inducing a complete correlation of the energy bins of a β spectrum. **(b)** Statistical uncertainties on the β spectra as well as systematic uncertainties in the case of ^{238}U, both being uncorrelated between the energy bins of a β spectrum. The uncertainties are taken from [116–119, 188, 189]

one from the BILL measurement normalization, $\sigma_{\text{norm BILL}}$, there is a second uncertainty on the absolute normalization of the measurement, $\sigma_{\text{norm exp}}$. Finally, the ^{238}U β spectrum presents statistical and systematic uncertainties, the latter originating from the background model and the energy calibration [189]. These uncertainties along with the ones on the normalization are presented in Fig. 5.11. The statistical uncertainties dominate over the whole energy range and reach more than 10% above 6 MeV.

Simulation of fission product inventories

The evolution of the composition of the irradiated target foils is governed by the initial composition of these foils, the list of independent FY that can be obtained from the JEFF-3.3 database [136] as well as by the neutron flux of the HFR. A simulation of the HFR using MCNP [321, 322] was used by the Saclay group to model the HFR neutron flux. This neutron flux was then used as input for the FISPACT-II program [157] to simulate the FP inventories resulting from the irradiation of the HFR fuel under this specific neutron flux. These calculations were provided by the Saclay group and were used in this study [323]. FY have been derived from these calculations for 12 h, 36 h and 48 h of irradiation respectively in the case of ^{235}U, ^{239}Pu and ^{241}Pu. These irradiation times correspond to the published β spectra for ^{235}U and ^{239}Pu. Regarding the ^{241}Pu measurement, the corresponding irradiation time is 43 h, and it was checked that the change in the ^{241}Pu FP inventory between 36 h and 48 h was not significant above 1 MeV ($<0.2\%$). Thus, the FP inventory at 48 h can be used to model the ^{241}Pu aggregate spectrum. Uncertainties were not propagated with FISPACT-II, and the CFY uncertainties from the JEFF-3.3 database have been then considered on the provided FY as a first approximation. This is a relevant approximation for FP with short half-lives that have reached or are close to reach an equilibrium state, and which contribute typically to the spectra above $\sim$ 3 MeV. It has been verified that assuming CFY uncertainties for FP that were not expected to be in an equilibrium state had a small impact on the total uncertainties of the fission spectra. The irradiation conditions and the geometry of the FRM II measurement have not been simulated. In [189], the ^{238}U off-equilibrium effects above 3 MeV were considered to be of the same order of magnitude than those of ^{235}U, ^{239}Pu and ^{241}Pu, and thus could be neglected. Therefore, the ^{238}U spectrum computed at equilibrium can be compared with the measurement above 3 MeV as the ^{238}U spectrum should not evolve by more than 1% at 3 MeV and even less at higher energies. The ^{238}U β spectrum can then be modeled above 3 MeV by using the fast CFY from the JEFF-3.3 database.

β spectrum comparison

The measured β spectra and the corresponding B-21 predictions are presented in Fig. 5.13 along with their ratios. A χ^2 test, presented in App. D, is used to determine if there is a statistically significant difference between the measured β spectra and the predictions as well as to evaluate the local agreement. Local p-values quantifying the significance of deviations are computed by considering free parameters on the energy bins located in a 1 MeV window. These free parameters allow the data points to float toward the model and to minimize the χ^2 value. The impact of the energy window on the overall agreement is thus estimated. Let us point out that a small local p-value does not indicate that the tension over the energy bins in the window is small, but rather that the overall tension is not significantly decreased when the energy bins in the window are let free. The modeled and measured β spectra are only compared up to 8 MeV, beyond which the large statistical uncertainties and the small fluxes result in a poor contribution of these energy bins to the χ^2 value. In the case of ^{238}U, only the measured data above 3 MeV are compared to our prediction in order to not introduce a tension due to off-equilibrium effects.

The comparison of the ILL ^{235}U β spectrum with the corresponding B-21 prediction leads to an overall agreement of $\chi^2/\text{NDF} = 398.1/131$, which indicates a significant tension. This tension is mostly driven by the discrepancies of up to $\sim$ 10% below 3.5 MeV, where the local deviations are particularly significant as shown by the p-value in Fig. 5.13a, and where the majority of the flux is emitted. The discrepancies above 5 MeV are not significant due to the large uncertainties dominated by the prediction uncertainties and by the experimental normalization uncertainties.

The comparison of the FRM II ^{238}U β spectrum with the corresponding B-21 prediction leads to an overall agreement of $\chi^2/\text{NDF} = 25.6/16$, which indicates a relatively small tension. The tension is driven by the differences around 3.5 MeV and around 5 MeV. The tension remains small despite large discrepancies of more than 10% above 5 MeV that are not significant due to the large experimental statistical uncertainties above 5 MeV.

The comparison of the ILL ^{239}Pu β spectrum with the corresponding B-21 prediction leads to an overall agreement of $\chi^2/\text{NDF} = 149.3/66$, which indicates a significant tension. The large tension is driven by the discrepancies below 3.5 MeV, and particularly around 2 MeV where the local deviations are significant. The large discrepancies superior to 20% above 6 MeV are not significant due to the large statistical uncertainties and prediction uncertainties.

The comparison of the ILL ^{241}Pu β spectrum with the corresponding B-21 prediction leads to an overall agreement of $\chi^2/\text{NDF} = 118.0/66$, which indicates a significant tension. The tension is led by the discrepancies below 3.5 MeV, and particularly around 2 MeV where the differences are significant due to the strong correlations between the energy bins induced by the experimental normalization uncertainty in this energy region. Nonetheless, the tension is also important above 5 MeV with a value of $\chi^2/\text{NDF} = 61.4/31$, although the large discrepancies in this region have a lower contribution to the tension as it concerns a small portion of the flux where large statistical uncertainties and prediction uncertainties dominate.

The four ratios of prediction over measurement exhibit a general increase when the energy increases. Fig. 5.12 shows the contributions of different types of transition to the four β spectrum modelings, where the transitions assumed to be correctly modeled are separated from the transitions whose modeling is based on approximations. The transitions assumed to be correctly modeled are the allowed and unique forbidden transitions with spin-parity data provided in ENSDF, the three non-unique forbidden transitions from ^{92}Rb, ^{96}Y and ^{144}Pr modeled with nuclear shell model (see Sec. 3.5.1), as well as the isotopes modeled with Tengblad's data. The remaining transitions are those with missing spin-parity data modeled as allowed by default, the non-unique forbidden transitions modeled with the ξ-approximation and the missing isotopes modeled with the Q_β effective modeling. It can be seen that the contribution from missing isotopes is particularly important for the ^{238}U, ^{239}Pu and ^{241}Pu β spectra, about 15% at 6 MeV and about 25% at 7 MeV. For each actinide, the increase above 5 MeV (or above 6 MeV in the case of ^{235}U) is very sensitive to the choice of the effective modeling used for the isotopes with missing nuclear data. The spectral changes induced by the choice of the effective modeling are negligible below 4 MeV. Modeling these missing isotopes with different effective modelings can reduce their contribution above 5 MeV and can have an important impact on the shapes of the B-21 spectra above 6 MeV, thus indicating a possible bias in the modeling of these isotopes. However, for each actinide, the tension originates mainly from the energy region below 5 MeV where the majority of the flux is emitted. As a result, the spectral changes above 5 MeV induced by the choice of the effective modeling have a small impact on the tensions. Nonetheless, the uncertainties associated to the Q_β effective modeling are potentially underestimated over the full energy range, which could then have a more important impact on the tensions.

Another important contribution to the β spectra comes from the modeling of non-unique forbidden transitions with the ξ-approximation which can induce a possible bias on the spectrum shapes. The uncertainty derived for the modeling of non-unique forbidden transitions with the ξ-approximation is expected to cover the possible bias at the level of individual transitions. If these modeling uncertainties are not taken into account, the χ^2/NDF values increase significantly for the four actinides. Nonetheless, considering the difficulty to define a modeling uncertainty associated to a potential mismodeling of the non-unique forbidden transitions, it is possible that the modeling uncertainty considered in our model is not enough to fully encompass this potential unknown bias, thus leading to some tension. Further investigation should be conducted to assess the impact of the non-unique forbidden transitions on the tensions.

The presence of isotopes with nuclear data still impacted by the Pandemonium effect could also contribute to the increases in the ratios of β spectra. The correction of the Pandemonium effect in nuclear data has been shown to systematically reduce the high energy part of the spectra and to increase the spectra in the lower energy region [176, 178, 179]. A possible bias originating from these data still uncorrected from the Pandemonium effect (see Tab. B.1) is not yet taken into account in B-21, and could thus contribute to the observed discrepancies.

The FY distribution has an important impact on the shape and on the normalization of the fission spectra. A possible bias in the used FY distribution has not been evaluated and could contribute to the observed differences and to the tensions. Furthermore, the assumption of uncorrelated FY is expected to underestimate the induced uncertainty on fission spectra, which would also impact the tensions.

The tensions could also be impacted by a possible bias in the normalization of the ILL spectra. A first study has concluded that the normalization of the ^{235}U β spectrum measurement performed at the ILL was overestimated by 5% [191, 192]. Another study is currently ongoing to investigate the impact of a possible bias in the different parameters used at the ILL to perform the relative normalization of the β spectrum measurements [193].

Finally, it is worth to stress that the discrepancies and the tensions with the ILL β spectra are not expected to be completely reduced once the different aforementioned biases will be accounted for in the B-21 predictions. The reactor antineutrino anomaly (RAA) and the anomaly on the shape of the $\bar{\nu}_e$ spectra observed in IBD experiments indicate that the $\bar{\nu}_e$ spectra predicted with the conversion method are biased both in normalization and in shape. In turn, it indicates that the ILL β spectra, from which the converted $\bar{\nu}_e$ spectra are based on, are potentially biased in normalization and in shape. The biases are expected to be similar at first order in both the measured ILL β spectra and the converted $\bar{\nu}_e$ spectra. As such, tensions are expected to remain in the finalized B-21 prediction when compared to the ILL spectra, which is required to observe better agreements with IBD experiment data.

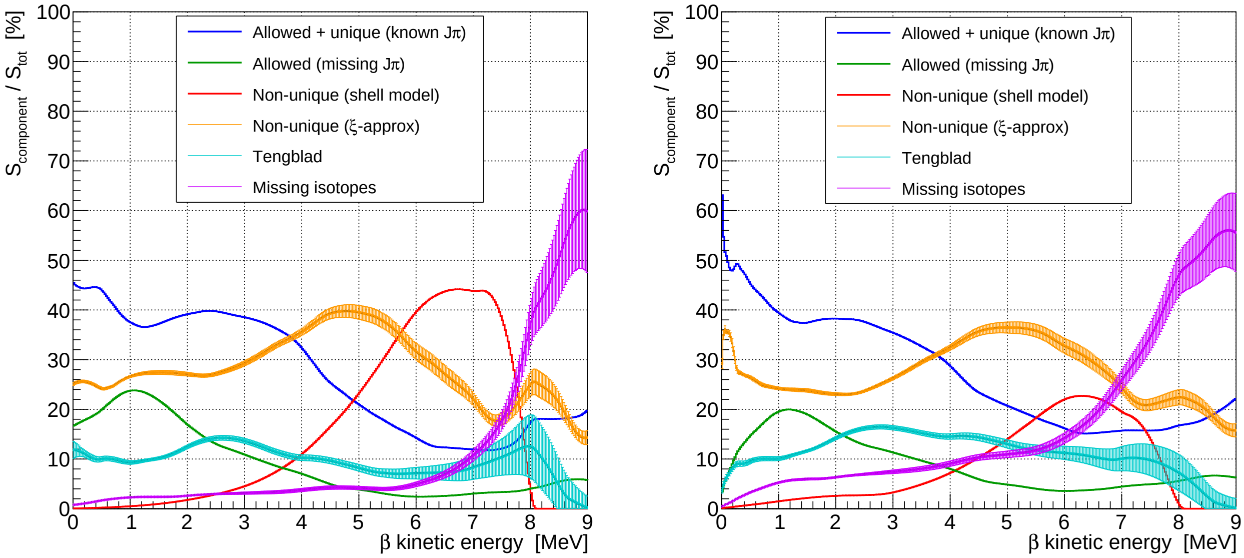

(a) ^{235}U branch contribution.

(b) ^{238}U branch contribution.

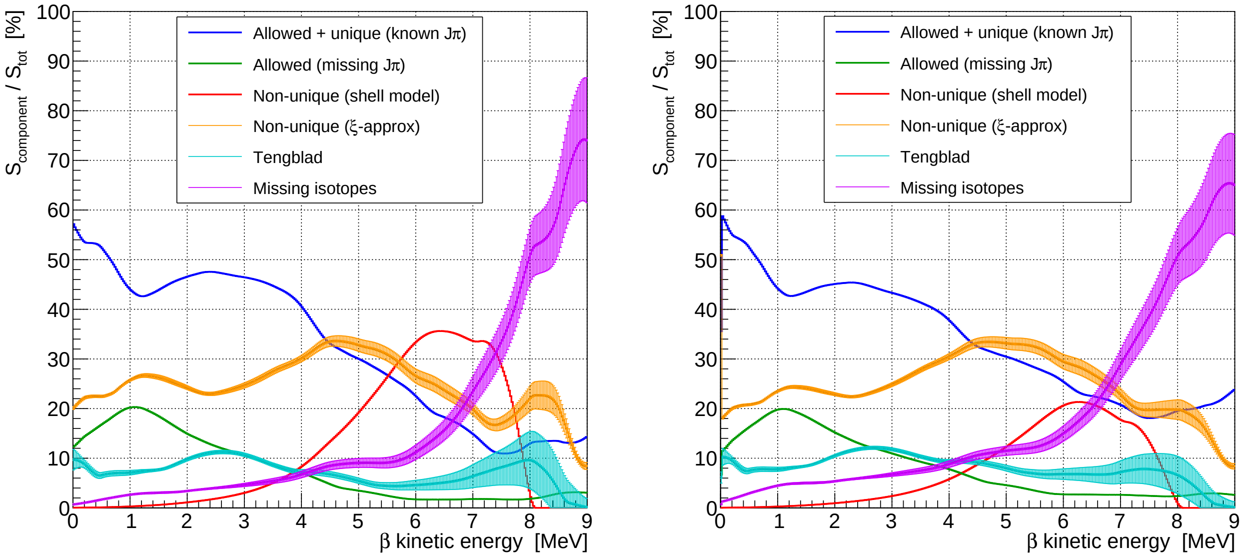

(c) ^{239}Pu branch contribution.

(d) ^{241}Pu branch contribution.

Figure 5.12: Contributions from different type of transitions to the β fission spectra of ^{235}U, ^{238}U, ^{239}Pu and ^{241}Pu. The contributions sum up to 100%. The ^{235}U, ^{239}Pu and ^{241}Pu spectra have been computed at respectively 12 h, 36 h and 48 h of irradiation, while the ^{238}U spectrum has been computed with CFY from JEFF-3.3. Transitions are sorted into the components based on the completeness of their spin-parity data and on the accuracy of the B-21 modeling. The transitions without spin-parity data are always modeled as allowed transitions in B-21. The non-unique forbidden transition computed with nuclear shell model calculation are separated from the non-unique forbidden transitions modeled with the ξ-approximation. The modeling uncertainty derived for the ξ-approximated non-unique forbidden transitions are represented on the corresponding contribution. The uncertainty associated to the Q_β effective modeling of missing isotopes are represented on the corresponding contribution, and likewise for the uncertainty on the isotopes modeled with Tengblad's data. The uncertainties induced by the FY are not represented by these three uncertainties.

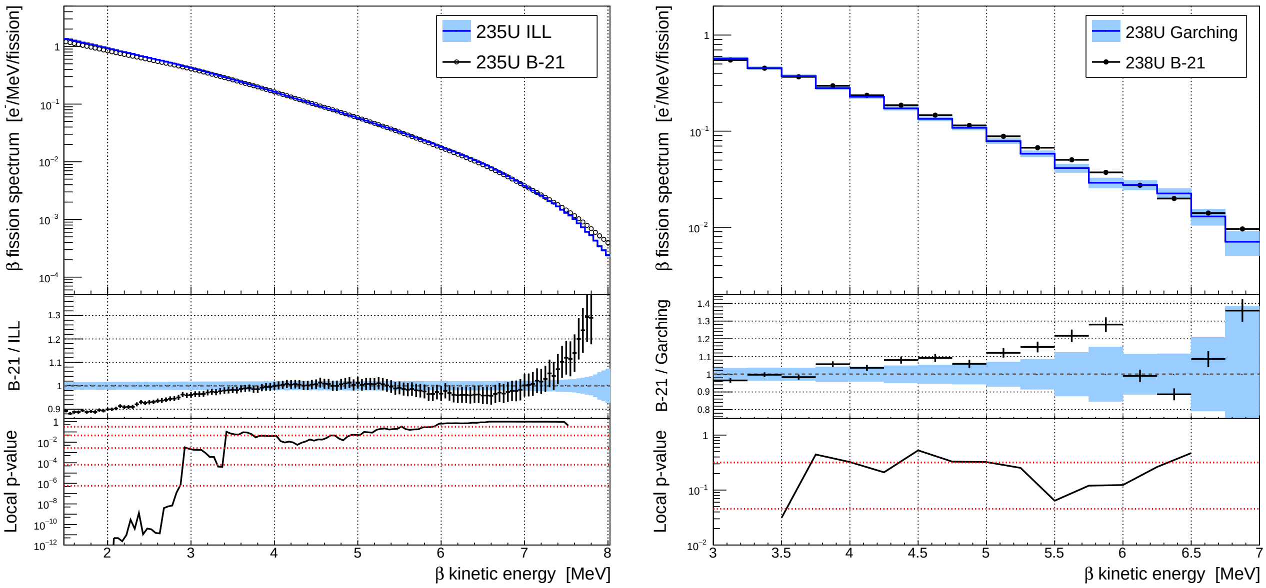

(a) ^{235}U. **(b)** ^{238}U.

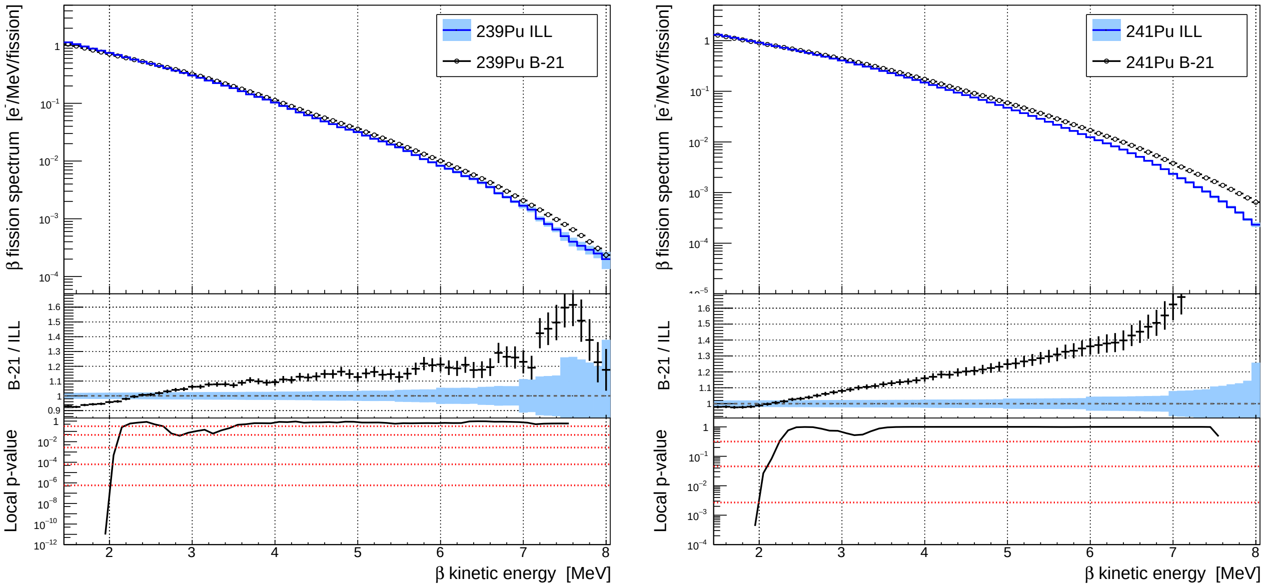

(c) ^{239}Pu. **(d)** ^{241}Pu.

Figure 5.13: (Top) Aggregate beta spectra of ^{235}U **(a)**, ^{238}U **(b)**, ^{239}Pu **(c)** and ^{241}Pu **(d)** computed with the B-21 modeling along with the experimental data collected at ILL and at the FRM II [188, 189]. **(Middle)** Ratios of the predictions over the experimental spectra. The blue bands centered at one represent the experimental uncertainties, while the uncertainties from the B-21 spectra are represented on the ratios. **(Bottom)** Local p-value quantifying the significance of the deviations between the experimental data and the B-21 prediction for a 1 MeV sliding window. The local p-values are represented at the center of each window. The red dotted lines represent the p-values associated to different levels of deviations, starting with the 1σ level with the top line, 2σ level with the second top line, etc.

5.3 Comparison with reactor antineutrino spectrum predictions

Comparison with conversion spectra

Based on the β spectrum measurements performed at the ILL in the 1980s, $\bar{\nu}_e$ spectra were predicted in 2011 by Huber using a revisited conversion method [14]. The predicted $\bar{\nu}_e$ spectra were corresponding to the short irradiation time of the ILL measurements. The measured β spectra were fitted using a set of virtual branches distributed with equidistant endpoint energies E_{0i}, starting with the highest endpoint energies. The ^{235}U β spectrum was fitted with 30 virtual branches, the ^{239}Pu spectrum with 23 branches and the ^{239}Pu spectrum with 25 branches. Each virtual branch β spectrum was then converted into the corresponding $\bar{\nu}_e$ spectrum based on energy conservation, $E_{0i} = E_\beta + E_{\bar{\nu}_e}$.

In the Huber conversion approach, a virtual branch is modeled with the $V - A$ theory of β-decay using several corrections. The corrections applied to the modeling from [14] are the same as those detailed in the "F-12" column of Tab. 3.5. The most important uncertainty in the model was assumed to be on the WM correction, with a 100% uncertainty applied at the level of each virtual branch. The resulting uncertainty on a $\bar{\nu}_e$ spectrum is fully correlated between the energy bins. Because a virtual branch is associated to a virtual FP, it must be based on an effective nuclear charge $\bar{Z}(E_{0i})$. The empirical mean proton number of the FP as a function of the endpoint energy is obtained by fitting the content of nuclear databases. The effective nuclear charge is impacted by the incompleteness of nuclear databases, which induces an uncertainty on the converted $\bar{\nu}_e$ spectra. The induced systematic uncertainty is correlated between the energy bins of a spectrum and between the ^{235}U, ^{239}Pu and ^{241}Pu spectra. The converted $\bar{\nu}_e$ spectra depends on the starting endpoint energy and on the number of energy bins fitted by a virtual branch during the conversion procedure. A small bias is thus induced on the $\bar{\nu}_e$ spectra by the procedure and a corresponding uncertainty has been quantified in [14]. The uncertainty on the bias of the procedure is uncorrelated between the energy bins of a spectrum. The statistical uncertainties of the β spectra is also propagated through the conversion procedure, and similarly for the BILL normalization uncertainties. Similarly to the β spectra, the statistical uncertainty is uncorrelated between the energy bins of a spectrum while the normalization uncertainty fully correlates the energy bins of a spectrum. All these uncertainties are represented in Fig. 5.14 for the converted $\bar{\nu}_e$ spectra of ^{235}U, ^{239}Pu and ^{241}Pu. For ^{235}U, the uncertainties are dominated by the normalization uncertainty of about 2% below 5.5 MeV and by the uncertainties of a few percents induced by the WM correction beyond. The statistical uncertainty and the uncertainty induced by the parametrization of the effective nuclear charge become significant in the last bins, above 7 MeV. For ^{239}Pu and ^{241}Pu, the normalization and the statistical uncertainties are about 2% each and dominate below 4 MeV, while the statistical uncertainty dominates above 4 MeV.

As for the direct comparison with the aggregate β spectra measured at the ILL and at the FRM II, the modeling of the $\bar{\nu}_e$ spectra with B-21 has been performed using FY provided by the Saclay group [323] using FISPACT-II [157] for irradiation times of 12 h, 36 h and 48 h respectively for ^{235}U, ^{239}Pu and ^{241}Pu. The $\bar{\nu}_e$ spectra modeled with B-21 and the converted $\bar{\nu}_e$ spectra from Huber are presented in Fig. 5.15 along with their ratio.

The overall agreement for ^{235}U is of $\chi^2/\mathrm{NDF} = 98.6/25$, which indicates a significant tension. The large tension is driven by the discrepancies of up to 15% below 3.5 MeV where the majority of the flux is emitted, and where the local deviations around 2.5 MeV are particularly

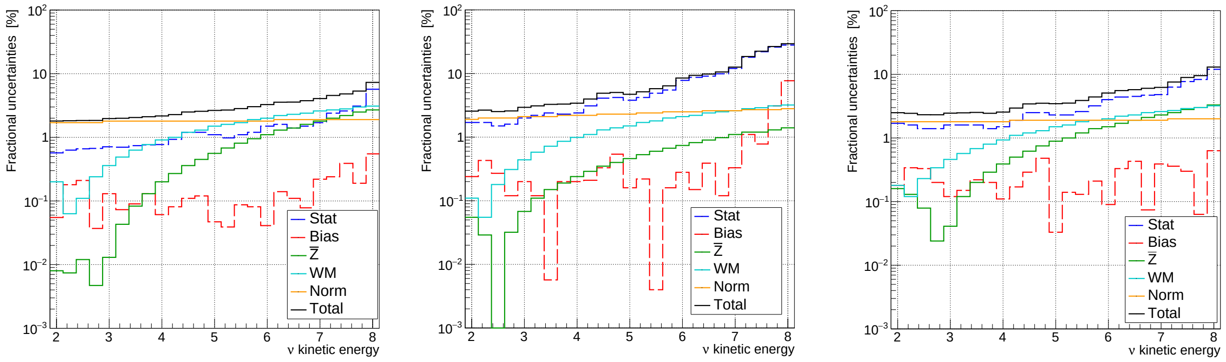

(a) ^{235}U uncertainties. **(b)** ^{239}Pu uncertainties. **(c)** ^{241}Pu uncertainties.

Figure 5.14: Uncertainties associated to the $\bar{\nu}_e$ spectra obtained with the conversion method from Huber [14]. The uncertainties sum quadratically to the total fractional uncertainties (solid black line). Beside the total uncertainty, the uncertainties in solid lines fully correlates the energy bins of a $\bar{\nu}_e$ spectrum, while the uncertainties in dashed lines are uncorrelated among the energy bins of a $\bar{\nu}_e$ spectrum.

significant. The discrepancies above 3.5 MeV are not significant due to the large uncertainties on the converted spectrum coming from the normalization of the measured spectrum and from the WM correction.

The overall agreement for ^{239}Pu is of $\chi^2/\mathrm{NDF} = 61.2/25$, which indicates a significant tension. The large tension is driven by the discrepancies of about 5% below 4 MeV which are significant, where the majority of the flux is emitted, and where the local deviations around 2.5 MeV are particularly significant. The large discrepancies superior to 10% above 5 MeV are not significant due to the large statistical uncertainties on the converted spectrum.

The overall agreement for ^{241}Pu is of $\chi^2/\mathrm{NDF} = 62.8/25$, which indicates a significant tension. The tension is led by the discrepancies below 4.5 MeV, and particularly around 2.5 MeV where the differences are significant. Nonetheless, the tension is also important above 4.5 MeV with a value of $\chi^2/\mathrm{NDF} = 37.4/15$, although the large discrepancies in this region have a lower contribution to the tension as it concerns a small portion of the flux where large statistical uncertainties and prediction uncertainties dominate.

The ratios of the predicted B-21 $\bar{\nu}_e$ fission spectra over the converted $\bar{\nu}_e$ spectra from Huber are close to the ratios of the β spectra discussed in Sec. 5.2, although with local differences. This is expected, as the Huber $\bar{\nu}_e$ spectra are converted from the ILL β spectra. The B-21 ^{235}U $\bar{\nu}_e$ spectrum is generally lower than the Huber prediction. Oppositely, the B-21 ^{239}Pu and ^{241}Pu spectra are generally higher than the Huber predictions. As such, the ^{235}U contributions to the RAA would be decreased with the B-21 prediction, while the ^{239}Pu and ^{241}Pu contributions would be increased. These opposite effects will be discussed in Sec. 5.4.1. The distortion of the B-21 $\bar{\nu}_e$ spectra compared to the Huber spectra could also impact the shape anomaly when compared to measured IBD spectra, which will be discussed in Sec. 5.4.2.

The contribution from different transition types in a $\bar{\nu}_e$ fission spectrum is very similar to those shown in Fig. 5.12 for a β spectrum, only with a slight shift of about 0.5 MeV toward higher energy. As such, the possible biases discussed in Sec. 5.2 in the context of the ILL β spectra could impact the shapes of the B-21 $\bar{\nu}_e$ spectra in a similar manner. Potential biases could then come from isotopes not corrected from the Pandemonium effect, from isotopes with missing nuclear data and modeled with the Q_β effective modeling, from non-unique forbidden transitions, from the FY distribution and from the normalization of the ILL β spectra. The uncertainty budget must be completed in order to fully take into account these potential biases.

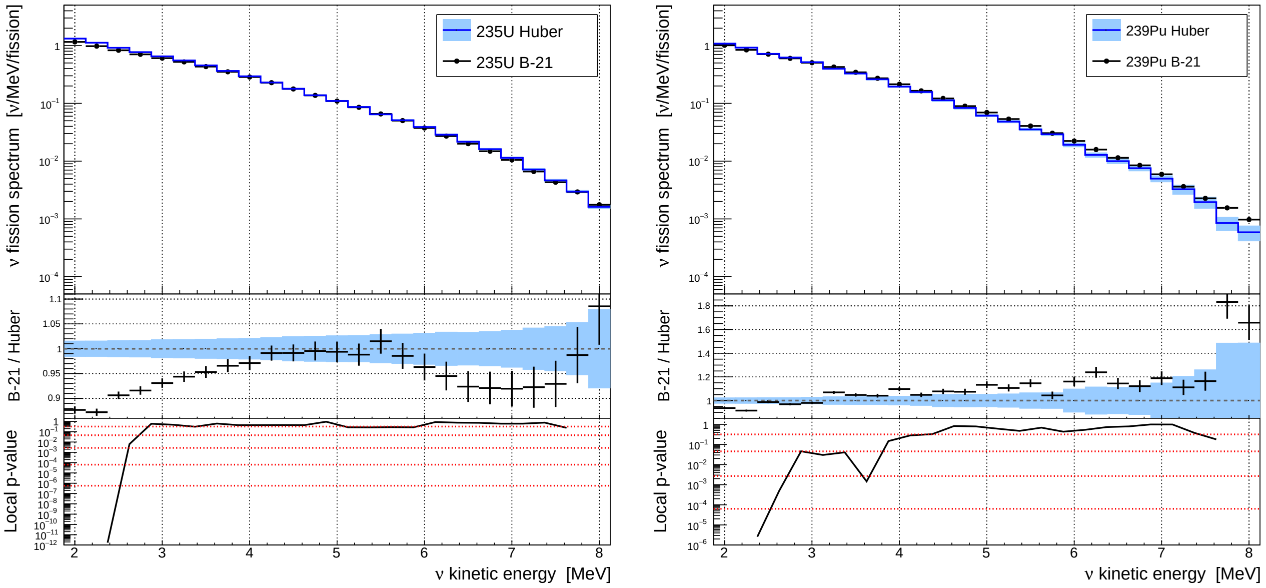

(a) ^{235}U spectra. **(b)** ^{239}Pu spectra.

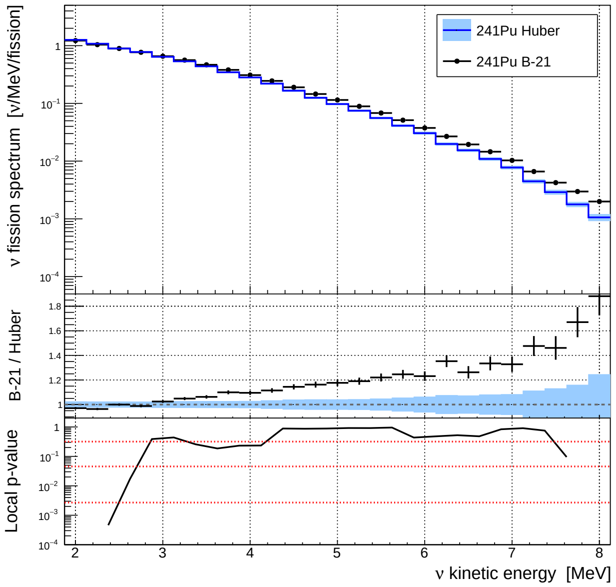

(c) ^{241}Pu spectra.

Figure 5.15: (Top) Spectra of ^{235}U **(a)**, ^{239}Pu **(b)** and ^{241}Pu **(c)** computed with the B-21 modeling along with the converted spectra from Huber [14]. **(Middle)** Ratios of the B-21 prediction over the Huber converted spectra. The blue bands centered at one represent the uncertainties from the converted spectra, while the uncertainties from the B-21 spectra are represented on the ratios. **(Bottom)** Local p-value quantifying the significance of the deviations between the Huber spectra and the B-21 prediction for a 1 MeV sliding window. The red dotted lines represent the p-values associated to different levels of deviations, starting with the 1σ level with the top line, 2σ level with the second top line, etc.

Comparison with summation spectra

The β and $\bar{\nu}_e$ fission spectra of ^{238}U were modeled with the summation method in 2011 [13]. The predictions were based on a previous version of BESTIOLE, labeled B-11, which has been detailed in Ch. 3 and Ch. 4. The B-11 predictions used nuclear data from the ENSDF database from 2011, Tengblad's data, TAGS data from Greenwood's campaign, and isotopes with missing nuclear data were modeled based on the evaluated data from the JENDL database and with an effective modeling. The corrections used in B-11 are detailed in Tab. 3.5. The different sources of uncertainty were sorted into four categories. The first one gathered the uncertainty on the evaluated nuclear data, *i.e.* the uncertainties on the BR and on the endpoint energies from the ENSDF database from 2011, and the uncertainties on the FY from the JEFF-3.1.1 database. In the B-11 uncertainty propagation, the BR were not normalized to the β^- intensity and would introduce strong positive correlations between the energy bin of a FP spectrum. The uncertainties induced by the FP uncertainties also fully correlate the energy bins of a FP spectrum. These two normalization uncertainties would dominate the nuclear data uncertainties, inducing large correlations between proximate energy bins of the ^{238}U spectra. Let us point out that the treatment of the FY uncertainty and of the endpoint energy uncertainty is very close in B-21 and in B-11. The difference in the uncertainty on the evaluated nuclear data, smaller in B-21, mainly originates from the different treatment of the BR uncertainty. The second category provided an estimation of the uncertainty associated to the treatment of forbidden unique transition compared to the case where all the transitions would be modeled as allowed ones. The third category evaluated the uncertainty on the spectrum shape induced by the WM and by the correction due to the finite size of the nucleus by comparing the fission spectrum with and without these corrections. In B-21, the correction to a transition spectrum induced by the finite size of the nucleus is computed numerically and no uncertainty is assumed on this correction (see Sec. 3.4.3 and 3.5). The uncertainty on the WM correction is evaluated with the method described in Sec. 4.2.1, and result in an uncertainty on the fission spectrum that is one order of magnitude lower than the uncertainty assumed on the Mueller ^{235}U spectrum. Finally, the fourth category was providing a rough estimate of the uncertainties induced by the missing nuclear data and by the Pandemonium effect. This last uncertainty would dominate the uncertainty budget, ranging from 10% at 2 MeV up to 20% at 8 MeV. All these uncertainties are represented in Fig. 5.16.

The ^{238}U β and $\bar{\nu}_e$ spectra have been modeled with B-21 and with CFY from the JEFF-3.3 database [136]. The ^{238}U β and $\bar{\nu}_e$ spectra from [13] were computed with FP activities evaluated with the MURE code [324] at 450 days of irradiation. It is noteworthy that no correlation were provided for the uncertainties of the Mueller spectra presented in Fig. 5.16, and that the same uncertainties are provided for both the ^{238}U β and $\bar{\nu}_e$ spectra. The uncertainties coming from the nuclear data category can be assumed to be fully correlated as a first approximation. The BR used in the Mueller spectra are correlated with those used in B-21 for the isotopes that have not been updated in ENSDF since then. However, the propagation of the BR uncertainty is different in the two modelings, and the correlations induced by the BR uncertainties between the energy bins of the fission spectra differ significantly in the two treatments. As a first approximation, the BR uncertainties are assumed to be uncorrelated between the Mueller spectra and the B-21 spectra. The endpoint energies and the FY come from different sources in the Mueller spectra and in the B-21 spectra and are thus uncorrelated. The second and third categories of uncertainty source only impact the spectrum shape of an isotope transition. As such, they should not result in a normalization uncertainty. In absence of provided correlations, these uncertainties are assumed to be uncorrelated between the energy bins of the Mueller spectra as a first approximation. Finally, the uncertainty on the missing information dominates the uncertainty budget, and as such the assumption on the induced correlations have a very

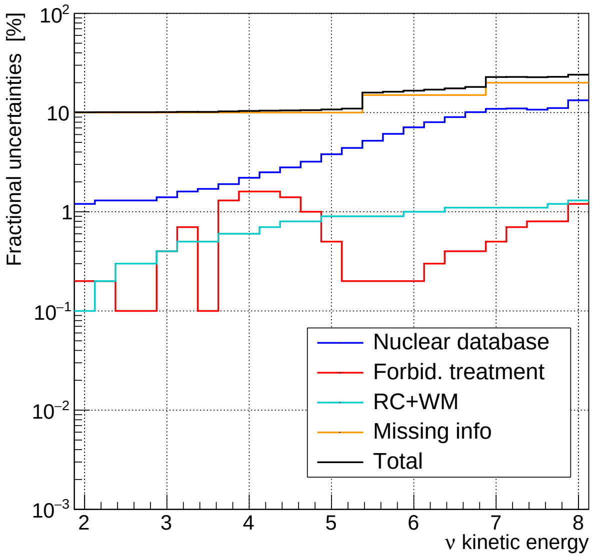

Figure 5.16: Uncertainties associated to the ^{238}U β and $\bar{\nu}_e$ spectra obtained with the summation method from Mueller [13]. The uncertainties sum quadratically to the total fractional uncertainties (solid black line).

important impact when comparing the Mueller spectra and the B-21 spectra. Two cases are considered for the uncertainty induced by the missing information: either the uncertainty does not induce any correlation between the energy bins of the Mueller spectra, or the uncertainty fully correlates the energy bins. The B-21 spectra and the Mueller spectra are presented along with their ratio in Fig. 5.18.

If the uncertainty induced by the missing information is assumed to be uncorrelated between the energy bins of the Mueller spectra, each energy bin can vary by more than 10% independently from the other bins. This variation is far larger than the observed differences between the B-21 and the Mueller spectra, and results in a very good agreement for both the β and $\bar{\nu}_e$ spectra predicted with B-21 compared to those of Mueller. If the uncertainty induced by the missing information is assumed to fully correlate the energy bins of the Mueller spectra, the energy bins are almost completely correlated and must then vary in the same direction. As a result, the differences between the B-21 and the Mueller predictions are much more significant and induce some tensions.

The differences between the Mueller spectra, computed with the 2011 version of BESTIOLE, and the B-21 spectra are mainly explained by the update of the nuclear data. Indeed, the improvements introduced at the level of individual transition spectra have a small impact on a reactor spectrum as mentioned in Sec. 5.1.2. The update of the evaluated nuclear data from ENSDF between 2011 and 2020 results in a decrease of the spectra below approximately 4 MeV and in an increase beyond. This is shown by the red curves in Fig. 5.17, which represent the ratio of ^{238}U spectra computed with B-21 and using nuclear data from the ENSDF 2011 database (for the spectra at the denominator) or from the ENSDF 2020 database (for the spectra at the numerator). The spectra also contain Greenwood's TAGS data, Tengblad's data and isotopes with missing nuclear data modeled with the Q_β effective modeling with 3 branches. The addition of TAGS data for 34 isotopes measured during the last decade results in a general decrease of the β and $\bar{\nu}_e$ fission spectra above 2 MeV. This is shown by the blue curves in Fig. 5.17, which represent the ratio of ^{238}U spectra where the spectra at the denominator are the same as for the red curves, and the spectra at the numerator include recent TAGS data in addition to the updated nuclear data from ENSDF 2020. The use of nuclear shell model calculations to model the main non-unique forbidden transitions of ^{92}Rb, ^{96}Y and ^{144}Pr increases the spectra above 6 MeV. This is shown in Fig. 5.6 as well as by the green curves in Fig. 5.17, which represent the ratio of ^{238}U spectra where the spectra at the denominator are the same as for the red curves, and the spectra at the numerator include nuclear shell model calculations for the three main non-unique forbidden transitions of ^{92}Rb, ^{96}Y and ^{144}Pr in addition to the recent TAGS data and to the updated nuclear data from ENSDF 2020. The structures exhibited by the green ratios in Fig. 5.17, with a decrease below 5 MeV and an increase between 5 MeV and 6 MeV and then above 7 MeV, can be distinguished in the ratios in Fig. 5.17. The remaining differences observed between the Mueller and the B-21 ^{238}U spectra are explained by the treatment of the isotopes with missing nuclear data and by the difference between the FY calculated with MURE and the FY obtained from the JEFF-3.3 database.

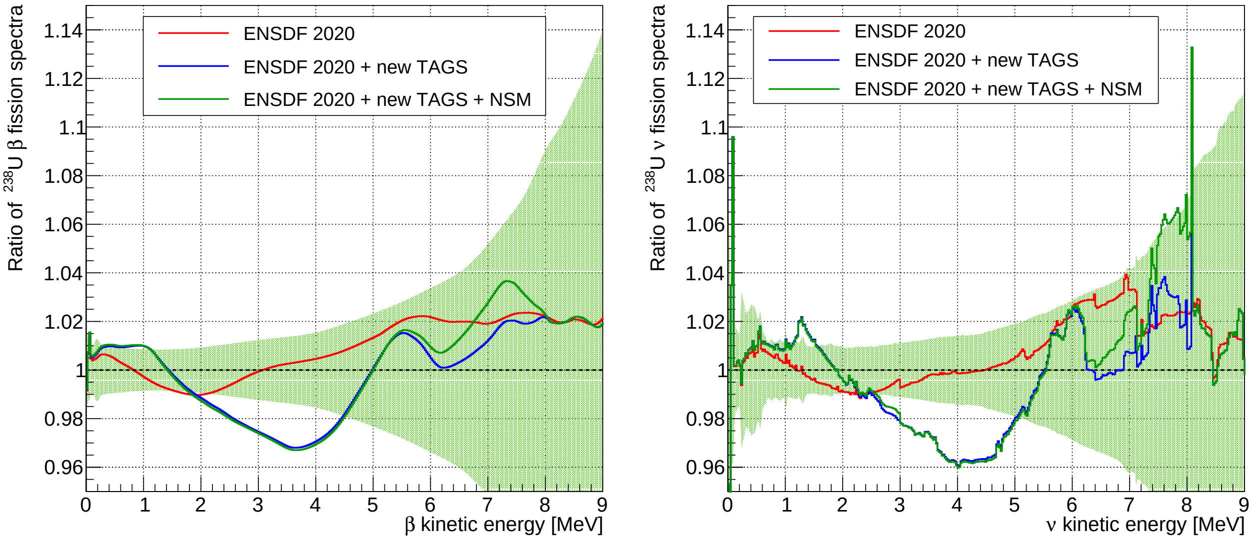

(a) Ratio of ^{238}U β spectra. **(b)** Ratio of ^{238}U $\bar{\nu}_e$ spectra.

Figure 5.17: Ratio of ^{238}U β fission spectra **(a)** and $\bar{\nu}_e$ fission spectra **(b)** computed with B-21 and with different BESTIOLE databases. For all the ratios, the spectra at the denominator include data from ENSDF 2011, Greenwood's TAGS data, Tengblad's data and isotopes with missing nuclear data modeled with the Q_β effective modeling with 3 branches. The blue curves, red curves and green curves each include additional data sources as detailed in the text, and the differences with the spectra at the denominator are written in the legend. The green bands represent the final B-21 ^{238}U spectrum uncertainties. The spectra have been computed with CFY from the JEFF-3.3 database [136].

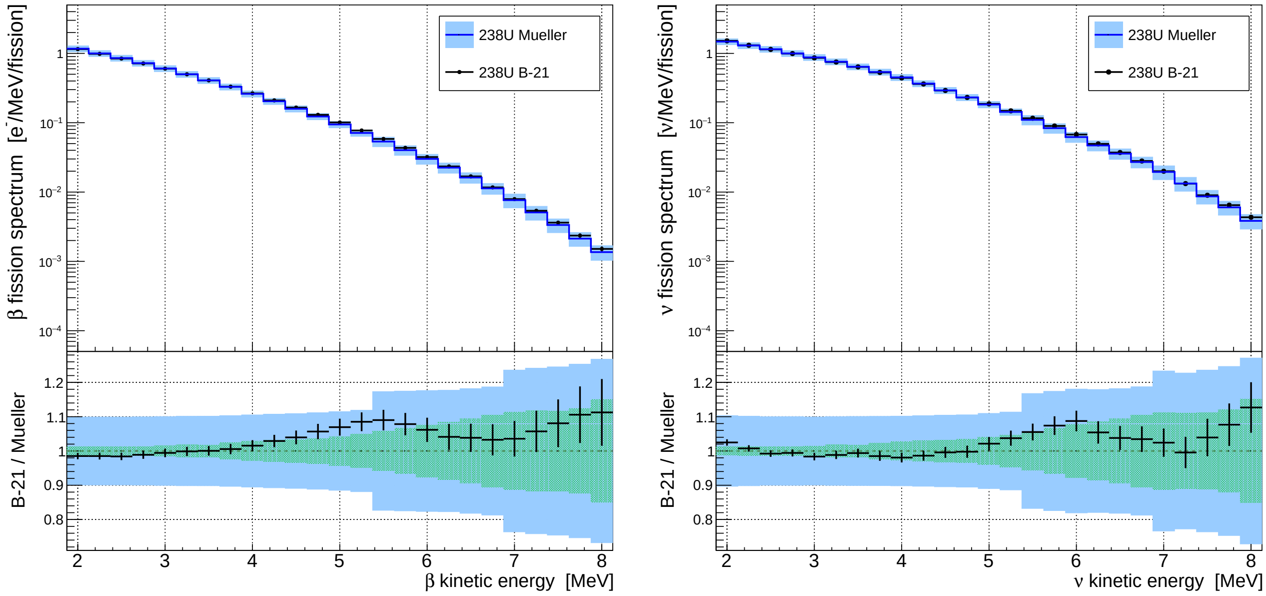

(a) ^{238}U β spectra. **(b)** ^{238}U $\bar{\nu}_e$ spectra.

Figure 5.18: (Top) β spectra **(a)** and $\bar{\nu}_e$ spectra **(b)** of ^{238}U computed with the B-21 modeling along with the summation spectra from Mueller [13]. **(Bottom)** Ratios of the B-21 prediction over the Mueller summation spectra. The blue bands centered at one represent the total uncertainties of the Mueller spectra, while the green bands represent the uncertainty without the one induced by the missing information. The uncertainties from the B-21 spectra are represented on the ratios.

5.4 Comparison with experimental reactor antineutrino spectra

Many reactor experiments have measured the shape and the rate of $\bar{\nu}_e$ fluxes detected with the IBD technique. Experiments located at commercial power plants have measured prompt energy spectra originating from a mix of the fission spectra emitted by ^{235}U, ^{238}U, ^{239}Pu and ^{241}Pu. On the other hand, experiments located at research reactors have measured an almost pure ^{235}U $\bar{\nu}_e$ flux. While most experiments have provided the measured prompt spectrum, only a limited number of experiments have provided an unfolded spectrum in true $\bar{\nu}_e$ energy. This is the case of Daya Bay [194], of RENO [325] and of STEREO [207] for instance. In this section, the IBD mean cross-section per fission and the IBD spectra obtained with the B-21 modeling are compared with the measurements from Daya Bay and STEREO, both of which provide currently the most precise data for commercial and research reactors. This will allow to sketch a panorama in which we can situate our work.

5.4.1 IBD mean cross-section per fission

The Daya Bay experiment is located near six identical 2.9 GW$_{\text{th}}$ PWR cores, and measures the emitted $\bar{\nu}_e$ with eight identical detectors distributed at two near-site experiment halls (two detectors in each hall) and one far-site experiment hall (four detectors) [326]. The $\bar{\nu}_e$ flux measured by Daya Bay is emitted predominantly by ^{235}U and ^{239}Pu with a secondary contribution from ^{238}U and ^{241}Pu. Each detector measures the superimposed $\bar{\nu}_e$ fluxes originating from the six reactors with different baselines and thus with different survival probabilities driven by the θ_{13} oscillation. The IBD mean cross-section per fission resulting from the measurements of the four near-site detectors is $\langle\sigma_{IBD}^{exp}\rangle = (5.91 \pm 0.09) \times 10^{-43}$ cm^2/fission [212].

The fractional contribution of each actinide to the total number of IBD events in the near-sites detectors is given by the effective fission fraction of the total prompt energy spectrum. This effective fission fraction takes into account the different baselines between the four near-sites detectors and the six reactor cores, the different survival probabilities, the fission fraction from each reactor core, and the predicted number of fissions from each reactor core based on their respective thermal power. Daya Bay has provided the average effective fission fractions for the four actinides over the data taking period relative to the data set from [212], which are $\alpha_{235} = 0.564$, $\alpha_{238} = 0.076$, $\alpha_{239} = 0.304$ and $\alpha_{241} = 0.056$. The predicted IBD yield is then given by the sum of the four actinide contributions using these average effective fission fractions. The uncertainty on the fission fractions is assumed to be taken into account in the measurement according to [212], so that the fission fraction uncertainty is not propagated on the IBD yield predicted with B-21. Other uncertainties listed in Tab. 5.1 are propagated on the IBD yield predicted with B-21, which is then equal to $\langle\sigma_{IBD}^{th,B-21}\rangle = (6.27 \pm 0.07) \times 10^{-43}$ cm^2/fission. The ratio of the Daya Bay measured IBD yield over the predicted one is 0.943 ± 0.014 (exp) ± 0.011 (B-21), indicating a significant tension. Interestingly, this is about the same value as the RAA. This is due to the fact that the differences in the dominant ^{235}U and ^{239}Pu IBD yields predicted with the B-21 and HM modelings compensate each other once the typical fission fractions of a PWR are considered. As a result, the RAA is almost unchanged when considering predictions made with B-21.

Daya Bay has also extracted the individual ^{235}U and ^{239}Pu IBD yields and prompt spectra using the evolution of the total prompt spectrum with the actinide fission fractions [195]. The obtained ^{235}U IBD yield is $\langle\sigma_{IBD}^{235}\rangle = (6.10 \pm 0.15) \times 10^{-43}$ cm^2/fission, and the

^{239}Pu IBD yield is $\langle\sigma_{IBD}^{239}\rangle = (4.32 \pm 0.25) \times 10^{-43}$ cm^2/fission. The ratios to the individual IBD yields predicted with B-21 are 0.938 ± 0.023 (exp) $\pm\, 0.013$ (model) for ^{235}U, and 0.915 ± 0.053 (exp) $\pm\, 0.014$ (model) for ^{239}Pu. The ^{235}U ratio indicates a significant tension similar to the tension observed for the total IBD yield, which reflect the fact that ^{235}U is the main contributor to the total IBD yield. The ^{239}Pu ratio, although exhibiting a larger discrepancy due to the large B-21 prediction, is less significant due to the large experimental uncertainty.

The detector of the STEREO experiment is installed 10 m away from the HFR research reactor core located at the ILL, which was operated at a thermal power of 49.2 MW$_{\text{th}}$ during the data taking period [158]. The ^{235}U enrichment of the core fuel is of 93%, which results in 99.3% of the $\bar{\nu}_e$ flux produced by the fission of ^{235}U on average during a 50-day reactor cycle. The remaining 0.7% of the $\bar{\nu}_e$ flux originates from the fission of ^{239}Pu. The impact of the ^{239}Pu $\bar{\nu}_e$ flux is small and decreases the emitted $\bar{\nu}_e$ rate by 0.3% compared to a pure ^{235}U $\bar{\nu}_e$ rate averaged on a reactor cycle [158]. Because of the short cycle of the HFR, an off-equilibrium correction needs to be applied to the CFY from the JEFF-3.3 database. A FISPACT-II [157] simulation of the ^{235}U FP inventory of the HFR has been provided by the Saclay group [323]. This inventory results from the irradiation of the fuel under the HFR neutron flux during the STEREO data taking period modeled with MCNP [321, 322] . The FP inventory at mid-cycle, *i.e.* at 25 days of irradiation, is assumed to correspond to the average FP inventory over the data taking period. FY values have been evaluated from this inventory, and CFY uncertainties from the JEFF-3.3 database have been assumed as a first approximation as the FP activity uncertainties were not propagated with FISPACT-II. This approximation is relevant for FP with short half-lives that have reached or are close to reach an equilibrium state, and which contribute typically to the spectra above $\sim$ 3 MeV. It has been verified that assuming CFY uncertainties for FP that were not expected to be in an equilibrium state had a small impact on the total uncertainties of the fission spectrum.

STEREO has measured a pure ^{235}U IBD yield of $\langle\sigma_{IBD}^{235}\rangle = (6.34 \pm 0.06 \text{ (stat)} \pm 0.15 \text{ (syst)} \pm 0.15 \text{ (model)}) \times 10^{-43}$ cm^2/fission [158]. The model uncertainty arises from the use of the Huber-Mueller (HM) model to normalize the detected number of events in STEREO. The uncertainty induced by the HM model is assumed to be uncorrelated with the uncertainty on the IBD yield predicted with B-21. The ratio of STEREO measured IBD yield with the one predicted with B-21 is then 0.975 ± 0.025 (exp) $\pm\, 0.023$ (HM) $\pm\, 0.014$ (B-21). Contrarily to the Daya Bay case, the ^{235}U IBD yield measured by STEREO is consistent with the B-21 prediction. This is due to the larger IBD yield measured by STEREO and to the larger experimental uncertainty.

The IBD yields measured by several experiments are displayed in Tab. 5.3 and in Fig. 5.19. The ^{235}U IBD yield predicted with B-21 is smaller than the HM ^{235}U IBD yield. The ratio of the ^{235}U IBD yield prediction from B-21 over Huber-Muller is 0.972 ± 0.026 assuming that the models are uncorrelated. The two IBD yield predictions are then in good agreement with each other. The B-21 IBD yields of the three other actinides are all larger than the HM predictions. Due to the dominant contributions from ^{235}U and ^{239}Pu to the IBD yield measured at PWR, the total IBD yields predicted with B-21 and with the HM models are very close and do not exhibit a significant tension. The agreement with the SM-2018 IBD yields from [178] cannot be quantified as the uncertainty is not provided. There is a 3.5% difference between the ^{235}U IBD yield predicted with SM-2018 and with B-21, corresponding to about 2.4 standard deviations of the B-21 ^{235}U IBD yield. The difference between the ^{235}U IBD yield predicted with SM-2018 and with B-21 is of 6.8%, corresponding to about 9 standard deviations of the B-21 ^{239}Pu IBD yield. The resulting difference between the total predicted IBD yields is then of 4.3%, which is about 6 standard deviations of the B-21 total IBD yield. In their current state, the B-21 and SM-2018 predictions would have very different impact on the RAA.

	Fission fraction				$\langle\sigma_{IBD}\rangle$ [10^{-43}cm^2/fis]				
	$\alpha_{^{235}\mathrm{U}}$	$\alpha_{^{238}\mathrm{U}}$	$\alpha_{^{239}\mathrm{Pu}}$	$\alpha_{^{241}\mathrm{Pu}}$	Mix	^{235}U	^{238}U	^{239}Pu	^{241}Pu
Model									
BESTIOLE-2021					6.27 ± 0.07	6.50 ± 0.09	10.32 ± 0.15	4.72 ± 0.07	6.93 ± 0.10
SM-2018 [178]					6.01	6.28	10.14	4.42	6.23
Huber-Mueller [223]					6.20 ± 0.14	6.69 ± 0.15	10.10 ± 1.00	4.36 ± 0.11	6.04 ± 0.60
PWR									
Daya Bay [212]	0.564	0.076	0.304	0.056	5.91 ± 0.09	6.10 ± 0.15		4.32 ± 0.25	
Double Chooz [327]	0.520	0.087	0.333	0.060	5.71 ± 0.06				
RENO [224, 325]	0.571	0.073	0.300	0.056	5.89 ± 0.12	6.15 ± 0.19		4.18 ± 0.26	
Bugey-4 [68]	0.538	0.078	0.328	0.056	5.75 ± 0.08				
Research									
STEREO [158]	0.993	-	0.007	-		6.34 ± 0.22			

Table 5.3: Measured and predicted reactor antineutrino IBD yields of ^{235}U, ^{238}U, ^{239}Pu and ^{241}Pu of several reactor experiments over their respective period of data taking, along with their effective fission fractions. The "Mix" IBD yield in the "Model" rows have been computed with the Daya Bay effective fission fractions.

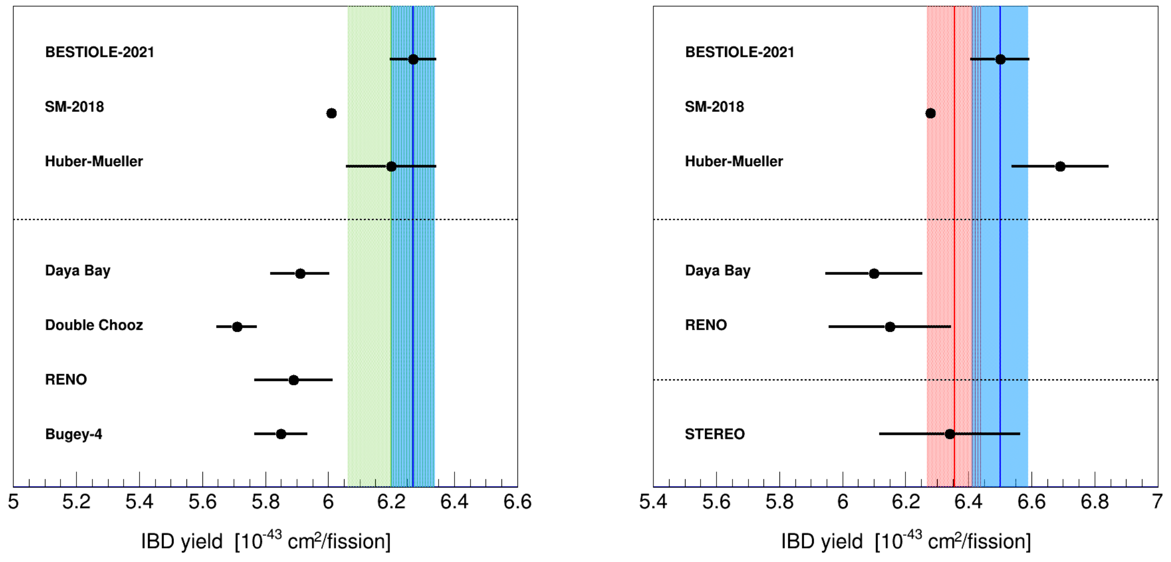

(a) Mix IBD yield.

(b) ^{235}U IBD yield.

Figure 5.19: Measured and predicted reactor antineutrino IBD yields of several reactor experiments. The predicted IBD yield (top) are separated from measurements at PWR (middle) and at research reactors (bottom). **(a)** Averaged IBD yields for PWR experiments over their respective period of data taking. The predicted IBD yields at the top use the Daya Bay effective fission fractions. The blue and green bands represent respectively the B-21 and the HM IBD yields. Note that the different fission fractions among experiments can induce a difference in the measured IBD yields that can reach up to 0.5%. **(b)** ^{235}U IBD yield. The blue and red bands represent respectively the B-21 IBD yield and the world average from [158].

5.4.2 Shape difference

The individual ^{235}U prompt spectra, the combined prompt spectra of ^{239}Pu and ^{241}Pu and the total prompt spectra measured by Daya Bay have been recently unfolded [194]. These spectra are compared with those modeled with B-21 using CFY from the JEFF-3.3 database in Fig. 5.20. The B-21 spectra are area-normalized to the Daya Bay spectra. The combination of the ^{239}Pu and ^{241}Pu spectra, label as Pu combo, is given by ($^{239}\mathrm{Pu} + 0.183 \times {}^{241}\mathrm{Pu}$), where the factor of 0.183 is the average fission fraction ratio of ^{241}Pu to ^{239}Pu over the data taking period [194]. The unfolded spectrum published by STEREO is a pure ^{235}U spectrum corrected for the contribution of $\bar{\nu}_e$ from activated ^{28}Al and ^{56}Mn, whose $\bar{\nu}_e$ spectra and uncertainties modeled with B-21 are given for completeness in App. F, as well as the contamination of fission from ^{239}Pu [207]. The B-21 modeling of the ^{235}U $\bar{\nu}_e$ spectrum is compared to the unfolded ^{235}U $\bar{\nu}_e$ spectrum in Fig. 5.21. The B-21 spectrum is area-normalized to the STEREO spectrum. For each case, the experimental uncertainty on the unfolded spectra dominates with respect to the B-21 uncertainty.

The ratio of the unfolded spectra over the B-21 spectra exhibit similar significant distortions than the shape anomaly observed with the HM model. A distortion between 5 MeV and 7 MeV is observed in the ratio with the Daya Bay ^{235}U unfolded spectrum, and between 5 MeV and 6 MeV in the ratio with unfolded Pu combo spectrum. The ratio with the unfolded total spectrum presents a distortion between 5 MeV and 7 MeV where the contribution from both ^{235}U and Pu combo distortions can be seemingly observed as two distinct peaks. The peak at 5.5 MeV would then correspond to ^{239}Pu, while the peak at 6.2 MeV would correspond to ^{235}U. The ratio of the STEREO ^{235}U unfolded spectrum with the B-21 prediction is similar to the ratio obtained with the HM prediction presented in [207] and reproduced as red dots in Fig. 5.21. The distortion between 4.5 MeV and 6 MeV is smaller with the B-21 prediction than with the HM prediction by up to 3%.

The distortion of the IBD spectrum shape appears for both the B-21 summation and the HM model, and thus despite the differences observed between the fission spectra predicted with the two modelings (see Fig. 5.15). The difference between the ratios STEREO/HM and STEREO/B-21 are expected to result from the differences between the HM and the B-21 fission spectra. The similar shape of the ratios STEREO/HM and STEREO/B-21 could suggest a common bias in the modelings. Furthermore, the difference in the distortion amplitudes for the STEREO ^{235}U spectrum could also suggest that the bias is smaller in the B-21 modeling than in the HM modeling. Finally, the distortion appears to be located at different energy regions in the ^{235}U fission spectrum and in the Pu combo fission spectrum, and to be smaller for the Pu combo fission spectrum. Similar characteristics can be observed in the contributions of the non-unique forbidden transitions, as seen in Fig. 5.12, which could indicate that it plays a role in the distortions. Indeed, the contribution from non-unique forbidden transitions is not taken into account the HM predictions. On the other hand, including the three non-unique forbidden transitions calculated from nuclear shell model in B-21 mostly modifies the predictions above 6 MeV, and thus has a very small impact on the distortion as shown by the green dots in Fig. 5.21. The peak of the contribution from non-unique forbidden transitions is between 5 MeV and 6 MeV for the four actinides, and is more important for the ^{235}U spectrum than for the Pu spectra. The different locations of the distortions in the ^{235}U and Pu combo spectra could be due to a specific isotope or group of isotopes having different weights in these spectra. The most important contributors to the IBD spectrum in the 5-7 MeV energy window has already been established using the B-21 modeling (see Sec. 3.5.1 and Tab. 3.3), and FP with important non-unique forbidden transitions that could potentially induce such bias will be included in priority using a nuclear shell model calculation. This could help to determine the potential role of non-unique forbidden transitions in the observed distortion and in the shape anomaly in general.

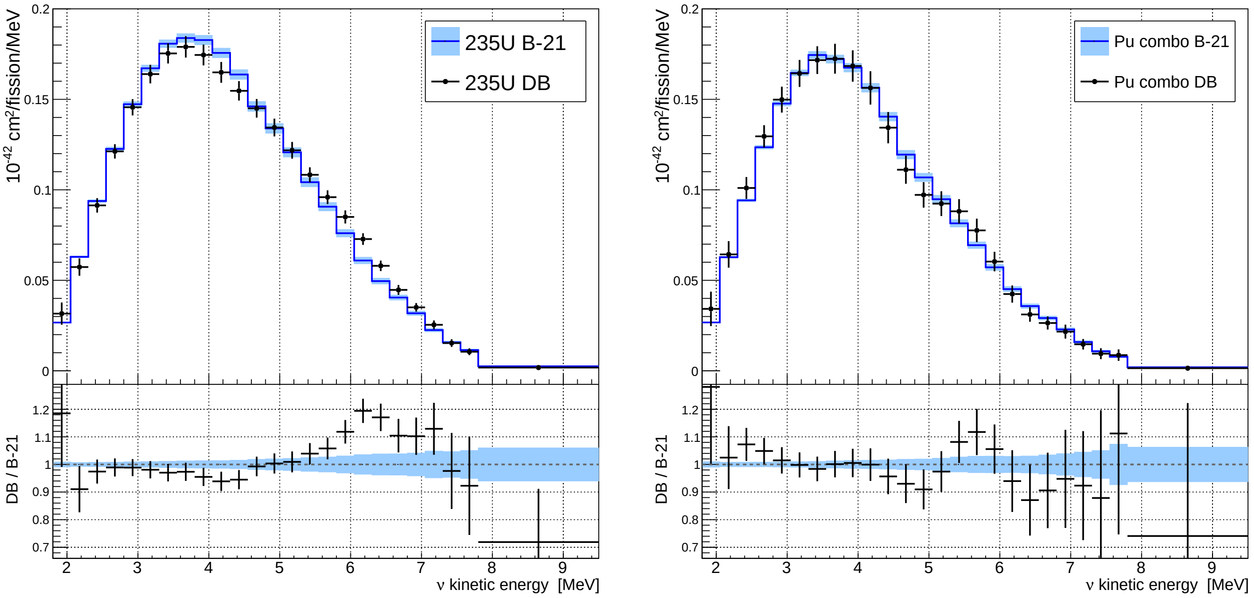

(a) ^{235}U spectra.

(b) Pu combo spectra.

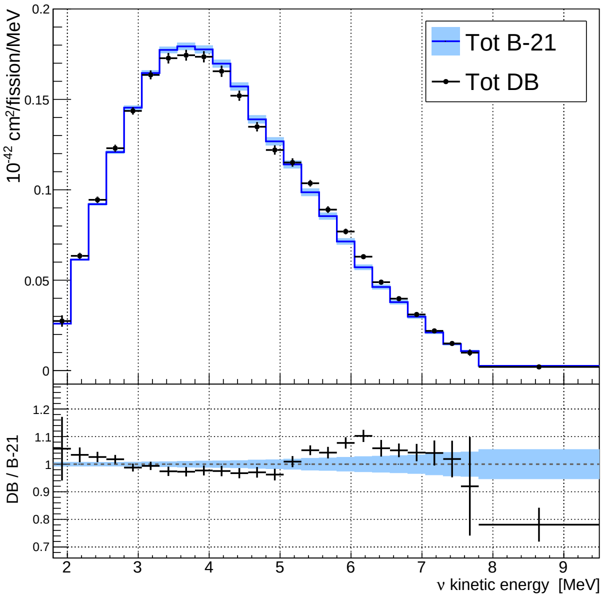

(c) Total spectra.

Figure 5.20: **(Top)** Comparison of the unfolded ^{235}U spectrum **(a)**, Pu combo spectrum (^{239}Pu $+ 0.183 \times {}^{241}$Pu) **(b)** and total spectrum from Daya Bay [194] with the corresponding B-21 predictions. The B-21 spectra are area-normalized to the Daya Bay unfolded spectra. **(Bottom)** Ratio of the unfolded spectra over the B-21 predicted spectra. The blue bands centered at one represent the uncertainties from the B-21 spectra, while the uncertainties from the unfolded spectra are represented on the ratios.

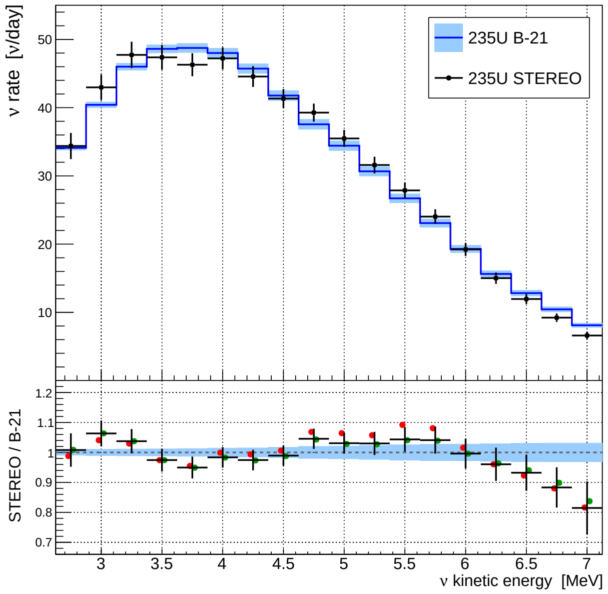

Figure 5.21: **(Top)** Comparison of the unfolded ^{235}U spectrum from STEREO [194] with the corresponding B-21 predictions. The B-21 spectrum is area-normalized to the STEREO unfolded spectra, and has been computed for an irradiation time of 25 days. **(Bottom)** Ratio of the unfolded spectrum over the B-21 predicted spectrum. The blue band centered at one represents the uncertainty from the B-21 spectrum, while the uncertainty from the unfolded spectra is represented on the ratio. The red dots represent the ratio between STEREO data and the HM spectrum. The green dots represent the ratio with a B-21 prediction where the non-unique transitions of ^{92}Rb, ^{96}Y and ^{144}Pr are ξ-approximated to allowed transitions. The dots are shifted for readability.

5.5 Discussion on the revised prediction uncertainties

All along the comparisons conducted in this chapter, significant tensions have been observed on the predicted β and $\bar{\nu}_e$ fission spectra, on the predicted IBD yields and on the shapes of the predicted IBD spectrum. A brief discussion is made is this section to summarize the limitations and the potential biases associated to the B-21 prediction and uncertainty model in perspective of the work already done.

The uncertainties on the BR and on the β^- intensities are well defined experimentally. Correlations between the BR, which are not provided in nuclear databases, have been conservatively estimated to maximize the uncertainty induced on the IBD yield. The resulting IBD yield uncertainty is reliable and small, about 0.6%. The uncertainties on the endpoint energies are also well defined experimentally. The endpoint energies of the different transitions of an isotope have been treated as fully correlated. The uncertainty induced by the multiplicity of spin-parity data has been integrated to the propagation of the endpoint energy uncertainty in order to account for the impact of the endpoint on the different types of transition. The resulting IBD yield uncertainty for the combined endpoint energy and spin-parity uncertainties is expected to be reliable and is small, about 0.2%. Hence, it is very unlikely that the predicted IBD yield uncertainty or the shape uncertainty of the fission spectra are underestimated because of these four uncertainty sources.

The FY are treated as uncorrelated, which results in an IBD uncertainty of about 1.1%, which currently makes it the main contributor to the total uncertainty budget. The actual IBD yield uncertainty induced by the FY uncertainty could be higher with a correct treatment of the FY correlations. Several studies have been conducted in the last decade regarding the possibility to evaluate FY correlations [311–316]. These studies represent a solid lead toward quantifying the bias induced by the current treatment of FY, which should be treated with a high level of priority considering that the FY uncertainty is the main contributor to the IBD yield uncertainty budget. The choice of the FY nuclear database can also be responsible for significant changes in the shape and in the normalization of a fission spectrum [328].

The uncertainties associated to the WM correction, to the outer radiative correction and to the modeling of non-unique forbidden transitions have been derived with the method proposed in Sec. 4.2.1, which is a first tentative to assess a shape uncertainty at the level of a transition spectrum respecting the transition normalization. In each case, the correction is assumed to be specific to a branch spectrum and to be uncorrelated with other branch corrections. As such, the derived modeling uncertainties have been treated as uncorrelated between the different branch spectra of an isotope. As a result, the relative modeling uncertainties on a fission spectrum decrease with the number of branches. If the assumption regarding the correlations is not correct, then this could result in an underestimation of the corresponding uncertainties in the region of the fission spectra where many transitions are stacked, which coincides with the region where the majority of the $\bar{\nu}_e$ flux is emitted. The uncertainty associated to the modeling of non-unique forbidden transitions has been derived by considering the dominant behavior of the differences between the ξ-approximated spectra and a more reliable modeling based on nuclear shell model calculations for a restrained set of transitions. As such, the modeled uncertainty is expected to cover the bias induced by the ξ-approximation for most of the non-unique forbidden transitions. A large uncertainty on the shape of about 30% at the endpoint energy and at the origin has been derived in this case. The IBD yield uncertainties induced by this non-unique modeling uncertainty is about 5% to 10% for the most important non-unique forbidden transition. Considering that the mismodeled non-unique forbidden transitions make about 25% of the IBD spectra (see Fig. 5.4b and 5.12 showing the contributions in fission spectra, which are identical for IBD spectra), and if one expects a similar uncertainty of about 5% on the corresponding IBD yield contribution, fully correlating the modeling uncertainty would result in an uncertainty of about 1.25% on the total IBD yield. The non-unique modeling uncertainty would then become one of the main contributors to the IBD yield uncertainty budget, and would slightly reduce the observed tensions, qualifying it to be treated with high priority. Due to the smaller impact of the WM correction and of the outer radiative correction at the level of a transition, a bad assessment of the corresponding uncertainties would be expected to have a lower impact on the total IBD yield. As such, it could be treated with a lower level of priority.

The presence of potentially Pandemonium-impacted FP making up about 20% of the $\bar{\nu}_e$ spectra up to 5 MeV and contributing to about 16% of the IBD yield (see Tab. 5.2) could be at the origin of a sizable bias. This bias is currently not accounted for in the B-21 uncertainty budget. The impact of including the TAGS data measured over the last decade is to decrease the predicted total IBD yield by about 3%. The IBD yield contribution of these remaining Pandemonium-impacted FP could reach half the contribution of isotopes modeled with these recent TAGS data. Hence, if one assumes as a first approximation a similar impact from correcting the Pandemonium effect on these potentially Pandemonium-impacted FP, it would further reduce the total IBD yield by another 1.5%. An uncertainty covering this bias would certainly be significant in regards with the current uncertainty budget, and could have an important impact on the observed tensions. As such, a high priority should be given to evaluated an uncertainty in order to cover this potential bias.

The possible bias induced by the use of Tengblad's data is covered at the level of individual isotopes, with large uncertainties on the BR and on the endpoint energies that can typically induce a 50% uncertainty on the individual isotope spectrum shape. However, the stacking of

FP result in a decreased relative uncertainty associated to these isotopes as they are treated as uncorrelated. The uncertainty on the aggregate spectrum of Tengblad's isotopes is then very small below 5 MeV, where the majority of the flux is emitted. The validity of the uncertainty on the aggregate spectra of Tengblad's isotopes should be further tested. A possibility could be to compare the modeling of these isotopes using different nuclear databases and using Tengblad's data in order to verify if the uncertainties cover correctly the differences.

Finally, the uncertainties on the isotopes modeled with the Q_β effective modeling have been treated by assuming a 10% uncertainty on the BR and a 20% uncertainty on the endpoint energies. The use of such effective modeling is most certainly at the origin of a sizable bias above 6 MeV. Indeed, differences higher than 10% can be observed above 6 MeV depending on the considered effective modeling. The current uncertainty associated to these isotopes do not cover such bias (see Fig. 5.12). Moreover, the fission spectra did not vary significantly below 4 MeV. As such, the potential bias remains to be quantified below 4 MeV. Further investigations are required to assess an uncertainty at the level of individual isotopes that would consistent at the level of the fission spectra with the expected bias of 10% or so. This could be achieved by selecting the uncertainties on the BR and endpoint energies based on the comparison of the aggregate spectrum of missing isotopes with an aggregate spectrum made of well-known isotopes.

5.6 Summary

The fission spectra of ^{235}U, ^{238}U, ^{239}Pu and ^{241}Pu computed with B-21 and based on a revised summation method and uncertainty propagation have been presented in this chapter, along with a detailed breakdown per uncertainty source and per nuclear data source. The final uncertainties are small, with total IBD yield uncertainties of about 1.3% and fractional uncertainties of about 1% at 2 MeV and inferior to 10% at 8 MeV. In particular, the propagation of known nuclear data uncertainties is robust, and is unlikely to at the origin of some tension.

IBD yields and IBD spectra predicted with B-21 have been compared with the measured IBD yields and the unfolded IBD spectra published by Daya Bay and by STEREO. The small uncertainty on the current B-21 predictions is secondary with respect to the experimental uncertainties. As a result, the IBD yields predicted with B-21 exhibit significant tensions with the total IBD yield and the ^{235}U IBD yield measured by Daya Bay, as shown by the respective ratios of 0.943 ± 0.014 (exp) $\pm\, 0.011$ (model) and of 0.938 ± 0.023 (exp) $\pm\, 0.013$ (model). The tension with the ^{239}Pu IBD yield measured by Daya Bay is less significant due to the larger experimental uncertainty, as shown by the ratio of 0.915 ± 0.053 (exp) $\pm\, 0.014$ (model). Nonetheless, a smaller ^{235}U IBD yield and a larger ^{239}Pu IBD yield predicted with B-21 compared to the HM predictions result in a ratio for the total IBD yield with a value about the same as the RAA. On the other hand, the ^{235}U IBD yields measured by STEREO is consistent with the B-21 IBD yield, with a ratio of 0.975 ± 0.025 (exp) $\pm\, 0.014$ (model) where the model uncertainty only consists in B-21. This is due to the large experimental uncertainty, to a larger measured IBD yield and to a smaller predicted IBD yield compared to the HM prediction. Finally, the comparisons of the shape of the B-21 IBD spectra with Daya Bay and STEREO unfolded spectra exhibit similar shape distortions between 5 MeV and 7 MeV than the comparisons with HM predictions. The difference in the shape distortions with respect to B-21 and the HM model is expected to originate from the difference between the fission spectrum predictions.

Significant differences have been observed with the β spectrum measurements performed at the ILL and with the converted $\bar{\nu}_e$ spectra from Huber. B-21 predictions of the ^{235}U β

and $\bar{\nu}_e$ fission spectra are higher than the ILL data and the predictions from Huber, while the B-21 predictions are generally lower in the case of ^{239}Pu and ^{241}Pu. While part of the observed discrepancies could originate from a mismodeling of non-unique forbidden transitions, of Pandemonium-impacted isotopes, and of isotopes with missing nuclear data, it is important to remind that the validity of both the normalization and the shape of the ILL spectra are questioned as they exhibit significant discrepancies with the spectra measured by IBD experiments. The ^{238}U β spectrum measured at the FRM II presents important differences superior to 10% but remains consistent with the B-21 prediction due to the large experimental uncertainties. The ^{238}U $\bar{\nu}_e$ spectrum computed with the summation method from Mueller can exhibit significant differences with the B-21 modeling that are mostly understood as an update of the nuclear data sources. In a next step, the B-21 predictions will be compared with other theoretical modelings such as the SM-2018 summation spectra published by [178] and the summation spectra from [225].

Several potentially significant biases have been identified in the B-21 modeling. The potential bias induced by the Q_β effective modeling for isotopes with missing nuclear data is not covered by the corresponding uncertainties. This bias could be particularly important above 6 MeV, and is yet to be determined below 4 MeV. Treating the modeling uncertainties derived for the WM, for the outer radiative correction and for the modeling of the non-unique forbidden transitions with the ξ-approximation as uncorrelated between the branch spectra may be an incorrect assumption. It could result in an incorrect evaluation of the uncertainties at the level of a fission spectrum. The modeling uncertainty of non-unique forbidden transitions could have an important impact on the tensions considering that these transitions contribute significantly to the fission spectra. This requires to develop further our first attempt at proposing a consistent uncertainty at the level of individual transitions. Another significant bias not taken into account in the current uncertainty budget is due to the possible Pandemonium effect present in the evaluated branching ratios of several important FP. All these different biases could lead to an underestimated uncertainty budget. As a rough estimation, it is reasonable to considered that the total IBD yield uncertainty could reach about $\sim 3\%$ once these biases have been evaluated.

Conclusion and outlook

More than 90 years have passed since the words of Pauli resonated at the Tübingen conference, signing the birth of the neutrino. Since its experimental observation in 1953 by Reines and Cowan, the neutrino has been at the origin of groundbreaking discoveries and of relentless questions for the physicist community. The reactor antineutrino anomaly is a great example. Highlighted in 2011 after a reevaluation of the modeling of reactor antineutrino spectra, this systematic deficit in the measured $\bar{\nu}_e$ rates emitted by nuclear reactors compared to the predictions raises the possibility of a neutrino oscillation toward a new neutrino massive state with a mass of $\sim$ 1 eV. After a decade of experiments, the sterile neutrino hypothesis seems to fade away and a possible bias in the modeling of reactor antineutrino spectra has become a privileged hypothesis to explain the anomaly. Such bias in the modeling could also explain two other anomalies, the first one being a distortion in the shapes of the predicted spectra with respect to the measured ones, and the second being a discrepancy observed in the fuel-dependent evolution of the measured $\bar{\nu}_e$ rate compared to the prediction. In this context, a revision of the summation method that can be used to predict reactor antineutrino spectra has been conducted. The current state of this revised summation modeling has been presented in this thesis.

Nuclear reactors emit an intense and pure flux of electron antineutrinos through the thousands of β-decays originating from the hundreds of fission products generated by the chain of fission. The modeling of the energy spectra of the electron and the antineutrino emitted during a β-decay has been improved by revising the most important corrections and by lifting commonly used approximations when possible. A home-made program has been developed in order to lift the "$\lambda_k = 1$" approximation, and to include the effect of the finite size of the nucleus and of the atomic screening on the β-decay spectra for any given potential with a spherical symmetry. These effects have been encompassed in Coulomb functions that have been tabulated on a very fine energy grid, thus giving the possibility to be independent from outdated tables of Coulomb functions. Different prescriptions for the weak magnetism correction have also been considered at the level of individual transitions. These improvements can have an important impact at the level of a transition, whose spectrum shape can be modified by several percents. The implemented corrections are expected to be the leading corrections at the level of individual transitions. Nonetheless, subleading corrections such as the impact of the spherical nucleus model could be investigated in a next step in order to evaluate the accuracy of the current hypothesis.

The so-called ξ-approximation, commonly used to model non-unique forbidden transitions, has also been discussed. The computation of some of the most important non-unique forbidden transitions in the context of reactor antineutrinos is currently performed by the Saclay group, using a detailed nuclear structure based on the nuclear shell model. At the moment, the main transitions of ^{92}Rb, ^{96}Y, and ^{144}Pr have been provided and included in the revised summation model. This computation has shown important differences with the usual spectra computed with the ξ-approximation, with a change in the spectrum shapes of up to tens of percents. An important priority will be given to the computation of additional non-unique forbidden transitions in future studies, with the aim to include the 10 principal transitions in a first step and then more.

The modeling of each fission product spectrum entering a reactor spectrum requires the use of a large amount of nuclear data. Different nuclear data sources exist, and a careful revision of the nuclear data selected for our summation model has been conducted. Isotopes impacted by the Pandemonium effect have been corrected by including TAGS measurements when available as well as data from direct β measurements. Assessing a reliable uncertainty budget to reactor antineutrino spectra computed with the summation method is a complicated task due to the numerous uncertainty sources originating from nuclear data and from modeling assumptions and corrections. A thorough work has been started in this thesis to quantify the impact of the different uncertainty sources. A first objective has been to improve the propagation of the uncertainties on evaluated nuclear data. For this purpose, a Monte-Carlo simulation propagating endpoint and branching ratio uncertainties has been developed. A careful and robust treatment of knows and unknown correlations has been realized. Unknown correlations are defined in order to maximize the uncertainty on the IBD yield. A second objective has been to derived an uncertainty to take into account possible biases induced by the weak magnetism correction, the radiative correction and the modeling of non-unique forbidden transitions. A method has been proposed to define covariance matrices at the level of individual β transitions that conserve the normalization of each transition spectrum while accounting for large shape uncertainties. Because of the important contribution of non-unique forbidden transitions in a reactor $\bar{\nu}_e$ spectrum, the robustness of this approach will need further investigation to validate or eventually refine the proposed modeling. Several inaccuracies arising from nuclear data sources are still not fully covered by our uncertainty budget. Inaccuracies induced by the effective modeling of isotopes without nuclear data and of isotopes modeled with Tengblad's data is not completely covered. More importantly, the presence of isotopes potentially impacted by the Pandemonium effect could be at the origin of a sizable bias that is not yet taken into account. These biases will be treated in a next step, with a particular focus on the one associated to possible Pandemonium-impacted isotopes.

Finally, the fission spectra and IBD mean cross-section per fissions computed with B-21 have been compared to different measurements performed at commercial and research reactors as well as with other theoretical predictions. Significant tensions have been observed, and are expected to be partially reduced once the uncertainty budget will be finalized. Other comparisons will then be conducted with the remaining experimental data from reactor experiments. An important application of the reactor antineutrino spectrum computed in this work will be in the context of the reactor experiments aiming at measuring the CEνNS mean cross-section per fission. The reactor neutrino flux prediction will contribute to the systematic uncertainty of the measurement, and must therefore be completed before any actual use. Future studies will investigate the impact of the prediction on the possible precision of CEνNS experiments at reactors, and will emphasize the impact of the neutrino flux emitted below the IBD threshold of 1.8 MeV. The revised BESTIOLE modeling developed in this thesis is also involved in two other studies conducted by the Saclay group. The first one consists in evaluating the residual antineutrino flux emitted from irradiated assemblies in the context of the Double Chooz experiment. The second study consists in evaluating the flux of geoneutrinos originating from the Earth.

Several other groups are investigating the summation and conversion methods in order to improve the accuracy and the precision of the reactor antineutrino spectrum predictions. The impact of non-unique forbidden transitions in the summation method is investigated by the groups of Hayen et al., while the impact of a more accurate weak magnetism correction in the conversion method has been addressed by Hayes et al. Furthermore, the impact of

TAGS measurements and the role of the Pandemonium effect in the summation method is studied by the group of Estienne et al. Regarding the TAGS measurements, the list of candidate-isotopes should continue to be measured by different teams from València and from Oak Ridge National Laboratory for instance, hence providing additional accurate data to include in summation predictions.

Appendices

A

The DIRAC program

The wavefunction of an electron moving within the electromagnetic field generated by a nucleus satisfies the radial Dirac equations Eq. 3.22 if the associated potential has a spherical symmetry. The Coulomb amplitudes correspond to the normalization of the radial electron wavefunctions, and can be computed by numerically solving the radial Dirac equations on a large grid. This task is performed by the Directives for an Improved Result of the Amplitudes of Coulomb (DIRAC) algorithm following the work of Behrens and Bühring [263]. The algorithm is based on a local power series expansion of the radial wavefunctions and of the nuclear potential. The algorithm can easily be adapted to any potential, assuming it has a spherical symmetry and can be power expanded at any point of space.

The wavefunction and potential power series have different expressions according to the point of space around which they are performed (power series around singular points are treated in [263]). An accurate description of the radial wavefunctions must be continuous at each point of space and correctly normalized at infinity, where the potential is always seen as a Coulomb potential in the case of a β-decay. These two requirements can be met numerically by connecting the wavefunction power series in each point of a radial grid. The gap between two radial points of the grid can be determined at each step, and is easily controlled to allow the power series to converge at each point. Hence, the radial gaps are not a relevant source of uncertainty on the wavefunctions. The Coulomb amplitudes are obtained as a result of the reconnection of the power series around the origin of the nucleus with the power series at infinity, or rather at a radial value large enough to assume that the asymptotic wavefunction behavior is valid. The reader is invited to read carefully the chapter 3 of [263], where the details of the different power series at each point of space of interest are described along the general steps to perform the reconnection of the power series. This work has been described in detail as an internal CEA technote to ensure the proper implementation of the DIRAC algorithm.

During the reconnection procedure, the power series must be truncated at each point of space. The bias induced by the truncation propagates and accumulates at each point of the grid, from the origin up to the reconnection point. The bias originating from the truncation is determined by the amplitude of the remainder which is bounded by the last term included in the computation. The index N of the last term is determined individually at each point of space when the relative difference of the remainder compared with the sum of all previous order terms is below a given tolerance. For instance, the relative tolerance in DIRAC is set to

10^{-13}. Hence, the terms neglected in the power series do not impact the numerical result and the wavefunctions computed locally are exact up to this relative tolerance.

The Coulomb functions such as the Fermi function and the λ_k functions are computed by combining the Coulomb amplitudes obtained for different values of the κ eigenvalue defined at Eq. 3.19. The Coulomb functions can be included in the BESTIOLE spectrum computation by following two different approaches. The first possibility is to implement the reconnection algorithm directly in BESTIOLE. The advantage of this method is that the computed Coulomb functions are exact up to numerical errors. However, the computation of a Coulomb function is relatively time consuming as the power series reconnection must be performed at a large radial value R_2 beyond which the asymptotic wavefunction behavior is ensured. Moreover, the Coulomb functions are independent of the type of the transition and of the endpoint energy. Thus, there is a large redundancy when computing multiple transitions of an isotope.

Let us point out that the radial value R_2 used to reconnect the power series is not provided in Behrens and Jänecke's tables [269]. However, the value $R_2 = 350W_e/p$ is used in [329] and more recently in [277]. In the case of a screened potential, an intermediate radial value R_1 is necessary to describe the transition of the exponential behavior of the screening potential into the asymptotic Coulomb behavior. This value is set to $R_1 = 150W_e/p$ in [277, 329]. In DIRAC, the used radial values are $R_2 = 3W_e/(\alpha p)$ and $R_1 = W_e/(\alpha p)$, with α the fine-structure constant. Although the use of α does not change significantly the values of R_1 and R_2, it has a more physical interpretation as the Bohr radius is equal to $1/\alpha$ and represents the natural length of the atomic scale. The necessity to define R_2 as proportional to W_e/p is due to the wavefunction oscillation frequency, $2\pi/p$. If R_2 were fixed at a constant value, there would be a range of momenta for which the length of the wavefunction oscillation would become of the same order of magnitude than R_2. Hence, the reconnection would be performed in a region of space where the asymptotic behavior is not valid, thus invalidating the algorithm. The momentum dependency of R_2 ensures that a minimum number of oscillations take place before reconnecting the different power series as the R_2 value increases linearly with p for large momenta. These definitions of R_1 and R_2 also keep reasonable the required computing time with modern computers. For instance, computing the electron wavefunctions from the origin to R_2 can last up to a few minutes for a β energy of a tens of MeV. However, it is difficult to accept few minutes for a single beta transition when thousands of branches have to be calculated, with a Monte Carlo propagation of the uncertainties of the input parameters for each.

The second approach is to generate Coulomb tables. The advantage is that the Coulomb functions need only to be computed once. However, the inclusion of the Coulomb functions in BESTIOLE must rely on an interpolation method in this approach. The accuracy of the reproduced Coulomb functions then depends entirely on the number of tabulated energies. For instance, Behrens and Janecke's tables only provide screened Coulomb functions for a handful of energies [269]. A polynomial interpolation is not appropriate over such a small number of tabulated energies, and a linear interpolation introduces an important bias in the isotope β and $\bar{\nu}_e$ spectra. Moreover, the energies are limited to a few keV and up to a couple of MeV at maximum, thus limiting the accuracy of an extrapolation method outside of this energy range.

Generating Coulomb tables is the only viable option to compute reactor antineutrino spectra made of thousands of transitions, due to time management. It is then necessary to selected the tabulated β energies to capture the Coulomb function behaviors in the best fashion. The Fermi functions and the λ_k functions change slowly above 1 MeV as illustrated in Fig. A.1. Hence, a small number of energies are required beyond 1 MeV. The Fermi function and the λ_k functions increase by several orders of magnitude below 1 MeV, and the number of tabulated energies must increase as a consequence. At very low energy, typically below 10 keV, the Coulomb functions display fine behaviors resulting from the atomic screening effects as shown in Fig. A.2. The tabulated energies in this energy range must allow to reproduce these behaviors, hence an increased number of energy points.

Threshold energy steps

A straightforward approach is to defined the gap between two tabulated energies depending on the energy range, decreasing the value of the gap as the β energy tends to zero. Coulomb functions are then tabulated identically even though their behaviors may display important variations between isotopes and even between the type of Coulomb function. Furthermore, the accuracy of interpolation Coulomb functions cannot be inferred when generating the Coulomb tables. As a result, numerical fluctuations due to the interpolation method can appear if the number of energy points is not appropriate. A simple solution is to increase the number of tabulated energies in a given region until the numerical fluctuations disappear, although it does not provide any information on the residual bias.

Adaptive ”on-the-fly” energy steps

Another approach is to probe the Coulomb function behaviors and refine automatically the number of points when fine behaviors are displayed. The DIRAC program uses an adaptive ”on-the-fly” algorithm that aims to control very precisely the precision over the interpolation of the tables. The principle of the ”on-the-fly” algorithm is to compute the exact values of a Coulomb function at three energy points: E_0, E_1 and at the middle energy $E_m = (E_0 + E_1)/2$. The Coulomb function is then interpolated between E_0 and E_1 and the interpolated value at E_m is compared to the exact value. If the relative difference between the interpolated and the exact values is below a given tolerance, the Coulomb function interpolation is considered to be accurate in the energy window limited by E_0 and E_1, and the procedure is repeated over the next energy window. If the difference between the interpolated and the exact values is above the tolerance threshold, the point E_1 is replaced with E_m, and the procedure is repeated between E_0 and E_m. Starting with E_0 set at high energy values, the complete energy range is tabulated by sliding down the energy window. The resulting Coulomb tables can then be

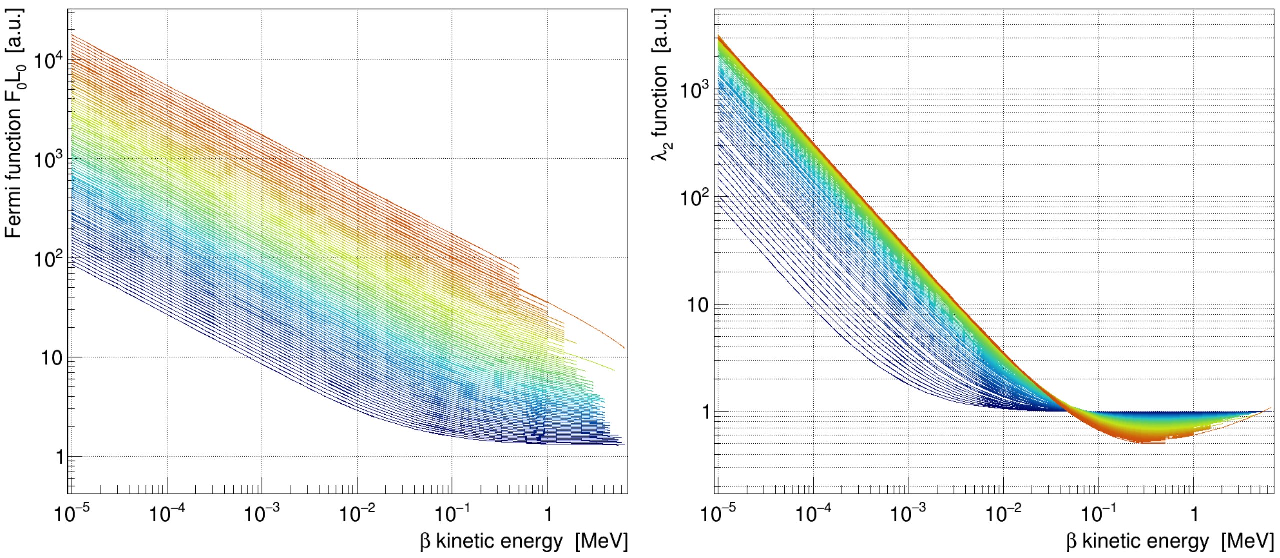

(a) Fermi function.

(b) λ_2 function.

Figure A.1: Fermi functions **(a)** and λ_2 functions **(b)** computed for a potential based on a finite-size nucleus and with atomic screening. The Coulomb functions have been computed with the DIRAC program for all the isotopes in the database [161] and only up to the isotopes Q_β energies. The gradient of color represents the increase of mass and of charge of the nuclei, low-mass nuclei being associated to the dark blue curves and high-mass nuclei with red curves.

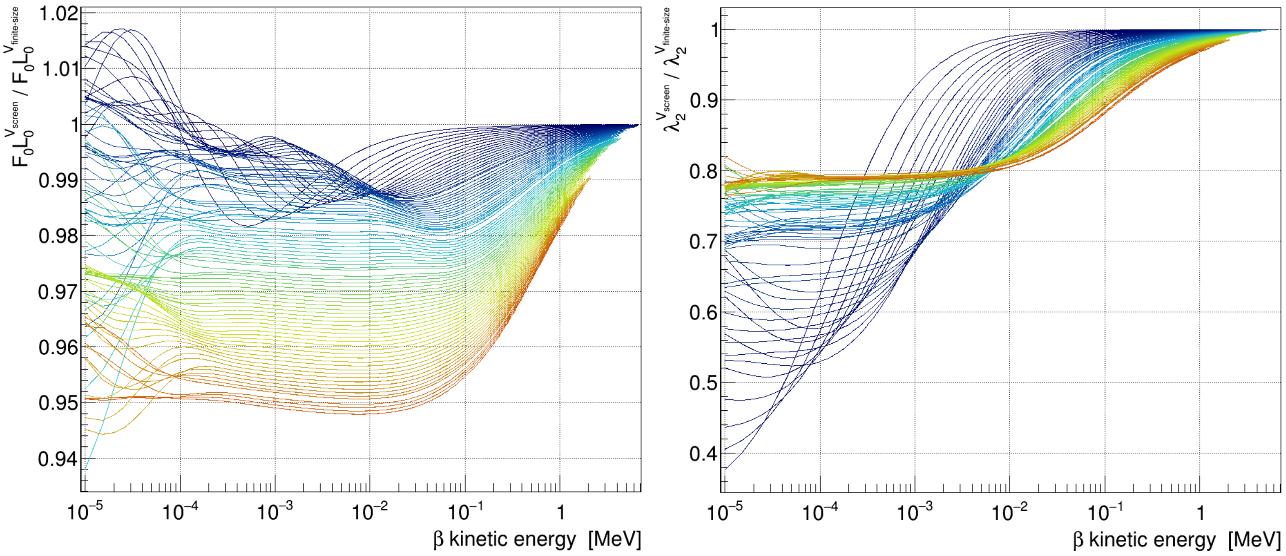

(a) Ratio of Fermi functions.

(b) Ratio of λ_2 functions.

Figure A.2: Ratios of Coulomb functions illustrating the low-energy behavior of the Fermi functions **(a)** and of the λ_2 **(b)** functions due to screening. Coulomb functions at the denominator have been computed for potentials based on finite-size nuclei, while the potentials used for the functions at the numerator also include an atomic screening. The Coulomb functions have been computed with the DIRAC program for all the isotopes in the database [161] and only up to the isotopes Q_β energies. The gradient of color represents the increase of mass and of charge of the nuclei, low-mass nuclei being associated to the dark blue curves and high-mass nuclei with red curves.

accurately interpolated for any energy range. The adaptive "on-the-fly" algorithm works best if the Coulomb function has a low curvature or if it is monotonic in the considered energy window. Should this not be the case, there is a risk to assume that an energy window can be correctly interpolated while it is not.

The "on-the-fly" algorithm has been applied in DIRAC by using a linear interpolation over each energy window. The interpolation is considered to be accurate if the relative difference at the middle point is inferior to $10^{-4}\%$. It has been verified that the bias induced in BESTIOLE is indeed inferior to $10^{-4}\%$ if a linear or a second order polynomial interpolation is used in BESTIOLE. When the tolerance condition is met for an energy window, the limits of the next energy window are defined such that the new upper limit is equal to the former lower limit, and the new lower limit is equal to half of the new upper limit. With this setting, the number of tabulated energies increases naturally in the region of lower β energy. To model accurately each Coulomb function, the tolerance criterion should be evaluated in each case. In practice, the tolerance criterion has been verified only for the Fermi functions, as they are the ones with the finest behaviors at low β energy compared to the λ_k functions as seen in Fig. A.2. It has been verified that the tabulated energies in that case allow to reproduce the λ_k functions with a similar degree of accuracy. However, this was not done for Coulomb functions unused in this work. Finally, Coulomb tables generated with threshold energy steps have been used to verify that the "on-the-fly" algorithm correctly works and does not miss any fine behavior.

B

List of priority for Total Absorption γ-ray Spectroscopy measurements

To improve the calculations of decay heat and reactor spectra, two meetings were held in 2009 [305] and 2014 [300] following the recommendations of the Subgroup 25 of the OECD-NEA Working Party on International Evaluation Cooperation of the Nuclear Science Committee. During these meetings, potential candidates to the Pandemonium effect have been identified. The candidate isotopes have been sorted in prioritizing order to be measured (or remeasured) with the Total Absorption γ-ray Spectroscopy (TAGS) technique. This list has been reproduced below.

The priority order discussed in [300, 305] in the context of reactor $\bar{\nu}_e$ spectra is reported in the ”TAGS” column. The ”IBD”, ”CEνNS” and ”$\bar{\nu}_e$” columns indicate the isotope contribution in percent to an IBD flux, a CEνNS flux or a reactor $\bar{\nu}_e$ flux corresponding to ^{235}U. Ranks are indicated in brackets and have been obtained by computing the fluxes with the 2021 version of the BESTIOLE software and with cumulative fission yields from the JEFF-3.3 database [136]. The CEνNS flux has been computed for a germanium detector with a 20 eV recoil energy threshold. Available TAGS measurements of these isotopes are reported in the ”Source” column. If several sources are listed for a given isotope, the first reference is the one included in the 2021 BESTIOLE database.

Radionuclide	Contribution [%] and priority order				Source	Comment
	TAGS	IBD	CEνNS	$\bar{\nu}_e$		
^{76}Ga		1.36E-03 (306)	1.33E-03 (335)	6.64E-04 (404)	[330]	
^{85}Se		3.86E-01 (73)	3.56E-01 (83)	1.74E-01 (136)		
^{86}Se		1.39E-01 (110)	1.79E-01 (109)	1.67E-01 (142)		
^{84}Br		1.18E-01 (115)	1.38E-01 (124)	1.63E-01 (143)	[331]	
^{85}Br		3.53E-02 (157)	1.11E-01 (131)	2.15E-01 (131)	[331]	
^{86}Br		6.53E-01 (45)	5.63E-01 (57)	2.85E-01 (120)	[332] [331, 333]	
^{87}Br		2.86E-01 (85)	2.93E-01 (92)	3.02E-01 (115)	[334]	
^{88}Br		5.18E-01 (56)	4.64E-01 (67)	2.27E-01 (127)	[334]	

Table B.1 continued from previous page

Radionuclide	Priority				Source	Comment
	TAGS	IBD	CEνNS	$\bar{\nu}_e$		
^{89}Br		4.96E-01 (61)	4.45E-01 (68)	1.71E-01 (137)		Tengblad's data
^{90}Br		3.35E-01 (78)	2.78E-01 (95)	8.02E-02 (171)		Tengblad's data
^{87}Kr		3.11E-01 (81)	4.43E-01 (70)	4.23E-01 (96)		Tengblad's data
^{89}Kr		1.57E-01 (101)	2.41E-01 (101)	7.30E-01 (64)	[333]	Tengblad's data
^{90}Kr		5.12E-01 (58)	7.50E-01 (44)	7.76E-01 (61)	[333]	
^{91}Kr	2	1.77E+00 (11)	1.56E+00 (16)	5.36E-01 (83)		Tengblad $\simeq$ ENSDF
^{94}Kr		1.66E-01 (99)	1.31E-01 (125)	2.97E-02 (215)	[335]	
^{88}Rb	1	1.58E+00 (14)	1.45E+00 (18)	5.82E-01 (79)		
^{89}Rb		3.02E-01 (83)	4.27E-01 (72)	7.76E-01 (62)	[302] [333]	
^{90}Rb	1	1.91E+00 (9)	1.64E+00 (11)	6.95E-01 (70)	[302] [333]	
^{90}Rb^{m}		1.08E-01 (117)	1.65E-01 (114)	2.21E-01 (129)	[302] [333]	
^{91}Rb		1.06E+00 (31)	1.12E+00 (27)	8.91E-01 (51)	[332] [302, 336]	
^{92}Rb	1	6.74E+00 (1)	4.69E+00 (1)	7.19E-01 (65)	[281] [337]	
^{93}Rb	1	2.06E+00 (8)	1.69E+00 (10)	5.48E-01 (81)	[281] [302]	
^{94}Rb	2	1.27E+00 (25)	1.01E+00 (32)	2.62E-01 (125)	[334]	
^{95}Rb		6.25E-01 (47)	5.20E-01 (61)	1.40E-01 (153)	[338] [283]	
^{89}Sr		-	6.36E-02 (150)	7.78E-01 (60)		
^{92}Sr		3.98E-04 (362)	9.27E-03 (237)	9.92E-01 (26)		
^{93}Sr		1.52E-01 (103)	3.39E-01 (86)	1.05E+00 (12)	[302]	Unresolved energies
^{94}Sr		2.65E-02 (169)	2.77E-01 (96)	1.01E+00 (22)	[336] [302]	
^{95}Sr	1	2.09E+00 (7)	1.93E+00 (8)	8.76E-01 (53)	[302]	
^{96}Sr	1	1.29E+00 (23)	1.38E+00 (22)	6.62E-01 (71)		Tengblad's data
^{97}Sr	2	1.11E+00 (30)	9.78E-01 (33)	3.11E-01 (113)		Tengblad's data
^{93}Y		3.62E-01 (76)	7.65E-01 (43)	1.06E+00 (9)		
^{94}Y	1	1.89E+00 (10)	2.00E+00 (7)	1.05E+00 (11)	[302]	
^{95}Y	1	1.31E+00 (20)	1.40E+00 (21)	1.05E+00 (10)	[302]	
^{96}Y	1	5.64E+00 (2)	4.18E+00 (2)	7.66E-01 (63)	[337]	
^{96}Y^{m}		1.94E-01 (95)	2.59E-01 (99)	1.87E-01 (133)		
^{97}Y	2	1.21E+00 (27)	1.04E+00 (30)	3.56E-01 (107)		Tengblad $\simeq$ ENSDF
^{97}Y^{m}	1	1.05E+00 (32)	1.03E+00 (31)	4.13E-01 (99)		Tengblad's data
^{98}Y^{m}	1	1.29E+00 (22)	1.04E+00 (29)	2.68E-01 (124)		
^{99}Y	1	1.30E+00 (21)	1.13E+00 (26)	3.50E-01 (110)	[282]	
^{98}Zr		5.52E-02 (141)	3.39E-01 (85)	9.34E-01 (44)		
^{99}Zr		1.01E+00 (34)	1.34E+00 (23)	9.47E-01 (41)		
^{100}Zr		4.65E-01 (66)	8.28E-01 (40)	8.87E-01 (52)		
^{101}Zr	1	1.75E+00 (12)	1.58E+00 (15)	5.44E-01 (82)		
^{98}Nb	1	1.44E+00 (18)	1.64E+00 (12)	9.37E-01 (43)		
^{98}Nb^{m}	1	4.32E-04 (359)	2.16E-03 (313)	8.66E-03 (257)		
^{99}Nb		4.02E-01 (71)	6.06E-01 (54)	6.55E-01 (73)		Tengblad's data
^{99}Nb^{m}		3.30E-01 (79)	4.24E-01 (75)	3.53E-01 (108)		
^{100}Nb	1	3.53E+00 (3)	3.01E+00 (3)	9.12E-01 (47)	[339] [283]	
^{100}Nb^{m}		1.40E-01 (109)	1.65E-01 (115)	1.02E-01 (164)	[339]	
^{101}Nb	1	1.47E+00 (17)	1.60E+00 (13)	8.06E-01 (57)	[340] [341]	
^{102}Nb	1	9.20E-01 (36)	9.52E-01 (36)	4.42E-01 (93)	[339] [283]	
^{102}Nb^{m}		8.81E-01 (37)	6.75E-01 (47)	1.47E-01 (149)	[339]	
^{104}Nb^{m}	2	2.98E-01 (84)	2.23E-01 (103)	5.48E-02 (193)		
^{101}Mo		2.73E-02 (168)	1.19E-01 (129)	8.52E-01 (55)		
^{103}Mo		3.63E-01 (75)	5.38E-01 (58)	5.07E-01 (87)	[283]	
^{105}Mo		2.73E-01 (88)	2.90E-01 (94)	1.42E-01 (152)	[340] [341]	
^{100}Tc		9.19E-08 (540)	1.64E-07 (583)	1.77E-07 (624)	[342] [283]	
^{102}Tc		1.37E+00 (19)	1.46E+00 (17)	7.06E-01 (68)	[343] [341]	
^{103}Tc		6.77E-02 (132)	2.39E-01 (102)	5.12E-01 (86)	[283]	
^{104}Tc		9.34E-02 (122)	1.68E-01 (113)	3.10E-01 (114)	[343] [341]	
^{105}Tc		1.22E-02 (203)	3.43E-02 (179)	1.55E-01 (147)	[343] [341]	
^{106}Tc		1.38E-01 (111)	1.40E-01 (123)	6.65E-02 (184)	[341]	
^{107}Tc		4.77E-02 (145)	4.86E-02 (164)	2.17E-02 (226)	[341]	
^{107}Ru		6.51E-03 (231)	1.44E-02 (215)	2.28E-02 (225)		
^{106}Rh		4.81E-02 (143)	7.39E-02 (142)	6.74E-02 (182)		

Table B.1 continued from previous page

Radionuclide	Priority				Source	Comment
	TAGS	IBD	CEνNS	$\bar{\nu}_e$		
^{108}Rh		1.49E-02 (198)	1.70E-02 (208)	9.31E-03 (251)		
^{129}Sn^{m}		5.02E-03 (247)	1.57E-02 (212)	6.84E-02 (181)		
^{128}Sb^{m}		2.71E-04 (380)	9.16E-04 (361)	1.90E-03 (343)		
^{129}Sb^{m}		3.68E-03 (259)	1.57E-02 (213)	3.58E-02 (203)		
^{130}Sb		1.79E-02 (183)	5.39E-02 (160)	1.80E-01 (135)		
^{130}Sb^{m}		2.13E-02 (179)	5.94E-02 (155)	1.14E-01 (161)		
^{131}Sb		9.32E-02 (123)	1.76E-01 (110)	4.09E-01 (101)		Tengblad's data
^{132}Sb		5.18E-01 (57)	5.24E-01 (60)	3.15E-01 (112)		
^{132}Sb^{m}		2.55E-01 (90)	2.52E-01 (100)	1.43E-01 (151)		
^{133}Sb		5.96E-04 (340)	2.52E-02 (196)	4.13E-01 (100)		Tengblad's data
^{133}Te		3.42E-02 (159)	1.51E-01 (118)	6.24E-01 (77)		
^{133}Te^{m}		1.53E-02 (193)	3.59E-02 (177)	4.42E-01 (92)		
^{134}Te		-	-	1.15E+00 (2)		
^{135}Te	1	2.54E+00 (6)	2.14E+00 (5)	5.92E-01 (78)		
^{134}I		1.73E-02 (185)	1.63E-01 (117)	1.27E+00 (1)		
^{136}I	2	9.83E-01 (35)	9.65E-01 (34)	4.28E-01 (94)		Tengblad's data
^{136}I^{m}	1	1.02E+00 (33)	9.59E-01 (35)	3.52E-01 (109)		
^{137}I	1	1.63E+00 (13)	1.42E+00 (19)	5.23E-01 (84)	[338] [283]	
^{138}I	2	1.23E+00 (26)	9.39E-01 (38)	2.22E-01 (128)	[282]	
^{139}I		5.07E-01 (60)	4.26E-01 (73)	1.24E-01 (158)		Tengblad's data
^{140}I		6.35E-02 (135)	6.20E-02 (152)	3.22E-02 (210)		Tengblad's data
^{137}Xe		1.16E+00 (29)	1.42E+00 (20)	9.89E-01 (27)	[344]	
^{138}Xe		1.04E-01 (118)	3.04E-01 (88)	1.04E+00 (15)		
^{139}Xe	1	1.51E+00 (15)	1.59E+00 (14)	8.30E-01 (56)	[333]	
^{140}Xe		2.49E-01 (91)	5.01E-01 (62)	6.62E-01 (72)		
^{141}Xe	2	1.29E+00 (24)	1.11E+00 (28)	3.27E-01 (111)		
^{138}Cs	2	5.09E-01 (59)	9.36E-01 (39)	1.09E+00 (5)	[302]	
^{138}Cs^{m}	2	3.89E-03 (255)	6.34E-03 (250)	6.17E-03 (268)	[302]	
^{139}Cs	1	1.48E+00 (16)	1.72E+00 (9)	1.03E+00 (19)	[302]	
^{140}Cs	1	2.59E+00 (5)	2.31E+00 (4)	9.61E-01 (39)	[283] [302]	
^{141}Cs	2	1.20E+00 (28)	1.25E+00 (24)	8.05E-01 (58)	[302]	Unresolved energies
^{142}Cs	1	2.62E+00 (4)	2.04E+00 (6)	4.97E-01 (88)	[282] [337]	
^{139}Ba		7.44E-02 (129)	4.06E-01 (77)	1.04E+00 (16)		
^{141}Ba		1.56E-01 (102)	4.45E-01 (69)	9.63E-01 (35)	[302]	
^{142}Ba		1.32E-03 (307)	3.81E-02 (175)	9.56E-01 (40)	[302] [345]	Unresolved energies
^{143}Ba		4.30E-01 (68)	7.77E-01 (42)	9.43E-01 (42)	[302]	Unresolved energies
^{144}Ba		8.66E-02 (125)	3.44E-01 (84)	8.01E-01 (59)	[302]	Unresolved energies
^{145}Ba		4.90E-01 (63)	5.75E-01 (56)	4.17E-01 (97)	[302]	Unresolved energies,
^{141}La		1.47E-01 (106)	4.99E-01 (63)	9.65E-01 (33)		
^{142}La		5.27E-01 (55)	6.75E-01 (48)	9.61E-01 (38)	[302, 346]	
^{143}La		6.17E-01 (48)	9.50E-01 (37)	9.79E-01 (32)	[302]	Unresolved energies
^{144}La		2.45E-01 (92)	5.27E-01 (59)	8.95E-01 (50)	[302]	
^{145}La		5.59E-02 (140)	2.14E-01 (104)	6.26E-01 (76)	[302]	Unresolved energies
^{146}La	2	7.55E-01 (40)	6.54E-01 (50)	2.59E-01 (126)		Tengblad's data
^{146}La^{m}		3.72E-01 (74)	3.56E-01 (82)	1.37E-01 (154)		
^{145}Ce		1.98E-03 (284)	9.73E-02 (134)	6.51E-01 (75)	[302]	Unresolved energies
^{146}Ce		-	5.80E-05 (467)	4.93E-01 (90)	[302]	Unresolved energies
^{147}Ce		5.62E-02 (139)	1.23E-01 (126)	3.68E-01 (105)	[302]	Unresolved energies
^{148}Ce		8.40E-05 (419)	3.82E-02 (174)	2.72E-01 (123)	[302]	Unresolved energies
^{146}Pr		4.95E-01 (62)	5.99E-01 (55)	4.93E-01 (89)	[302]	
^{147}Pr		9.31E-03 (210)	7.96E-02 (140)	3.70E-01 (104)	[302]	Unresolved energies
^{148}Pr		3.03E-01 (82)	3.38E-01 (87)	2.73E-01 (122)	[302]	
^{148}Pr^{m}		1.70E-03 (295)	2.58E-03 (302)	3.19E-03 (303)	[302]	Unresolved energies
^{149}Pr		2.90E-02 (166)	6.54E-02 (149)	1.68E-01 (141)	[302]	
^{151}Pr		3.03E-02 (165)	4.96E-02 (163)	6.11E-02 (189)	[302]	Unresolved energies
^{149}Nd		-	8.20E-03 (240)	1.69E-01 (139)	[302]	
^{151}Nd		1.86E-03 (289)	1.17E-02 (228)	7.06E-02 (180)	[302]	Unresolved energies
^{152}Nd		-	2.19E-04 (422)	4.17E-02 (201)		

Table B.1 continued from previous page

Radionuclide	Priority				Source	Comment
	TAGS	IBD	CEνNS	$\bar{\nu}_e$		
^{153}Nd		1.20E-02 (205)	2.00E-02 (200)	2.38E-02 (221)	[302]	Unresolved energies
^{154}Nd		1.11E-03 (319)	4.26E-03 (279)	1.16E-02 (245)	[302]	Unresolved energies
^{155}Nd		3.10E-03 (263)	4.54E-03 (273)	4.43E-03 (287)	[302]	Unresolved energies
^{152}Pm		2.84E-02 (167)	4.36E-02 (166)	4.17E-02 (200)	[302]	Unresolved energies
^{153}Pm		3.69E-05 (431)	4.55E-03 (272)	2.41E-02 (219)	[302]	Unresolved energies
^{154}Pm^m		4.18E-05 (429)	1.04E-04 (446)	2.42E-04 (452)	[302]	Unresolved energies
^{155}Pm		1.65E-03 (298)	3.46E-03 (288)	4.98E-03 (278)	[302]	Unresolved energies
^{156}Pm		1.22E-03 (316)	1.94E-03 (319)	2.09E-03 (334)	[302]	Unresolved energies
^{157}Pm		9.10E-04 (330)	1.14E-03 (346)	8.26E-04 (390)	[302]	Unresolved energies
^{157}Sm		1.26E-04 (403)	4.48E-04 (395)	1.09E-03 (381)	[302]	Unresolved energies
^{158}Sm		2.23E-08 (561)	2.66E-05 (476)	3.16E-04 (443)	[302]	Unresolved energies
^{158}Eu		4.13E-05 (430)	1.20E-04 (439)	3.22E-04 (442)	[302]	Unresolved energies

Table B.1: List of candidates to the Pandemonium effect and their contributions in percent to ^{235}U IBD flux, CEνNS flux and $\bar{\nu}_e$ flux. The "Unresolved energies" comment refers to Greenwood's data (see Sec. 4.1.2.2 for more details). The "Tengblad's data" comment indicates a measurement in [307] (see Sec. 4.1.2.3 for more details), and "Tengblad $\simeq$ ENSDF" means that the β spectra from Tengblad's data and from ENSDF data are consistent with each other.

C

Propagation of the uncertainties

Contents

C.1 Analytical uncertainty propagation

Uncertainties can be analytically propagated with the Jacobian matrix formalism, using for instance the formalism from [347]. Any differentiable function f of d variables $x_{k\leq d}$ can be Taylor-expanded at first order around $\{x_1^0, \cdots, x_d^0\}$.

$$f(x_1, ..., x_d) \simeq f(x_1^0, \cdots, x_d^0) + \sum_{k\leq d} \left.\frac{\partial f}{\partial x_k}\right|_{x_k^0} (x_k - x_k^0). \tag{C.1}$$

For a vector-valued function $\boldsymbol{f}$ with n components, the matrix notation of Eq. C.1 is

$$\boldsymbol{f}(\boldsymbol{x}) \simeq \boldsymbol{f}(\boldsymbol{x}^0) + J\left(\boldsymbol{x} - \boldsymbol{x}^{\mathbf{0}}\right), \tag{C.2}$$

where $\boldsymbol{x}$ and $\boldsymbol{x}^0$ are d-dimensional column vectors and J is the Jacobian matrix evaluated at $\boldsymbol{x}^0$. The Jacobian matrix is defined as the matrix of the first order derivative of the function:

$$J = \begin{pmatrix} \frac{\partial f_1}{\partial x_1} & \cdots & \frac{\partial f_1}{\partial x_d} \\ \vdots & \ddots & \vdots \\ \frac{\partial f_n}{\partial x_1} & \cdots & \frac{\partial f_n}{\partial x_d} \end{pmatrix}. \tag{C.3}$$

A spectrum computed with n energy bins can be considered as a n-dimensional function $\boldsymbol{S}$, where the value of each energy bin is a function of d variables $x_{k\leq d}$:

$$\boldsymbol{S} = \begin{pmatrix} S_1(x_1, \cdots, x_d) \\ \cdots \\ S_n(x_1, \cdots, x_d) \end{pmatrix}. \tag{C.4}$$

The covariance matrix V between the d variables is given by:

$$V = \begin{pmatrix} \sigma_1^2 & \rho_{12}\sigma_1\sigma_2 & \cdots & \rho_{1d}\sigma_1\sigma_d \\ \rho_{12}\sigma_1\sigma_2 & \sigma_2^2 & \cdots & \rho_{2d}\sigma_1\sigma_2 \\ \vdots & \vdots & \ddots & \vdots \\ \rho_{1d}\sigma_1\sigma_d & \rho_{2d}\sigma_1\sigma_2 & \cdots & \sigma_d^2 \end{pmatrix}, \tag{C.5}$$

where $\sigma(x_k) \equiv \sigma_k$ is the uncertainty on x_k and ρ_{kl} is the correlation between x_k and x_l. The covariance matrix Σ associated to the spectrum $\boldsymbol{S}$ is then given by

$$\Sigma = JVJ^t, \tag{C.6}$$

with J^t the transpose of the Jacobian matrix. When the sources of uncertainty are independent, the covariance matrices of each uncertainty source and associated to the spectrum can be computed separately. The total covariance matrix of the spectrum is then given as the sum of the covariance matrix of each source.

This propagation method is appropriated when the first partial derivatives are expressed in relatively simple terms, for instance when the spectrum is a linear function of the variable. The computation time required for this method is negligible, which make it the method of uncertainty propagation of choice. However, it is limited by the requirement that the expansion Eq. C.1 should be correct at first order with negligible higher-order terms.

C.2 Monte-Carlo uncertainty propagation

When additional constrains needs to be included in the covariance matrix, when higher order terms are required in the Jacobian approach, or when the partial derivatives cannot be easily derived, uncertainties can be propagated with a Monte-Carlo (MC) simulation as described for instance in [348]. The drawback is that it costs in computation time, and that the generated uncertainties are associated to randomly generated variables.

The MC is an iterative approach where two variables x_k and x_l are drawn randomly from their distribution at each iteration. The covariance $V(x_k, x_l) \equiv V_{kl}$ between x_k and x_l is then given by

$$V_{kl} = \langle x_k x_l \rangle - \langle x_k \rangle \langle x_l \rangle, \tag{C.7}$$

where the brackets represent the average over the number of iterations. If x_k follows a Gaussian distribution $\mathcal{N}(\mu_k, \sigma_k^2)$, considering the Bessel's correction for an unbiased estimator and considering that $\langle x_k \rangle \simeq \mu_k$, Cochran's theorem states that the x_k variance $V_{kk} = \sigma_k^2$ follows a χ^2 distribution with $c-1$ degrees of freedom after c iterations of the MC. The uncertainty on V_{kk} is then given by

$$\sigma(V_{kk}) = \sqrt{\frac{2}{c-1}}\sigma_k^2. \tag{C.8}$$

If a second variable x_l follows a Gaussian distribution $\mathcal{N}(\mu_l, \sigma_l^2)$, then the uncertainty on the covariance $V_{kl} = \rho_{kl}\sigma_k\sigma_l$ between x_k and x_l after c iterations is given by

$$\sigma(V_{kl}) = \sqrt{\frac{V_{kl}^2 + V_{kk}V_{ll}}{c-1}} = \sqrt{\frac{1 + {}^1\!/_{\rho_{kl}^2}}{c-1}}\, |\rho_{kl}|\, \sigma_k\sigma_l \tag{C.9}$$

In both cases, the uncertainties on the covariance matrix values decrease with the inverse square root of the number of iterations. The precision on the covariance matrix values generated with a MC can then be inferred by the number of iterations in the MC.

$$\left|\frac{\sigma(V_{kl})}{V_{kl}}\right| = \sqrt{\frac{1+{}^{1}/_{\rho_{kl}^2}}{c-1}} \qquad \Longrightarrow \qquad c = 1 + \frac{10^4}{p^2}\left(1+\frac{1}{\rho_{kl}^2}\right) \tag{C.10}$$

where $p = 100\left|\frac{\sigma(V_{kl})}{V_{kl}}\right|$ is the precision in percent.

D

Statistical analysis to compare reactor antineutrino spectra

A χ^2 test can be used to quantify the discrepancies between a measured spectrum S_m and a predicted spectrum S_p each composed of n energy bins, taking in to account their corresponding covariance matrices V_m and V_p [158, 164, 194]. The χ^2 value associated to two spectra is defined as:

$$\chi^2 = \sum_{i,j} \left[S_m(E_i) - S_p(E_i)\right] \left(V_{tot}^{-1}\right)_{ij} \left[S_m(E_j) - S_p(E_j)\right] \equiv \sum_{i,j} \chi^2_{ij} \tag{D.1}$$

where E_i is the energy bin i, and $V_{tot} = V_m + V_p$. The χ^2 value can then be compared to a χ^2 distribution with n degree of freedom, $\chi^2(n)$. The right-tailed p-value associated to the χ^2 value is defined as the integral of $\chi^2(n)$ between χ^2 and infinity. The p-value indicates that there is a $p\%$ probability of observing a measured spectrum S_m at least this discrepant from the prediction S_p, assuming the prediction is correct. The usual p-values used in statistical analysis are 68.27%, 95.45%, 99.73%, 99.99% and 99.9999%. They are commonly referred to as deviations at the level of respectively 1σ, 2σ, 3σ, 4σ and 5σ.

The local significance of the deviations between the data and the model over an energy window W containing k energy bins can be quantify by adding free parameters α_i on the energy bins in W. The value χ^2_{min} is then computed as:

$$\chi^2_{\text{min}} = \sum_{i,j} \Delta_i \left(V_{tot}^{-1}\right)_{ij} \Delta_j, \tag{D.2}$$

where $\Delta_i = S_m(E_i) \times \alpha_i - S_p(E_i)$ for $E_i \in W$ and $\Delta_i = S_m(E_i) - S_p(E_i)$ otherwise. This allows the data points to float toward the model and to minimize the χ^2 value. The value $\Delta\chi^2_W = \chi^2 - \chi^2_{\text{min}}$ then quantities the deterioration of the agreement between the data and the model when the data in W are at their measured value instead of free-floating. The impact of the energy window on the overall agreement is thus estimated. A local p-value can be computed from $\Delta\chi^2_W$ by comparing it to a χ^2 distribution with k degree of freedom, and quantifies the discrepancy between the data and the model in the energy window.

E

Summation modeling of the fission spectra of ^{235}U, ^{238}U, ^{239}Pu and ^{241}Pu

Contents

E.1 Fission spectra and details of the correlations between the energy bins

The $\bar{\nu}_e$ fission spectra of ^{235}U, ^{238}U, ^{239}Pu and ^{241}Pu computed with the 2021 version of the BESTIOLE software are presented with energy bins of 25 keV width. Fractional uncertainties associated to the different uncertainty sources listed in Tab. 5.1 are shown along with the corresponding correlation matrices. The uncertainty propagation for each source is detailed in Sec. 4.2.

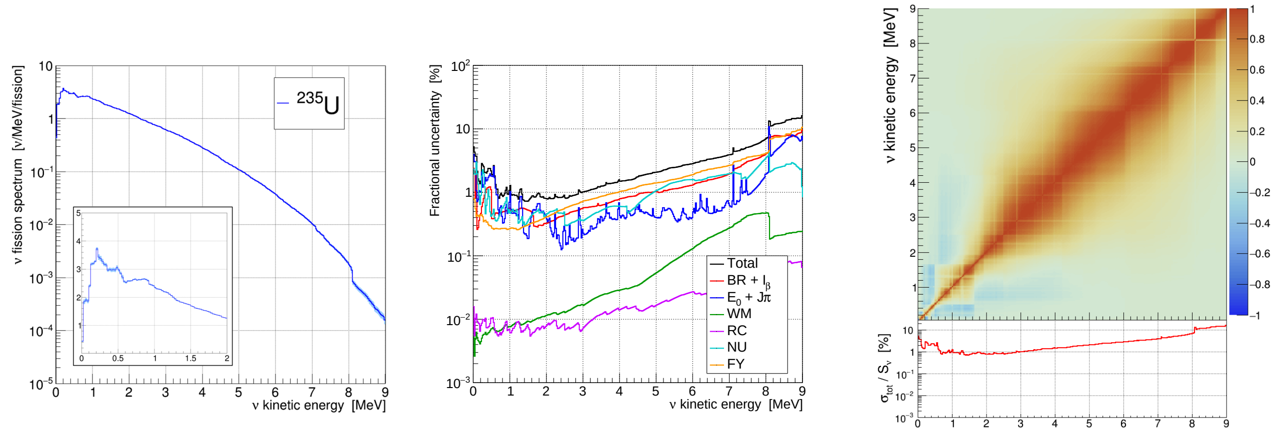

(a) Fission spectrum. **(b)** Fractional uncertainties. **(c)** Total correlation matrix.

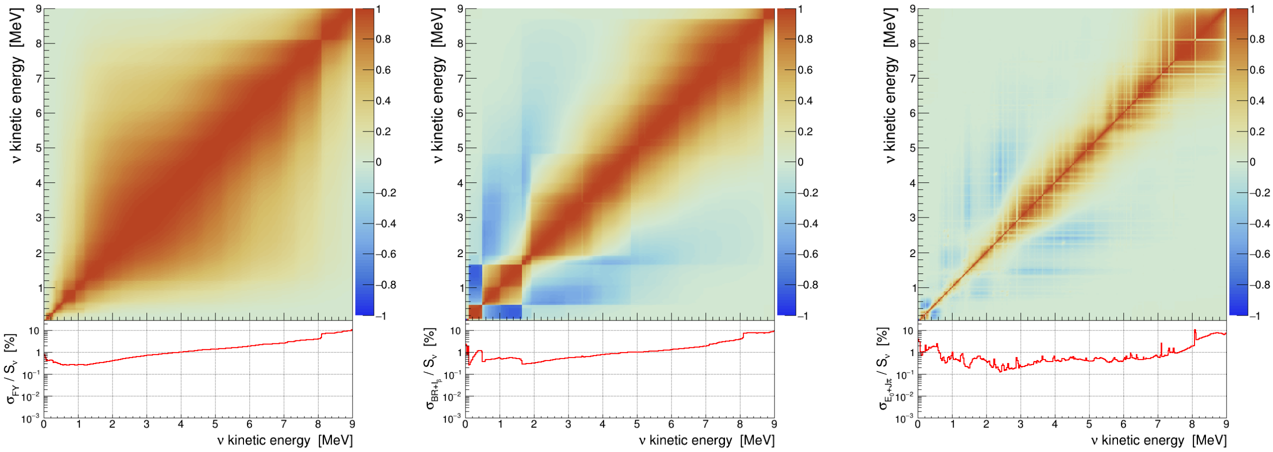

(d) FY. **(e)** BR and I_β. **(f)** E_0 and $J\pi$.

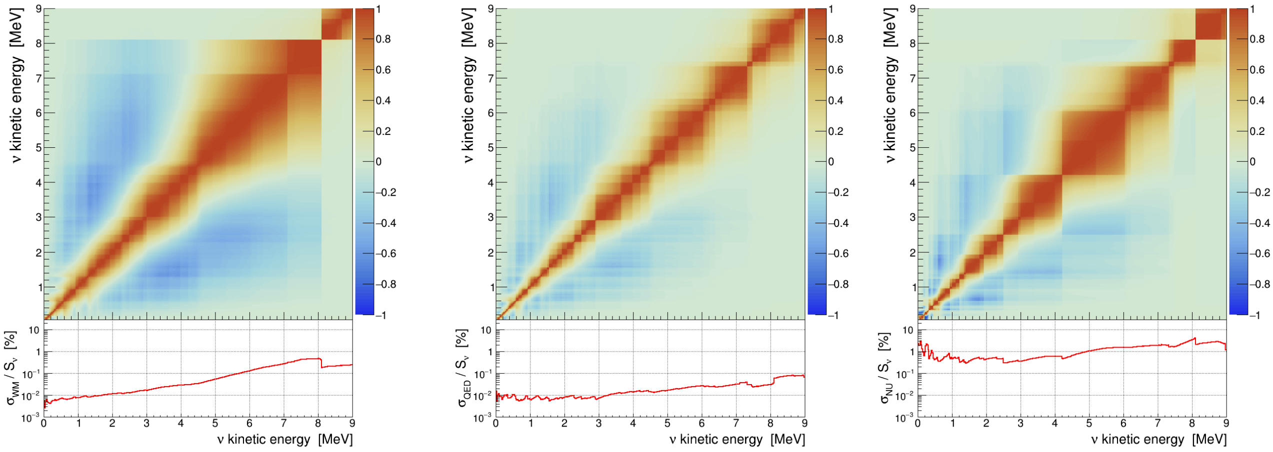

(g) WM. **(h)** RC. **(i)** NU.

Figure E.1: ^{235}U fission spectrum, fractional uncertainties and correlation matrix per uncertainty source. The inset in the plot **(a)** zooms in the region below 2 MeV. The uncertainties are induced by nuclear data uncertainties (FY: fission yield, BR: branching ratio, I_β: β^- intensity, E_0: endpoint energy, $J\pi$: spin-parity) and modeling uncertainties (WM: weak magnetism, RC: radiative correction, NU: modeling of non-unique transitions).

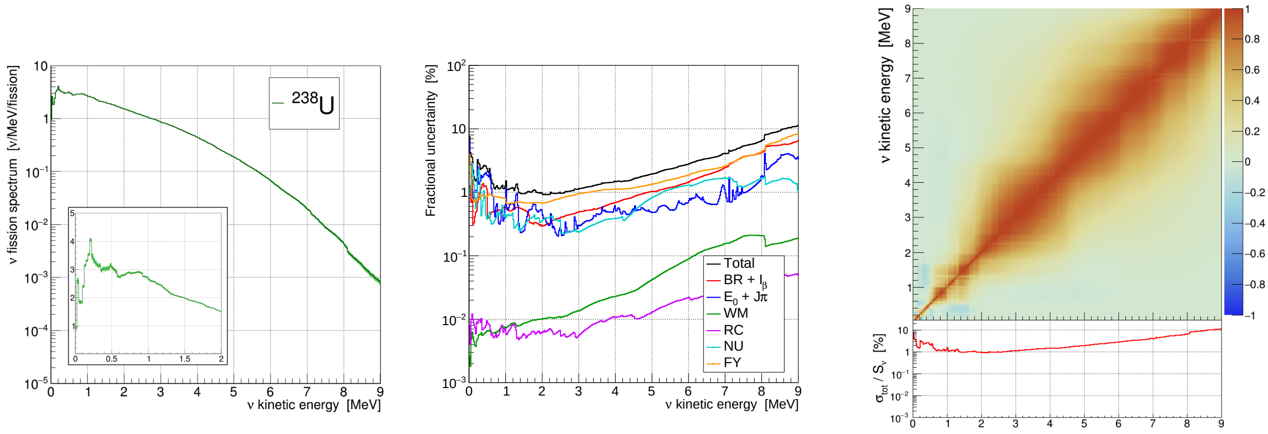

(a) Fission spectrum.

(b) Fractional uncertainties.

(c) Total correlation matrix.

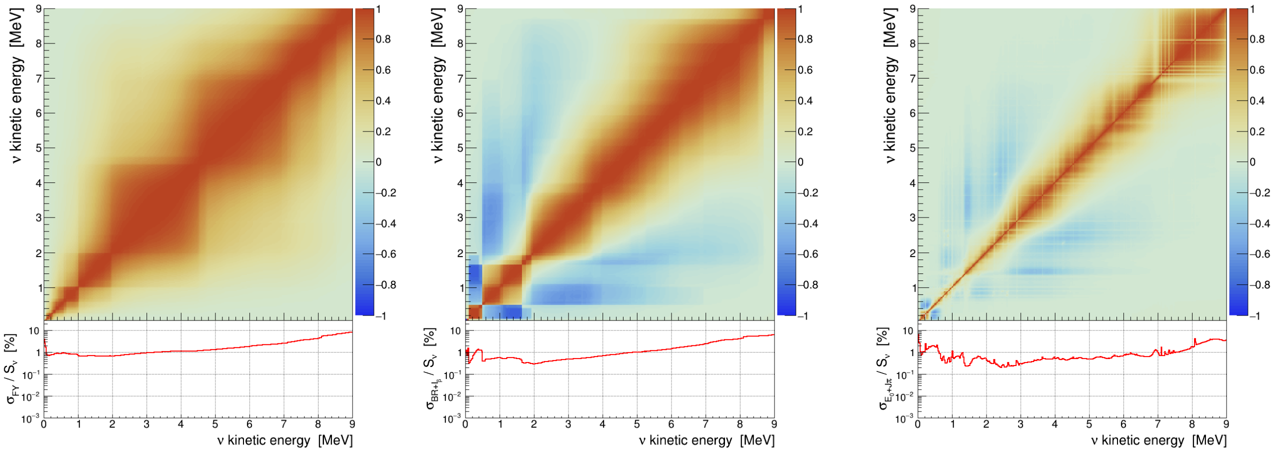

(d) FY.

(e) BR and I_β.

(f) E$_0$ and $J\pi$.

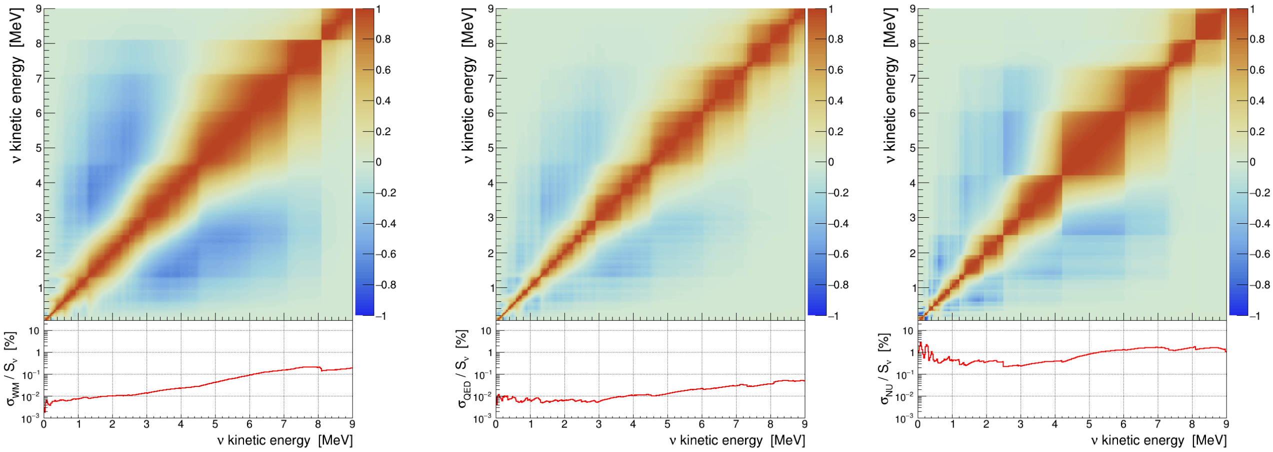

(g) WM.

(h) RC.

(i) NU.

Figure E.2: ^{238}U fission spectrum, fractional uncertainties and correlation matrix per uncertainty source. The inset in the plot **(a)** zooms in the region below 2 MeV. The uncertainties are induced by nuclear data uncertainties (FY: fission yield, BR: branching ratio, I_β: β^- intensity, E$_0$: endpoint energy, $J\pi$: spin-parity) and modeling uncertainties (WM: weak magnetism, RC: radiative correction, NU: modeling of non-unique transitions).

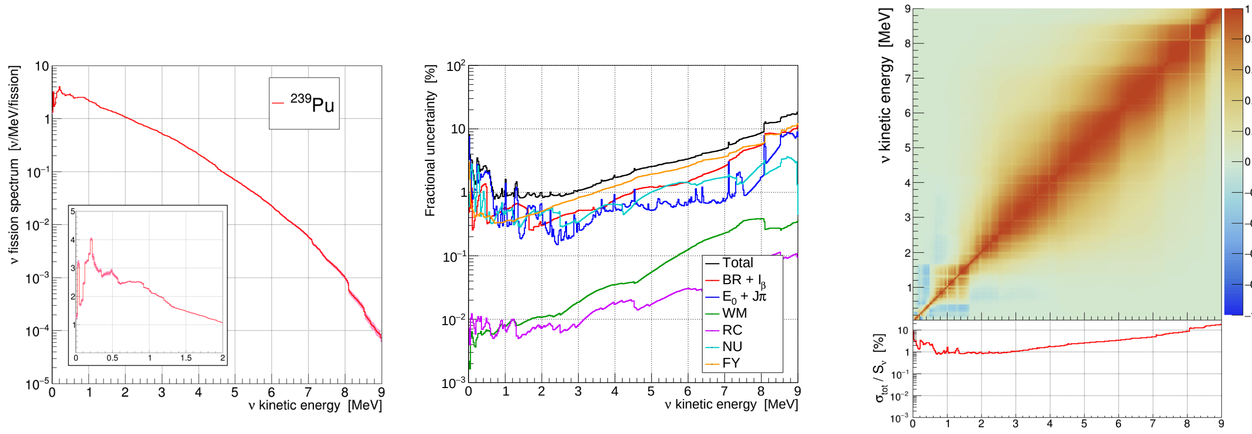

(a) Fission spectrum.

(b) Fractional uncertainties.

(c) Total correlation matrix.

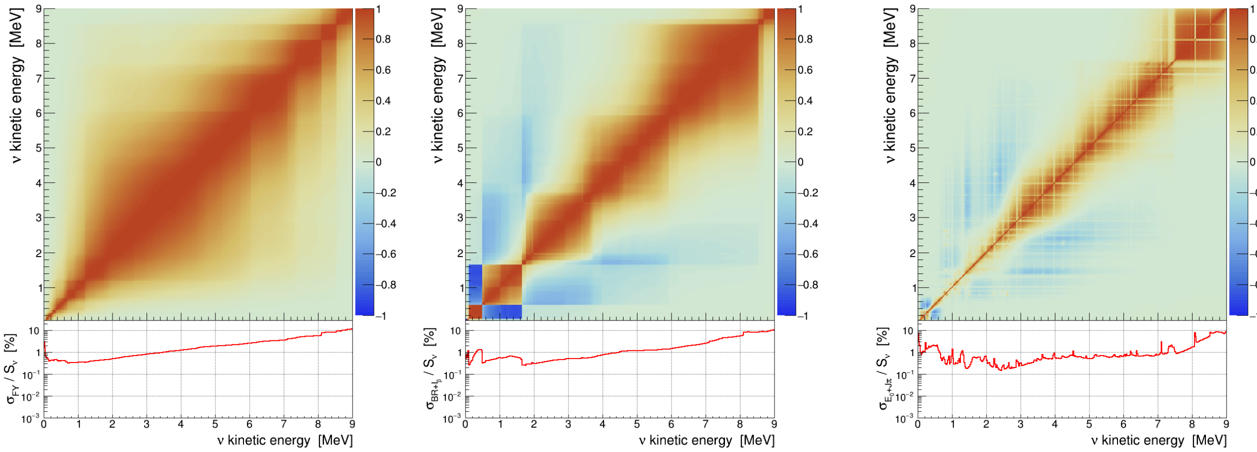

(d) FY.

(e) BR and I_β.

(f) E_0 and $J\pi$.

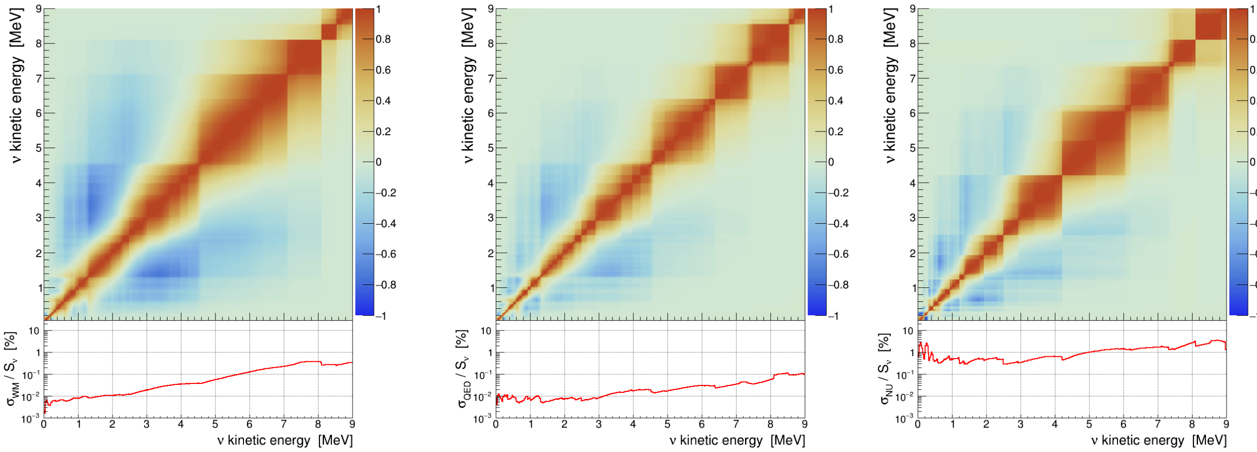

(g) WM.

(h) RC.

(i) NU.

Figure E.3: ^{239}Pu fission spectrum, fractional uncertainties and correlation matrix per uncertainty source. The inset in the plot **(a)** zooms in the region below 2 MeV. The uncertainties are induced by nuclear data uncertainties (FY: fission yield, BR: branching ratio, I_β: β^- intensity, E_0: endpoint energy, $J\pi$: spin-parity) and modeling uncertainties (WM: weak magnetism, RC: radiative correction, NU: modeling of non-unique transitions).

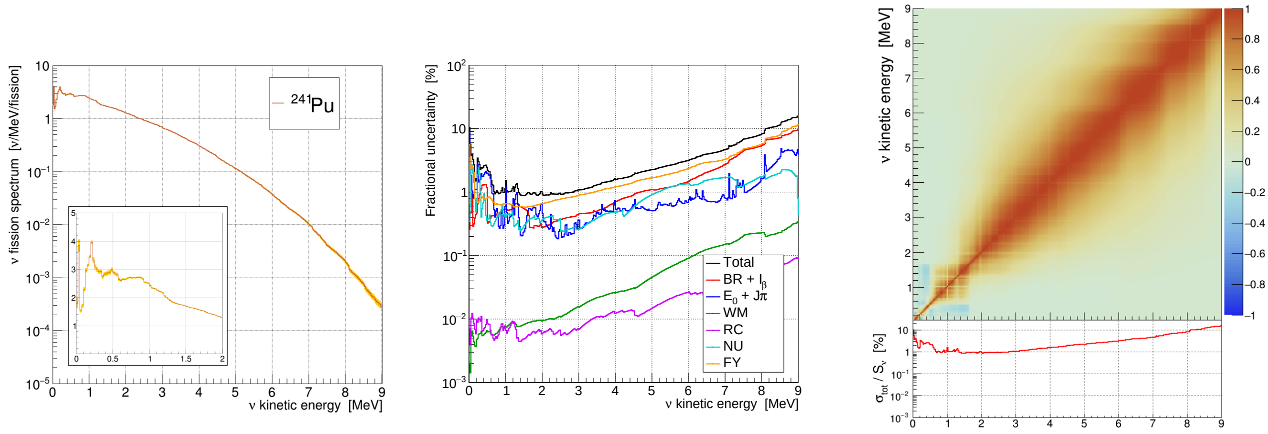

(a) Fission spectrum. **(b)** Fractional uncertainties. **(c)** Total correlation matrix.

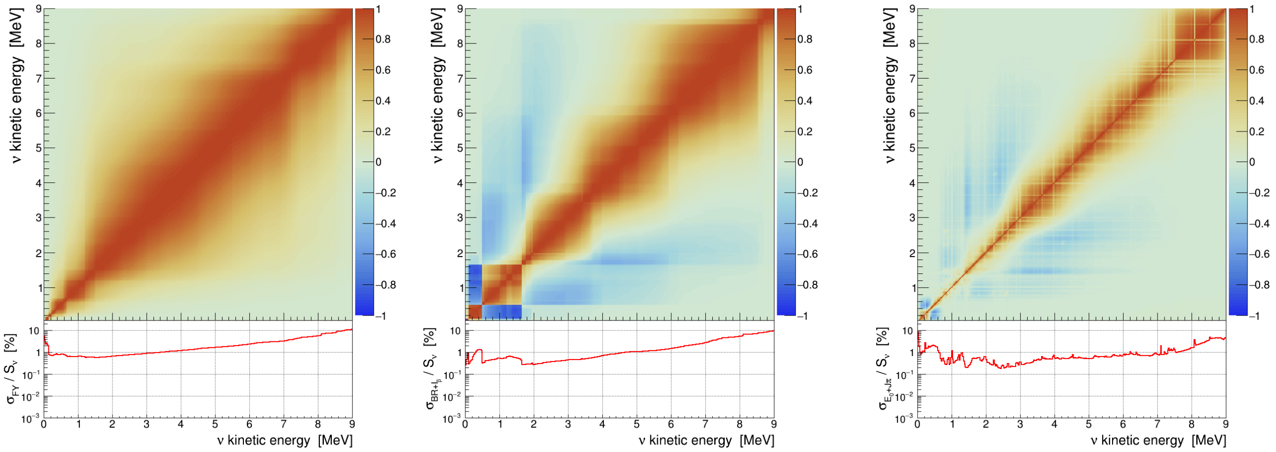

(d) FY. **(e)** BR and I_β. **(f)** E_0 and $J\pi$.

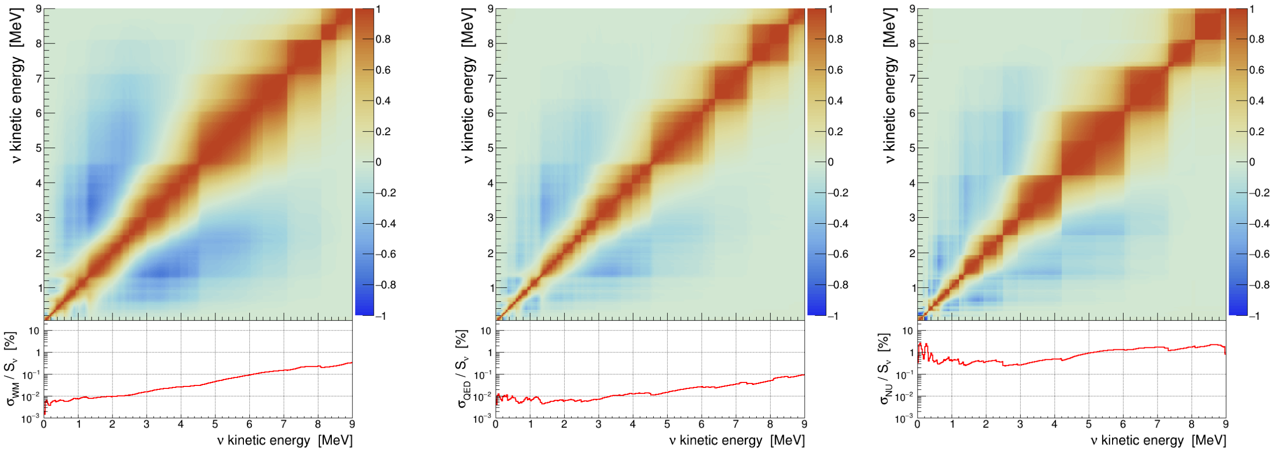

(g) WM. **(h)** RC. **(i)** NU.

Figure E.4: ^{241}Pu fission spectrum, fractional uncertainties and correlation matrix per uncertainty source. The inset in the plot **(a)** zooms in the region below 2 MeV. The uncertainties are induced by nuclear data uncertainties (FY: fission yield, BR: branching ratio, I_β: β^- intensity, E_0: endpoint energy, $J\pi$: spin-parity) and modeling uncertainties (WM: weak magnetism, RC: radiative correction, NU: modeling of non-unique transitions).

E.2 Correlation between the actinide spectra due to the summation modeling

Numerous fission product spectra enter the composition of several of the actinide fission spectra. As such, the spectrum of a fission product p is fully correlated between the different fission spectra. The covariance matrix between the actinides f_1 and f_2 resulting from the superimposition of hundreds of fission product spectra is then given by

$$V^{FP}_{f_1 f_2} = \sum_p \mathcal{Y}^{f_1}_p \mathcal{Y}^{f_2}_p V_p, \tag{E.1}$$

where $\mathcal{Y}^{f_i}_p$ is the fission yield of the fission product p associated to the actinide f_i and V_p is the total covariance matrix of the fission product p computed with the 2021 version of the BESTIOLE software. The resulting correlation matrices between the four actinides are presented in Fig. E.5.

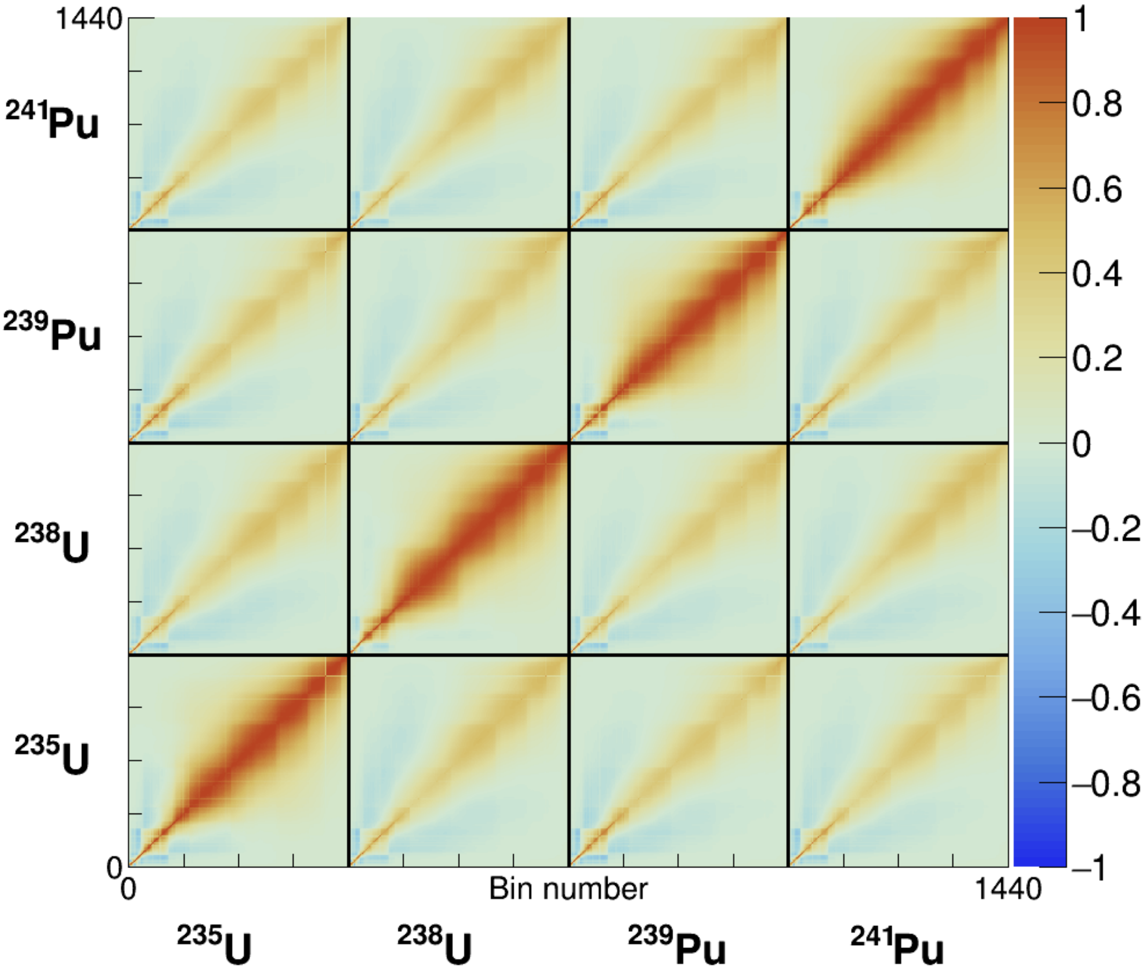

Figure E.5: Correlation matrices between ^{235}U, ^{238}U, ^{239}Pu and ^{241}Pu fission spectra (from left to right and from bottom to top) induced by the correlation of individual fission product spectra shared between the fission spectra. Each correlation matrix is made of 360 × 360 energy bins with 25 keV width and ranges from 0 MeV to 9 MeV.

F

Modeling of $\bar{\nu}_e$ spectra from activated elements

Contents

The $\bar{\nu}_e$ spectra of the most important activated elements contributing to PWR and research reactor spectra computed with the 2021 version of the BESTIOLE software are presented. The spectra are normalized to the β^- intensity of the parent nucleus. The fractional uncertainties per uncertainty source are also presented, along with the total correlation matrix of the isotope spectrum. The correlations evaluated between the branching ratios in order to maximize the uncertainty on the isotope IBD yield are shown (see Sec. 4.2.2 for the details about the method). For simplicity, a transition between the parent nuclear state and an energy level of the daughter nucleus at x MeV will be referred to as a ”x MeV transition”.

F.1 Spectrum and uncertainties of ^{239}U

The main β-decays of ^{239}U have completely known spin-parity data, as shown in Tab.F.1. The ^{239}U spectrum is dominated by the 74 keV transition which is a non-unique forbidden transition that does not satisfy the ξ-approximation. The uncertainty derived for the modeling of this non-unique forbidden transition dominates as shown in Fig. F.1b. The sharp decrease of the fractional uncertainty observed around 0.8 MeV corresponds to the anchor point of the 74 keV transition, which is the energy where the uncertainty associated to the modeling of the non-unique forbidden transition is minimal. The total correlation matrix in Fig. F.1d is then almost entirely induced by the uncertainty on the modeling of the non-unique forbidden transitions, except above 1.2 MeV where the dominant transitions are allowed.

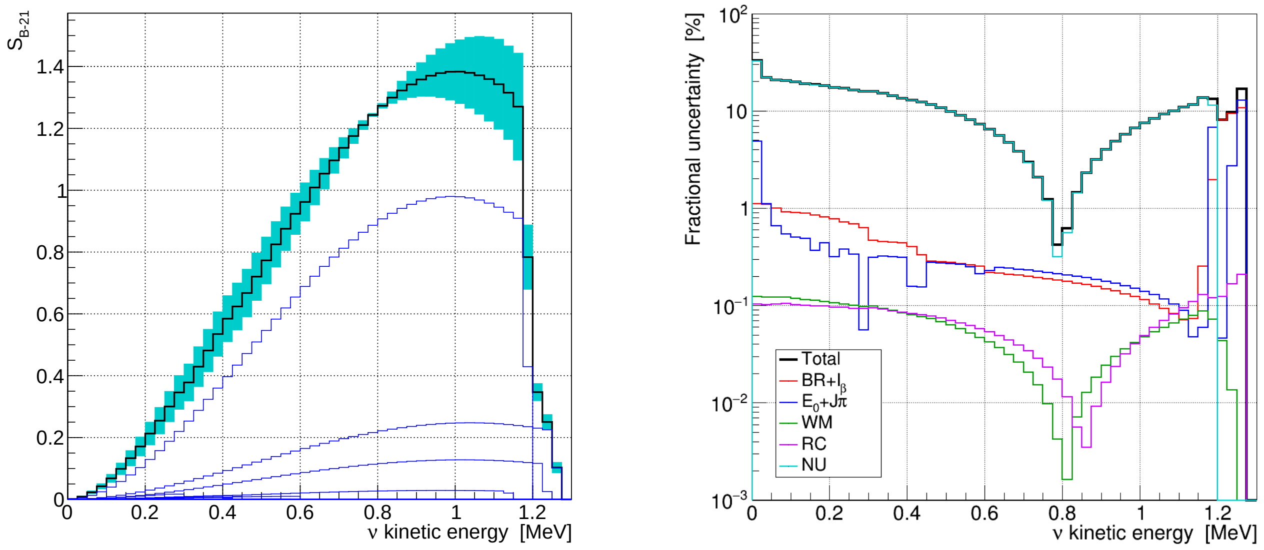

(a) ^{239}U $\bar{\nu}_e$ spectrum. **(b)** Fractional uncertainties.

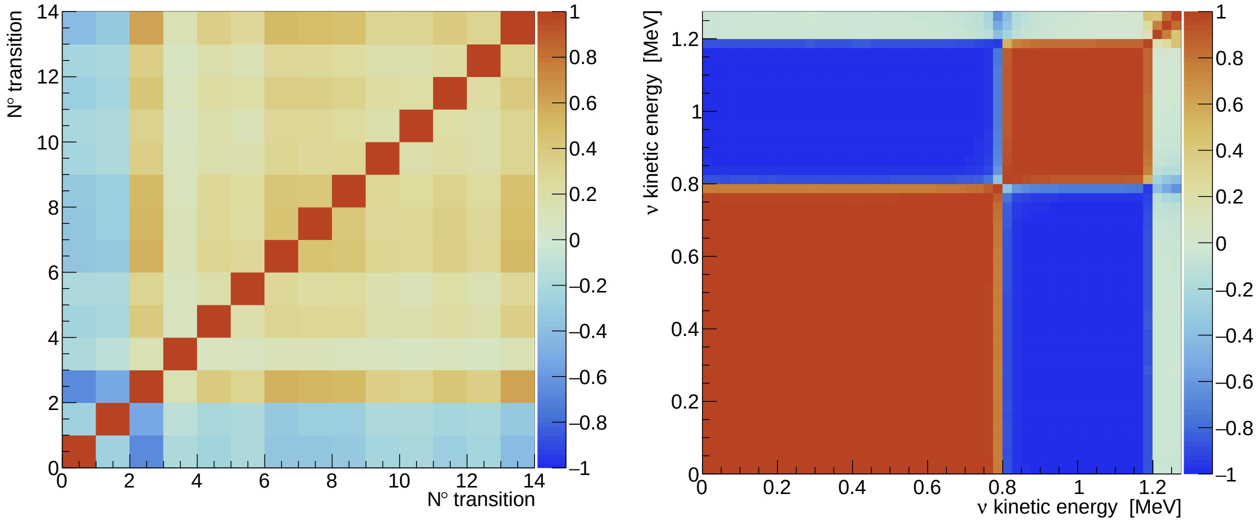

(c) Correlations between BR. **(d)** $\bar{\nu}_e$ spectrum correlation matrix.

Figure F.1: **(a)** ^{239}U $\bar{\nu}_e$ spectrum. The black line represents the isotope spectrum, while the blue lines represent each transition spectrum. The total uncertainty is displayed as a cyan band on the isotope spectrum. **(b)** Fractional uncertainties associated to the different uncertainty sources (BR: branching ratio, I_β: β^- intensity, E$_0$: endpoint energy, $J\pi$: spin-parity, WM: weak magnetism, QED: radiative correction, NU: modeling of non-unique forbidden transition). **(c)** Correlations between the branching ratios maximizing the ^{239}U IBD yield. The ordering of the transitions follows the one from Tab.F.1, the first one being the transition to the ground-state and so on. **(d)** Correlation matrix of the ^{239}U $\bar{\nu}_e$ spectrum.

The 844 keV and 1040 keV transitions have two possible spin-parity couples, which result in each case in the same forbiddenness degree. The 844 keV transition is either a Fermi or a Gamow-Teller transition (differing only by their weak magnetism correction) and the 1040 keV transition is a non-unique transition satisfying the ξ-approximation. These two transitions then do no have a spin-parity uncertainty. The final spin-parity states of the 1013 and 1197 keV transitions are unknown and are modeled as allowed transitions. Nonetheless, an uncertainty is induced by considering the possibility that they are 1st, 2nd or 3rd first unique forbidden transitions (see Sec. 4.2.4).

The null I_β uncertainty induces anticorrelations between the highest branching ratios associated to the ground-state transition, to the 31 keV transition and to the 74 keV transition, as displayed in Fig. F.1c. The branching ratios of the ground-state transition and of the 31 keV transition are also slightly anticorrelated with those of other transitions, while the transition to the 74 keV energy level and the rest of the transitions have slightly correlated branching ratios.

^{239}U				$\longrightarrow$	^{239}Np		
Q_β (keV)	I_β (%)	$J\pi$	$T_{1/2}$		E_{lvl} (keV)	BR (%)	$J\pi$
1261.663 ± 1.494	100	5/2+	23.45 ± 0.02 min		0	18.7 ± 2.4	5/2+
					31.131 ± 0.001	9.4 ± 1.9	7/2+
					74.664 ± 0.001	69 ± 1.4	5/2−
					117.71 ± 0.020	1.96 ± 0.24	7/2−
					662.258 ± 0.015	0.3 ± 0.02	5/2−
					695.097 ± 0.040	0.049 ± 0.004	7/2−
					819.206 ± 0.018	0.27 ± 0.01	7/2
					844.069 ± 0.015	0.26 ± 0.01	5/2, 7/2
					964.205 ± 0.017	0.24 ± 0.01	7/2−
					992.047 ± 0.030	0.027 ± 0.002	7/2−
					1013.407 ± 0.060	0.013 ± 0.001	
					1040.387 ± 0.040	0.035 ± 0.002	5/2−, 7/2−
					1096.977 ± 0.050	0.013 ± 0.001	7/2+
					1197.137 ± 0.100	0.0032 ± 0.0001	

Table F.1: β decay scheme of ^{239}U. The data are taken from ENSDF [161] as detailed in Sec. 4.1.1, except for the Q_β which is taken from [296].

F.2 Spectrum and uncertainties of ^{239}Np

All the spin-parity data of ^{239}Np are well known, as seen in Tab.F.2. The 391 keV, 492 keV, 505 keV and 556 keV transitions are 1st non-unique forbidden, but satisfies the conservative ξ-approximation criterion and are assumed to be correctly modeled as allowed transitions. Thus, the uncertainty is dominated by the uncertainties originating from the endpoint energies and by the branching ratios, as seen in Fig. F.2b. The null I_β uncertainty induces large anticorrelations between the highest BR uncertainties associated to the 285 keV, 330 keV and 391 keV transitions, as displayed in Fig. F.2c. The bloc structure of the total correlation matrix in Fig. F.2c is mainly induced by the BR correlation matrix.

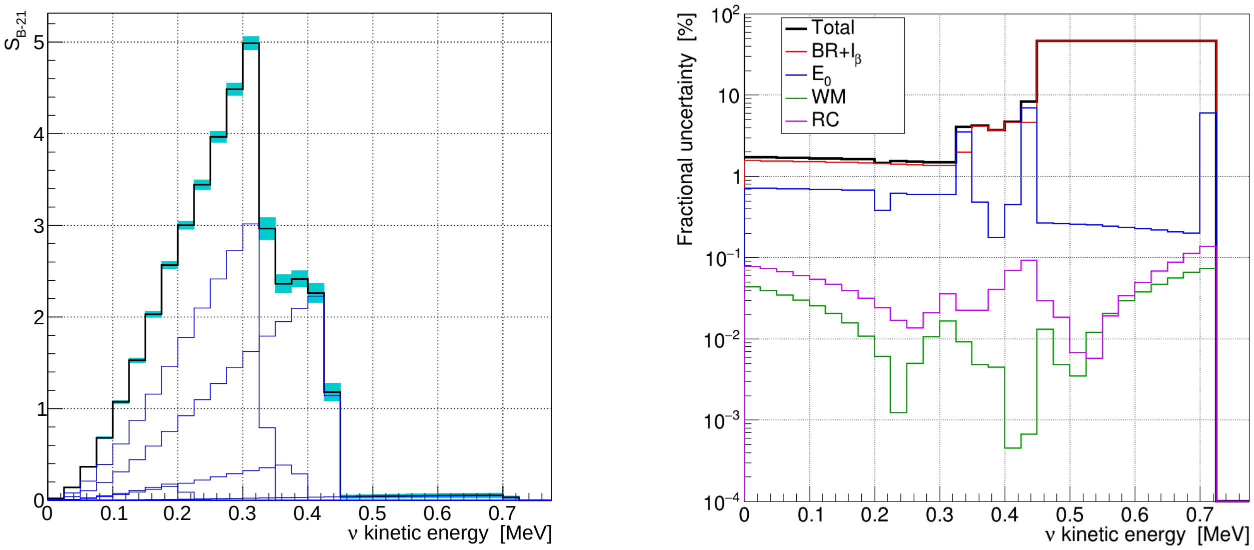

(a) ^{239}Np $\bar{\nu}_e$ spectrum. **(b)** Fractional uncertainties.

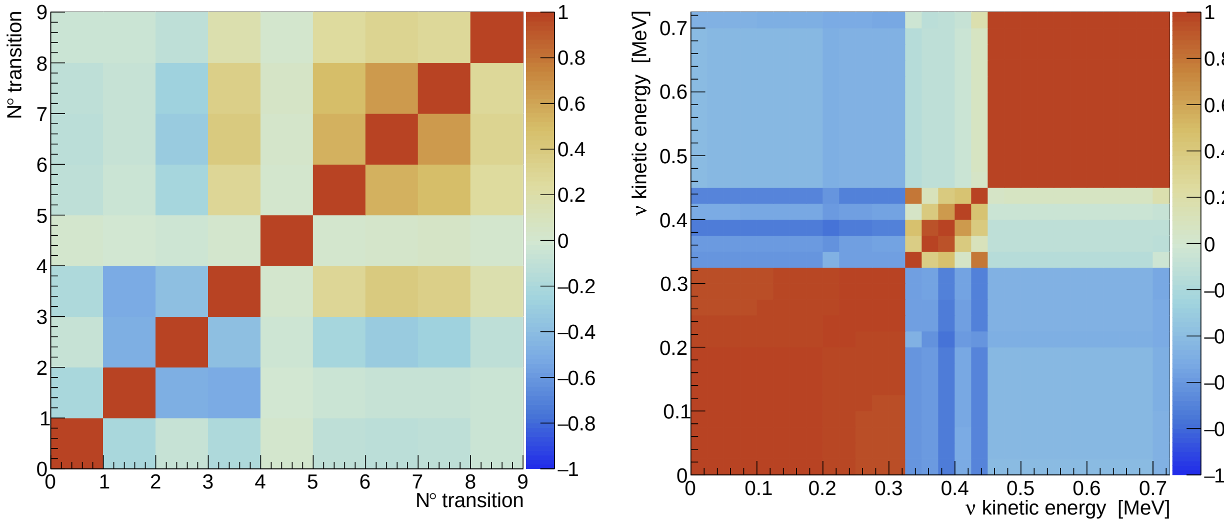

(c) Correlations between BR. **(d)** $\bar{\nu}_e$ spectrum correlation matrix.

Figure F.2: (a) ^{239}Np $\bar{\nu}_e$ spectrum. The black line represents the isotope spectrum, while the blue lines represent each transition spectrum. The total uncertainty is displayed as a cyan band on the isotope spectrum. **(b)** Fractional uncertainties associated to the different uncertainty sources (BR: branching ratio, I_β: β^- intensity, E_0: endpoint energy, $J\pi$: spin-parity, WM: weak magnetism, QED: radiative correction, NU: modeling of non-unique forbidden transition). **(c)** Correlations between the branching ratios maximizing the ^{239}Np IBD yield. The ordering of the transitions follows the one from Tab.F.2, the first one being the transition to the ground-state and so on. **(d)** Correlation matrix of the ^{239}Np $\bar{\nu}_e$ spectrum.

^{239}Np				$\longrightarrow$	^{239}Pu		
Q_β (keV)	I_β (%)	$J\pi$	$T_{1/2}$		E_{lvl} (keV)	BR (%)	$J\pi$
722.785 ± 0.930	100	5/2+	2.356 ± 0.003 d		7.861	2 ± 1	3/2+
					285.46	45 ± 3	5/2+
					330.125	7 ± 2	7/2+
					391.58	44 ± 2	7/2−
					469.8	0.13615 ± 0.077	1/2−
					492.2	0.020 ± 0.001	3/2−
					505.2	0.0074 ± 0.0002	5/2−
					511.81	1.70 ± 0.06	7/2+
					556.2	0.003 ± 0.0003	7/2−

Table F.2: β decay scheme of ^{239}Np. The data are taken from ENSDF [161] as detailed in Sec. 4.1.1, except for the Q_β which is taken from [296]. Uncertainties for the level energies are not provided in ENSDF and a 10% uncertainty is considered on the energy levels in BESTIOLE. The branching ratio of the 469 keV transition is given in ENSDF as "≥ 0.0027", and is modeled with a uniform distribution in BESTIOLE.

F.3 Spectrum and uncertainties of ^{56}Mn

The ^{56}Mn transitions are well known. The spectrum is made of only allowed transitions with complete spin-parity data. The uncertainty is dominated by the one induced by the branching ratio, as seen in Fig. F.3b, and remains small, about 1% over the spectrum. The null I_β uncertainty induces anticorrelations between the 846 keV transition and the 2657 keV, 2959 keV and 3369 keV transitions, which have the highest branching ratio uncertainties. The other branching ratios are too low to have a significant impact and they remain almost uncorrelated. The bloc structure of the total correlation matrix in Fig. F.3d is thus mainly due to the correlation between the branching ratios of the 846 keV, 2657 keV, 2959 keV and 3369 keV transitions. The four diagonal blocs of correlation are associated to the four principal transitions at 846 keV, 2657 keV, 2959 keV and 3369 keV, while the off-diagonal anticorrelated bands result from the anticorrelation between the branching ratio of 846 keV transition with the other three.

^{56}Mn				$\longrightarrow$	^{56}Fe		
Q_β (keV)	I_β (%)	$J\pi$	$T_{1/2}$		E_{lvl} (keV)	BR (%)	$J\pi$
3695.497 ± 0.207	100	3+	2.5789 ± 0.0001 h		846.776 ± 0.002	56.6 ± 0.7	2+
					2085.064 ± 0.003	0.057 ± 0.006	4+
					2657.547 ± 0.004	27.5 ± 0.4	2+
					2959.935 ± 0.006	14.5 ± 0.3	2+
					3122.908 ± 0.004	0.040 ± 0.004	4+
					3369.91 ± 0.04	1.20 ± 0.03	2+
					3445.279 ± 0.005	0.020 ± 0.002	3+

Table F.3: β decay scheme of ^{56}Mn. The data are taken from ENSDF [161] as detailed in Sec. 4.1.1, except for the Q_β which is taken from [296].

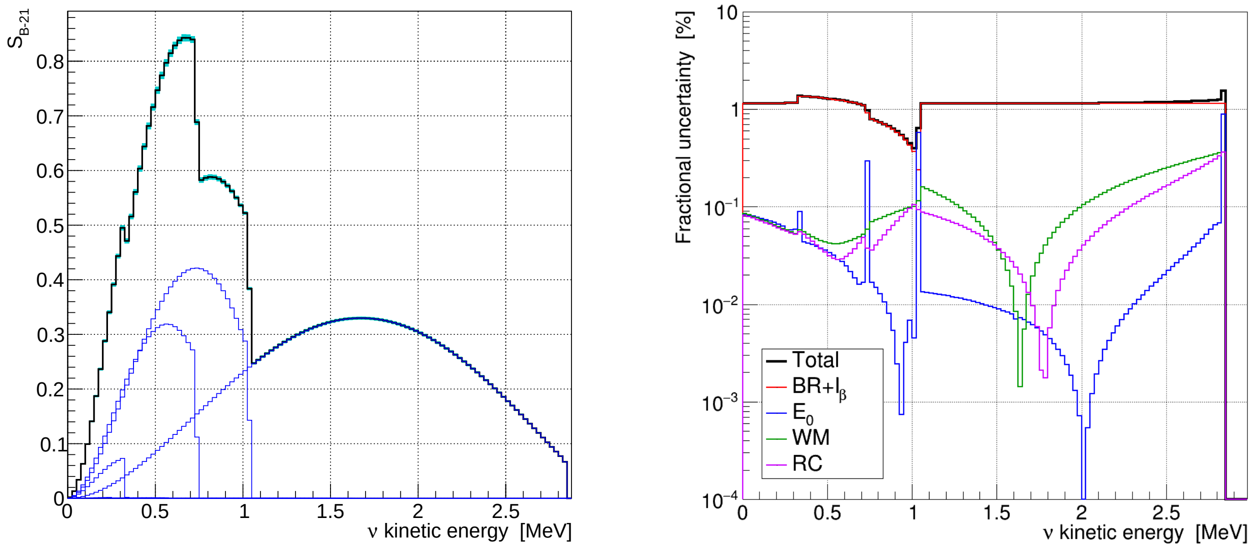

(a) ^{56}Mn $\bar{\nu}_e$ spectrum.

(b) Fractional uncertainties.

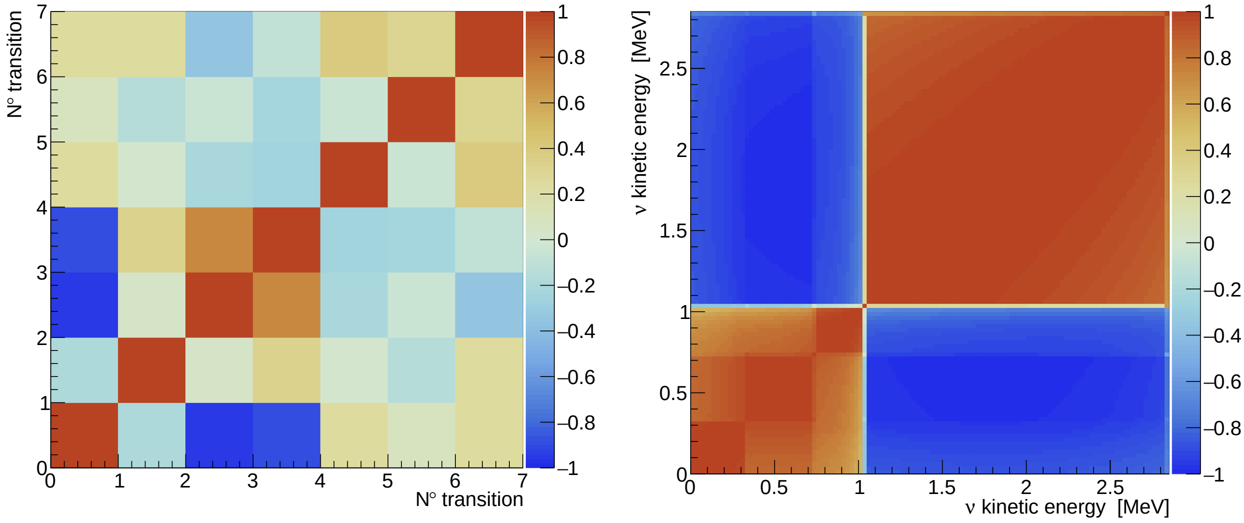

(c) Correlations between BR.

(d) $\bar{\nu}_e$ spectrum correlation matrix.

Figure F.3: **(a)** ^{56}Mn $\bar{\nu}_e$ spectrum. The black line represents the isotope spectrum, while the blue lines represent each transition spectrum. The total uncertainty is displayed as a cyan band on the isotope spectrum. **(b)** Fractional uncertainties associated to the different uncertainty sources (BR: branching ratio, I_β: β^- intensity, E_0: endpoint energy, $J\pi$: spin-parity, WM: weak magnetism, QED: radiative correction, NU: modeling of non-unique forbidden transition). **(c)** Correlations between the branching ratios maximizing the ^{56}Mn IBD yield. The ordering of the transitions follows the one from Tab.F.3, the first one being the transition to the 846 keV level and so on. **(d)** Correlation matrix of the ^{56}Mn $\bar{\nu}_e$ spectrum.

F.4 Spectrum and uncertainties of ^{28}Al

The ^{28}Al spectrum is a textbook case of a transition. It it composed of a single allowed transition with no missing data, as seen in Tab.F.4. The uncertainty induced by the branching ratio and by the β^- intensity is null as ^{28}Al is a complete β^- emitter. The uncertainty is dominated by the modeling uncertainty derived for the weak magnetism and for the radiative correction, as shown in Fig. F.4b. The anchor points associated to these two corrections are very close, which results in an anticorrelated bloc structure in the total correlation matrix in Fig. F.4c.

^{28}Al				$\longrightarrow$	^{28}Si		
Q_β (keV)	I_β (%)	$J\pi$	$T_{1/2}$		E_{lvl} (keV)	BR (%)	$J\pi$
4642.078 ± 0.049	100	3+	2.245 ± 0.002 min		1778.987 ± 0.015	99.99 ± 0.01	2+

Table F.4: β decay scheme of ^{28}Al. The data are taken from ENSDF [161] as detailed in Sec. 4.1.1, except for the Q_β which is taken from [296].

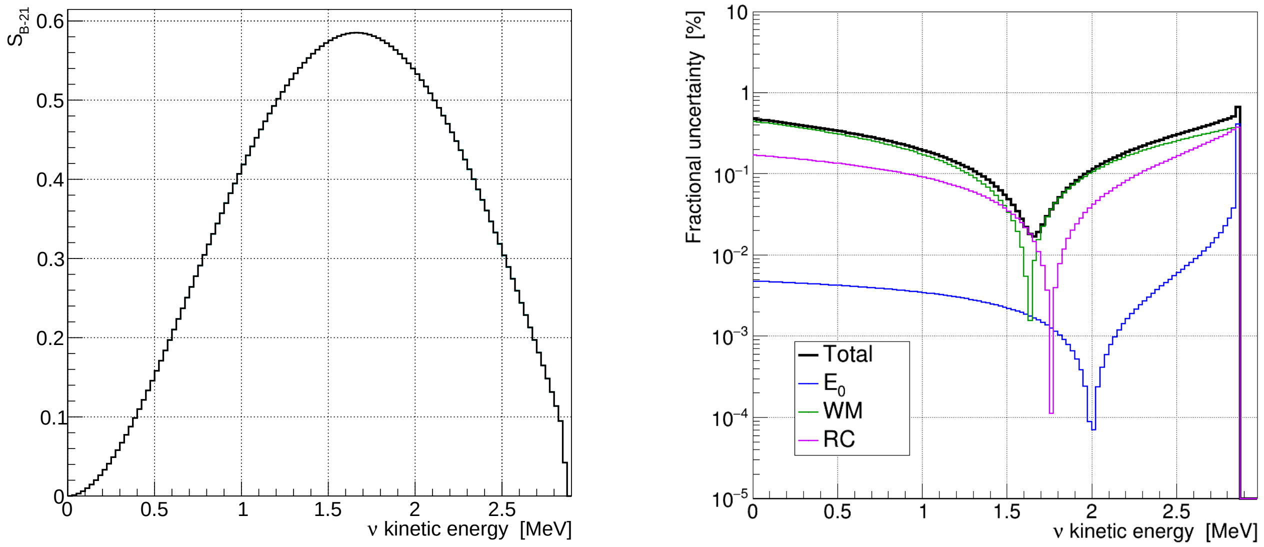

(a) ^{28}Al $\bar{\nu}_e$ spectrum.

(b) Fractional uncertainties.

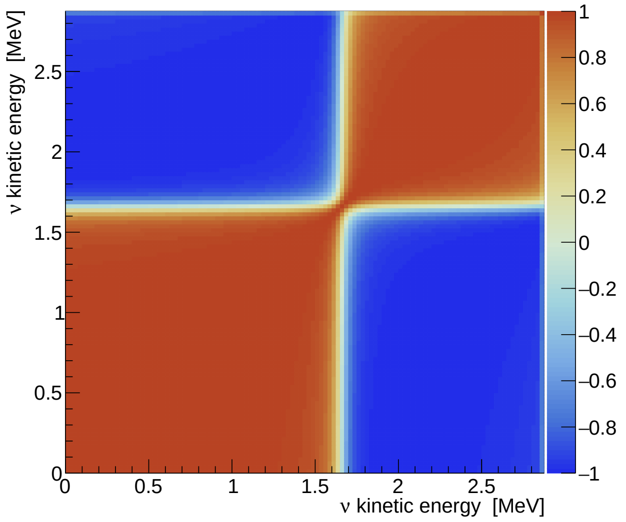

(c) $\bar{\nu}_e$ spectrum correlation matrix.

Figure F.4: (a) ^{28}Al $\bar{\nu}_e$ spectrum. The black line represents the isotope spectrum, while the blue lines represent each transition spectrum. The total uncertainty is displayed as a cyan band on the isotope spectrum. **(b)** Fractional uncertainties associated to the different uncertainty sources (E_0: endpoint energy, $J\pi$: spin-parity, WM: weak magnetism, QED: radiative correction, NU: modeling of non-unique forbidden transition). **(c)** Correlation matrix of the ^{28}Al $\bar{\nu}_e$ spectrum.

F.5 Spectrum and uncertainties of ^{52}V

The ^{52}V spectrum is dominated by the 1434 keV transition which is an allowed transition. The uncertainty induced by the branching ratio of the 1434 keV transition is lower than the 1% expected from the ENSDF data in Tab.F.5, as seen in the corresponding fractional uncertainty above 1.5 MeV in Fig. F.5b. This is a result of the Monte-Carlo simulation used to propagate the β^- intensity uncertainty which is null for ^{52}V. The maximization of the branching ratio uncertainty with respect to the IBD yield then impacts the branching ratios of the 2369 keV, 2767 keV and 2964 keV transitions, which thus present large correlations.

Above 0.5 MeV, the modeling uncertainty derived for the weak magnetism of the 1434 keV transition dominates, followed closely by the modeling uncertainty derived for the radiative correction. The general structure of the correlation matrix is induced by these two modeling uncertainties of the 1434 keV transition. The bloc structure below 1.5 MeV is also induced by the branching ratio uncertainties of the other transitions.

^{52}V				$\longrightarrow$	^{52}Cr		
Q_β (keV)	I_β (%)	$J\pi$	$T_{1/2}$		E_{lvl} (keV)	BR (%)	$J\pi$
3976.476 ± 0.160	100	3+	3.743 ± 0.005 min		1434.081 ± 0.010	99.2 ± 1.0	2+
					2369.596 ± 0.022	0.052 ± 0.010	4+
					2767.75 ± 0.03	0.570 ± 0.013	4+
					2964.775 ± 0.015	0.116 ± 0.002	2+
					3161.65 ± 0.14	0.008 ± 0.001	2+
					3415.22 ± 0.04	0.03 ± 0.01	4+
					3472.4 ± 0.3	0.002 ± 0.001	3+
					3771.9 ± 0.5	0.0025 ± 0.0014	2+

Table F.5: β decay scheme of ^{52}V. The data are taken from ENSDF [161] as detailed in Sec. 4.1.1, except for the Q_β which is taken from [296].

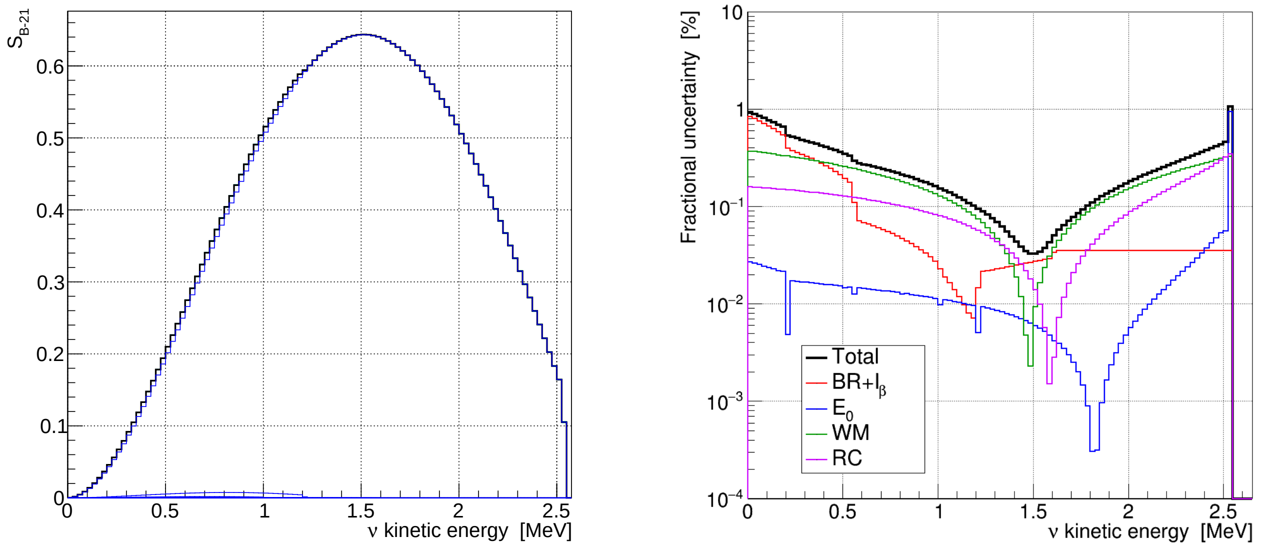

(a) ^{52}V $\bar{\nu}_e$ spectrum.

(b) Fractional uncertainties.

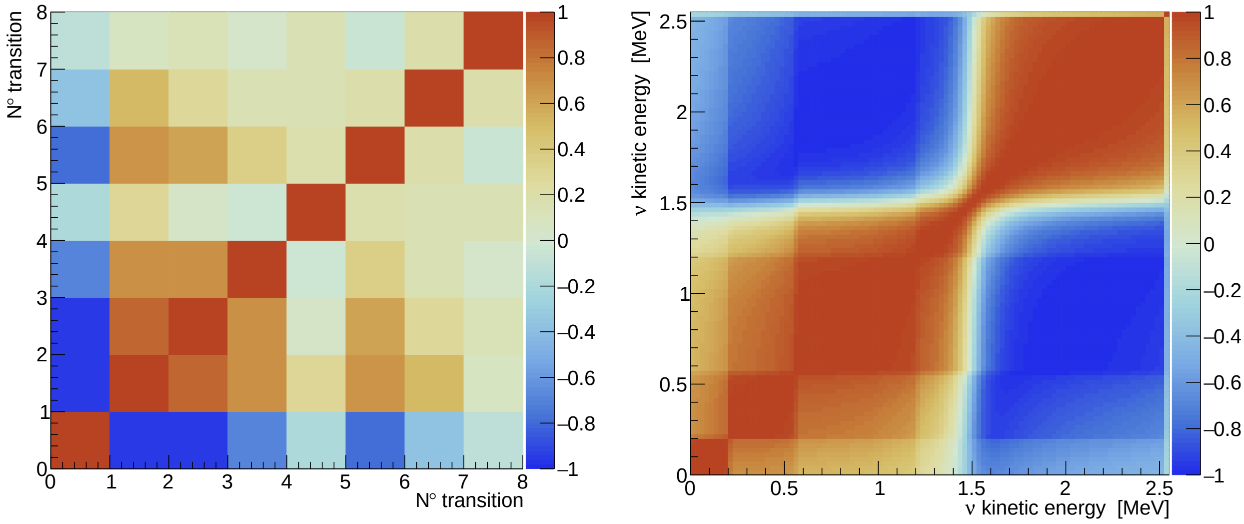

(c) Correlations between BR.

(d) $\bar{\nu}_e$ spectrum correlation matrix.

Figure F.5: **(a)** ^{52}V $\bar{\nu}_e$ spectrum. The black line represents the isotope spectrum, while the blue lines represent each transition spectrum. The total uncertainty is displayed as a cyan band on the isotope spectrum. **(b)** Fractional uncertainties associated to the different uncertainty sources (BR: branching ratio, I_β: β^- intensity, E$_0$: endpoint energy, $J\pi$: spin-parity, WM: weak magnetism, QED: radiative correction, NU: modeling of non-unique forbidden transition). **(c)** Correlations between the branching ratios maximizing the ^{52}V IBD yield. The ordering of the transitions follows the one from Tab.F.5, the first one being the transition to the 1434 keV level and so on. **(d)** Correlation matrix of the ^{52}V $\bar{\nu}_e$ spectrum.

F.6 Spectrum and uncertainties of ^{6}He

^{6}He is also a complete β^- emitter whose spectrum is made of a single transition with very well known data, as seen in Tab.F.6. Hence, there is no BR uncertainty on its spectrum and the endpoint uncertainty has a very low impact except at the endpoint. The main uncertainty on its allowed shape comes from the WM uncertainty, followed closely by the radiative correction uncertainty. As for ^{28}Al, the anticorrelated bloc structure observed in the total correlation matrix in Fig. F.6c result from the similar impact of these two uncertainties which have close anchor points.

^{6}He				$\longrightarrow$	^{6}Li		
Q_β (keV)	I_β (%)	$J\pi$	$T_{1/2}$		E_{lvl} (keV)	BR (%)	$J\pi$
3505.215 ± 0.053	100	0+	806.7 ± 0.1 ms		0	100	1+

Table F.6: β decay scheme of ^{6}He. The data are taken from ENSDF [161] as detailed in Sec. 4.1.1, except for the Q_β which is taken from [296].

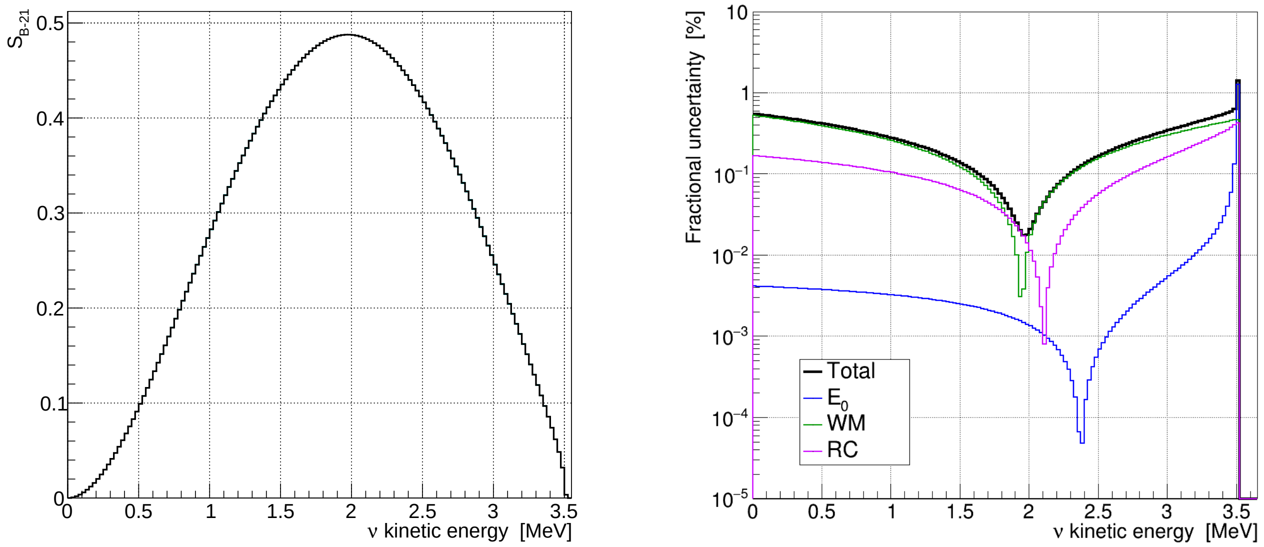

(a) ^{6}He $\bar{\nu}_e$ spectrum. **(b)** Fractional uncertainties.

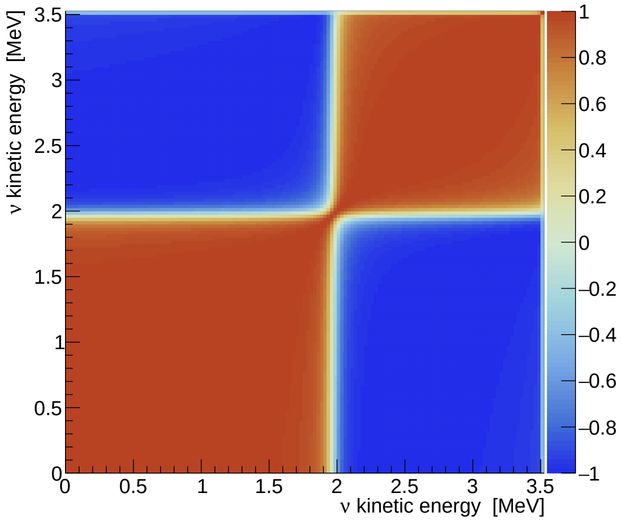

(c) $\bar{\nu}_e$ spectrum correlation matrix.

Figure F.6: **(a)**: ^{6}He $\bar{\nu}_e$ spectrum. The black line represents the isotope spectrum, while the blue lines represent each transition spectrum. The total uncertainty is displayed as a cyan band on the isotope spectrum. **(b)** Fractional uncertainties associated to the different uncertainty sources (E_0: endpoint energy, $J\pi$: spin-parity, WM: weak magnetism, QED: radiative correction, NU: modeling of non-unique forbidden transition). **(c)** Correlation matrix of the ^{6}He $\bar{\nu}_e$ spectrum.

G
Summary in French

Contents

G.1 La physique du neutrino

L'existence du neutrino a été prédite par Wolfgang Pauli en 1930, afin d'expliquer le spectres continu des électons émis lors d'une désintegration beta observé par Walter Kaufmann et Henry Becquerel [1]. Le neutrino fut alors décrit comme une particule électriquement neutre avec un spin de $^1/_2$ et une masse positive, et a rapidement été intégré dans la première théorie de la désintégration beta développée par Enrico Fermi en 1934 [2]. La théorie de Fermi a ouvert la voie à deux décennies de travaux théoriques et d'expériences, et l'existence des neutrinos a finalement été confirmée en 1953. Cette prouesse a été réalisée par Frederick Reines et Clyde Cowan, qui ont détecté des antineutrinos émis par le réacteur nucléaire de Savannah River en utilisant une technique de détection par scintillation basée sur le processus de désintégration beta inverse (IBD) [3], toujours utilisée par les expériences actuelles. La zoologie des neutrinos a ensuite été complétée par deux autres saveurs de neutrinos : le neutrino muon, observé en 1962 au Brookhaven Alternating Gradient Synchrotoron [4], et le neutrino tau, découvert en 1975 par l'expérience DONUT [5]. En 1968, seul un tiers du flux prédit de neutrinos émis par le Soleil a été mesuré lors de l'expérience Homestake [6]. Ce déficit en neutrinos solaires a été confirmé par SAGE [7], GALLEX [8] et GNO [8] dans les années 1990. Le problème des neutrinos solaires a été suivi par le problème des neutrinos atmosphériques, dans lequel seule la moitié des neutrinos prédit provenant des collisions de rayons cosmiques dans la haute atmosphère a été observée par les détecteurs Cherenkov tels que IMB [9], Kamiokande [10] et Super-Kamiokande [11]. Une origine possible des déficits en neutrinos solaires et atmosphériques est décrite par la théorie des oscillations de saveur des neutrinos, postulée en 1962 par Ziro Maki, Masami Nakagawa et Shoichi Sakata après la détection du neutrino muonique et basée sur l'oscillation neutrino-antineutrino proposée par Bruno Pontecorvo la même année. Les déficits en neutrinos solaires et atmosphériques ont été confirmés comme provenant des oscillations de neutrinos par des mesures concluantes effectuées par Super-Kamiokande [11] et l'Observatoire de neutrinos de Sudbury [12], respectivement en 1998 et 2001. Cette observation est devenue importante car les oscillations de neutrinos ont mis en évidence avec certitude la masse non nulle des neutrinos.

La plupart des expériences observant des oscillations de neutrinos peuvent être interprétées dans un cadre d'oscillation à trois états de neutrinos massifs. Ces états de neutrinos massifs sont liés aux états de neutrinos de saveur par l'intermédiaire de la matrice complexe 3 × 3 dite de "Pontecorvo-Maki-Nakagawa-Sakata" (PMNS). Le phénomène d'oscillation provient alors du fait que les états propres de masse des neutrinos ne coïncident pas avec les états propres de saveur. Sur la base d'une phénoménologie déduite des expériences, la matrice PMNS peut être paramétrisée par trois angles de mélange et une phase induisant la violation de la symétrie $\mathcal{CP}$ dans les oscillations de neutrinos. Les probabilités d'oscillation dépendent également des différences entre le carré de la masse des états propres massifs. Deux des angles de mélange, respectivement θ_{12} et θ_{23}, ont été mesurés dans des expériences de neutrino solaires et atmosphériques. Le troisième angle de mélange, θ_{13}, a été mesuré en observant les flux de neutrinos et d'antineutrinos émis par des accélérateurs ainsi que par des réacteurs nucléaires. En ce qui concerne les réacteurs nucléaires, une réévaluation des prédictions du spectre des antineutrinos de réacteur en 2011 [13, 14] a conduit à un déficit systématique des antineutrinos mesurés dans vingt expériences de réacteur, significatif au niveau de $2,8\sigma$ et appelé anomalie des antineutrinos de réacteur (RAA) [15]. La RAA ne peut pas être expliquée par les trois angles de mélange connus, et n'est pas la seule divergence entre les expériences et les prédictions. Par exemple, les taux de capture de neutrinos mesurés et théoriques sur le gallium observés dans GALLEX et dans SAGE diffèrent significativement les uns des autres, même après avoir inclus les effets de l'oscillation à trois saveurs, et constituent l'anomalie du gallium [16]. L'anomalie LSND et MiniBooNE fait référence aux résultats incohérents des expériences éponymes par rapport aux prédictions incluant les paramètres d'oscillation solaire et atmosphérique [17, 18]. Toutes ces anomalies peuvent être expliquées dans le cadre de l'oscillation des neutrinos si des neutrinos stériles supplémentaires sont considérés. Ces neutrinos stériles pourraient se mélanger avec les autres états de masse des neutrinos mais ne pourraient pas interagir avec les états de saveur. Si les neutrinos stériles existaient, ce serait une preuve évidente d'une physique au-delà du modèle standard. Cependant, l'interprétation des neutrinos stériles du RAA a été largement exclue par les récentes expériences de réacteurs à très courte base, et aucune preuve d'un biais expérimental n'a été détectée. En outre, les expériences d'antineutrinos IBD menées à courtes et longues lignes de vol ont révélé deux autres différences significatives sur le taux et sur la forme des spectres mesurés par rapport aux prédictions. La validité des prédictions est alors remise en question comme source des divergences observées dans les expériences en réacteur. Cette dernière piste a motivé une révision des modélisations du spectre des antineutrinos des réacteurs.

G.2 Antineutrinos de réacteur et motivations physiques

La réaction en chaîne qui se produit dans un réacteur nucléaire entraîne un flux intense d'antineutrinos électroniques ($\bar{\nu}_e$) d'environ 2×10^{20} $\bar{\nu}_{\mathrm{e}}$/s par $\mathrm{GW_{th}}$, ce qui fait des réacteurs commerciaux et de recherche des sources de $\bar{\nu}_e$ par exellence pour les expériences sur les neutrinos. Ce flux est produit par quatre isotopes fissiles dans un réacteues à eau préssurisé (REP) (^{235}U, ^{238}U, ^{239}Pu, ^{241}Pu), et presque entièrement par ^{235}U dans un réacteur de recherche. Elle se traduit par l'émission d'environ 6 Nu par fission dans les deux types de réacteurs, avec une contribution dominante de l'^{235}U suivie de l'^{239}Pu dans les REP, respectivement de 55% et 30% en moyenne sur un cycle de réacteur. Le flux de neutrons produit par la réaction en chaîne active également plusieurs isotopes qui peuvent contribuer à hauteur de 10% à 20% au flux de neutrons d'un réacteur, en fonction du combustible et du matériau structurel. On peut donc s'attendre à des différences significatives dans le flux et les spectres émis par un REP et un réacteur de recherche. Bien que la puissance thermique d'un réacteur de recherche soit inférieure de deux ordres de grandeur à celle d'un REP, elle est compensée par sa compacité qui permet de mener des expériences plus près du coeur.

Les expériences sur les réacteurs ont présenté des divergences entre les prédictions et les données expérimentales. La RAA est un écart de taux significatif d'environ $2,8\sigma$ entre les mesures et les prédictions basées sur des modèles de conversion récents qui est observé dans toutes les expériences IBD. Une nouvelle génération d'expériences de réacteurs IBD situées à des lignes de base très courtes a été déployée pour étudier l'hypothèse du neutrino stérile comme explication possible du RAA. Pour le moment, une partie significative de la région autorisée du RAA a été exclue, et un biais par rapport aux prédictions est maintenant privilégié comme origine du RAA. Un tel biais pourrait également expliquer la différence de forme observée entre les spectres IBD mesurés et les prédictions. De plus, le biais dans les prédictions est à l'origine d'une divergence avec la variation du rendement IBD en fonction du combustible mesurée à Daya Bay. Les modèles de conversion, utilisés dans toutes les prédictions récentes, présentent des incertitudes d'environ 2-3Ces incertitudes des modèles de conversion sont équivalentes aux incertitudes expérimentales concernant l'anomalie de forme du spectre, tandis que l'incertitude expérimentale domine l'analyse de la variation du rendement des IBD en fonction du combustible. Une autre possibilité pour prédire les spectres du réacteur est la méthode de sommation. Cependant, les modèles de sommation actuels présentent une incertitude de 10%, principalement due à des bases de données nucléaires incomplètes, ou sont dépourvus d'incertitudes en raison de la complexité de la tâche.

Les modèles de conversion et de sommation présentent tous deux des limites importantes et doivent être affinés afin de prendre en compte la RAA, l'écart de forme et l'évolution du rendement des IBD en fonction du combustible. Les spectres du réacteur doivent également être prédits jusqu'à 0 MeV pour les futures expériences CEνNS ce qui n'est pas possible avec les modèles par conversion. Le processus CEνNS permettra de mesurer le flux de $\bar{\nu}_e$ provenant de réacteur et émis sous le seuil d'énergie du processus IBD. Jusqu'à 75% du flux de $\bar{\nu}_e$ se trouve sous ce seuil en énergie de 1,8 MeV, en dessous dequel le processus IBD ne peut pas se réaliser. Les $\bar{\nu}_e$ d'activation qui ne peuvent pas être détectés dans les expériences IBD menées sur les réacteurs commerciaux peuvent alors contribuer de manière significative au flux de $\bar{\nu}_e$ mesuré dans les futures expériences CEνNS. La prédiction contribuera de manière significative à l'incertitude systématique de la mesure, et doit présenter un budget d'incertitude fiable en dessous du seuil IBD. Dans ce contexte, la méthode de sommation et les incertitudes associées ont été revisitées dans cette thèse, en utilisant une théorie avancée de la désintégration et des données nucléaires récentes.

G.3 Modélisation revisitée des spectres issus de la désintégration β

Beta Energy Spectrum Tool for an Improved Optimal List of Elements (BESTIOLE) est un logiciel développé au CEA dont le but est de modéliser les spectres électron et antineutrino émis lors d'une désintégration β. Écrit en C++ et utilisant ROOT [256], BESTIOLE prend en entrée une base de données écrit dans un format dédié et qui contient le détail des différentes transitions pour tous les isotopes d'intérêt. BESTIOLE enregistre dans un fichier ROOT les spectres β et $\bar{\nu}_e$ de chaque isotope ainsi que leurs matrices de covariance respectives. BESTIOLE a été développé en 2011 par le groupe de Saclay pour modéliser les spectres $\bar{\nu}_e$ de fission [13]. A partir de la version 2011 de BESTIOLE, la modélisation a été améliorée étape par étape dans ce travail de thèse en levant plusieurs approximations et en affinant certaines corrections. De plus, un travail approfondi a été réalisé pour caractériser les incertitudes associées. La propagation des incertitudes induites par la modélisation des spectres de désintégration β et les incertitudes liées à l'origine des données nucléaires ont été entièrement revues.

En partant de la règle d'or de Fermi, la probabilité de transition d'un électron émis lors d'une désintégration β s'exprime comme

$$P(W_e)\,\mathrm{d}W_e = K\ F(Z,W_e)\ C(W_e)\ (W_0-W_e)^2 p_e W_e\ (1+\delta_R^{e^-}+\delta_{WM})\,\mathrm{d}W_e, \tag{G.1}$$

où $F(Z,W_e)$ et $C(W_e)$ sont respectivement la *fonction de Fermi* et le *facteur de forme*, et où toutes les constantes ont été rassemblées en un seul facteur de normalisation $K = 1/\int P(W_e)\mathrm{d}W_e$. L'effet principal de l'interaction électromagnétique entre le noyau et l'électron émis est englobé dans $F(Z,W_e)$, tandis que les effets de structure nucléaire sont rassemblés dans $C(W_e)$. Le magnétisme faible est un effet du facteur de forme couramment traité comme une correction, et en tant que tel il est explicitement retiré du facteur de forme via δ_{WM}. Une autre correction importante des spectres de désintégration β provient de l'électrodynamique quantique, les corrections radiatives externes δ_R. Le spectre $\bar{\nu}_e$ émis simultanément lors d'une désintégration β est donné en miroir de l'équation G.1 basé sur la conservation de l'énergie, $W_\nu + W_e = W_0$, à l'exception de la correction radiative externe qui est spécifique au lepton émis, $\delta_R^{e^-}. \to \delta_R^{\bar{\nu}_e}$.

Il existe différents types de désintégration β classés en fonction du spin et de la parité des états nucléaires initial et final, respectivement donnés par $(J_i\pi_i)$ et $(J_f\pi_f)$. Ces spins et parités des états initial et final sont liés par des règles de sélection induites par l'interaction faible:

$$J_i = J_f + l + s, \tag{G.2}$$

$$\pi_i\pi_f = (-1)^l, \tag{G.3}$$

avec $l = l_e + l_\nu$ le moment angulaire leptonique total et $s = s_e + s_\nu$ le spin leptonique total. Le spin s peut être égal à 0 ou 1, ce qui correspond respectivement à un spin électron-neutrino antiparallèle ou parallèle. La classification des désintégrations β basée sur ces règles de sélection est résumée dans la Table G.1.

La fonction d'onde d'un électron se déplaçant dans le champ électromagnétique généré par un noyau satisfait aux équations de Dirac radiales si le potentiel associé a une symétrie sphérique. Les amplitudes coulombiennes correspondent à la normalisation des fonctions d'onde radiales des électrons, et peuvent être calculées en résolvant numériquement l'équation de Dirac radiale sur une large grille en énergie. Un programme appelé Directives for an Improved Result of the Amplitudes of Coulomb (DIRAC) a été développé lors de cette thèse pour résoudre l'équation de Dirac radiale, sur la base de l'algorithme numérique développé par [263]. L'algorithme est

Type de désintégration β	l	s	$\Delta J = \lvert J_f - J_i \rvert = l + s$	$\pi_f \pi_i = (-1)^l$
Autorisée	0	0,1	0,1	$+$
$1^{\text{ère}}$ interdite non-unique	0,1	0	0,1	$-$
$n^{\text{ème}}$ interdite non-unique	n	0	n	$(-1)^{\Delta J}$
$n^{\text{ème}}$ interdite unique	n	1	$n+1$	$(-1)^{\Delta J - 1}$

Table G.1: Classification des différents types de désintégration β et règles de sélection associées.

basé sur une expansion locale en série des fonctions d'onde radiales et du potentiel nucléaire. L'algorithme peut facilement être adapté à n'importe quel potentiel, à condition qu'il ait une symétrie sphérique et qu'il puisse être développé en série en tout point de l'espace. Cet algorithme calcule deux effets importants dans le calcul de la fonction de Fermi et du facteur de forme : l'extension spatiale du noyau et l'écrantage atomique. De plus, il calcule des fonctions qui permettent de lever l'approximation $\lambda_k = 1$ couramment utilisée pour calculer les facteurs de forme. Ces effets sont englobés dans des fonctions dites "de Coulomb" qui ont été tabulées pour une grille en énergie très fine, donnant ainsi la possibilité d'être indépendant des anciennes tables de fonctions de Coulomb peu précise et utilisant des modèles nucléaires dépassés.

Au niveau d'une transition, l'impact typique de la taille finie du noyau sur la forme des spectres β et $\bar{\nu}_e$ est d'environ 1-2% induit par la fonction de Fermi. L'impact de la levée de l'approximation $\lambda_k = 1$ et de l'inclusion de l'effet de la taille finie sur le facteur de forme est d'environ 5-10%. L'effet de l'écrantage est opposé à l'effet de taille finie, avec un impact typique d'environ 0.5-1% induit par la fonction de Fermi et d'environ 0.5% induit par le facteur de forme. Enfin, l'utilisation de rayons nucléaires basés sur des données expérimentales au lieu de formules théoriques a un faible impact, typiquement de 0.1%, sur la forme des spectres de transition. Les incertitudes sur les fonctions de Coulomb calculées avec DIRAC sont faibles et peuvent être négligées. Cependant, il est important de souligner que les incertitudes sur les paramètres d'écrantage ne sont pas fournies dans la littérature et n'ont donc pas pu être étudiées. Les incertitudes associées aux paramètres d'écrantage de Salvat pourraient avoir un impact sur la correction d'écrantage.

Le calcul des facteurs de forme interdits non-uniques est actuellement hors de portée pour une utilisation généralisée. Leur étude dans cette thèse est limitée aux deux transitions interdites non uniques les plus importantes contribuant au flux IBD d'un spectre de réacteur, associées à ^{92}Rb et ^{96}Y, ainsi qu'à une transition interdite non unique supplémentaire de ^{144}Pr calculée dans le contexte des géoneutrinos. Un calcul avancé des facteurs de forme interdits non uniques utilisant une structure nucléaire détaillée basée sur le modèle en couches a montré un impact significatif sur la forme des spectres de ces trois transitions, supérieur à 2% au centre des spectre et jusqu'à plusieurs dizaines de pourcents aux énergies maximales. D'autres transitions non uniques seront calculées dans de futures études, dans le but d'inclure les 10 principaux contributeurs aux spectres IBD dans une première étape, puis davantage.

En utilisant les corrections analytiques actualisées du magnétisme faible et de la correction radiative externe, la modélisation améliorée de BESTIOLE a été comparée à trois autres modélisations de la désintégration β décrites dans la littérature. La nouvelle modélisation de BESTIOLE, nommée B-21, présente des différences importantes sur la forme des spectres β et $\bar{\nu}_e$ au niveau d'une transition par rapport aux autres modèles. Il convient de souligner que de nombreuses corrections théoriques entrant dans la description complète de la désintégration β n'ont pas été pris en compte. Cependant, les effets de ces corrections sont généralement plus faible de plusieurs ordres de grandeur que ceux des corrections incluses dans B-21. La modélisation des transitions interdites non uniques reste le point critique à améliorer. Des données nucléaires doivent être couplées à la modélisation d'un spectre afin de produire des spectres de réacteur basé sur la méthode par sommation.

G.4 Révision et amélioration du traitement des données nucléaires

La construction d'une base de données pour BESTIOLE est basée sur l'utilisation de différentes sources de données expérimentales. D'un côté, un ensemble très large de données éxpérimentales provient de la base de donnée ENSDF, couvrant environ 70% des produits de fission entrant dans la composition d'un spectre de réacteur. Les autres données sont des données éxperimentales corrigées de l'effet Pandémonium et provenant des mesures TAGS et des mesures effectuées par Tengblad et al. Enfin, les isotopes n'ayant aucune donnée nucléaire sont modélisés par un modèle effectif. La lecture des données ENSDF a été revue pour améliorer la cohérence des spectres modélisés avec les données expérimentales, en incluant notamment l'intensité β^- des produits de fission et la possibilité de prendre en compte la multiplicité des données de parité et de spin disponibles. De plus, les données TAGS mesurées par Greenwood ont été incluses dans B-21 selon une nouvelle prescription, ce qui permet d'obtenir des spectres plus cohérents et un budget d'incertitude fiable. Ces révisions ont un impact potentiellement important au niveau d'un isotope, avec une différence allant jusqu'à 10% sur les formes des spectres isotopiques pertinents pour un flux IBD de réacteur. Cependant, la superposition de centaines de spectres de produits de fission réduit l'impact de ces révisions au niveau d'un spectre de réacteur, avec typiquement un impact sur la forme de l'ordre de 0.1%. Les données de 34 expériences TAGS récentes ont également été incluses, et devraient réduire le biais systématique provenant de l'effet Pandemonium.

Un examen complet de la propagation des incertitudes des données nucléaires évaluées et des incertitudes de modélisation a été effectué dans BESTIOLE. Une simulation Monte-Carlo a été développée pour propager les incertitudes associées aux données nucléaires évaluées. Cette simulation tient compte des corrélations potentielles entre les branches d'un isotope. Bien que des corrélations puissent exister entre les rapports d'embranchement d'un isotope, elles ne sont pas connues et ne sont pas pourvues dans la base de donnée ENSDF. Cette simulation Monte-Carlo consiste à générer aléatoirement des matrices de corrélation associées aux rapports d'embranchement et à sélectionner celle qui maximise l'incertitude sur le rendement IBD.

Enfin, une méthode a été proposée pour modéliser des incertitudes qui tiennent compte de la possibilité d'une mauvaise modélisation d'un spectre de transition. Cette méthode a été appliquée pour dériver des incertitudes sur la modélisation des transitions interdites non-uniques modélisées avec l'approximation ξ ou avec les calculs du modèle en couche, et qui contribuent de manière significative au spectre d'un réacteur. Le biais induit par l'approximation ξ utilisée abusivement est difficile à estimer, et même si la méthode proposée dans ce travail est probablement trop grossière pour prétendre le contraire, elle devrait être suffisamment conservatrice. Cette méthode à aussi été utilisée pour générer des incertitudes pour la correction de magnétisme faible et pour la correction radiative externe.

G.5 Spectres antineutrino de réacteur obtenus par la méthode par sommation révisée

Les spectres antineutrino de réacteur et les incertitudes fractionnelles associées obtenus avec B-21 sont présentés en Figure G.1. Les incertitudes totales sur les spectres antineutrino de fission sont faibles, avec des incertitudes fractionnelles d'environ 1% à 2 MeV et inférieures à 10% à 8 MeV, et des incertitudes totales de rendement IBD d'environ 1.3%. En particulier, la propagation des incertitudes des données nucléaires est robuste et il est peu probable qu'elle soit à l'origine d'un biais significatif. En revanche, plusieurs biais potentiellement significatifs ont été identifiés. Les biais induits par la modélisation effective des isotopes sans donnée nucléaire etceux induits par les isotopes modélisés avec les données Tengblad ne sont pas couverts par les incertitudes correspondantes. Les incertitudes de modélisation dérivées pour le magnétisme faible, pour la correction radiative externe et pour la modélisation des transitions interdites non uniques avec l'approximation ξ peuvent également être sujettes à un biais potentiel. Le biais sur l'incertitude de modélisation des transitions interdites non uniques pourrait être important étant donné que ces transitions contribuent de manière significative aux spectres de fission, et nécessite de développer davantage notre première tentative de proposer une incertitude cohérente au niveau d'une transition. Deux biais importants ne sont pas encore pris en compte dans le bilan d'incertitude actuel. Le premier est dû à l'éventuel effet Pandemonium présent dans les données de plusieurs produits de fission importants. Le second est dû au traitement des rendements de fission, qui sont supposés être non corrélés d'une part, et qui peuvent différer entre différentes bases de donnée d'autre part. Tous ces différents biais pourraient conduire à un budget d'incertitude sous-estimé. Une estimation grossière de l'incertitude totale du rendement des IBD une fois ces biais pris en compte serait d'environ 2.5%.

Des écarts significatifs ont été observés avec les mesures de spectres β effectuées à l'ILL et avec les spectres $\bar{\nu}_e$ convertis modélisés par Huber. B-21 surestime de manière générale les spectres de fissionβ et $\bar{\nu}_e$ pour ^{235}U par rapport à ceux mesurés à l'ILL et ceux prédits par

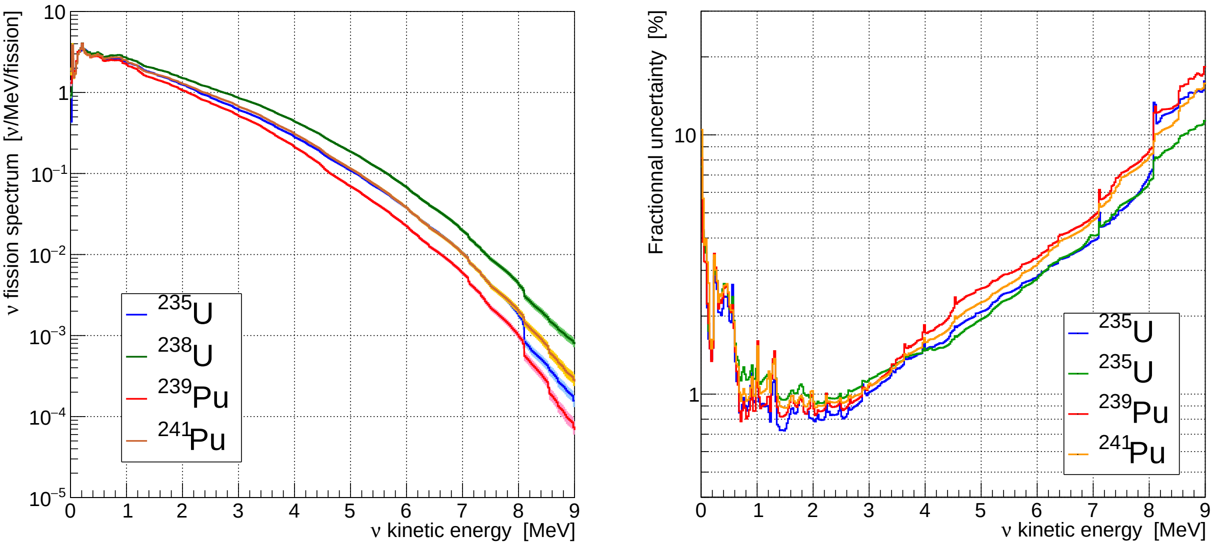

(a) Fission spectra. **(b)** Fractional uncertainties.

Figure G.1: **(a)** Spectres antineutrino de fission pour ^{235}U, ^{238}U, ^{239}Pu et ^{241}Pu et **(b)** incertitudes fractionelles totales correspondantes en fonction de l'énergie cinétique du neutrino. Les spectres ont été calculés avec des rendements de fission cumulaitf issus de la base de données JEFF-3.3 [136].

Huber, alors qu'ils sont généralement sous-estimés dans le cas de ^{239}Pu et ^{241}Pu. L'origine de ces divergences n'a pas été clairement identifiée, bien que différentes origines soient possibles, comme une mauvaise modélisation des transitions interdites non uniques, des isotopes impactés par le Pandemonium, et des isotopes pour lesquels des données nucléaires manquent. Le spectre ^{238}U β mesuré à Garching présente des différences importantes supérieures à 10% mais reste cohérent avec la prédiction B-21 en raison des grandes incertitudes expérimentales. Le spectre ^{238}U $\bar{\nu}_e$ calculé avec la méthode par sommation de Mueller peut présenter des écarts significatifs avec la modélisation B-21 en fonction de l'hypothèse sur les incertitudes fournies par Mueller et al. La sous-estimation du spectre $\bar{\nu}_e$ de ^{235}U et la surestimation du spectre $\bar{\nu}_e$ de ^{239}Pu par rapport aux spectres Huber-Mueller se compense lors du calcul de rendement IBD. Ainsi, les rendements IBD calculés avec B-21 et avec le modèle Huber-Mueller sont proches et ne présentent pas de tension particulière. Dans une prochaine étape, les prédictions de B-21 seront comparées avec d'autres modélisations théoriques telles que les spectres de sommation SM-2018 publiés par [178] et les spectres de sommation de [225].

Les rendements IBD et les spectres IBD prédits avec B-21 ont été comparés aux rendements IBD mesurés et aux spectres IBD dépliés publiés par Daya Bay et par STEREO. Un résumé des rendements IBD des modèles de référence, de B-21 et des experiences réacteurs est présenté dans la Table G.2 et dans la Figure. G.2. La faible incertitude sur les prédictions actuelles de B-21 est secondaire par rapport aux incertitudes expérimentales. Par conséquent, les rendements IBD prédits avec B-21 présentent de fortes tensions avec le rendement IBD total et le rendement IBD ^{235}U mesuré par Daya Bay, comme le montrent les rapports respectifs de 0.943 ± 0.014 (exp) $\pm\, 0.011$ (modèle) et de 0.938 ± 0.023 (exp) $\pm\, 0.013$ (modèle). La tension avec le rendement de l'IBD ^{239}Pu mesuré par Daya Bay est moins importante en raison de la plus grande incertitude expérimentale, comme le montre le rapport de 0.915 ± 0.053 (exp) $\pm\, 0.014$ (model). D'un autre côté, le rendement IBD de ^{235}U mesuré par STEREO est cohérent avec le rendement IBD de B-21, avec un rapport de 0.975 ± 0.025 (exp) $\pm\, 0.014$(modèle) où l'incertitude du modèle provient uniquement de B-21. Ceci est dû à la grande incertitude expérimentale, à un rendement IBD mesuré plus important et à un rendement IBD prédit plus faible par rapport à la prédiction de Huber-Mueller. Enfin, les comparaisons de la forme des spectres IBD de B-21 avec les spectres de Daya Bay et de STEREO présentent des distorsions similaires entre 5 MeV et 7 MeV que les comparaisons avec les prédictions de Huber-Mueller.

Des tensions significatives sont observées pour les rendements IBD et dans la forme des spectres prédits par B-21 lorsque comparés aux données experimentales. Ces tensions devraient être partiellement réduites lorsque le budget d'incertitude sera finalisé. D'autres comparaisons seront alors effectuées avec les données expérimentales restantes des expériences réacteur. Une application importante du spectre antineutrino de réacteur calculé avec B-21 dans ce travail sera dans le contexte des expériences réacteur visant à mesurer le rendement CEνNS. La prédiction du flux de neutrinos du réacteur contribuera à l'incertitude systématique de la mesure, et doit donc être complétée avant toute utilisation. Les études futures examineront l'impact de la prédiction sur la précision possible des expériences CEνNS dans les réacteurs, et mettront l'accent sur l'impact du flux de neutrinos émis en dessous du seuil IBD de 1.8 MeV.

	Fission fractionnelle				$\langle\sigma_{IBD}\rangle$ $[10^{-43}\text{cm}^2/\text{fis}]$				
	$\alpha_{^{235}\text{U}}$	$\alpha_{^{238}\text{U}}$	$\alpha_{^{239}\text{Pu}}$	$\alpha_{^{241}\text{Pu}}$	Mix	^{235}U	^{238}U	^{239}Pu	^{241}Pu
Modèle									
BESTIOLE-2021					6.27 ± 0.07	6.50 ± 0.09	10.32 ± 0.15	4.72 ± 0.07	6.93 ± 0.10
SM-2018 [178]					6.01	6.28	10.14	4.42	6.23
Huber-Mueller [223]					6.20 ± 0.14	6.69 ± 0.15	10.10 ± 1.00	4.36 ± 0.11	6.04 ± 0.60
REP									
Daya Bay [212]	0.564	0.076	0.304	0.056	5.91 ± 0.09	6.10 ± 0.15		4.32 ± 0.25	
Double Chooz [327]	0.520	0.087	0.333	0.060	5.71 ± 0.06				
RENO [224, 325]	0.571	0.073	0.300	0.056	5.89 ± 0.12	6.15 ± 0.19		4.18 ± 0.26	
Bugey-4 [68]	0.538	0.078	0.328	0.056	5.75 ± 0.08				
Recherche									
STEREO [158]	0.993	-	0.007	-		6.34 ± 0.22			

Table G.2: Rendements IBD d'antineutrino de réacteur mesurés et prédits de ^{235}U, ^{238}U, ^{239}Pu et ^{241}Pu de plusieurs expériences réacteur sur leur période respective de prise de données, ainsi que leurs fractions de fission effectives. Le rendement IBD "Mix" dans les rangées "Modèle" a été calculé avec les fissions fractionnelles effectives de Daya Bay.

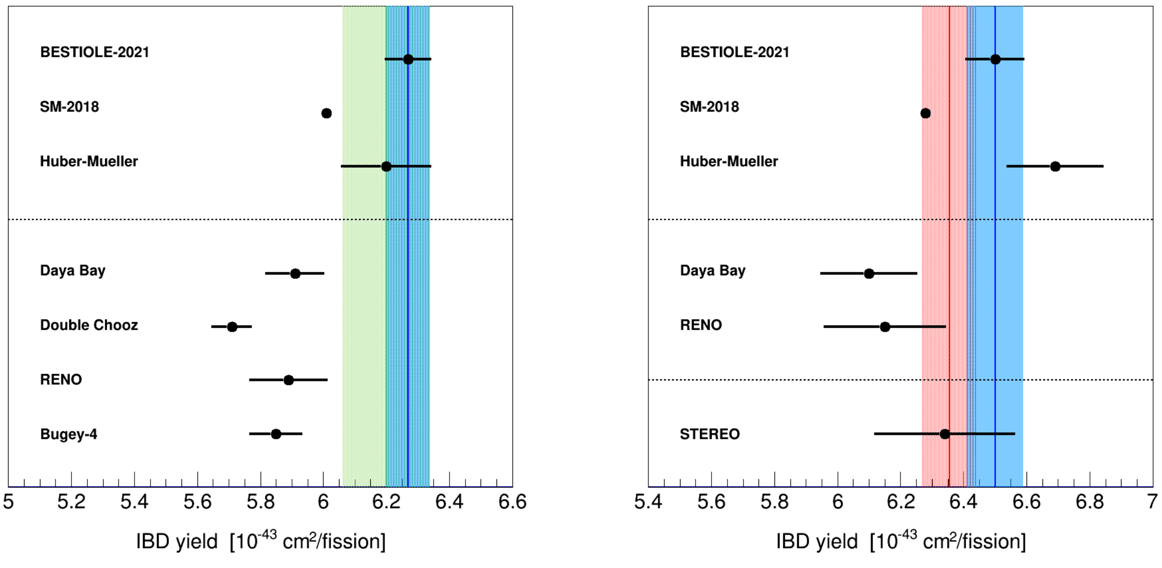

(a) Rendements IBD de REP.

(b) Rendements IBD de l'^{235}U.

Figure G.2: Rendements IBD antineutrinos mesurés et prédits de plusieurs expériences réacteur, ainsi que leurs fractions de fission effectives. Les rendements IBD prédits (en haut) sont séparés des mesures effectuées sur les réacteurs REP (au milieu) et sur les réacteurs de recherche (en bas). **(a)** Rendements IBD moyens pour les expérience REP sur leur période respective de prise de données et remis à l'échelle des fractions de fission de Daya Bay. Les rendements IBD prédits en haut utilisent les fractions de fission effectives de Daya Bay. Les bandes bleues et rouges représentent respectivement les rendements IBD de B-21 et de Huber-Mueller. **(b)** Rendement IBD de l'^{235}U. Les bandes bleues et rouges représentent respectivement le rendement IBD de B-21 et la moyenne mondiale de [158].

References

[1] W. Pauli. "Dear radioactive ladies and gentlemen". In: *Phys. Today* 31N9 (1930), p. 27 (see pp. 1, 7, 204).

[2] E. Fermi. "Versuch einer Theorie der beta-Strahlen. I". In: *Zeitschrift fur Physik* 88 (1934), pp. 161–177. DOI: `10.1007/BF01351864` (see pp. 1, 7, 8, 21, 70, 72, 79, 204).

[3] C. L. Cowan et al. "Detection of the Free Neutrino: a Confirmation". In: *Science* 124.3212 (1956), pp. 103–104. DOI: `10.1126/science.124.3212.103` (see pp. 1, 7, 204).

[4] G. Danby et al. "Observation of High-Energy Neutrino Reactions and the Existence of Two Kinds of Neutrinos". In: *Phys. Rev. Lett.* 9 (1 1962), pp. 36–44. DOI: `10.1103/PhysRevLett.9.36` (see pp. 1, 9, 204).

[5] M. L. Perl et al. "Evidence for Anomalous Lepton Production in $e^+ - e^-$ Annihilation". In: *Phys. Rev. Lett.* 35 (22 1975), pp. 1489–1492. DOI: `10.1103/PhysRevLett.35.1489` (see pp. 9, 204).

[6] Raymond Davis, Don S. Harmer, and Kenneth C. Hoffman. "Search for Neutrinos from the Sun". In: *Phys. Rev. Lett.* 20 (21 1968), pp. 1205–1209. DOI: `10.1103/PhysRevLett.20.1205` (see pp. 1, 14, 204).

[7] A. I. Abazov et al. "Search for neutrinos from the Sun using the reaction $^{71}\mathrm{Ga}(\nu,^-)^{71}$ Ge". In: *Phys. Rev. Lett.* 67 (24 1991), pp. 3332–3335. DOI: `10.1103/PhysRevLett.67.3332` (see pp. 1, 14, 204).

[8] M. Altmann et al. "GNO solar neutrino observations: results for GNO I". In: *Physics Letters B* 490.1 (2000), pp. 16 –26. DOI: `https://doi.org/10.1016/S0370-2693(00)00915-1` (see pp. 1, 14, 204).

[9] R. Becker-Szendy et al. "Electron- and muon-neutrino content of the atmospheric flux". In: *Phys. Rev. D* 46 (9 1992), pp. 3720–3724. DOI: `10.1103/PhysRevD.46.3720` (see pp. 1, 16, 204).

[10] Y. Fukuda et al. "Atmospheric v ve ratio in the multi-GeV energy range". In: *Physics Letters B* 335.2 (1994), pp. 237 –245. DOI: `https://doi.org/10.1016/0370-2693(94)91420-6` (see pp. 1, 16, 204).

[11] Y. Fukuda et al. "Evidence for Oscillation of Atmospheric Neutrinos". In: *Phys. Rev. Lett.* 81 (8 1998), pp. 1562–1567. DOI: `10.1103/PhysRevLett.81.1562` (see pp. 1, 9, 16, 17, 204, 205).

[12] Q. R. Ahmad et al. "Direct Evidence for Neutrino Flavor Transformation from Neutral-Current Interactions in the Sudbury Neutrino Observatory". In: *Phys. Rev. Lett.* 89 (1 2002), p. 011301. DOI: `10.1103/PhysRevLett.89.011301` (see pp. 1, 14, 205).

[13] Th. A. Mueller et al. "Improved predictions of reactor antineutrino spectra". In: *Phys. Rev. C* 83 (5 2011), p. 054615. DOI: `10.1103/PhysRevC.83.054615` (see pp. 2, 26, 42, 48–50, 70, 77, 80–82, 86, 92, 93, 95–97, 102, 106, 107, 110–112, 133, 147, 157, 158, 160, 205, 207).

[14] Patrick Huber. "Determination of antineutrino spectra from nuclear reactors". In: *Phys. Rev. C* 84 (2 2011), p. 024617. DOI: `10.1103/PhysRevC.84.024617` (see pp. 2, 26, 49–51, 96, 97, 154–156, 205).

[15] G. Mention et al. "Reactor antineutrino anomaly". In: *Phys. Rev. D* 83 (7 2011), p. 073006. DOI: `10.1103/PhysRevD.83.073006` (see pp. 2, 18, 23, 26, 53, 54, 57, 111, 205).

[16] Carlo Giunti and Marco Laveder. "Statistical significance of the gallium anomaly". In: *Phys. Rev. C* 83 (6 2011), p. 065504. DOI: `10.1103/PhysRevC.83.065504` (see pp. 2, 24, 205).

[17] A. Aguilar et al. "Evidence for neutrino oscillations from the observation of $\overline{\nu}$ appearance in a $\overline{\nu}_\mu$ beam". In: *Phys. Rev. D* 64 (11 2001), p. 112007. DOI: `10.1103/PhysRevD.64.112007` (see pp. 2, 25, 205).

[18] A. A. Aguilar-Arevalo et al. "Updated MiniBooNE neutrino oscillation results with increased data and new background studies". In: *Phys. Rev. D* 103 (5 2021), p. 052002. DOI: `10.1103/PhysRevD.103.052002` (see pp. 2, 25, 205).

[19] M. Fierz and W. Pauli. "On Relativistic Wave Equations for Particles of Arbitrary Spin in an Electromagnetic Field". In: *Proceedings of the Royal Society of London Series A* 173.953 (Nov. 1939), pp. 211–232. DOI: `10.1098/rspa.1939.0140` (see p. 4).

[20] W. Pauli. "The Connection Between Spin and Statistics". In: *Phys. Rev.* 58 (8 1940), pp. 716–722. DOI: `10.1103/PhysRev.58.716` (see p. 4).

[21] D. DeCamp et al. "Determination of the number of light neutrino species". In: *Physics Letters B* 231.4 (1989), pp. 519 –529. DOI: `https://doi.org/10.1016/0370-2693(89)90704-1` (see p. 4).

[22] M Tanabashi et al. "Review of Particle Physics: Particle Data Group". In: *Physical Review D* 98 (Aug. 2018) (see p. 5).

[23] M. Aker et al. "Improved Upper Limit on the Neutrino Mass from a Direct Kinematic Method by KATRIN". In: *Phys. Rev. Lett.* 123 (22 2019), p. 221802. DOI: `10.1103/PhysRevLett.123.221802` (see p. 5).

[24] F. Englert and R. Brout. "Broken Symmetry and the Mass of Gauge Vector Mesons". In: *Phys. Rev. Lett.* 13 (9 1964), pp. 321–323. DOI: `10.1103/PhysRevLett.13.321` (see p. 6).

[25] Peter W. Higgs. "Broken Symmetries and the Masses of Gauge Bosons". In: *Phys. Rev. Lett.* 13 (16 1964), pp. 508–509. DOI: `10.1103/PhysRevLett.13.508` (see p. 6).

[26] G. S. Guralnik, C. R. Hagen, and T. W. B. Kibble. "Global Conservation Laws and Massless Particles". In: *Phys. Rev. Lett.* 13 (20 1964), pp. 585–587. DOI: `10.1103/PhysRevLett.13.585` (see p. 6).

[27] G. Aad et al. "Observation of a new particle in the search for the Standard Model Higgs boson with the ATLAS detector at the LHC". In: *Physics Letters B* 716.1 (2012), pp. 1 –29. DOI: `https://doi.org/10.1016/j.physletb.2012.08.020` (see p. 6).

[28] S. Chatrchyan et al. "Observation of a new boson at a mass of 125 GeV with the CMS experiment at the LHC". In: *Physics Letters B* 716.1 (2012), pp. 30 –61. DOI: `https://doi.org/10.1016/j.physletb.2012.08.021` (see p. 6).

[29] H. Becquerel. "Sur les Radiations Emises par Phosphorescence." In: *Comptes Rendus des Séances de L'Académie des Sciences* 122 (189), pp. 420–421 (see p. 6).

[30] H. Becquerel. "Sur les Radiations Invisibles Emises par les Sels d'Uranium." In: *Comptes Rendus des Séances de L'Académie des Sciences* 122 (189), pp. 689–694 (see p. 6).

[31] H. Becquerel. “Sur les Propriétés Différentes des Radiations Invisibles Emises par les Sels d’Uranium, et du Rayonnement de la Paroi Anticathodique d’un Tube de Crookes.” In: *Comptes Rendus des Séances de L’Académie des Sciences* 122 (189), pp. 762–767 (see p. 6).

[32] E. Rutherford. “VIII. Uranium radiation and the electrical conduction produced by it”. In: *The London, Edinburgh, and Dublin Philosophical Magazine and Journal of Science* 47.284 (1899), pp. 109–163. DOI: `10.1080/14786449908621245`. eprint: `https://doi.org/10.1080/14786449908621245` (see p. 6).

[33] M M Villard. “Sur la reflexion et la refraction des rayons cathodiques et des rayons deviables du radium”. In: *C. R. Acad. Sci. Paris* 130 (1900), p. 1010 (see p. 6).

[34] J. Chadwick. “Intensiẗtsverteilung im magnetischen Spectrum der β-Strahlen von radium B + C”. In: *Verhandl. Dtsc. Phys. Ges.* 16 (1914), p. 383 (see p. 6).

[35] H. Bethe and R. Peierls. “The Neutrino”. In: *Nature* 133 (1934), p. 532. DOI: `10.1038/133532a0` (see p. 7).

[36] T. D. Lee and C. N. Yang. “Question of Parity Conservation in Weak Interactions”. In: *Phys. Rev.* 104 (1 1956), pp. 254–258. DOI: `10.1103/PhysRev.104.254` (see p. 8).

[37] C. S. Wu et al. “Experimental Test of Parity Conservation in Beta Decay”. In: *Phys. Rev.* 105 (4 1957), pp. 1413–1415. DOI: `10.1103/PhysRev.105.1413` (see pp. 8, 70).

[38] M. Goldhaber, L. Grodzins, and A. W. Sunyar. “Helicity of Neutrinos”. In: *Phys. Rev.* 109 (3 1958), pp. 1015–1017. DOI: `10.1103/PhysRev.109.1015` (see p. 8).

[39] J. C. Palathingal. “Helicity of Antineutrinos Emitted by Nuclei”. In: *Phys. Rev. Lett.* 24 (10 1970), pp. 524–526. DOI: `10.1103/PhysRevLett.24.524` (see p. 8).

[40] P. Aarnio et al. “Measurement of the mass and width of the Z0-particle from multihadronic final states produced in e+e− annihilations”. In: *Physics Letters B* 231.4 (1989), pp. 539 –547. DOI: `https://doi.org/10.1016/0370-2693(89)90706-5` (see p. 9).

[41] B. Adeva et al. “A determination of the properties of the neutral intermediate vector boson Z0”. In: *Physics Letters B* 231.4 (1989), pp. 509 –518. DOI: `https://doi.org/10.1016/0370-2693(89)90703-X` (see p. 9).

[42] M.Z. Akrawy et al. “Measurement of the Z0 mass and width with the opal detector at LEP”. In: *Physics Letters B* 231.4 (1989), pp. 530 –538. DOI: `https://doi.org/10.1016/0370-2693(89)90705-3` (see p. 9).

[43] G. S. Abrams et al. “Initial measurements of Z-boson resonance parameters in e^+e^- annihilation”. In: *Phys. Rev. Lett.* 63 (7 1989), pp. 724–727. DOI: `10.1103/PhysRevLett.63.724` (see p. 9).

[44] The L3 Collaboration The OPAL Collaboration The SLD Collaboration The LEP Electroweak Working Group The SLD Electroweak The ALEPH Collaboration The DELPHI Collaboration and Heavy Flavour Groups. “Precision electroweak measurements on the Z resonance”. In: *Physics Reports* 427.5 (2006), pp. 257 –454. DOI: `https://doi.org/10.1016/j.physrep.2005.12.006` (see p. 9).

[45] K. Kodama et al. “Observation of tau neutrino interactions”. In: *Physics Letters B* 504.3 (2001), pp. 218 –224. DOI: `https://doi.org/10.1016/S0370-2693(01)00307-0` (see pp. 1, 9).

[46] B. Pontecorvo. “Mesonium and anti-mesonium”. In: *Sov. Phys. JETP* 6 (1957). [Zh. Eksp. Teor. Fiz.33,549(1957)], p. 429 (see p. 9).

[47] Ziro Maki, Masami Nakagawa, and Shoichi Sakata. “Remarks on the Unified Model of Elementary Particles”. In: *Progress of Theoretical Physics* 28.5 (Nov. 1962), pp. 870–880. DOI: `10.1143/PTP.28.870`. eprint: `https://academic.oup.com/ptp/article-pdf/28/5/870/5258750/28-5-870.pdf` (see p. 9).

[48] C. Giunti et al. “Treatment of neutrino oscillations without resort to weak eigenstates”. In: *Phys. Rev. D* 48 (9 1993), pp. 4310–4317. DOI: `10.1103/PhysRevD.48.4310` (see p. 10).

[49] Carlo Giunti and Chung W. Kim. *Fundamentals of Neutrino Physics and Astrophysics*. 2007 (see pp. 10, 11, 20, 21).

[50] C. Giganti, S. Lavignac, and M. Zito. “Neutrino oscillations: The rise of the PMNS paradigm”. In: *Progress in Particle and Nuclear Physics* 98 (2018), pp. 1 –54. DOI: `https://doi.org/10.1016/j.ppnp.2017.10.001` (see pp. 10, 11, 15–17, 22).

[51] E. Kh. Akhmedov and A. Yu. Smirnov. “Paradoxes of neutrino oscillations”. In: *Physics of Atomic Nuclei* 72.8 (Aug. 2009), pp. 1363–1381. DOI: `10.1134/S1063778809080122`. arXiv: `0905.1903 [hep-ph]` (see p. 10).

[52] Ivan Esteban et al. “The fate of hints: updated global analysis of three-flavor neutrino oscillations”. In: *JHEP* 09 (2020), p. 178. DOI: `10.1007/JHEP09(2020)178`. arXiv: `2007.14792 [hep-ph]` (see pp. 13, 15, 17, 18).

[53] Bruce T. Cleveland et al. “Measurement of the Solar Electron Neutrino Flux with the Homestake Chlorine Detector”. In: *The Astrophysical Journal* 496.1 (1998), pp. 505–526. DOI: `10.1086/305343` (see p. 14).

[54] B. Pontecorvo. “Neutrino Experiments and the Problem of Conservation of Leptonic Charge”. In: *Sov. Phys. JETP* 26 (1968), pp. 984–988 (see p. 14).

[55] V. Gribov and B. Pontecorvo. “Neutrino astronomy and lepton charge”. In: *Physics Letters B* 28.7 (1969), pp. 493 –496. DOI: `https://doi.org/10.1016/0370-2693(69)90525-5` (see p. 14).

[56] J. N. Abdurashitov et al. “Measurement of the solar neutrino capture rate with gallium metal”. In: *Phys. Rev. C* 60 (5 1999), p. 055801. DOI: `10.1103/PhysRevC.60.055801` (see p. 14).

[57] K. Eguchi et al. “First Results from KamLAND: Evidence for Reactor Antineutrino Disappearance”. In: *Phys. Rev. Lett.* 90 (2 2003), p. 021802. DOI: `10.1103/PhysRevLett.90.021802` (see p. 15).

[58] A. Gando et al. “Reactor on-off antineutrino measurement with KamLAND”. In: *Phys. Rev. D* 88 (3 2013), p. 033001. DOI: `10.1103/PhysRevD.88.033001` (see pp. 15, 16).

[59] J N Bahcall. “Solar Models and Solar Neutrinos”. In: *Physica Scripta* T121 (2005), pp. 46–50. DOI: `10.1088/0031-8949/2005/t121/006` (see p. 16).

[60] M. H. Ahn et al. “Measurement of neutrino oscillation by the K2K experiment”. In: *Phys. Rev. D* 74 (7 2006), p. 072003. DOI: `10.1103/PhysRevD.74.072003` (see p. 16).

[61] P. Adamson et al. “Combined Analysis of ν_μ Disappearance and $\nu_\mu \rightarrow \nu_e$ Appearance in MINOS Using Accelerator and Atmospheric Neutrinos”. In: *Phys. Rev. Lett.* 112 (19 2014), p. 191801. DOI: `10.1103/PhysRevLett.112.191801` (see p. 16).

[62] N. Agafonova et al. “Discovery of τ Neutrino Appearance in the CNGS Neutrino Beam with the OPERA Experiment”. In: *Phys. Rev. Lett.* 115 (12 2015), p. 121802. DOI: `10.1103/PhysRevLett.115.121802` (see p. 16).

[63] K. Abe et al. “Indication of Electron Neutrino Appearance from an Accelerator-Produced Off-Axis Muon Neutrino Beam”. In: *Phys. Rev. Lett.* 107 (4 2011), p. 041801. DOI: `10.1103/PhysRevLett.107.041801` (see pp. 16, 18).

[64] P. Adamson et al. “Measurement of the Neutrino Mixing Angle θ_{23} in NOvA”. In: *Phys. Rev. Lett.* 118 (15 2017), p. 151802. DOI: `10.1103/PhysRevLett.118.151802` (see p. 16).

[65] Sacha E. Kopp. “Accelerator neutrino beams”. In: *Physics Reports* 439.3 (2007), pp. 101 –159. DOI: `https://doi.org/10.1016/j.physrep.2006.11.004` (see pp. 16, 17).

[66] H. Kwon et al. “Search for neutrino oscillations at a fission reactor”. In: *Phys. Rev. D* 24 (5 1981), pp. 1097–1111 (see p. 17).

[67] Achkar et al. “Comparison of anti-neutrino reactor spectrum models with the Bugey 3 measurements”. In: (1996) (see p. 17).

[68] Y. Declais et al. “Study of reactor antineutrino interaction with proton at Bugey nuclear power plant”. In: *Physics Letters B* 338.2 (1994), pp. 383 –389. DOI: `https://doi.org/10.1016/0370-2693(94)91394-3` (see pp. 17, 163, 212).

[69] G. Zacek et al. “Neutrino-oscillation experiments at the Gøsgen nuclear power reactor”. In: *Phys. Rev. D* 34 (9 1986), pp. 2621–2636. DOI: `10.1103/PhysRevD.34.2621` (see p. 17).

[70] Ketov S.N. Kopeikin V.I. Mikaelyan L.A. Skorokhvatov M.D. Tolokonnikov S.V.v Afonin A.I. “A study of the reaction ve + P → e+ +n on a nuclear reactor”. In: *Soviet Physics - JETP* 67.2 (1988), pp. 213 –221 (see p. 17).

[71] Vyrodov V.N. Gurevich I.I. Kozlov Yu.V. Martem
yanov V.P. Sukhotin S.V. Tarasenkov V.G. Khakimov S.Kh. Vidyakin G.S. “Detecting of antineutrinos in beam from two reactors”. In: *Soviet Physics - JETP* 93.8 (1987), pp. 424–431 (see p. 17).

[72] Z. D. Greenwood et al. “Results of a two-position reactor neutrino-oscillation experiment”. In: *Phys. Rev. D* 53 (11 1996), pp. 6054–6064. DOI: `10.1103/PhysRevD.53.6054` (see p. 17).

[73] Carlo Bemporad, Giorgio Gratta, and Petr Vogel. “Reactor-based neutrino oscillation experiments”. In: *Rev. Mod. Phys.* 74 (2 2002), pp. 297–328. DOI: `10.1103/RevModPhys.74.297` (see p. 18).

[74] M. Apollonio et al. “Limits on neutrino oscillations from the CHOOZ experiment”. In: *Physics Letters B* 466.2 (1999), pp. 415 –430. DOI: `https://doi.org/10.1016/S0370-2693(99)01072-2` (see p. 18).

[75] S. Yamamoto et al. “Improved Search for $\nu_\mu \to \nu_e$ Oscillation in a Long-Baseline Accelerator Experiment”. In: *Phys. Rev. Lett.* 96 (18 2006), p. 181801. DOI: `10.1103/PhysRevLett.96.181801` (see p. 18).

[76] P. Adamson et al. “Improved Search for Muon-Neutrino to Electron-Neutrino Oscillations in MINOS”. In: *Phys. Rev. Lett.* 107 (18 2011), p. 181802. DOI: `10.1103/PhysRevLett.107.181802` (see p. 18).

[77] F. P. An et al. “Measurement of electron antineutrino oscillation based on 1230 days of operation of the Daya Bay experiment”. In: *Phys. Rev. D* 95 (7 2017), p. 072006. DOI: `10.1103/PhysRevD.95.072006` (see p. 18).

[78] Y. Abe et al. “Improved measurements of the neutrino mixing angle theta(13) with the Double Chooz detector”. In: *Journal of High Energy Physics* (Feb. 2015). DOI: `10.1007/JHEP02(2015)074` (see p. 18).

[79] F. P. An et al. “Observation of Electron-Antineutrino Disappearance at Daya Bay”. In: *Phys. Rev. Lett.* 108 (17 2012), p. 171803. DOI: `10.1103/PhysRevLett.108.171803` (see p. 20).

[80] F. Ardellier et al. “Double Chooz: A Search for the neutrino mixing angle theta(13)”. In: (2006). arXiv: `hep-ex/0606025 [hep-ex]` (see p. 20).

[81] J. K. on behalf of the RENO Collaboration Ahn. “RENO: An Experiment for Neutrino Oscillation Parameter theta_13 Using Reactor Neutrinos at Yonggwang”. In: *arXiv e-prints*, arXiv:1003.1391 (Mar. 2010), arXiv:1003.1391. arXiv: `1003.1391 [hep-ex]` (see p. 20).

[82] Mauro Mezzetto and Thomas Schwetz. “ 13: phenomenology, present status and prospect”. In: *Journal of Physics G: Nuclear and Particle Physics* 37.10 (2010), p. 103001. DOI: `10.1088/0954-3899/37/10/103001` (see p. 19).

[83] M. Rayner. *Tuning in to neutrinos.* 2020. URL: `https://cerncourier.com/a/tuning-in-to-neutrinos/` (see p. 19).

[84] Michelle J. Dolinski, Alan W.P. Poon, and Werner Rodejohann. “Neutrinoless Double-Beta Decay: Status and Prospects”. In: *Annual Review of Nuclear and Particle Science* 69.1 (2019), pp. 219–251. DOI: `10.1146/annurev-nucl-101918-023407`. eprint: `https://doi.org/10.1146/annurev-nucl-101918-023407` (see p. 20).

[85] M. Agostini et al. “Probing Majorana neutrinos with double- decay”. In: *Science* 365.6460 (2019), pp. 1445–1448. DOI: `10.1126/science.aav8613`. eprint: `https://science.sciencemag.org/content/365/6460/1445.full.pdf` (see p. 20).

[86] S. I. Alvis et al. “Search for neutrinoless double-β decay in ^{76}Ge with 26 kg yr of exposure from the Majorana Demonstrator”. In: *Phys. Rev. C* 100 (2 2019), p. 025501. DOI: `10.1103/PhysRevC.100.025501` (see p. 20).

[87] O. Azzolini et al. “Final Result of CUPID-0 Phase-I in the Search for the ^{82}Se Neutrinoless Double-β Decay”. In: *Phys. Rev. Lett.* 123 (3 2019), p. 032501. DOI: `10.1103/PhysRevLett.123.032501` (see p. 20).

[88] J. Argyriades et al. “Measurement of the two neutrino double beta decay half-life of Zr-96 with the NEMO-3 detector”. In: *Nuclear Physics A* 847.3 (2010), pp. 168 –179. DOI: `https://doi.org/10.1016/j.nuclphysa.2010.07.009` (see p. 20).

[89] R. Arnold et al. “Results of the search for neutrinoless double-β decay in ^{100}Mo with the NEMO-3 experiment”. In: *Phys. Rev. D* 92 (7 2015), p. 072011. DOI: `10.1103/PhysRevD.92.072011` (see p. 20).

[90] R. Arnold et al. “Measurement of the $2\nu\beta\beta$ decay half-life of ^{150}Nd and a search for $0\nu\beta\beta$ decay processes with the full exposure from the NEMO-3 detector”. In: *Phys. Rev. D* 94 (7 2016), p. 072003. DOI: `10.1103/PhysRevD.94.072003` (see p. 20).

[91] A. S. Barabash et al. “Final results of the Aurora experiment to study 2β decay of ^{116}Cd with enriched ^{116}CdWO$_4$ crystal scintillators”. In: *Phys. Rev. D* 98 (9 2018), p. 092007. DOI: `10.1103/PhysRevD.98.092007` (see p. 20).

[92] D. Q. Adams et al. “Improved Limit on Neutrinoless Double-Beta Decay in ^{130}Te with CUORE”. In: *Phys. Rev. Lett.* 124 (12 2020), p. 122501. DOI: `10.1103/PhysRevLett.124.122501` (see p. 20).

[93] A. Gando et al. “Search for Majorana Neutrinos Near the Inverted Mass Hierarchy Region with KamLAND-Zen”. In: *Phys. Rev. Lett.* 117 (8 2016), p. 082503. DOI: `10.1103/PhysRevLett.117.082503` (see p. 20).

[94] G. Anton et al. “Search for Neutrinoless Double-β Decay with the Complete EXO-200 Dataset”. In: *Phys. Rev. Lett.* 123 (16 2019), p. 161802. DOI: `10.1103/PhysRevLett.123.161802` (see p. 20).

[95] C. Kraus et al. “Final results from phase II of the Mainz neutrino mass searchin tritium decay”. In: *European Physical Journal C* 40 (Apr. 2005), pp. 447–468 (see p. 21).

[96] V. N. Aseev et al. “Upper limit on the electron antineutrino mass from the Troitsk experiment”. In: *Phys. Rev. D* 84 (11 2011), p. 112003. DOI: `10.1103/PhysRevD.84.112003` (see p. 21).

[97] M. Aker et al. *First direct neutrino-mass measurement with sub-eV sensitivity.* 2021. arXiv: `2105.08533 [hep-ex]` (see p. 21).

[98] Nathalie Palanque-Delabrouille et al. “Constraint on neutrino masses from SDSS-III/BOSS Ly forest and other cosmological probes”. In: *Journal of Cosmology and Astroparticle Physics* 2015.02 (2015), pp. 045–045. DOI: `10.1088/1475-7516/2015/02/045` (see p. 21).

[99] I. Gil-Botella. “Neutrino Physics”. In: arXiv:1504.03551 (2015). 50 pages, contribution to the 2011 CERN-Latin-American School of High-Energy Physics, Natal, Brazil, 23 March-5 April 2011, edited by C. Grojean, M. Mulders and M. Spiropulu. arXiv admin note: text overlap with arXiv:1010.5112, arXiv:1010.4131, arXiv:0704.1800 by other authors, 157–205. 50 p. DOI: `10.5170/CERN-2013-003.157` (see p. 21).

[100] Haoqi Lu. “Status of the JUNO reactor anti-neutrino experiment”. In: *Nuclear and Particle Physics Proceedings* 287-288 (2017). The 14th International Workshop on Tau Lepton Physics, pp. 143 –146. DOI: `https://doi.org/10.1016/j.nuclphysbps.2017.03.063` (see p. 22).

[101] DUNE Collaboration et al. “Long-Baseline Neutrino Facility (LBNF) and Deep Underground Neutrino Experiment (DUNE) Conceptual Design Report Volume 2: The Physics Program for DUNE at LBNF”. In: *arXiv e-prints*, arXiv:1512.06148 (Dec. 2015), arXiv:1512.06148. arXiv: `1512.06148 [physics.ins-det]` (see p. 22).

[102] DUNE Collaboration et al. *Long-baseline neutrino oscillation physics potential of the DUNE experiment.* 2020. arXiv: `2006.16043 [hep-ex]` (see pp. 22, 23).

[103] Stephen F King and Christoph Luhn. “Neutrino mass and mixing with discrete symmetry”. In: *Reports on Progress in Physics* 76.5 (2013), p. 056201. DOI: `10.1088/0034-4885/76/5/056201` (see p. 23).

[104] J. Bernabéu and A. Segarra. “Stimulated transitions in resonant atom Majorana mixing”. In: *Journal of High Energy Physics* 2018 (2017), pp. 1–16 (see p. 23).

[105] K. Abe et al. “Combined Analysis of Neutrino and Antineutrino Oscillations at T2K”. In: *Phys. Rev. Lett.* 118 (15 2017), p. 151801. DOI: `10.1103/PhysRevLett.118.151801` (see p. 23).

[106] M.V. Smirnov et al. “The possibility of leptonic CP-violation measurement with JUNO”. In: *Nuclear Physics B* 931 (2018), pp. 437–445. DOI: `https://doi.org/10.1016/j.nuclphysb.2018.05.003` (see p. 23).

[107] Carlo Giunti and Marco Laveder. “$3 + 1$ and $3 + 2$ sterile neutrino fits”. In: *Phys. Rev. D* 84 (7 2011), p. 073008. DOI: `10.1103/PhysRevD.84.073008` (see p. 24).

[108] J. Kopp et al. “Sterile neutrino oscillations: the global picture”. In: *Journal of High Energy Physics* 5, 50 (May 2013), p. 50. DOI: `10.1007/JHEP05(2013)050`. arXiv: `1303.3011 [hep-ph]` (see p. 24).

[109] P Anselmann et al. "First results from the 51Cr neutrino source experiment with the GALLEX detector". In: *Physics Letters B* 342.1 (1995), pp. 440 –450. DOI: `https://doi.org/10.1016/0370-2693(94)01586-2` (see p. 24).

[110] W Hampel et al. "Final results of the 51Cr neutrino source experiments in GALLEX". In: *Physics Letters B* 420.1 (1998), pp. 114 –126. DOI: `https://doi.org/10.1016/S0370-2693(97)01562-1` (see p. 24).

[111] V.I. Barsanov et al. "Artificial neutrino source based on the Ar-37 isotope". In: *Phys. Atom. Nucl.* 70 (2007), pp. 300–310. DOI: `10.1134/S1063778807020111` (see p. 24).

[112] J. Kostensalo et al. "The gallium anomaly revisited". In: *Physics Letters B* 795 (2019), pp. 542–547. DOI: `https://doi.org/10.1016/j.physletb.2019.06.057` (see p. 24).

[113] A. A. Aguilar-Arevalo et al. "Significant Excess of Electronlike Events in the MiniBooNE Short-Baseline Neutrino Experiment". In: *Phys. Rev. Lett.* 121 (22 2018), p. 221801. DOI: `10.1103/PhysRevLett.121.221801` (see p. 25).

[114] A.A. Aguilar-Arevalo et al. "The MiniBooNE detector". In: *Nuclear Instruments and Methods in Physics Research Section A: Accelerators, Spectrometers, Detectors and Associated Equipment* 599.1 (2009), pp. 28 –46. DOI: `https://doi.org/10.1016/j.nima.2008.10.028` (see p. 25).

[115] R. Acciarri et al. "Design and construction of the MicroBooNE detector". In: *Journal of Instrumentation* 12.02 (2017), P02017–P02017. DOI: `10.1088/1748-0221/12/02/p02017` (see p. 25).

[116] F. Von Feilitzsch A.A. Hahn K. Hawerkamp J.L. Vuilleumier Schreckenbach H.R. Faust. "Absolute measurement of the beta spectrum from 235U fission as a basis for reactor antineutrino experiments". In: (1981). Ed. by Physics letter. DOI: `https://doi.org/10.1016/0370-2693(81)91120-5` (see pp. 25, 49, 51, 147, 148).

[117] Feilitzsch Schreckenbach Hahn. "Experimental beta spectra from 239Pu and 235U thermal neutron fission products and their correlated antineutrino spectra". In: Volume1 18B,n umbe1r , 2, 3 PHYSICS LETTERS 2 Decembe1r (1982). Ed. by PHYSICS LETTERS. DOI: `10.1016/0370-2693(82)90622-0` (see pp. 25, 49, 131, 147, 148).

[118] W. Gelletly F. Von Feilitzsch Schreckenbach G. Colvin. "Determination of the antineutrino sprectrum from 235U thermal neutron fission products up to 9.5 MeV". In: (1985). Ed. by PHYSICS LETTERS. DOI: `10.1016/0370-2693(85)91337-1` (see pp. 25, 49, 51, 131, 147, 148).

[119] W. Gelletly F. Von Ferlitzsch G. Colvin B. Krusche Schreckenbach Hahn. "Antineutrino spectra from 241Pu and 239Pu thermal neutron fission products". In: (1989). Ed. by Physics letter. DOI: `10.1016/0370-2693(89)91598-0` (see pp. 25, 49, 131, 147, 148).

[120] S. Gariazzo et al. "Updated global 3+1 analysis of short-baseline neutrino oscillations". In: *Journal of High Energy Physics* 2017.6 (2017), p. 135. DOI: `10.1007/JHEP06(2017)135` (see pp. 26, 57).

[121] M. Aker et al. "Bound on 3 + 1 Active-Sterile Neutrino Mixing from the First Four-Week Science Run of KATRIN". In: *Phys. Rev. Lett.* 126 (9 2021), p. 091803. DOI: `10.1103/PhysRevLett.126.091803` (see pp. 27, 59).

[122] P. Adamson et al. "Search for Sterile Neutrinos in MINOS and MINOS+ Using a Two-Detector Fit". In: *Phys. Rev. Lett.* 122 (9 2019), p. 091803. DOI: `10.1103/PhysRevLett.122.091803` (see p. 27).

[123] M. G. Aartsen et al. “Searches for Sterile Neutrinos with the IceCube Detector”. In: *Phys. Rev. Lett.* 117 (7 2016), p. 071801. DOI: `10.1103/PhysRevLett.117.071801` (see p. 27).

[124] Pedro A.N. Machado, Ornella Palamara, and David W. Schmitz. “The Short-Baseline Neutrino Program at Fermilab”. In: *Annual Review of Nuclear and Particle Science* 69.1 (2019), pp. 363–387. DOI: `10.1146/annurev-nucl-101917-020949`. eprint: `https://doi.org/10.1146/annurev-nucl-101917-020949` (see p. 27).

[125] S. Ajimura et al. “Technical Design Report (TDR): Searching for a Sterile Neutrino at J-PARC MLF (E56, JSNS2)”. In: (May 2017) (see p. 27).

[126] Jeffrey M. Berryman. “Constraining sterile neutrino cosmology with terrestrial oscillation experiments”. In: *Phys. Rev. D* 100 (2 2019), p. 023540. DOI: `10.1103/PhysRevD.100.023540` (see p. 27).

[127] G. Agnolet et al. “Background studies for the MINER Coherent Neutrino Scattering reactor experiment”. In: *Nuclear Instruments and Methods in Physics Research Section A: Accelerators, Spectrometers, Detectors and Associated Equipment* 853 (2017), pp. 53 –60. DOI: `https://doi.org/10.1016/j.nima.2017.02.024` (see pp. 27, 66, 67).

[128] F. Gönnenwein. “Ternary and quaternary fission”. In: *Nuclear Physics A* 734 (2004), pp. 213 –216. DOI: `https://doi.org/10.1016/j.nuclphysa.2004.01.037` (see p. 30).

[129] Kenneth S. Krane. *Introductory nuclear physics* (see pp. 30, 42).

[130] G. Naudet and P. Reuss. *Énergies, électricité et nucléaire.* Génie atomique. EDP Sciences, 2008 (see pp. 30–32, 34, 35, 37).

[131] Elmer E. Lewis. *Fundamentals of Nuclear Reactor Physics.* Academic Press, 2008 (see pp. 30, 32, 39, 40).

[132] C. de la Vaissière. IN2P3 / EDP Sciences, (accessed June 9, 2021). URL: `https://www.radioactivity.eu.com/site/pages/Slow_Fast_Neutrons.htm` (see p. 31).

[133] G. Naudet and P. Reuss. *Précis de neutronique.* Génie atomique. EDP Sciences, 2008 (see pp. 31, 32, 34).

[134] D.A. Brown et al. “ENDF/B-VIII.0: The 8th Major Release of the Nuclear Reaction Data Library with CIELO-project Cross Sections, New Standards and Thermal Scattering Data”. In: *Nuclear Data Sheets* 148 (2018). Special Issue on Nuclear Reaction Data, pp. 1 –142. DOI: `https://doi.org/10.1016/j.nds.2018.02.001` (see pp. 32, 40, 113).

[135] Aldo Dall’Osso and Léandre Brault. “On the neutron spectrum and multiplication factor in the infinite homogeneous reactor”. In: *Annals of Nuclear Energy* 36.8 (2009), pp. 1287 –1293. DOI: `https://doi.org/10.1016/j.anucene.2009.04.008` (see p. 33).

[136] Arjan Plompen et al. “The joint evaluated fission and fusion nuclear data library, JEFF-3.3”. In: *The European Physical Journal A* 56 (July 2020). DOI: `10.1140/epja/s10050-020-00141-9` (see pp. 33, 39–41, 43, 65, 89, 104, 108, 113, 132, 134, 136, 138, 140, 142, 148, 157, 160, 178, 210).

[137] S. Marguet. *The Physics of Nuclear Reactors.* Springer, 2017 (see pp. 32, 35, 37, 39, 42).

[138] Walt Patterson Gennadi Pshakin M.V. Ramana Mycle Schneider Tatsujiro Suzuki Frank von Hippel Thomas B. Cochran Harold A. Feiveson. *Fast Breeder Reactor Programs:History and Status.* (accessed June 10, 2021). URL: `http://fissilematerials.org/library/rr08.pdf` (see p. 34).

[139] Commissariat à l’Énergie Atomique et aux Énergies Alternatives. *ELECNUC: Nuclear power plants in the world.* CEA, 2019 (see p. 34).

[140] Pierre Coppolani et al. *La chaudière des réacteurs à eau sous pression*. Génie atomique. EDP Sciences, 2008 (see pp. 34, 35).

[141] Encyclopædia Britannica. (accessed November 11, 2020). URL: `https://www.britannica.com/technology/pressurized-water-reactor` (see p. 36).

[142] Anthony Onillon. "Estimation of the Chooz cores fission rates and associated errors in the framework of the Double Chooz experiment". Theses. Ecole des Mines de Nantes, May 2014 (see p. 35).

[143] Juris Meija et al. "Isotopic compositions of the elements 2013 (IUPAC Technical Report)". In: *Pure and Applied Chemistry* 88.3 (1Mar. 2016), pp. 293 –306. DOI: `https://doi.org/10.1515/pac-2015-0503` (see p. 35).

[144] N. Kerkar and P. Paulin. *Exploitation des coeurs REP*. Génie atomique. EDP Sciences, 2008 (see p. 37).

[145] Anthony Onillon, Matthieu Vivier, and Alex Wex. *Neutrino flux prediction - antineutrino spectra review -*. Internal communication (talk) to the NUCLEUS collaboration. 2021 (see pp. 37, 42, 43, 45, 65).

[146] N. Allemandou et al. "The STEREO experiment". In: *Journal of Instrumentation* 13.07 (2018), P07009–P07009. DOI: `10.1088/1748-0221/13/07/p07009` (see pp. 37, 38).

[147] J. Ashenfelter et al. "The PROSPECT reactor antineutrino experiment". In: *Nuclear Instruments and Methods in Physics Research Section A: Accelerators, Spectrometers, Detectors and Associated Equipment* 922 (2019), pp. 287 –309. DOI: `https://doi.org/10.1016/j.nima.2018.12.079` (see pp. 37, 56, 58).

[148] Ivochkin V.G. Samoilov R.M. et al. Serebrov A.P. "First Observation of the Oscillation Effect in the Neutrino-4 Experiment on the Search for the Sterile Neutrino". In: *Jetp Lett.* 109 (2019), pp. 213–221. DOI: `10.1134/S0021364019040040` (see pp. 37, 58).

[149] Y. Abreu et al. "A novel segmented-scintillator antineutrino detector". In: *Journal of Instrumentation* 12.04 (2017), P04024–P04024. DOI: `10.1088/1748-0221/12/04/p04024` (see pp. 37, 58).

[150] Ghita Zaz. "Post Examination of a High Flux Reactor Single Element with Ultra-Sounds". Theses. Université Montpellier, Dec. 2015 (see p. 38).

[151] H. Almazán et al. "Improved sterile neutrino constraints from the STEREO experiment with 179 days of reactor-on data". In: *Phys. Rev. D* 102 (5 2020), p. 052002. DOI: `10.1103/PhysRevD.102.052002` (see pp. 38, 44, 45, 56, 58).

[152] Institut Laue-Langevin (ILL) Grenoble. (accessed June 10, 2021). URL: `https://www.encyclopedie-energie.org/les-reacteurs-de-recherche/` (see p. 39).

[153] Robert W. Mills. "Fission product yield evaluation". PhD thesis. 1995 (see pp. 38, 40, 113).

[154] H. Bateman. "Solution of a system of differential equations occurring in the theory of radioactive transformations". In: *Proc. Cambridge Phil. Soc.* 15 (1910), pp. 423–427 (see p. 39).

[155] F.G. Kondev et al. "The NUBASE2020 evaluation of nuclear physics properties $*$". In: *Chinese Physics C* 45.3 (2021), p. 030001. DOI: `10.1088/1674-1137/abddae` (see pp. 41, 105, 111).

[156] Jun-ichi Katakura. *JENDL FP decay data file 2011 and fission yields data file 2011*. 2012 (see p. 40).

[157] J.-Ch. Sublet et al. “FISPACT-II: An Advanced Simulation System for Activation, Transmutation and Material Modelling”. In: *Nuclear Data Sheets* 139 (2017). Special Issue on Nuclear Reaction Data, pp. 77–137. DOI: `https://doi.org/10.1016/j.nds.2017.01.002` (see pp. 43, 148, 154, 162).

[158] H. Almazán et al. “Accurate Measurement of the Electron Antineutrino Yield of ^{235}U Fissions from the STEREO Experiment with 119 Days of Reactor-On Data”. In: *Phys. Rev. Lett.* 125 (20 2020), p. 201801. DOI: `10.1103/PhysRevLett.125.201801` (see pp. 44, 57, 162, 163, 185, 212).

[159] Keiichi SHIBATA et al. “JENDL-4.0: A New Library for Nuclear Science and Engineering”. In: *Journal of Nuclear Science and Technology* 48.1 (2011), pp. 1–30. DOI: `10.1080/18811248.2011.9711675`. eprint: `https://doi.org/10.1080/18811248.2011.9711675` (see pp. 44, 45, 47, 113).

[160] V. I. Kopeikin. “Flux and spectrum of reactor antineutrinos”. In: *Physics of Atomic Nuclei* 75.2 (2012), pp. 143–152. DOI: `10.1134/s1063778812020123` (see p. 44).

[161] From ENSDF database as of June 29th 2020. Version available at. URL: `http://www.nndc.bnl.gov/ensarchivals/` (see pp. 44, 47, 81, 82, 84, 86, 88, 90, 97, 102–104, 125, 176, 177, 194, 196, 198, 200, 202).

[162] Andrew James Conant. “Antineutrino spectrum characterization at the high flux isotope reactor using neutronic simulations”. Theses. Georgia Tech, Aug. 2019 (see pp. 44, 45).

[163] A. B. Balantekin et al. “Nonfuel antineutrino contributions in the ORNL High Flux Isotope Reactor (HFIR)”. In: *Phys. Rev. C* 101 (5 2020), p. 054605. DOI: `10.1103/PhysRevC.101.054605` (see pp. 44, 45).

[164] J. Ashenfelter et al. “Measurement of the Antineutrino Spectrum from ^{235}U Fission at HFIR with PROSPECT”. In: *Phys. Rev. Lett.* 122 (25 2019), p. 251801. DOI: `10.1103/PhysRevLett.122.251801` (see pp. 45, 58, 60, 185).

[165] X. B. Ma et al. “Improved calculation of the energy release in neutron-induced fission”. In: *Phys. Rev. C* 88 (1 2013), p. 014605. DOI: `10.1103/PhysRevC.88.014605` (see p. 46).

[166] Zhigang Ge et al. “CENDL-3.2: The new version of Chinese general purpose evaluated nuclear data library”. In: *European Physical Journal Web of Conferences*. Vol. 239. European Physical Journal Web of Conferences. May 2020, 09001, p. 09001. DOI: `10.1051/epjconf/202023909001` (see p. 47).

[167] R. W. King and J. F. Perkins. “Inverse Beta Decay and the Two-Component Neutrino”. In: *Phys. Rev.* 112 (3 1958), pp. 963–966. DOI: `10.1103/PhysRev.112.963` (see p. 47).

[168] F. T. Avignone, S. M. Blakenship, and C. W. Darden. “Theoretical Fission-Antineutrino Spectrum and Cross Section of the Reaction $^{3}\mathrm{He}(\overline{\nu}_e, e^+)^{3}\mathrm{H}$”. In: *Phys. Rev.* 170 (4 1968), pp. 931–934. DOI: `10.1103/PhysRev.170.931` (see p. 47).

[169] F. T. Avignone. “$V - A$ Elastic Scattering of Electrons by Fission Antineutrinos”. In: *Phys. Rev. D* 2 (11 1970), pp. 2609–2612. DOI: `10.1103/PhysRevD.2.2609` (see p. 47).

[170] A A Borovoi, Y L Dobrynin, and V I Kopeikin. “Energy spectra of electrons and antineutrinos from fragments in thermal-neutron fission of /sup 235/U and /sup 239/Pu”. In: *Sov. J. Nucl. Phys. (Engl. Transl.); (United States)* 25 (Feb. 1977) (see p. 47).

[171] J.C. Hardy et al. “The essential decay of pandemonium: A demonstration of errors in complex beta-decay schemes”. In: *Physics Letters B* 71.2 (1977), pp. 307 –310. DOI: `https://doi.org/10.1016/0370-2693(77)90223-4` (see pp. 47, 106).

[172] F. T. Avignone III, L. P. Hopkins, and Z. D. Greenwood. "Theoretical Beta Spectrum from Uranium-235 Fission Fragments in Secular Equilibrium". In: *Nuclear Science and Engineering* 72.2 (1979), pp. 216–221. DOI: `10.13182/NSE79-A19465`. eprint: `https://doi.org/10.13182/NSE79-A19465` (see p. 47).

[173] F. T. Avignone and Z. D. Greenwood. "Calculated spectra of antineutrinos from the fission products of ^{235}U, ^{238}U, and ^{239}Pu, and antineutrino-induced reactions". In: *Phys. Rev. C* 22 (2 1980), pp. 594–605. DOI: `10.1103/PhysRevC.22.594` (see p. 47).

[174] B. R. Davis et al. "Reactor antineutrino spectra and their application to antineutrino-induced reactions". In: *Phys. Rev. C* 19 (6 1979), pp. 2259–2266. DOI: `10.1103/PhysRevC.19.2259` (see pp. 47, 49).

[175] P. Vogel et al. "Reactor antineutrino spectra and their application to antineutrino-induced reactions. II". In: *Phys. Rev. C* 24 (4 1981), pp. 1543–1553. DOI: `10.1103/PhysRevC.24.1543` (see pp. 47, 49).

[176] M. Fallot et al. "New Antineutrino Energy Spectra Predictions from the Summation of Beta Decay Branches of the Fission Products". In: *Phys. Rev. Lett.* 109 (20 2012), p. 202504. DOI: `10.1103/physrevlett.109.202504` (see pp. 48, 77, 86, 95–97, 106, 111, 112, 150).

[177] M. Fallot et al. "Total absorption spectroscopy of fission fragments relevant for reactor antineutrino spectra". In: *European Physical Journal Web of Conferences*. Vol. 146. European Physical Journal Web of Conferences. Sept. 2017, 10002, p. 10002. DOI: `10.1051/epjconf/201714610002` (see p. 48).

[178] M. Estienne et al. "Updated Summation Model: An Improved Agreement with the Daya Bay Antineutrino Fluxes". In: *Phys. Rev. Lett.* 123 (2 2019), p. 022502. DOI: `10.1103/PhysRevLett.123.022502` (see pp. 48, 61, 96, 150, 162, 163, 169, 211, 212).

[179] M. Estienne et al. "Summation Calculations for Reactor Antineutrino Spectra, Decay Heat and Delayed Neutron Fractions Involving New TAGS Data and Evaluated Databases". In: *European Physical Journal Web of Conferences*. Vol. 211. European Physical Journal Web of Conferences. Oct. 2019, 01001, p. 01001. DOI: `10.1051/epjconf/201921101001` (see pp. 48, 106, 150).

[180] L Hayen. "Spurring the beta spectrum hydra towards the reactor anomaly". eng. PhD thesis. 2018 (see p. 48).

[181] L. Hayen et al. "First-forbidden transitions in the reactor anomaly". In: *Phys. Rev. C* 100 (5 2019), p. 054323. DOI: `10.1103/PhysRevC.100.054323` (see pp. 48, 51, 60, 120).

[182] D. A. Dwyer and T. J. Langford. "Spectral Structure of Electron Antineutrinos from Nuclear Reactors". In: *Phys. Rev. Lett.* 114 (1 2015), p. 012502. DOI: `10.1103/PhysRevLett.114.012502` (see p. 48).

[183] A. A. Sonzogni, M. Nino, and E. A. McCutchan. "Revealing fine structure in the antineutrino spectra from a nuclear reactor". In: *Phys. Rev. C* 98 (1 2018), p. 014323. DOI: `10.1103/PhysRevC.98.014323` (see p. 48).

[184] JUNO Collaboration et al. "TAO Conceptual Design Report: A Precision Measurement of the Reactor Antineutrino Spectrum with Sub-percent Energy Resolution". In: *arXiv e-prints*, arXiv:2005.08745 (May 2020), arXiv:2005.08745. arXiv: `2005.08745 [physics.ins-det]` (see pp. 48, 56).

[185] C. O. Muelhause and S. Oleksa. "Antineutrino Flux from a Reactor". In: *Phys. Rev.* 105 (4 1957), pp. 1332–1334. DOI: `10.1103/PhysRev.105.1332` (see pp. 49, 51).

[186] R. E. Carter et al. “Free Antineutrino Absorption Cross Section. II. Expected Cross Section from Measurements of Fission Fragment Electron Spectrum”. In: *Phys. Rev.* 113 (1 1959), pp. 280–286. DOI: 10.1103/PhysRev.113.280 (see pp. 49, 51).

[187] W. Mampe et al. “The double focusing iron-core electron-spectrometer “BILL” for high resolution (n, e—) measurements at the high flux reactor in Grenoble”. In: *Nuclear Instruments and Methods* 154.1 (1978), pp. 127 –149. DOI: https://doi.org/10.1016/0029-554X(78)90671-7 (see p. 49).

[188] N. Haag et al. “Re-publication of the data from the BILL magnetic spectrometer: The cumulative β spectra of the fission products of ^{235}U, ^{239}Pu, and ^{241}Pu”. In: *ArXiv e-prints* (May 2014). arXiv: 1405.3501 [nucl-ex] (see pp. 49, 51, 147, 148, 153).

[189] N. Haag et al. “Experimental Determination of the Antineutrino Spectrum of the Fission Products of ^{238}U”. In: *Phys. Rev. Lett.* 112 (12 2014), p. 122501. DOI: 10.1103/PhysRevLett.112.122501 (see pp. 49, 51, 131, 147–149, 153).

[190] N. Tsoulfanidis, B. W. Wehring, and M. E. Wyman. “Measurements of Time-Dependent Energy Spectra of Beta Rays from Uranium-235 Fission Fragments”. In: *Nuclear Science and Engineering* 43.1 (1971), pp. 42–53. DOI: 10.13182/NSE71-A21244. eprint: https://doi.org/10.13182/NSE71-A21244 (see p. 51).

[191] V. I. Kopeikin, Yu. N. Panin, and A. A. Sabelnikov. “Measurement of the Ratio of Cumulative Spectra of Beta Particles from ^{235}U and ^{239}Pu Fission Products for Solving Problems of Reactor-Antineutrino Physics”. In: *Phys. Atom. Nucl.* 84.1 (2021), pp. 1–10. DOI: 10.1134/S1063778821010129 (see pp. 51, 151).

[192] V. Kopeikin, M. Skorokhvatov, and O. Titov. *Reevaluating reactor antineutrino spectra with new measurements of the ratio between ^{235}U and ^{239}Pu β spectra.* 2021. arXiv: 2103.01684 [nucl-ex] (see pp. 51, 151).

[193] A. Onillon and A. Letourneau. “Investigation of the ILL spectra normalization”. In: *Applied Antineutrino Physics 2018 Proceedings*, arXiv:1911.06834 (2019). arXiv: 1911.06834 (see pp. 51, 151).

[194] Daya Bay collaboration et al. “Antineutrino Energy Spectrum Unfolding Based on the Daya Bay Measurement and Its Applications”. In: *arXiv e-prints*, arXiv:2102.04614 (Feb. 2021), arXiv:2102.04614. arXiv: 2102.04614 [hep-ex] (see pp. 52, 161, 164–166, 185).

[195] D. Adey et al. “Extraction of the ^{235}U and ^{239}Pu Antineutrino Spectra at Daya Bay”. In: *Phys. Rev. Lett.* 123 (11 2019), p. 111801. DOI: 10.1103/PhysRevLett.123.111801 (see pp. 52, 60, 161).

[196] J. A. Formaggio and G. P. Zeller. “From eV to EeV: Neutrino cross sections across energy scales”. In: *Rev. Mod. Phys.* 84 (3 2012), pp. 1307–1341. DOI: 10.1103/RevModPhys.84.1307 (see p. 52).

[197] P. Vogel and J. F. Beacom. “Angular distribution of neutron inverse beta decay, $\overline{\nu}_e + \overrightarrow{p}$ $e^+ + n$”. In: *Phys. Rev. D* 60 (5 1999), p. 053003. DOI: 10.1103/PhysRevD.60.053003 (see pp. 53, 54).

[198] Artur Ankowski. “Improved estimate of the cross section for inverse beta decay”. In: *Journal of Physics: Conference Series* 1216 (Jan. 2016). DOI: 10.1088/1742-6596/1216/1/012015 (see p. 53).

[199] Particle Data Group et al. “Review of Particle Physics”. In: *Progress of Theoretical and Experimental Physics* 2020.8 (Aug. 2020). 083C01. DOI: 10.1093/ptep/ptaa104. eprint: https://academic.oup.com/ptep/article-pdf/2020/8/083C01/34673722/ptaa104.pdf (see pp. 53, 54, 63).

[200] D.H. Wilkinson. "Analysis of neutron -decay". In: *Nuclear Physics A* 377.2 (1982), pp. 474 –504. DOI: `https://doi.org/10.1016/0375-9474(82)90051-3` (see p. 53).

[201] D.H. Wilkinson. "Phase space for neutron beta-decay: an update". In: *Nuclear Instruments and Methods in Physics Research Section A: Accelerators, Spectrometers, Detectors and Associated Equipment* 404.2 (1998), pp. 305–310. DOI: `https://doi.org/10.1016/S0168-9002(97)01153-4` (see p. 53).

[202] P. Vogel. "Analysis of the antineutrino capture on protons". In: *Phys. Rev. D* 29 (9 1984), pp. 1918–1922. DOI: `10.1103/PhysRevD.29.1918` (see pp. 54, 77, 81, 92, 97).

[203] S. A. Fayans. "Radiative Corrections and Recoil Effects in the Reaction $\bar{\nu}_e + P \to N + e^+$ at Low-energies. (In Russian)". In: *Sov. J. Nucl. Phys.* 42 (1985). [Yad. Fiz.42,929(1985)], p. 590 (see pp. 54, 92).

[204] C. Caso et al. (Particle Data Group). "Review of Particle Physics". In: *The European Physical Journal C3* (1998) (see p. 54).

[205] F. P. An et al. "Improved measurement of the reactor antineutrino flux and spectrum at Daya Bay". In: *Chinese Physics C* 41.1 (2017), p. 013002. DOI: `10.1088/1674-1137/41/1/013002` (see pp. 55, 58, 141).

[206] Jun Cao and Kam-Biu Luk. "An overview of the Daya Bay reactor neutrino experiment". In: *Nuclear Physics B* 908 (2016). Neutrino Oscillations: Celebrating the Nobel Prize in Physics 2015, pp. 62 –73. DOI: `https://doi.org/10.1016/j.nuclphysb.2016.04.034` (see p. 55).

[207] H Almazán et al. "First antineutrino energy spectrum from 235U fissions with the STEREO detector at ILL ∗". In: *Journal of Physics G: Nuclear and Particle Physics* 48.7 (2021), p. 075107. DOI: `10.1088/1361-6471/abd37a` (see pp. 55, 58, 60, 161, 164).

[208] Celine Moortgat. "The SoLid antineutrino detector: construction and commissioning with cosmic ray muons: Ćline Moortgat". English. Score=30. PhD thesis. UGent - Universiteit Gent, Feb. 2018 (see p. 56).

[209] I. Alekseev et al. "DANSS: Detector of the reactor AntiNeutrino based on Solid Scintillator". In: *Journal of Instrumentation* 11.11 (2016), P11011–P11011. DOI: `10.1088/1748-0221/11/11/p11011` (see pp. 56, 58).

[210] R. Leitner. "Recent results of Daya Bay reactor neutrino experiment". In: *Nuclear and Particle Physics Proceedings* 285-286 (2017). Sixth Workshop on Theory, Phenomenology and Experiments in Flavour Physics Interplay of Flavour Physics with Electroweak symmetry breaking, pp. 32 –37. DOI: `https://doi.org/10.1016/j.nuclphysbps.2017.03.007` (see p. 56).

[211] Alex Wex. *Prediction of Low Energy Coherent Neutrino Scattering in the NUCLEUS Cryogenic Detector*. Internal communication to the NUCLEUS collaboration. 2021 (see p. 57).

[212] D. Adey et al. "Improved measurement of the reactor antineutrino flux at Daya Bay". In: *Phys. Rev. D* 100 (5 2019), p. 052004. DOI: `10.1103/PhysRevD.100.052004` (see pp. 57, 58, 161, 163, 212).

[213] C. Giunti et al. "Diagnosing the reactor antineutrino anomaly with global antineutrino flux data". In: *Phys. Rev. D* 99 (7 2019), p. 073005. DOI: `10.1103/PhysRevD.99.073005` (see p. 57).

[214] Mikhail Danilov. "Recent results of the DANSS experiment". In: *arXiv e-prints*, arXiv:1911.10140 (Nov. 2019), arXiv:1911.10140. arXiv: `1911.10140 [hep-ex]` (see p. 58).

[215] M. Andriamirado et al. “Improved Short-Baseline Neutrino Oscillation Search and Energy Spectrum Measurement with the PROSPECT Experiment at HFIR”. In: *arXiv e-prints*, arXiv:2006.11210 (June 2020), arXiv:2006.11210. arXiv: `2006.11210 [hep-ex]` (see pp. 58, 59).

[216] Y. J. Ko et al. “Sterile Neutrino Search at the NEOS Experiment”. In: *Phys. Rev. Lett.* 118 (12 2017), p. 121802. DOI: `10.1103/PhysRevLett.118.121802` (see pp. 58, 60).

[217] Private communication with G. Mention et al. “Reactor antineutrino shoulder explained by energy scale nonlinearities ?” In: *Physics Letters B* 773 (Oct. 2017), pp. 307–312. DOI: `10.1016/j.physletb.2017.08.035`. arXiv: `1705.09434 [hep-ex]` (see p. 59).

[218] Y. Abe et al. “Erratum: Improved measurements of the neutrino mixing angle θ $_{13}$ with the Double Chooz detector (vol 10, 086, 2014)”. In: *Journal of High Energy Physics* 02 (2015), p. 074. DOI: `10.1007/JHEP02(2015)074` (see pp. 58, 60).

[219] J. H. Choi et al. “Observation of Energy and Baseline Dependent Reactor Antineutrino Disappearance in the RENO Experiment”. In: *Phys. Rev. Lett.* 116 (21 2016), p. 211801. DOI: `10.1103/PhysRevLett.116.211801` (see p. 58).

[220] Seon-Hee Seo and. “New Results from RENO using 1500 Days of Data”. In: *Journal of Physics: Conference Series* 1342 (2020), p. 012045. DOI: `10.1088/1742-6596/1342/1/012045` (see p. 58).

[221] A. C. Hayes et al. “Systematic Uncertainties in the Analysis of the Reactor Neutrino Anomaly”. In: *Phys. Rev. Lett.* 112 (20 2014), p. 202501. DOI: `10.1103/PhysRevLett.112.202501` (see pp. 60, 92, 93, 97, 132, 133).

[222] Patrick Huber. “NEOS Data and the Origin of the 5 MeV Bump in the Reactor Antineutrino Spectrum”. In: *Phys. Rev. Lett.* 118 (4 2017), p. 042502. DOI: `10.1103/PhysRevLett.118.042502` (see p. 60).

[223] F. P. An et al. “Evolution of the Reactor Antineutrino Flux and Spectrum at Daya Bay”. In: *Phys. Rev. Lett.* 118 (25 2017), p. 251801. DOI: `10.1103/PhysRevLett.118.251801` (see pp. 60, 61, 163, 212).

[224] G. Bak et al. “Fuel-Composition Dependent Reactor Antineutrino Yield at RENO”. In: *Phys. Rev. Lett.* 122 (23 2019), p. 232501. DOI: `10.1103/PhysRevLett.122.232501` (see pp. 60, 61, 163, 212).

[225] A. C. Hayes et al. “Analysis of the Daya Bay Reactor Antineutrino Flux Changes with Fuel Burnup”. In: *Phys. Rev. Lett.* 120 (2 2018), p. 022503. DOI: `10.1103/PhysRevLett.120.022503` (see pp. 61, 169, 211).

[226] Daniel Z. Freedman. “Coherent effects of a weak neutral current”. In: *Phys. Rev. D* 9 (5 1974), pp. 1389–1392. DOI: `10.1103/PhysRevD.9.1389` (see p. 62).

[227] V. B. Kopeliovich and L. L. Frankfurt. “Isotopic and chiral structure of neutral current”. In: *JETP Lett.* 19 (1974), pp. 145–147 (see p. 62).

[228] Vadim A. Bednyakov and Dmitry V. Naumov. “Coherency and incoherency in neutrino-nucleus elastic and inelastic scattering”. In: *Phys. Rev. D* 98 (5 2018), p. 053004. DOI: `10.1103/PhysRevD.98.053004` (see p. 62).

[229] J. Barranco, O.G. Miranda, and T.I. Rashba. “Probing new physics with coherent neutrino scattering off nuclei”. In: *JHEP* 12 (2005), p. 021. DOI: `10.1088/1126-6708/2005/12/021`. arXiv: `hep-ph/0508299` (see p. 62).

[230] Manfred Lindner, Werner Rodejohann, and Xun-Jie Xu. “Coherent Neutrino-Nucleus Scattering and new Neutrino Interactions”. In: *Journal of High Energy Physics* 2017 (Dec. 2016). DOI: `10.1007/JHEP03(2017)097` (see p. 62).

[231] Dimitrios K. Papoulias, Theocharis S. Kosmas, and Yoshitaka Kuno. “Recent Probes of Standard and Non-standard Neutrino Physics With Nuclei”. In: *Frontiers in Physics* 7 (2019), p. 191. DOI: `10.3389/fphy.2019.00191` (see p. 62).

[232] J. Engel. “Nuclear form factors for the scattering of weakly interacting massive particles”. In: *Physics Letters B* 264.1 (1991), pp. 114 –119. DOI: `https://doi.org/10.1016/0370-2693(91)90712-Y` (see p. 62).

[233] J. Piekarewicz et al. “Power of two: Assessing the impact of a second measurement of the weak-charge form factor of ^{208}Pb”. In: *Phys. Rev. C* 94 (3 2016), p. 034316. DOI: `10.1103/PhysRevC.94.034316` (see p. 62).

[234] Richard H. Helm. “Inelastic and Elastic Scattering of 187-Mev Electrons from Selected Even-Even Nuclei”. In: *Phys. Rev.* 104 (5 1956), pp. 1466–1475. DOI: `10.1103/PhysRev.104.1466` (see p. 62).

[235] G. Angloher et al. “Exploring CEvNS with NUCLEUS at the Chooz nuclear power plant”. In: *The European Physical Journal C* 79.12 (2019). DOI: `10.1140/epjc/s10052-019-7454-4` (see pp. 64, 65, 67).

[236] P. Vogel and J. Engel. “Neutrino electromagnetic form factors”. In: *Phys. Rev. D* 39 (11 1989), pp. 3378–3383. DOI: `10.1103/PhysRevD.39.3378` (see p. 64).

[237] T. S. Kosmas et al. “Probing light sterile neutrino signatures at reactor and Spallation Neutron Source neutrino experiments”. In: *Phys. Rev. D* 96 (6 2017), p. 063013. DOI: `10.1103/PhysRevD.96.063013` (see p. 64).

[238] D. Akimov et al. “Observation of coherent elastic neutrino-nucleus scattering”. In: *Science* 357.6356 (2017), pp. 1123–1126. DOI: `10.1126/science.aao0990`. eprint: `https://science.sciencemag.org/content/357/6356/1123.full.pdf` (see p. 64).

[239] COHERENT Collaboration et al. “First Detection of Coherent Elastic Neutrino-Nucleus Scattering on Argon”. In: *arXiv e-prints*, arXiv:2003.10630 (Mar. 2020), arXiv:2003.10630. arXiv: `2003.10630 [nucl-ex]` (see p. 64).

[240] R. Strauss et al. “The ν -cleus experiment: a gram-scale fiducial-volume cryogenic detector for the first detection of coherent neutrino-nucleus scattering”. In: *European Physical Journal C* 77.8, 506 (Aug. 2017), p. 506. DOI: `10.1140/epjc/s10052-017-5068-2`. arXiv: `1704.04320 [physics.ins-det]` (see p. 65).

[241] R. Strauss et al. “Gram-scale cryogenic calorimeters for rare-event searches”. In: *Phys. Rev. D* 96 (2 2017), p. 022009. DOI: `10.1103/PhysRevD.96.022009` (see p. 65).

[242] Bhaskar Dutta et al. “Sensitivity to oscillation with a sterile fourth generation neutrino from ultralow threshold neutrino-nucleus coherent scattering”. In: *Phys. Rev. D* 94 (9 2016), p. 093002. DOI: `10.1103/PhysRevD.94.093002` (see p. 66).

[243] H. Bonet et al. “First constraints on elastic neutrino nucleus scattering in the fully coherent regime from the Conus experiment”. In: *arXiv e-prints*, arXiv:2011.00210 (Oct. 2020), arXiv:2011.00210. arXiv: `2011.00210 [hep-ex]` (see p. 66).

[244] V. Belov et al. “The νGeN experiment at the Kalinin Nuclear Power Plant”. In: *Journal of Instrumentation* 10.12 (2015), P12011–P12011. DOI: `10.1088/1748-0221/10/12/p12011` (see pp. 66, 67).

[245] A.G. Beda et al. “Gemma experiment: The results of neutrino magnetic moment search”. In: *Phys. Part. Nucl. Lett.* 10 (2013), pp. 139–143. DOI: `10.1134/S1547477113020027` (see p. 66).

[246] S. Kerman et al. “Coherency in neutrino-nucleus elastic scattering”. In: *Phys. Rev. D* 93 (11 2016), p. 113006. DOI: `10.1103/PhysRevD.93.113006` (see p. 66).

[247] Lakhwinder Singh and H.T. Wong. "Studies of neutrino interactions at the Kuo-Sheng Neutrino Laboratory with sub-keV Ge-detectors". In: *Journal of Physics: Conference Series* 1342 (2020), p. 012078. DOI: `10.1088/1742-6596/1342/1/012078` (see pp. 66, 67).

[248] Alexis Aguilar-Arevalo et al. "Exploring low-energy neutrino physics with the Coherent Neutrino Nucleus Interaction Experiment". In: *Phys. Rev. D* 100 (9 2019), p. 092005. DOI: `10.1103/PhysRevD.100.092005` (see p. 67).

[249] A. Aguilar-Arevalo et al. "Results of the engineering run of the Coherent Neutrino Nucleus Interaction Experiment (CONNIE)". In: *Journal of Instrumentation* 11.07 (2016), P07024–P07024. DOI: `10.1088/1748-0221/11/07/p07024` (see p. 67).

[250] J. J. Choi et al. "Improving the light collection using a new NaI(Tl) crystal encapsulation". In: *Nuclear Instruments and Methods in Physics Research A* 981, 164556 (Nov. 2020), p. 164556. DOI: `10.1016/j.nima.2020.164556`. arXiv: `2006.02573 [physics.ins-det]` (see p. 67).

[251] D.Y. Akimov et al. "First ground-level laboratory test of the two-phase xenon emission detector RED-100". In: *Journal of Instrumentation* 15.02 (2020), P02020–P02020. DOI: `10.1088/1748-0221/15/02/p02020` (see p. 67).

[252] B A Dolgoshein, V N Lebedenko, and B U Rodionov. "NEW METHOD OF REGISTRATION OF IONIZING-PARTICLE TRACKS IN CONDENSED MATTER." In: *JETP Lett. (USSR) (Engl. Transl.) 11: 351-3 (5 Jun 1970).* (Jan. 1970) (see p. 67).

[253] J Billard et al. "Coherent neutrino scattering with low temperature bolometers at Chooz reactor complex". In: *Journal of Physics G: Nuclear and Particle Physics* 44.10 (2017), p. 105101. DOI: `10.1088/1361-6471/aa83d0` (see p. 67).

[254] C Buck et al. "A novel experiment for coherent elastic neutrino nucleus scattering: CONUS". In: *Journal of Physics: Conference Series* 1342 (2020), p. 012094. DOI: `10.1088/1742-6596/1342/1/012094` (see p. 67).

[255] D Yu Akimov et al. "RED-100 detector for the first observation of the elastic coherent neutrino scattering off xenon nuclei". In: *Journal of Physics: Conference Series* 675.1 (2016), p. 012016. DOI: `10.1088/1742-6596/675/1/012016` (see p. 67).

[256] Rene Brun and Fons Rademakers. "ROOT - An Object Oriented Data Analysis Framework". In: *Phys. Res. A* 389 (1997), pp. 81–86 (see pp. 70, 207).

[257] G. Gamow and E. Teller. "Selection Rules for the β-Disintegration". In: *Phys. Rev.* 49 (12 1936), pp. 895–899. DOI: `10.1103/PhysRev.49.895` (see pp. 70, 72).

[258] G. Gamow and E. Teller. "Some Generalizations of the β Transformation Theory". In: *Phys. Rev.* 51 (4 1937), pp. 289–289. DOI: `10.1103/PhysRev.51.289` (see p. 70).

[259] R. P. Feynman and M. Gell-Mann. "Theory of the Fermi Interaction". In: *Phys. Rev.* 109 (1 1958), pp. 193–198. DOI: `10.1103/PhysRev.109.193` (see p. 70).

[260] Sheldon L. Glashow. "Partial-symmetries of weak interactions". In: *Nuclear Physics* 22.4 (1961), pp. 579–588. DOI: `https://doi.org/10.1016/0029-5582(61)90469-2` (see p. 70).

[261] Steven Weinberg. "A Model of Leptons". In: *Phys. Rev. Lett.* 19 (21 1967), pp. 1264–1266. DOI: `10.1103/PhysRevLett.19.1264` (see p. 70).

[262] Abdus Salam. "Weak and electromagnetic interactions". In: (1968), pp. 244–254. DOI: `10.1142/9789812795915_0034`. eprint: `https://www.worldscientific.com/doi/pdf/10.1142/9789812795915_0034` (see p. 70).

[263] W. Bühring H. Behrens. *Electron radial wave functions and nuclear beta-decay.* Clarendon press. Oxford, 1982 (see pp. 70–74, 76, 77, 85, 88, 89, 94, 96, 97, 120, 174, 207).

[264] M. Thomson. *Modern Particle Physics.* Cambridge University press, 2013 (see p. 72).

[265] Geoffrey F. Chew. “The Inelastic Scattering of High Energy Neutrons by Deuterons According to the Impulse Approximation”. In: *Phys. Rev.* 80 (2 1950), pp. 196–202. DOI: `10.1103/PhysRev.80.196` (see p. 73).

[266] Walter E. Meyerhof. *Elements of Nuclear Phsycis.* McGraw-Hill, Inc, 1967 (see p. 74).

[267] Lloyd Armstrong and C. W. Kim. “Comparison of Impulse-Approximation and Elementary-Particle Treatments in Nuclear β Decay”. In: *Phys. Rev. C* 6 (6 1972), pp. 1924–1934. DOI: `10.1103/PhysRevC.6.1924` (see p. 74).

[268] L. Armstrong and C.W. Kim. “Limitation on the use of impulse approximation in nuclear -decay”. In: *Physics Letters B* 41.1 (1972), pp. 39–42. DOI: `https://doi.org/10.1016/0370-2693(72)90362-0` (see p. 74).

[269] H. Behrens, J. Jänecke (auth.), and H. Schopper (eds.) *Numerical Tables for Beta-Decay and Electron Capture.* 1st ed. Landolt-Börnstein - Group I Elementary Particles, Nuclei and Atoms 4 : Elementary Particles, Nuclei and Atoms. Springer-Verlag Berlin Heidelberg, 1969 (see pp. 76–78, 97, 175).

[270] I Angeli. *Table of nuclear root mean square charge radii (INDC(HUN)–033).* International Atomic Energy Agency (IAEA), 1999 (see pp. 77–79, 97).

[271] D.H. Wilkinson. “Evaluation of beta-decay: II. Finite mass and size effects”. In: *Nuclear Instruments and Methods in Physics Research Section A: Accelerators, Spectrometers, Detectors and Associated Equipment* 290.2 (1990), pp. 509 –515. DOI: `https://doi.org/10.1016/0168-9002(90)90570-V` (see pp. 77, 96, 97).

[272] L. R. B. Elton. “A semi-empirical formula for the nuclear radius”. In: 5 (Mar. 1958), pp. 173–178. DOI: `10.1016/0029-5582(58)90016-6` (see pp. 77, 97).

[273] István Angeli and Krassimira Marinova. “Table of experimental nuclear ground state charge radii: An update”. In: *Atomic Data and Nuclear Data Tables* 99 (Jan. 2013), pp. 69–95. DOI: `10.1016/j.adt.2011.12.006` (see pp. 77, 97).

[274] I.S. Towner, J.C. Hardy, and M. Harvey. “Analogue symmetry breaking in superallowed fermi -decay”. In: *Nuclear Physics A* 284.2 (1977), pp. 269 –281. DOI: `https://doi.org/10.1016/0375-9474(77)90123-3` (see p. 78).

[275] E. J. Konopinski. *The theory of beta radioactivity.* Clarendon press. Oxford, 1966 (see pp. 79, 83).

[276] F. Salvat et al. “Analytical Dirac-Hartree-Fock-Slater screening function for atoms (Z=1–92)”. In: *Phys. Rev. A* 36 (2 1987), pp. 467–474. DOI: `10.1103/PhysRevA.36.467` (see pp. 82, 83, 85, 97).

[277] X. Mougeot and C. Bisch. “Consistent calculation of the screening and exchange effects in allowed β^- transitions”. In: *Phys. Rev. A* 90 (1 2014), p. 012501. DOI: `10.1103/PhysRevA.90.012501` (see pp. 82, 83, 85, 175).

[278] L. Hayen et al. “High precision analytical description of the allowed beta spectrum shape”. In: *Reviews of Modern Physics* 90.1, 015008 (Jan. 2018), p. 015008. DOI: `10.1103/revmodphys.90.015008`. arXiv: `1709.07530 [nucl-th]` (see pp. 82, 85, 92, 95, 100).

[279] Herwig F. Schopper. *Weak Interactions and Nuclear Beta Decay.* Amsterdam, North-Holland Pub. Co., 1966 (see p. 88).

[280] X. Mougeot. "Reliability of usual assumptions in the calculation of beta and nu spectra". In: *Phys. Rev. C* 91 (5 2015), p. 055504. DOI: `10.1103/PhysRevC.91.055504` (see p. 88).

[281] Abdoul-Aziz Zakari. "Étude des propriétés de désintégration bêta de produits de fission d'intérêt pour les spectres en énergie des antineutrinos et la puissance résiduelle des réacteurs nucléaires". Thèse de doctorat dirigée par Haddad, FeridFallot, Muriel et Porta, Amanda Physique nucléaire – Constituants élémentaires et physique théorique Nantes 2015. PhD thesis. 2015, 1 vol. (140 p.) (See pp. 90, 106, 179).

[282] Loïc Le Meur. "Etude des propriétés de désintégration bêta de noyaux exotiques d'intérêts pour la physique des réacteurs, la structure nucléaire et l'astrophysique nucléaire, à l'aide de la technique de Spectroscopie Gamma par Absorption Totale (TAGS)". Thèse de doctorat dirigée par Sami, Taklit et Fallot, Muriel Physique Nantes 2018. PhD thesis. 2018 (see pp. 90, 179, 180).

[283] Víctor Guadilla Gómez. "TAGS measurements for neutrino physics and applications". PhD thesis. U. Valencia (main), 2017 (see pp. 90, 107, 179, 180).

[284] X. Mougeot. "Towards high-precision calculation of electron capture decays". In: *Applied Radiation and Isotopes* 154 (2019), p. 108884. DOI: `https://doi.org/10.1016/j.apradiso.2019.108884` (see pp. 89, 97).

[285] B.A. Brown and W.D.M. Rae. "The Shell-Model Code NuShellX@MSU". In: *Nuclear Data Sheets* 120 (2014), pp. 115–118. DOI: `https://doi.org/10.1016/j.nds.2014.07.022` (see p. 89).

[286] I. S. Towner and J. C. Hardy. "Improved calculation of the isospin-symmetry-breaking corrections to superallowed Fermi β decay". In: *Phys. Rev. C* 77 (2 2008), p. 025501. DOI: `10.1103/PhysRevC.77.025501` (see pp. 89, 97, 98).

[287] A. Sirlin. "Radiative correction to the $\overline{\nu}_e(\nu_e)$ spectrum in β decay". In: *Phys. Rev. D* 84 (1 2011), p. 014021. DOI: `10.1103/PhysRevD.84.014021` (see pp. 89, 95, 97, 132).

[288] A. Sirlin. "General Properties of the Electromagnetic Corrections to the Beta Decay of a Physical Nucleon". In: *Phys. Rev.* 164 (5 1967), pp. 1767–1775. DOI: `10.1103/PhysRev.164.1767` (see pp. 94, 95, 97, 132).

[289] William J. Marciano and Alberto Sirlin. "Improved Calculation of Electroweak Radiative Corrections and the Value of V_{ud}". In: *Phys. Rev. Lett.* 96 (3 2006), p. 032002. DOI: `10.1103/PhysRevLett.96.032002` (see p. 94).

[290] Chien-Yeah Seng et al. "Reduced Hadronic Uncertainty in the Determination of V_{ud}". In: *Phys. Rev. Lett.* 121 (24 2018), p. 241804. DOI: `10.1103/PhysRevLett.121.241804` (see p. 94).

[291] Alberto Sirlin and Andrea Ferroglia. "Radiative corrections in precision electroweak physics: A historical perspective". In: *Rev. Mod. Phys.* 85 (1 2013), pp. 263–297. DOI: `10.1103/RevModPhys.85.263` (see p. 95).

[292] Mougeot, Xavier. "BetaShape: A new code for improved analytical calculations of beta spectra". In: *EPJ Web Conf.* 146 (2017), p. 12015. DOI: `10.1051/epjconf/201714612015` (see p. 97).

[293] Wolfgang Bühring. "The screening correction to the Fermi function of nuclear beta-decay and its model dependence". In: *Nuclear Physics A* 430.1 (1984), pp. 1 –20. DOI: `https://doi.org/10.1016/0375-9474(84)90190-8` (see p. 97).

[294] L. R. B. Elton. *Nuclear sizes.* 1961 (see p. 97).

[295] Rikard Lundmark, Carl Toft, and Philippe Klintefelt Collet. Version of ENSDF++ available at. URL: `https://github.com/gsize/ENSDFpp` (see p. 102).

[296] Meng Wang et al. "The AME 2020 atomic mass evaluation (II). Tables, graphs and references∗". In: *Chinese Physics C* 45.3 (2021), p. 030003. DOI: `10.1088/1674-1137/abddaf` (see pp. 105, 111, 194, 196, 198, 200, 202).

[297] W.J. Huang et al. "The AME 2020 atomic mass evaluation (I). Evaluation of input data, and adjustment procedures∗". In: *Chinese Physics C* 45.3 (2021), p. 030002. DOI: `10.1088/1674-1137/abddb0` (see p. 105).

[298] (See p. 106).

[299] A.-A. Zakari-Issoufou et al. "Total Absorption Spectroscopy Study of ^{92}Rb Decay: A Major Contributor to Reactor Antineutrino Spectrum Shape". In: *Phys. Rev. Lett.* 115 (10 2015), p. 102503. DOI: `10.1103/PhysRevLett.115.102503` (see p. 106).

[300] A.L. Nichols and Paraskevi Dimitriou. "Total Absorption Gamma-ray Spectroscopy for Decay Heat Calculations and Other Applications Summary Report of Consultants' Meeting". In: vol. INDC(NDS) - 0676. International Atomic Energy Agency, 2015, p. 36. DOI: `https://www-nds.iaea.org/publications/indc/indc-nds-0676.pdf` (see pp. 106, 109, 178).

[301] R.C. Greenwood et al. "Total absorption gamma-ray spectrometer for measurement of beta-decay intensity distributions for fission product radionuclides". In: *Nuclear Instruments and Methods in Physics Research Section A: Accelerators, Spectrometers, Detectors and Associated Equipment* 314.3 (1992), pp. 514 –540. DOI: `https://doi.org/10.1016/0168-9002(92)90243-W` (see p. 107).

[302] R.C. Greenwood et al. "Measurement of —-decay intensity distributions of several fission-product isotopes using a total absorption -ray spectrometer". In: *Nuclear Instruments and Methods in Physics Research Section A: Accelerators, Spectrometers, Detectors and Associated Equipment* 390.1 (1997), pp. 95 –154. DOI: `https://doi.org/10.1016/S0168-9002(97)00356-2` (see pp. 107, 108, 124, 179–181).

[303] Meng Wang et al. "The AME2016 atomic mass evaluation (II). Tables, graphs and references". In: *Chinese Physics C* 41.3 (2017), p. 030003. DOI: `10.1088/1674-1137/41/3/030003` (see p. 108).

[304] G. Audi et al. "The NUBASE2016 evaluation of nuclear properties". In: *Chinese Physics C* 41.3 (2017), p. 030001. DOI: `10.1088/1674-1137/41/3/030001` (see p. 108).

[305] A.L. Nichols. "Total absorption gamma-ray spectroscopy (TAGS): Current status of measurement programmes for decay heat calculations and other applications Summary report of consultants' meeting". In: vol. INDC(NDS) - 0551. International Atomic Energy Agency, 2009, p. 26. DOI: `http://www-nds.iaea.org/reports-new/indc-reports/indc-nds/indc-nds-0551.pdf` (see pp. 109, 178).

[306] O. Tengblad et al. "Integral -spectra derived from experimental -spectra of individual fission products". In: *Nuclear Physics A* 503.1 (1989), pp. 136 –160. DOI: `https://doi.org/10.1016/0375-9474(89)90258-3` (see p. 110).

[307] G. Rudstam et al. "Beta and gama spectra of short-lived fission products". In: *Atomic Data and Nuclear Data Tables* 45.2 (1990), pp. 239 –320. DOI: `https://doi.org/10.1016/0092-640X(90)90009-9` (see pp. 110, 181).

[308] Thomas Mueller. "Expérience double Chooz : simulation des spectres antineutrinos issus de réacteurs". Thèse de doctorat dirigée par Lhuillier, David Physique. Physique des neutrinos Paris 11 2010. PhD thesis. 2010, 1 vol. (VIII–183 p.) (See pp. 111, 112).

[309] Kohji Takahashi and Masami Yamada. “Gross Theory of Nuclear -Decay”. In: *Progress of Theoretical Physics* 41.6 (June 1969), pp. 1470–1503. DOI: `10.1143/PTP.41.1470`. eprint: `https://academic.oup.com/ptp/article-pdf/41/6/1470/5406988/41-6-1470.pdf` (see p. 111).

[310] Kohji Takahashi. “Gross Theory of First Forbidden -Decay”. In: *Progress of Theoretical Physics* 45.5 (May 1971), pp. 1466–1492. DOI: `10.1143/PTP.45.1466`. eprint: `https://academic.oup.com/ptp/article-pdf/45/5/1466/5397305/45-5-1466.pdf` (see p. 111).

[311] Nicholas J. Terranova. “Covariance Evaluation for Nuclear Data of Interest to the Reactivity Loss Estimation of the Jules Horowitz Material Testing Reactor”. PhD thesis. 2016 (see pp. 113, 167).

[312] N. Terranova et al. “Fission Product Yields Covariance Generation Methodologies and Uncertainty Propagation Using the URANIE Platform”. In: (May 2016) (see pp. 113, 167).

[313] Nicholas Terranova et al. “Covariance generation and uncertainty propagation for thermal and fast neutron induced fission yields”. In: *EPJ Web of Conferences* 146 (Jan. 2017), p. 02013. DOI: `10.1051/epjconf/201714602013` (see pp. 113, 167).

[314] N. Terranova et al. “Fission yield covariance matrices for the main neutron-induced fissioning systems contained in the JEFF-3.1.1 library”. In: *Annals of Nuclear Energy* 109 (2017), pp. 469 –489. DOI: `https://doi.org/10.1016/j.anucene.2017.05.052` (see pp. 113, 167).

[315] L. Fiorito et al. “Fission yield covariance generation and uncertainty propagation through fission pulse decay heat calculation”. In: *Annals of Nuclear Energy* 69 (2014), pp. 331 –343. DOI: `https://doi.org/10.1016/j.anucene.2014.01.038` (see pp. 113, 167).

[316] L. Fiorito et al. “Generation of fission yield covariances to correct discrepancies in the nuclear data libraries”. In: *Annals of Nuclear Energy* 88 (2016), pp. 12 –23. DOI: `https://doi.org/10.1016/j.anucene.2015.10.027` (see pp. 113, 167).

[317] Daniel Lewandowski, Dorota Kurowicka, and Harry Joe. “Generating random correlation matrices based on vines and extended onion method”. In: *Journal of Multivariate Analysis* 100.9 (2009), pp. 1989 –2001. DOI: `https://doi.org/10.1016/j.jmva.2009.04.008` (see p. 124).

[318] Z Djurcic et al. “Uncertainties in the anti-neutrino production at nuclear reactors”. In: *Journal of Physics G: Nuclear and Particle Physics* 36.4 (2009), p. 045002. DOI: `10.1088/0954-3899/36/4/045002` (see p. 141).

[319] A. Onillon. “Reactor and Antineutrino Spectrum Calculations for the Double Chooz First Phase Results”. In: *Nuclear Data Sheets* 120 (2014), pp. 153 –156. DOI: `https://doi.org/10.1016/j.nds.2014.07.032` (see p. 141).

[320] Y. Abe et al. “Reactor $\overline{\nu}_e$ disappearance in the Double Chooz experiment”. In: *Phys. Rev. D* 86 (5 2012), p. 052008. DOI: `10.1103/PhysRevD.86.052008` (see p. 141).

[321] C.J. Werner and et al. *MCNP6.2 Release Notes*. 2018. URL: `https://mcnp.lanl.gov/` (see pp. 148, 162).

[322] C.J. Werner (editor). *MCNP Users Manual - Code Version 6.2*. 2017. URL: `https://mcnp.lanl.gov/` (see pp. 148, 162).

[323] Private communication with Alain Letourneau. 2021 (see pp. 148, 154, 162).

[324] *Program Package NEA-1845 MURE*. 2011. URL: `http://www.nea.fr/tools/abstract/detail/nea-1845` (see p. 157).

[325] Z. Atif et al. “Measurement of Reactor Antineutrino Flux and Spectrum at RENO”. In: *arXiv e-prints*, arXiv:2010.14989 (Oct. 2020), arXiv:2010.14989. arXiv: 2010.14989 [hep-ex] (see pp. 161, 163, 212).

[326] F.P. An et al. “A side-by-side comparison of Daya Bay antineutrino detectors”. In: *Nuclear Instruments and Methods in Physics Research Section A: Accelerators, Spectrometers, Detectors and Associated Equipment* 685 (2012), pp. 78 –97. DOI: https://doi.org/10.1016/j.nima.2012.05.030 (see p. 161).

[327] The Double Chooz Collaboration. “Double Chooz 13 measurement via total neutron capture detection”. In: *Nature Physics* 16.5 (2020), pp. 558–564. DOI: 10.1038/s41567-020-0831-y (see pp. 163, 212).

[328] A. A. Sonzogni et al. “Effects of Fission Yield Data in the Calculation of Antineutrino Spectra for ^{235}U(n, fission) at Thermal and Fast Neutron Energies”. In: *Phys. Rev. Lett.* 116 (13 2016), p. 132502. DOI: 10.1103/PhysRevLett.116.132502 (see p. 167).

[329] Wolfgang Bühring. “Beta decay theory using exact electron radial wave functions: (III). The influence of screening”. In: *Nuclear Physics* 61sch.1 (1965), pp. 110 –128. DOI: https://doi.org/10.1016/0029-5582(65)90939-9 (see p. 175).

[330] A. C. Dombos et al. “Total absorption spectroscopy of the β decay of ^{76}Ga”. In: *Phys. Rev. C* 93 (6 2016), p. 064317. DOI: 10.1103/PhysRevC.93.064317 (see p. 178).

[331] K. Goetz. “Total Absorption Spectroscopy of Neutron Rich Nuclei Across the N=50 Neutron Shell Closure”. PhD thesis. 2017 (see p. 178).

[332] S. Rice et al. “Total absorption spectroscopy study of the β decay of ^{86}Br and ^{91}Rb”. In: *Phys. Rev. C* 96 (1 2017), p. 014320. DOI: 10.1103/PhysRevC.96.014320 (see pp. 178, 179).

[333] A. Fijałkowska et al. “Impact of Modular Total Absorption Spectrometer measurements of β decay of fission products on the decay heat and reactor $\overline{\nu}_e$ flux calculation”. In: *Phys. Rev. Lett.* 119 (5 2017), p. 052503. DOI: 10.1103/PhysRevLett.119.052503 (see pp. 178–180).

[334] E. Valencia et al. “Total absorption γ-ray spectroscopy of the β-delayed neutron emitters ^{87}Br, ^{88}Br, and ^{94}Rb”. In: *Phys. Rev. C* 95 (2 2017), p. 024320. DOI: 10.1103/PhysRevC.95.024320 (see pp. 178, 179).

[335] K. Miernik et al. “β-decay study of ^{94}Kr”. In: *Phys. Rev. C* 94 (2 2016), p. 024305. DOI: 10.1103/PhysRevC.94.024305 (see p. 179).

[336] S. Rice. “Decay Heat Measurements of FissionFragments 86Br,91Rb & 94Sr Using Total Absorption Gamma-ray Spectroscopy”. PhD thesis. 2014 (see p. 179).

[337] B. C. Rasco et al. “Decays of the Three Top Contributors to the Reactor $\overline{\nu}_e$ High-Energy Spectrum, ^{92}Rb, ^{96gs}Y, and ^{142}Cs, Studied with Total Absorption Spectroscopy”. In: *Phys. Rev. Lett.* 117 (9 2016), p. 092501. DOI: 10.1103/PhysRevLett.117.092501 (see pp. 179, 180).

[338] V. Guadilla et al. “Total absorption γ-ray spectroscopy of the β-delayed neutron emitters ^{137}I and ^{95}Rb”. In: *Phys. Rev. C* 100 (4 2019), p. 044305. DOI: 10.1103/PhysRevC.100.044305 (see pp. 179, 180).

[339] V. Guadilla et al. “Total absorption γ-ray spectroscopy of niobium isomers”. In: *Phys. Rev. C* 100 (2 2019), p. 024311. DOI: 10.1103/PhysRevC.100.024311 (see p. 179).

[340] A. Algora et al. “Reactor Decay Heat in ^{239}Pu: Solving the γ Discrepancy in the 4–3000-s Cooling Period”. In: *Phys. Rev. Lett.* 105 (20 2010), p. 202501. DOI: 10.1103/PhysRevLett.105.202501 (see p. 179).

[341] M. Dolores Jordán Martín. “Beta-decay total absorption spectroscopy measurements for reactor decay heat calculations”. PhD thesis. 2010 (see p. 179).

[342] V. Guadilla et al. “Experimental study of ^{100}Tc β decay with total absorption γ-ray spectroscopy”. In: *Phys. Rev. C* 96 (2017), p. 014319. DOI: `10.1103/PhysRevC.96.014319` (see p. 179).

[343] D. Jordan et al. “Total absorption study of the β decay of ^{102,104,105}Tc”. In: *Phys. Rev. C* 87 (4 2013), p. 044318. DOI: `10.1103/PhysRevC.87.044318` (see p. 179).

[344] B. C. Rasco et al. “Complete β-decay pattern for the high-priority decay-heat isotopes ^{137}I and ^{137}**Xe** determined using total absorption spectroscopy”. In: *Phys. Rev. C* 95 (5 2017), p. 054328. DOI: `10.1103/PhysRevC.95.054328` (see p. 180).

[345] Marzena Wolińska-Cichocka et al. “Beta-strength and anti-neutrino spectra from total absorption spectroscopy of a decay chain ^{142}Cs→^{142}Ba→^{142}La”. In: *European Physical Journal Web of Conferences*. Vol. 146. European Physical Journal Web of Conferences. Sept. 2017, 10005, p. 10005. DOI: `10.1051/epjconf/201714610005` (see p. 180).

[346] M. Wolińska-Cichocka et al. “Modular Total Absorption Spectrometer at the HRIBF (ORNL, Oak Ridge)”. In: *Nuclear Data Sheets* 120 (2014), pp. 22 –25. DOI: `https://doi.org/10.1016/j.nds.2014.06.131` (see p. 180).

[347] A. M. Mathai. “Jacobians of matrix transformations and functions of matrix argument”. In: 1997 (see p. 182).

[348] Nick Thomopoulos. *Essentials of Monte Carlo simulation: Statistical methods for building simulation models*. Nov. 2013, pp. 1–171. DOI: `10.1007/978-1-4614-6022-0` (see p. 183).

universite
PARIS-SACLAY

ÉCOLE DOCTORALE
Particules, hadrons, énergie et noyau : instrumentation, imagerie, cosmos et simulation (PHENIICS)

Titre: Modélisation de spectres antineutrino de réacteur.

Mots clés: neutrino, réacteur, particule, modélisation, calcul numérique, désintégration β.

Résumé: Au cours des dernières décennies, les expériences visant à mesurer des antineutrinos menées à courtes et longues distances de réacteurs nucléaires et utilisant des détecteurs basées sur la désintégration β inverse (IBD) ont révélé un déficit systématique et significatif d'antineutrinos détectés par rapport aux flux prédits. Outre cet écart de flux, appelé anomalie des antineutrinos de réacteur (RAA), une différence dans la forme des spectres mesurés par rapport aux prédictions reflétant l'état de l'art a été observée. Aucune preuve d'un biais expérimental n'a été mis en évidence comme étant à l'origine de ces divergences, et l'interprétation de la RAA comme une nouvelle oscillation de neutrino avec un état stérile est pour l'instant défavorisée par de récentes expériences placées à courtes lignes de vol d'un réacteur. La validité des prédictions est aussi remise en question comme source des divergences observées, ce qui a motivé une révision des modèles de spectres d'antineutrino de réacteur. Dans ce contexte, une nouvelle prédiction a été développée et est présentée dans cette thèse de doctorat. Les antineutrinos de réacteur sont émis lors de la désintégration β^- des produits issus de la fission du combustible nucléaire (^{235}U, ^{238}U, ^{239}Pu, ^{241}Pu). Lors d'une telle transition, un noyau excité éjecte en corrélation un électron et un antineutrino. La probabilité d'émission totale et les spectres en énergie associés à chacune de ces deux particules sont caractéristiques du noyau initial et du noyau final, et dépendent de leurs structures nucléaire et atomique. Le spectre antineutrino émis par un cœur de réacteur résulte ainsi de la superposition de milliers de spectres β. La prédiction revisitée est basée sur la méthode par sommation qui consiste à modéliser chacune de ces transitions β. Une modélisation avancée de la théorie de la désintégration β a été utilisée pour inclure différents effets dus à l'interaction électromagnétique entre l'électron émis et le noyau fils par un traitement numérique. Les données nucléaires experimentales les plus récentes sont utilisées pour modéliser les milliers de désintégrations contribuant au spectre antineutrinos d'un réacteur, incluant les mesures de spectroscopie d'absorption totale γ. Une propagation détaillée des incertitudes associées à la fois à la modélisation et à l'évaluation des données nucléaires a également été effectuée, permettant de générer un budget d'incertitude cohérent et conservatif pour les spectres ainsi modélisés. La nouvelle modélisation par sommation est finalement comparée à l'état de l'art des prédictions de spectre de réacteur, et ses améliorations et limitations sont discutées en considérant des jeux de données IBD collectées par de récentes expériences réacteurs à courtes et longues lignes de vol.

universite
PARIS-SACLAY

ÉCOLE DOCTORALE
Particules, hadrons, énergie et noyau :
instrumentation, imagerie, cosmos
et simulation (PHENIICS)

Title: Modeling of reactor antineutrino spectra.

Keywords: neutrino, reactor, particle, modeling, numerical computation, β-decay.

Abstract: Over the last decades, antineutrino experiments conducted at short and long baselines from nuclear reactors and using detection techniques based on the inverse β-decay (IBD) have revealed a systematic and significant deficit of detected antineutrinos compared to the predicted fluxes. Besides this flux discrepancy, called the reactor antineutrino anomaly, a difference in the shape of the measured spectra compared to state-of-the-art predictions has been observed. No evidence for an experimental bias has so far been detected as the origin of these discrepancies, and the interpretation of the reactor antineutrino anomaly as a neutrino oscillation with a sterile neutrino state is currently disfavored by recent very short baseline reactor experiments. The validity of the predictions is also questioned as the source of the observed discrepancies, and has motivated a revision of the modelings of reactor antineutrino spectra. In this context, a revisited prediction has been developed and is presented in this PhD dissertation. In a nuclear reactor, antineutrinos are typically emitted during the β-decays of the products originating from the fission of four actinides making up more than 99% of the thermal power released in the core (^{235}U, ^{238}U, ^{239}Pu, ^{241}Pu). During a β-decay, an excited nucleus ejects in correlation an electron and an antineutrino. The total emission probability and the energy spectra associated to each of these two particles are characteristic of the parent and daughter nuclei, and depend on their nuclear and atomic structures. The antineutrino spectrum emitted by a reactor core then results from the superposition of thousands of β spectra. The revised prediction is based on the summation method which consists in modeling each of these β transitions. An advanced modeling of the β-decay theory has been used to include various effects due to the Coulomb interaction between the emitted electron and the daughter nucleus through a numerical treatment. The latest evaluated nuclear data are used to model the thousands β-decays contributing to a reactor antineutrino spectrum, including the most recent data from total absorption γ spectroscopy measurements. A thorough propagation of the uncertainties associated to both the modeling and the nuclear data evaluation has also been investigated, allowing to produce a consistent and conservative uncertainty budget for the revisited spectra. The new summation modeling is finally compared with other state-of-the-art predictions, and its improvements and limitations are discussed in regards to IBD datasets from recent short and long baseline reactor experiments.